

UNIVERSITÉ DE STRASBOURG

HABILITATION À DIRIGER DES RECHERCHES

Spécialité : Géophysique interne

Présentée par
Zacharie DUPUTEL

Institut Terre et Environnement de Strasbourg
École et Observatoire des Sciences de la Terre

**Caractérisation de la source sismique :
de la microseismicité volcanique aux mégaséismes de subduction**

Soutenue publiquement le 12 février 2021 à 14h.

Composition du Jury :

Pascal BERNARD.	Physicien, IPGP, Paris	Rapporteur
Alessia MAGGI	Professeur, IPGS, Strasbourg	Rapportrice
Martin VALLÉE	Physicien adjoint, IPGP, Paris.	Rapporteur
Françoise COURBOULEX	Directrice de Recherche, Géoazur, Nice	Examinateuse
Luis RIVERA	Professeur, IPGS, Strasbourg	Examinateur

Remerciements

Nous avons une responsabilité limitée dans les résultats que nous obtenons. Nos réussites sont en effet le reflet des rencontres qui ont influencé nos vies et des opportunités qui se sont présentées. Je souhaite donc ici remercier les nombreuses personnes qui ont rendu possible cette habilitation.

Je suis reconnaissant au jury d'avoir évalué mon travail dans un contexte particulier. Merci donc à Pascal Bernard, Françoise Courboulex et Martin Vallée pour leurs retours et la discussion qui a suivi. Je remercie également Alessia Maggi d'avoir accepté d'être à la fois rapportrice et présidente du jury.

Je suis particulièrement reconnaissant à Luis Rivera d'avoir largement façonné la manière dont mon travail de recherche se déroule aujourd'hui. Au delà de tout ce que tu m'as transmis, tu as été un soutien essentiel dans mon parcours. Merci également à Valérie Ferrazzini qui m'a mis le pied à l'étrier et m'a convaincu de poursuivre en doctorat. Les mois passés à l'observatoire m'ont donné la motivation nécessaire pour arriver jusqu'ici.

Merci à Hiroo Kanamori, Mark Simons, Pablo Ampuero et Victor Tsai pour leur enthousiasme indéfectible et communicatif lors de mon post-doctorat à Caltech. Merci à Olivier Lençliné, Romain Jolivet, Piyush Agram et aux collègues de Strasbourg pour leur sympathie. Nos discussions m'ont souvent aiguillé et ont parfois réorienté mon regard.

Je remercie les doctorants et post-doctorants avec qui j'ai eu le plaisir de travailler ces dernières années : Emmanuel Caballero, Agnès Chouinet, Baptiste Gombert, Emilie Klein, Catalina Morales, Luc Moutote et Cédric Twardzik. Ils ont largement contribué aux résultats présentés dans ce mémoire.

Du fond de mon cœur, je remercie mes parents pour leurs encouragements et pour m'avoir transmis leur soif d'apprendre. Je suis reconnaissant pour toujours du soutien que vous m'avez apporté. Je regrette de ne pas toujours pouvoir en apporter autant en retour.

Je veux enfin remercier Indrah pour son amour constant qui a transformé ma vie. Je suis désolé de t'avoir embarqué dans ce délicat jeu d'équilibre entre vie académique et vie privée. Je te remercie infiniment de m'avoir offert les deux amours de ma vie, Anjali et Aditya. Je savoure tous les moments passés avec vous trois.

कर्मण्येवाधिकारस्ते मा फलेषु कदाचन ।
मा कर्मफलहेतुभूर्मा ते सङ्गोऽस्त्वकर्मणि ॥

Ton choix est dans l'action et jamais dans ses résultats.
Ne te prends pas pour l'auteur des résultats de l'action.
Ne t'abandonne pas non plus à l'inaction.

— श्रीमद् भगवद् गीता ॥ २,४७ ॥

Sommaire

Introduction	1
1 Données et méthodes	3
1.1 Les observations de surface	4
1.1.1 Données sismologiques	5
1.1.2 Données GNSS : de la géodésie à la sismo-géodésie	8
1.1.3 Imagerie satellite et aérienne	10
1.1.4 Données tsunami	11
1.2 Le problème direct	12
1.2.1 Représentation en point source	13
1.2.2 Représentation en source étendue	14
1.2.2.1 Cas statique : modélisation de données géodésiques	15
1.2.2.2 Cas cinématique : Approche linéaire en fenêtres multiples	16
1.2.2.3 Cas cinématique : Approche non-linéaire	17
1.2.3 Calcul des fonctions de Green	19
1.3 Le problème inverse	20
1.3.1 Approche par régularisation de Tikhonov	22
1.3.2 Approche Bayésienne	23
1.3.3 Modélisation de données dans le domaine fréquentiel ou en ondelettes	26
1.4 Modèles de glissement : implications sur la physique des séismes	27
2 Détermination des caractéristiques principales de la rupture sismique	33
2.1 Caractérisation de la source à longue période : alerte rapide et complexité de la rupture.	33
2.2 Utilisation du délai barycentrique pour identifier des séismes atypiques	34
2.3 Impact des hétérogénéités structurales 3D sur les solutions phase W	44
2.4 Le séisme de Gorkha en 2015	59
2.5 Analyse longue-période du séisme de Kaikoura en Novembre 2016	69
2.6 Conclusion et perspectives : prise en compte de la structure 3D et extension aux plus faibles magnitudes	75
3 Caractérisation détaillée du glissement sur les failles à partir de données multiples	77
3.1 Prise en compte de l'incertitude associée au problème direct	78
3.2 Modélisation bayésienne du séisme d'Iquique en 2014 ($M_W = 8.1$)	98
3.3 Exploration bayésienne du glissement et de l'endommagement co-sismique lors du séisme Landers en 1992 ($M_W = 7.3$)	108
3.4 Budget de déformation le long de la subduction équatorienne	123

3.5	La source impulsive du séisme d'Ezgeleh en 2017 ($M_W = 7.3$)	136
3.6	Perspectives	147
3.6.1	Détection de séismes lents potentiellement récurrents au Chili	147
3.6.2	Glissement sismique et asismique lors de la préparation de grands séismes.	148
4	Sismicité volcanique	149
4.1	Différences entre sismicité volcanique et sismicité tectonique	149
4.2	Réalimentation profonde du réservoir magmatique superficiel au Piton de la Fournaise	151
4.3	Caractéristiques spatiotemporelles du transport magmatique superficiel au Piton de la Fournaise	161
4.4	Mécanisme à la source de l'effondrement de caldeira en 2007 au Piton de la Fournaise	171
4.5	Perspectives	182
4.5.1	Caractérisation des mécanismes à la source des séismes volcaniques	182
4.5.2	Suivi du transport magmatique à partir de la sismicité	183
4.5.3	Analyse comparative des effondrements de Caldeira basaltiques	184
4.5.4	Sismicité au nord de l'Île de la Réunion : origine tectonique ou processus magmatique ?	184
Bibliographie		203
Annexes		205
A.1	Curriculum Vitae	205
A.2	Activités d'enseignement et d'encadrement	207
A.3	Liste des publications	209
A.4	Participation au montage de projets	214
A.5	Détection de séismes lents profonds dans la région de l'Atacama au Chili	215
A.6	Suivi de la propagation du dike à l'origine de l'éruption de mai 2018 au Kīlauea .	227

Introduction

Ce mémoire synthétise mes travaux de recherche effectués après mon doctorat. Ils sont principalement focalisés sur la compréhension des mécanismes physiques à la source des séismes dans différents systèmes géologiques actifs (failles et volcans). Le Chapitre 1 introduit les observations de surface et les principales méthodes permettant de caractériser la source des séismes. On y discute également de l'apport des modèles cinématiques sur notre compréhension de la source sismique.

Le Chapitre 2 concerne la détermination des caractéristiques principales de la rupture sismique à partir d'observations sismologiques à longue période. J'ai participé au développement de la méthode phase W qui est aujourd'hui utilisée par différentes agences pour caractériser rapidement la source des grands séismes. Cette approche étant basée sur l'hypothèse d'une Terre à symétrie sphérique, on s'intéressera à l'impact de la structure 3D sur l'estimation des paramètres de la source. Bien que les données longue période ne fournissent pas d'informations détaillées sur la rupture, elles permettent une caractérisation systématique et robuste des paramètres au premier ordre de la source pour un grand nombre de séismes. Ces observations peuvent ainsi fournir des informations importantes sur la diversité et la complexité des séismes.

Le Chapitre 3 aborde le détail du processus de rupture via l'intégration de données variées à proximité de la source (données sismologiques, géodésiques et tsunami). Même lorsque de nombreuses données sont disponibles, il existe généralement différents modèles de glissement qui ajustent correctement les observations de surface. Ce chapitre abordera ainsi l'utilisation de méthodes d'échantillonnage de type Monte-Carlo pour caractériser notre information sur le processus de rupture. Dans ce cadre, on traitera en particulier des incertitudes liées au problème direct (e.g., modèle de Terre) qui sont généralement négligées mais qui jouent un rôle important dans l'estimation des paramètres de source. On verra comment cette approche probabiliste permet d'aborder différentes questions telles que (1) le déficit de glissement à faible profondeur sur les failles décrochantes, (2) Le budget de déformation sismique/asismique le long de zones de subduction et (3) le caractère naturellement impulsif des ruptures sismiques.

Le Chapitre 4 concerne la sismicité volcanique en se focalisant sur mes travaux qui concernent l'activité du Piton de la Fournaise. Notre compréhension des processus magmatiques est principalement limitée par le manque d'observations précises sur les séismes volcaniques. On verra d'abord comment l'utilisation de méthodes de "comparaison à modèle" (template matching) permettent de caractériser en détail le transport magmatique au sein du Piton de la Fournaise. On s'intéressera ensuite aux signaux de très longue période associés aux effondrements de caldeira observés sur différents volcans mais dont les mécanismes à la source restent encore mal compris. On traitera en particulier de l'effondrement de caldeira en 2007 au Piton de la Fournaise et ce que la source des signaux longue période nous apprend sur la dynamique du phénomène.

Des éléments introductifs et de perspectives sont présentés au début et à la fin de chaque chapitre.

Données et méthodes

La plupart des séismes correspondent à la rupture d'une faille à l'intérieur de la Terre. Ces phénomènes sont généralement causés par le mouvement relatif des plaques tectoniques à la surface terrestre. Lorsque les contraintes tectoniques augmentent et finissent par dépasser la résistance de la faille, une rupture se produit en déformant brusquement le milieu environnant et en générant des ondes sismiques. Bien que cette description soit correcte en général, on sait aujourd'hui qu'il y a une grande diversité dans la façon dont les séismes se produisent. Tout d'abord, la taille des séismes varie de plusieurs ordres de grandeur. Les plus petits ne durent qu'une fraction de seconde alors que les plus grandes ruptures se produisent sur des centaines de kilomètres en quelques minutes. Par ailleurs, alors que les tremblements de terre correspondent souvent à des ruptures "cassantes" générant des ondes sismiques, d'autres séismes se produisent lentement de façon silencieuse. Certains séismes impliquent des processus dissipatifs avec une libération importante de chaleur. D'autres tremblements de terre ne sont même pas causés par l'activité des failles tectoniques. Parmi les sources alternatives d'activité sismique, on trouve ainsi les volcans qui sont des systèmes particulièrement actifs avec des taux de sismicité pouvant atteindre plusieurs milliers de séismes par jour dans des régions de taille kilométrique. La grande diversité des sources sismiques observées dans la nature reste encore mal comprise. Pourquoi certains séismes s'arrêtent rapidement après quelques mètres alors que d'autres continuent de rompre une faille sur plusieurs centaines de kilomètres ? Pourquoi certaines ruptures se produisent de façon catastrophique en générant des ondes sismiques alors que d'autres impliquent le glissement lent d'une faille ? Quelle est l'interaction entre les modes de glissements sismiques et asismiques ?

Plusieurs modèles ont été développés pour tenter d'expliquer la diversité des modes de glissements observée sur les failles tectoniques. Au cours des dernières décennies, une vision dominante consistait à considérer les failles comme segmentées en grandes régions avec différentes propriétés frictionnelles contrôlant le caractère sismique ou asismique dans ces régions (Lay and Kanamori, 1981). Ce modèle conceptuel d'aspérité suggère un partitionnement exclusif entre les modes de glissements et prédit notamment la notion de "séismes caractéristiques" qui rompent toujours la même aspérité de façon périodique, prédictible en temps ou prédictible en glissement (Schwartz and Coppersmith, 1984 ; Shimazaki and Nakata, 1980). Cependant, il existe aujourd'hui de nombreuses observations suggérant une superposition entre glissements sismiques et asismiques (voir par exemple Lay and Kanamori, 2011 ; Johnson et al., 2012 ; Bedford et al., 2013). Par ailleurs, une région de faille peut être entièrement rompue par un seul grand séisme mais aussi rompre de façon séquentielle en une série de séismes plus petits comme cela a été observé au Japon, à Sumatra ou en Equateur (Simons et al., 2011 ; Lay, 2015 ; Nocquet et al., 2017). Cette diversité des phénomènes observés est vraisemblablement associée à une grande hétérogénéité des pro-

priétés frictionnelles sur les failles (Avouac, 2015), avec des zones en régime conditionnement stable pour expliquer l'occurrence de ruptures sismiques dans des zones glissant habituellement de façon stable (Scholz, 1998). Cette variabilité spatiale peut notamment expliquer certains comportements complexes observés au cours du cycle sismique comme la variabilité de la taille des séismes se produisant dans la même zone de faille (Kaneko et al., 2010).

La diversité des signaux sismiques observés sur les volcans est encore plus importante que sur les structures tectoniques. Les observations sismo-volcaniques typiques incluent les séismes volcano-tectoniques, les évènements basse fréquence, les séismes hybrides et les trémors volcaniques (Kawakatsu and Yamamoto, 2007). Cette variété s'explique en partie par le large éventail de styles éruptifs s'étalant du volcanisme effusif au volcanisme explosif dépendant notamment de la teneur en gaz et de la viscosité du magma (Newhall, 2007). La grande variété des signaux observés reflète également la diversité et la complexité des sources volcaniques. Parmi les sources volcaniques communément citées, on distingue ainsi des ruptures cassantes déclenchées par le mouvement de magma, des oscillations de pressions accompagnant la dynamique des liquides et gaz, la fracturation et la fragmentation magmatique (Chouet and Matoza, 2013). Dans beaucoup de cas, les mécanismes de génération des signaux volcaniques sont peu contraints et leur lien avec le dynamisme magmatique reste mal compris.

Les méthodes de caractérisation des paramètres de la source sont le sujet central de ce chapitre. On résumera d'abord les principales données géophysiques utilisées aujourd'hui pour caractériser la rupture sismique. On s'intéressera ensuite au problème direct c'est à dire à la formulation permettant de prédire les observations de surface à partir d'une source sismique. Nous traiterons ensuite le problème inverse consistant à estimer les paramètres de source à partir des données de surface. Enfin, nous discuterons certaines implications des modèles de glissement sur la dynamique des ruptures sismiques. Ce chapitre est largement inspiré d'une introduction à la détermination des paramètres de la source en cours de publication dans un ouvrage ISTE concernant le cycle sismique.

1.1 Les observations de surface

La quantité de mesures disponibles pour étudier la source des séismes a considérablement augmenté au cours des dernières décennies. Nous résumons ici les principales données géophysiques utilisées aujourd'hui pour caractériser les séismes. On détaillera en particulier les données sismologiques qui sont un ingrédient essentiel pour déterminer l'évolution temporelle du glissement lors des séismes. Ces observations sont généralement associées à des données géodésiques de différents types (GNSS, GNSS haute-fréquence, interférométrie radar, corrélation d'images). Les données tsunami peuvent également apporter des contraintes importantes pour les ruptures sous le fond océanique. En complément de ces mesures, les études de la source bénéficient également des observations de terrain. Ces observations permettent par exemple de cartographier la trace des failles ou même de mesurer directement le glissement en surface.

1.1.1 Données sismologiques

Le sismomètre est l'instrument le plus répandu pour quantifier les mouvements sismiques. Ces capteurs sont composés d'une masse attachée au sol au travers d'un ressort et d'un amortisseur. Pendant longtemps, le déplacement de la masse relative au sol a été utilisé pour mesurer le mouvement du sol. Les instruments modernes sont basés sur le même système inertiel mais avec un système de rétroaction électromagnétique qui empêche la masse de bouger. C'est le signal de correction nécessaire à l'asservissement de la masse qui est enregistré. Ce système permet d'avoir un instrument compact enregistrant des signaux sur une large gamme de fréquence et d'amplitude en conservant la linéarité du capteur. Pour plus d'information sur la sismométrie, le lecteur peut se référer par exemple au chapitre 12 de Aki and Richards (2002).

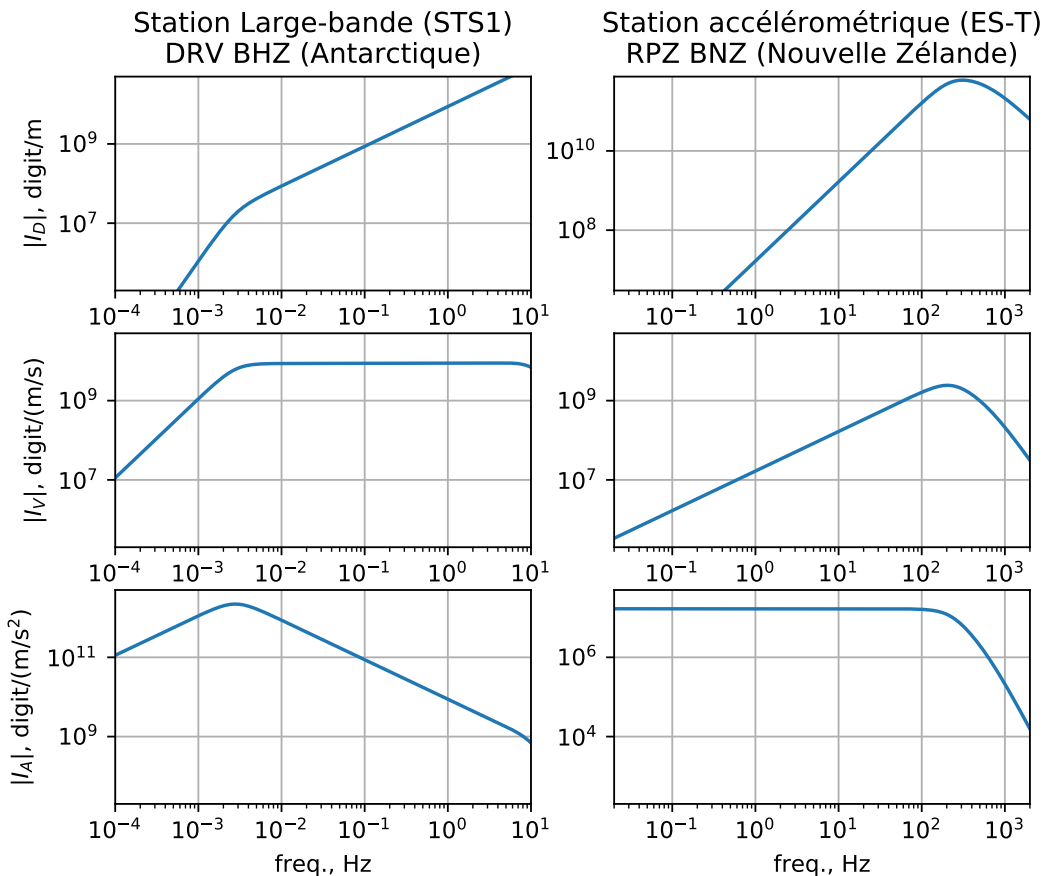


FIG. 1 – Exemples de réponses instrumentales pour un sismomètre large-bande (à gauche) et un accéléromètre (à droite). L'amplitude spectrale des fonctions de transfert en déplacement I_D , en vitesse I_V et en accélération I_A est présentée dans chaque cas. La station large-bande est équipée d'un capteur Streckeisen STS-1 avec une fréquence coin à 2.7mHz. Le capteur "strong motion" est un accéléromètre kinematics EpiSensor (ES-T) avec une fréquence coin à 200 Hz. Ces deux capteurs sont asservis.

Les formes d'ondes sismologiques fournissent une information essentielle pour caractériser la source des séismes. Deux types de capteur sismologiques sont aujourd'hui largement utilisés : les sismomètres large bande et les capteurs de mouvements forts ("strong motion" en anglais). Les données sismologiques peuvent être vues comme le produit de convolution entre le déplacement

du sol dans la direction enregistrée et la fonction de transfert du capteur. Ainsi, dans le domaine fréquentiel, les enregistrements sismologiques $S(\omega)$ peuvent être décrits comme :

$$S(\omega) = I_D(\omega)U(\omega) \quad (1.1)$$

avec ω la fréquence angulaire, $U(\omega)$ le spectre de déplacement du sol et $I_D(\omega)$ la fonction de transfert du capteur en déplacement. Les réponses du capteur par rapport à la vitesse de déplacement du sol ($I_V(\omega)$) ou à son accélération ($I_A(\omega)$) peuvent alternativement être utilisés dans l'équation ci-dessus $S(\omega) = I_V(\omega)V(\omega) = I_A(\omega)A(\omega)$ où $V(\omega)$ et $A(\omega)$ correspondent respectivement à la vitesse et à l'accélération du sol. La Figure 1 présente les réponses d'un sismomètre large-bande (station Dumont d'Urville en Antarctique) et d'un capteur de mouvement fort en Nouvelle Zélande. L'instrument large-bande présente une fonction de transfert en vitesse ($I_V(\omega)$) quasiment plate sur une large gamme de fréquence, c'est à dire avec une réponse proportionnelle à la vitesse du sol jusqu'à une période de 360 s (il s'agit ici d'un capteur STS1). Pour des périodes plus longues, l'amplitude de la réponse instrumentale diminue proportionnellement à ω^2 . Le capteur "strong motion" présenté sur la Figure 1 est un accéléromètre, c'est à dire qu'il a une réponse "plate" en accélération à partir de la fréquence nulle jusqu'à sa fréquence coin (ici à 200 Hz).

Pour travailler avec des données interprétables physiquement, il faut corriger les signaux enregistrés de la réponse instrumentale. L'approche la plus répandue consiste à déconvoluer la réponse instrumentale du signal. Ainsi, si on veut extraire le déplacement du sol :

$$U(\omega) \sim F(\omega) \frac{S(\omega)}{I_D(\omega)} \quad (1.2)$$

Lors de cette déconvolution, on utilise un filtre passe-bande $F(\omega)$ qui filtre les données dans une bande proche de celle utilisée par la suite lors de l'inversion.

La Figure 2 présente des exemples de signaux enregistrés lors du séisme de Kaikoura en 2016 (Nouvelle Zélande, $M_W = 7.8$) par la station large-bande DRV (Dumont d'Urville en Antarctique) et la station accélérométrique RPZ (Rata Peaks en Nouvelle Zélande) dont les réponses sont présentées sur la Figure 1. Les données brutes sont en haut et les données après correction de la réponse instrumentale sont présentées dessous (en déplacement, vitesse et accélération du sol). On voit clairement que les données en accélération et en vitesse sont plus haute fréquence que les données en déplacement. Cet effet est lié à la relation de dérivée temporelle entre ces signaux qui se traduit par un facteur $i\omega$ dans le domaine spectral (où i est l'unité imaginaire). Les données en accélération ou en vitesse sont donc plus sensibles aux complexités de la rupture visibles à haute fréquence. Ces données sont également plus sensibles aux hétérogénéités dans le milieu de propagation qui ne sont pas nécessairement bien prises en compte dans le modèle de vitesse utilisé. En pratique, on utilise généralement des données corrigées en déplacement ou en vitesse (l'accélération du sol étant souvent difficile à modéliser).

Les stations large-bande étant très sensibles au mouvement du sol, elles permettent d'observer des ondes sismiques à de grandes distances (à plus de 3000 km de l'épicentre sur la Figure 2). À ces distances télémétriques, on utilise classiquement des ondes de volume (généralement des ondes P et SH) pour déterminer l'histoire temporelle de la rupture. Sur la Figure 2 à gauche, les

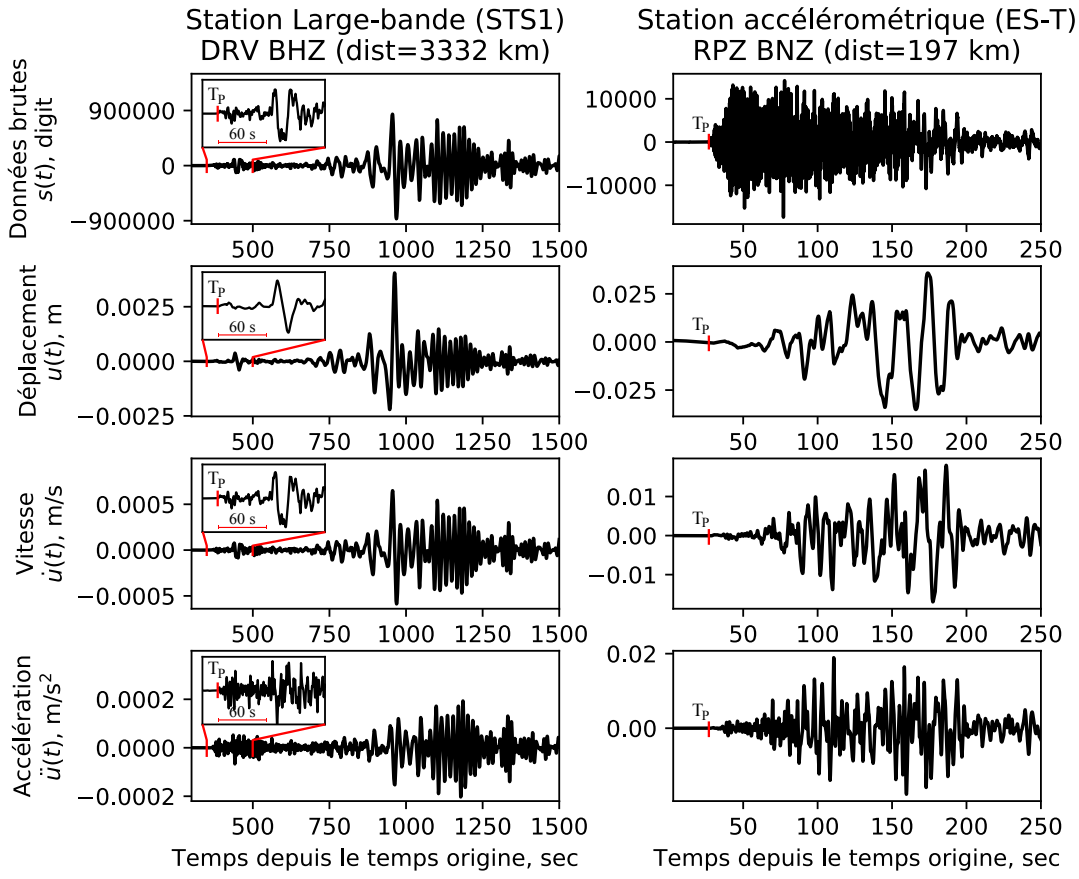


FIG. 2 – Enregistrements sismologiques lors du séisme de Kaikoura en 2016 ($M_W = 7.8$, Nouvelle Zélande). Les formes d’ondes présentées correspondent au sismomètre large-bande (STS1, à gauche) et à l’accéléromètre (EpiSensor ES-T) dont les réponses sont présentées sur la Figure 1. Dans chaque cas, on présente les données brutes $s(t)$, les données en déplacement $u(t)$, en vitesse $\dot{u}(t)$ et en accélération $\ddot{u}(t)$. La correction de la réponse instrumentale est effectuée entre 5 et 125 s de période (0.008-0.2 Hz). L’insert dans les figures de gauche présentent un agrandissement de l’arrivée P télésismique à la station DRV (T_P indique le temps d’arrivée des ondes P).

ondes P télésismiques émergent assez faiblement jusqu’à une arrivée très énergétique environ 60 s après la première arrivée. Cette arrivée correspond à un glissement important qui s’est produit ~60 s après le temps origine du séisme dans la partie nord de la rupture du séisme de Kaikoura (voir par exemple Wang et al., 2018). Si on s’intéresse aux paramètres au premier ordre de la source comme le moment sismique ou la directivité de la rupture, on peut également utiliser des ondes plus longue période comme les ondes de surface (Rayleigh et Love) ou leurs harmoniques à longue période correspondant à la phase W (cf., Chapitres 2 et 4; Dziewonski et al., 1981; Kanamori and Rivera, 2008; Vallée et al., 2011). Contrairement aux sismomètres large-bande, les accéléromètres ont une sensibilité généralement beaucoup plus faible (cf., Figure 1) ce qui permet d’enregistrer de très forts mouvements sans saturer. Ces données étant proches de la source sismique, elles sont peu affectées par le milieu de propagation et apportent ainsi une information importante sur la rupture. Sur la Figure 2 à droite, on voit à nouveau que le signal émerge faiblement et que les arrivées énergétiques arrivent tardivement (~60 s après la première

arrivée comme pour les données télésismiques).

1.1.2 Données GNSS : de la géodésie à la sismo-géodésie

Parmi les données les plus utilisées pour étudier la source, on trouve les données basées sur les systèmes GNSS (Global Navigation Satellite System), dont fait partie le Global Positioning System (GPS), le système russe GLONASS ou encore le système européen Galileo. En estimant la position d'un point par rapport à un système de référence défini par une constellation de satellites, ces données permettent de mesurer déplacement co-sismique dans trois directions (verticale, Est et Nord). Deux types de mesures peuvent être acquises : les mesures de campagnes et les mesures de stations permanentes. Dans le premier cas, les déplacements mesurés peuvent contenir une part importante de déplacements inter- et post-sismiques ou de mouvements liés à des répliques, qui peuvent être corrigés en combinant les observations avec d'autres données disponibles (voir par exemple Klein et al., 2017). Dans le cas des mesures continues par les stations permanentes pour lesquelles une position journalière est estimée, la mesure du déplacement co-sismique se fait à partir du décalage entre les positions estimées avant et après l'événement. Les données journalières co-sismiques peuvent également être affectées par les déformations post-sismiques (Twardzik et al., 2019) ou les répliques se produisant rapidement après le choc principal (Simons et al., 2011).

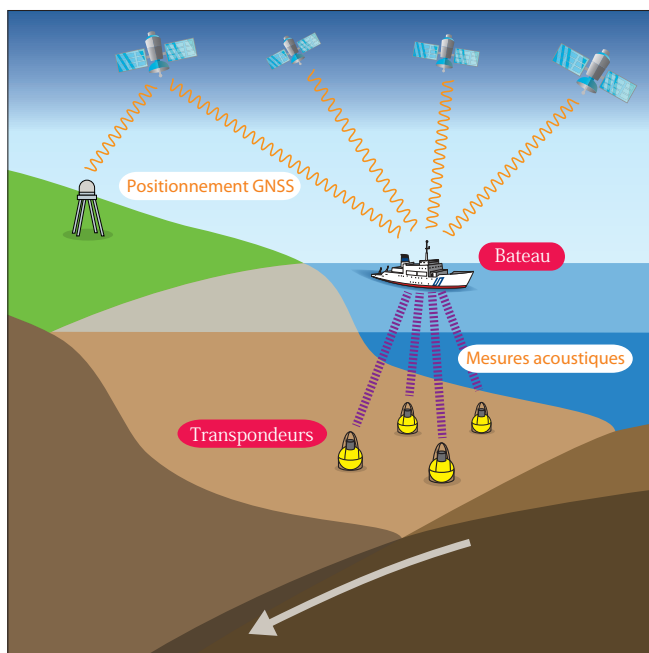


FIG. 3 – Système d’observation géodésique de fond de mer GNSS-A. Ce système combine le positionnement GNSS d’un bateau (ou d’un robot autonome) et des mesures acoustiques pour le positionnement de transpondeurs placés au fond de la mer. Cette figure est modifiée d’après Yokota and Ishikawa (2020).

Au niveau des zones de subduction, les données géodésiques à terre sont quasiment insensibles aux processus de déformations au large de la côte. Pour palier à ce problème, plusieurs approches de géodésie de fond de mer ont été proposées depuis les années 1980 (Spiess, 1980 ; Bürgmann and Chadwell, 2014). En particulier, une approche combinant observations GNSS et acoustiques

(GNSS-A ; Figure 3) est aujourd’hui utilisée dans différentes régions (Chadwell et al., 1999 ; Yokota and Ishikawa, 2020). Cette méthode repose sur le positionnement GNSS d’un bateau (ou d’un robot autonome) depuis lequel sont localisés des transpondeurs placés au fond de la mer par mesure acoustique des distances. Une approche également répandue est le déploiement de capteurs de pression permettant de mesurer les déplacements verticaux. Beaucoup d’autres méthodes sont également proposées comme l’installation d’inclinomètres de fond de mer, la cartographie sonar répétitive ou la mesure de déformations par fibre optique (Bürgmann and Chadwell, 2014).

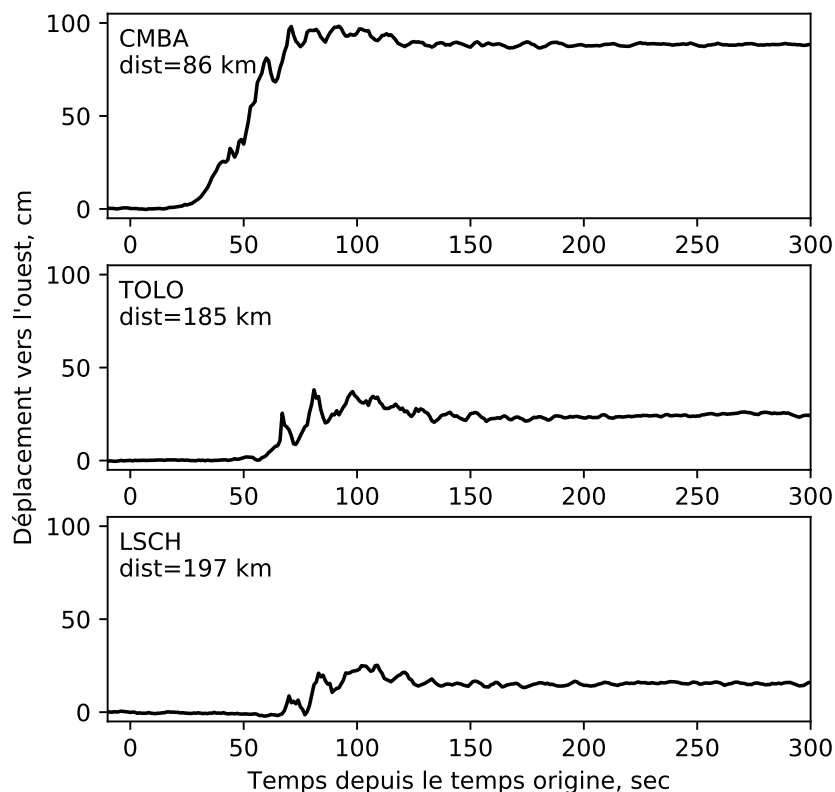


FIG. 4 – Déplacements GNSS haute-fréquence obtenus lors du séisme de Illapel au Chili en 2015 ($M_W = 8.3$). Les déplacements vers l’ouest sont présentés pour trois stations GPS à différentes distances épcentrales (indiquées dans chaque cas). Ces données échantillonées à 1 Hz ont été calculées au Jet Propulsion Laboratory en utilisant le code GIPSY-OASIS en mode Precise Point Positioning (Zumberge et al., 1997, , données traitées par S. Owen, A. Moore et M. Simons)).

Au cours de la dernière décennie, un effort important a également été effectué pour obtenir des mesures GNSS échantillonées à plus haute fréquence (c-à-d, ≥ 1 Hz, Larson et al., 2003 ; Vigny et al., 2011). Avec un tel échantillonnage, ces mesures correspondent en réalité à des sismogrammes avec trois différences principales : (1) ces données mesurent directement le déplacement du sol, ce qui élimine les problèmes d’intégration des données sismologiques, (2) ces mesures ne saturent pas (contrairement aux sismogrammes conventionnels), (3) la sensibilité des données GNSS est bien inférieure aux données sismologiques (ce qui limite leur utilisation aux plus grands séismes à de faibles distances épcentrales). Un exemple de donnée GNSS haute-fréquence est présentée sur la Figure 4 pour le séisme de Illapel en 2015 (Chili, $M_W = 8.3$). On

voit clairement la superposition du champ d'onde dynamique (oscillations courtes périodes) et du déplacement statique (rampe longue période). Ces données sont très utiles en champ proche car elles informent à la fois sur le glissement final et sur l'histoire temporelle de la rupture.

1.1.3 Imagerie satellite et aérienne

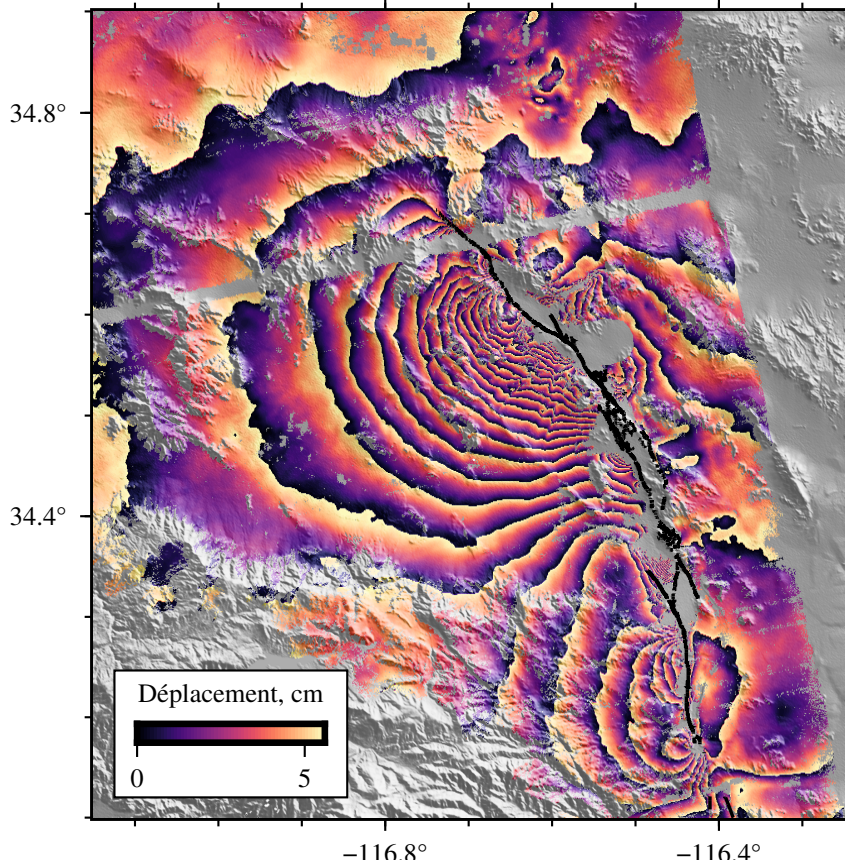


FIG. 5 – Interférogramme montrant la déformation associée au séisme de Landers en 1992 (Californie, $M_W = 7.2$). Ces données ont été obtenues à partir de deux images SAR obtenues par le satellite ERS-1 en orbite ascendante le 26 mai et le 30 juin 1992 (cf., Gombert et al. (2018a)). Les couleurs indiquent le déplacement mesuré dans la ligne de visée du satellite. La phase a été déroulée puis ré-enroulée à 5.17cm par frange. La trace en surface de la rupture du séisme de Landers est indiquée en noir.

Les données d'imagerie satellite ou aérienne ont considérablement amélioré notre vision du champ de déformation associé aux failles actives. Les données satellitaires sont notamment très utiles car elles permettent d'accéder globalement à la déformation de surface, même dans des régions mal instrumentées. Ces méthodes d'imagerie sont basées sur la combinaison de données satellites ou aériennes acquises avant et après le séisme étudié. En plus du signal co-sismique, les mesures effectuées peuvent donc contenir une part non négligeable de signal inter-sismique, post-sismique ou associé aux répliques du séisme étudié.

Parmi les méthodes employées pour mesurer le champ de déplacement co-sismique, l'interférométrie radar est particulièrement répandue (Massonnet et al., 1993 ; Hernandez et al., 1999 ; Simons et al., 2002 ; Delouis et al., 2010). Cette approche repose sur l'utilisation de deux

images SAR (*Synthetic-Aperture Radar*) acquises avant et après un séisme. Les images SAR sont obtenues en émettant une série de pulses électromagnétiques à partir d'une antenne fixée latéralement sur un satellite ou un système aéroporté (Simons and Rosen, 2007). Les échos de chaque pulse sont combinés pour obtenir une image de la zone observée. En mesurant les différences de phases pour chaque point imagé avant et après un séisme, on peut ensuite générer une carte de déplacement co-sismique dans la ligne de visée du satellite. Cette méthode est communément appelée InSAR pour *Interferometric Synthetic-Aperture Radar*. Il faut noter que lorsque le déplacement devient trop important, les données InSAR souffrent d'une perte de cohérence qui affecte parfois les déformations mesurées à proximité de la rupture. De nombreuses sources de bruit peuvent également contaminer les données InSAR. Parmi les plus fréquentes, on trouve l'effet de l'atmosphère dans l'ionosphère et/ou dans la troposphère, notamment du fait de la teneur en vapeur d'eau retardant la propagation de l'onde radar et entraînant un déphasage dans l'interférogramme. L'amplitude de ces erreurs peut être très importante et même parfois dépasser le signal tectonique. Alors que l'effet ionosphérique est plus difficile à estimer, plusieurs techniques ont été développées pour évaluer le signal d'origine troposphérique et corriger les interférogrammes de ces effets (voir par exemple Doin et al., 2009 ; Jolivet et al., 2011 ; Liang and Fielding, 2017). Une autre source de bruit provient de la mauvaise connaissance de la trajectoire du satellite, induisant un signal grande longueur d'onde dans l'image. Une correction orbitale peut alors être estimée pour en limiter l'impact sur les modèles de glissement (Simons and Rosen, 2007).

Un exemple d'image InSAR est présentée sur la Figure 5 pour le séisme de Landers en 1992 ($M_W = 7.2$). Il s'agit du premier séisme imagé grâce à l'interférométrie radar (Massonnet et al., 1993). Les données présentées incluent majoritairement le déplacement co-sismique associé au choc principal mais également 2 jours de déformations post-sismiques ainsi qu'une réplique de magnitude $M_W = 6.5$ qui s'est produit quelques heures après le choc principal (au sud de l'image).

Une autre approche répandue est la corrélation d'images prises avant et après un séisme. Ces images peuvent correspondre à des images satellites optiques (Avouac et al., 2014 ; Vallage et al., 2016), à des photographies aériennes (Ayoub et al., 2009 ; Gombert et al., 2018a) ou encore à des images d'amplitude SAR (Michel et al., 1999 ; Simons and Rosen, 2007). Contrairement au SAR qui illumine la zone étudiée, la couverture nuageuse est un paramètre limitant lors de l'utilisation d'images optiques. Bien que peu sensible aux perturbations atmosphériques, les principales difficultés à l'application de cette méthode sont liées à la co-registration des images entre elles et aux nuisances orbitales pouvant affecter l'une ou les deux images. La corrélation d'images est une méthode tout à fait complémentaire à l'InSAR car elle informe sur la composante horizontale du mouvement, mais elle permet aussi d'estimer les déplacements forts à proximité des failles souvent associés à une perte de cohérence interférométrique.

1.1.4 Données tsunami

Les séismes de subduction peuvent être associés à une forte déformation du fond océanique. Ces déplacements occasionnés sur le plancher océanique engendrent une variation du niveau de la mer par rapport à son niveau d'équilibre créant ainsi des vagues tsunami. Les données

tsunami sont donc un atout capital car elles apportent une information importante sur le champ de déplacement au fond de la mer, où peu voire aucune observation n'est disponible.

Les données tsunami sont mesurés en estimant la variation de hauteur de la surface de l'océan. Ces enregistrements peuvent prendre plusieurs formes. Depuis les années 2000, un réseau de bouées DART (*Deep-ocean Assessment and Reporting of Tsunamis*) est déployé par l'agence américaine NOAA (*National Oceanic and Atmospheric Administration*). Ces bouées déployées en pleine mer transmettent en temps réel des enregistrements d'un capteur de pression posé sur le plancher océanique pour estimer les variations de la hauteur de la colonne d'eau. Les tsunamis peuvent également être enregistrés à la côte grâce à des marégraphes qui fournissent des données généralement plus sensibles aux variations locales de bathymétrie. D'autres outils peuvent éventuellement être utilisés. En 2004 par exemple, le satellite d'altimétrie Jason a pu mesurer le tsunami généré par le séisme de Sumatra-Andaman ($M_W = 9.0$, Hébert, 2008).

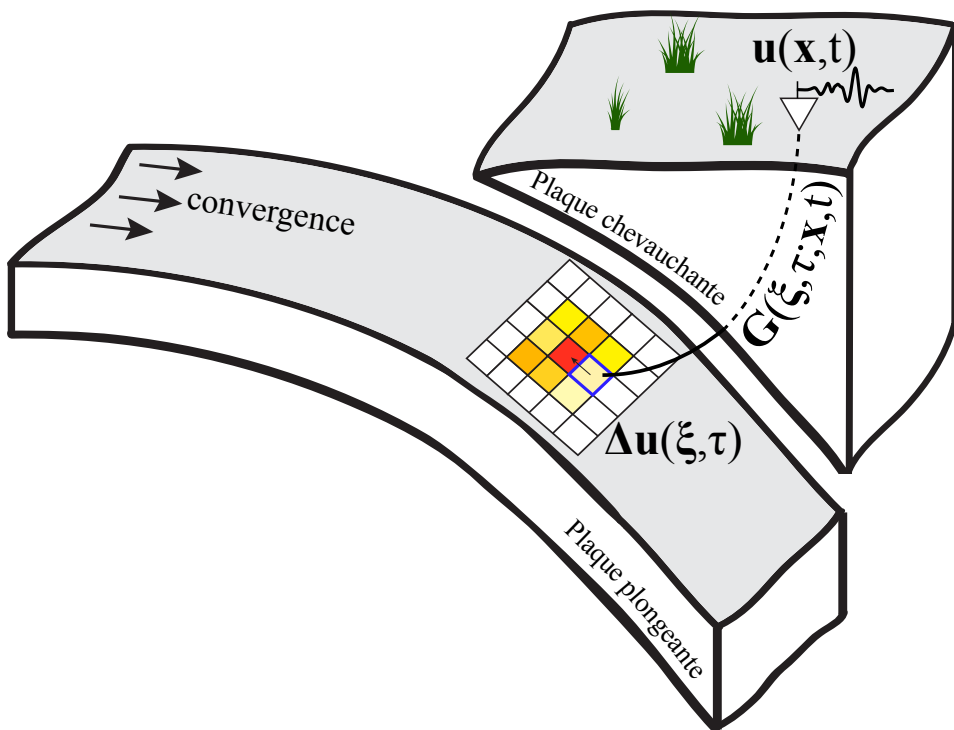


FIG. 6 – **Problème direct dans le cas d'un séisme de subduction.** Dans cet exemple, la faille est discrétisée spatialement avec des sous-failles rectangulaires (ici colorés en fonction de l'amplitude du glissement). La distribution de glissement $\Delta\mathbf{u}(\xi, \tau)$ dans l'espace (ξ) et dans le temps (τ) est reliée aux observations de surface $\mathbf{u}(\mathbf{x}, t)$ grâce à la fonction $\mathbf{G}(\mathbf{x}, t; \xi, \tau)$ comme indiqué dans l'équation 1.3. Figure modifiée d'après Gombert (2018)

1.2 Le problème direct

Nous introduisons ici la formulation permettant de relier la source sismique aux données en surface (listées dans la section 1.1). On considère qu'un séisme correspond à une discontinuité de déplacement $\Delta\mathbf{u}(\xi, \tau)$ pendant une durée de rupture T au travers d'une ou de plusieurs failles correspondant à une surface notée Σ . La fonction $\Delta\mathbf{u}(\xi, \tau)$ décrit donc le glissement dans le temps (τ) et dans l'espace (ξ) sur la faille considérée (voir Figure 6). On suppose également

qu'aux échelles de temps considérées, le milieu se comporte de façon élastique linéaire. D'après le théorème de représentation (cf., équation 3.2 de Aki and Richards, 2002), la discontinuité de déplacement $\Delta\mathbf{u}(\boldsymbol{\xi}, \tau)$ sur la faille Σ est reliée au déplacement observé à la surface $\mathbf{u}(\mathbf{x}, t)$ via l'expression suivante :

$$u_i(\mathbf{x}, t) = \int_0^T d\tau \int_{\Sigma} \Delta u_j(\boldsymbol{\xi}, \tau) c_{j k p q}(\boldsymbol{\xi}) \nu_k(\boldsymbol{\xi}) G_{i p, q}(\mathbf{x}, t; \boldsymbol{\xi}, \tau) d\Sigma \quad (1.3)$$

où G_{ip} est la fonction de Green qui décrit la composante i du déplacement au récepteur en (\mathbf{x}, t) due à une force impulsionale en $(\boldsymbol{\xi}, \tau)$ qui agit dans la direction p . L'indice q dans $G_{ip,q}$ indique la dérivée de la fonction de Green G_{ip} par rapport à la direction ξ_q . Dans cette équation, on note également c_{ijpq} le tenseur des coefficients élastiques et $\boldsymbol{\nu}(\boldsymbol{\xi})$ la normale à la surface de la faille. On se limitera ici au cas où la discontinuité de déplacement $\Delta\mathbf{u}(\boldsymbol{\xi}, \tau)$ est perpendiculaire à $\boldsymbol{\nu}(\boldsymbol{\xi})$. Pour plus de détails sur cette représentation de la source sismique, le lecteur peut se référer au chapitres 2 et 3 de Aki and Richards (2002).

1.2.1 Représentation en point source

L'équation (1.3) a été développée pour une faille Σ étendue dans l'espace. En pratique, lorsque nous utilisons des données télesismiques filtrées à longue période, la contribution des différents éléments de surface $d\Sigma$ sont approximativement en phase et l'ensemble de la faille Σ peut être représentée par un point source $\boldsymbol{\xi}^0$. Pour ce point source effectif, on peut alors écrire :

$$u_i(\mathbf{x}, t) = \int_0^T M_{pq}(\tau) G_{ip, q}(\mathbf{x}, t; \boldsymbol{\xi}^0, \tau) d\tau \quad (1.4)$$

Où on définit le tenseur moment sismique

$$M_{pq}(\tau) = \int_{\Sigma} \Delta u_j(\boldsymbol{\xi}, \tau) c_{j k p q}(\boldsymbol{\xi}) \nu_k(\boldsymbol{\xi}) d\Sigma \quad (1.5)$$

La caractérisation des paramètres de la source consistera alors à déterminer $M_{pq}(\tau)$ ainsi que la localisation du point source $\boldsymbol{\xi}^0$ qui permettra d'ajuster au mieux les données. La meilleure localisation du point source est souvent appelée localisation barycentrique ("centroid location" en anglais ; Dziewonski et al., 1981). Lorsqu'on considère une faille plane avec un glissement unidirectionnel, on peut en effet démontrer que l'approximation en point source est optimum au niveau du barycentre de l'histoire spatiale et temporelle de la rupture (voir chapitre 5 de Dahlen and Tromp, 1998).

En considérant que le mécanisme ne change pas significativement au cours de la rupture, on considère généralement $M_{pq}(\tau) = M_{pq} S(\tau)$ et on peut écrire :

$$u_i(\mathbf{x}, t) = \int_0^T M_{pq} S(\tau) G_{ip, q}(\mathbf{x}, t; \boldsymbol{\xi}^0, \tau) d\tau \quad (1.6)$$

où M_{pq} est le tenseur moment sismique statique et $S(\tau)$ est une fonction normalisée (croissante entre 0 et 1) décrivant l'évolution temporelle du moment sismique scalaire qui peut être défini

comme (Silver and Jordan, 1982) :

$$M_0 = \frac{1}{\sqrt{2}}(\mathbf{M} : \mathbf{M})^{1/2} \quad (1.7)$$

Différentes approches peuvent être employées pour décrire pour la fonction $S(\tau)$. Un choix classique est de considérer que sa dérivée temporelle $\dot{S}(\tau)$ est une fonction porte ou une fonction triangulaire isocèle centrée sur un temps barycentrique τ^0 à déterminer lors de l'inversion (Ekström and Dziewonski, 1985 ; Ekström et al., 2012 ; Kanamori and Rivera, 2008). Une autre approche est de considérer une forme quelconque qui peut être déterminée sous certaines contraintes (par exemple le fait que $\dot{S}(\tau)$ est strictement positive avec une durée correspondant à la durée de rupture ; Vallée et al., 2011). Ces deux approches sont employées dans le Chapitre 2 de ce mémoire.

1.2.2 Représentation en source étendue

Comme on le verra dans le Chapitre 3, les données de surface nous informent également sur l'étendue spatiale et temporelle de la source sismique. C'est le cas pour les sismogrammes filtrés à courte période ou pour les données sismo-géodésiques dans la zone épicentrale. Pour décrire la distribution de glissement dans le temps et dans l'espace, on paramétrise la vitesse de glissement en la décomposant sur N_s fonctions de base spatiales de la façon suivante (Ide, 2007) :

$$\Delta \dot{u}_i(\xi, \tau) = \sum_{j=1}^{N_s} p^j \hat{u}_i^j(\tau) \phi^j(\xi) h^j(\xi, \tau) \quad (1.8)$$

où on définit :

- $\Delta \dot{u}_i$ la i -ème composante du vecteur de glissement sur la faille,
- $\phi^j(\xi)$ la j -ème fonction de base spatiale associée au coefficient p^j ,
- p^j un coefficient dont la dimension est le produit du glissement par une aire,
- $h^j(\xi, \tau)$ une fonction décrivant l'évolution temporelle de la rupture,
- $\hat{u}_i^j(\tau)$ un vecteur unitaire représentant la direction de glissement au temps τ .

Les fonctions $\phi^j(\xi)$ et $h^j(\xi, \tau)$ sont normalisées tel que $\int \int_{\Sigma} \phi^j(\xi) d\Sigma(\xi) = 1$ et $\int_{-\infty}^{+\infty} h^j(\xi, \tau) d\tau = 1$.

Un choix courant pour la paramétrisation spatiale du glissement est de "quadriller" la faille avec des sous-failles dans lesquelles le glissement est considéré constant à un temps donné. Des sous-failles rectangulaires (comme sur la Figure 6) ou triangulaires sont couramment employées dans la littérature. Dans les équations précédentes, on définit alors $\phi^j(\mathbf{x})$ comme une fonction porte sur la faille. Pour la j -ème sous-faille, on a donc

$$\begin{aligned} \phi^j(\xi) &= 1/\Sigma^j \text{ lorsque } \xi \in \Sigma^j \\ \phi^j(\xi) &= 0 \text{ sinon} \end{aligned} \quad (1.9)$$

où Σ^j correspond à la surface de la sous-faille j . Dans ce cas là, les coefficients p^j correspondent directement au produit entre le glissement et l'aire de chaque sous-faille. On parle alors de "seismic potency" en anglais qui pourrait se traduire par "puissance sismique".

1.2.2.1 Cas statique : modélisation de données géodésiques

Si on ne s'intéresse qu'à la distribution finale du glissement, on peut utiliser des données géodésiques co-sismiques qui ne sont sensibles qu'à la distribution statique du glissement. Pour des séismes de taille modérée, les données tsunami rentrent également dans cette catégorie car elles ont une faible sensibilité à l'histoire de la rupture. Les séismes de magnitude $M_W > 8$ ont une durée de rupture importante ($T > 1$ min) qu'il faudra généralement prendre en compte lors de la modélisation de données tsunami. Pour modéliser les données statiques, on intègre les équations précédentes dans le temps jusqu'à la durée de rupture T . On obtient :

$$\Delta u_i(\xi) = \sum_{j=1}^{N_s} p^j \hat{u}_i^j \phi^j(\xi) \quad (1.10)$$

où \hat{u}_i^j représente cette fois la direction finale du glissement sur la faille. On peut ensuite décomposer le vecteur de glissement en deux composantes :

$$\Delta u_i(\xi) = \sum_{j=1}^{N_s} (p^{j1} v_i^1 + p^{j2} v_i^2) \phi^j(\xi) \quad (1.11)$$

où p^{j1} et p^{j2} sont les composantes de p^j dans la direction des deux vecteurs unitaires orthogonaux \mathbf{v}^1 et \mathbf{v}^2 . Ainsi par exemple, \mathbf{v}^1 et \mathbf{v}^2 peuvent correspondre aux directions le long du pendage et le long de l'azimut de la faille. En remplaçant cette formulation dans l'équation (1.3), on obtient :

$$u_i(\mathbf{x}) = \sum_{l=1}^{N_s} (p^{l1} v_j^1 + p^{l2} v_j^2) \mathcal{G}_{ij}^l(\mathbf{x}) \quad (1.12)$$

où on a :

$$\mathcal{G}_{ij}^l(\mathbf{x}) = \int \int_{\Sigma} \phi^l(\xi) c_{jkpq}(\xi) \nu_k(\xi) G_{ip,q}(\mathbf{x}; \xi) d\Sigma(\xi) \quad (1.13)$$

Dans le cas où on utilise une paramétrisation en sous-failles, on a :

$$\mathcal{G}_{ij}^l(\mathbf{x}) = \frac{1}{\Sigma^l} \int \int_{\Sigma^l} c_{jkpq}(\xi) \nu_k(\xi) G_{ip,q}(\mathbf{x}; \xi) d\Sigma(\xi) \quad (1.14)$$

où Σ^l correspond à la surface de la sous-faille l pour laquelle $\phi^l(\xi) = 1/\Sigma^l$ (voir équation 1.9). Dans les équations ci-dessus, $\mathcal{G}_{ij}^l(\mathbf{x})$ décrit le déplacement à la surface (en \mathbf{x}) causé par un glissement unitaire sur la sous-faille l . Dans un demi-espace homogène, cette fonction peut être calculée analytiquement (Mansinha and Smylie, 1971 ; Okada, 1985). Pour un milieu hétérogène, il existe différents outils pour calculer numériquement la réponse d'un milieu tabulaire (par ex. Zhu and Rivera, 2002) ou d'un milieu 3D (par ex. Aagaard et al., 2013).

Dans le cas statique, on peut donc décrire la distribution finale de glissement en utilisant deux composantes de "slip potency" p^{l1} et p^{l2} pour chaque sous-faille l (c.-à-d. pour chaque fonction de base ϕ^l). Il s'agit d'un problème linéaire :

$$\mathbf{d}_s = \mathbf{G}_s \mathbf{m}_s \quad (1.15)$$

où \mathbf{d}_s est le vecteur donnée contenant les mesures géodésiques en surface, \mathbf{m}_s correspond au

vecteur modèle contenant les coefficients p^{l1} et p^{l2} , \mathbf{G}_s est la matrice contenant les fonctions $\mathcal{G}_{ij}^l(\mathbf{x})$ définie dans les équations 1.13 et 1.14).

Les données géodésiques statiques n’informent que sur la distribution finale du glissement sur la faille. Si on s’intéresse à la façon dont la rupture se propage, il faut choisir une paramétrisation pour décrire l’évolution temporelle du glissement. Traditionnellement, il existe deux approches qui sont détaillées dans les deux sections suivantes.

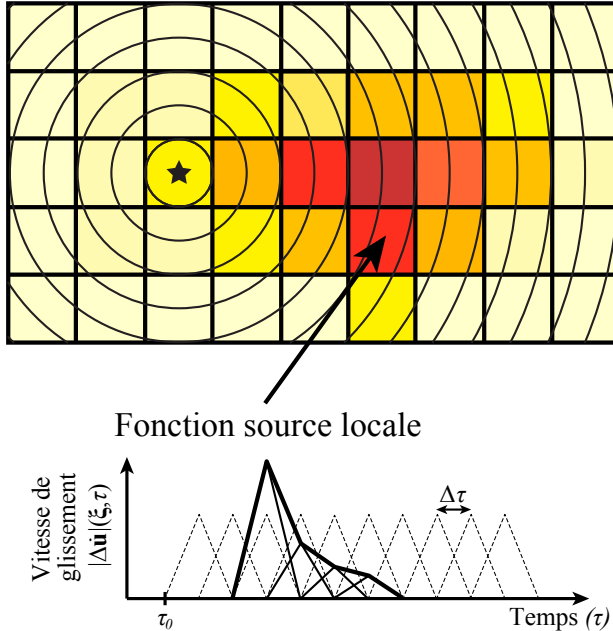


FIG. 7 – **Paramétrisation en fenêtres multiples.** Exemple de formulation basée sur l’utilisation de fonctions de base triangulaires en temps et rectangulaires dans l’espace. La couleur de chaque sous-faille indique l’amplitude du glissement. Les temps de rupture minimums τ_0 sont représentés par des isocontours de temps sur la faille. La vitesse de glissement est présentée en noir pour une des sous-failles après sommation des fonctions temporelles (triangles en pointillés).

1.2.2.2 Cas cinématique : Approche linéaire en fenêtres multiples

Comme illustré sur la Figure 7, la paramétrisation en fenêtre multiple consiste à développer la fonction $\hat{u}_i^j(\tau) h^j(\xi, \tau)$ dans l’équation (1.8) en utilisant une série de N_t coefficients :

$$\Delta \dot{u}_i(\xi, \tau) = \sum_{j=1}^{N_s} \sum_{k=1}^{N_t} (p^{jk1} v_i^1 + p^{jk2} v_i^2) \phi^j(\xi) f(\tau - (k-1)\Delta\tau - \tau_0(\xi)) \quad (1.16)$$

Dans cette équation $f(\tau)$ est une fonction de base temporelle qui est nulle pour $\tau < 0$ avec une intégrale unitaire et un support fini. Un choix typique pour $f(\tau)$ est une fonction porte ou une fonction triangulaire (Olson and Apsel, 1982 ; Hartzell and Heaton, 1983). Ces fonctions représentent une série de fenêtres décalées tous les $\Delta\tau$ entre un temps de rupture minimum $\tau = \tau_0(\xi)$ et un temps de rupture maximum $\tau = \tau_0(\xi) + (N_t - 1)\Delta\tau$. Cette paramétrisation décompose donc la vitesse de glissement $\Delta\dot{\mathbf{u}}$ en une série de coefficients p^{jk1} associés à la j -ème direction de glissement sur la j -ème fonction de base spatiale et une fenêtre temporelle décalée

de $(k - 1)\Delta\tau + \tau_0(\xi)$ (voir Figure 7).

En substituant cette équation dans (1.3), on obtient une expression assez similaire au cas statique. En considérant une fonction porte $\phi^j(\xi)$ pour la j -ème sous-faille et un temps initial de rupture $\tau_0(\xi \in \Sigma^j) = \tau_0^j$:

$$u_i(\mathbf{x}, t) = \sum_{l=1}^{N_s} \sum_{k=1}^{N_t} (p^{lk1} v_j^1 + p^{lk2} v_j^2) \mathcal{G}_{ij}^{lk}(\mathbf{x}, t - (k - 1)\Delta\tau - \tau_0^j) \quad (1.17)$$

avec :

$$\mathcal{G}_{ij}^{lk}(\mathbf{x}, t) = \frac{1}{\Sigma^l} \int_0^T d\tau \int \int_{\Sigma^l} f(\tau) c_{jkpq}(\xi) \nu_k(\xi) G_{ip,q}(\mathbf{x}, t; \xi, \tau) d\Sigma(\xi) \quad (1.18)$$

Comme dans le cas statique, on obtient un problème linéaire :

$$\mathbf{d}_k = \mathbf{G}_k \mathbf{m}_k \quad (1.19)$$

où \mathbf{d}_k est le vecteur donnée, \mathbf{m}_k inclut les coefficients p^{jkl} et \mathbf{G}_k est la matrice contenant les formes d'ondes calculés pour chaque fonction de base dans l'espace et dans le temps (cf., équation 1.18).

Cette paramétrisation est fréquemment utilisée car elle aboutit à un système d'équations linéaires qui peut être résolu avec des approches classiques comme la méthode des moindres carrés. Le modèle en fenêtre multiple est aussi avantageux car il autorise une certaine flexibilité dans l'évolution temporelle du glissement. Cependant, un inconvénient important de cette formulation est qu'elle repose sur un grand nombre de paramètres à estimer. Pour les grands séismes se produisant sur de grandes failles avec des durées de rupture importantes, on peut facilement aboutir à plusieurs milliers de paramètres. Pour diminuer la dimension du problème, on considère donc généralement un nombre limité de fenêtres temporelles à partir d'un temps de rupture minimum $\tau_0(\xi) = |\xi - \xi_0|/V_R^{max}$ déterminé par une vitesse de rupture V_R^{max} et la position de l'hypocentre ξ_0 sur la faille (fixée a priori).

1.2.2.3 Cas cinématique : Approche non-linéaire

Dans l'approche non-linéaire de l'inversion cinématique, les temps de rupture sont traités comme des paramètres à déterminer. On a donc :

$$\Delta \dot{u}_i(\xi, \tau) = \sum_{j=1}^{N_s} (p^{j1} v_i^1 + p^{j2} v_i^2) \phi^j(\xi) f(\tau - \tau^j, r^j) \quad (1.20)$$

avec :

- $f(\tau, r)$ une fonction qui est nulle pour $\tau < 0$ et $\tau > r$ et d'intégrale unitaire,
- τ^j correspond au temps de rupture pour la sous-faille j (ou la fonction ϕ^j),
- r^j est la durée locale du glissement, appellée "rise-time" ou temps de montée.

Dans l'approche non-linéaire, la forme de la fonction source locale $f(\tau, r)$ est identique pour toutes les sous-failles j (contrairement à l'approche linéaire en fenêtres multiples). On peut utiliser différentes formes pour la fonction $f(\tau, r)$: fonction porte, fonction triangulaire sont des choix typiques (cf., Figure 8). Il est également possible d'utiliser des expressions qui représentent mieux la dynamique de la rupture (une fonction de Yoffe est présentée par exemple sur la Figure 8

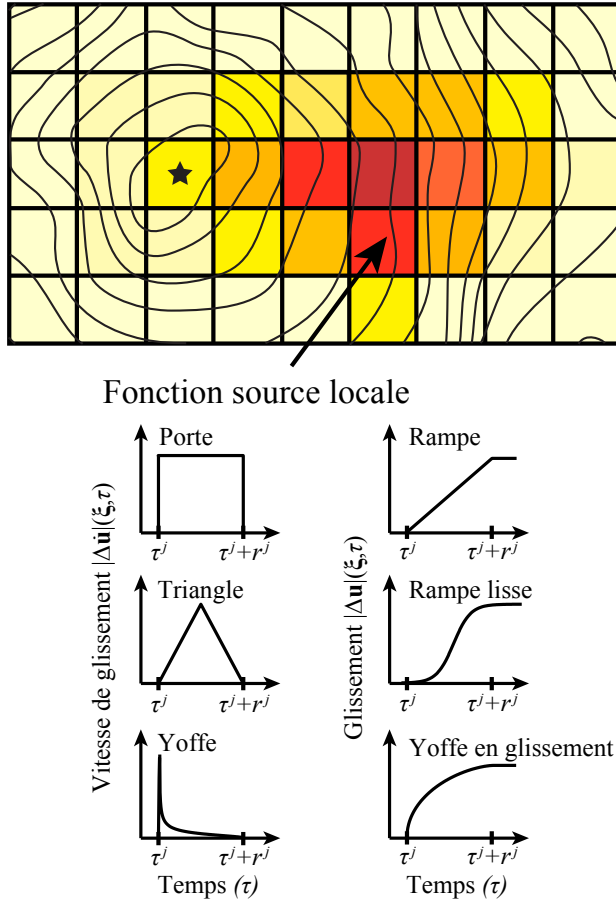


FIG. 8 – Paramétrisation non-linéaire. Formulation non-linéaire où l'évolution temporelle du glissement est paramétrisée avec un temps de rupture τ^j et un temps de montée r^j . On considère une paramétrisation spatiale en sous-faille où la couleur indique l'amplitude du glissement. Les temps de rupture sont indiqués sur la faille par des isocontours. Différents choix pour la fonction $f(\tau, r)$ sont présentés sous la faille en vitesse de glissement à gauche (fonction porte, triangulaire et Yoffe) avec leur équivalent en glissement à droite (rampe, rampe lisse, Yoffe en glissement).

Yoffe, 1951 ; Tinti et al., 2005a).

En intégrant cette paramétrisation dans l'équation (1.3), on obtient un problème direct non linéaire :

$$\mathbf{d}_k = \mathbf{G}_k(\mathbf{m}_k) \quad (1.21)$$

Dans cette équation, le vecteur modèle \mathbf{m}_k inclut les coefficients p^{jl} , les temps de montée r^j et les temps de rupture τ^j . \mathbf{G}_k représente la fonction non linéaire permettant de relier ces paramètres au vecteur donnée \mathbf{d}_k . Certaines approches décrivent la vitesse de rupture V_R^j dans chaque sous-faille à la place des temps de rupture τ^j (voir par exemple Minson et al., 2013). Le calcul direct $\mathbf{G}_k(\mathbf{m}_k)$ inclut alors la résolution de l'équation eikonal

$$|\nabla \tau^j| = 1/V_R^j \quad (1.22)$$

permettant d'obtenir les temps de rupture τ^j (avec $\tau^j = 0$ à l'hypocentre du séisme). Ce type d'approche (employé notamment dans le chapitre 3) permet notamment d'imposer la causalité

du front de rupture.

Une paramétrisation non-linéaire permet de réduire significativement la dimension du problème. Avec cette formulation, le nombre de paramètres est de $4 \times N_s$ qui est généralement bien inférieur aux $2 \times N_s \times N_t$ paramètres de l'approche en fenêtres multiples (cf., équation 1.17). L'inconvénient majeur est la non-linéarité du problème direct qui complique la résolution du problème inverse et peut aboutir à l'existence de minimums locaux. Comme on le verra dans le Chapitre 3 et dans la section 1.3.2 ci-dessous, cette non-unicité peut être traitée en caractérisant l'ensemble des modèles expliquant les observations de surface et notre connaissance a priori sur la rupture.

1.2.3 Calcul des fonctions de Green

Les formulations du problème direct présentées ci-dessus reposent sur les dérivées spatiales des fonctions de Green $G_{ip,q}$ qui doivent être calculées en chaque point de la faille dans le cas d'une inversion en source étendue. Suivant la paramétrisation et les données utilisées, différentes stratégies peuvent être employées pour le calcul de $G_{ip,q}$.

Comme décrit dans la section 1.2.2.1 dans le cas statique, il existe des solutions analytiques pour calculer les fonctions de Green dans un demi-espace homogène (Okada, 1985). Il existe également différents outils numériques pour simuler les déplacements statiques dans un milieu 2D ou 3D (Zhu and Rivera, 2002 ; Aagaard et al., 2013). Lorsque des données tsunami sont utilisées, ces fonctions de Green statiques doivent être couplés à des modèles décrivant la propagation du tsunami à partir d'un champ de déplacement du fond marin (Satake, 2007). La longueur d'onde tsunami étant généralement largement supérieure à la profondeur d'eau et son amplitude étant petite devant la profondeur océanique en pleine mer, la modélisation tsunami est généralement effectuée en considérant des approximations dites en eau peu profonde et de petite vague. Un des codes les plus populaires basé sur ces approximations est (pour CORNELL Multi-grid COupled Tsunami Model ; Liu et al., 1998). Bien que ce code soit adapté pour la modélisation de données DART en pleine mer, il ne conviendra pas pour les données marégraphiques cotières pour lesquelles l'hypothèse de petite vague n'est souvent pas valide. Par ailleurs, des effets dispersifs liés à l'élasticité du fond marin et à la variation de densité d'eau sont généralement négligés (Tsai et al., 2013). Ces effets engendrent des retards dans la propagation tsunami pouvant atteindre plusieurs minutes. Des codes ont été développés pour modéliser ces effets (Allgayer and Cummins, 2014) et il est également possible d'appliquer des corrections au premier ordre sur les temps de trajet (Tsai et al., 2013) ou la profondeur océanique (Inazu and Saito, 2013).

La modélisation des données sismologiques repose souvent sur la simulation de formes d'ondes pour un milieu tabulaire. Dans le cas de données télésismiques à courte période, on emploie généralement la méthode de la matrice de propagation couplée à la théorie des rais (Bouchon, 1976 ; Kikuchi and Kanamori, 1991). Les ondes P et S télésismiques sont alors modélisées en considérant des milieux tabulaires à la source, aux récepteurs et éventuellement aux points de réflexion PP si ces phases sont utilisées. Pour des données plus longue période (ondes de surface, phase W), il est courant de calculer les sismogrammes synthétiques via sommation de modes propres (Dahlen and Tromp, 1998). Pour le calcul de formes d'ondes en champ proche, l'utilisation de méthodes basées sur l'intégration en nombre d'ondes est très répandue (Bouchon, 1981) et de

nombreux codes basées sur ces méthodes sont distribués (voir par exemple Herrmann, 2013). La prise en compte de la structure 3D est de plus en plus répandue dans les études de source (voir Chapitre 2 ; Hjörleifsdóttir et al., 2009). Pour ce faire, il existe de nombreuses méthodes de modélisation de formes d'onde 3D telles que des approches en différence finies ou en éléments spectraux (Komatitsch and Tromp, 1999). Bien que la prise en compte de l'hétérogénéité latérale soit importante pour améliorer la caractérisation de la source, des modèles détaillés de structure 3D ne sont pas toujours disponibles. Pour limiter l'impact des imprécisions dans le modèle de Terre, certaines approches reposent sur la calibration empirique des fonctions de Green (Wei et al., 2013). Une bonne alternative est l'utilisation de fonctions de Green empiriques (EGF) qui consiste à utiliser des enregistrements de petits séismes co-localisés avec le séisme étudié (Hartzell, 1978). Toutefois la couverture en EGFs n'est souvent pas suffisante pour couvrir toute la faille et cette approche repose sur l'hypothèse que le séisme étudié et les EGFs sont associés au même mécanisme au foyer.

Les imprécisions dans le modèle de vitesse utilisé pour le calcul des fonctions de Green peuvent avoir un impact important lors de l'inversion du glissement. Comme on le verra dans le Chapitre 3 et dans la section suivante, l'incertitude associée au modèle de Terre peut être prise en compte dans le problème inverse. Pour limiter l'impact des imprécisions du modèle de vitesse, une pratique courante est d'aligner les arrivées d'ondes prédictes et observées pour minimiser la différence entre les phases correspondantes. Cette approche reste cependant complexe en champ proche où les ondes S dominent les enregistrements mais pour lesquelles un temps d'arrivée est difficile à déterminer car il est souvent masqué par les ondes P. Un mauvais alignement des arrivées P et/ou S peut avoir un impact considérable sur le résultat de l'inversion et peut en partie expliquer la variabilité de certains modèles de source. Il est donc impératif d'utiliser un modèle de vitesse fiable pour limiter son impact sur le résultat final.

1.3 Le problème inverse

Le problème inverse consiste à retrouver un modèle de glissement \mathbf{m} à partir des données \mathbf{d}_{obs} , de notre formulation du problème direct et de notre connaissance *a priori* sur le modèle. Il existe de nombreux ouvrages détaillant différentes approches pour la résolution du problème inverse. Nous ne présentons ici que quelques approches pour introduire l'optimisation régularisée et l'inversion Bayésienne.

On se limitera ici aux approches où une norme L^2 est utilisée pour caractériser l'écart aux données. On définit ainsi une fonction d'ajustement aux données :

$$\chi(\mathbf{m}) = \|\mathbf{d}_{\text{obs}} - \mathbf{G}(\mathbf{m})\|_2^2 \quad (1.23)$$

Le vecteur données \mathbf{d}_{obs} est généralement construit en concaténant les formes d'ondes sismologiques et les autres observables (géodésiques, tsunami, etc.). Le problème peut également être résolu en représentant les données sismologiques dans le domaine fréquentiel. Cependant, comme on le verra dans la section 1.3.3, modéliser les données en fréquence est théoriquement identique à le faire dans le domaine temporel.

Les données étant affectées par des erreurs de mesure et notre connaissance limitée du sous-

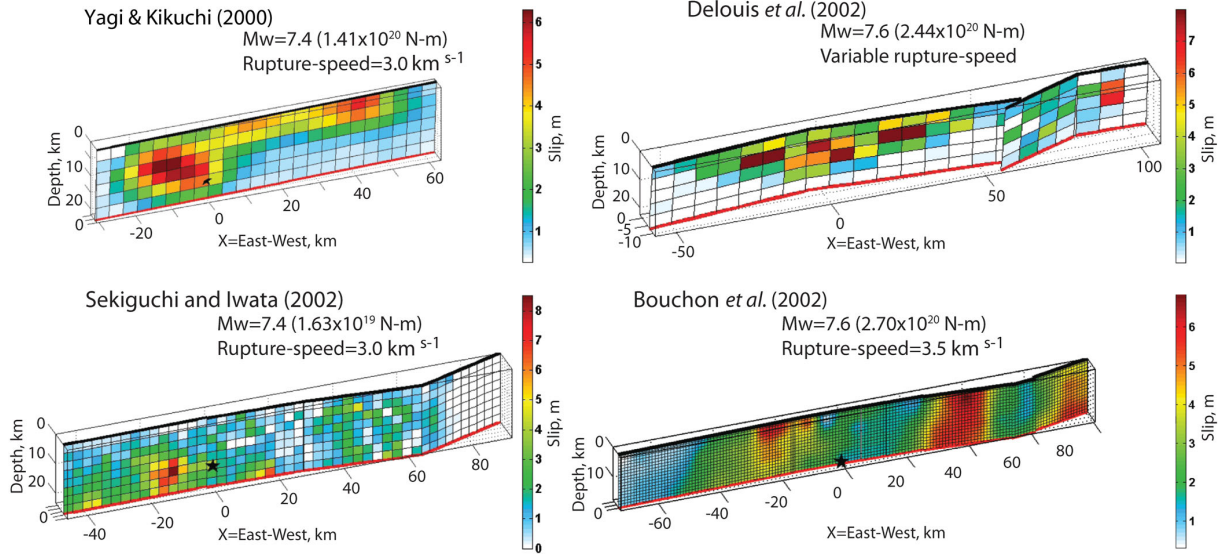


FIG. 9 – **Une illustration de la variabilité des modèles de source cinématiques.** Résultats de l'inversion de glissement obtenus par différentes équipes pour le séisme d'Izmit en 1999 (Yagi and Kikuchi, 2000 ; Bouchon et al., 2002 ; Delouis et al., 2002 ; Sekiguchi and Iwata, 2002). Ces modèles de source sont disponibles via la base de données SRCMOD Mai (2012). Figure modifiée d'après Duputel et al. (2014).

sol, la solution du problème inverse est généralement non-unique. Il existe alors plusieurs modèles de glissement associés à un écart aux données $\chi(\mathbf{m})$ similaire. Même lorsque les incertitudes sont faibles, l'utilisation de données en surface pour caractériser un processus de rupture complexe en profondeur est un problème fondamentalement mal posé. Ainsi par exemple, si on se place dans un cas linéaire gaussien $\mathbf{G}(\mathbf{m}) = \mathbf{G}\mathbf{m}$, en considérant des données suffisantes, indépendantes et identiquement distribuées, la minimisation de $\chi(\mathbf{m})$ aboutit à la solution des moindres carrés :

$$\widetilde{\mathbf{m}} = (\mathbf{G}^t \mathbf{G})^{-1} \mathbf{G}^t \mathbf{d}_{\text{obs}} \quad (1.24)$$

où l'exposant t indique la transposition de matrice. Cette solution est classiquement employée pour l'estimation du tenseur moment sismique dans la représentation en point source. Dans le cas de l'inversion phase W par exemple, cette solution est couplée à une recherche sur grille pour déterminer la location optimum du point source dans le temps et dans l'espace. Dans ce cas de figure, \mathbf{m} correspond au tenseur moment sismique et la localisation du point source est estimée de façon à minimiser l'écart aux données (équation 1.23) pour toutes les localisations testées sur une grille pré-définie autour de l'hypocentre du séisme (voir Duputel et al., 2012c).

Lors de l'inversion du glissement en source étendue, la matrice $\mathbf{G}^t \mathbf{G}$ dans l'équation (1.24) est généralement mal conditionnée. Il existe alors une infinité de solutions minimisant l'écart aux données. Cette variabilité dans les résultats de l'inversion est illustrée sur la Figure 9 dans le cas du séisme d'Izmit (Turquie) en 1999 ($M_W = 7.6$). Le séisme d'Izmit en 1999 n'est pas un cas isolé. Pour beaucoup d'événements, de petites différences dans le jeu de données ou la formulation du problème aboutissent à des différences importantes dans les distributions de glissement obtenues (Wald and Heaton, 1994 ; Hernandez et al., 1999 ; Pritchard et al., 2007). Pour traiter ce problème de non-unicité de la solution, une pratique répandue est de régulariser l'inversion pour se placer

dans un problème d'optimisation bien conditionné. Une approche alternative est de caractériser l'ensemble des modèles plausibles qui expliquent les données en considérant nos connaissances a priori sur la rupture. Ces deux approches sont décrites ci-dessous.

1.3.1 Approche par régularisation de Tikhonov

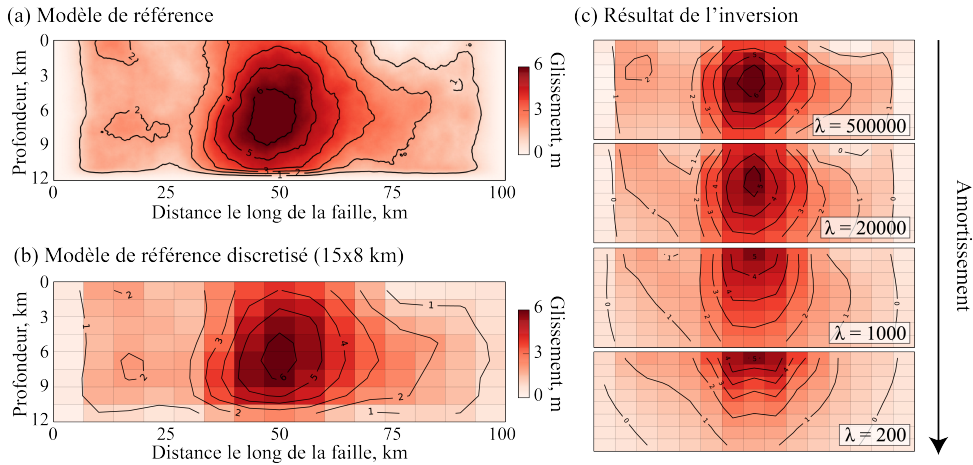


FIG. 10 – **Impact de la régularisation sur les modèles de glissement.** (a) Modèle synthétique décrivant une distribution hétérogène de glissement. (b) Modèle synthétique discréte dans des cellules de 15x8 km. (c) Résultat de l'inversion en considérant un amortissement croissant. Ce test est effectué en supposant un réseau de stations GNSS espacées régulièrement tous les 10 km autour de la faille. Le lissage est contrôlé par l'amortissement λ comme indiqué dans l'équation (1.25).

La régularisation de Tikhonov est une méthode de régularisation très répandue pour la résolution de problèmes inverses mal posés. Cette méthode est également connue sous le nom de régression de crête (ridge regression). Pour limiter la non-unicité du problème inverse, un terme de régularisation est introduit dans la minimisation. La solution est alors donnée par :

$$\widetilde{\mathbf{m}} = \arg \min(\|\mathbf{d}_{\text{obs}} - \mathbf{G}(\mathbf{m})\|_2^2 + \lambda^2 \|\boldsymbol{\Gamma}\mathbf{m}\|_2^2) \quad (1.25)$$

où $\boldsymbol{\Gamma}$ est la matrice de Tikhonov et λ et le paramètre d'amortissement. Dans l'équation ci-dessus, " $\arg \min(f(\mathbf{m}))$ " définit la valeur de \mathbf{m} minimisant ma fonction coût $f(\mathbf{m})$. La matrice $\boldsymbol{\Gamma}$ peut prendre différentes formes suivant les caractéristiques du modèle que l'on souhaite favoriser. Un choix classique est $\boldsymbol{\Gamma} = \mathbf{I}$ qui privilégiera les modèles avec une norme L_2 faible (voir par exemple Olson and Apsel, 1982). Dans le contexte de l'inversion du glissement, cette régularisation peut cependant biaiser les modèles vers des magnitudes de moment faibles (en réduisant l'amplitude du glissement sur la faille). Un autre choix répandu est l'opérateur Laplacien spatial $\boldsymbol{\Gamma} = \nabla^2$ qui consiste à minimiser la "rugosité" du modèle afin d'obtenir une distribution de glissement relativement lisse sur la faille (Segall and Harris, 1987).

On se place maintenant dans un cas linéaire $\mathbf{d} = \mathbf{G}\mathbf{m}$ comme dans le cas statique (section 1.2.2.1) ou dans une paramétrisation en fenêtres multiples (section 1.2.2.2). Pour traiter le problème inverse, on considère le cas pondéré $\mathbf{W}\mathbf{d} = \mathbf{W}\mathbf{G}\mathbf{m}$ avec \mathbf{W} une matrice diagonale dont les éléments W_{ii} donnent le poids associé au i -ème échantillon de donnée. L'équation (1.25)

devient alors :

$$\tilde{\mathbf{m}} = (\mathbf{G}^t \mathbf{W}^2 \mathbf{G} + \lambda^2 \mathbf{\Gamma}^t \mathbf{\Gamma})^{-1} \mathbf{G}^t \mathbf{W}^2 \mathbf{d}_{\text{obs}} \quad (1.26)$$

Cette équation est peu utilisée en pratique car elle aboutit souvent à des solutions incorporant du glissement dans la direction négative (c.-à-d. dans le sens opposé au glissement moyen sur la faille). Même si l'existence d'un tel phénomène est débattue, il est difficile d'imaginer une inversion radicale de la direction de glissement dans un environnement sous contrainte tel que la croûte terrestre. Pour limiter de telles oscillations du modèle, on intègre alors des contraintes de positivité : la minimisation de l'équation (1.25) peut alors être résolue en utilisant une méthode d'optimisation comme les moindres carrés non-négatifs, les gradients conjugués ou le recuit simulé (Lawson and Hanson, 1995 ; Tarantola, 2005).

La solution de l'équation 1.25 est un compromis entre l'ajustement des données $\|\mathbf{d}_{\text{obs}} - \mathbf{G}(\mathbf{m})\|_2^2$ et la régularisation du modèle $\|\mathbf{\Gamma}\mathbf{m}\|_2^2$ dont le poids relatif est contrôlé par le paramètre d'amortissement (λ). Le choix de λ a donc un impact direct sur la solution. Comme illustré sur la Figure 10, un λ^2 élevé aboutira à un modèle très lisse alors qu'un λ^2 plus faible renforcera l'ajustement des données. L'approche la plus répandue consiste à calculer la courbe en L de l'écart aux données $\|\mathbf{d}_{\text{obs}} - \mathbf{G}(\mathbf{m})\|_2^2$ en fonction de $\|\mathbf{\Gamma}\mathbf{m}\|_2^2$. On choisira alors une valeur de λ au coin de la courbe (offrant un compromis acceptable). Ce choix reste cependant relativement arbitraire et a un impact important sur le modèle obtenu (cf., Causse et al., 2010).

1.3.2 Approche Bayésienne

La régularisation de Tikhonov est un outil pratique pour résoudre rapidement l'inversion du glissement comme un problème d'optimisation. Cette approche repose cependant sur un amortissement du modèle qui n'a pas de réelle base physique. Cette régularisation peut par ailleurs avoir un impact important sur la solution (cf., Figure 10). L'approche Bayésienne aborde différemment le problème de la non-uniquité de la solution. L'idée est de caractériser l'ensemble des modèles pouvant expliquer les données au regard des différentes sources d'incertitudes et de notre connaissance *a priori* sur le modèle. L'ensemble des modèles obtenus est alors présenté comme la solution du problème inverse.

Cette approche repose sur le théorème de Bayes permettant de caractériser la densité de probabilité *a posteriori* du modèle \mathbf{m} étant données nos observations \mathbf{d}_{obs} :

$$p(\mathbf{m} | \mathbf{d}_{\text{obs}}) = \frac{p(\mathbf{d}_{\text{obs}} | \mathbf{m}) p(\mathbf{m})}{p(\mathbf{d}_{\text{obs}})} \quad (1.27)$$

Dans cette équation, $p(\mathbf{m})$ est la distribution de probabilité représentant nos connaissances *a priori* sur le modèle \mathbf{m} . Le terme $p(\mathbf{d}_{\text{obs}} | \mathbf{m})$ est la fonction de vraisemblance des données, représentant la plausibilité de nos observations \mathbf{d}_{obs} pour différents modèles \mathbf{m} . Même si la vraisemblance des données est ici une fonction de \mathbf{m} , il ne s'agit pas d'une densité de probabilité sur \mathbf{m} (son intégrale en fonction de \mathbf{m} n'est d'ailleurs pas nécessairement unitaire). Le dénominateur dans l'équation 1.27 est une constante de normalisation que l'on peut définir comme :

$$p(\mathbf{d}_{\text{obs}}) = \int p(\mathbf{d}_{\text{obs}} | \mathbf{m}) p(\mathbf{m}) d\mathbf{m} \quad (1.28)$$

Dans un cadre Bayésien, la solution du problème est donc la distribution de probabilité *a posteriori* $p(\mathbf{m}|\mathbf{d}_{\text{obs}})$. Cette distribution caractérise l'information sur le modèle \mathbf{m} étant données les observations \mathbf{d}_{obs} , la formulation du problème direct $\mathbf{G}(\mathbf{m})$, les incertitudes associées et nos hypothèses *a priori* sur le modèle. Formellement, on peut réécrire le problème direct en considérant les incertitudes associées :

$$\mathbf{d}_{\text{obs}} = \mathbf{G}(\mathbf{m}) + \mathbf{e}_d + \mathbf{e}_p \quad (1.29)$$

où \mathbf{e}_d représente l'incertitude sur les données (c-à-d., l'erreur de mesure) et \mathbf{e}_p correspond à l'incertitude associée au problème direct (liées aux imprécisions de modélisation). Bien que l'incertitude sur le problème direct \mathbf{e}_p soit généralement négligée, son amplitude peut être plus importante que l'incertitude \mathbf{e}_d liée aux données. \mathbf{e}_p peut provenir d'imprécisions dans le modèle de Terre utilisé pour calculer les fonctions de Green, d'une géométrie de faille trop simpliste ou d'approximations lors de la paramétrisation du processus de rupture (cf., section 1.2). Les incertitudes \mathbf{e}_d et \mathbf{e}_p sont couramment considérées comme Gaussiennes (un choix qui peut être justifié via le principe d'entropie maximale étant données les covariances correspondantes ; Jaynes, 2003). La fonction de vraisemblance $p(\mathbf{d}_{\text{obs}}|\mathbf{m})$ dans l'équation (1.27) peut alors s'écrire (Tarantola and Valette, 1982) :

$$p(\mathbf{d}_{\text{obs}}|\mathbf{m}) = \frac{1}{(2\pi)^{N/2} |\mathbf{C}_\chi|^{1/2}} e^{-\frac{1}{2} [\mathbf{d}_{\text{obs}} - \mathbf{G}(\mathbf{m})]^t \mathbf{C}_\chi^{-1} [\mathbf{d}_{\text{obs}} - \mathbf{G}(\mathbf{m})]} \quad (1.30)$$

où N est le nombre de données (la taille du vecteur \mathbf{d}_{obs}) et \mathbf{C}_χ est la matrice de covariance définie par :

$$\mathbf{C}_\chi = \mathbf{C}_d + \mathbf{C}_p \quad (1.31)$$

où \mathbf{C}_d et \mathbf{C}_p sont les matrices de covariances associées à \mathbf{e}_d et \mathbf{e}_p , respectivement. En utilisant cette forme gaussienne de la fonction de vraisemblance, l'écart aux données est caractérisé par une norme L^2 comme dans l'équation (1.23). La matrice de covariance \mathbf{C}_d associée aux incertitudes observationnelles \mathbf{e}_d peut prendre différentes formes suivant les données considérées. Ainsi par exemple, dans le cas de données sismologiques, \mathbf{C}_d caractérise le niveau de bruit à chaque station ainsi que la corrélation temporelle des données filtrées (voir par exemple Duputel et al., 2012b). Comme on le verra dans le Chapitre 3, il est possible de construire une matrice de covariance \mathbf{C}_p associée aux incertitudes sur le problème direct, en particulier en ce qui concerne les imprécisions du modèle de Terre (Duputel et al., 2014) et de la géométrie de faille (Ragon and Simons, 2018).

On considère maintenant le cas linéaire (comme dans les sections 1.2.2.1 et 1.2.2.2), avec un *a priori* Gaussien de la forme :

$$p(\mathbf{m}) = \frac{1}{(2\pi)^{M/2} |\mathbf{C}_m|^{1/2}} e^{-\frac{1}{2} (\mathbf{m} - \mathbf{m}_{\text{prior}})^t \mathbf{C}_m^{-1} (\mathbf{m} - \mathbf{m}_{\text{prior}})} \quad (1.32)$$

où M est le nombre de paramètres du modèle (la taille du vecteur \mathbf{m}), $\mathbf{m}_{\text{prior}}$ est le modèle moyen *a priori* et \mathbf{C}_m est la matrice de covariance *a priori*. Dans cette configuration, la distribution *a*

posteriori est Gaussienne (Tarantola and Valette, 1982) :

$$p(\mathbf{m}|\mathbf{d}_{\text{obs}}) = \frac{1}{(2\pi)^{M/2} |\tilde{\mathbf{C}}_m|^{1/2}} e^{-\frac{1}{2} (\mathbf{m} - \tilde{\mathbf{m}})^t \tilde{\mathbf{C}}_m^{-1} (\mathbf{m} - \tilde{\mathbf{m}})} \quad (1.33)$$

avec $\tilde{\mathbf{m}}$ le modèle moyen *a posteriori* (également le maximum *a posteriori*) et $\tilde{\mathbf{C}}_m$ et la covariance *a posteriori* qui s'écrivent respectivement :

$$\begin{aligned} \tilde{\mathbf{m}} &= (\mathbf{G}^t \mathbf{C}_\chi^{-1} \mathbf{G} + \mathbf{C}_m^{-1})^{-1} (\mathbf{G}^t \mathbf{C}_\chi^{-1} \mathbf{d}_{\text{obs}} + \mathbf{C}_m^{-1} \mathbf{m}_{\text{prior}}) \\ \tilde{\mathbf{C}}_m &= (\mathbf{G}^t \mathbf{C}_\chi^{-1} \mathbf{G} + \mathbf{C}_m^{-1})^{-1} \end{aligned} \quad (1.34)$$

Le cas linéaire Gaussien est utile car il offre une solution analytique à la formulation Bayésienne du problème inverse. Le terme \mathbf{C}_m^{-1} dans l'équation (1.34) agit comme un terme de régularisation. En considérant $\mathbf{m}_{\text{prior}} = \mathbf{0}$, $\mathbf{C}_\chi^{-1} = \mathbf{W}^2$ et $\mathbf{C}_m^{-1} = \lambda^2 \mathbf{\Gamma}^t \mathbf{\Gamma}$, on obtient d'ailleurs la solution moindre carrés régularisés de l'équation (1.26). Dans le cas linéaire Gaussien, il y a donc un lien très clair entre la formulation Bayésienne et la régularisation Tikhonov. Si la matrice de poids \mathbf{W} est choisie de façon ad hoc, on peut aussi voir le paramètre d'amortissement λ comme le rapport entre la variance *a priori* sur le modèle et l'incertitude sur les données. Dans le cas de l'inversion du glissement, cette forme analytique est souvent problématique car elle n'offre pas la possibilité d'imposer des contraintes de positivité. Or, une des informations dont nous disposons *a priori* est la positivité du glissement dans une direction donnée (à partir des observations longue période ou du glissement attendu à partir du mouvement relatif des plaques tectoniques). Certains de nos paramètres sont donc associés à une information *a priori* $p(\mathbf{m})$ non Gaussienne (typiquement une distribution uniforme définie positive), ne permettant pas d'utiliser les équations (1.33) et (1.34). Par ailleurs, il n'existe pas de forme analytique pour $p(\mathbf{m}|\mathbf{d}_{\text{obs}})$ dans le cas d'un problème non-linéaire comme lorsque nous inversons la vitesse de rupture et le temps de montée en incorporant des données cinématiques (cf., section 1.2.2.3).

Pour résoudre le problème dans le cas général (non-linéaire et/ou non-Gaussien), on peut utiliser une approche d'échantillonnage. C'est la stratégie employée dans le Chapitre 3 pour l'inversion statique et cinématique du glissement. L'échantillonnage Bayésien consiste à générer une population de modèles qui seront distribués statistiquement selon $p(\mathbf{m}|\mathbf{d}_{\text{obs}})$. La solution est alors composée d'un ensemble de modèles distribués avec une densité d'autant plus forte qu'ils expliquent les observations et qu'ils sont plausibles au regard de l'information *a priori* $p(\mathbf{m})$. La distribution *a posteriori* sera obtenue en générant un grand nombre d'échantillons de modèles pour lesquels nous évaluerons $p(\mathbf{m}|\mathbf{d}_{\text{obs}})$. Malgré un coût important en terme de calcul, cette approche est intéressante pour des problèmes mal posés car elle ne nécessite pas d'évaluer l'inverse de \mathbf{G} (ou de $\mathbf{G}^t \mathbf{G}$). Contrairement aux équations (1.26) et (1.34), il n'est donc pas nécessaire de régulariser l'inversion de \mathbf{G} en lissant le modèle. L'information contenue dans $p(\mathbf{m})$ doit comprendre les contraintes physiques s'appliquant au modèle. Prenons l'exemple d'un séisme pour lequel on souhaite trouver la distribution du glissement le long de la faille (dans la direction horizontale, le long de l'azimut de la faille). Si les analyses du tenseur moment sismique à longue période révèlent qu'il s'agit d'un séisme en décrochement de magnitude 7, on peut choisir une distribution *a priori* du type $p(\mathbf{m}) = \mathcal{U}(-1m, 15m)$, c'est à dire une distribution uniforme entre -1 et 15 mètres de glissement. On ne s'attend pas à avoir plus de 15 m de glissement pour

une telle magnitude, et on interdit à la faille de glisser significativement dans l'autre sens. Toutes les valeurs de glissement entre -1 m et 15 m sont quant à elles *a priori* équiprobables. Ce choix d'un *a priori* peu informatif permet de réduire l'espace des modèles à explorer tout en laissant les données guider la solution, ce qui fait l'une des forces de l'échantillonnage Bayésien. Pour plus d'information sur l'échantillonnage Bayésien, le lecteur peut se référer à Bishop (2006) ou dans le contexte de l'inversion du glissement Minson et al. (2013) et Dettmer et al. (2014).

1.3.3 Modélisation de données dans le domaine fréquentiel ou en ondelettes

Dans la plupart des approches d'inversion du glissement, le vecteur données \mathbf{d}_{obs} est construit en concaténant les formes d'ondes sismologiques avec les autres jeux de données (GNSS, InSAR, tsunami, etc.). Le problème peut également être résolu en représentant les données sismologiques dans le domaine fréquentiel (Olson and Anderson, 1988 ; Cotton and Campillo, 1995) ou après transformation en ondelettes (Ji et al., 2002). On démontre ici que la modélisation des données sismologiques dans ces différents domaines (temporel, fréquentiel ou en ondelettes) devraient théoriquement aboutir à des modèles de glissements identiques (Ide, 2007).

On commence par réécrire la fonction d'ajustement aux données dans l'équation (1.23) sous la forme :

$$\chi(\mathbf{m}) = [\mathbf{d}_{\text{obs}} - \mathbf{G}(\mathbf{m})]^t \mathbf{C}_\chi^{-1} [\mathbf{d}_{\text{obs}} - \mathbf{G}(\mathbf{m})] \quad (1.35)$$

Dans les développements qui suivent, l'inverse de la matrice de covariance \mathbf{C}_χ peut être invariablement remplacée par la matrice de poids \mathbf{W}^2 utilisée dans l'équation (1.26). A noter également que $\chi(\mathbf{m})$ apparaît dans la fonction de vraisemblance Gaussienne introduite dans l'équation (1.30). La transformée de Fourier ou la transformation en ondelettes peuvent être représentées sous la forme d'un opérateur linéaire \mathbf{T} . On peut alors définir :

$$\begin{aligned} \hat{\mathbf{d}}_{\text{obs}} &= \mathbf{T}\mathbf{d}_{\text{obs}} \\ \hat{\mathbf{G}}(\mathbf{m}) &= \mathbf{T}\mathbf{G}(\mathbf{m}) \end{aligned} \quad (1.36)$$

Dans cette équation, $\hat{\mathbf{d}}_{\text{obs}}$ and $\hat{\mathbf{G}}(\mathbf{m})$ correspondent à la transformée de Fourier (ou en ondelettes) des données \mathbf{d}_{obs} et des prédictions $\mathbf{G}(\mathbf{m})$ dans le domaine temporel. On considère ici que \mathbf{T} est un opérateur orthonormal, tel que :

$$\mathbf{T}^t \mathbf{T} = \mathbf{T} \mathbf{T}^t = \mathbf{I} \quad (1.37)$$

où \mathbf{I} est la matrice identité. C'est effectivement le cas pour la transformée de Fourier et les transformées en ondelettes utilisées habituellement dans l'inversion dans la source. On peut alors définir la fonction d'ajustement aux données dans le domaine fréquentiel (ou en ondelettes) comme :

$$\hat{\chi}(\mathbf{m}) = [\hat{\mathbf{d}}_{\text{obs}} - \hat{\mathbf{G}}(\mathbf{m})]^t \mathbf{C}_{\hat{d}}^{-1} [\hat{\mathbf{d}}_{\text{obs}} - \hat{\mathbf{G}}(\mathbf{m})] \quad (1.38)$$

où $\mathbf{C}_{\hat{d}}$ est la matrice de covariance en fréquence/ondelettes qui peut être obtenue à partir de la covariance \mathbf{C}_d dans le domaine temporel en utilisant :

$$\mathbf{C}_{\hat{d}} = \mathbf{T} \mathbf{C}_d \mathbf{T}^t \quad (1.39)$$

En insérant les équations (1.36) et (1.39) dans l'équation (1.38) puis en utilisant l'équation (1.37), on peut alors démontrer :

$$\begin{aligned}
 \hat{\chi}(\mathbf{m}) &= [\mathbf{Td}_{\text{obs}} - \mathbf{TG}(\mathbf{m})]^t \left(\mathbf{TC}_d \mathbf{T}^t \right)^{-1} [\mathbf{Td}_{\text{obs}} - \mathbf{TG}(\mathbf{m})] \\
 &= [\mathbf{d}_{\text{obs}} - \mathbf{G}(\mathbf{m})]^t \mathbf{T}^t \mathbf{TC}_d^{-1} \mathbf{T}^t \mathbf{T} [\mathbf{d}_{\text{obs}} - \mathbf{G}(\mathbf{m})] \\
 &= [\mathbf{d}_{\text{obs}} - \mathbf{G}(\mathbf{m})]^t \mathbf{C}_d^{-1} [\mathbf{d}_{\text{obs}} - \mathbf{G}(\mathbf{m})] \\
 &= \chi(\mathbf{m})
 \end{aligned} \tag{1.40}$$

L'égalité entre les fonctions d'ajustement $\chi(\mathbf{m}) = \hat{\chi}(\mathbf{m})$ pour un même modèle \mathbf{m} démontre que l'inversion de données dans le domaine temporel ou dans le domaine fréquentiel aboutissent théoriquement à des solutions identiques. Bien entendu, cela n'est valable que si les matrices de covariances \mathbf{C}_d et \mathbf{C}_d sont statistiquement équivalentes (c.-à-d., si l'équation (1.39) est vraie). Représenter les données en fréquence/ondelettes permet d'associer facilement différents poids à différentes bandes fréquentielles (Ji et al., 2002). En pratique, cela est fait en construisant \mathbf{C}_d dans le domaine fréquentiel. Il reste cependant possible de faire l'inversion dans le domaine temporel en utilisant l'équation (1.39) pour calculer la matrice de covariance \mathbf{C}_d correspondante.

1.4 Modèles de glissement : implications sur la physique des séismes

Les modèles de glissement obtenus grâce aux méthodes décrites ci-dessus présentent certaines propriétés génériques qui sont activement discutés dans la littérature. Dans cette section nous traitons en particulier du mode de propagation de la rupture, de la vitesse de rupture, de la chute de contrainte et du partitionnement énergétique des séismes.

Une propriété intéressante des modèles cinématiques est qu'ils montrent généralement l'existence d'un pulse de glissement correspondant à une bande cassante se propageant sur la faille avec une largeur étroite par rapport à la taille totale de la rupture (Heaton, 1990 ; Melgar and Hayes, 2017). Cette observation a des implications importantes sur l'état de contrainte et la friction des failles. Un exemple est montré sur la Figure 11 dans le cas du séisme d'Ezgeleh de 2017 en Iran ($M_W = 7.3$) présenté dans le Chapitre 3. Ce modèle montre qu'un pulse de glissement apparaît rapidement : en moins de 4 s et à moins de 7 km de l'épicentre (Figure 11d). Si ce pulse était contrôlée par la taille de la rupture, on devrait obtenir un temps de montée $r = 0.5 \times W/V_R$, avec W la largeur de la faille (Day, 1982). La Figure 11b montre qu'on a systématiquement $r < 0.5 \times W/V_R$, ce qui indique que le pulse apparaît avant que le front de rupture atteigne les bords de la faille. On parle alors de pulse de glissement autocicatrisant (Heaton, 1990). Ces pulses étroites par rapport à la taille de la rupture peuvent résulter de différents facteurs tels que les propriétés frictionnelles sur la faille, l'hétérogénéité de contrainte ou la réflexion d'ondes dans la zone de faible vitesse autour de la faille (Cochard and Madariaga, 1994 ; Peyrat et al., 2001 ; Huang and Ampuero, 2011). Ce mode de rupture en pulse a également des implications du point de vue de l'aléa sismique et de la génération des mouvements forts. Dans le cas du séisme d'Ezgeleh, la vitesse de glissement élevée, le temps de montée rapide et la forte directivité de la rupture vers le sud semblent avoir exacerbé les dégâts au sud de l'hypocentre

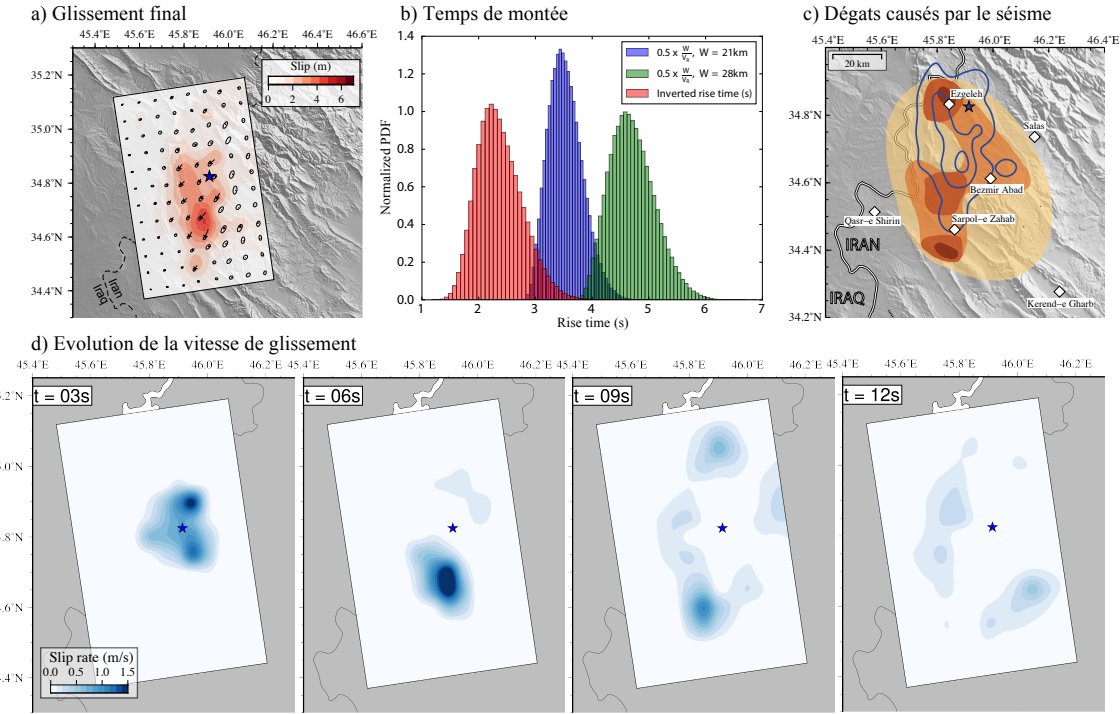


FIG. 11 – Pulse de glissement lors du séisme d’Ezgeleh de 2017 en Iran ($M_W = 7.3$). a) Glissement final. Les couleurs et les flèches indiquent l’amplitude et la direction du glissement. Les ellipses représentent 95% d’incertitude a posteriori. L’étoile indique la localisation de l’hypocentre. b) Comparaison des temps de montée estimés avec les prédictions de Day (1982). L’histogramme en rouge est la distribution a posteriori des temps de montée (rise-time r) moyennés le long de la rupture. Les histogrammes bleu et vert correspondent aux prédictions $r = 0.5 \times W/V_R$ avec V_R la vitesse de rupture estimée le long de la rupture et W la largeur de faille. Deux cas sont considérés $W = 21\text{ km}$ (correspondant à 3 sous-failles) et $W = 28\text{ km}$ (correspondant à 4 sous-failles). c) Dégâts causés par le séisme. Les couleurs indiquent le niveau de dégâts estimés par le service géologique iranien. Les couleurs plus foncées indiquent des dommages plus intenses. Les lignes bleues correspondent aux lignes de contour de 1.5 m du glissement final. d) Evolution de la vitesse de glissement sur la faille 3, 6, 9 et 12 s après le temps origine. Figure modifiée d’après Gombert et al. (2019) présenté dans le Chapitre 3.

(cf., Figure 11c). Ces pulses de glissement peuvent être difficiles à arrêter car ils impliquent des contraintes dynamiques importantes au niveau du front de rupture. Ces ruptures pourraient ainsi se propager dans des régions faiblement chargées ou re-rompre des zones de faille ayant récemment été cassées par un autre séisme (Vallée and Satriano, 2014).

La vitesse de rupture V_R est également un paramètre que l’on peut extraire des modèles cinématiques et qui peut fournir des informations intéressantes sur la dynamique de la rupture. Cependant, V_R et les temps de ruptures τ associés sont souvent estimés avec de fortes incertitudes. La Figure 12 montre un exemple de modèle cinématique Bayésien obtenu pour le séisme de Pedernales en 2016 ($M_W = 7.8$, Equateur, également présenté dans le Chapitre 3). On constate assez clairement un compromis entre le temps de rupture τ et le temps de montée r avec une corrélation négative entre ces deux paramètres. Cela est lié au fait que le temps central du pulse est relativement bien contraint alors que les données filtrées ont une sensibilité plus limitée au temps initial de glissement et à la durée du pulse. Si la vitesse de rupture locale est générale-

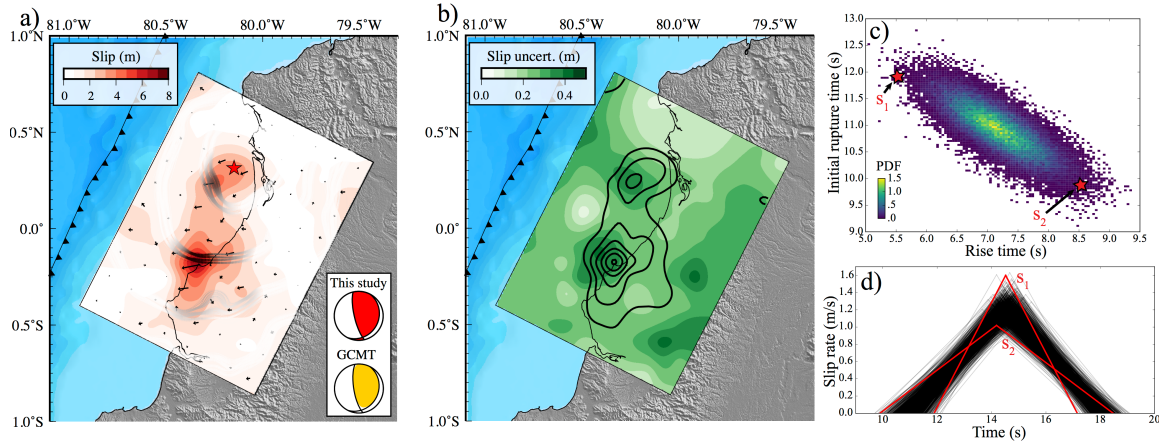


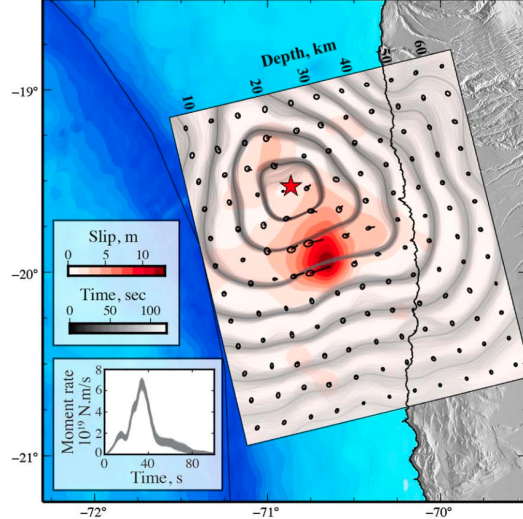
FIG. 12 – Modèle Bayésien du séisme de Pedernales de 2016 (Équateur, $M_W = 7.8$).
 a) Glissement final. Les couleurs et les flèches indiquent l'amplitude et la direction du glissement. Les lignes grises sont des fronts de rupture stochastiques déduits de l'ensemble a posteriori et affichés à 10, 20 et 30 s. L'étoile rouge indique la localisation de l'hypocentre. b) Incertitude sur le glissement final. c) Distribution marginale a posteriori de temps de montée (rise time) et de temps de rupture (rupture time) dans l'aspérité de glissement localisée proche de l'épicentre. d) Ensemble a posteriori des fonctions sources locales correspondantes. Les fonctions sources notés s_1 et s_2 correspondent aux temps de rupture et de montée indiqués avec des étoiles rouges sur la sous-figure c. Figure modifiée d'après Gombert et al. (2018b) présenté dans le Chapitre 3.

ment difficile à contraindre, la vitesse moyenne est généralement plus facile à caractériser (en particulier si des observations sont disponibles à faible distance épcentrale). Typiquement les vitesses de rupture observées sont de l'ordre de 70% de la vitesse des ondes S aux environs de la faille (Geller, 1976 ; Ide, 2007). Pour certains séismes, on observe cependant des vitesses de rupture dépassant la vitesses des ondes S. Cela est théoriquement possible pour des ruptures en mode II, c'est à dire lorsque la faille glisse dans la même direction que la propagation de la rupture. En pratique, ces ruptures supershear ont été observées principalement pour des séismes en décrochement (Frankel, 2004 ; Bouchon and Karabulut, 2008 ; Socquet et al., 2019 ; Bao et al., 2019) mais ont également été rapportées pour d'autres types de mécanismes (Zhan et al., 2014).

A des périodes inférieures à 2 s (c-à-d., des longueurs d'ondes inférieures à ~ 5 km), l'hétérogénéité du milieu et les complexités de la rupture produisent des formes d'ondes trop complexes pour être expliquées par un modèle simple (Kanamori and Brodsky, 2004). En particulier, la complexité des formes d'ondes à courte distance suggère une importante hétérogénéité du processus de rupture (Zeng et al., 1994). De part l'utilisation de données filtrées à basse fréquence et les contraintes de lissage spatial, beaucoup de modèles cinématiques peuvent être vus comme la distribution à grande longueur d'onde du glissement sur la faille. Cependant, les sources de radiation haute fréquence ne sont pas nécessairement colocalisées avec les zones de glissement important sur la faille. Ainsi par exemple, l'émission d'ondes à haute fréquence peut être associée à des variations de vitesse de rupture (Madariaga, 1977 ; Sato, 1994). L'endommagement dynamique causé par les ruptures sismiques autour de la faille peut également expliquer une partie du contenu haute fréquence observé à courte distance (Thomas et al., 2017). Au niveau des zones de subduction, plusieurs études rapportent l'existence de sources haute-fréquence dans la partie profonde du domaine sismogénique (Simons et al., 2011 ; Lay et al., 2012 ; Grandin et al.,

2015). Cette observation traduit potentiellement une augmentation du niveau d'hétérogénéité frictionnelle et de contrainte avec la profondeur (Huang et al., 2012 ; Lay, 2015).

a) Modèle de glissement



b) Chute de contrainte

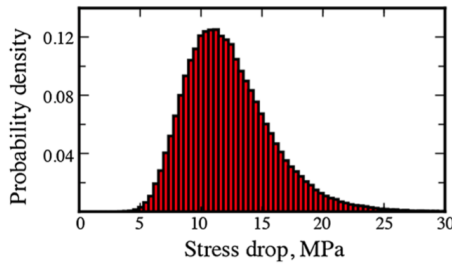


FIG. 13 – Modèle cinématique du séisme de Iquique de 2014 au Chili ($M_W = 8.1$).
a) Glissement final. Les couleurs et les flèches indiquent l'amplitude et la direction du glissement. Les ellipses représentent 95% d'incertitude a posteriori. Les lignes grises indiquent les fronts de rupture stochastiques déduits de l'ensemble des modèles a posteriori (les couleurs grises indiquent le temps de rupture correspondant). L'étoile rouge indique la localisation de l'hypocentre. L'insert en bas à gauche présente l'ensemble a posteriori des fonctions taux de moment. b) Distribution a posteriori de la chute de contrainte moyenne (voir équation 1.42). Modifié d'après Duputel et al. (2015) présenté dans le Chapitre 3.

La distribution de glissement finale donne une information directe sur la chute de contrainte causée par la rupture. La distribution finale de glissement est ainsi communément utilisée pour caractériser la chute de contrainte statique moyenne $\overline{\Delta\sigma}$ associée à un séisme. Une approche répandue en sismologie est basée sur le moment sismique M_0 et l'aire de la rupture A :

$$\overline{\Delta\sigma} = C \frac{M_0}{A^{3/2}} \quad (1.41)$$

où C est un paramètre géométrique dépendant de la forme de la zone rompue (Kanamori and Anderson, 1975). La détermination de la surface rompue A est cependant difficile en pratique. Par exemple, le lissage spatial ($\|\Gamma\mathbf{m}\|$ dans l'équation 1.25) induit des zones de glissement faible qui sont généralement mal contraintes. Pour limiter l'impact du lissage, l'aire A est souvent définie à partir des régions où le glissement excède une fraction s_{th} du glissement maximum.

Cette approche reste cependant problématique car la valeur estimée de $\overline{\Delta\sigma}$ dépend fortement de la valeur du seuil s_{th} choisie. Une approche alternative est de calculer le changement co-sismique de traction $\Delta\sigma$ au centre de chaque sous-faille (par exemple en utilisant la formulation de (Okada, 1992)). Dans le cas où la paramétrisation repose sur des fonctions de base continues et dérivables, on peut également évaluer la distribution continue de $\Delta\sigma$. On exprime ensuite la chute de contrainte moyenne (Noda et al., 2013) :

$$\overline{\Delta\sigma} = \frac{\int \Delta\mathbf{u} \Delta\sigma d\Sigma}{\int \Delta\mathbf{u} \mathbf{e}_1 d\Sigma} \quad (1.42)$$

où \mathbf{e}_1 est le vecteur unitaire le long de la direction moyenne de glissement, $\Delta\mathbf{u}$ est la distribution de glissement co-sismique. Un exemple d'estimation de $\overline{\Delta\sigma}$ basé sur cette approche est présenté pour le séisme d'Iquique en 2014 sur la Figure 13. Malgré une incertitude non-négligeable sur cette estimation, les valeurs estimées entre 5 et 25 MPa démontrent une source compacte pour ce séisme (la moyenne globale étant située aux alentours de 3 MPa (Allmann and Shearer, 2009)).

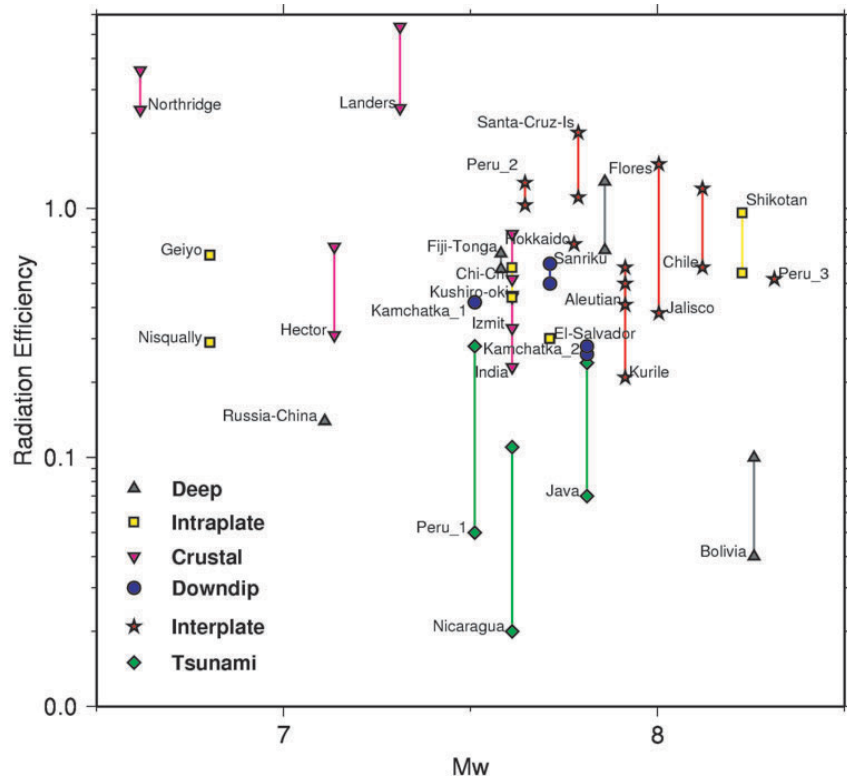


FIG. 14 – Efficacité de radiation estimée pour différents grands séismes. L'efficacité de radiation $\eta_R = \frac{E_R}{E_R + E_G}$ est présentée en fonction de la magnitude de moment M_W . Les différents symboles correspondent à différents types de séismes (profonds, interplaques, crustaux, etc.). Figure modifiée d'après Venkataraman and Kanamori (2004)

La distribution spatiotemporelle du glissement peut également être utilisée comme condition aux limites pour le calcul de l'évolution du changement de contrainte au cours de la rupture (Bouchon, 1997). Ce travail permet d'analyser les relations glissement-contrainte et d'explorer ainsi l'affaiblissement sur la faille. Plusieurs études montrent cependant que le détail de cette relation est mal contraint par les données filtrées et la paramétrisation utilisée lors de la modélisation cinématique (Guatteri and Spudich, 2000 ; Piatanesi et al., 2004 ; Spudich and

Guatteri, 2004). En revanche, l'énergie de fracture E_G , qui correspond à l'intégrale de la courbe contrainte-glisement au dessus du niveau de friction dynamique, est souvent bien caractérisée par les données (Tinti et al., 2005b). E_G correspond à l'énergie dissipée par de nombreux processus tels que la déformation plastique en tête de fissure, la création de microfissures en dehors de la faille, la pressurisation fluide, etc (Kanamori and Rivera, 2006). De façon similaire, les modèles de glissement peuvent permettre d'évaluer l'énergie radiée E_R par un séisme sous forme d'ondes sismiques (Rivera and Kanamori, 2005). En combinant ces différents observables, on peut ainsi évaluer le partitionnement énergétique des ruptures sismiques. Lors d'un séisme, l'énergie potentielle (énergie de déformation élastique et gravitationnelle accumulée lors de la période intersismique) est libérée sous forme d'énergie radiée E_R , d'énergie de fracture E_G et d'énergie frictionnelle E_F (Kanamori and Rivera, 2006). L'énergie frictionnelle E_F est associée au travail contre la résistance au glissement sur la faille et est principalement dissipée sous forme de chaleur. Peu d'information est disponible sur E_F car les données sismologiques ne fournissent pas d'information sur le niveau de contrainte absolu sur la faille. Pour cette raison, on s'intéresse généralement au partitionnement de l'énergie disponible à la propagation de la rupture $E_{T0} = E_R + E_G$ en terme d'énergie radiée E_R et d'énergie de fracture E_G . En particulier, on peut estimer le rapport entre l'énergie radiée E_R et cette énergie disponible E_{T0} à partir de différents paramètres dérivables à partir des modèles de glissement :

$$\eta_R = \frac{E_R}{E_R + E_G} \sim \frac{2\mu}{\Delta\sigma} \frac{E_R}{M_0} \quad (1.43)$$

où μ est le module de cisaillement autour de la faille, $\Delta\sigma$ la chute de contrainte moyenne (cf., équation 1.42) et M_0 le moment sismique. Ce paramètre η_R , appelé efficacité de radiation, est utile pour caractériser le comportement dynamique d'un séisme. Si $\eta_R = 1$, le séisme est très efficace pour radier de l'énergie sismique. Si $\eta_R = 0$, l'énergie disponible (E_{T0}) est dissipée mécaniquement et il n'y a pas d'énergie radiée. La Figure 14 montre η_R pour différents séismes pour lequel ce paramètre a pu être estimé. On constate que la plupart des séismes ont des valeurs de η_R supérieures à 0.25. Cependant, certains séismes ont une très faible efficacité de radiation ($\eta_R < 0.25$). C'est le cas pour les séismes tsunami qui correspondent à des ruptures très lentes générant des tsunamis anormalement importants par rapport à leur magnitude. Ces séismes seraient donc associés à des processus dissipatifs importants. Une interprétation possible est que la plupart des séismes tsunami impliquent des ruptures dans des sédiments déformables à faible profondeur et qu'une grande partie de l'énergie disponible est utilisée pour la déformation de ces matériaux. Certains séismes profonds (à des profondeurs > 600 km) sont également associés à un $\eta_R < 0.25$ comme le séisme de Bolivie en 1994. La mécanique de ces séismes est encore mal comprise mais ces événements pourrait impliquer une dissipation importante liée à de la déformation plastique (Kanamori et al., 1998). D'un autre côté, les valeurs élevées de η_R pour beaucoup de séismes superficiels suggèrent une faible énergie de fracture E_G avec des implications importantes concernant ces ruptures. Dans un modèle d'affaiblissement en vitesse, ces valeurs élevées de η_R suggèrent une faible distance d'affaiblissement (autrement dit un affaiblissement rapide en fonction du glissement (Kanamori and Brodsky, 2004)). Cela suggère également une certaine facilité pour l'emballage de ruptures (en anglais "runaway ruptures") qui grandissent facilement et sont difficiles à arrêter.

Détermination des caractéristiques principales de la rupture sismique

2.1 Caractérisation de la source à longue période : alerte rapide et complexité de la rupture.

Depuis les années 1990, un effort considérable a été effectué pour développer des outils dédiés à la quantification rapide des paramètres physiques de la source des séismes. Avec la disponibilité des données en temps réel, différents systèmes d'alerte ont été mis en place pour quantifier rapidement la taille d'un séisme à partir d'une quantité limitée de données (par exemple en utilisant les arrivées P des stations les plus proches de l'épicentre). Si ces approches sont fonctionnelles pour les séismes de taille modérée ($6.0 \leq M_w \leq 7.0$), elles sont beaucoup plus difficiles à mettre en place pour les plus grands séismes. Lors des très grands événements ($M_W > 7.0$), la faille peut rompre pendant plusieurs minutes de façon complexe, ce qui aboutit inévitablement à une variabilité des magnitudes estimées à courte période ou dans des bandes fréquentielles étroites. Le délai d'alerte peut être considérablement allongé par la durée de rupture elle-même. Si il existe des modèles permettant de prédire une magnitude à partir des premiers instants de rupture (e.g., Colombelli et al., 2014), plusieurs études récentes suggèrent que la croissance des ruptures est en réalité identique pour les grands et les petits séismes (e.g., Meier et al., 2016, 2017; Renou et al., 2019).

Le séisme de Sumatra en 2004 a véritablement démontré la nécessité de développer des méthodes permettant de déterminer rapidement les propriétés au premier ordre de la source des très grands tremblements de terre. Avec une rupture se propageant sur plus de 1300 km pendant environ 10 minutes, il a fallu plusieurs heures pour déterminer la magnitude de cet évènement. Parmi les différentes approches employées pour réduire ce délai, il a été proposé d'utiliser la phase W pour caractériser rapidement la source des grands séismes (Kanamori and Rivera, 2008). Il s'agit d'une phase sismique très longue période (entre 100 sec et 1000 sec) identifiée par Kanamori (1993) lors du séisme tsunami au Nicaragua en 1992. Cette phase présente plusieurs avantages. Tout d'abord, la phase W se propage rapidement (vitesses de groupe supérieures à 4.5 km/s), ce qui permet une détermination rapide des paramètres de source. Ensuite, son caractère très longue période permet de conserver une description relativement simple de la source sismique, même pour de très grands séismes. Enfin, la phase W correspond principalement à la superposition d'harmoniques de modes normaux peu affectés par les hétérogénéités superficielles de structure. Cela permet de considérer un modèle de terre à symétrie sphérique et ainsi d'accélérer le calcul des fonctions de Green nécessaires à l'estimation des paramètres de

la source (cf., Chapitre 1). Mon doctorat a principalement concerné l'utilisation de la phase W pour la détermination rapide des paramètres du tenseur moment sismique barycentrique (localisation spatio-temporelle, tenseur moment sismique ; Duputel et al., 2011, 2012c). Cette approche est aujourd'hui implantée dans plusieurs centres opérationnels (par exemple, NEIC-USGS, PTWC, JMA, CENALT) et fournit des paramètres de référence inclus dans différents catalogues (catalogue ComCat de l'USGS, catalogue ISC). La même approche a également été déployée à l'échelle régionale pour accélérer l'estimation des paramètres et s'intéresser à des séismes de magnitude plus faible (Zhao et al., 2017 ; Riquelme et al., 2018).

L'utilisation de données longue période permet une caractérisation robuste et systématique des paramètres de source à l'échelle globale. Ce double intérêt permet d'étudier les propriétés génériques des séismes et d'identifier les événements atypiques par rapport aux comportement classiques de rupture. La complexité et la diversité des phénomènes de ruptures apparaît d'autant plus visible qu'on s'intéresse aux grands séismes. Cette complexité de la source peut correspondre à une propagation de la rupture sur plusieurs segments (Duputel et al., 2012a ; Meng et al., 2012 ; Duputel and Rivera, 2017), à une complexité géométrique de la faille (Jolivet et al., 2015 ; Duputel et al., 2016) ou au déclenchement statique ou dynamique de plusieurs événements distincts (Lay et al., 2013). Parmi les exemples les plus récents, on peut citer le séisme de Samoa en 2009 ($M_W=8.1$), le séisme de Sumatra en 2012 ($M_W=8.6$) et le séisme de Kaikoura (Nouvelle Zélande) en 2016 ($M_W=7.8$). Cette complexité est abordée dans ce chapitre en utilisant différentes approches : (1) l'étude de la variabilité du délai barycentrique pour différents séismes, (2) le calcul de fonctions sources apparentes à partir des ondes de surface et (3) l'analyse en points sources multiples.

2.2 Utilisation du délai barycentrique pour identifier des séismes atypiques

La durée de rupture des grands séismes est souvent difficile à établir précisément. Leur histoire temporelle est parfois complexe et décroît souvent de façon graduelle, ce qui complique la détection de la fin de rupture. Dans l'article présenté ci-dessous, nous montrons que le délai barycentrique τ_c (i.e., "centroid time-delay" en anglais) fournit une estimation alternative à la durée de rupture. Le délai τ_c entre le temps origine et le temps barycentrique représente en effet une caractéristique temporelle au premier ordre de la rupture. On utilise les catalogues globaux phase W et Global Centroid Moment Tensor (GCMT) pour évaluer la relation entre τ_c et le moment sismique scalaire M_0 . Cette loi d'échelle très simple convient pour un grand nombre de séismes. Elle permet également d'identifier des séismes atypiques comme des événements impliquant un processus de rupture complexe ou encore des séismes caractérisés par des vitesses de rupture, des chutes de contrainte ou des rapports d'aspect peu communs.

L'article proposé ci-dessous a été publié en 2013 dans *Earth and Planetary Science Letters*. Ce travail a été effectué dans le cadre de mon post-doctorat au Caltech.



Using centroid time-delays to characterize source durations and identify earthquakes with unique characteristics

Zacharie Duputel ^{a,*}, Victor C. Tsai ^a, Luis Rivera ^b, Hiroo Kanamori ^a

^a Seismological Laboratory, California Institute of Technology, Pasadena, CA, USA

^b Institut de Physique du Globe de Strasbourg, UDS and EOST/CNRS UMR 7516, France



ARTICLE INFO

Article history:

Received 19 March 2013

Received in revised form

13 May 2013

Accepted 14 May 2013

Editor: P. Shearer

Available online 13 June 2013

Keywords:

rupture duration

tsunami earthquakes

transform fault

scaling laws

earthquake source observations

seismicity and tectonics

ABSTRACT

The relationship between M_0 and the rupture duration is often difficult to establish. This is particularly true for large earthquakes for which the moment rate functions (MRF) generally have complicated shapes, and the estimated durations can vary considerably depending on the methodology used to evaluate the MRF. In this work, we show that the centroid time-delay (τ_c) provides an alternative estimate of the source duration. Inverted MRFs often end gradually, making the end of coseismic rupture difficult to detect. In such cases, when the rupture duration is not well defined, the time-delay τ_c is a useful quantity to represent the first-order temporal characteristics of the rupture process. Variations in stress parameter $\Delta\sigma$ can be investigated by assuming a standard scaling relationship between the seismic moment M_0 and τ_c . This simple scaling relationship can also be used to identify unusual earthquakes, with unique source properties, such as events involving complicated rupture processes or earthquakes characterized by unusual rupture velocities, stress drops or aspect ratios.

© 2013 Elsevier B.V. All rights reserved.

1. Introduction

Scaling relations are often used in seismology to understand basic and common properties of the seismic source (Kanamori and Anderson, 1975). One of the most commonly used relationships is that between seismic moment (M_0) and rupture dimension (e.g., Aki, 1972; Romanowicz, 1992; Scholz, 1982), which can in turn be used to estimate common source properties (e.g., the stress drop). However, source dimensions are usually only indirectly estimated which can cause considerable uncertainties in the estimated source properties. Several studies have also focused on the link between M_0 and the corner frequency (f_c) of small earthquakes (e.g., Aki, 1967; Shearer et al., 2006). In such analyses, it is common practice to use seismic moment and corner frequency (f_c) measurements to estimate an average stress drop ($\Delta\sigma$). This estimate usually requires a number of assumptions about the source, such as the shape of the faulting area or the average rupture velocity (e.g., Brune, 1970). The resulting stress drop estimates usually vary over several orders of magnitude (Allmann and Shearer, 2009) and we may ask if this scatter is real or is a consequence of incorrect assumptions about the source model and of uncertainties in f_c estimates. Despite this variability in stress drop measurements, corner frequency observations are of primary importance as they contribute to various ongoing debates about earthquake self-similarity and regional variations of source properties. These

analyses are, however, more difficult to conduct for large earthquakes (i.e., $M_w \geq 6.5$), partly because source complexity is more apparent as magnitude increases.

Long-period seismology is a robust tool to characterize elastic structure (Dziewonski and Anderson, 1981) and quantify source parameters of earthquakes (Dziewonski et al., 1981; Kanamori and Given, 1981). With the advent of broad-band instrumentation (Wielandt and Stein, 1986; Wielandt and Streckeisen, 1982) and the expansion of global seismological networks, long-period observations today provide some of the most robust information on the characteristics of large earthquakes. In particular, we can now determine the relationship between M_0 and the source duration objectively and directly from seismograms. In this short note, we show that the centroid time-delay (τ_c) estimated from long-period source inversion provides a very straightforward and reliable estimate of the rupture duration. A scaling relation between the seismic moment M_0 and the centroid time-delay τ_c is discussed on the basis of an extensive set of earthquake data, including all events of $M_w \geq 6.5$ between 1990 and 2012. This scaling relation is used to study the relative variation of source properties and identify events with unique source characteristics.

2. Centroid time-delay measurements

Source inversion approaches such as the Global CMT (GCMT) or the W-phase source inversion algorithm (WCMT) use a very simple parameterization of the source with a small number of parameters

* Corresponding author. Tel.: +1 626 395 3801.

E-mail address: zacharie@gps.caltech.edu (Z. Duputel).

to be determined (Dziewonski et al., 1981; Kanamori and Rivera, 2008). The source is assumed to be a point source in space, with an isosceles-triangular moment rate function (MRF). The source parameters to be determined are then the elements of the seismic moment tensor, the point-source space-time coordinates (latitude, longitude, depth, time at the center of the MRF) and the rupture half-duration (i.e., half-width of the triangular MRF).

We use two catalogs that provide the point-source parameters of worldwide earthquakes of $M_w \geq 6.5$ between 1990 and 2012. The first catalog contains the WCMT solutions provided by Duputel et al. (2012) for 1990–2010 earthquakes (available at the url <http://wphase.unistra.fr>). We extended this catalog to 2011–2012 events using the same procedure. The second catalog is built with the GCMT solutions between 1990 and 2012 (Ekström et al., 2012; also available at the url: <http://www.globalcmt.org>). To focus on well-constrained point-source parameters, we rejected events whose signals are contaminated by large amplitude waveforms of a preceding event. These earthquakes, defined as “disturbed events” in Duputel et al. (2012), are listed in the Online Supplementary Information. Fig. 1a compares the moment magnitude estimates from the GCMT and WCMT catalogs for all events between 1990 and 2012. The reliability of such catalogs is well illustrated here with an absolute magnitude deviation smaller than 0.2 for 99% of the events.

The half-duration τ_h is generally poorly constrained in CMT inversions because of the long-period character of the waveforms used in these methods (i.e. periods of 40–350 s for GCMT, 100–1000 s for WCMT). In fact, in GCMT inversions, an empirical scaling between half-duration and seismic moment M_0 is assumed to set τ_h (Dziewonski and Woodhouse, 1983; Ekström, 1989; Ekström and Engdahl, 1989). The centroid time, on the other hand, is generally well constrained. In this study, we use the centroid time-delay τ_c as a proxy for the half-duration τ_h of the event. This assumption is explicitly used in the WCMT algorithm in which we assume $\tau_h = \tau_c$ after estimating τ_c . The time-delay, τ_c , is the difference between the MRF center time and the rupture nucleation time (i.e. the origin time). As we will see in the next section, the assumption $\tau_c = \tau_h$ is reasonable as long as the origin time, which is generally determined from body-wave travel-times, is accurate. The raw τ_c values in GCMT and WCMT solutions are generally given with respect to preliminary estimates of the origin time, which can be affected by large errors. To improve our measurements, we thus updated the time-delays τ_c using the origin times from the final USGS PDE catalog. Fig. 1b compares the resulting estimates from GCMT and WCMT catalogs for all events between 1990 and 2012. The total set of τ_c measurements is given in Table S2 of the Online supplementary information. Time-delays are compared with rupture duration estimates in the next section.

3. Comparison between centroid time-delay and rupture duration

The source duration, τ_d , is given by $\tau_d = t_e - t_0$ where t_0 is the time when the rupture on the fault begins (i.e. the origin time) and t_e is when the co-seismic slip motion ends. For the widely used Haskell model, $t_e = t_0 + L/V + \tau$ where L is the unilateral rupture length, V is the rupture speed, and τ is the rise-time of local slip function. The moment rate function (MRF) for this source is given by a trapezoid with a rise and fall time of τ , and a top flat portion of duration $L/V - \tau$. The rupture duration, τ_d , is usually determined from the MRF, $m(t)$, determined as part of the slip inversion using seismic waves.

On the other hand, the centroid time-delay is given by $\tau_c = \int (t - t_0) m(t) dt / \int m(t) dt$, where the time integrals are taken over the entire MRF. In GCMT and WCMT analyses, $m(t)$ is assumed

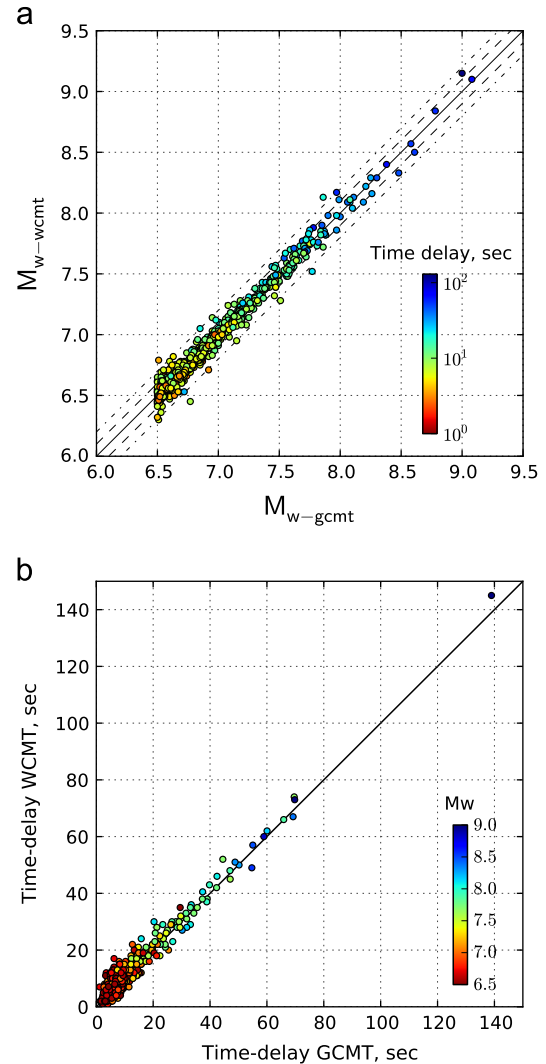


Fig. 1. An illustration of the consistency between GCMT and WCMT catalogs. (a) Comparison of moment magnitude estimates from the WCMT (M_{w-wcmt}) and GCMT (M_{w-gcmt}) catalogs. Symbols are colored according to the GCMT centroid time-delay. Dashed lines indicate ± 0.1 and dot-dashed lines ± 0.2 magnitude units. (b) Comparison of centroid time-delay estimates from WCMT and GCMT catalogs. Symbols are colored according to the GCMT moment magnitude. (For interpretation of the references to color in this figure legend, the reader is referred to the web version of this article.)

to be an isosceles triangle and the time at the center of the triangle (i.e., the centroid time t_c) is determined by inversion. The origin time, t_0 , is determined from high-frequency P-wave arrival times. If the centroid time-delay ($\tau_c = t_c - t_0$) is accurately determined, the source duration (τ_d) can be estimated by $\tau_d = 2\tau_c$. This assumption is reasonable since, for most earthquakes, $m(t)$ is well approximated by a symmetrical triangle, trapezoid, or a single sinusoid (e.g., 2010 Maule earthquake; 2011 Tohoku-oki earthquake; Lay and Kanamori, 2011).

Fig. 2a shows a comparison between GCMT and WCMT centroid time-delays and rupture duration measurements provided in the literature. We see that there is an overall consistency between duration and time-delay measurements. The centroid time-delay (τ_c) is a very straightforward observable and there is good agreement between τ_c measurements estimated from the GCMT and from the WCMT catalogs. This indicates a small uncertainty for τ_c , as expected for long-period robust CMT inversion techniques. In general, as long as the time-smoothed $m(t)$ is relatively simple and symmetric around the center, then $\tau_d = 2\tau_c$ is a good

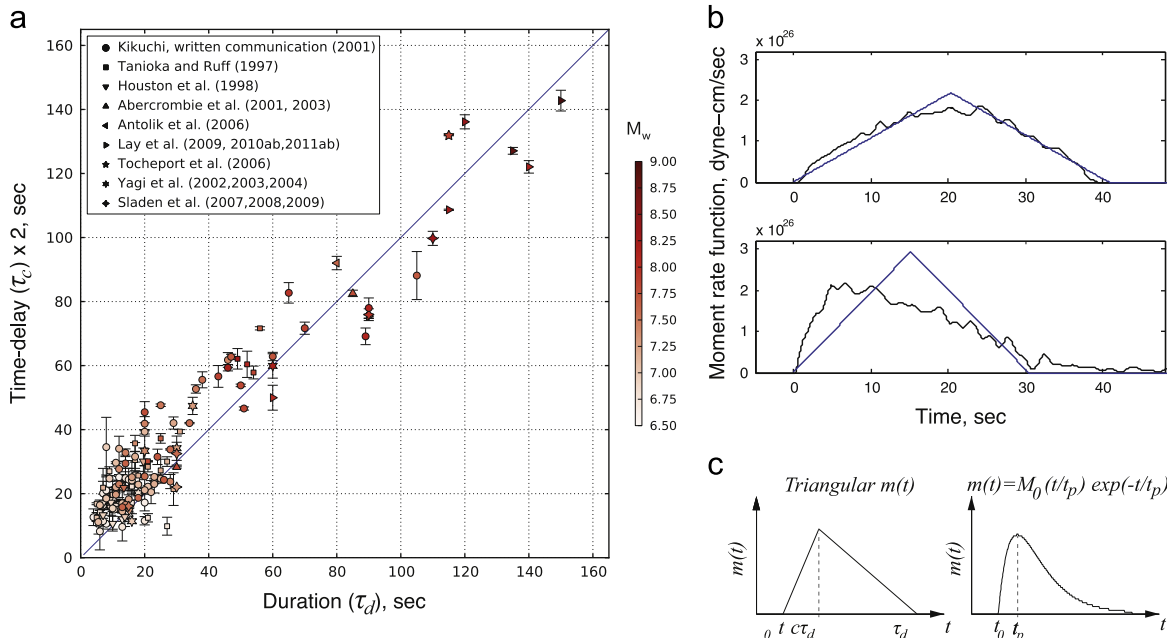


Fig. 2. Comparison between centroid time-delay (τ_c) and rupture duration (τ_d). (a) Rupture duration measurements provided in the literature for $M_w \geq 6.5$ earthquakes are compared with duration estimated from our time-shift measurements (Abercrombie et al., 2003, 2001; Antolik et al., 2006; Houston et al., 1998; Lay et al., 2011, 2010a, 2010b; Lay and Kanamori, 2011; Lay et al., 2009; Sladen, 2009a, 2009b, 2008a, 2008b, 2007a, 2007b; Kikuchi, written communication, 2001; Tanioka and Ruff, 1997; Tochepot et al., 2006; Yagi, 2004, 2003, 2002). Error bars represent the deviation between GCMT and WCMT measurements for each earthquake (the symbols correspond to the average time-shift). (b) Illustrations of moment rate functions (MRF, $m(t)$) for a triangular $m(t)$ (left) and $m(t) = M_0 (t/t_p) \exp(-t/t_p)$ (right). (c) Examples of time-shift measurement for synthetic MRF with different shapes. The time-shift is measured at the center of the isosceles triangle (blue) that best fit the MRF (black). (For interpretation of the references to color in this figure legend, the reader is referred to the web version of this article.)

approximation as illustrated in Fig. 2b. The time-delay τ_c at the center of the best-fitting triangle is thus a fairly effective and straightforward estimate of the rupture duration. On the other hand, the rupture duration estimates (τ_d) can be somewhat ambiguous. The MRFs often end gradually and in such cases, the rupture duration end (t_e) can be difficult to detect as shown in Fig. 2b (bottom). In such situations, when the rupture duration is not well defined, the time-delay τ_c is probably a more appropriate quantity to represent the average temporal characteristics of the rupture process.

There are exceptions, however, such as the 2004 Sumatra-Andaman Is. earthquake ($M_w = 9.2$). For this event, the MRF has a very long tail and $\tau_d \approx 3.5\tau_c$ instead of $\tau_d = 2\tau_c$ ($\tau_c = 139$ s from GCMT inversion and $\tau_c = 145$ s from WCMT). Assuming that the source time function $m(t)$ is a simple triangle with a duration τ_d and a maximum amplitude at a time $c\tau_d$, Fig. 2c (left) illustrates a schematic MRF of the Sumatra-Andaman Is. earthquake. In this case, we have a centroid time-delay given by $\tau_c = \tau_d(1 + c)/3$. We can also assume a long tailed MRF of the form $m(t) = M_0(t/t_p) \exp(-t/t_p)$ as shown in Fig. 2c (right) with a centroid time-delay of $\tau_c = 2t_p$. For the 2004 Sumatra-Andaman Is. earthquake, the MRF is not determined very well, which leads to a large variability of duration estimates between 400 s and 600 s. If we take $\tau_d = 500$ s, $c = 0.2$, $t_p = 100$ s from Ammon et al. (2005), τ_c should be about 200 s (i.e. $\tau_d \approx 2.5\tau_c$), which is still larger than WCMT and GCMT measurements (i.e., $\tau_d \approx 3.5\tau_c$). This event can, however, be considered as a very extreme case and $\tau_d = 2\tau_c$ can be considered as a good assumption for most earthquakes.

4. Absolute time-delay anomalies

In this section, we examine the difference between centroid time-delay measurements τ_c and predictions from scaling laws. This comparison is interesting because it allows for the identification

of anomalous earthquakes for which measurements and predictions significantly differ. The scaling relation used in WCMT inversions for the initial half-duration is (Duputel et al., 2012):

$$\tau_r = 1.2 \times 10^{-8} \times M_0^{1/3} \quad (1)$$

In this study, τ_r is a reference half-duration predicted for a given seismic moment M_0 (in dyne-cm). Fig. S1 in the Online Supplementary Information shows a comparison between rupture duration measurements (τ_d) and a scaling half-duration (τ_r). There are significant differences between τ_d and $2\tau_r$, unlike the general agreement between τ_d and $2\tau_c$ shown in Fig. 2. This indicates that rupture duration anomalies can be detected by looking at the difference $\Delta\tau = \tau_c - \tau_r$ between time-delay measurements τ_c and scaling predictions $\tau_r = 1.2 \times 10^{-8} \times M_0^{1/3}$. The values of $\Delta\tau$ are shown in Fig. 3 for all the events with $M_w \geq 6.5$ in chronological order for the period 1990–2012. Approximately 95% of the events are within ± 10 s, indicating that this scaling relationship represents the general behavior of moderate to large earthquakes. However, $\Delta\tau$ loses its significance for small earthquakes since it is generally small regardless of the source characteristics (e.g., $M_w \leq 7.1$ earthquakes have $\Delta\tau < 10$ s).

Here we focus on the events for which $\Delta\tau$ significantly deviates from 0. These earthquakes do not strictly follow the scaling relation, which suggests that each of them has unique source properties. Rupture duration anomalies can be interpreted as the result of (1) abnormal rupture or slip velocities, (2) stress-drop variations, (3) atypical fault geometries, or (4) complicated faulting processes (e.g., rupture partitioning in several subevents). Although measuring $\Delta\tau$ alone does not allow us to distinguish between these different possibilities, it provides a robust and straightforward way to identify events with peculiar characteristics.

Fig. 3 clearly shows that the two largest events of the 1990–2010 time-period have unique temporal characteristics. The 2004 $M_w = 9.2$ Sumatra-Andaman Is. earthquake has a large value of $\Delta\tau$. With a rupture duration of about 500 s, this event is indeed

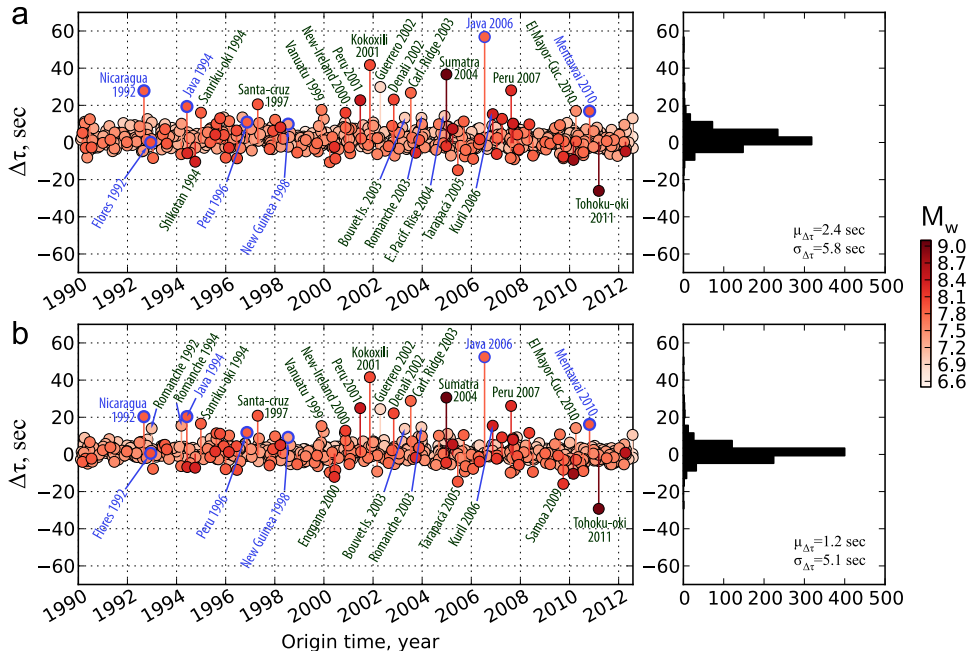


Fig. 3. Time-delay difference $\Delta\tau = \tau_c - \tau_r$ between measurements τ_c and predictions $\tau_r = 1.2 \times 10^{-8} \times M_0^{1/3}$ for the events which occurred during the period from January 1990 to September 2012. (a) Time-delays from the W phase catalog. (b) Time-delays from the Global CMT catalog. Tsunami earthquakes are highlighted in blue. Mean ($\mu_{\Delta\tau}$) and standard deviation ($\sigma_{\Delta\tau}$) of the $\Delta\tau$ distributions are shown on the histograms for both catalogs. (For interpretation of the references to color in this figure legend, the reader is referred to the web version of this article.)

the earthquake with the longest duration ever observed in the history of instrumental seismology (Ammon et al., 2005; Ishii et al., 2005; Lambotte et al., 2006; Tsai et al., 2005). On the other hand, the 2011 $M_w = 9.0$ Tohoku-oki earthquake is associated with a small $\Delta\tau$ and thus stands out as a very temporally compact event (Lay and Kanamori, 2011). Other earthquakes with high-stress drop can also be identified such as the $M_w = 8.2$ 1994 Shikotan event (Kikuchi and Kanamori, 1995) and the $M_w = 7.7$ 2005 Tarapacá earthquake (Kuge et al., 2010). Although the 2004 Sumatra-Andaman Is. and the 2011 Tohoku-oki earthquakes stand out because of their large absolute time-delay difference $|\Delta\tau| = |\tau_c - \tau_r|$ (i.e., $|\Delta\tau| > 20$ s), we note that the corresponding relative difference $|\Delta\tau|/\tau_r$ remains small because of the long duration expected for such large magnitude events (i.e., $|\Delta\tau|/\tau_r \leq 0.3$).

Another set of events that we can easily identify includes tsunami earthquakes. Defined initially by Kanamori (1972), these events produce unusually large tsunamis relative to their radiated seismic energy (Newman and Okal, 1998). They are currently interpreted as either having an anomalously slow rupture process or as being accompanied by underwater landslides and slumping. Events previously identified as tsunami earthquakes in the literature are highlighted in blue in Fig. 3. Four of them can be easily identified as $\Delta\tau$ outliers:

- (1) The first one is the 1992 Nicaragua earthquake ($M_w = 7.6$), which is a slow thrust event that probably occurred close to the middle America trench (Kanamori and Kikuchi, 1993; Satake, 1994).
- (2) The second outlier is the 1994 Java earthquake ($M_w = 7.8$). This event has a number of unusual characteristics and was a matter of debate in the literature. Abercrombie et al. (2001) argued that there is no evidence for slow and shallow rupture and interpreted the deficiency in high frequency as due to low average stress drop (~ 0.3 MPa). On the other hand, Polet and Thio (2003) proposed that it had a slow rupture velocity and/or a slow slip velocity.

- (3) The third event is the 2006 Java earthquake ($M_w = 7.7$) that has the largest $\Delta\tau$ anomaly of the 1990–2012 time-period. It is a classic example of a tsunami earthquake, with slow rupture velocity and large slip distributed close to the trench (Ammon et al., 2006).
- (4) The last one is the 2010 Mentawai earthquake ($M_w = 7.8$), for which the large value of $\Delta\tau$ is consistent with studies reporting a slow rupture process (Hill et al., 2012; Lay et al., 2011; Newman et al., 2011).

Some tsunami earthquakes, such as the 1992 Flores earthquake ($M_w = 7.7$) and the 1998 Papua-New-Guinea earthquake ($M_w = 7.0$), do not appear to have anomalously long rupture durations. This is consistent with observations from Polet and Kanamori (2000) indicating no particular high-frequency deficiency in the spectrum of these events. The unusually large tsunami amplitudes for these earthquakes can probably be explained by slumping or underwater landslides as suggested for the Flores event by Tsuji et al. (1995) and Hidayat et al. (1995), and for the Papua-New-Guinea earthquake by Heinrich et al. (2000) and Synolakis et al. (2002). For the 1996 Peru event ($M_w = 7.5$), the value of $\Delta\tau$ shows that the earthquake had a long duration but does not quite belong to the class of slow tsunami earthquakes (Ihmlé et al., 1998).

Although not classified as tsunami earthquakes, other events with anomalously long rupture duration can also be identified:

- (1) The 1994 Sanriku-oki earthquake ($M_w = 7.7$) is an interesting event with very large after-slip that lasted for about a year (Heiki et al., 1997). The long duration indicated by the large value of $\Delta\tau$ is consistent with a slow rupture initiation stage observed by Tanioka et al. (1996) and Nakayama and Takeo (1997).
- (2) The long duration of the 1997 Santa Cruz earthquake ($M_w = 7.8$) is also consistent with observations from Kaverina

- et al. (1998) that reported a low rupture velocity of about 1.9 km/s.
- (3) Another very interesting event is the April 18, 2002 Guerrero earthquake ($M_w = 6.7$), for which the estimated time-delay ($\tau_c \sim 30$ s) is nearly five times longer than what is expected from the scaling relation. This event can be interpreted as an aftershock of the large $M_w \sim 7.5$ slow-slip event in 2001–2002 and is deficient in high-frequency energy (Iglesias et al., 2003; Kostoglodov et al., 2003). This last observation, as well as the centroid location being close to the trench with the generation of a tsunami (which is quite surprising for such a small event), suggests a small tsunami earthquake-like event.

As proposed above, events with a complicated rupture process may also display abnormal time-delay values. Good examples are the $M_w = 7.9$ 2001 Kokoxili earthquake, the $M_w = 7.9$ 2002 Denali event and the $M_w = 7.2$ 2010 El Mayor–Cucapah earthquake (Eberhart-Phillips et al., 2003; Hauksson et al., 2010; Tocheport et al., 2006). These events are made of several subevents that involve large moment rate at a significant delay with respect to the origin time. Similarly, the rather long durations observed for the Peru earthquakes in 2001 ($M_w = 8.4$) and 2007 ($M_w = 8.0$), may be interpreted as a result of rupture partitioning into two subevents as reported by Sladen et al. (2010) and Lay et al. (2010a). Regarding the $M_w = 8.0$ 2000 New-Ireland earthquake, the large observed time-delays can probably be explained by the obvious source complexity of this event. This earthquake shows large differences between point-source and finite-fault inversion results (Duputel et al., 2012) and the occurrence of a late dip-slip subevent was also proposed (Earthquake Research Institute (ERI), 2000; Park and Mori, 2007). In a similar way, the small value of $\Delta\tau$ obtained by GCMT analysis for the 2009 Samoa earthquake can be seen as a consequence of its remarkable source complexity with two subevents having nearly opposite mechanisms (Lay et al., 2010c). The same interpretation can be made for the $M_w = 7.9$ 2000 Enggano earthquake that involved a combination of two subevents with strike-slip and thrust mechanisms (Abercrombie et al., 2003). The Samoa and Enggano earthquakes showed large differences between GCMT and WCMT solutions (Duputel et al., 2012) as well as important variations in estimated time-delays. This suggests that a single-point-source representation is not suitable for these events and that the estimated time-delays may therefore not be completely relevant.

Other events that stand out include oceanic fracture zone earthquakes such as the 2003 Carlsberg ridge earthquake ($M_w = 7.6$). The large value of $\Delta\tau$ that we obtained for this event is consistent with the long rupture duration observed by Antolik et al. (2006). Similar but smaller oceanic fracture zone earthquakes can also be identified in Fig. 3. These are the 2003 Bouvet Is. earthquake (April 17, $M_w = 6.5$), the 2004 East Pacific Rise event (November 28, $M_w = 6.6$) and the Romanche earthquakes in 1992 (December 26, $M_w = 6.8$), 1994 (March 14, $M_w = 7.0$) and 2003 (December 21, $M_w = 6.5$). As a result of their small magnitudes and associated time-delays, these earthquakes do not clearly stand out in Fig. 3. The discrepancies between measured (τ_c) and predicted (τ_r) time-delays for these events are discussed more in detail in the next section where we look at the normalized time-delay τ_c/τ_r .

5. Relative time-delay anomalies

In Fig. 3, time-delay anomalies are not scaled by event sizes. Thus, for small earthquakes, $\Delta\tau = \tau_c - \tau_r$ is generally small regardless of the source characteristics of the events. In other words, differences in source characteristics for small earthquakes do not show up in Fig. 3 (except for the $M_w = 6.7$ 2002 Guerrero

earthquake on April 18). Moreover, if we use $\Delta\tau$ as a variable, the distribution of time-delay anomalies is necessarily asymmetrical. Indeed, because of the time-delay positivity $\tau_c > 0$ and $\tau_r > 0$, there is a lower bound $\Delta\tau > -\tau_r$. This asymmetry in the distribution of $\Delta\tau$ will highlight events with long durations and de-emphasize temporally compact earthquakes. For instance, if we assume a $M_w = 7.7$ event, we have a prediction $\tau_r = 20$ s from Eq. (1) and the minimum expected time-delay anomaly will be $\Delta\tau_{min} = -20$ s. On the other hand, $\Delta\tau$ can be very large such as for the $M_w = 7.7$ 2006 Java earthquake, for which we have $\Delta\tau \approx 55$ s. To obtain a symmetrical distribution of time-delay anomalies, in this section we focus on the difference between the logarithms of τ_c and τ_r , i.e., $\log(\tau_c/\tau_r)$.

As discussed above, an alternative way to show the scaling relation is to scale τ_c by τ_r , and plot $\tau_c/\tau_r = \tau_c/(1.2 \times 10^{-8} \times M_0^{1/3})$ on a logarithmic scale as a function of M_0 . Fig. 4 shows τ_c and τ_c/τ_r as a function of M_0 for all $M_w \geq 6.5$ earthquakes from 1990 to 2012. As expected, we notice that the distribution of τ_c/τ_r on a log-scale is much more symmetrical than that of $\Delta\tau$ in Fig. 3a and b. It has been observed, however, that τ_c has a small (1–2 s) bias towards positive values (Dziewonski and Woodhouse, 1983), perhaps due to the different Earth models used by USGS PDE and GCMT catalogs (Smith and Ekström, 1995). To test the effect of this bias, in Fig. S2, we plot the same τ_c/τ_r as in Fig. 4 but account for a 1 s offset. As shown, there is no significant difference between Fig. S2 and Fig. 4, although small shifts are visible for the smallest events.

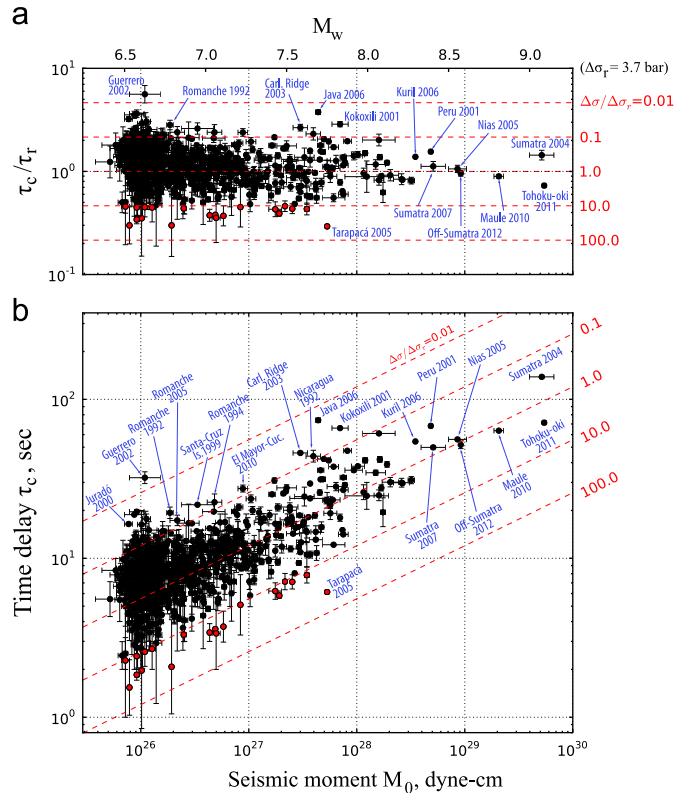


Fig. 4. Ratios τ_c/τ_r of observed time-delays τ_c to predictions $\tau_r = 1.2 \times 10^{-8} \times M_0^{1/3}$ for the events which occurred during the period from 1990 to 2012. (a) Relative time-delays τ_c/τ_r and (b) measured time-delays τ_c are shown as a function of the seismic moment. Black circles correspond to the geometric mean between GCMT and WCMT observations while error bars represent the deviation between GCMT and WCMT measurements for each earthquake. Stress circles indicate events for which $\Delta\sigma/\Delta\sigma_r > 10$ (also shown in Fig. 5). Event names are given for obvious τ_c/τ_r outliers and large events. Earthquakes with large τ_c/τ_r values that are not named for $M_0 < 2 \cdot 10^{26}$ dyne-cm, are identified in Fig. 6. (For interpretation of the references to color in this figure legend, the reader is referred to the web version of this article.)

In the following, we will therefore focus only on the raw time-delay measurements presented in Fig. 4. Notice that for smaller earthquakes ($M_w \leq 6.5$), a diagram similar to Fig. 4 is often shown for the corner frequency f_c as a function of M_0 (Mayeda and Malagnini, 2007). To facilitate comparison of Fig. 4 with such corner frequency diagrams, the scaling laws for the corner frequency and the centroid time-delay are discussed in the next paragraph.

If the centroid time-delay τ_c is taken as a proxy for the half-duration t_h (i.e., $\tau_c = t_h$), the spectrum of the triangular moment rate function (MRF) assumed in GCMT and WCMT inversions can be written as

$$\hat{m}(f) = M_0 \left[\frac{\sin(\pi f \tau_c)}{\pi f \tau_c} \right]^2, \quad (2)$$

where f is frequency and M_0 is the seismic moment. The corner frequency f_c for the moment rate spectrum (Eq. (2)) is given by

$$f_c = \frac{1}{\pi \tau_c}. \quad (3)$$

Before 2004, the MRF used in GCMT inversions was modeled as a boxcar, for which the spectrum decays as f^{-1} at high frequency in contrast to the f^{-2} decay for the triangular MRF. The corner frequency for a boxcar MRF spectrum is, however, identical to that of the triangular MRF (i.e., $f_c = 1/\pi \tau_c$). The corner frequency f_c for a Brune-type scaling relation is given by (Brune, 1971, 1970)

$$f_c = c_1 \beta \left(\frac{\Delta \sigma}{M_0} \right)^{1/3} \quad (4)$$

where c_1 is a scaling parameter, β is a representative shear wave speed and $\Delta \sigma$ is a reference scaling parameter with units of stress. The scaling constant in Brune's model is $c_1 = 0.49$ (if all quantities are in c.g.s. units). We might call $\Delta \sigma$ a stress parameter as proposed, for example, by Boore (1983). The stress parameter $\Delta \sigma$ is not the stress drop of the earthquake, but in studies of small earthquakes where the assumptions of a circular fault and a constant rupture speed are considered approximately valid, it is often used as a proxy for the earthquake stress drop. For the large earthquakes discussed in this paper, the stress drop depends on the geometry of the fault and the slip distribution, and cannot be approximated by the stress parameter. Combining Eqs. (3) and (4), we obtain

$$\tau_c = \frac{1}{c_1 \pi \beta} \left(\frac{M_0}{\Delta \sigma} \right)^{1/3}. \quad (5)$$

Comparing this with Eq. (1) and assuming $\beta = 3.5$ km/s, we find that the stress parameter $\Delta \sigma$ for our data set is $\Delta \sigma \equiv \Delta \sigma_r = 3.7$ bar (0.37 MPa).

In Fig. 4, the stress parameter ratio $\Delta \sigma / \Delta \sigma_r = (\tau_r / \tau_c)^3$ is indicated for reference. The stress parameter $\Delta \sigma$ varies mainly over 2 orders of magnitude, which is smaller than the 3–4 orders of magnitude variability observed for stress-drop measurements from corner frequencies (Allmann and Shearer, 2009; Shearer et al., 2006). Events identified previously in Fig. 3 are also visible here:

- (1) Tsunami earthquakes such as the 1992 Nicaragua earthquake and the 2006 Java earthquake.
- (2) The $M_w = 6.7$ 2002 Guerrero earthquake on April 18 can also be easily identified with a value of $\tau_c / \tau_r \sim 5$.
- (3) Earthquakes showing complicated rupture process such as the 2001 Kokoxili earthquake and the 2010 El-Mayor–Cucapah event.

Earthquakes associated with small values of τ_c / τ_r or large stress parameter ratios $\Delta \sigma / \Delta \sigma_r$ can also be identified in Fig. 4. Such temporally compact events can possibly be associated with

high stress drop, as is certainly the case for the 2005 Tarapacá earthquake (Kuge et al., 2010). Since all events with $\tau_c / \tau_r < 0.46$ (i.e., red circles for $\Delta \sigma / \Delta \sigma_r > 10$) correspond to intermediate to large depth earthquakes, another possible explanation is an effect of the increase of shear wave velocity (β) with depth as suggested previously by Vidale and Houston (1993). This is illustrated in Fig. 5a, on which we see that most events with depth larger than 80 km (i.e., below the lithosphere) correspond, in average, to relatively small values of τ_c / τ_r . To remove this effect, we can use PREM velocities (Dziewonski and Anderson, 1981) in Eq. (5) to adjust τ_r for intermediate to large depth events. The resulting corrected τ_c / τ_r ratios, shown in Fig. 5b, suggest that the τ_c / τ_r decrease seen in Fig. 5a (i.e., assuming $\beta = 3.5$ km/s) can be explained by the increase of β as a function of depth.

Another class of events that clearly stands out in Fig. 4 is oceanic transform strike-slip earthquakes such as the 2003 Carlsberg ridge earthquake ($M_w = 7.6$). The normalized time-delays τ_c / τ_r obtained for strike-slip earthquakes are presented in Fig. 6. In this figure we see that events showing anomalously large values of τ_c / τ_r are generally oceanic fracture zone earthquakes. This observation is consistent with observations from Pérez-Campos et al. (2003), who report some anomalous oceanic strike-slip events with large time-delays compared to their seismic moment. Using techniques developed initially by Silver and Jordan (1983), anomalously long rupture processes are also reported by Ihmlé and Jordan (1994) and McGuire et al. (1996), who interpret these observations as slow precursory slip preceding some oceanic fracture zone earthquakes. This interpretation is, however, disputed by Abercrombie and Ekström (2003, 2001) because of large uncertainties due to mismodeling (epicenter mislocation, inaccuracy of the Earth model, etc.). Likewise, the large positive centroid time-delays measured at long-period do not support such slow slip precursors but rather abnormal long rupture durations. Consistent with Beroza and Jordan (1990), Pérez-Campos et al. (2003) describe these long-duration oceanic earthquakes as having anomalously low

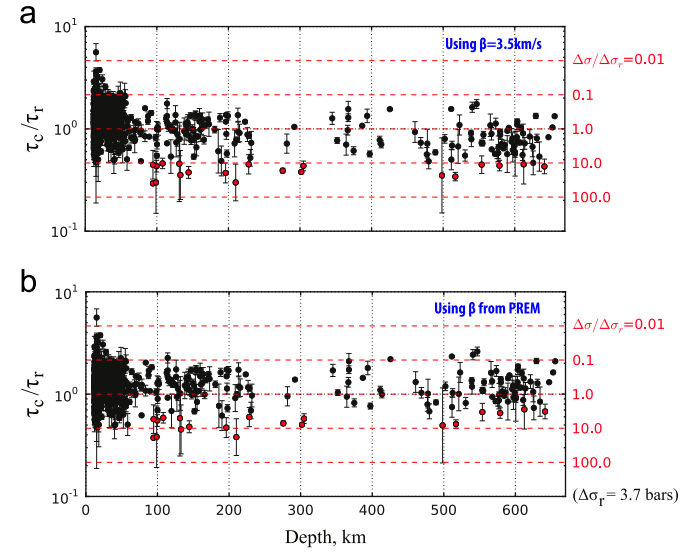


Fig. 5. Ratios τ_c / τ_r of observed time-delays τ_c to predictions τ_r for $M_0 \geq 6.5$ earthquakes from 1990 to 2012. The relative time-delays τ_c / τ_r are depicted (a) using $\tau_r = 1.2 \times 10^{-8} \times M_0^{1/3}$ (i.e., $\beta = 3.5$ km/s) and (b) by correcting τ_r from the shear-velocity variations as a function of depth (using values of β from the PREM model). Circles correspond to the geometric mean between GCMT and WCMT observations while error bars represent the deviation between GCMT and WCMT measurements for each earthquake. Red circles indicate events for which $\Delta \sigma / \Delta \sigma_r > 10$ in (a) and Fig. 4. (For interpretation of the references to color in this figure legend, the reader is referred to the web version of this article.)

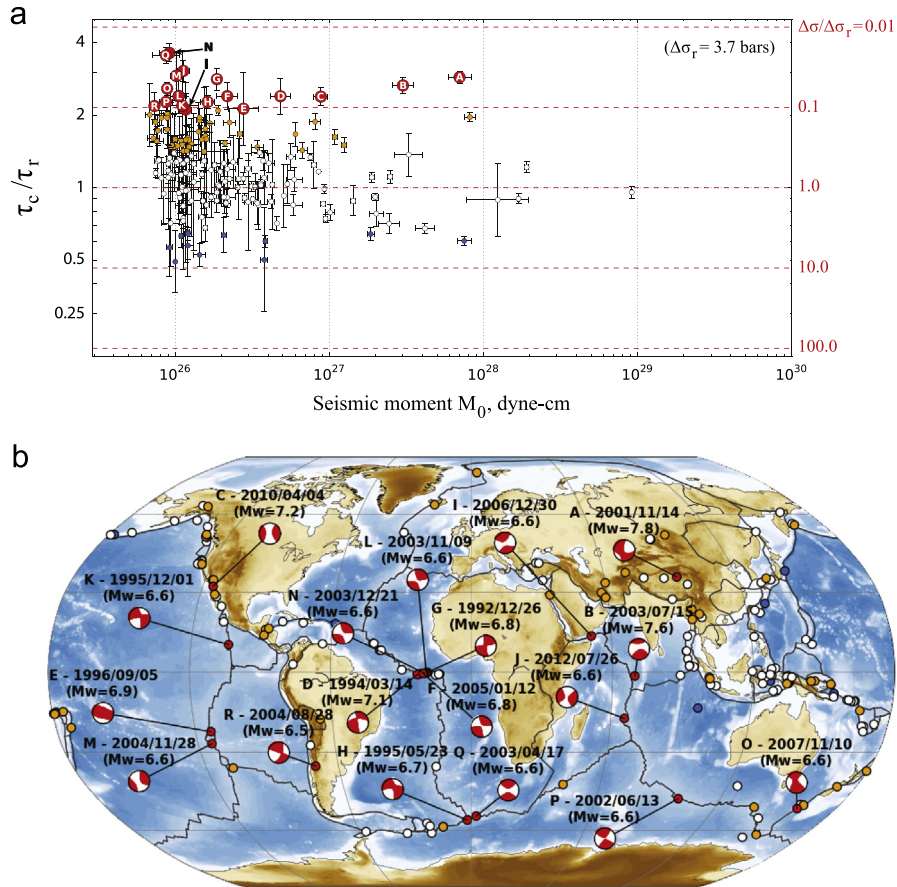


Fig. 6. Normalized time-delays τ_c/τ_r for strike-slip earthquakes for the events which occurred during the period from 1990 to 2012. (a) Similar to Fig. 4a but for strike-slip events only. (b) Map of normalized time-delays τ_c/τ_r for strike-slip earthquakes. Mechanisms with $\Delta\sigma/\Delta\sigma_r < 0.1$ bar identified with letters in (a) are shown. Circles in (a) and (b) are colored as a function of the stress parameter ratio $\Delta\sigma/\Delta\sigma_r$. (For interpretation of the references to color in this figure legend, the reader is referred to the web version of this article.)

apparent stresses as a consequence of slow rupture processes. Contrary to these observations, Choy and Boatwright (1995) and Choy and McGarr (2002) report high apparent stresses for oceanic transform zone earthquakes. Unfortunately, observations based on body-waves are subject to considerable uncertainties because of near-nodal take-off angles of body waves for strike-slip earthquakes (Schramm and Stein, 2009). The long rupture duration for some fracture zone earthquakes is, however, supported here by both W phase (WCMT) and fundamental-mode surface wave (GCMT) centroid time-delay measurements. Consistent with these observations, the finite-fault model obtained by Antolik et al. (2006) for the $M_w = 7.6$ Carlsberg ridge earthquake shows a long rupture process. Instead of a slow rupture component, the results of Antolik et al. (2006) indicate that this long duration is simply due to a very long rupture length. The finite-fault model proposed by Abercrombie and Ekström (2001) for the 1994 Romanche earthquake ($M_w = 7.1$) also shows an elongated rupture process involving normal or even high rupture velocities. These unusual aspect ratios can be explained by the location of these events on active ridges, where the seismogenic zone is restricted to very shallow depths because of the high temperature of the oceanic lithosphere. Such elongated rupture scenarios are consistent with large time-delay estimates that are mostly controlled by the fault length. This interpretation of elongated ruptures is also compatible with large corner frequencies and high stress drop observations reported by Allmann and Shearer (2009) that are most sensitive to the fault width (which can be small if the seismogenic zone is restricted to shallow depths).

6. Conclusions

In this short note, we show that the centroid time-delay provides a very straightforward and reliable estimate of the rupture duration. In some cases, such as for long-tailed moment-rate functions, the centroid time-delay provides a more meaningful way of quantifying the sources' temporal characteristics than other possible definitions of duration. We also present a simple scaling relationship between the seismic moment and the centroid time-delay, both of which can be determined accurately and objectively from the analysis of long-period seismic waves. This standard scaling relationship can be used to estimate the variability of the stress parameter and to identify events with unique source properties. Different types of unusual earthquakes can be identified from their anomalous centroid time-delays. First of all, events involving slow rupture processes, such as tsunami earthquakes, generally show larger centroid time-delay estimates than expected from their seismic moments (e.g., the 2006 Java event). Secondly, anomalous time-delays can also be observed for events with unusual aspect ratios. For instance, some oceanic fracture zone earthquakes involving elongated faults but ordinary rupture velocities can be associated with anomalously long time-delays (e.g., the 2003 Carlsberg ridge earthquake). Thirdly, high or low stress-drop earthquakes can induce significant time-delay variations. For example, high stress drop events can have small centroid time-shifts because these earthquakes generally have a temporally compact moment rate function (e.g., the 2011 Tohoku-oki earthquake). Also, earthquakes with complicated ruptures involving multiple sub-events, which often have a large moment

rate at a late stage of faulting, tend to have large time-shifts (e.g., the 2002 Denali earthquake). Despite these various interpretations for rupture duration anomalies, the centroid time-delay/moment scaling relation is useful for identifying events with unusual characteristics. In this study, many interesting events, which have been debated in earthquake seismology for the last 2 decades, have been identified using this approach. This very simple and straightforward analysis also has practical applications, such as the rapid identification of tsunami earthquakes in real-time.

Acknowledgments

We thank Zhongwen Zhan, Gavin Hayes, Göran Ekström and an anonymous reviewer for their helpful suggestions. This work uses Federation of Digital Seismic Networks (FDSN) seismic data, CMT solutions from the Global CMT catalog and event origin times from the USGS PDE catalog. The Incorporated Research Institutions for Seismology (IRIS) Data Management System (DMS) was used to access the data. This work made use of the Matplotlib python library created by John D. Hunter.

Appendix A. Supplementary material

Supplementary data associated with this article can be found in the online version at <http://dx.doi.org/10.1016/j.epsl.2013.05.024>.

References

- Abercrombie, R.E., Antolik, M., Ekström, G., 2003. The June 2000 Mw7.9 earthquakes south of Sumatra: deformation in the India–Australia Plate. *J. Geophys. Res.* 108, 2018.
- Abercrombie, R.E., Antolik, M., Felzer, K., Ekström, G., 2001. The 1994 Java tsunami earthquake—slip over a subducting seamount. *J. Geophys. Res.* 106, 6595–6607.
- Abercrombie, R.E., Ekström, G., 2001. Earthquake slip on oceanic transform faults. *Nature* 410, 74–77.
- Abercrombie, R.E., Ekström, G., 2003. A reassessment of the rupture characteristics of oceanic transform earthquakes. *J. Geophys. Res.* 108, 2225.
- Aki, K., 1967. Scaling law of seismic spectrum. *J. Geophys. Res.* 72, 1217.
- Aki, K., 1972. Earthquake mechanism. *Tectonophysics* 13, 423–446.
- Allmann, B.P., Shearer, P.M., 2009. Global variations of stress drop for moderate to large earthquakes. *J. Geophys. Res.* 114, B01310.
- Ammon, C.J., Chen, J., Thio, H.K., Robinson, D., Ni, S., Hjörleifsdóttir, V., Kanamori, H., Lay, T., Das, S., Helmberger, D., Ichinoise, G., Polet, J., Wald, D., 2005. Rupture process of the 2004 Sumatra–Andaman earthquake. *Science* 308, 1133–1139.
- Ammon, C.J., Lay, T., Velasco, A.A., Kanamori, H., 2006. The 17 July 2006 Java tsunami earthquake. *Geophys. Res. Lett.* 33, L24308.
- Antolik, M., Abercrombie, R.E., Pan, J., Ekström, G., 2006. Rupture characteristics of the 2003 Mw 7.6 mid-Indian Ocean earthquake: implications for seismic properties of young oceanic lithosphere. *J. Geophys. Res.* 111, B04302.
- Beroza, G.C., Jordan, T.H., 1990. Searching for slow and silent earthquakes using free oscillations. *J. Geophys. Res.* 95, 2485.
- Boore, D.M., 1983. Stochastic simulation of high-frequency ground motions based on seismological models of the radiated spectra. *Bull. Seismol. Soc. Am.* 73, 1865–1894.
- Brune, J.N., 1970. Tectonic stress and the spectra of seismic shear waves from earthquakes. *J. Geophys. Res.* 75, 4997–5009.
- Brune, J.N., 1971. Correction to tectonic stress and the spectra of seismic shear waves from earthquakes. *J. Geophys. Res.* 76, 5002.
- Choy, G.L., Boatwright, J.L., 1995. Global patterns of radiated seismic energy and apparent stress. *J. Geophys. Res.* 100, 18205–18228.
- Choy, G.L., McGarr, A., 2002. Strike-slip earthquakes in the oceanic lithosphere: observations of exceptionally high apparent stress. *Geophys. J. Int.* 150, 506–523.
- Duputel, Z., Rivera, L., Kanamori, H., Hayes, G., 2012. W phase source inversion for moderate to large earthquakes (1990–2010). *Geophys. J. Int.* 189, 1125–1147.
- Dziewonski, A., Chou, T.A., Woodhouse, J.H., 1981. Determination of earthquake source parameters from waveform data for studies of global and regional seismicity. *J. Geophys. Res.* 86, 2825–2852.
- Dziewonski, A.M., Anderson, D.L., 1981. Preliminary reference Earth model. *Phys. Earth Planet. Inter.* 25, 297–356.
- Dziewonski, A.M., Woodhouse, J.H., 1983. An experiment in systematic study of global seismicity: centroid-moment tensor solutions for 201 moderate and large earthquakes of 1981. *J. Geophys. Res.* 88, 3247.
- Earthquake Research Institute (ERI), 2000. EIC Seismological Note 94.
- Eberhart-Phillips, D., Haeussler, P.J., Freymueller, J.T., Frankel, A.D., Rubin, C.M., Craw, P., Ratchkovski, N.A., Anderson, G., Carver, G.A., Crone, A.J., Dawson, T.E., Fletcher, H., Hansen, R., Harp, E.L., Harris, R.A., Hill, D.P., Hreinsdóttir, S., Jibson, R.W., Jones, L.M., Kayen, R., Keefer, D.K., Larsen, C.F., Moran, S.C., Personius, S.F., Plafker, G., Sherrod, B., Sieh, K., Sitar, N., Wallace, W.K., 2003. The 2002 Denali Fault Earthquake, Alaska: a large magnitude, slip-partitioned event. *Science*, 300; pp. 1113–1118.
- Ekström, G., 1989. A very broad band inversion method for the recovery of earthquake source parameters. *Tectonophysics* 166, 73–100.
- Ekström, G., Engdahl, E.R., 1989. Earthquake source parameters and stress distribution in the Adak Island region of the central Aleutian Islands, Alaska. *J. Geophys. Res.* 94, 15499.
- Ekström, G., Nettles, M., Dziewonski, A.M., 2012. The global CMT project 2004–2010: centroid-moment tensors for 13,017 earthquakes. *Phys. Earth Planet. Inter.* 200–201, 1–9.
- Hauksson, E., Stock, J., Hutton, K., Yang, W., Vidal-Villegas, J.A., Kanamori, H., 2010. The 2010 Mw7.2 El Mayor–Cucapah Earthquake Sequence, Baja California, Mexico and Southernmost California, USA: active seismotectonics along the Mexican Pacific Margin. *Pure Appl. Geophys.* 168, 1255–1277.
- Heinrich, P., Piattesi, A., Okal, E.A., Hébert, H., 2000. Near-field modeling of the July 17, 1998 tsunami in Papua New Guinea. *Geophys. Res. Lett.* 27, 3037–3040.
- Heki, K., Miyazaki, S., Tsuji, H., 1997. Silent fault slip following an interplate thrust earthquake at the Japan Trench. *Nature* 386, 595–598.
- Hidayat, D., Barker, J.S., Satake, K., 1995. Modeling the seismic source and tsunami generation of the December 12, 1992 Flores Island, Indonesia, earthquake. *Pure Appl. Geophys.* 144, 537–554.
- Hill, E.M., Borroto, J.C., Huang, Z., Qiu, Q., Banerjee, P., Natawidjaja, D.H., Elosgui, P., Fritz, H.M., Suwargadi, B.W., Pranantyo, I.R., Li, L., Macpherson, K.A., Skanavis, V., Synolakis, C.E., Sieh, K., 2012. The 2010 Mw 7.8 Mentawai earthquake: very shallow source of a rare tsunami earthquake determined from tsunami field survey and near-field GPS data. *J. Geophys. Res.: Solid Earth* 117, B06402.
- Houston, H., Benz, H.M., Vidale, J.E., 1998. Time functions of deep earthquakes from broadband and short-period stacks. *J. Geophys. Res.* 103, 29895.
- Iglesias, A., Singh, S.K., Pacheco, J.F., Alcántara, L., Ortiz, M., Ordaz, M., 2003. Near-trench Mexican Earthquakes have anomalously low peak accelerations. *Bull. Seismol. Soc. Am.* 93, 953–959.
- Ihmlé, P.F., Jordan, T.H., 1994. Teleseismic search for slow precursors to large earthquakes. *Science* 266, 1547–1551.
- Ihmlé, P.F., Gomez, J.-M., Heinrich, P., Guibourg, S., 1998. The 1996 Peru tsunami-generating broadband source process. *Geophys. Res. Lett.* 25, 2691.
- Ishii, M., Shearer, P.M., Houston, H., Vidale, J.E., 2005. Extent, duration and speed of the 2004 Sumatra–Andaman earthquake imaged by the Hi-Net array. *Nature* 435, 933–936.
- Kanamori, H., 1972. Mechanism of tsunami earthquakes. *Phys. Earth Planet. Inter.* 6, 356–359.
- Kanamori, H., Anderson, D.L., 1975. Theoretical basis of some empirical relations in seismology. *Bull. Seismol. Soc. Am.* 65, 1073–1095.
- Kanamori, H., Given, J.W., 1981. Use of long-period surface waves for rapid determination of earthquake-source parameters. *Phys. Earth Planet. Inter.* 27, 8–31.
- Kanamori, H., Kikuchi, M., 1993. The 1992 Nicaragua earthquake: a slow tsunami earthquake associated with subducted sediments. *Nature* 361, 714–716.
- Kanamori, H., Rivera, L., 2008. Source inversion of W phase: speeding up seismic tsunami warning. *Geophys. J. Int.* 175, 222–238.
- Kaverina, A., Dreger, D., Antolik, M., 1998. Source process of the 21 April, 1997 Santa Cruz Island Earthquake (Mw7.8). *Geophys. Res. Lett.* 25, 4027.
- Kikuchi, M., Kanamori, H., 1995. The Shikotan Earthquake of October 4, 1994: lithospheric earthquake. *Geophys. Res. Lett.* 22, 1025–1028.
- Kostoglodov, V., Singh, S.K., Santiago, J.A., Franco, S.I., Larson, K.M., Lowry, A.R., Bilham, R., 2003. A large silent earthquake in the Guerrero seismic gap, Mexico. *Geophys. Res. Lett.* 30, 1807.
- Kuge, K., Kase, Y., Urata, Y., Campos, J., Perez, A., 2010. Rupture characteristics of the 2005 Tarapaca, northern Chile, intermediate-depth earthquake: evidence for heterogeneous fluid distribution across the subducting oceanic plate? *J. Geophys. Res.* 115, B09305.
- Lambotte, S., Rivera, L., Hinderer, J., 2006. Rupture length and duration of the 2004 Aceh–Sumatra earthquake from the phases of the Earth's gravest free oscillations. *Geophys. Res. Lett.* 33, L03307.
- Lay, T., Ammon, C.J., Hutko, A.R., Kanamori, H., 2010a. Effects of Kinematic Constraints on Teleseismic Finite-Source Rupture Inversions: Great Peruvian Earthquakes of 23 June 2001 and 15 August 2007. *Bull. Seismol. Soc. Am.* 100, 969–994.
- Lay, T., Ammon, C.J., Kanamori, H., Koper, K.D., Sufri, O., Hutko, A.R., 2010b. Teleseismic inversion for rupture process of the 27 February 2010 Chile (Mw8.8) earthquake. *Geophys. Res. Lett.* 37, L13301.
- Lay, T., Ammon, C.J., Kanamori, H., Rivera, L., Koper, K., Hutko, A.R., 2010c. The 2009 Samoa–Tonga great earthquake triggered doublet. *Nature* 466, 964–968.
- Lay, T., Ammon, C.J., Kanamori, H., Yamazaki, Y., Cheung, K.F., Hutko, A.R., 2011. The 25 October 2010 Mentawai tsunami earthquake (Mw 7.8) and the tsunami hazard presented by shallow megathrust ruptures. *Geophys. Res. Lett.* 38, L06302.
- Lay, T., Kanamori, H., 2011. Insights from the great 2011 Japan earthquake. *Phys. Today* 64, 33–39.
- Lay, T., Kanamori, H., Ammon, C.J., Hutko, A.R., Furlong, K., Rivera, L., 2009. The 2006–2007 Kuril Islands great earthquake sequence. *J. Geophys. Res.* 114, B11308.

- Mayeda, K., Malagnini, L., 2007. A new spectral ratio method using narrow band coda envelopes: evidence for non-self-similarity in the Hector Mine sequence. *Geophys. Res. Lett.* 34, L11303.
- McGuire, J.J., Ihmlé, P.F., Jordan, T.H., 1996. Time-domain observations of a slow precursor to the 1994 Romanche Transform Earthquake. *Science* 274, 82–85.
- Nakayama, W., Takeo, M., 1997. Slip history of the 1994 Sanriku-Haruka-Oki, Japan, earthquake deduced from strong-motion data. *Bull. Seismol. Soc. Am.* 87, 918–931.
- Newman, A., Hayes, G., Wei, Y., Converse, J., 2011. The 25 October 2010 Mentawai tsunami earthquake, from real-time discriminants, finite-fault rupture, and tsunami excitation. *Geophys. Res. Lett.* 38, L05302.
- Newman, A.V., Okal, E.A., 1998. Teleseismic estimates of radiated seismic energy: the E/M0 discriminant for tsunami earthquakes. *J. Geophys. Res.* 103, 26885.
- Park, S.-C., Mori, J., 2007. Triggering of earthquakes during the 2000 Papua New Guinea earthquake sequence. *J. Geophys. Res.* 112, B03302.
- Pérez-Campos, X., McGuire, J.J., Beroza, G.C., 2003. Resolution of the slow earthquake/high apparent stress paradox for oceanic transform fault earthquakes. *J. Geophys. Res.* 108, 2444.
- Polet, J., Kanamori, H., 2000. Shallow subduction zone earthquakes and their tsunamigenic potential. *Geophys. J. Int.* 142, 684–702.
- Polet, J., Thio, H.K., 2003. The 1994 Java tsunami earthquake and its “Normal” aftershocks. *Geophys. Res. Lett.* 30, 1474.
- Romanowicz, B., 1992. Strike-slip earthquakes on quasi-vertical transcurrent faults: inferences for general scaling relations. *Geophys. Res. Lett.* 19, 481–484.
- Satake, K., 1994. Mechanism of the 1992 Nicaragua tsunami earthquake. *Geophys. Res. Lett.* 21, 2519–2522.
- Scholz, C.H., 1982. Scaling laws for large earthquakes: consequences for physical models. *Bull. Seismol. Soc. Am.* 72, 1–14.
- Schramm, K., Stein, S., 2009. Apparent slow oceanic transform earthquakes due to source mechanism bias. *Seismol. Res. Lett.* 80, 102–107.
- Shearer, P.M., Prieto, G.A., Hauksson, E., 2006. Comprehensive analysis of earthquake source spectra in southern California. *J. Geophys. Res.* 111, B06303.
- Silver, P.G., Jordan, T.H., 1983. Total-moment spectra of fourteen large earthquakes. *J. Geophys. Res.* 88, 3273.
- Sladen, A., 2007a. Tectonics Observatory Source Models of Large Earthquakes—August/15/2007 (Mw 8.0), Peru http://www.tectonics.caltech.edu/slip_history.
- Sladen, A., 2007b. Tectonics Observatory Source Models of Large Earthquakes—September/12/2007 (Mw 8.4), South Sumatra, http://www.tectonics.caltech.edu/slip_history.
- Sladen, A., 2008a. Tectonics Observatory Source Models of Large Earthquakes—May/12/2008 (Mw 7.9), East Sichuan, http://www.tectonics.caltech.edu/slip_history.
- Sladen, A., 2008b. Tectonics Observatory Source Models of Large Earthquakes—November/16/2008 (Mw 7.3), Sulawesi, http://www.tectonics.caltech.edu/slip_history.
- Sladen, A., 2009a. Tectonics Observatory Source Models of Large Earthquakes—October/07/2009 (Mw 7.6), Vanuatu, http://www.tectonics.caltech.edu/slip_history.
- Sladen, A., 2009b. Tectonics Observatory Source Models of Large Earthquakes—September/30/2009 (Mw 7.6), Padang, http://www.tectonics.caltech.edu/slip_history.
- Sladen, A., Tavera, H., Simons, M., Avouac, J., 2010. Source model of the 2007 Mw 8.0 Pisco, Peru earthquake: implications for seismogenic behavior of subduction megathrusts. *J. Geophys. Res.* 114, B02405.
- Smith, G.P., Ekström, G., 1995. Using travel-time and waveform data to study the earthquake source. AGU Fall Meeting Abstracts, EOS Supplement 76, 389.
- Synolakis, C.E., Bardet, J.P., Borrero, J.C., Davies, H.L., Okal, E.A., Silver, E.A., Sweet, S., Tappin, D.R., 2002. The slump origin of the 1998 Papua New Guinea Tsunami. *Proc. R. Soc. A: Math. Phys. Eng. Sci.* 458, 763–789.
- Tanioka, Y., Ruff, L., Satake, K., 1996. The Sanriku-Oki, Japan, Earthquake of December 28, 1994 (Mw7.7): rupture of a different asperity from a previous earthquake. *Geophys. Res. Lett.* 23, 1465.
- Tanioka, Y., Ruff, L.J., 1997. Source time functions. *Seismol. Res. Lett.* 68, 386–400.
- Tochepart, A., Rivera, L., Van der Woerd, J., 2006. A study of the 14 November 2001 Kokoxili Earthquake: history and geometry of the rupture from teleseismic data and field observations. *Bull. Seismol. Soc. Am.* 96, 1729–1741.
- Tsai, V.C., Nettles, M., Ekström, G., Dziewonski, A.M., 2005. Multiple CMT source analysis of the 2004 Sumatra earthquake. *Geophys. Res. Lett.* 32, L17304.
- Tsuji, Y., Matsutomi, H., Imamura, F., Takeo, M., Kawata, Y., Matsuyama, M., Takahashi, T., Sunarjo, Harjadi, P., 1995. Damage to coastal villages due to the 1992 Flores Island earthquake tsunami. *Pure Appl. Geophys.* 144, 481–524.
- Vidale, J.E., Houston, H., 1993. The depth dependence of earthquake duration and implications for rupture mechanisms. *Nature* 365, 45–47.
- Wielandt, E., Stein, J.M., 1986. A digital very-broad-band seismograph. *Ann. Geophys. Ser.* 4, 227–232.
- Wielandt, E., Streckeisen, G., 1982. The leaf-spring seismometer: design and performance. *Bull. Seismol. Soc. Am.* 72, 2349.
- Yagi, Y., 2002. 2002 Northern Sumatra, Indonesia Earthquake, <http://iisee.kenken.go.jp/staff/yagi>.
- Yagi, Y., 2003. Source process of large and significant earthquakes in 2003. *Bull. Int. Inst. Seismol. Earthquake Eng.*, 145–153.
- Yagi, Y., 2004. Source rupture process of the 2003 Tokachi-oki earthquake determined by joint inversion of teleseismic body wave and strong ground motion data. *Earth Planets Space* 56, 311–316.

2.3 Impact des hétérogénéités structurales 3D sur les solutions phase W

Les modèles de source sismique sont affectés par différents types d'incertitude. Une première source d'incertitude est associée à l'imprécision des mesures (causée par le bruit ambiant, une mauvaise calibration instrumentale, etc.). Une autre source d'incertitude, souvent négligée est associée à l'imperfection des prédictions, liée en particulier à l'inexactitude du modèle de Terre utilisé lors de l'inversion de la source. Alors que différentes stratégies ont été développées pour quantifier l'incertitude dans les prédictions (voir Chapitre 3), la plupart des applications actuelles reposent encore sur un modèle de Terre 1D (ou sphérique). C'est le cas pour l'algorithme phase W qui permet de déterminer les paramètres du tenseur moment sismique barycentrique en supposant un modèle de Terre sphérique. Comme indiqué précédemment, la phase W correspond principalement à la superposition d'harmoniques de modes normaux à longue période qui ne sont pas fortement influencés par les hétérogénéités structurales proches de la surface. Même si la phase W est peu affectée par la structure superficielle, l'existence de biais de localisation dans certaines régions suggère clairement que les solutions phase W sont impactées par l'hétérogénéité 3D (Duputel et al., 2012b). Dans l'article présenté ci-dessous, on évalue l'impact de la structure 3D en effectuant des inversions phase W à partir d'un grand jeu de données synthétiques calculé dans des modèles 3D pour 250 séismes répartis globalement. Les résultats indiquent que l'hétérogénéité latérale affecte principalement la localisation barycentrique (i.e., centroid) alors que les autres paramètres de source sont peu impactés. Les séismes superficiels montrent une variabilité importante dans les composantes $M_{r\theta}$ et $M_{r\phi}$ du tenseur moment sismique, résultant à la fois de la faible amplitude et de la plus grande incertitude des fonctions d'excitation associées.

L'article proposé ci-dessous a été publié en 2020 dans *Geophysical Journal International*. Ce travail a été effectué dans le cadre du doctorat de Catalina Morales (thèse soutenue en Mai 2020).

Impact of 3-D Earth structure on W-phase CMT parameters

Catalina Morales-Yáñez, Zacharie Duputel and Luis Rivera

Institut de Physique du Globe de Strasbourg, UMR7516, Université de Strasbourg/EOST, CNRS, 67081 Strasbourg, France. E-mail: cmorales@unistra.fr

Accepted 2020 August 6. Received 2020 August 5; in original form 2020 January 31

SUMMARY

We investigate the impact of unmodelled 3-D structural heterogeneity on inverted W-phase source parameters. We generate a large data set of synthetic seismograms accounting for the Earth's 3-D structure for 250 earthquakes globally distributed. The W-phase algorithm is then used to invert for earthquake CMT parameters, assuming a spherical Earth model. The impact of lateral heterogeneity is assessed by comparing inverted source parameters with those used to compute the 3-D synthetics. Results show that the 3-D structure mainly affects centroid location while the effect on the other source parameters remains small. Centroid mislocations present clear geographical patterns. In particular, W-phase solutions for earthquakes in South America are on average biased 17 km to the east of the actual centroid locations. This effect is significantly reduced using an azimuthally well balanced distribution of seismological stations. Source parameters are generally more impacted by mantle heterogeneity while the scalar moment of shallow earthquakes seems to be mainly impacted by the crustal structure. Shallow earthquakes present a variability of $M_{r\theta}$ and $M_{r\phi}$ moment tensor elements, resulting both from the small amplitude and a larger uncertainty of the associated Green's functions.

Key words: Structure of the Earth; Inverse theory; Earthquake source observations; Surface waves and free oscillations; Wave propagation.

1 INTRODUCTION

The characterization of earthquake sources is based on different data types such as teleseismic body waves, surface waves, strong-motion waveforms, GNSS and InSAR data (e.g. Delouis *et al.* 2010; Polet & Thio 2011; Crowell *et al.* 2012; Ekström *et al.* 2012). Source inversions also rely on various representations such as centroid–moment-tensors (CMT; e.g. Dziewonski *et al.* 1981), multiple point sources (e.g. Tsai *et al.* 2005), linear and non-linear finite-fault parametrizations (e.g. Ide 2007). The resulting source models are affected by different types of uncertainties (e.g. Duputel *et al.* 2012b). A first source of uncertainty is the error induced by more or less imperfect measurements (e.g. ambient noise, incorrect instrument calibration, etc.). Another source of uncertainty, often overlooked, is associated with modeling errors (i.e. errors in model predictions) and in particular, prediction inaccuracies due to imperfections of the Earth model used for the inversion. While different strategies have been developed to quantify such uncertainties (Yagi & Fukahata 2011; Duputel *et al.* 2014; Hallo & Gallović 2016), most applications rely on a simple 1-D (or spherical) Earth model (Hallo *et al.* 2017; Gombert *et al.* 2018). It is the case for W-phase CMT inversions for which 3-D effects are supposedly small but have not yet been fully quantified (Kanamori & Rivera 2008; Duputel *et al.* 2016). The W-phase corresponds to a long period signal (100–1000 s) that is conspicuous for large earthquakes between the P wave and the surface waves. This phase can be described as the superposition

of normal mode overtones, that have limited sensitivity to shallow lateral heterogeneity compared to fundamental mode surface waves (Kanamori 1993).

Lateral structural heterogeneity can significantly affect the propagation of seismic waves, which in return can impact source estimates if they are not properly accounted for. Different corrections can be applied to mitigate the effect of 3-D Earth structures. For example, Nakanishi & Kanamori (1982) proposed to use path-dependent Rayleigh wave phase velocities for moment tensor inversions. Another example is the Global CMT algorithm in which S362ANI is used as the 3-D model. The seismograms are calculated using 3-D structure and the path-average approximation (Dziewonski *et al.* 1984; Woodhouse & Dziewonski 1984). Despite these corrections, CMT solutions can still be affected by errors due to lateral heterogeneity (Ferreira & Woodhouse 2006). In particular, the comparison between interferometric synthetic aperture radar (InSAR) data and CMT solutions suggests large uncertainties in centroid locations (Ferreira *et al.* 2011). In the same line, Hjörleifsdóttir & Ekström (2010) found that even with phase corrections, Global CMT solutions are still contaminated by the Earth's 3-D structure, causing an error close to 11 per cent in moment along with non-negligible regional biases in centroid locations (e.g. larger than 10–20 km in South America).

With the recent improvement of computing capabilities, several studies are now using more expensive numerical methods to better incorporate the effect of 3-D heterogeneity (Liu *et al.* 2004;

Duputel *et al.* 2016). This is particularly relevant to account for 3-D effects when using fundamental mode surface waves that are strongly affected by lateral heterogeneity near the surface (e.g. caused by oceans and continents; Dahlen & Tromp 1998). Some other phases, like the W-phase, are less impacted by shallow 3-D structures because they propagate deeper in the mantle where lateral heterogeneity is supposedly smaller. The inversion of W-phase proved to be very useful for rapid source characterization of large earthquakes (Duputel *et al.* 2012b) and has been implemented in various warning centres to quickly provide CMT solutions in near real time conditions (Hayes *et al.* 2009; Wang *et al.* 2017; Zhao *et al.* 2017; Riquelme *et al.* 2018). The robustness of this approach relies partially on the fact that the W-phase corresponds mainly to the superposition of normal-mode overtones at long period, which are not strongly influenced by the 3-D structure and can be efficiently synthesized in a spherical Earth model (Kanamori & Rivera 2008). Even if W-phase should be less affected by the 3-D structure, recent studies suggest that there might still be some impact (Duputel *et al.* 2016). However, such 3-D effects have not yet been quantified systematically. In this study, we assess the impact of 3-D Earth structures on W-phase CMT solutions. For this purpose, we evaluate the performance of the W-phase algorithm using a large data set of synthetic seismograms ($\sim 64\,000$ waveforms) computed for 3-D Earth models.

2 METHODOLOGY

To assess the effects of lateral structural heterogeneity on W-phase solutions, we compute a large database of 3-D synthetics for earthquakes at various locations and with different source parameters. From those synthetic seismograms, we then invert for CMT parameters using the (1-D) W-phase approach. The performance of the algorithm is then assessed by comparing inverted source parameters with those used to compute input 3-D synthetics.

2.1 Earthquake catalogue and 3-D synthetic database

We first define a set of earthquakes to be used in this study. To have a reasonably representative catalogue, we use a $5^\circ \times 5^\circ$ grid at the surface of the Earth and extract CMT parameters of the largest events ($M_W \geq 6.5$) in each cell from the Global CMT (GCMT) catalogue between 1995 and 2017 (Dziewonski *et al.* 1981; Ekström *et al.* 2012). This results into a catalogue of 252 earthquakes whose distribution and focal mechanisms are shown in Fig. 1. We also design a realistic network composed of 254 seismological stations. These stations, presented in Fig. 2, mainly belong to networks IU, II, GT, IC, CU, G, MN, CN, GE, CI and BK (for more information see caption Fig. 2).

Using the earthquake catalogue and seismic network described above, we compute synthetic seismograms assuming two different 3-D global mantle models: S362ANI (Kustowski *et al.* 2008) and S40RTS (Ritsema *et al.* 2011), which are both completed with the CRUST2.0 crust structure (Bassin *et al.* 2000). We use the spectral element method code SPECFEM3D_GLOBE (Komatsitsch *et al.* 2015) with a mesh-size ensuring accurate simulations for periods down to ~ 27 s. This resolution is compatible with the filter used for smaller magnitude earthquakes ($M_W = 6.5$) and allows to incorporate realistic features of the Earth. Simulations are conducted for each earthquake in our catalogue. Computing the complete catalogue takes ~ 40 hr using 48 Tesla K80 Nvidia GPUs on the University of Strasbourg HPC cluster. Using 24 GPUs, each earthquake

simulation is conducted in 20 min to obtain seismograms with a duration of 40 min. Beyond 3-D lateral heterogeneity, these computations include the effect of ellipticity, topography, rotation, attenuation and gravity (implemented using the Cowling approximation; Komatsitsch & Tromp 2002a, b).

The synthetics are computed such that they correspond to a unit scalar moment and a step source time history (i.e. a Dirac delta moment rate function). To assess the effect of ambient noise for different magnitudes, we add actual seismic noise after scaling the 3-D synthetics to different earthquake sizes. We use noise records for each used channel on time-periods with no significant earthquake activity (on 1995/06/01, 2005/11/3 and 2015/06/09, depending on the seismic station). The final noisy synthetics $s(t, M_0)$ at a given station can then be written as:

$$s(t, M_0) = M_0 \times \hat{s}(t) \otimes f(t, M_0) \otimes I(t) + n(t), \quad (1)$$

where the symbol \otimes is used to denote convolution. In this equation, M_0 is the scalar seismic moment, $\hat{s}(t)$ is the unit synthetic seismogram (i.e. computed for unit scalar moment and step time-history), $f(t, M_0)$ is the normalized moment rate function, $I(t)$ is the instrument response and $n(t)$ the raw noise record at the corresponding station. The source time function $f(t, M_0)$ is assumed to be an isosceles triangle function of unit area with a time-shift (t_c) and a half duration (h_c) defined as (Duputel *et al.* 2012b):

$$t_c(M_0) = h_c(M_0) = 2.6 \times 10^{-6} M_0^{1/3}. \quad (2)$$

In the above equations, M_0 is in N.m (i.e. 10^7 dyne.cm) and t_c is in seconds.

2.2 W-phase inversion

The W-phase inversion algorithm is based on a Green's functions database that is pre-computed for a 1-D Earth model. For consistency, we use the same code to compute 3-D synthetics and to create the 1-D Green's functions. We compute SPECFEM3D_GLOBE Green's functions using the 1-D Earth model STW105 (Kustowski *et al.* 2008), which is the reference model of S362ANI.

In general, for every source–station pair we have to compute 18 Green's functions (6 moment tensor components, 3 receiver orientations). However, for a spherical Earth model, only 10 Green's functions are required for every depth–distance pair (see Kanamori & Rivera 2008). We thus compute a database including those 10 elementary Green's functions for a range of epicentral distances and focal depths considered in the problem. Epicentral distances are discretized every 0.1° from 0° to 90° . The depth discretization is variable with 2, 5 and 10 km depth intervals, respectively, for depth ranges of 3.5–25.5 km, 25.5–50.5 km and 50–760 km.

The W-phase inversion algorithm consists of estimating the centroid moment tensor parameters (i.e. the moment tensor elements along with the centroid location in time and space). This relies on a grid-search approach to find the point source time and location that minimizes the RMS waveform misfit. For each explored point in time and space the inverse problem is linear for the moment tensor elements (Kanamori & Rivera 2008). As for standard W-phase implementations, we use stations within 5° – 85° of epicentral distance and a time-window starting at the P -wave arrival, with a duration (δt) proportional to the epicentral distance (Δ): $\delta t = 15[s/\text{km}] \Delta$. We also apply a data screening by iteratively removing channels having a relative RMS misfit larger than 500, 300 and 90 per cent of the data L2 norm (for more details, see Duputel *et al.* 2012b).

Table 1. Comparison of the impact of crustal and mantle lateral heterogeneity. We compare solutions obtained using a full 3-D structure with solutions retrieved from a 3-D crust with a 1-D mantle (3Dc–1Dm) or a 1-D crust with a 3-D mantle (1Dc–3Dm). $\langle \Delta M_W \rangle_{3D} - \langle \Delta M_W \rangle_{\text{model}}$ is the average difference of the magnitude discrepancy ΔM_W (measured for a 3-D model) and ΔM_W (where model is 3Dc–1Dm or 1Dc–3Dm). Similarly, $\langle \Delta_3D - \Delta_{\text{model}} \rangle$, $\langle \Delta \tau_{3D} - \Delta \tau_{\text{model}} \rangle$, $\langle \Delta h_{3D} - \Delta h_{\text{model}} \rangle$ and $\langle |\Delta \mathbf{x}_{3D}| - |\Delta \mathbf{x}_{\text{model}}| \rangle$ denote, respectively, the average beachball RMS difference, centroid time difference, depth difference and horizontal mislocations.

	3-D crust 1-D mantle	1-D crust 3-D mantle
$\langle \Delta M_W \rangle_{3D} - \langle \Delta M_W \rangle_{\text{model}}$	-0.00014	0.0041
$\langle \Delta_3D - \Delta_{\text{model}} \rangle$	0.0068	0.0052
$\langle \Delta \tau_{3D} - \Delta \tau_{\text{model}} \rangle$	0.012 s	-0.004 s
$\langle \Delta h_{3D} - \Delta h_{\text{model}} \rangle$	2.69 km	0.44 km
$\langle \Delta \mathbf{x}_{3D} - \Delta \mathbf{x}_{\text{model}} \rangle$	6.50 km	-3.34 km

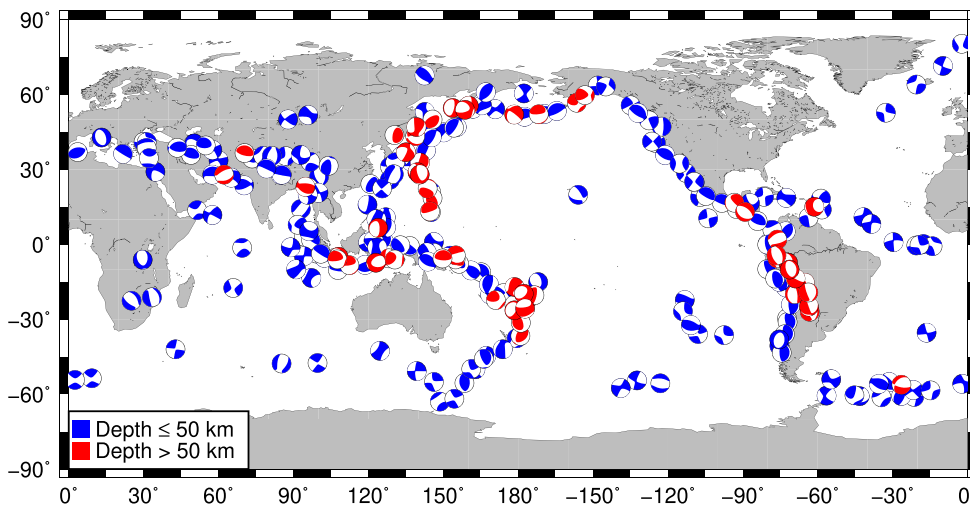


Figure 1. Earthquake catalogue. We use centroid moment tensor solutions from the GCMT database. Blue focal mechanisms represent earthquakes shallower than 50 km and red represents earthquakes deeper than 50 km.

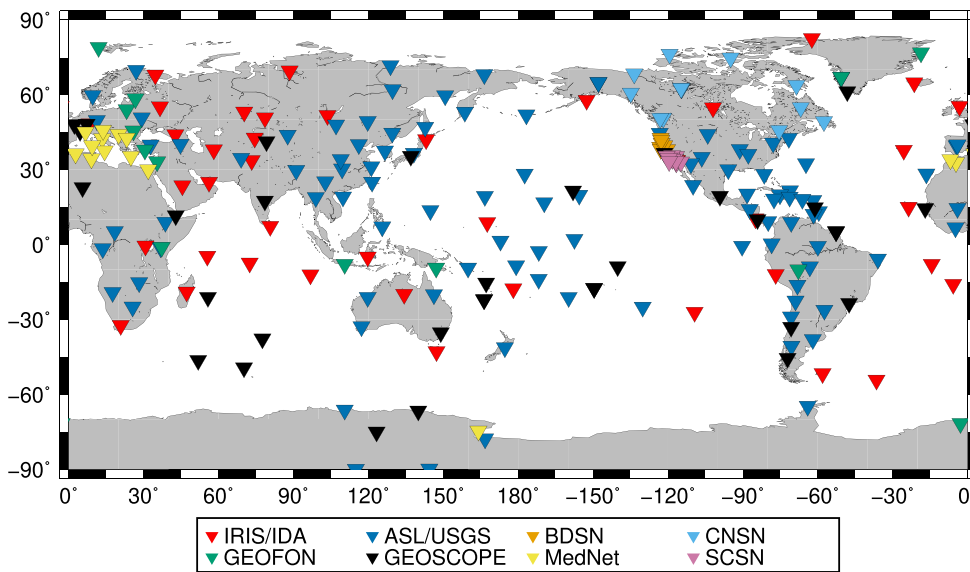


Figure 2. Seismological network. We use a combination of 254 stations from the IRIS/IDA (II; Scripps Institution of Oceanography 1986), ASL/USGS (IU; CU; IC; GT; Albuquerque Seismological Laboratory (ASL)/USGS 1988, 2006, 1992, 1993), BDSN (BK; Northern California Earthquake Data Center 2014), CNSN (CN; Geological Survey of Canada 1980), GEOFON (GE; GEOFON Data Centre 1993), GEOSCOPE (G; Institut de Physique du Globe de Paris IPGP 1982), MedNet (MN; MedNet Project Partner Institutions 1990) and Southern California Seismic Network (CI; California Institute of Technology and United States Geological Survey Pasadena (SCSN) 1926).

3 IMPACT OF 3-D STRUCTURE ON W-PHASE CMT PARAMETERS

To evaluate the impact of lateral heterogeneity, we compare the source parameters used to compute 3-D synthetic seismograms (input source parameters) with the retrieved W-phase CMT solutions (output source parameters).

3.1 Comparison between input and retrieved source parameters

We first focus on results obtained for $M_W = 7.5$ earthquakes. Before inversion, traces are filtered in the 150–500 s passband as proposed by Duputel *et al.* (2012b) for this magnitude. The comparison between input and retrieved source parameters is summarized in Fig. 3 for Earth models S362ANI and S40RTS. In order to have a complete view of the influence of 3-D structures on W-phase CMT parameters, we evaluate the performance of the algorithm using five different metrics.

First, we evaluate the magnitude difference, defined as:

$$\Delta M_W = M_W^{\text{output}} - M_W^{\text{input}} = \frac{2}{3} \log_{10} \frac{M_0^{\text{output}}}{M_0^{\text{input}}}, \quad (3)$$

where M_W^{input} and M_W^{output} are, respectively, the input and retrieved moment magnitude. M_0^{input} and M_0^{output} are the corresponding scalar moments, calculated using $M_0 = \sqrt{\frac{\mathbf{M} : \mathbf{M}}{2}}$ with \mathbf{M} the moment tensor (i.e. following the definition of the *total scalar moment* by Silver & Jordan 1982). Figs 3(a) and (f) show that magnitude difference is tightly centred around 0, with 83 per cent of earthquakes for which $|\Delta M_W| < 0.03$. Largest positive magnitude differences are observed in Greece, the Caspian Sea and Nepal, while the largest negative values are obtained for earthquakes in Indonesia and Northern Japan.

To measure the impact of 3-D heterogeneity on focal mechanisms, we estimate the beachball RMS difference (Δ), following Rivera & Kanamori (2014):

$$\Delta = \frac{1}{2\sqrt{2}} (\mathbf{D} : \mathbf{D})^{1/2} \quad (4)$$

\mathbf{D} is the difference between normalized moments tensor $\mathbf{D} = \hat{\mathbf{M}}^{\text{output}} - \hat{\mathbf{M}}^{\text{input}}$, with $\hat{\mathbf{M}} = \frac{\mathbf{M}}{M_0}$. With this definition, we have $\Delta = 0$ when the two moment tensors are equal and $\Delta = 1$ when they are opposite. Overall, beachball RMS difference (Figs 3b and g) are small with ~ 90 per cent of the events showing $\Delta < 0.1$.

We also evaluate the difference between centroid times,

$$\Delta\tau = t_s^{\text{output}} - t_s^{\text{input}} \quad (5)$$

In Figs 3(c) and (h), we note a clear geographical consistency in $\Delta\tau$. In the Northeast Pacific Ocean, the output centroid time is generally later than the input, while in the Northwest Pacific and South Atlantic we see the opposite behavior. The standard deviation in $\Delta\tau$ is ~ 2 s for the entire data set, which correspond to ~ 6 per cent of the input rupture duration for a $M_w = 7.5$ event (cf. eq. 2). This level of uncertainty is acceptable given that the used data set is sampled at 1 sample per second.

Figs 3(d) and (i) show the centroid depth difference defined as

$$\Delta h = h^{\text{output}} - h^{\text{input}} \quad (6)$$

The retrieved centroid depths are overall deeper than the input ones. For S362ANI the average depth bias is +3 km while it is 1 km for S40RTS. This bias remains relatively small given that the depth discretization of the W-phase Green's function ranges from 2 to

10 km. The absolute depth difference is smaller than 10 km for 85 and 90 per cent of the events calculated with the S362ANI and S40RTS models, respectively.

Finally, we evaluate the horizontal centroid mislocations as

$$\Delta\mathbf{x} = \mathbf{x}^{\text{output}} - \mathbf{x}^{\text{input}}, \quad (7)$$

where $\mathbf{x}^{\text{input}}$ and $\mathbf{x}^{\text{output}}$ are input and retrieved horizontal centroid locations. We estimate an average centroid mislocation $|\Delta\mathbf{x}| \sim 17$ km. Although such uncertainty is not negligible compared to the typical rupture length of $M_W = 7.5$ earthquakes, it is of the same order as the 0.1° source-receiver distance interval used in our Green's function database. Results in Figs 3(e) and (j) also indicate that there are significant geographical biases on retrieved centroid locations. In particular, earthquakes in central and south America seem to be biased towards the East while they seem to be biased towards the North in Alaska, the Aleutians and Japan.

If we compare Figs 3(a)–(e) and (f)–(j), we note that the impact of lateral heterogeneity on W-phase solutions is globally consistent between both models S362ANI and S40RTS. The S40RTS model has a higher resolution (up to 40 harmonic degree) than the S362ANI model (18 harmonic degrees). The consistency between both models confirms that the W-phase is not sensitive to small details of the structure, yet it is sensitive to large-scale heterogeneity that is present in both models.

3.2 Long-period ambient seismic noise

To assess the influence of ambient seismic noise on the inversion results, we compare in Fig. 4 solutions obtained for $M_W = 7.5$ earthquakes with solutions obtained for $M_W = 6.5$ events for the Earth model S362ANI with Crust2.0. We recall that actual seismic noise has been added to synthetic seismograms (see eq. 1) such that the long-period signal-to-noise ratio is naturally larger for a $M_W = 7.5$ earthquake than for a $M_W = 6.5$ event. To avoid any bias due to the use of different stations, the stations set is fixed prior to inversion.

Figs 4(a) and (b) show that noise-free moment tensor solutions obtained for $M_W = 6.5$ are very similar to those obtained for $M_W = 7.5$. On the other hand, the solutions are significantly affected when ambient noise is added to the synthetics (cf. Figs 4d and e). More specifically, we observe that the dispersion of beachball RMS difference (Δ) for $M_W = 6.5$ is more than two times larger than for $M_W = 7.5$ earthquakes. This difference results from long-period noise that is particularly prominent when analysing smaller magnitude earthquakes.

In order to limit the impact of ambient noise for moderate sized earthquakes, it has been previously proposed to use a magnitude dependent bandpass filtering (Hayes *et al.* 2009; Duputel *et al.* 2012b). Using the 100–250 s passband suggested by Duputel *et al.* (2012b) for $M_W = 6.5$ earthquakes (instead of 150–500 s for $M_W = 7.5$ events), we see in Fig. 4 f that the resulting solutions are significantly less affected by ambient seismic noise. A detailed comparison of input and inverted solutions for $M_W = 6.5$ is presented in Fig. S1 for Earth models S362ANI and S40RTS using the 100–250 s passband. Overall, we note a slightly larger dispersion for $M_W = 6.5$ than for $M_W = 7.5$ earthquakes (cf. Fig. 4). This likely results from the smaller signal-to-noise ratio of W-phase waveforms for moderate sized events and larger 3-D effects when using shorter period waveforms.

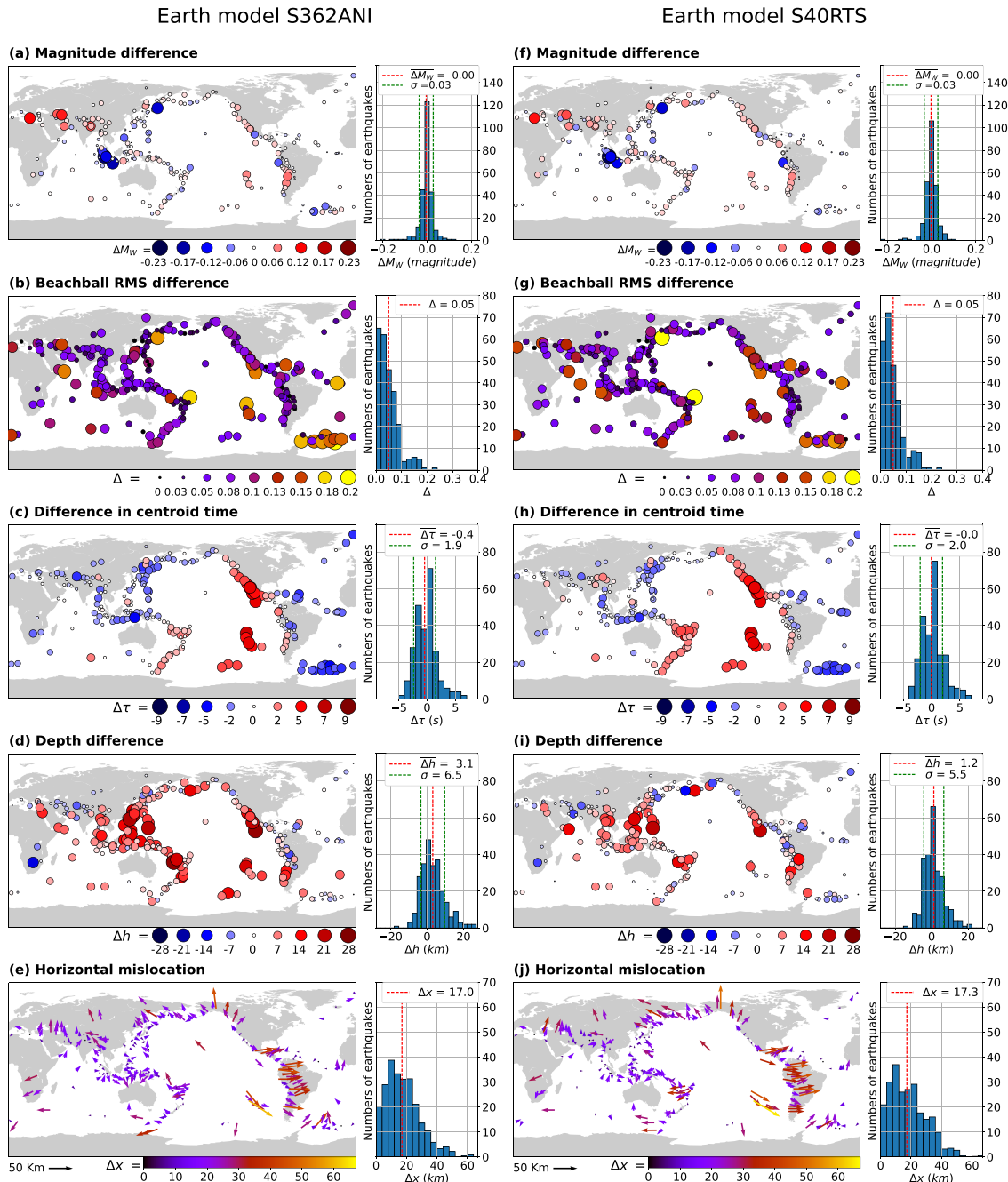


Figure 3. Effects of 3-D heterogeneity for $M_w = 7.5$ earthquakes. Maps shows the following quantities from top to bottom: moment magnitude difference, beachball RMS difference, difference in time-shift, depth difference and horizontal mislocation. Panels from (a) to (e) correspond to the inversion of synthetic seismograms created with the Earth model S362ANI. Panels (f) to (j) correspond to the inversion of synthetic seismograms created with the Earth model S40RTS. In both cases, seismic noise has been added to synthetics prior to source inversion (see Section 2.1).

3.3 Relative influence of crustal and mantle heterogeneity

To further investigate the influence of the 3-D structure on W-phase solutions, we analyse separately the influence of the crust and the mantle. Using the procedure described in section 2, we compute synthetics seismograms with noise, scaled to $M_w = 7.5$, with two different Earth models:

- (1) A model with a 3-D crust and a 1-D mantle (hereafter noted 3Dc–1Dm), using CRUST2.0 and STW105.

(2) A model with a 1-D crust and a 3-D mantle (hereafter noted 1Dc–3Dm), using STW105 and S362ANI.

As before we compare input and estimated parameters using the five metrics defined in Section 3.1.

The results are presented in Figs 5 and S3. To evaluate the relative impact of crust and mantle heterogeneity, we also show in Table 1 the average discrepancy in magnitude difference (ΔM_w) beachball RMS difference (Δ), centroid time difference ($\Delta\tau$), depth difference (Δh) and horizontal mislocations (Δx). If the average difference for the 3Dc–1Dm model is closer to zero than for the

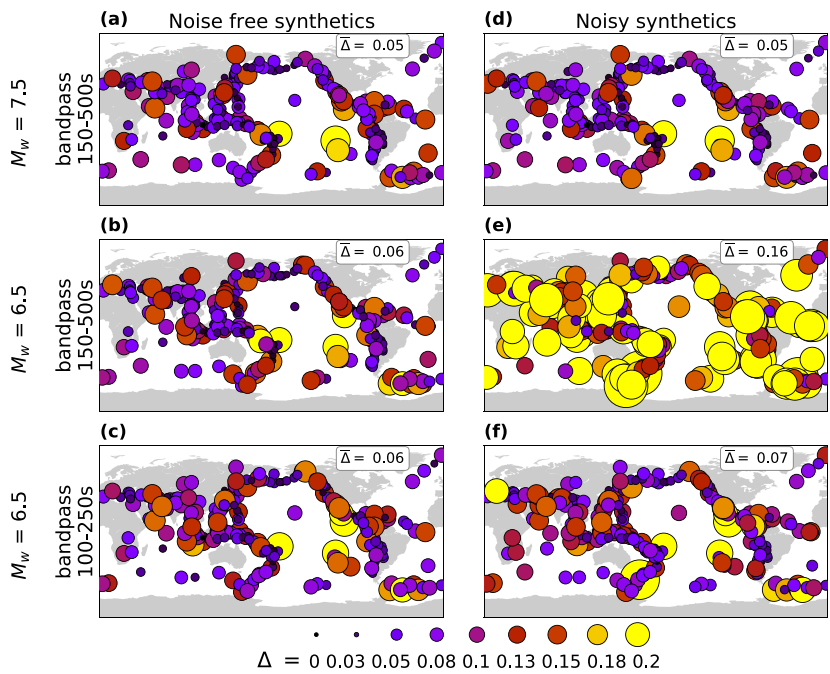


Figure 4. Beachball RMS difference (Δ) after W-phase inversion in different frequency passband with and without ambient seismic noise. Panels (a) and (d) correspond to $M_w = 7.5$ earthquakes inverted in the 150–500 s passband. Panels (b) and (e) are for the same passband but for $M_w = 6.5$. (c) and (f) are for $M_w = 6.5$ with the 100–250 passband.

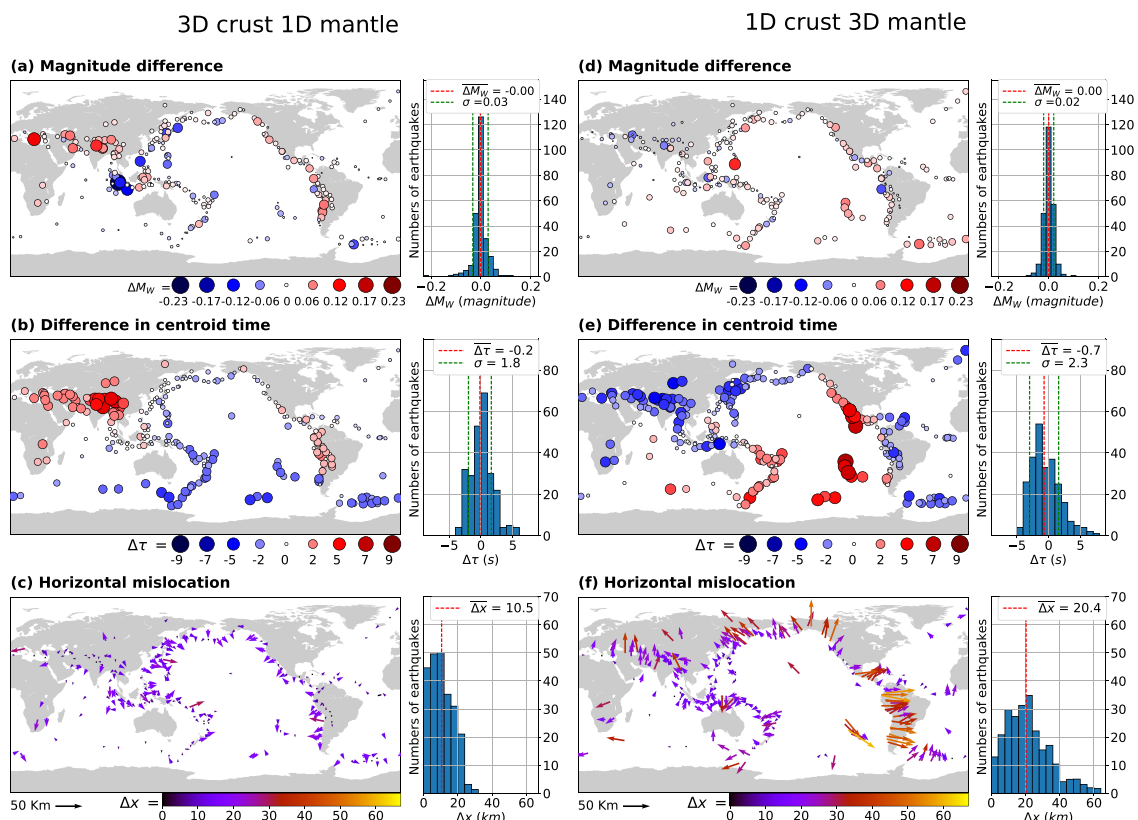


Figure 5. Effects of crustal and mantle heterogeneity on W-phase solutions obtained for $M_w = 7.5$ earthquakes. Maps show from top to bottom: magnitude difference, difference in time-shift and horizontal mislocation. Figures from (a) to (c) correspond to the inversion of synthetic seismograms created with a 3-D crust (CRUST2.0) and a 1-D mantle (STW105). Figures (d) to (f) correspond to the inversion of synthetic seismograms created with a 1-D crust (STW105) and a 3-D mantle (S362ANI). As described in the main text, ambient noise has been added to synthetics prior to source inversion.

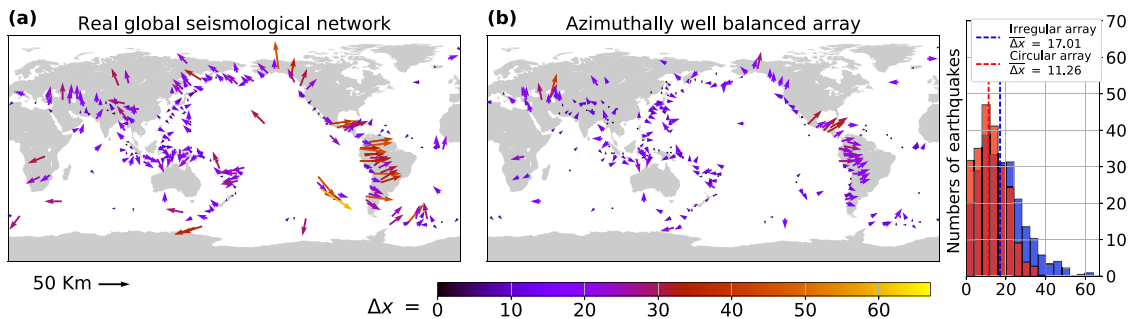


Figure 6. Impact of station distribution on horizontal mislocation. Maps show the horizontal mislocation, after inversion of noisy synthetic seismograms created with the Earth model S362ANI, computed for the real global seismological network (a) and for an azimuthally well balanced array (b).

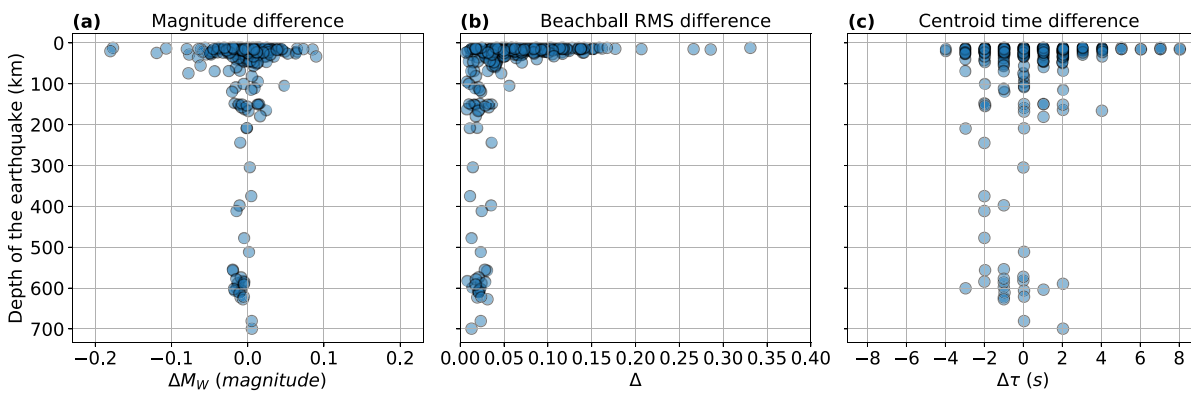


Figure 7. Effect of earthquake depth on retrieved source parameters. (a) Magnitude difference, (b) beachball RMS difference and (c) centroid time difference is shown for as a function of centroid depth.

1Dc–3Dm model, we can postulate that the evaluated parameter is more sensitive to crustal heterogeneity than to the mantle, and vice versa. Table 1 suggests that the crust has a larger impact on the magnitude difference than mantle. This is consistent with Figs 5(a) and (d) that shows a larger dispersion of the magnitude difference with the Earth model 3Dc–1Dm than 1Dc–3Dm. Table 1 indicates that the other parameters seem to be mainly impacted by mantle heterogeneity (consistently with Figs 5 and S3). This is particularly true for the centroid location, for which mantle heterogeneity induces mislocations that are much larger than those induced by the crust (see Figs 5c and f). Interestingly, we see in Figs 6(b)–(c) and (e)–(f) that 3-D heterogeneity in the crust and in the mantle results into anti-correlated effects in terms of centroid time and horizontal mislocation (this is further discussed in Section 4.2).

4 DISCUSSION

4.1 Centroid depth and location uncertainties

As shown in Fig. 3, lateral heterogeneity induces non-negligible uncertainties both in terms of centroid depth and centroid location. We note a centroid depth bias of about +3 km to larger depths (Figs 3d, i and Figs S1d, i). A similar effect was noted by Hjörleifsdóttir & Ekström (2010), who reported a bias of +6 km in GCMT solutions due to 3-D heterogeneity. Similar to GCMT solutions, our results indicate negligible trade-offs between centroid times and centroid depths. While GCMT depths seem to be mainly impacted by local velocity structures at the source and receivers, Figs S3(b) and 3(d)

suggest that W-phase depths are more affected by upper mantle heterogeneity, where the W-phase travel. The measured W-phase depths bias (ranging from 1.2 to 4.5 km in Figs 3d, i and Fig. S1) remains however small relative to the value reported by Hjörleifsdóttir & Ekström (2010) and is of the same order as the depth discretization of the W-phase Green's function database (ranging from 2 to 10 km, see Section 2.2). The comparison between this work and Hjörleifsdóttir & Ekström (2010), can be problematic because the GCMT algorithm uses different phases (body, mantle and surface waves) and filter passbands (between 40 and 350 s for $M_w = 6.0$) for the inversion. In addition, Hjörleifsdóttir & Ekström (2010) focuses mainly on moderate sized earthquakes ($M_w = 5.5$ and $M_w = 6.0$) while we focus on larger earthquakes ($M_w = 6.5$ and $M_w = 7.5$). Nevertheless, the procedure to assess the effect of 3-D heterogeneity on CMT solutions is similar to our study.

As pointed out in Section 3.1, there are clear geographical patterns in centroid mislocations. Centroid locations in the Circum-Pacific belt seem to be biased outward of the Pacific Ocean while events in the middle east are typically shifted 10–20 km to the north. Such geographical patterns are also reported for GCMT locations that are biased towards West in South America (Hjörleifsdóttir & Ekström 2010; Weston *et al.* 2011, 2012). Interestingly, GCMT solutions in the western part of the Americas are biased in the direction opposite to W-phase solutions. This is consistent with actual observations showing that GCMT locations are systematically located at the west of W-phase centroids in this region (Duputel *et al.* 2012a). Such difference is likely related to the fact that GCMT incorporates 3-D corrections (SH8/U4L8 Earth model before 2011 and S362ANI

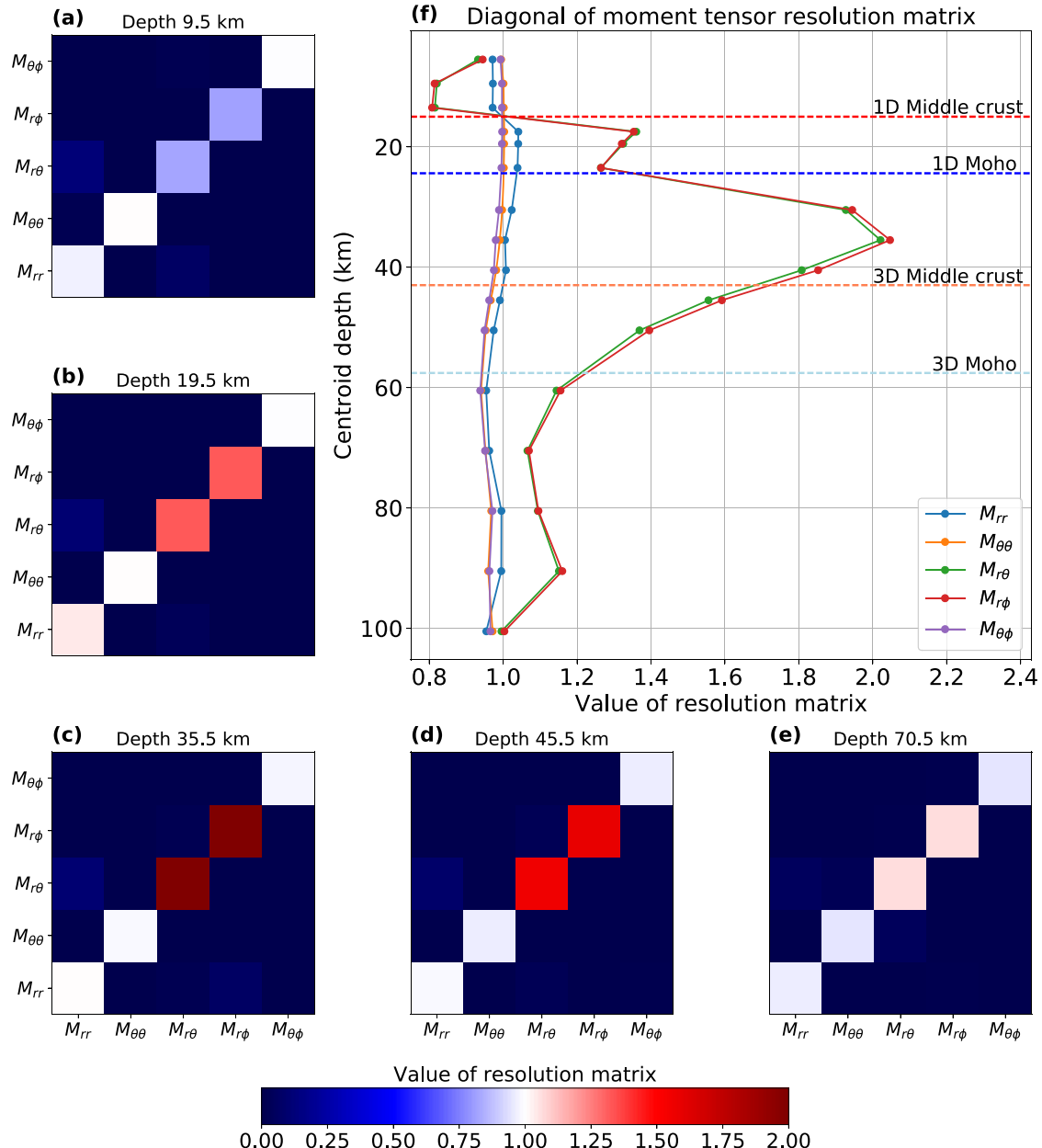


Figure 8. Moment tensor resolution matrix as a function of depth for an earthquake in Nepal (lat = 27.91°N, lon = 85.33°E). Panels (a)–(e) correspond to the resolution matrix at different depths. Panel (f) shows the variation in depth of the diagonal elements of the resolution matrix, horizontal lines show the Moho and middle crust depth for STW105 (1-D model) and CRUST2.0 (3-D model).

since 2011, Dziewonski *et al.* 1992) while W-phase solutions are computed at much longer period assuming a spherical model.

Unmodelled 3-D heterogeneity can cause errors in earthquake locations that can be amplified by an uneven distribution of seismological stations with limited path coverage (Bondár *et al.* 2004; Bai *et al.* 2006; Bondár & Storchak 2011). To evaluate the effect of station distribution on W-phase estimates, we compute another set of 3-D synthetic seismograms assuming an azimuthally well balanced array around each earthquake. For each event in our database, we assume a circular array made of stations distributed at 15°, 30°, 45°, 60° and 75° of epicentral distances (see Fig. S2). Fig. 6 compares centroid mislocations obtained using the actual global seismological network and an azimuthally well balanced array of stations. It can

readily be observed that the use of a well balanced array yields to significantly smaller mislocations. Geographical patterns are in fact similar to that observed for the real global network but the average centroid mislocation is reduced from 17 to 11 km. This suggests that largest centroid mislocations are actually due to a combined effect of lateral velocity variations and limited path coverage (e.g. with paths only crossing the Pacific Ocean).

4.2 Variation of uncertainty as a function of depth

The impact of 3-D heterogeneity on W-phase solutions changes dramatically with the source depth. Fig. 7 shows that uncertainties

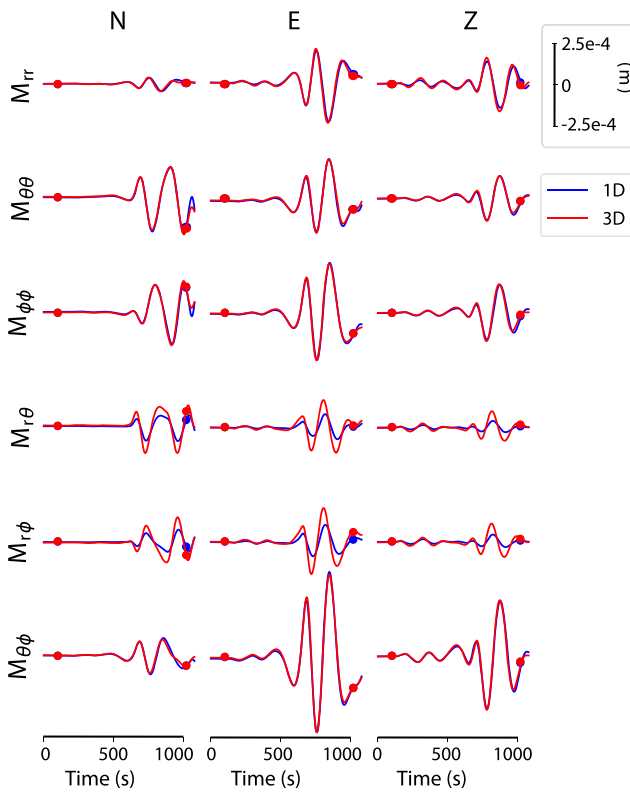


Figure 9. Comparison of Green's function waveforms for 1-D and 3-D Earth models. These seismograms are computed for an earthquake in Nepal at a depth of 35.5 km for the station BFO (II, 60° from the epicentre). Green's functions are for each moment tensor element computed assuming $M_{ij} = 10^{28}$ dyne.cm (where i, j are moment tensor indexes). Waveforms are filtered in the 150–500 s bandpass using a causal 4th order butterworth filter. The two red dots indicate the time-window of the W-phase. The blue waveform corresponds to the 1-D Earth model STW105 and the red waveform corresponds to the 3-D Earth model S362ANI with Crust2.0.

on the magnitude, focal mechanism and centroid time are significantly larger at shallow depth. Magnitude differences larger than 0.1, beachball RMS differences larger than 0.06 and centroid time differences larger than 3 s are only found for earthquakes shallower than 50 km. To analyse these results, we explore how the moment tensor resolution evolves as a function of depth. Let us first write the W-phase moment tensor solution obtained assuming a 1-D (spherical) Earth model as:

$$\tilde{\mathbf{m}} = \mathbf{G}_{\text{1D}}^{-g} \mathbf{d}. \quad (8)$$

In this equation, $\tilde{\mathbf{m}}$ is the inverted moment tensor, \mathbf{d} is the data vector (i.e. concatenated W-phase waveforms) and $\mathbf{G}_{\text{1D}}^{-g}$ is the least-squares generalized inverse operator computed assuming a 1-D Earth model (i.e. $\mathbf{G}_{\text{1D}}^{-g} = (\mathbf{G}_{\text{1D}}^T \mathbf{G}_{\text{1D}})^{-1} \mathbf{G}_{\text{1D}}^T$, where \mathbf{G}_{1D} is the 1-D Green's function matrix; Kanamori & Rivera 2008). The data vector can be represented as

$$\mathbf{d} = \mathbf{G}_{\text{3D}} \mathbf{m} + \epsilon, \quad (9)$$

where \mathbf{G}_{3D} are Green's functions accounting for 3-D heterogeneity, \mathbf{m} is the ‘true’ moment tensor (used to compute SPECFEM3D_GLOBE synthetics) and ϵ is the ambient seismic noise in the data. We can then rewrite eq. (8):

$$\tilde{\mathbf{m}} = \mathbf{R}_{\text{3D}} \mathbf{m} + \mathbf{G}_{\text{1D}}^{-g} \epsilon, \quad (10)$$

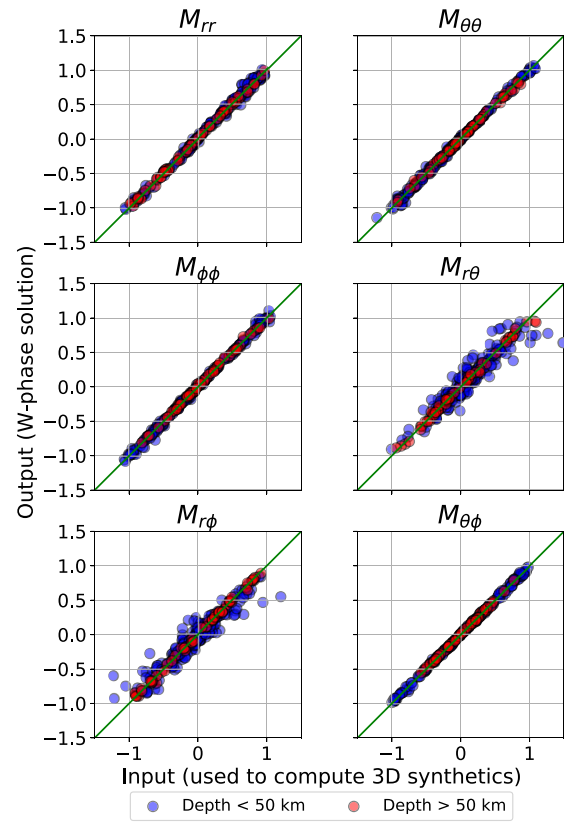


Figure 10. Comparison between input and output moment tensor solutions (for $M_W = 7.5$ earthquakes and the S362ANI Earth model). Blue dots correspond to shallow earthquakes (depth < 50 km) and red dots correspond to event depths larger than 50 km. We see a larger dispersion for $M_{r\theta}$ and $M_{r\phi}$ components for shallow earthquakes.

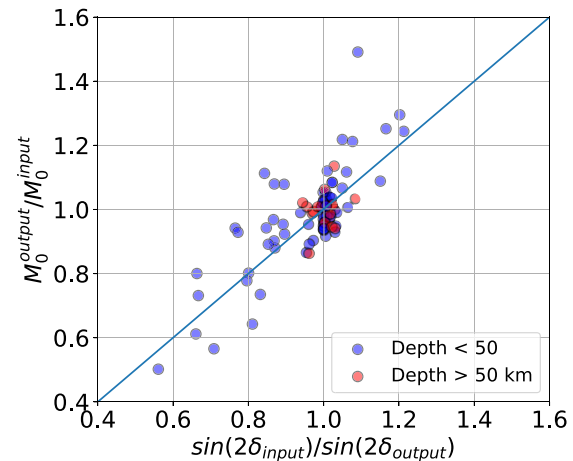


Figure 11. Comparison between the scalar moment ratio and the ratio of $\sin(2\delta)$ (δ is the dip angle) for dip-slip earthquakes in our catalogue. These results correspond to solutions obtained for $M_W = 7.5$ and the S362ANI model with a rake angle $80^\circ < |\lambda| < 100^\circ$. Earthquakes at depth shallower than 50 km are colored in blue while deeper events are colored in red.

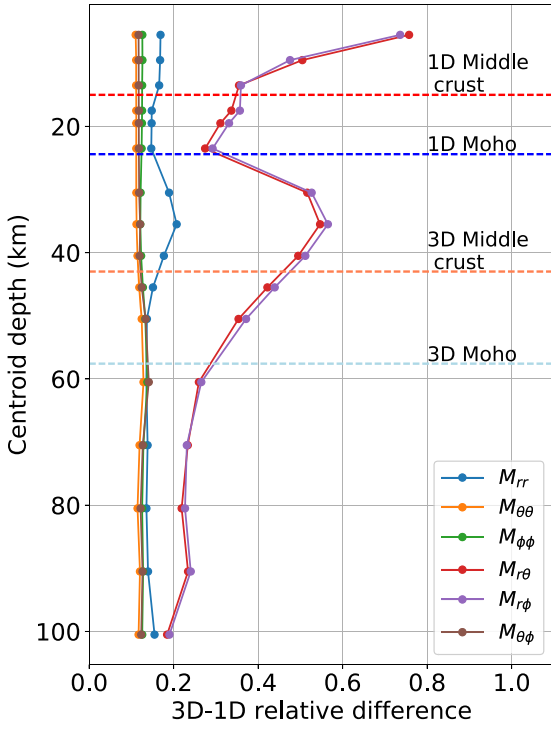


Figure 12. Relative difference between Green's functions computed for 1-D and 3-D Earth models for an earthquake in Nepal (same event as in Figs 8 and 9). The relative difference is defined as $D = \sum_{i=1}^N \int |s_i^{3D}(t) - s_i^{1D}(t)|dt / \sum_{i=1}^N \int |s_i^{3D}(t)|dt$, where $s_i^{1D}(t)$ and $s_i^{3D}(t)$ are, respectively, 1-D and 3-D seismograms, i is the channel index and N is the total number of channels in our data set ($N \sim 360$). We note larger difference for Green's functions calculated for $M_{r\theta}$ and $M_{r\phi}$. To a lesser extent, we also note that differences are generally larger for M_{rr} than for the other moment tensor elements.

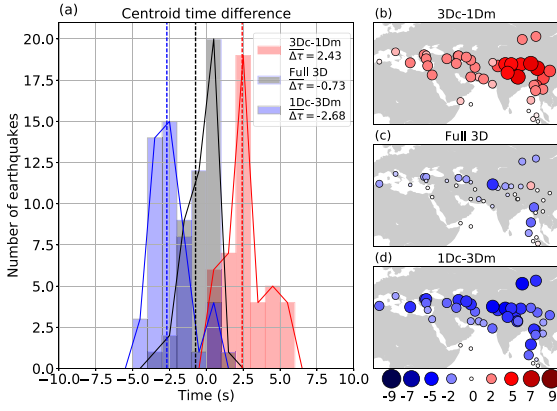


Figure 13. Centroid time differences in Eurasia, for different Earth models and $M_W = 7.5$ earthquakes. (a) histograms of centroid time difference for the 1-D crust and 1-D mantle (red), model S362ANI (black) and the 1-D crust and 1-D mantle (blue) and (b), (c) and (d) show the corresponding distribution of centroid time differences.

where the resolution matrix \mathbf{R}_{3D} is defined as:

$$\mathbf{R}_{3D} = \mathbf{G}_{1D}^{-g} \mathbf{G}_{3D}. \quad (11)$$

The matrix \mathbf{R}_{3D} provides a direct measure of the impact of 3-D structure on moment tensor inversion results. From eq. (10) the difference between inverted and input moment tensor can then be

written as:

$$\tilde{\mathbf{m}} - \mathbf{m} = (\mathbf{R}_{3D} - \mathbf{I})\mathbf{m} + \mathbf{G}_{1D}^{-g} \epsilon \quad (12)$$

where \mathbf{I} is the identity matrix. If the resolution matrix is not the identity \mathbf{I} , then the error in the estimated moment tensor will result both from the impact of 3-D heterogeneity (i.e. the term $(\mathbf{R}_{3D} - \mathbf{I})\mathbf{m}$) and from the propagation of noise on the estimated solution (i.e. the term $\mathbf{G}_{1D}^{-g} \epsilon$). We can see that when the values of \mathbf{R}_{3D} are close to \mathbf{I} , the moment tensor components are not significantly affected by 3-D heterogeneity (error in model estimates will then only be caused by ambient noise ϵ).

Fig. 8 illustrates the variation of \mathbf{R}_{3D} with depth for an earthquake in Nepal (lat = 27.9°N, lon = 85.3°E), where the crust is thicker than the 1-D model used to compute the Green's functions. We note that off-diagonal elements of \mathbf{R}_{3D} are close to zero, indicating that elements on the diagonal can roughly be interpreted as scaling factors between true and inverted moment tensor components. Results show that most diagonal elements of \mathbf{R}_{3D} remain close to one, with the exception of those associated with $M_{r\theta}$ and $M_{r\phi}$ moment tensor components. The elements of \mathbf{R}_{3D} corresponding to $M_{r\theta}$ and $M_{r\phi}$ show large variations as function of depth. Other examples provided in the online supplementary for earthquakes in Chile and Turkey also show larger variations for $M_{r\theta}$ and $M_{r\phi}$ components (see Figs S5 and S6). In Nepal, from the surface to the middle crust of the 1-D model they are smaller than one (Fig. 8a). These elements then increase to reach ~ 2 in the vicinity of the 1-D Moho and the 3-D middle crust (Fig. 8c). Finally, they decrease and stay close to one at depths larger than the 3-D Moho (Fig. 8e). This depth variation of \mathbf{R}_{3D} indicates that $|M_{r\theta}|$ and $|M_{r\phi}|$ will systematically be overestimated below the 1-D middle crust in Nepal. This is consistent with inversion results in the region presented in Fig. 3, showing that the scalar moment is overestimated at depth larger than 15 km (i.e. below the 1-D middle crust). Fig. 9 compares 1-D and 3-D Green's functions computed at a centroid depth of 35.5 km. It clearly appears that 1-D Green's functions for $M_{r\theta}$ and $M_{r\phi}$ are smaller than Green's functions computed in a 3-D Earth, which explains the overestimation of $M_{r\theta}$ and $M_{r\phi}$ and the corresponding large values in \mathbf{R}_{3D} .

More generally, if we compare inverted moment tensor solutions with the input values (as shown in Fig. 10), we observe larger dispersion on $M_{r\theta}$ and $M_{r\phi}$ elements, for shallower events. Such, larger dispersion on $M_{r\theta}$ and $M_{r\phi}$ can also be observed when comparing W-phase and GCMT solutions (Duputel *et al.* 2012b). For shallow dip-slip earthquakes, the larger uncertainty on $M_{r\theta}$ and $M_{r\phi}$ results in a moment-dip trade-off, where different solutions corresponding to a constant value of $M_0 \sin 2\delta$ (where δ is the dip angle) will be associated with the same data misfit (e.g. Bukchin 2006). We should therefore have the relation

$$\frac{M_0^{\text{output}}}{M_0^{\text{input}}} = \frac{\sin(2\delta_{\text{input}})}{\sin(2\delta_{\text{output}})}. \quad (13)$$

Fig. 11 compares the moment ratio $M_0^{\text{output}} / M_0^{\text{input}}$ with the right side of eq. (13), for earthquakes with dip-slip mechanisms in our catalogue (i.e. with a rake angle $80^\circ < |\lambda| < 100^\circ$). Although there is some variability induced by ambient noise and 3-D heterogeneity, the estimated scalar moments and dip angles for earthquakes deeper than 50 km are relatively close to the input values. On the other hand, shallow earthquakes clearly depict an additional variability that can largely be attributed to the $M_0 \sin 2\delta$ trade-off. There is some scatter around the trade-off curve in eq. (13). This can be induced by observational and modeling errors and can also be related to deviations from a pure dip-slip mechanism.

Table 2. Overall impact of 1-D heterogeneity on source parameters. For the two studied 1-D Earth models and for both $M_W = 7.5$ and $M_W = 6.5$ earthquakes, we show the mean and standard deviation of the magnitude difference (ΔM_W), the beachball RMS difference (Δ), the centroid time difference ($\Delta\tau$), the centroid depth difference (Δh) and the centroid mislocation ($|\Delta x|$).

Model		ΔM_W	Δ	$\Delta\tau$ [s]	Δh [km]	$ \Delta x $ [km]
S362ANI	($M_W = 7.5$)	0 ± 0.03	0.05 ± 0.04	-0.4 ± 1.9	3.1 ± 6.5	17.0
S40RTS	($M_W = 7.5$)	0 ± 0.03	0.05 ± 0.04	0 ± 2	1.2 ± 5.5	17.3
S362ANI	($M_W = 6.5$)	0 ± 0.03	0.06 ± 0.05	0.1 ± 2	4.5 ± 5.7	16.5
S40RTS	($M_W = 6.5$)	0 ± 0.03	0.06 ± 0.05	0.6 ± 2.1	2 ± 5.4	17.3

The larger uncertainty on $M_{r\theta}$ and $M_{r\phi}$ estimates at long period is usually interpreted as a direct consequence of the low amplitude of the associated Green's functions close to the free surface (e.g. Dziewonski *et al.* 1981; Kanamori & Given 1982). Moreover, we note in Fig. 9 that Green's functions associated with $M_{r\theta}$ and $M_{r\phi}$ are also more affected by the 3-D structure than the other components. This is confirmed in Figs 12 and S7 showing that, for earthquakes at different locations, the relative impact of lateral heterogeneity is generally larger for $M_{r\theta}$ and $M_{r\phi}$. It shows that 3-D heterogeneity in the source region is a significant contributor to the observed differences for $M_{r\theta}$ and $M_{r\phi}$ components of shallow earthquakes.

4.3 Anticorrelation between crustal and mantle effects

In Section 3.4, we found that 3-D heterogeneity in the crust and in the mantle seems to have an anticorrelated impact on spatio-temporal centroid coordinates.

For example, we see that 3-D crustal heterogeneity induces positive centroid time delays in Eurasia and South America, while mantle heterogeneity induces negative delays in the same regions (see Figs 5b and e). In the same way, the crust induces negative delays at the interface between Australian, Pacific and Antarctic plates, while mantle heterogeneity induces positive delays. Although such anticorrelation is less clear for centroid locations, we see that the crust induces a westward bias in South America, while the mantle biases locations towards the east in the same area (see Figs 5c and f).

Fig. 13 presents a detailed analysis of the relative effect of crust and mantle heterogeneity on centroid times estimated in Eurasia, where the differences of 3Dc–1Dm (3-D crust and 1-D mantle) and 1Dc–3Dm (1-D crust and 1-D mantle) are quite clear. Fig. 13(a) shows the distribution of centroid time differences ($\Delta\tau$) for 3Dc–1Dm, 1Dc–3Dm and the full 1-D model assuming $M_W = 7.5$ earthquakes (W-phase solutions obtained using a 150–500 s bandpass filter). It clearly illustrates the anticorrelation between crustal and mantle effects on centroid times that is also visible in Figs 13(b) and (d). On the other hand, we note that values of $\Delta\tau$ for the full 1-D model are smaller, suggesting that mantle and crustal effects compensates. Such anticorrelation is also found for $M_W = 6.5$ earthquakes (using a 100–250 s bandpass filter) in Fig. S8 that also show a larger impact of crustal heterogeneity on centroid times (resulting into larger $\Delta\tau$ values). The larger crustal effects for $M_W = 6.5$ earthquakes is most likely due to the use of shorter period waveforms that are more sensitive to shallow heterogeneity.

The 1-D Global mantle models used in this study are obtained by assuming a specific crustal model (the CRUST2.0 model). The crust structure is then linked to the mantle as these models rely on a fixed crustal model to fit the observations. We think that this could explain partly the observed anticorrelation of centroid times estimates in Fig. 13. Such mutual cancellation of crustal and mantle

effects has also been reported in another context by Koelemeijer (2014).

5 CONCLUSIONS

We quantify the impact of lateral structural heterogeneity on W-phase CMT solutions by simulating synthetic earthquakes in 1-D Earth models and comparing the retrieved source parameters with the input values. To assess the influence of long-period noise, we add actual ambient noise to synthetics assuming two earthquake magnitudes ($M_W = 6.5$ and $M_W = 7.5$). The results obtained for 1-D Earth models S362ANI and S40RTS and moment magnitudes $M_W = 6.5$ and 7.5 are summarized in Table 2.

On average, the impact of 1-D heterogeneity is relatively small on retrieved W-phase solutions. The resulting discrepancy on moment magnitude estimates is smaller than 0.03 for 80 per cent of earthquakes. Beachball RMS differences are smaller than 0.1 for ~90 per cent of earthquakes. The impact on centroid time is of the same order as the sampling period. Overall, lateral heterogeneity mainly impacts centroid locations, especially if the station coverage is limited. This is particularly visible in the Circum-Pacific belt for which many earthquakes have paths that only cross the Pacific Ocean for large ranges of source to station azimuths.

Results show that the impact of 1-D heterogeneity is consistent between Earth models S362ANI and S40RTS, suggesting that the W-phase is mainly sensitive to large-scale heterogeneity that exists in both models. Although uncertainties estimated for $M_W = 6.5$ earthquakes are often larger than for $M_W = 7.5$ events, shifting the passband towards higher frequencies clearly mitigates the impact of long period ambient noise. The remaining larger dispersion observed for $M_W = 6.5$ events likely results from larger 1-D effects when using shorter period waveforms.

Results also indicate that most source parameters seems to be mostly affected by mantle heterogeneity, where most of the W-phase propagating energy is confined. However, crustal heterogeneity seems to have a larger impact on scalar moment estimates for shallow earthquakes. In general, the uncertainty on scalar seismic moment, focal mechanism and centroid time increases significantly at shallow depth. This can be attributed to the difficulty to constrain $M_{r\theta}$ and $M_{r\phi}$ moment tensor elements at long period due to the small amplitude of the associated Green's functions for shallow earthquakes. In addition, our tests indicate that Green's functions for $M_{r\theta}$ and $M_{r\phi}$ are more impacted by lateral heterogeneity than the other components.

Although the impact of lateral heterogeneity on W-phase solutions is relatively moderate on average, source models can clearly be improved by incorporating 1-D Green's functions (e.g. Ferreira *et al.* 2011; Duputel *et al.* 2016; Hejrani *et al.* 2017). While it is still challenging for global real-time applications, the improvement of

computational capabilities makes rapid 1-D CMT inversions already possible at regional scale (Wang & Zhan 2019). As lateral heterogeneity can have non-negligible impact on earthquake locations, such improvements could be instrumental for rapid earthquake response and tsunami warning purposes.

ACKNOWLEDGEMENTS

The authors would like to acknowledge the Editor, Ana Ferreira, an anonymous reviewer and Göran Ekström for their comments. We also would like to thank Stephen Beller, Hiroo Kanamori, Javier Ruiz and Sophie Lambotte for helpful discussion at various stages of this work. Some of the computations were performed on the facilities of the High Performance Computing Center of the University of Strasbourg. This work was supported by the Initiative d'Excellence (IDEX) funding framework (Université de Strasbourg). This project has also received funding from the European Research Council (ERC, under the European Union's Horizon 2020 research and innovation programme under grant agreement No. 805256) and from Agence Nationale de la Recherche (project ANR-17-ERC3-0010). We wish to thank the network and station operators for their commitment to collect high-quality seismic data. Some figures were made using the Generic Mapping Tools (GMT) software version 5.3.1 (Wessel *et al.* 2013).

REFERENCES

- Albuquerque Seismological Laboratory (ASL)/USGS, 1988. Global Seismograph Network (GSN - IRIS/USGS). International Federation of Digital Seismograph Networks.
- Albuquerque Seismological Laboratory (ASL)/USGS, 1992. New China Digital Seismograph Network. International Federation of Digital Seismograph Networks.
- Albuquerque Seismological Laboratory (ASL)/USGS, 1993. Global Telemetered Seismograph Network (USAF/USGS). International Federation of Digital Seismograph Networks.
- Albuquerque Seismological Laboratory (ASL)/USGS, 2006. Caribbean USGS Network. International Federation of Digital Seismograph Networks.
- Bai, L., Wu, Z., Zhang, T. & Kawasaki, I., 2006. The effect of distribution of stations upon location error: statistical tests based on the double-difference earthquake location algorithm and the bootstrap method, *Earth, Planets Space*, **58**(2), e9–e12, doi.org/10.1186/BF03353364.
- Bassin, C., Laske, G. & Masters, G., 2000. The current limits of resolution for surface wave tomography in North America, *EOS, Trans. Am. Geophys. Un.*, **81**(F897).
- Bondár, I. & Storchak, D., 2011. Improved location procedures at the international seismological centre, *J. geophys. Int.*, **186**(3), 1220–1244, doi.org/10.1111/j.1365-246X.2011.05107.x.
- Bondár, I., Myers, S.C., Engdahl, E.R. & Bergman, E.A., 2004. Epicentre accuracy based on seismic network criteria, *J. geophys. Int.*, **156**(3), 483–496, doi.org/10.1111/j.1365-246X.2004.02070.x.
- Bukchin, B.G., 2006. Specific features of surface wave radiation by a shallow source, *Izvest. Phys. Solid Earth*, **42**(8), 712–717, doi.org/10.1134/S1069351306080088.
- California Institute of Technology and United States Geological Survey Pasadena (SCSN), 1926. Southern California Seismic Network. International Federation of Digital Seismograph Networks.
- Crowell, B.W., Bock, Y. & Melgar, D., 2012. Real-time inversion of GPS data for finite fault modeling and rapid hazard assessment, *Geophys. Res. Lett.*, **39**(9), doi:10.1029/2012GL051318.
- Dahlen, F. & Tromp, J., 1998. *Theoretical Global Seismology*, Princeton Univ. Press.
- Delouis, B., Nocquet, J.-M. & Vallée, M., 2010. Slip distribution of the February 27, 2010 Mw = 8.8 Maule earthquake, central Chile, from static and high-rate GPS, InSAR, and broadband teleseismic data, *Geophys. Res. Lett.*, **37**(17), doi:10.1029/2010GL043899.
- Duputel, Z., Rivera, L., Fukahata, Y. & Kanamori, H., 2012a. Uncertainty estimations for seismic source inversions, *J. geophys. Int.*, **190**(2), 1243–1256, doi.org/10.1111/j.1365-246X.2012.05554.x.
- Duputel, Z., Rivera, L., Kanamori, H. & Hayes, G., 2012b. W phase source inversion for moderate to large earthquakes (1990–2010), *J. geophys. Int.*, **189**(2), 1125–1147, doi.org/10.1111/j.1365-246X.2012.05419.x.
- Duputel, Z., Agram, P.S., Simons, M., Minson, S.E. & Beck, J.L., 2014. Accounting for prediction uncertainty when inferring subsurface fault slip, *J. geophys. Int.*, **197**(1), 464–482, doi.org/10.1093/gji/ggt517.
- Duputel, Z., Vergne, J., Rivera, L., Wittlinger, G., Farra, V. & Hetényi, G., 2016. The 2015 Gorkha earthquake: a large event illuminating the main Himalayan thrust fault, *Geophys. Res. Lett.*, **43**(6), 2517–2525, doi.org/10.1002/2016GL068083.
- Dziewonski, A., Franzen, J. & Woodhouse, J., 1984. Centroid-moment tensor solutions for January–March, 1984, *Phys. Earth planet. Inter.*, **34**(4), 209–219.
- Dziewonski, A.M., Chou, T.-A. & Woodhouse, J.H., 1981. Determination of earthquake source parameters from waveform data for studies of global and regional seismicity, *J. geophys. Res.*, **86**(B4), 2825–2852, doi.org/10.1029/JB086iB04p02825.
- Dziewonski, A.M., Ekström, G. & Salganik, M.P., 1992. Centroid-moment tensor solutions for July–September 1991, *Phys. Earth planet. Inter.*, **72**(1–2), 1–11.
- Ekström, G., Nettles, M. & Dziewonski, A., 2012. The global CMT project 2004–2010: centroid-moment tensors for 13,017 earthquakes, *Phys. Earth planet. Inter.*, **200–201**, 1–9.
- Ferreira, A.M.G. & Woodhouse, J.H., 2006. Long-period seismic source inversions using global tomographic models, *J. geophys. Int.*, **166**(3), 1178–1192, doi.org/10.1111/j.1365-246X.2006.03003.x.
- Ferreira, A. M.G., Weston, J. & Funning, G.J., 2011. Global compilation of interferometric synthetic aperture radar earthquake source models: 2. Effects of 3-D earth structure, *J. geophys. Res.*, **116**(B8), doi:10.1029/2010JB008132.
- GEOFON Data Centre, 1993. Geofon seismic network. deutsches geoforschungszentrum gfz.
- Geological Survey of Canada, 1980. Canadian National Seismograph Network (CNSN). International Federation of Digital Seismograph Networks.
- Gombert, B., Duputel, Z., Jolivet, R., Simons, M., Jiang, J., Liang, C., Fielding, E. & Rivera, L., 2018. Strain budget of the Ecuador–Colombia subduction zone: a stochastic view, *Earth planet. Sci. Lett.*, **498**, 288–299, doi.org/10.1016/j.epsl.2018.06.046.
- Hallo, M. & Gallovič, F., 2016. Fast and cheap approximation of green function uncertainty for waveform-based earthquake source inversions, *J. geophys. Int.*, **207**(2), 1012–1029, doi.org/10.1093/gji/ggw320.
- Hallo, M., Asano, K. & Gallovič, F., 2017. Bayesian inference and interpretation of centroid moment tensors of the 2016 Kumamoto earthquake sequence, Kyushu, Japan, *Earth, Planets Space*, **69**(1), 134.
- Hayes, G.P., Rivera, L. & Kanamori, H., 2009. Source inversion of the W-phase: real-time implementation and extension to low magnitudes, *Seismol. Res. Lett.*, **80**(5), 817.
- Hejrani, B., Tkalcic, H. & Fichtner, A., 2017. Centroid moment tensor catalogue using a 3-D continental scale earth model: application to earthquakes in Papua New Guinea and the Solomon Islands, *J. geophys. Res.*, **122**(7), 5517–5543.
- Hjörleifsdóttir, V. & Ekström, G., 2010. Effects of three-dimensional earth structure on cmt earthquake parameters, *Phys. Earth planet. Inter.*, **179**(3), 178–190.
- Ide, S., 2007. 4.07 - slip inversion, in *Treatise on Geophysics*, pp. 193–223, ed. Schubert, G., Elsevier.
- Institut de Physique du Globe de Paris (IPGP) and Ecole et Observatoire des Sciences de la Terre de Strasbourg (EOST), 1982. Geoscope, French Global Network of Broad Band Seismic Stations. Institut de Physique du Globe de Paris (IPGP).
- Kanamori, H., 1993. W phase, *Geophys. Res. Lett.*, **20**(16), 1691–1694.

- Kanamori, H. & Given, J.W., 1982. Use of long-period surface waves for rapid determination of earthquake source parameters 2. Preliminary determination of source mechanisms of large earthquakes ($ms \geq 6.5$) in 1980, *Phys. Earth planet. Inter.*, **30**(2), 260–268.
- Kanamori, H. & Rivera, L., 2008. Source inversion of W-phase: speeding up seismic tsunami warning, *J. geophys. Int.*, **175**(1), 222–238, doi.org/10.1111/j.1365-246X.2008.03887.x.
- Koellemeijer, P., 2014. Normal mode studies of long wavelength structures in Earth's lowermost mantle, *PhD thesis*, University of Cambridge.
- Komatitsch, D. & Tromp, J., 2002a. Spectral-element simulations of global seismic wave propagation – I. Validation, *J. geophys. Int.*, **149**(2), 390–412.
- Komatitsch, D. & Tromp, J., 2002b. Spectral-element simulations of global seismic wave propagation – II. Three-dimensional models, oceans, rotation and self-gravitation, *J. geophys. Int.*, **150**(1), 303–318.
- Komatitsch, D., et al., 2015. SPECFEM3D globe v7.0.0 [software].
- Kustowski, B., Ekström, G. & Dziewoski, A.M., 2008. Anisotropic shear-wave velocity structure of the earth's mantle: a global model, *J. geophys. Res.*, **113**(B6), doi:10.1029/2007JB005169.
- Liu, Q., Polet, J., Komatitsch, D. & Tromp, J., 2004. Spectral-element moment tensor inversions for earthquakes in southern California, *Bull. seism. Soc. Am.*, **94**(5), 1748.
- MedNet Project Partner Institutions, 1990. Mediterranean Very Broadband Seismographic Network (mednet).
- Nakanishi, I. & Kanamori, H., 1982. Effects of lateral heterogeneity and source process time on the linear moment tensor inversion of long-period rayleigh waves, *Bull. seism. Soc. Am.*, **72**(6A), 2063.
- Northern California Earthquake Data Center, 2014. Berkeley Digital Seismic Network (BDSN) [data set].
- Polet, J. & Thio, H.K., 2011. Rapid calculation of a centroid moment tensor and waveheight predictions around the north Pacific for the 2011 off the Pacific coast of Tohoku earthquake, *Earth, Planet Space*, **63**, doi:10.5047/eps.2011.05.005.
- Riquelme, S., Medina, M., Bravo, F., Barrientos, S., Campos, J. & Cisternas, A., 2018. W-phase real-time implementation and network expansion from 2012 to 2017: the experience in Chile, *Seismol. Res. Lett.*, **89**(6), 2237.
- Ritsema, J., Deuss, A., van Heijst, H.J. & Woodhouse, J.H., 2011. S40rts: a degree-40 shear-velocity model for the mantle from new Rayleigh wave dispersion, teleseismic traveltimes and normal-mode splitting function measurements, *J. geophys. Int.*, **184**(3), 1223–1236.
- Rivera, L. & Kanamori, H., 2014. Diagnosing source geometrical complexity of large earthquakes, *Pure appl. Geophys.*, **171**(10), 2819–2840.
- Scripps Institution of Oceanography, 1986. Global Seismograph Network (GSN - IRIS/USGS). International Federation of Digital Seismograph Networks.
- Silver, P.G. & Jordan, T.H., 1982. Optimal estimation of scalar seismic moment, *Geophys. J. Int.*, **70**(3), 755–787.
- Tsai, V.C., Nettles, M., Ekström, G. & Dziewoski, A.M., 2005. Multiple CMT source analysis of the 2004 Sumatra earthquake, *Geophys. Res. Lett.*, **32**(17), L17304.
- Wang, D., et al., 2017. Evaluation of W phase CMT based PTWC real-time tsunami forecast model using DART observations: events of the last decade, *AGU Fall Meeting Abstracts*, , abstract #NH21D-02.
- Wang, X. & Zhan, Z., 2019. Moving from 1-D to 3-D velocity model: automated waveform-based earthquake moment tensor inversion in the Los Angeles region, *Geophys. J. Int.*, **220**(1), 218–234, doi.org/10.1093/gji/ggz435.
- Wessel, P., Smith, W.H.F., Scharroo, R., Luis, J. & Wobbe, F., 2013. Generic mapping tools: improved version released, *EOS, Trans. Am. Geophys. Un.*, **94**(45), 409–410.
- Weston, J., Ferreira, A. M.G. & Funning, G.J., 2011. Global compilation of interferometric synthetic aperture radar earthquake source models: 1. Comparisons with seismic catalogs, *J. geophys. Res.*, **116**(B8), doi:10.1029/2010JB008131.
- Weston, J., Ferreira, A.M. & Funning, G.J., 2012. Systematic comparisons of earthquake source models determined using InSAR and seismic data, *Tectonophysics*, **532–535**, 61–81, doi.org/10.1016/j.tecto.2012.02.001.
- Woodhouse, J.H. & Dziewonski, A.M., 1984. Mapping the upper mantle: three-dimensional modeling of earth structure by inversion of seismic waveforms, *J. geophys. Res.*, **89**(B7), 5953–5986, doi.org/10.1029/JB089iB07p05953.
- Yagi, Y. & Fukahata, Y., 2011. Introduction of uncertainty of green's function into waveform inversion for seismic source processes, *J. geophys. Int.*, **186**(2), 711–720, doi.org/10.1111/j.1365-246X.2011.05043.x.
- Zhao, X., Duputel, Z. & Yao, Z., 2017. Regional w-phase source inversion for moderate to large earthquakes in china and neighboring areas, *J. geophys. Res.*, **122**(12), 10 052–10 068, doi.org/10.1002/2017JB014950.

SUPPORTING INFORMATION

Supplementary data are available at *GJI* online.

Figure S1 Effects of 1-D heterogeneity for $M_W = 6.5$ earthquakes. Maps shows the following quantities from top to bottom: moment magnitude difference, beachball RMS difference, difference in time-shift, depth difference and horizontal mislocation. Panels from (a) to (e) correspond to the inversion of synthetic seismograms created with the Earth model S362ANI. Panels (f) to (j) correspond to the inversion of synthetic seismograms created with the Earth model S40RTS. In both cases, seismic noise has been added to synthetics prior to source inversion (see Section 2.1 of the main text).

Figure S2 Example of circular array for an earthquake in the middle of the Pacific. The inset on the lower left-hand corner show the station distribution from the actual seismological network that would have been used for that earthquake.

Figure S3 Effects of crustal and mantle heterogeneity on W-phase solutions obtained for $M_W = 7.5$ earthquakes. Top maps indicate beachball RMS difference (Δ) and bottom map show the depth difference (Δh). Panels (a) and (b) correspond to the inversion of synthetic seismograms created with a 1-D crust (CRUST2.0) and a 1-D mantle (STW105). Panels (c) and (d) correspond to the results of the inversion of synthetic seismograms created with a 1-D crust (STW105) and a 1-D mantle (S362ANI). As described in the main text, ambient noise has been added to synthetics prior to source inversion.

Figure S4 Effects of crustal and mantle heterogeneity on W-phase solutions obtained for $M_W = 6.5$ earthquakes. Maps show from top to bottom: moment magnitude difference, beachball RMS difference, difference in time-shift, depth difference and horizontal mislocation. Panels from (a) to (e) correspond to the inversion of synthetic seismograms created with a 1-D crust (CRUST2.0) and a 1-D mantle (STW105). Panels (f) to (j) correspond to the inversion of synthetic seismograms created with a 1-D crust (STW105) and a 1-D mantle (S362ANI). As described in the main text, ambient noise has been added to synthetics prior to source inversion.

Figure S5 Moment tensor resolution matrix as a function of depth for an earthquake in Chile ($lat = 40.64^\circ S$, $lon = 75.37^\circ W$). Figures from (a) to (e) correspond to the resolution matrix at different depths. Panel (f) shows the variation in depth of the value of the diagonal components of the resolution matrix, horizontal lines show the Moho and middle crust depth for STW105 (1-D model) and crust 2.0 (1-D model).

Figure S5 Moment tensor resolution matrix as a function of depth an earthquake in Turkey ($lat = 41.01^\circ N$, $lon = 29.97^\circ E$). Panels from (a) to (e) correspond to the resolution matrix at different depths. Panel (f) shows the variation in depth of the value of the diagonal components of the resolution matrix, horizontal lines show the Moho and middle crust depth for STW105 (1-D model) and crust 2.0 (1-D model).

Figure S6 Relative difference between Green's functions computed for 1-D and 1-D Earth models for earthquakes in (a) Chile and (b) Turkey (same events as in Figs S5 and S6). The relative difference is defined as in Fig. 12 of the main text.

Figure S7 Centroid time differences in Eurasia, for different Earth models and $M_W = 6.5$ earthquakes. (a) histograms of centroid time difference for the 1-D crust and 1-D mantle (red), model S362ANI

(black) and the 1-D crust and 1-D mantle (blue) and (c) and (d) show the corresponding distribution of centroid time differences.

Please note: Oxford University Press is not responsible for the content or functionality of any supporting materials supplied by the authors. Any queries (other than missing material) should be directed to the corresponding author for the paper.

2.4 Le séisme de Gorkha en 2015

La séquence de séismes de Gorkha en 2015 a fourni une opportunité unique de caractériser la géométrie du chevauchement principal himalayen. Pour limiter l'impact des hétérogénéités latérales de structure discutées précédemment, nous effectuons l'inversion du tenseur moment sismique dans un modèle de Terre 3D pour le choc principal et ses plus grandes répliques. En parallèle, nous recalculons les fonctions récepteur S-P et P-S à partir des données HI-CLIMB. Les séismes de la séquence de Gorkha sont localisés dans une zone de faible vitesse à une profondeur de 10-15 km correspondant à la partie plate du chevauchement principal himalayen. Au nord de l'hypocentre, les fonctions récepteurs indiquent une structure à pendage vers le nord correspondant à la rampe crustale connectant la partie plate du chevauchement à sa partie profonde. Notre analyse indique que l'énergie longue période émise lors du choc principal est localisée au sud des sources de radiations à haute fréquence, ce qui pourrait s'expliquer par différents facteurs tels que la géométrie de la faille ou la présence de fluides.

L'article proposé ci-dessous a été publié en 2016 dans *Geophysical Research Letters*. Ce travail a été effectué suite à mon recrutement à l'IPGS.



Geophysical Research Letters

RESEARCH LETTER

10.1002/2016GL068083

Key Points:

- We conduct a joint analysis of receiver functions and 3-D CMT solutions for the 2015 Gorkha sequence to explore the geometry of the MHT
- Results outline the ramp-flat-ramp geometry of the MHT and show that the flat seismogenic portion of the MHT is confined within a LVZ
- The frequency-dependent behavior of the Gorkha rupture can be explained by a downdip fault kink and the presence of fluids in the LVZ

Supporting Information:

- Supporting Information S1

Correspondence to:

Z. Duputel,
zacharie.duputel@unistra.fr

Citation:

Duputel, Z., J. Vergne, L. Rivera, G. Wittlinger, V. Farra, and G. Hetényi (2016), The 2015 Gorkha earthquake: A large event illuminating the Main Himalayan Thrust fault, *Geophys. Res. Lett.*, 43, doi:10.1002/2016GL068083.

Received 2 FEB 2016

Accepted 1 MAR 2016

Accepted article online 7 MAR 2016

The 2015 Gorkha earthquake: A large event illuminating the Main Himalayan Thrust fault

Zacharie Duputel¹, Jérôme Vergne¹, Luis Rivera¹, Gérard Wittlinger¹, Véronique Farra², and György Hetényi³

¹IPGS-EOST, CNRS/Université de Strasbourg, Strasbourg, France, ²Institut de Physique du Globe de Paris, Paris, France,

³Institute of Earth Sciences, University of Lausanne, Lausanne, Switzerland

Abstract The 2015 Gorkha earthquake sequence provides an outstanding opportunity to better characterize the geometry of the Main Himalayan Thrust (MHT). To overcome limitations due to unaccounted lateral heterogeneities, we perform Centroid Moment Tensor inversions in a 3-D Earth model for the main shock and largest aftershocks. In parallel, we recompute S-to-P and P-to-S receiver functions from the Hi-CLIMB data set. Inverted centroid locations fall within a low-velocity zone at 10–15 km depth and corresponding to the subhorizontal portion of the MHT that ruptured during the Gorkha earthquake. North of the main shock hypocenter, receiver functions indicate a north dipping feature that likely corresponds to the midcrustal ramp connecting the flat portion to the deep part of the MHT. Our analysis of the main shock indicates that long-period energy emanated updip of high-frequency radiation sources previously inferred. This frequency-dependent rupture process might be explained by different factors such as fault geometry and the presence of fluids.

1. Introduction

The Main Himalayan Thrust (MHT) is one of the largest and fastest-slipping continental megathrust on Earth. It absorbs most of the convergence between India and southern Tibet and represents the largest source of seismic hazard in Nepal and North India (Figure 1) [Ader *et al.*, 2012]. The largest instrumentally recorded earthquake in this region is the $M=8.2$ 1934 Bihar earthquake shown in Figure 1, which propagated up to the front of the Himalaya where the MHT emerges at the surface [Geller and Kanamori, 1977; Sapkota *et al.*, 2013] as the Main Frontal Thrust (MFT). From paleoseismological studies, historical events in 1255 and 1505 might have also ruptured the MHT and reached the surface [Sapkota *et al.*, 2013; Bollinger *et al.*, 2014]. Other large earthquakes affected the area of Kathmandu in 1344 and 1833 but whether they occurred on the MHT is debated [Bilham, 1995; Bollinger *et al.*, 2014].

The geometry of the MHT has been investigated through various geological and geophysical field campaigns [Brunel, 1986; Zhao *et al.*, 1993; Brown *et al.*, 1996; Hauck *et al.*, 1998; Lemonnier *et al.*, 1999; Lavé and Avouac, 2001; Nabelek *et al.*, 2009; Wittlinger *et al.*, 2009; Schulte-Pelkum *et al.*, 2005; Caldwell *et al.*, 2013]. Among them, analysis of receiver functions (RF) from the Hi-CLIMB (Himalayan-Tibetan Continental Lithosphere during Mountain Building) experiment reveals a low-velocity zone (LVZ) extending from the Lesser Himalayas to southern Tibet and interpreted as the signature of the MHT beneath Lesser and Higher Himalayas [Nabelek *et al.*, 2009]. Below Nepal this LVZ appears almost horizontal and located at 10 to 15 km depth [Nabelek *et al.*, 2009], but the horizontal and vertical resolutions are limited by the smoothing of the migrated cross section and the frequency range used to produce the receiver functions. Moreover, because of large depth uncertainties in previous earthquake catalogs, the depth of the MHT relative to the LVZ is still unclear [Nabelek *et al.*, 2009; Caldwell *et al.*, 2013]. Between the Lesser and Higher Himalayas, debate is still ongoing regarding the presence of a midcrustal ramp along the MHT at the front of the Higher Himalayas [Lavé and Avouac, 2001; Bollinger *et al.*, 2004; Wobus *et al.*, 2005; Elliott *et al.*, 2016].

On 25 April 2015, a large $M_w=7.8$ earthquake occurred close to Kathmandu (28.230°N , 84.731°E , 06:11:25 UTC; U.S. Geological Survey (USGS) National Earthquake Information Center: <http://earthquake.usgs.gov>). This event was followed by a $M_w=7.2$ aftershock on 12 May 2015. *W* phase inversion was performed both for the main shock and the largest aftershock (Figure S1 in the supporting information). The *W* phase moment tensor estimates are similar to global centroid moment tensor (GCMT) solutions, and the northward low-dipping planes suggest that both events ruptured the MHT. However, centroid depth estimates vary significantly between the different catalogs; *W* phase and SCARDEC (Seismic source characteristics retrieved from deconvolving

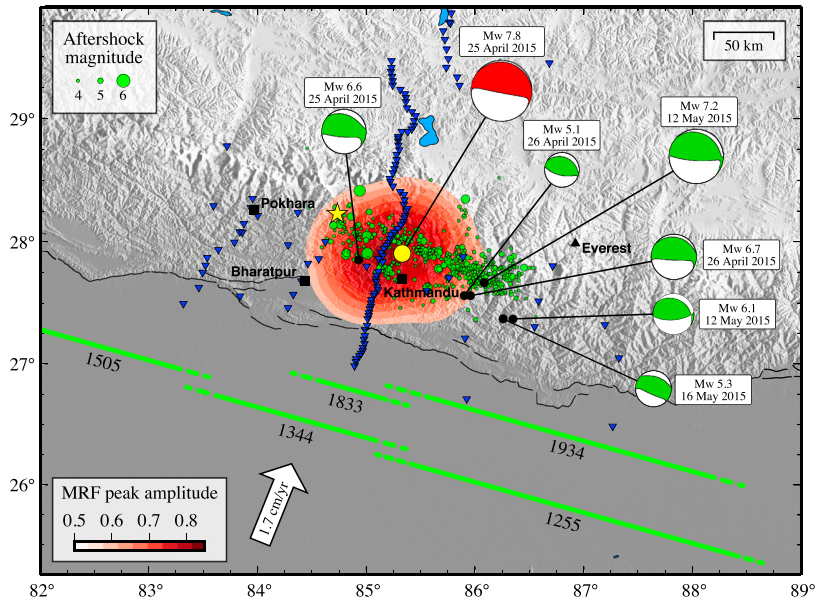


Figure 1. The 2015 Nepal earthquake sequence. Centroid moment tensor (CMT) inversions are conducted using body waves and surface waves assuming a 3-D Earth model. The red focal mechanism is the CMT solution obtained for the $M_w = 7.8$ main shock. Yellow circle is the corresponding centroid location, and yellow star is the USGS hypocenter. Green focal mechanisms are solutions obtained for $M_w \geq 5$ aftershocks. Red colors indicate peak-stacked amplitude in the source region from moment rate functions (MRF) backprojected relative to the main shock epicentral location. Green lines indicate the supposed rupture zones for the 1255, 1344, 1505, 1833, and 1934 earthquakes. Green circles are aftershocks of magnitude $M \geq 4$ from Adhikari et al. [2015] (2015/04/25 to 2015/06/07).

teleseismic body waves) yield to depths larger than 20 km (<http://wphase.unistra.fr>, <http://geoscope.ipgp.fr>), while GCMT converges to its minimum allowed depth of 12 km [Ekström et al., 2012]. On the other hand, preliminary finite-fault inversions [Avouac et al., 2015; Galetzka et al., 2015; Grandin et al., 2015; Yagi and Okuwaki, 2015] fixed the hypocentral depth to ~ 15 km according to the USGS preliminary determined hypocenter location, which was later updated to 8.2 km (<http://geoscope.ipgp.fr>).

The 2015 Gorkha earthquake sequence offers an outstanding occasion to better constrain and resolve the geometry of the MHT. We exploit global long-period data to perform centroid moment tensor (CMT) inversion in a 3-D Earth model. This new CMT approach enables more accurate centroid depth estimates and is accompanied by a detailed directivity analysis of apparent moment rate functions. In parallel, we reprocessed both S-to-P and P-to-S receiver functions under Nepal using a selection of teleseismic events with $M_w > 6$ recorded by the Hi-CLIMB broadband network. The low-dip angle of the MHT (optimum for receiver function imaging) and the coincidence of having the deployment of Hi-CLIMB stations above the Gorkha rupture area is a rare opportunity to image a fault that ruptured in a large earthquake.

2. Depth and Geometry of the Main Himalayan Thrust

As discussed above, the centroid depths of the 2015 Gorkha earthquake sequence are uncertain. The quality of centroid depth estimates depends on many factors like the size of the event, the azimuthal coverage, and the type of used data (W phase, body waves, mantle waves, and surface waves). The inaccuracy of Earth models used for Green's function calculation is a major source of uncertainty in source inversions [Nakanishi and Kanamori, 1982; Smith and Ekström, 1996; Duputel et al., 2014]. The W phase approach is based on a 1-D Earth model and is usually associated with centroid depth uncertainties of the order of 15 km [Vallée et al., 2010; Duputel et al., 2012]. Global CMT corrects 1-D Earth synthetic seismograms using first-order path-averaged phase perturbations [Dziewonski et al., 1992]. Although these corrections yield smaller location uncertainties, GCMT solutions are affected by an average bias of 5–8 km to greater depths [Hjörleifsdóttir and Ekström, 2010].

To determine a range of reasonable centroid depths and to get rid of uncertainty due to unaccounted 3-D structures, we perform CMT inversions for the main shock and $M_w \geq 5.0$ aftershocks based on a 3-D Earth

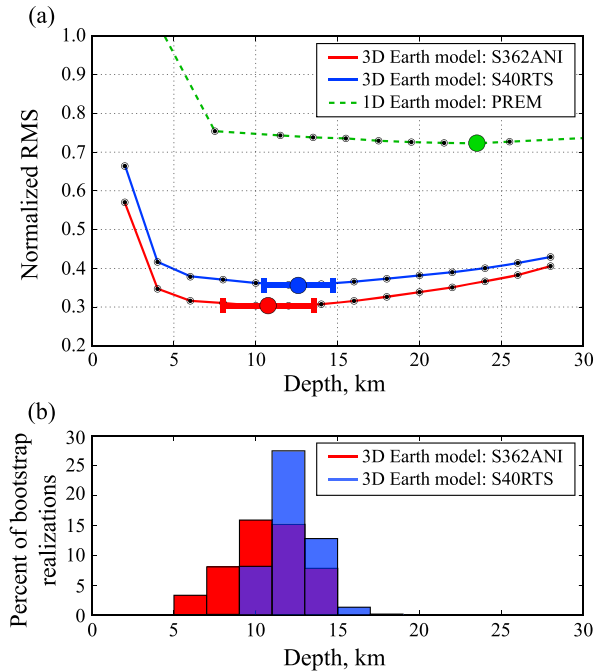


Figure 2. Centroid depth estimates in a 3-D Earth model for the 2015 Gorkha main shock. (a) Normalized RMS with respect to centroid depth. (b) Histogram of depth estimates from 5000 bootstrap realizations. Results are shown in red for S362ANI and in blue for S40RTS. Error bars in Figure 2a correspond to standard deviations estimated from 5000 bootstrap realizations presented in Figure 2b. Results obtained using the 1-D Earth model PREM are shown for reference in green.

the main shock and $M_w \geq 5.0$ aftershocks are presented in Figure 1. These results are obtained using body waves and surface waves filtered between 80 and 200 s for $M_w \geq 6.0$ earthquakes and between 60 and 150 s for smaller events. We use a selected set of 139 broadband seismograms including 77 vertical and 62 horizontal components from global seismological networks. Being contaminated by large amplitude wave trains of the main shock and of the $M_w = 7.2$ aftershock, the $M_w \geq 6$ aftershocks on 25 April and 12 May are analyzed using a smaller data set, after careful selection of nondisturbed waveforms (cf. supporting information). The centroid depth grid search is presented in Figure 2 for the main shock and in Figure S2 for $M_w \geq 5$ aftershocks. For each explored depth, the normalized root-mean-square (RMS) misfit is computed using

$$\rho = \|\mathbf{s} - \mathbf{d}\|_2 / \|\mathbf{s}\|_2 \quad (1)$$

where \mathbf{d} and \mathbf{s} are, respectively, the data and synthetic traces. After grid search, all optimum centroid depths are between 8 km and 14 km. Observed and predicted waveforms computed for our preferred CMT solutions are presented in Figures S3–S11 in the supporting information.

To analyze the variability of these depth estimates, we perform bootstrapping analysis based on 5000 random resampling of the channels used in the inversion [Efron and Tibshirani, 1994]. The histograms in Figures 2 and S2 show the distribution of centroid depths estimated from these 5000 realizations. The number of random samples has been chosen to ensure stability of bootstrapping estimates. In practice, histograms of centroid depths are stable when using more than 1000 realizations. The bootstrap results indicate centroid depths shallower than 15 km (except for the 25 April aftershock associated with large uncertainty). These estimates are globally consistent with aftershock locations from Adhikari *et al.* [2015] shown in Figure 3d and relocations from Bai *et al.* [2016] showing that more than 65% of aftershocks occurred at depth between 10 and 15 km. Such bootstrapping analysis does not fully capture the uncertainty due to inaccuracies in the Earth model used to compute the Green's functions. To investigate this effect, Figure 2 shows the result of

model. The parameters to be determined are the elements of the seismic moment tensor as well as the centroid location and timing. At this stage, the horizontal coordinates of the centroid are fixed to the global CMT location, and the effect of finite-source duration is accounted for by assuming the moment rate function (MRF) to be an isosceles triangle (this hypothesis will be relaxed in the next section). Using an inversion procedure similar to Duputel *et al.* [2012], the centroid depth is estimated by grid searching the best point source location (minimizing the data misfit). The source duration and the centroid timing (i.e., the width and center of the triangular MRF) are evaluated using the same approach. The Green's functions are computed using the spectral-element method (SEM) [Komatitsch and Tromp, 1999] for a 3-D Earth model composed of S362ANI [Kustowski *et al.*, 2008] and Crust2.0 [Basson *et al.*, 2000].

Our preferred CMT solutions for

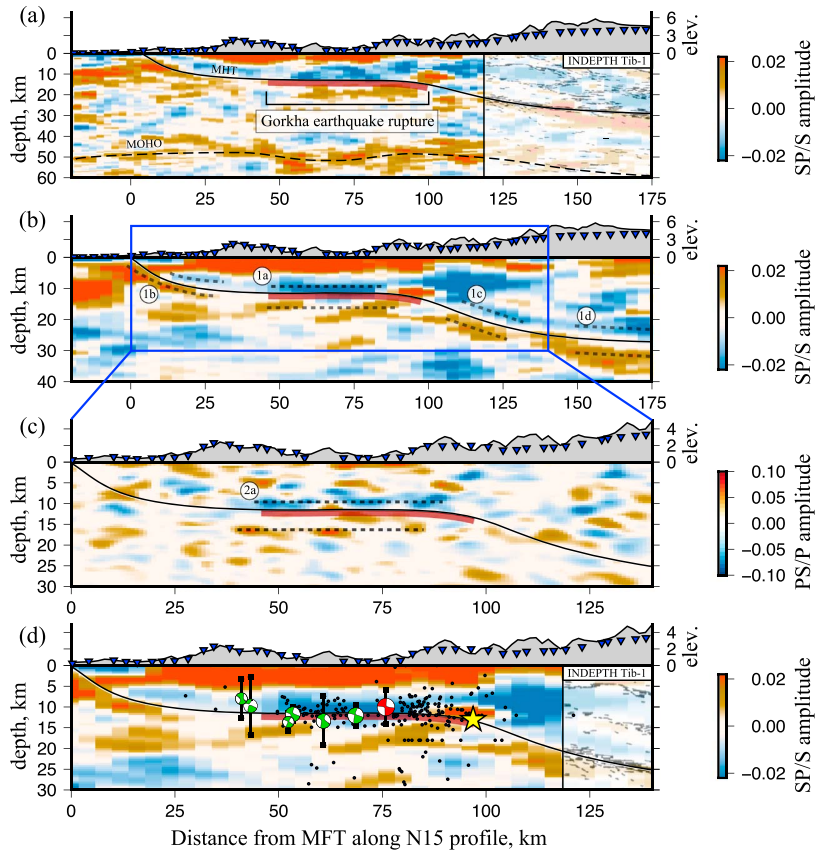


Figure 3. Imaging the Main Himalayan Thrust. (a) S-to-P receiver function migration image in the 0.2–2 Hz passband showing MHT and Moho. (b) S-to-P receiver function migration image in the 0.2–5 Hz passband. (c) P-to-S receiver function migration image. (d) Seismicity over the S-to-P image (also shown in Figure 3b). Back hemisphere focal mechanisms for the main shock (in red) and largest aftershocks (in green) are obtained from CMT inversion using 3-D SEM Green's functions. Dashed black lines and circles with letters mark features discussed in the main text. Black line shows our interpretation of the MHT geometry. Yellow star indicates the hypocenter of the main shock from USGS projected on the MHT interface. Black dots are aftershocks from Adhikari *et al.* [2015] within ± 40 km of the Hi-CLIMB profile. Blue triangles are station locations. The right inset in Figures 3a and 3d corresponds to the INDEPTH Tib-1 reflection profile [Hauck *et al.*, 1998] presented at matching distance from the MFT. Notice that the Tib-1 profile has a different orientation and is located about 400 km east of the Hi-CLIMB profile. Raw receiver function images are also presented in Figures S13 and S14 available in the supporting information.

the centroid depth grid search for the main shock by replacing S362ANI with S40RTS [Ritsema *et al.*, 2011]. The inversion results obtained using both models are quite similar with $M_w \sim 7.8$, dip $\sim 7^\circ$, and depth ~ 12 km. S40RTS is associated with slightly larger RMS misfits but with smaller variability in bootstrapped depth estimates. The depth grid search performed using the 1-D Earth model preliminary reference Earth model (PREM) [Dziewonski and Anderson, 1981] is also shown for reference. Since fundamental mode surface waves are sensitive to shallow structures, PREM is associated with larger misfit and leads to a larger depth of ~ 23 km. Our CMT analysis being based on long-period surface waves, the computed Green's functions, must account for crustal heterogeneities but also incorporate effects of deeper structures in the upper mantle. This is illustrated in Figure S12, showing that records are poorly predicted by a model composed of Crust2.0 over a 1-D mantle contrarily to a full 3-D model.

In parallel to long-period CMT inversions, we reinvestigated the receiver functions from the Hi-CLIMB experiment [Nabelek *et al.*, 2009] in order to compare centroid locations with major crustal impedance contrasts. The Hi-CLIMB stations were operated between 2002 and 2004 and were located along a N15°E oriented profile that runs on top of the rupture area of the Gorkha earthquake (Figure 1). We process both P-to-S (PS) and S-to-P (SP) RFs from a selection of teleseismic events with magnitude $M_w \geq 5.8$ using an iterative time domain

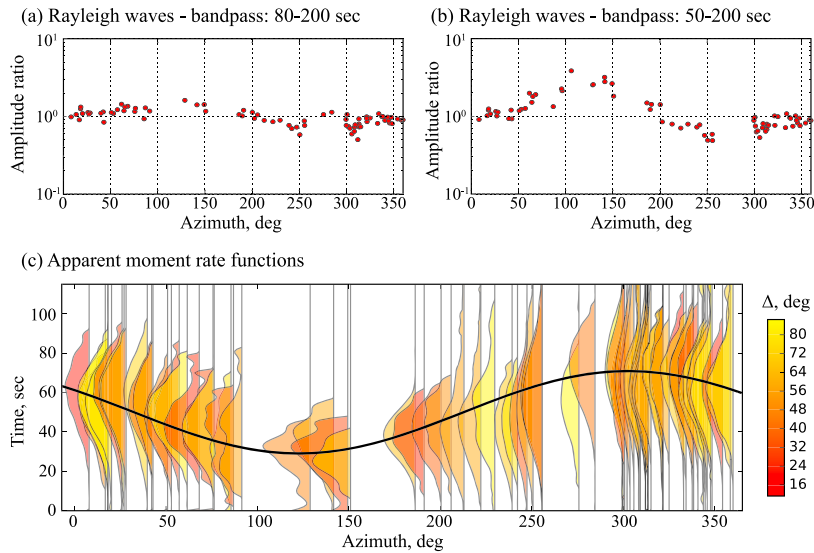


Figure 4. Directivity effects. Rayleigh wave amplitude ratios are shown using different passbands. (a) Amplitude ratios between 80 and 200 s. (b) Ratios between 50 and 200 s. Directivity effects are particularly visible when short periods are included. (c) Apparent moment rate functions are shown as a function of azimuth and colored by epicentral distance. These represent seismic moment as a function of time observed at different stations. The black curve corresponds to the centroid location, showing the predicted arrival time of energy radiated from this location (see yellow circle in Figure 1).

deconvolution approach [Ligorria and Ammon, 1999]. RF migration is performed using the common conversion point technique [Dueker and Sheehan, 1998; Zhu, 2000] and the 1-D velocity model for Nepal from Grandin *et al.* [2015]. To attain the best possible resolution in the shallow part of the MHT, seismograms are filtered in the 0.5–2 Hz passband for PS-RFs and in the 0.2–5 Hz and 0.2–2 Hz passbands for SP-RFs. The main advantage of SP-RFs compared to PS-RFs is that they are free from crustal reverberations that can contaminate PS-RFs cross sections.

SP and PS migrations are presented in Figures 3, S13, and S14. Between 40 km and 90 km north of the MFT, the images show a marked negative impedance contrast at ~10 km depth followed by a broader positive contrast at a depth of ~15 km (1a and 2a in Figure 3). These features being consistent on both SP and PS images, we are confident that they correspond to a quasi horizontal LVZ below Nepal and also are visible on the shallow portion of the broader sections of Nabelek *et al.* [2009] and Wittlinger *et al.* [2009] and along other profiles crossing the Himalayas [Schulte-Pelkum *et al.*, 2005; Caldwell *et al.*, 2013] but generally not providing such a high resolution as the RF images presented here. Comparison with centroid depths of the Gorkha earthquake sequence in Figure 3d confirms that this LVZ corresponds to the receiver function signature of the MHT. Interestingly, we also notice that the horizontal extent of the LVZ seems to match the along dip distribution of coseismic slip and the aftershock epicenters [Adhikari *et al.*, 2015; Bai *et al.*, 2016].

In addition to the horizontal LVZ, the SP cross sections presented in Figures 3a, 3b, S13, and S14 show several features. (i) A shallow ~20° north dipping weak negative impedance over a positive contrast at 0–30 km from the MFT (1b in Figure 3b, also visible in Figure 3a). (ii) A ~17° dipping structure at 100–130 km of the MFT (1c in Figure 3) connecting the horizontal LVZ with (iii) a deeper, subhorizontal LVZ at distances larger than 140 km (1d in Figure 3). These features are interpreted here as receiver function signatures of the MHT outlined with a black line in Figures 3 and S14. The southernmost feature (1b) likely corresponds to the shallow ramp at the MFT found in several geological cross sections [e.g., Lavé and Avouac, 2000] or the base of under-thrust Ganges sediments below the MHT. The northern deep structure (1d) corresponds to the deeper part of the MHT and is consistent both with the northern midcrustal LVZ segment observed by Nabelek *et al.* [2009] and with the International Deep Profiling of Tibet and the Himalaya (INDEPTH) Tib-1 seismic profile (shown in Figures 3a and 3d) [Hauck *et al.*, 1998]. The intermediate dipping structure (1c) is consistent with the midcrustal MHT ramp mentioned in previous geological reconstructions [e.g., Lavé and Avouac, 2001] and suggested by joint analysis of interseismic and coseismic geodetic observations [Elliott *et al.*, 2016].

3. Surface Wave Directivity

To investigate possible rupture directivity effects visible at long period for the $M_w=7.8$ Nepal earthquake, we measure the ratio between observed and predicted surface wave amplitudes in the 50–200 s and 80–200 s passbands. The effect of radiation pattern, dispersion, and attenuation are removed using single-point-source synthetic SEM seismograms computed for the optimum CMT solution obtained in the previous section. We focus here on the variation of the amplitude ratio (observed/predicted) as a function of azimuth. We use minor-arc Rayleigh waves (R1) which provides relatively good azimuthal coverage for epicentral distances $\Delta < 90^\circ$. If directivity effects are negligible, the observed/predicted amplitude ratios would be unity for all azimuths. For the $M_w=7.8$ Nepal earthquake, we clearly see in Figures 4a and 4b that the Rayleigh wave amplitudes are enhanced in azimuths around N120°E. The directivity effects are stronger at shorter period (i.e., in Figure 4b), in agreement with what one would expect for a rupture with unilateral propagation toward east-southeast [Ben-Menahem, 1961; Haskell, 1963].

We also compute apparent Rayleigh wave moment rate functions (MRFs) to extract long-period finiteness observables. The dispersive wave-propagation effects are removed by deconvolving the data by point-source synthetic seismograms computed from our preferred CMT solution in section 2. We use broadband (periods of 10–200 s) SEM synthetics computed for a 3-D Earth model (S362ANI and Crust2.0). We use the projected Landweber deconvolution method [Bertero *et al.*, 1999; Lanza *et al.*, 1999] imposing causality, positivity, and a maximum rupture duration of 100 s. The MRFs are shown in Figure 4c. Azimuthal variation in apparent duration and peak MRF amplitude is clearly visible. This directivity effect is consistent with unilateral rupture propagation toward east-southeast as suggested by amplitude ratios and the location of the centroid relative to the hypocenter (cf. yellow star and yellow circle in Figure 1). To study this apparent directivity, we image the spatial distribution of long-period seismic wave radiation. To do so, the MRFs are averaged in 10° azimuthal windows and back projected over a gridded region around the $M_w=7.8$ epicenter assuming an average phase velocity of 4.0 km/s. The resulting peak stacked amplitude, shown in Figure 1, provides an image of where long-period radiation emanated from the source region (darker colors indicate stronger long-period source radiation). This suggests a fairly simple rupture process with a primary source of long-period energy concentrated in the area north of Kathmandu.

4. Discussion and Conclusion

To resolve the geometry of the MHT below central Nepal, we performed a joint analysis of CMT solutions for the 2015 Gorkha sequence and receiver functions from the Hi-CLIMB experiment. We conducted long-period CMT inversions using SEM Green's functions for 3-D Earth models. We also processed both PS and SP receiver functions to enable high-resolution imaging below Lesser and Higher Himalayas. Below Nepal, this analysis confirmed the presence of a LVZ at 10–15 km depth as reported previously by Nabelek *et al.* [2009]. On the other hand, our CMT analysis revealed that the Gorkha main shock and $M_w \geq 5.0$ aftershocks occurred at depths ranging between 8 km and 14 km, which clearly show that the flat portion of MHT is located within the LVZ revealed by receiver function analysis. Other observations of such LVZ has been reported along other profiles crossing the Himalayas [Schulte-Pelkum *et al.*, 2005; Caldwell *et al.*, 2013] indicating that the geometry and receiver function signature of the MHT is similar along the Himalayan front. On a larger scale, SP receiver function migration outlines the ramp-flat-ramp geometry of the MHT, with a shallow thrust fault flattening at depths between 10 and 15 km followed by a midcrustal ramp connecting to a deeper low-dipping thrust at depths larger than 25 km.

Reconciling the subhorizontal portion of the ruptured area of the MHT as imaged by the LVZ with the ~7° dip of our CMT solution for the Gorkha earthquake requires that this event also ruptured a steeper part of the MHT presumably corresponding to the upper end of the midcrustal ramp. This interpretation is consistent with the main shock hypocenter located on the updip edge of the crustal ramp as shown in Figure 3d. The existence of this steeper thrust also agrees with previous geological, geodetic, and geomorphological studies and may play a strong role on the uplift of the high Himalaya as advocated by Elliott *et al.* [2016]. At distances larger than 130 km from the MFT this steep thrust roots into a lower dipping LVZ having a thickness of 5 to 10 km in our SP images that can be interpreted as the aseismic shear zone discussed in previous studies [e.g., Cattin and Avouac, 2000].

To further interpret our image of the LVZ in the subhorizontal portion of the MHT, we designed a simple velocity model able to fit both SP and PS receiver functions in this region (cf. Text S1 in the supporting information). Our preferred model presented in Figure S16 includes a sharp ~10% shear velocity decrease at ~10 km

depth followed by a smooth velocity recovery. Such a sharp velocity decrease clearly reinforces previous hypotheses suggesting the existence of fluids released by dewatering of underthrust sediments around the flat portion of the MHT [Nabelek *et al.*, 2009]. This interpretation is in good agreement with high conductivity features revealed by magnetotelluric studies [Lemonnier *et al.*, 1999; Patro and Harinarayana, 2009] and with temperature conditions inferred from thermokinematic modeling [Bollinger *et al.*, 2006; Hetényi *et al.*, 2007]. Whether the MHT corresponds to the negative impedance contrast at ~10 km depth or to the broader positive impedance contrast between 15 and 20 km is unsure since the vertical resolution of receiver functions is about 2 km. However, we favor the hypothesis that the MHT lies between 10 and 15 km, where the seismic velocity is the lowest and where most earthquakes occur. The spreading of aftershocks within the LVZ might correspond to uncertainties in depth estimates but may also be due to the occurrence of aftershocks on subfaults surrounding the MHT. As discussed in Bai *et al.* [2016], the ~25° dip angle of some small aftershocks suggests that some events might occur on steeper faults in the hanging wall. The activation of such steeper faults during the Gorkha earthquake sequence remains however uncertain as dip angle estimates are affected by the moment-dip trade-off for shallow thrust events [Tsai *et al.*, 2011].

Our long-period analysis of the $M_w=7.8$ Gorkha earthquake indicates a simple unilateral rupture propagation toward east-southeast. MRF backprojection shows that long-period seismic energy mainly emanated in the north of Kathmandu, in agreement with preliminary finite-fault models [Avouac *et al.*, 2015; Galetzka *et al.*, 2015; Grandin *et al.*, 2015; Yagi and Okuwaki, 2015; Elliott *et al.*, 2016]. High-frequency radiators revealed by back-projection results are located downdip of these long-period radiation sources [Avouac *et al.*, 2015; Fan and Shearer, 2015; Grandin *et al.*, 2015]. Although the spatial resolution is lower than short-period P wave backprojections, imaging long-period seismic energy provides a good indication of seismic moment distribution independent of any assumption on the fault geometry [Yue *et al.*, 2012]. These observations suggest similar behavior as subduction zone earthquakes, where high-frequency sources are distributed at the downdip edge of the seismogenic domain, which is usually interpreted as variations in frictional and stress heterogeneity with depth [Huang *et al.*, 2012; Lay *et al.*, 2012]. In addition, the location of high-frequency sources matches the position of the hinge line between the flat and the deeper ramp that also marks the transition zone between locked and stable sliding portions of the MHT [Ader *et al.*, 2012]. As discussed by Denolle *et al.* [2015] and Elliott *et al.* [2016], this suggests possible structural control on the generation of high-frequency energy.

The smooth rupture process in the updip part of the rupture with a depletion of high-frequency emissions can also be related to the presence of fluids revealed by the LVZ in receiver function images. As shown in Figure 3d, the horizontal extent of the LVZ seems to match the along-dip distribution of coseismic slip and aftershock epicenters. Such reverse polarities associated with elevated fluid pressures have been previously observed in shallow portions of subduction zones [Bangs *et al.*, 1996; Park *et al.*, 2002; Tobin and Saffer, 2009] and has been invoked to explain frequency-dependent rupture process of megathrust earthquakes such as the 2004 Sumatra-Andaman event [Lay *et al.*, 2012] or the 2011 Tohoku-oki event [Huang *et al.*, 2012]. Increase in fluid pressure results in a local decrease of the effective normal stress and is often associated with a depletion of high-frequency emissions [Ito and Obara, 2006; Lengliné *et al.*, 2014]. Elevated pore fluid pressure due to sediment dewatering might therefore explain the frequency-dependent rupture process observed for the Gorkha event, with a smooth updip rupture process causing moderate peak ground acceleration in Kathmandu. Whether such phenomenon is present in most subduction megathrusts is not yet established and other parameters such as temperature and fault geometry might also affect rupture behavior. Full quantification of mechanisms governing depth-varying seismic characteristics and along-dip segmentation of megathrust faults is an important challenge for the future and has important impacts on seismic hazard assessment.

Acknowledgments

This research was supported by the Initiative d'Excellence (IDEX) funding framework (Université de Strasbourg), the Institut National des Sciences de l'Univers (INSU), and the CNRS international program for scientific cooperation (PICS). The research described herein used data from various global networks (including II, IU, G, and GE) and from the first phase of the Hi-CLIMB experiment (doi: 10.7914/SN/XF_2002). All used data are available through the IRIS DMC. We are grateful to the operators of these networks for ensuring the high quality of the data and making them publicly available. We thank R. Jolivet, H. Yue, J. Van der Woerd, and C. Satriano for helpful discussions. We thank the Editor, J. Ritsema, and two anonymous reviewers for their constructive comments, which helped improve this manuscript.

References

- Ader, T., *et al.* (2012), Convergence rate across the Nepal Himalaya and interseismic coupling on the Main Himalayan Thrust: Implications for seismic hazard, *J. Geophys. Res.*, 117, B04403, doi:10.1029/2011JB009071.
- Adhikari, L. B., *et al.* (2015), The aftershock sequence of the 2015 April 25 Gorkha–Nepal earthquake, *Geophys. J. Int.*, 203(3), 2119–2124.
- Avouac, J.-P., L. Meng, S. Wei, T. Wang, and J.-P. Ampuero (2015), Lower edge of locked Main Himalayan Thrust unzipped by the 2015 Gorkha earthquake, *Nat. Geosci.*, doi:10.1038/ngeo2518.
- Bai, L., H. Liu, J. Ritsema, J. Mori, T. Zhang, Y. Ishikawa, and G. Li (2016), Faulting structure above the Main Himalayan Thrust as shown by relocated aftershocks of the 2015 Mw7.8 Gorkha, Nepal, earthquake, *Geophys. Res. Lett.*, 43, 637–642, doi:10.1002/2015GL066473.
- Bangs, N. L., T. H. Shipley, and G. F. Moore (1996), Elevated fluid pressure and fault zone dilation inferred from seismic models of the northern Barbados Ridge decollement, *J. Geophys. Res.*, 101(B1), 627–642.

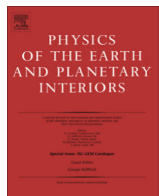
- Bassin, C., G. Laske, and G. Masters (2000), The current limits of resolution for surface wave tomography in North America, *Eos Trans. AGU*, 81, F897.
- Ben-Menahem, A. (1961), Radiation of seismic surface-waves from finite moving sources, *Bull. Seismol. Soc. Am.*, 51, 401–435.
- Bertero, M., D. Bindi, P. Boccacci, M. Cattaneo, C. Eva, and V. Lanza (1999), Application of the projected Landweber method to the estimation of the source time function in seismology, *Inverse Prob.*, 13(2), 465–486, doi:10.1088/0266-5611/13/2/017.
- Bilham, R. (1995), Location and magnitude of the 1833 Nepal Earthquake and its relation to the rupture zones of Contiguous Great Himalayan Earthquakes, *Curr. Sci.*, 69(2), 101–128.
- Bollinger, L., J. P. Avouac, O. Beyssac, E. J. Catlos, T. M. Harrison, M. Grove, et al. (2004), Thermal structure and exhumation history of the Lesser Himalaya in central Nepal, *Tectonics*, 23, TC5015, doi:10.1029/2003TC001564.
- Bollinger, L., P. Henry, and J. Avouac (2006), Mountain building in the Nepal Himalaya: Thermal and kinematic model, *Earth Planet. Sci. Lett.*, 244(1–2), 58–71, doi:10.1016/j.epsl.2006.01.045.
- Bollinger, L., S. N. Sapkota, P. Tapponnier, Y. Klinger, M. Rizza, J. Van der Woerd, D. R. Tiwari, R. Pandey, A. Bitri, and S. B. de Berc (2014), Estimating the return times of great Himalayan earthquakes in eastern Nepal: Evidence from the Patu and Bardibas strands of the Main Frontal Thrust, *J. Geophys. Res. Solid Earth*, 119, 7123–7163, doi:10.1002/2014JB010970.
- Brown, L. D., W. Zhao, K. D. Nelson, M. Hauck, D. Alsdorf, A. Ross, M. Cogan, M. Clark, X. Liu, and J. Che (1996), Bright spots, structure, and magmatism in southern Tibet from INDEPTH seismic reflection profiling, *Science*, 274(5293), 1688–1690, doi:10.1126/science.274.5293.1688.
- Brunel, M. (1986), Ductile thrusting in the Himalayas: Shear sense criteria and stretching lineations, *Tectonics*, 5(2), 247–265, doi:10.1029/TC005i002p00247.
- Caldwell, W. B., S. L. Klempner, J. F. Lawrence, S. S. Rai, and Ashish (2013), Characterizing the Main Himalayan Thrust in the Garhwal Himalaya, India with receiver function CCP stacking, *Earth Planet. Sci. Lett.*, 367, 15–27.
- Cattin, R., and J. P. Avouac (2000), Modeling mountain building and the seismic cycle in the Himalaya of Nepal, *J. Geophys. Res.*, 105, 13,389–13,407, doi:10.1029/2000JB900032.
- Denolle, M. A., W. Fan, and P. M. Shearer (2015), Dynamics of the 2015 M_{7.8} Nepal earthquake, *Geophys. Res. Lett.*, 42, 7467–7475, doi:10.1002/2015GL065336.
- Dueker, K. G., and A. F. Sheehan (1998), Mantle discontinuity structure beneath the Colorado Rocky Mountains and High Plains, *J. Geophys. Res.*, 103(B4), 7153–7169, doi:10.1029/97JB03509.
- Duputel, Z., L. Rivera, H. Kanamori, and G. Hayes (2012), W phase source inversion for moderate to large earthquakes (1990–2010), *Geophys. J. Int.*, 189(2), 1125–1147, doi:10.1111/j.1365-246X.2012.05419.x.
- Duputel, Z., P. S. Agram, M. Simons, S. E. Minson, and J. L. Beck (2014), Accounting for prediction uncertainty when inferring subsurface fault slip, *Geophys. J. Int.*, 197(1), 464–482, doi:10.1093/gji/gjt517.
- Dziewonski, A. M., and D. L. Anderson (1981), Preliminary reference Earth model, *Phys. Earth Planet. Inter.*, 25(4), 297–356, doi:10.1016/0031-9201(81)90046-7.
- Dziewonski, A. M., G. Ekström, and M. P. Salganik (1992), Centroid-moment tensor solutions for July–September 1991, *Phys. Earth Planet. Inter.*, 72(1–2), 1–11.
- Elliott, J. R., R. Jolivet, P. J. González, J. P. Avouac, J. Hollingsworth, M. P. Searle, and V. L. Stevens (2016), Himalayan megathrust geometry and relation to topography revealed by the Gorkha earthquake, *Nat. Geosci.*, doi:10.1038/ngeo2623.
- Efron, B., and R. J. Tibshirani (1994), *An Introduction to the Bootstrap*, Monographs on Statistics Applied Probability, Chapman and Hall/CRC, New York.
- Ekström, G., M. Nettles, and A. M. Dziewonski (2012), The global CMT project 2004–2010: Centroid-moment tensors for 13,017 earthquakes, *Phys. Earth Planet. Inter.*, 200–201, 1–9.
- Fan, W., and P. M. Shearer (2015), Detailed rupture imaging of the 25 April 2015 Nepal earthquake using teleseismic Pwaves, *Geophys. Res. Lett.*, 42, 5744–5752, doi:10.1002/2015GL064587.
- Galetzka, J., et al. (2015), Slip pulse and resonance of Kathmandu basin during the 2015 M_w 7.8 Gorkha earthquake, Nepal imaged with geodesy, *Science*, doi:10.1126/science.aac6383.
- Geller, R., and H. Kanamori (1977), Magnitudes of great shallow earthquakes from 1904 to 1952, *Bull. Seismol. Soc. Am.*, 67, 587–598.
- Grandin, R., M. Vallée, C. Satriano, R. Lacassini, Y. Klinger, M. Simoes, and L. Bollinger (2015), Rupture process of the M_w=7.9 2015 Gorkha earthquake (Nepal): Insights into Himalayan megathrust segmentation, *Geophys. Res. Lett.*, 42, 8373–8382, doi:10.1002/2015GL066044.
- Haskell, N. A. (1963), Radiation pattern of Rayleigh waves from a fault of arbitrary dip and direction of motion in a homogeneous medium, *Bull. Seismol. Soc. Am.*, 53, 619–642.
- Hauck, M. L., K. D. Nelson, L. D. Brown, W. Zhao, and A. R. Ross (1998), Crustal structure of the Himalayan orogen at ~90° east longitude from Project INDEPTH deep reflection profiles, *Tectonics*, 17(4), 481–500, doi:10.1029/98TC01314.
- Hetényi, G., R. Cattin, F. Brunet, L. Bollinger, J. Vergne, J. L. Nábělek, and M. Diamant (2007), Density distribution of the India plate beneath the Tibetan plateau: Geophysical and petrological constraints on the kinetics of lower-crustal eclogitization, *Earth Planet. Sci. Lett.*, 264(1–2), 226–244.
- Hjörleifsdóttir, V., and G. Ekström (2010), Effects of three-dimensional Earth structure on CMT earthquake parameters, *Phys. Earth Planet. Inter.*, 179, 178–190.
- Huang, Y., L. Meng, and J.-P. Ampuero (2012), A dynamic model of the frequency-dependent rupture process of the 2011 Tohoku-Oki earthquake, *Earth Planets Space*, 64(12), 1061–1066.
- Ito, Y., and K. Obara (2006), Very low frequency earthquakes within accretionary prisms are very low stress-drop earthquakes, *Geophys. Res. Lett.*, 33, L09302, doi:10.1029/2006GL025883.
- Komatitsch, D., and J. Tromp (1999), Introduction to the spectral element method for three-dimensional seismic wave propagation, *Geophys. J. Int.*, 139(3), 806–822.
- Kustowski, B., G. Ekström, and A. M. Dziewonski (2008), Anisotropic shear-wave velocity structure of the Earth's mantle: A global model, *J. Geophys. Res.*, 113, B06306, doi:10.1029/2007JB005169.
- Lanza, V., D. Spallarossa, M. Cattaneo, D. Bindi, and P. Augliera (1999), Source parameters of small events using constrained deconvolution with empirical Green's functions, *Geophys. J. Int.*, 137(3), 651–662.
- Lavé, J., and J. P. Avouac (2000), Active folding of fluvial terraces across the Siwaliks Hills, Himalayas of central Nepal, *J. Geophys. Res.*, 105(B3), 5735–5770, doi:10.1029/1999JB000292.
- Lavé, J., and J. P. Avouac (2001), Fluvial incision and tectonic uplift across the Himalayas of central Nepal, *J. Geophys. Res.*, 106(B11), 26,561–26,591, doi:10.1029/2001JB000359.
- Lay, T., H. Kanamori, C. J. Ammon, K. D. Koper, A. R. Hutko, L. Ye, H. Yue, and T. M. Rushing (2012), Depth-varying rupture properties of subduction zone megathrust faults, *J. Geophys. Res.*, 117, B04311, doi:10.1029/2011JB009133.

- Lengliné, O., L. Lamourette, L. Vivin, N. Cuenot, and J. Schmittbuhl (2014), Fluid-induced earthquakes with variable stress drop, *J. Geophys. Res. Solid Earth*, 119, 8900–8913, doi:10.1002/2014JB011282.
- Lemonnier, C., G. Marquis, F. Perrier, J. P. Avouac, G. Chitrakar, B. Kafle, S. Sapkota, U. Gautam, D. Tiwari, and M. Bano (1999), Electrical structure of the Himalaya of Central Nepal: High conductivity around the mid-crustal ramp along the MHT, *Geophys. Res. Lett.*, 26(21), 3261–3264, doi:10.1029/1999GL008363.
- Ligorria, J. P., and C. J. Ammon (1999), Iterative deconvolution and receiver-function estimation, *Bull. Seismol. Soc. Am.*, 89(5), 1395–1400.
- Nabelek, J., G. Hetényi, J. Vergne, S. Sapkota, B. Kafle, M. Jiang, H. Su, J. Chen, B. S. Huang, and T. H. C. Team (2009), Underplating in the Himalaya-Tibet collision zone revealed by the Hi-CLIMB experiment, *Science*, 325(5946), 1371–1374.
- Nakanishi, I., and H. Kanamori (1982), Effects of lateral heterogeneity and source process time on the linear moment tensor inversion of long-period Rayleigh waves, *Bull. Seismol. Soc. Am.*, 72(6A), 2063–2080.
- Park, J.-O., T. Tsuru, S. Kodaira, P. R. Cummins, and Y. Kaneda (2002), Splay fault branching along the Nankai Subduction Zone, *Science*, 297(5584), 1157–1160.
- Patro, P. K., and T. Harinarayana (2009), Deep geoelectric structure of the Sikkim Himalayas (NE India) using magnetotelluric studies, *Phys. Earth Planet. Inter.*, 173(1–2), 171–176, doi:10.1016/j.pepi.2008.10.011.
- Ritsema, J., A. Deuss, H. J. van Heijst, and J. H. Woodhouse (2011), S40RTS: A degree-40 shear-velocity model for the mantle from new Rayleigh wave dispersion, teleseismic traveltimes and normal-mode splitting function measurements, *Geophys. J. Int.*, 184(3), 1223–1236.
- Sapkota, S. N., L. Bollinger, Y. Klinger, P. Tapponnier, Y. Gaudemer, and D. Tiwari (2013), Primary surface ruptures of the great Himalayan earthquakes in 1934 and 1255, *Nat. Geosci.*, 6(1), 71–76, doi:10.1038/ngeo1669.
- Schulte-Pelkum, V., G. Monsalve, A. Sheehan, M. R. Pandey, S. Sapkota, R. Bilham, and F. Wu (2005), Imaging the Indian subcontinent beneath the Himalaya, *Nature*, 435(7046), 1222–1225.
- Smith, G. P., and G. Ekström (1996), Improving teleseismic event locations using a three-dimensional earth model, *Bull. Seismol. Soc. Am.*, 86(3), 788–796.
- Tobin, H. J., and D. M. Saffer (2009), Elevated fluid pressure and extreme mechanical weakness of a plate boundary thrust, Nankai Trough subduction zone, *Geology*, 37(8), 679–682.
- Tsai, V. C., G. P. Hayes, and Z. Duputel (2011), Constraints on the long-period moment-dip tradeoff for the Tohoku earthquake, *Geophys. Res. Lett.*, 38, L00G17, doi:10.1029/2011GL049129.
- Vallée, M., J. Charléty, and A. Ferreira (2010), SCARDEC: A new technique for the rapid determination of seismic moment magnitude, focal mechanism and source time functions for large earthquakes using body-wave deconvolution, *Geophys. J. Int.*, 184, 338–358.
- Wittlinger, G., V. Farra, G. Hetényi, J. Vergne, and J. Nabelek (2009), Seismic velocities in Southern Tibet lower crust: A receiver function approach for eclogite detection, *Geophys. J. Int.*, 177(3), 1037–1049.
- Wobus, C., A. Heimsath, K. Whipple, and K. Hodges (2005), Active out-of-sequence thrust faulting in the central Nepalese Himalaya, *Nature*, 434(7036), 1008–1011.
- Yagi, Y., and R. Okuwaki (2015), Integrated seismic source model of the 2015 Gorkha, Nepal, earthquake, *Geophys. Res. Lett.*, 42, 6229–6235, doi:10.1002/2015GL064995.
- Yue, H., T. Lay, and K. D. Koper (2012), En echelon and orthogonal fault ruptures of the 11 April 2012 great intraplate earthquakes, *Nature*, 490, 245–249.
- Zhao, W., K. D. Nelson, J. Che, J. Quo, D. Lu, C. Wu, and X. Liu (1993), Deep seismic reflection evidence for continental underthrusting beneath southern Tibet, *Nature*, 366(6455), 557–559.
- Zhu, L. (2000), Crustal structure across the San Andreas Fault, southern California from teleseismic converted waves, *Earth Planet. Sci. Lett.*, 179(1), 183–190.

2.5 Analyse longue-période du séisme de Kaikoura en Novembre 2016

Le séisme de Kaikoura du 13 Décembre 2016 ($M_W=7.8$) a impliqué une rupture remarquablement complexe impliquant de nombreux segments de failles dans une zone de transition entre la faille Alpine, au sud de la Nouvelle Zélande, et la zone de subduction Kermadec-Tonga. Dans l'article présenté ci-dessous, nous montrons comment les observations sismologiques à longue période couplées à des simulations 3D de formes d'ondes permettent de contraindre les caractéristiques principales d'une telle rupture complexe. Les résultats montrent que le séisme a débuté comme une petite rupture décrochante qui s'est propagée vers le Nord-Est en déclenchant un glissement important à la fois sur des failles décrochantes et inverses. Ce séisme est un bon exemple qui démontre la nécessité de prendre en compte les failles secondaires lors de l'évaluation de l'aléa sismique associé aux failles actives majeures.

L'article proposé ci-dessous a été publié en 2016 dans le journal *Physics of the Earth and Planetary Interiors*. Ce travail a été effectué suite à mon recrutement à l'IPGS.



Short communication

Long-period analysis of the 2016 Kaikoura earthquake



Z. Duputel*, L. Rivera

Institut de Physique du Globe de Strasbourg, UMR7516, Université de Strasbourg/EOST, CNRS, Strasbourg, France

ARTICLE INFO

Article history:

Received 23 January 2017

Received in revised form 6 February 2017

Accepted 8 February 2017

Available online 17 February 2017

Keywords:

New Zealand

Earthquake

Megathrust

Strike-slip

Surface waves

ABSTRACT

The recent $M_w = 7.8$ Kaikoura (New Zealand) earthquake involved a remarkably complex rupture propagating in an intricate network of faults at the transition between the Alpine fault in the South Island and the Kermadec-Tonga subduction zone. We investigate the main features of this complicated rupture process using long-period seismological observations. Apparent Rayleigh-wave moment-rate functions reveal a clear northeastward directivity with an unusually weak rupture initiation during 60 s followed by a major 20 s burst of moment rate. To further explore the rupture process, we perform a Bayesian exploration of multiple point-source parameters in a 3-D Earth model. The results show that the rupture initiated as a small strike-slip rupture and propagated to the northeast, triggering large slip on both strike-slip and thrust faults. The Kaikoura earthquake is thus a rare instance in which slip on intraplate faults trigger extensive interplate thrust faulting. This clearly outlines the importance of accounting for secondary faults when assessing seismic and tsunami hazard in subduction zones.

© 2017 Elsevier B.V. All rights reserved.

1. Introduction

On November 13, 2016, a large earthquake struck the northeast coast of the South Island in New Zealand (GeoNet hypocenter: latitude = -42.69° , longitude = 173.02° , depth = 14 km, O.T. = 11:02:56 UTC; Global CMT $M_w = 7.8$). This earthquake occurred in the Marlborough Fault system, an intricate network of right lateral strike-slip faults connecting the Alpine fault in the South Island to the Hikurangi subduction zone (cf., Fig. 1). A tsunami swept onto the coastlines with wave-heights of 2.5 m at Kaikoura (<https://www.geonet.org.nz/tsunami>). This earthquake is the largest event in the region since a magnitude 7.5 earthquake that occurred 100 km to the northeast in October 1848 (Grapes et al., 1998; Mason and Little, 2006). The 1848 earthquake ruptured ~100 km of the Awatere Fault near Blenheim with horizontal displacements as large as 6 m causing significant damages in Wellington and the Awatere valley.

Several facts indicate that the 2016 Kaikoura earthquake involved a complex rupture. Long-period moment tensor solutions indicate an oblique thrust focal mechanism with a large non-double couple component. Using the definition of Hara et al. (1996), the non-double couple component of Global CMT (GCMT) and USGS W-phase solutions are $\epsilon = -0.12$ and $\epsilon = -0.21$ respectively. This suggest that the mainshock is not well represented by a single fault plane. Both GCMT and W-phase solutions have large

centroid time-delay $\tau_c \sim 57$ s that indicate an anomalously long rupture duration, more than 2.5 times longer than what is expected from standard scaling laws (Duputel et al., 2013). In addition, preliminary fields reports indicate that multiple faults were involved with surface strike-slip offsets as large as 10 m across the Kekerengu fault and coastal uplift between 2 and 5 m northeast of Kaikoura (Litchfield et al., 2016).

In this study, we investigate the mainshock rupture using long-period records available at teleseismic distances. Using this dataset, we conduct a directivity analysis using apparent moment rate functions and perform a multiple-point-source inversion accounting for 3-D Earth structures.

2. Rayleigh-wave moment rate functions

To study the time-history of the rupture and investigate possible directivity effects visible at long-period for the $M_w = 7.8$ Kaikoura earthquake, we compute apparent Rayleigh-wave moment rate functions (MRFs). The dispersive wave-propagation effects are removed by deconvolving the data by point-source synthetic seismograms. To reduce biases in Rayleigh-wave MRFs due to unaccounted lateral heterogeneities, we use broadband (10–600 s) SEM synthetics computed for a 3D Earth model (S362ANI and CRUST2.0) using the spectral element code SPECFEM3D-GLOBE (Komatitsch and Tromp, 2002). Deconvolution is performed using the projected Landweber deconvolution method (Bertero et al., 1999; Lanza et al., 1999) imposing causality and positivity (Duputel et al., 2016).

* Corresponding author.

E-mail address: zacharie.duputel@unistra.fr (Z. Duputel).

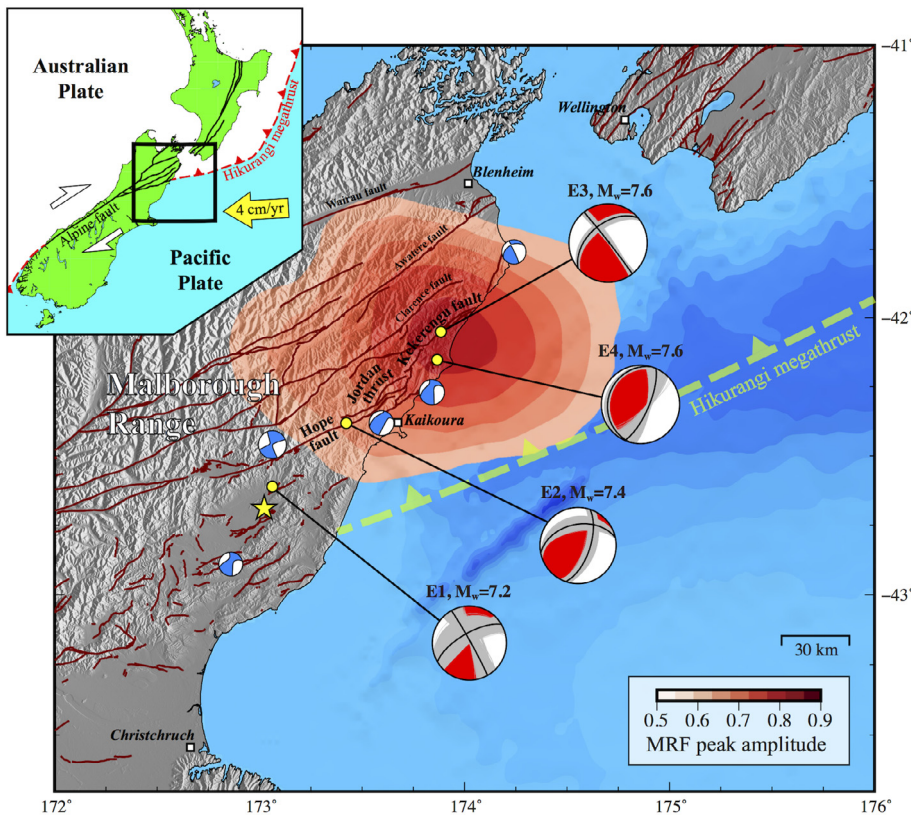


Fig. 1. The 2016 Kaikoura earthquake sequence. Red mechanisms correspond to our preferred four-point-source model obtained using body waves and surface waves assuming a 3-D Earth model. Red colors indicate peak-stacked amplitude in the source region from moment rate functions (MRF) backprojected relative to the main shock epicentral location. Blue mechanisms are the Global CMT solutions obtained for $M_w \geq 5$ aftershocks (2016/11/14 to 2016/11/22). Red lines are faults traces from the New Zealand Active Faults Database (GNS Science, <https://data.gns.cri.nz/af>). Yellow dashed line shows the approximate trench location of the Hikurangi megathrust. (For interpretation of the references to color in this figure legend, the reader is referred to the web version of this article.)

The MRFs shown in Fig. 2 indicate an unusual initiation with very small moment rate in the first 60 s. Following this slow initiation phase, the moment rate rises abruptly during ~ 20 s. This main energy burst shows clear azimuth-dependent time-shifts that are consistent with unilateral rupture propagation to the northeast. Such directivity is in agreement with both GCMT and W-phase centroid location that lie ~ 120 km northeast of the epicenter. To study this apparent directivity, we image the spatial distribution of long-period seismic wave radiation. To do so, the MRFs are averaged in 10° azimuthal windows and back-projected over a gridded region around the epicenter assuming an average phase-velocity of 4 km/s. The resulting peak stacked amplitude shown in Fig. 1 indicates that this main moment-rate burst emanated from a region including the Kekerengu fault and the east coast of the upper South Island.

3. Multiple point source analysis of the 2016 Kaikoura earthquake

3.1. Multiple CMT inversion approach

We employ a strategy similar to Duputel et al. (2012) where multiple moment tensor sources are inverted simultaneously using W-phase waveforms. Here, we extend this approach to surface waves using a larger time-window in the period range of 100–450 s. The W-phase being mainly sensitive to first-order source parameters, incorporating surface waves and extending our passband to shorter periods improve our ability to capture more details of the rupture process. While most of the W-phase energy propagates into the mantle and are therefore not strongly affected by shallow structures, fundamental mode surface waves are sensitive

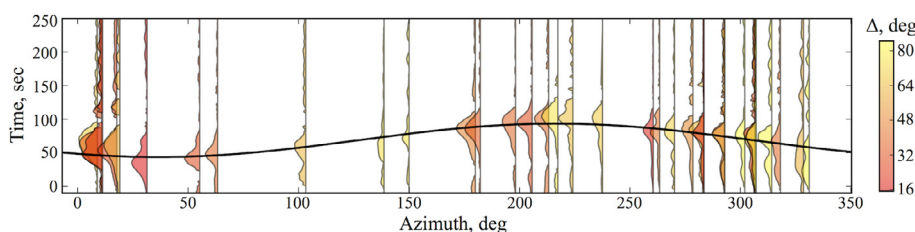


Fig. 2. Rayleigh-wave moment rate functions. Apparent moment rate functions (MRFs) are shown as a function of azimuth and colored by epicentral distance. These represent seismic moment as a function of time observed at different stations. The black curve corresponds to the maximum MRF peak amplitude, showing the predicted arrival time of energy radiated from this location (cf., Fig. 1). (For interpretation of the references to color in this figure legend, the reader is referred to the web version of this article.)

to shallow lateral heterogeneities such as those associated by the oceans and continents. As for Rayleigh-wave MRFs (Section 2), such 3D effects are accounted for using SEM Green's functions that are computed for the 3D Earth model S362ANI (Kustowski et al., 2008).

Using a Bayesian approach, we invert for multiple double-couple parameters (i.e., the strike, dip, rake, seismic moment and centroid time of each sub-event), while sub-event locations are fixed based on field and satellite observations (e.g., Litchfield et al., 2016). From Bayes' theorem, the posterior probability density function (PDF) is given by:

$$p(\mathbf{m}|\mathbf{d}_{\text{obs}}) \propto p(\mathbf{m})p(\mathbf{d}_{\text{obs}}|\mathbf{m}), \quad (1)$$

where $p(\mathbf{d}_{\text{obs}}|\mathbf{m})$ is the likelihood function representing the ability of a source model \mathbf{m} to fit the observations \mathbf{d}_{obs} and $p(\mathbf{m})$ is the *a priori* PDF, which describes our prior knowledge about the source. We define the likelihood function as

$$p(\mathbf{d}_{\text{obs}}|\mathbf{m}) \propto \exp\left(-\frac{1}{2}[\mathbf{d}_{\text{obs}} - \mathbf{g}(\mathbf{m})]^T \mathbf{C}_\chi^{-1} [\mathbf{d}_{\text{obs}} - \mathbf{g}(\mathbf{m})]\right) \quad (2)$$

where \mathbf{d}_{obs} and $\mathbf{g}(\mathbf{m})$ are the observed and predicted waveforms for a multiple-point-source model \mathbf{m} and \mathbf{C}_χ is the misfit covariance matrix. We assume a block-diagonal \mathbf{C}_χ , which is given by the following expression for a station n :

$$(\mathbf{C}_\chi)_n^{ij} = (\sigma_n)^2 \exp(-|\Delta t^{ij}|/t_0). \quad (3)$$

In the previous equation, σ_n is the data uncertainty at station n , t_0 represents a characteristic correlation duration and Δt^{ij} is the time difference between data samples i and j (Duputel et al., 2012). As discussed in Minson et al. (2013) and Duputel et al. (2014), model prediction error is expected to be roughly proportional with data amplitude. We use a conservative estimate of 20% uncertainty (i.e., $\sigma_n = 0.2 \times \max(\mathbf{d}^n)$, where \mathbf{d}^n is the long-period waveform recorded at station n) that is consistent with the variability in RMS misfits obtained using different 3D Earth models (e.g., S362ANI and S40RTS in Duputel et al., 2016). The correlation duration t_0 is estimated to match the main lobe of the auto-correlation of the residual vector $\mathbf{r} = \mathbf{d}_{\text{obs}} - \mathbf{g}(\tilde{\mathbf{m}})$, where $\tilde{\mathbf{m}}$ is the maximum a posteriori model obtained from a first inversion. After different tests using different number of sub-events, we found that $t_0 = 30$ s is appropriate for the dataset used in this study (cf., Fig. S1b).

Our solution is thus not a single “optimum” model but the full posterior PDF $p(\mathbf{m}|\mathbf{d}_{\text{obs}})$ describing the ensemble of source models that are consistent with observations and prior assumptions. With this purpose, we employ a Monte Carlo strategy that allows us to generate an ensemble of models that are statistically distributed according to $p(\mathbf{m}|\mathbf{d}_{\text{obs}})$. This is done using an adaptive Metropolis Method (Brooks et al., 2011), which is described in the Supplementary material.

3.2. Results

We use records from 60 broadband stations within an epicentral distance of 90°. Before inversion, waveforms are deconvolved to displacement and band-pass filtered in the period range of 100–450 s. Using this dataset, we perform a three-point source inversion with sub-events placed along the main ruptures planes reported by field and satellite observations: (1) Sub-event E1 is located in the Humps fault zone close to the epicenter, (2) Sub-event E2 is put along the Hope fault and Jordan thrust, (3) Sub-event E3 is placed along the Kekerengu fault (Litchfield et al., 2016; <http://comet.nerc.ac.uk>; <http://www.gsi.go.jp/cais/topic161117-index-e.html>). Despite a limited sensitivity with respect to source depths, we observe smaller RMS misfits when

using shallow focal depths for sub-events E1 and E2 (~ 10 km) and a deeper source for sub-events E3 (~ 20 km; cf., Table S2). The resulting solution shown in Fig. 3a present oblique strike-slip mechanisms with strike angles that are globally consistent with fault orientations. There is a dominant moment contribution from sub-event E3 with a centroid time-shift of 73 s, in good agreement with the time and location of the main burst of moment-rate seen in Figs. 1 and 2. Comparison between data and predictions in Fig. 3b indicate that fundamental mode rayleigh-wave amplitudes are slightly overestimated for stations located north of the epicenter (in the Pacific Ocean) and underestimated for stations located to the south (in Antarctic and the Southern Ocean). This suggest that a stronger directivity toward the north is needed to better match the observed waveforms.

To investigate the possibility that the rupture triggered slip along the Hikurangi megathrust, we add a fourth sub-event to our multiple point-source model. This additional point source is also motivated by field reports and InSAR observations indicating significant vertical displacement southeast of the Kekerengu fault that cannot be explained by our three-point source model (3–5 m coastal uplift measured by Litchfield et al. (2016), up to 5 m uplift according to <http://www.gsi.go.jp/cais/topic161117-index-e.html>). We thus perform a four double-couple inversion adding sub-event E4 where large uplift is observed. The solution presented in Fig. 4 shows oblique strike-slip mechanisms for sub-events E1, E2 and E3 (quite similar to our three double-couple solution in Fig. 3) and a pure thrust mechanism for sub-event E4. Waveform fits are significantly improved, which suggest that this additional thrust source fulfill the northward directivity that was missing in our three point-source model. Moreover, the composite mechanism in Fig. 4a obtained by summing moment tensors of the four sub-events is remarkably consistent with GCMT, while the composite three sub-event solution show larger differences (cf., Fig. 3a).

4. Discussion and conclusion

Long-period analysis of the Kaikoura earthquake reveals a rather unique source process. Apparent MRFs indicate a northeastward directivity with an unusually weak radiation during the first 60 s followed by a major 20 s burst of moment rate around the Kekerengu fault. This slow rupture initiation results in an anomalously long rupture duration, with a centroid time-shift more than 2.5 times longer than what is expected from standard scaling laws (Duputel et al., 2013).

In addition, our multiple point source analysis reveals a remarkably complex rupture process. The first sub-event (E1) suggests that the Kaikoura earthquake initiated as a small strike-slip rupture consistent with field reports of ~1 m horizontal offsets in the Humps fault zone close to the epicenter (Litchfield et al., 2016). As the rupture propagated to the northeast with large strike-slip motion (sub-event E3), significant thrust-slip was also triggered on a deeper shallow-dipping thrust fault (sub-event E4). This model explains W-phase and Global CMT single point-source solutions involving a significant non-double component with a large thrust slip motion (Fig. 4). This also agrees with field and satellite observations showing large horizontal offsets along the Kekerengu and Papatea faults accompanied by significant coastal uplifts along with 2.5 m tsunami waves recorded at Kaikoura (<https://www.geonet.org.nz/tsunami>). Notice that sub-event E2 involves a non-negligible thrust component suggesting that dip-slip motion might have started during the early stages of the rupture process. We are aware that this model only describe the first order features of the overall rupture process, which in detail might involve additional complexities (e.g., slip on the Papatea

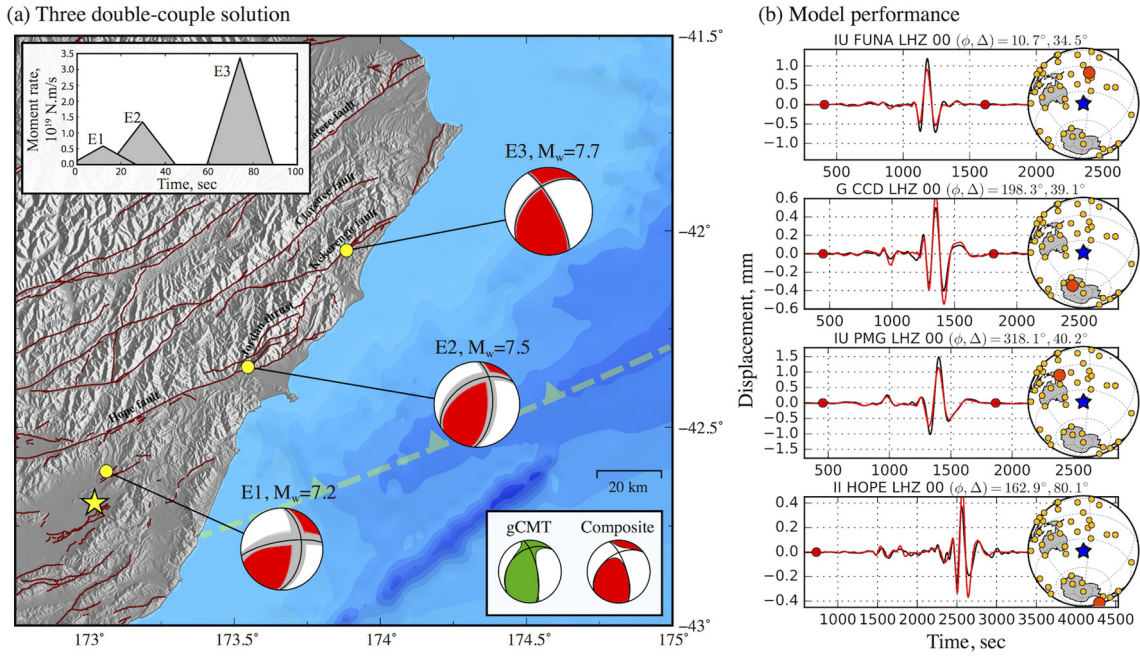


Fig. 3. Three double-couple inversion. (a) Red mechanisms correspond to our three-point-source model obtained from Bayesian inversion of long-period seismic waves assuming a 3-D Earth model. Grey lines indicate the posterior population of double-couple mechanisms and the black lines correspond to the posterior mean model. Top left inset shows the timing and moment-rate function of each sub-event. Bottom right inset presents a comparison of the Global CMT (GCMT) solution and a composite mechanism corresponding to the sum of moment tensors for sub-events E1, E2 and E3. (b) Comparison between data (black) and synthetic (red) waveforms for representative stations. The part of the signal used for multiple point source determination is delimited by red dots. Yellow circles in right insets show the global distribution of stations used for the inversion. The station azimuth (ϕ) and epicentral distance (Δ) is indicated on top of each seismic trace. (For interpretation of the references to color in this figure legend, the reader is referred to the web version of this article.)

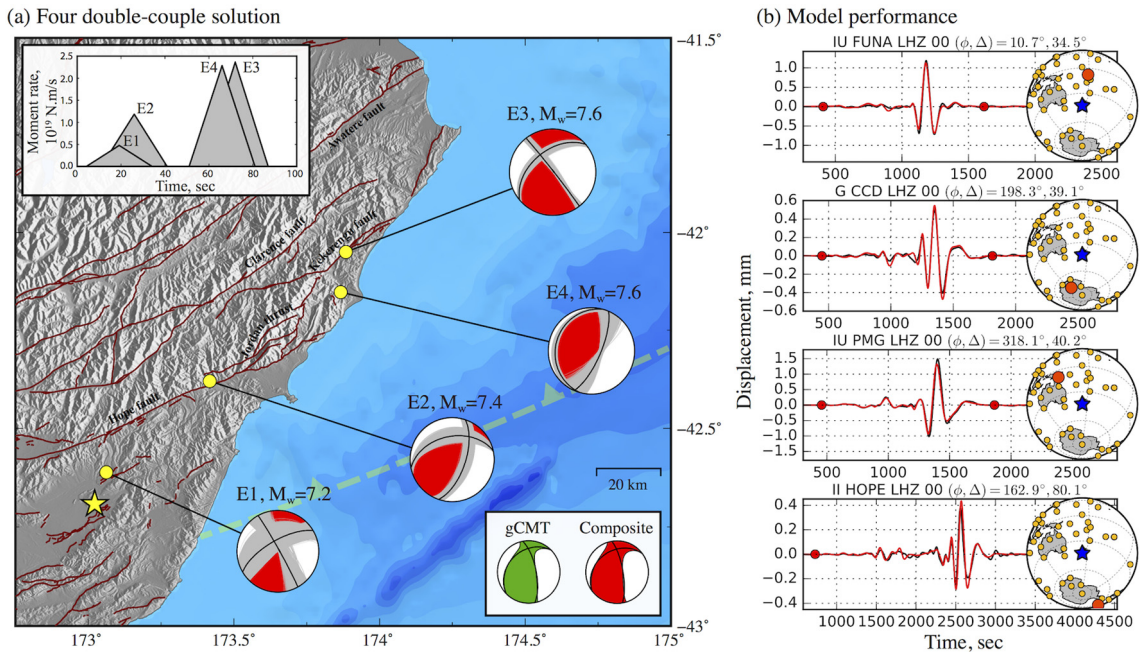


Fig. 4. Four double-couple inversion. (a) Red mechanisms correspond to our four-point-source model obtained from Bayesian inversion of long-period seismic waves assuming a 3-D Earth model. Grey lines indicate the posterior population of double-couple mechanisms and the black lines correspond to the posterior mean model (cf., Table S1 and S3). Top left inset shows the timing and moment-rate function of each sub-event. Bottom right inset presents a comparison of the Global CMT (GCMT) solution and a composite mechanism corresponding to the sum of moment tensors for sub-events E1, E2, E3 and E4. (b) Comparison between data (black) and synthetic (red) waveforms for representative stations. The part of the signal used for multiple point source determination is delimited by red dots. Yellow circles in right insets show the global distribution of stations used for the inversion. The station azimuth (ϕ) and epicentral distance (Δ) is indicated on top of each seismic trace. Additional waveform comparisons for this inversion are shown in the [Supplementary material](#). (For interpretation of the references to color in this figure legend, the reader is referred to the web version of this article.)

fault that is nearly orthogonal to the Kekerengu fault). We leave to further investigations the determination of a refined source model providing a detailed mapping of slip from available near-field geodetic and seismic data.

The strike-slip and thrust focal mechanisms of the two largest sub-events (E3 and E4) can be interpreted as slip on the Kekerengu fault splaying from a deeper thrust fault underlying the Marlborough coastline. This previously undocumented shallow-dipping fault might correspond to the southwest extension of the Hikurangi Megathrust or some other thrust fault within the forearc wedge (Barnes and Audru, 1999). The strike of sub-event E4 thrust mechanism is consistent with the azimuth of the Kekerengu Bank fault, although our probabilistic results yield a relatively large uncertainty on the strike angle. Activation of secondary faults are common during large megathrust earthquakes (Li et al., 2014). Triggering of splay faults have been identified on many subduction margins and represent significant seismic and tsunami threats (Park et al., 2002; Wendt et al., 2009; Melnick et al., 2012). However, the Kaikoura earthquake is a rare instance clearly showing that megathrust ruptures can also be triggered by slip on secondary faults. Another example of such interactions with intraplate earthquakes was observed during the 2009 Samoa-Tonga sequence in which an outer-rise event triggered extensive interplate faulting along the subduction interface (Lay et al., 2010). Those rare instances reverse the typical pattern between megathrust and secondary faults and expand seismic and tsunami hazard in subduction zones.

Acknowledgments

This work was supported by the Initiative d'Excellence (IDEX) funding framework (Université de Strasbourg). The research described herein used seismological data from various global networks available through the IRIS DMC (including Geoscope and IRIS/USGS stations in Antarctica and the Southern Ocean). We are grateful to the operators of these networks for ensuring the high quality of the data and making them publicly available. We also acknowledge the New Zealand GeoNet project and its sponsors EQC, GNS Science and LINZ, for providing data/images used in this study. We also thank COMET and GSI for providing InSAR images. This study contributed from fruitful discussions with Lingling Ye and James Hollingsworth. We thank the Editor, Vernon F. Cormier, and an anonymous reviewer for his constructive comments, which helped improve this manuscript.

Appendix A. Supplementary data

Supplementary data associated with this article can be found, in the online version, at <http://dx.doi.org/10.1016/j.pepi.2017.02.004>.

References

- Barnes, P.M., Audru, J.C., 1999. Recognition of active strike-slip faulting from high-resolution marine seismic reflection profiles: Eastern Marlborough fault system, New Zealand. *Geol. Soc. Am. Bull.* 111 (4), 538–559.
- Bertero, M., Bindi, D., Boccacci, P., Cattaneo, M., Eva, C., Lanza, V., 1999. Application of the projected Landweber method to the estimation of the source time function in seismology. *Inverse Probl.* 13 (2), 465–486. <http://dx.doi.org/10.1088/0266-5611/13/2/017>.
- Brooks, S., Gelman, A., Jones, G.L., Meng, X.-L., 2011. *Handbook of Markov Chain Monte Carlo*. Chapman & Hall/CRC, New York.
- Duputel, Z., Kanamori, H., Tsai, V.C., Rivera, L., 2012. The 2012 Sumatra great earthquake sequence. *Earth Planet. Sci. Lett.* 351–352, 247–257.
- Duputel, Z., Rivera, L., Fukahata, Y., Kanamori, H., 2012. Uncertainty estimations for seismic source inversions. *Geophys. J. Int.* 190 (2), 1243–1256.
- Duputel, Z., Tsai, V.C., Rivera, L., Kanamori, H., 2013. Using centroid time-delays to characterize source durations and identify earthquakes with unique characteristics. *Earth Planet. Sci. Lett.* 374, 92–100. <http://dx.doi.org/10.1016/j.epsl.2013.05.024>.
- Duputel, Z., Agram, P.S., Simons, M., Minson, S.E., Beck, J.L., 2014. Accounting for prediction uncertainty when inferring subsurface fault slip. *Geophys. J. Int.* 197 (1), 464–482. <http://dx.doi.org/10.1093/gji/gjt517>.
- Duputel, Z., Vergne, J., Rivera, L., Wittlinger, G., Farra, V., Hetényi, G., 2016. The 2015 Gorkha earthquake: a large event illuminating the Main Himalayan Thrust fault. *Geophys. Res. Lett.* 43 (6), 2517–2525. <http://dx.doi.org/10.1002/2016GL068083>.
- Grapes, R., Little, T., Downes, G., 1998. Rupturing of the awatere fault during the 1848 October 16 Marlborough earthquake, New Zealand: historical and present day evidence. *N. Z. J. Geol. Geophys.* 41 (4), 387–399.
- Hara, T., Kuge, K., Kawakatsu, H., 1996. Determination of the isotropic component of deep focus earthquakes by inversion of normal-mode data. *Geophys. J. Int.* 127, 515–528.
- Komatitsch, D., Tromp, J., 2002. Spectral-element simulations of global seismic wave propagation—II. Three-dimensional models, oceans, rotation and self-gravitation – Komatitsch – 2002 – Geophysical Journal International – Wiley Online Library, *Geophys. J. Int.*
- Kustowski, B., Ekström, G., Dziewonski, A.M., 2008. Anisotropic shear-wave velocity structure of the Earth's mantle: a global model. *J. Geophys. Res.* 113 (B06), 306.
- Lanza, V., Spallarossa, D., Cattaneo, M., Bindi, D., Augliera, P., 1999. Source parameters of small events using constrained deconvolution with empirical Green's functions. *Geophys. J. Int.* 137 (3), 651–662. <http://dx.doi.org/10.1046/j.1365-246x.1999.00809.x>.
- Lay, T., Ammon, C.J., Kanamori, H., Rivera, L., Koper, K., Hutko, A.R., 2010. The 2009 Samoa-Tonga great earthquake triggered doublet. *Nature* 466 (7309), 964–968.
- Li, S., Moreno, M., Rosenau, M., Melnick, D., Oncken, O., 2014. Splay fault triggering by great subduction earthquakes inferred from finite element models. *Geophys. Res. Lett.* 41 (2), 385–391. <http://dx.doi.org/10.1002/2013GL058598>.
- Litchfield, N.J., Barrell, D.J.A., Begg, J.G., Benson, A., Berryman, K.J., Clark, Cochran, U. A., Cox, S.C., Gasston, C., Glassey, P.J., Heron, D.W., Howarth, J.D., Langridge, R.M., Little, T., Lukovic, B., Nicol, A., Pettinga, J., Ries, W.F., J. R., Stirling, M.W., Townsend, D.B., Upton, P., Van Dissen, R.J., Villamor, P., 2016. 4th November 2016 Kaikoura Earthquake: Preliminary earthquake geology observations, GNS Science. <http://dx.doi.org/10.21420/G2MW2D>.
- Mason, D.P.M., Little, T.A., 2006. Refined slip distribution and moment magnitude of the 1848 Marlborough earthquake, Awatere Fault, New Zealand. *N. Z. J. Geol. Geophys.* 49 (3), 375–382. <http://dx.doi.org/10.1080/00288306.2006.9515174>.
- Melnick, D., Moreno, M., Motagh, M., Cisternas, M., Wesson, R.L., 2012. Splay fault slip during the Mw 8.8 2010 Maule Chile earthquake. *Geology* 40 (3), 251–254. <http://dx.doi.org/10.1130/G32712.1>.
- Minson, S.E., Simons, M., Beck, J.L., 2013. Bayesian inversion for finite fault earthquake source models I—theory and algorithm. *Geophys. J. Int.* 194 (3), 1701–1726. <http://dx.doi.org/10.1093/gji/ggt180>.
- Park, J.-O., Tsuru, T., Kodaira, S., Cummins, P.R., Kaneda, Y., 2002. Splay fault branching along the nankai subduction zone. *Science* 297 (5584), 1157–1160. <http://dx.doi.org/10.1126/science.1074111>.
- Wendt, J., Oglesby, D.D., Geist, E.L., 2009. Tsunamis and splay fault dynamics. *Geophys. Res. Lett.* 36 (15). <http://dx.doi.org/10.1029/2009GL038295>.

2.6 Conclusion et perspectives : prise en compte de la structure 3D et extension aux plus faibles magnitudes

Les résultats présentés dans cette section peuvent être obtenus de manière systématique et robuste pour un grand nombre de tremblements de terre. Cette démarche permet de s'intéresser au comportement d'un grand nombre d'évènements et de mettre en évidence des séismes anormaux qui s'éloignent des comportements classiques. La structure 3D peut avoir un impact non négligeable sur les modèles de source. En particulier, le mode fondamental des ondes de surface est largement affecté par les hétérogénéités superficielles (e.g., entre la lithosphère continentale et la lithosphère océanique). Bien que d'autres phases soient relativement peu affectées par les hétérogénéités de surface, les modèles de source qui en résultent peuvent être biaisés par les hétérogénéités plus profondes. C'est notamment le cas pour les solutions phase W en Amérique du Sud qui montrent un biais systématique de localisation lié à la structure 3D du manteau supérieur.

Pour améliorer les modèles de source, il est donc nécessaire de prendre en compte la structure 3D de la Terre. Différentes applications ont été présentées dans ce chapitre. Le calcul des fonctions d'excitation reste couteux malgré l'utilisation de nouvelles technologies de calcul basées sur le GPGPU. Le temps de calcul peut cependant être grandement réduit via l'utilisation de la réciprocité source-récepteur. En plaçant une force simple à chaque récepteur, nous pouvons ainsi calculer le tenseur de déformation de Green sur une grille fine dans la région-source étudiée. Ces tenseurs peuvent ensuite être recombinés pour calculer les fonctions d'excitation nécessaires à l'inversion du tenseur moment sismique. Cette approche a récemment été employée dans le cadre du doctorat de Catalina Morales pour l'analyse de la sismicité associée à la crise sismo-volcanique débutée en Mai 2018 au large de Mayotte (travail en cours de préparation pour publication).

La prise en compte systématique de la structure 3D peut être utile à différents niveaux. Tout d'abord, la prise en compte des hétérogénéités latérales permet d'améliorer nos modèles de source (en particulier de limiter les biais de localisation). La prise en compte de la structure 3D permet également d'inclure des observations plus courtes périodes et ainsi d'étendre l'analyse systématique des caractéristiques de source à des séismes de plus faible magnitude. L'incorporation de données plus courte période nous donne aussi accès à plus de détail sur la rupture des grands séismes. L'analyse conjointe des fonctions sources apparentes et de la répartition azimutale des amplitudes observées pourrait par exemple permettre une caractérisation systématique de la vitesse et de la direction de rupture pour un grand nombre de séismes. Cela permettrait notamment de vérifier des observations récentes sur la direction de rupture ou l'anticorrélation entre chute de contrainte et vitesse de rupture (Chouhet et al., 2018).

Caractérisation détaillée du glissement sur les failles à partir de données multiples

De part leur nature multi-échelle, les failles sont un système physique difficile à étudier. Les déformations inter-sismiques sont accumulées pendant des dizaines voire des centaines d'années sur des failles bloquées ou partiellement bloquées. Ces déformations accumulées sont ensuite relâchées brusquement lors de ruptures sismiques ou beaucoup plus progressivement lors de séismes lents. Les dernières décennies ont vu une amélioration considérable des moyens de calcul directs et une expansion substantielle des observations géophysiques avec une densification des réseaux sismiques, le déploiement de réseaux GNSS permanents et le lancement de constellations satellites radar ou optiques (Blewitt, 2015 ; Komatitsch and Tromp, 2002 ; Meltzer et al., 1999 ; Simons and Rosen, 2007). Ces efforts ouvrent constamment de nouvelles perspectives sur des aspects fondamentaux du comportement sismogénique des failles actives.

Malgré ces améliorations, de nombreuses questions subsistent sur les interrelations entre glissement sismique et asismique. Plusieurs observations récentes remettent en question l'idée selon laquelle le mode de glissement est une caractéristique permanente d'une zone de faille (Johnson et al., 2012 ; Bedford et al., 2013 ; Thomas et al., 2014). De nombreux mécanismes peuvent être invoqués pour expliquer un possible recouvrement entre glissement sismique et asismique (Avouac, 2015). Ainsi par exemple, si on considère des propriétés frictionnelles hétérogènes, les aspérités voisines sur la faille vont rompre parfois indépendamment et parfois ensemble suivant la répartition des contraintes au moment de la rupture. Une autre possibilité prédictive par les modèles de friction "rate and state", est que la contrainte normale effective doit être suffisamment petite pour autoriser les deux modes de glissement dans les zones de faille en affaiblissement cinétique (en régime conditionnellement stable ; Scholz, 1998). Il a également été démontré que les complexités géométriques de faille peuvent produire des séquences spontanément complexes alternant glissement sismique et asismique (Romanet et al., 2018).

Du point de vue observationnel, le recouvrement entre glissement sismique et asismique est souvent mal contraint et possiblement biaisé par le lissage employé pour régulariser le problème inverse. Le développement de modèles non lissés, avec des estimations d'incertitude fiables est donc important pour évaluer le partitionnement entre ces différents modes de glissement. La résolution du problème inverse est également compliquée par la difficulté à combiner plusieurs types de données présentant une sensibilité variable aux processus en jeu sur la faille. La pondération relative entre les différents jeux de données est souvent définie arbitrairement, ce qui

peut impacter fortement les modèles de glissement. Dans un contexte Bayésien, le poids relatif entre différentes observations est généralement dicté par la matrice de covariance qui décrit les incertitudes observationnelles et de modélisation (Tarantola, 2005).

Dans ce chapitre, on s'intéressera d'abord à la prise en compte des incertitudes et en particulier de celles associées au problème direct. On verra comment cette prise en compte des incertitudes couplée à un échantillonnage Bayésien permet de résoudre le problème d'inversion du glissement sans introduire de lissage arbitraire. Cette approche sera appliquée dans différents contextes (séismes de subduction, séismes décrochants, couplage inter-sismique, séismes lents, phase de nucléation).

3.1 Prise en compte de l'incertitude associée au problème direct

Comme indiqué précédemment, la prise en compte des incertitudes est essentielle dans l'inversion du glissement. Bien que l'erreur observationnelle soit souvent prise en compte, l'incertitude associée au problème direct est généralement négligée. L'erreur associée aux prédictions peut cependant être beaucoup plus importante que l'erreur observationnelle, en particulier pour les grands séismes. Les incertitudes sont généralement intégrées dans le problème inverse sous la forme d'une matrice de covariance \mathbf{C}_χ qui combine la matrice de covariance \mathbf{C}_d associée aux observations et la matrice de covariance \mathbf{C}_p associée aux prédictions. Dans cette section, on développe un modèle direct stochastique pour traiter l'incertitude dans les prédictions, et on montre comment \mathbf{C}_p peut être construite explicitement pour prendre en compte l'incertitude dans le modèle de Terre. Un exemple d'application est présenté dans le cas simple d'une faille infinie en strike-slip dans l'approximation quasi-statique. On discute également comment ce formalisme peut être étendu à d'autres paramètres comme la géométrie de faille. La prise en compte de l'incertitude dans les prédictions permet de produire des modèles plus résistants aux biais induits par un sur-ajustement des observations et permet une estimation plus réaliste de l'incertitude a posteriori.

L'article proposé ci-dessous a été publié en 2014 dans *Geophysical Journal International*. Ce travail a été effectué dans le cadre de mon post-doctorat au Caltech.



Accounting for prediction uncertainty when inferring subsurface fault slip

Zacharie Duputel,^{1,*} Piyush S. Agram,^{1,†} Mark Simons,¹ Sarah E. Minson¹ and James L. Beck²

¹Seismological Laboratory, California Institute of Technology, 1200 E California Blvd., Pasadena, CA 91125-2100, USA. E-mail: zacharie.duputel@unistra.fr

²Division of Engineering and Applied Science, California Institute of Technology, 1200 E California Blvd., Pasadena, CA 91125-2100, USA

Accepted 2013 December 20. Received 2013 December 20; in original form 2013 August 1

SUMMARY

This study lays the groundwork for a new generation of earthquake source models based on a general formalism that rigorously quantifies and incorporates the impact of uncertainties in fault slip inverse problems. We distinguish two sources of uncertainty when considering the discrepancy between data and forward model predictions. The first class of error is induced by imperfect measurements and is often referred to as observational error. The second source of uncertainty is generally neglected and corresponds to the prediction error, that is the uncertainty due to imperfect forward modelling. Yet the prediction error can be shown to scale approximately with the size of earthquakes and thus can dwarf the observational error, particularly for large events. Both sources of uncertainty can be formulated using the misfit covariance matrix, \mathbf{C}_χ , which combines a covariance matrix for observation errors, \mathbf{C}_d and a covariance matrix for prediction errors, \mathbf{C}_p , associated with inaccurate model predictions. We develop a physically based stochastic forward model to treat the model prediction uncertainty and show how \mathbf{C}_p can be constructed to explicitly account for some of the inaccuracies in the earth model. Based on a first-order perturbation approach, our formalism relates \mathbf{C}_p to uncertainties on the elastic parameters of different regions (e.g. crust, mantle, etc.). We demonstrate the importance of including \mathbf{C}_p using a simple example of an infinite strike-slip fault in the quasi-static approximation. In this toy model, we treat only uncertainties in the 1-D depth distribution of the shear modulus. We discuss how this can be extended to general 3-D cases and applied to other parameters (e.g. fault geometry) using our formalism for \mathbf{C}_p . The improved modelling of \mathbf{C}_p is expected to lead to more reliable images of the earthquake rupture, that are more resistant to overfitting of data and include more realistic estimates of uncertainty on inferred model parameters.

Key words: Inverse theory; Probability distributions; Earthquake source observations.

1 INTRODUCTION

Inferring earthquake source models is an essential ingredient in efforts to understand the physics of seismic rupture phenomena and the relationship of an earthquake with its tectonic and geodynamic environment. As such, the earthquake source model is not only an end unto itself but serves as input into a variety of other related applications such as studies of fault zone rheology (e.g. Rice & Cocco

2007), earthquake energy budget analysis (e.g. Kanamori & Rivera 2006) and Coulomb stress transfer calculations (e.g. King 2007). Source estimates are also useful for rapid assessment and response to seismic disasters when they occur (e.g. Duputel *et al.* 2012b). However, source inversion algorithms usually do not include realistic error analyses and their results are generally not accompanied by reliable estimates of uncertainty. These limitations reduce the utility of inferred rupture models and associated by-products. Furthermore, uncertainty in both data and model predictions can cause current source models to be significantly biased due to overfitting of seismic and geodetic observations.

Descriptions of earthquake sources come in various flavours depending on the nature of the data (e.g. seismological, geodetic, geological), the observation scale (i.e. regional or global), the

*Now at: Institut de Physique du Globe de Strasbourg, UDS and EOST/CNRS UMR 7516, France.

†Now at: Jet Propulsion Laboratory, California Institute of Technology, Pasadena, California 91109, USA.

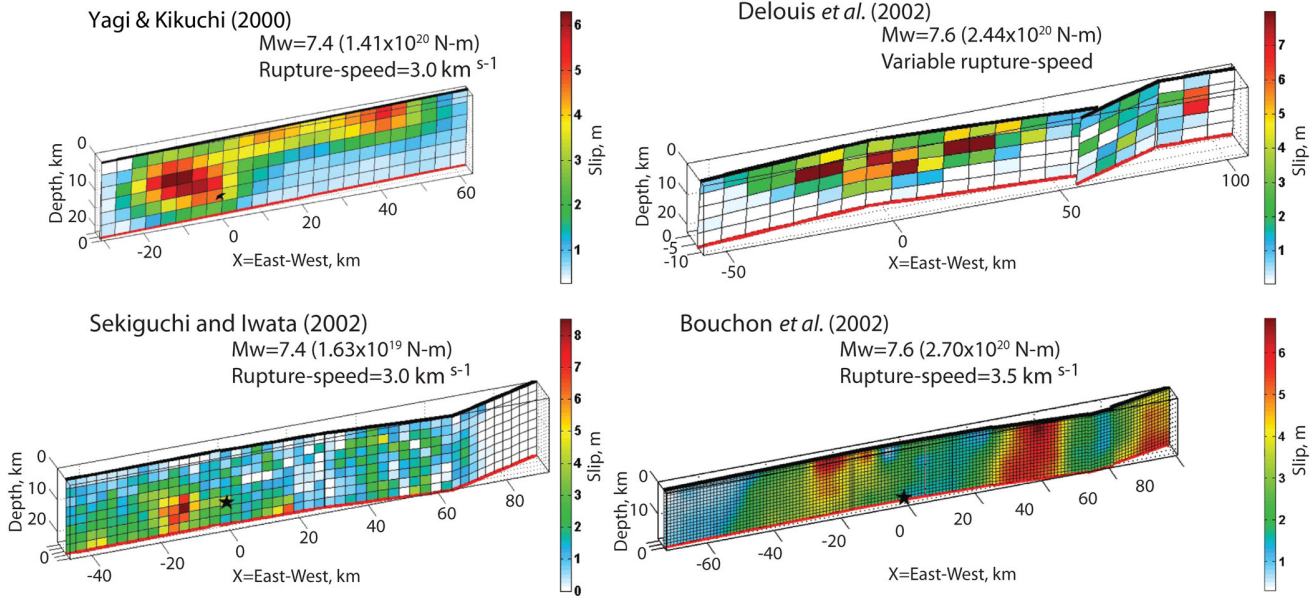


Figure 1. An illustration of variability of kinematic earthquake source models. Results of finite-source rupture modelling obtained by different research groups are presented for the 1999 Izmit earthquake (Yagi & Kikuchi 2000; Bouchon *et al.* 2002; Delouis *et al.* 2002; Sekiguchi & Iwata 2002). The origin of XY-coordinates is set at the epicentre location. These source models are available through the SRCMOD source inversion database (Mai 2012).

parametrization of the source (e.g. linear versus non-linear) and the approach used to infer relevant parameters (e.g. Yabuki & Matsuzura 1992; Wald & Heaton 1994; Ji *et al.* 2002; Minson *et al.* 2013). The reliability of any source inversion depends on many factors including the size and complexity of the event, the amount and quality of data, the way in which data sample the source region and, while usually disregarded, uncertainties in our forward models (i.e. our model predictions).

The last decade has seen considerable improvements in the fidelity of forward modelling capability (e.g. Komatitsch & Vilotte 1998; Williams *et al.* 2005) and a substantial expansion of geophysical observations including broad-band data from dense seismic networks (e.g. USArray, <http://www.usarray.org>; Geonet, <http://geonet.org.nz>; CENC, <http://www.csndmc.ac.cn>; F-net, Okada *et al.* 2004), continuously recording geodetic positioning data from permanent GPS installations (e.g. the Plate Boundary Observatory, <http://pbo.unavco.org>; Geonet, <http://geonet.org.nz>, Taiwan GPS Network, Yu *et al.* 1997) and spatially synoptic geodetic imaging data from orbiting radar and optical satellites (e.g. Simons & Rosen 2007). Despite this progress in forward modelling and data acquisition, one of the biggest obstacles to significant progress in earthquake source modelling arises from imperfect predictions of geodetic and seismic data due to uncertainties in (or imperfect knowledge of) the Earth structure—whose impact is generally ignored. Indeed, for large earthquakes and even aseismic processes, our ability to measure ground motions frequently far exceeds our ability to model them. As discussed latter in Section 2 for linear elastic deformation, the prediction errors due to earth model inaccuracies scale with the fault slip. This aspect is particularly important since large events with large amounts of slip will magnify earth model errors in contrast to small earthquakes for which measurement errors are dominant. Besides the necessity to continue improving the accuracy and efficiency of forward calculations, one of the main challenges today is thus to develop an accurate stochastic model that better describes modelling uncertainty in predicting geodetic and seismic data.

One approach to estimate the uncertainty in source parameters for a given earthquake is to compare fault slip models obtained by various research groups using different inversion approaches (Mai 2012). Fig. 1 shows selected kinematic rupture models for the 1999 Izmit earthquake. Although these models are generally derived from similar data sets, there is a large variability in inversion results. The 1999 Izmit earthquake is not an isolated case. For many events, such as the 1992 Landers or 2001 Arequipa earthquakes, small differences in modelling techniques and data lead to striking differences in inferred slip models (Wald & Heaton 1994; Hernandez *et al.* 1999; Pritchard *et al.* 2007). When different methodologies yield different results for the same event, it is not obvious how any conclusion about the rupture process can be drawn.

This study focus on theoretical and algorithmic developments needed for the next generation of finite-fault earthquake source models by providing a general formalism to explicitly quantify the impact of uncertainties in our forward models and to rigorously incorporate such uncertainties in large ill-posed source inversion problems. We stress the importance of using a stochastic forward modelling approach in this process. It allows us to describe a probability distribution of predictions for a given source model, contrary to a deterministic approach that provides a single set of (potentially inaccurate) predictions. This idea of incorporating stochastic (probabilistic) models in the inverse problem is not new and was introduced in geophysics around 1980, notably by Tarantola & Valette (1982). More recently, Yagi & Fukahata (2011) used such a formalism and proposed a stochastic forward model based on adding Gaussian noise to the unattenuated 1-D teleseismic Green's functions. This Gaussian noise is characterized by a covariance matrix that is partially specified *a priori*. Minson *et al.* (2013) also presented a Gaussian model for the uncertain prediction error in the forward modelling, taking a diagonal covariance matrix with variances that scale with the square of observed amplitudes. In the two approaches, the scale factor that controls the prediction-error variances is incorporated in the model parameters to be inverted. Based on these early studies, we develop here a new formulation exploiting more of the

physics of the forward problem to improve the modelling of the prediction covariance matrix. This general formalism can be used for various problems (e.g. earthquake or volcanic source inversions based on seismic or geodetic data) and relates input uncertainties in the earth model or source geometry to the corresponding distribution of predictions. As recognized by Yagi & Fukahata (2011) and Minson *et al.* (2013), a physically based stochastic model must also account for the dependence of the prediction uncertainty upon the slip model.

We begin by developing the concept of the misfit covariance matrix as used in inversions of slip on subsurface faults. This matrix is the sum of a covariance matrix for observations (often assumed independent) and a covariance matrix for prediction errors associated with inaccurate model predictions (often entirely ignored). We then describe how a physically informed prediction covariance matrix can be obtained. In particular, we consider the effect of uncertainties in the earth model. Our description is based on a Bayesian formulation of the inverse problem but our formalism can also be used in optimization methods. Although our approach is general and can be used for various seismic and geodetic data sets, we explore here the advantage of including more structured reasonable prediction covariance matrices by using simple quasi-static models. We also discuss how to account for other sources of prediction uncertainty such as inaccurate fault geometries. Given the increased computational complexity, we leave a similar development of the prediction covariance for kinematic modelling to a future study.

2 ON THE IMPORTANCE OF PREDICTION UNCERTAINTY IN SOURCE INVERSION PROBLEMS

Let $\mathbf{d}_{\text{obs}} = [d_1^{\text{obs}}, d_2^{\text{obs}}, \dots, d_N^{\text{obs}}]^T$ be the set of N field observations used in the source inversion process. Let also define \mathbf{m} as the set of source model parameters in the M -dimensional model space \mathfrak{M} . In the source inversion process, we want to use \mathbf{d}_{obs} to learn about \mathbf{m} . As in many inverse problems, error models play a central role in the formulation of uncertainties and our knowledge of \mathbf{m} will strongly depend on the information they provide. In our problem, we can separate two sources of error that we can account for using appropriate stochastic models. These two fundamental probability models are discussed in the following.

The first source of uncertainty comes from the observational error that is induced by the measurement process. When measuring an N -dimensional quantity \mathbf{d} , measurements are associated with an uncertain error \mathbf{e} given by

$$\mathbf{e} = \mathbf{d}^* - \mathbf{d}. \quad (1)$$

In this equation, \mathbf{d}^* is a stochastic variable representing uncertain measurement and \mathbf{d} is the actual displacement value. The set of field observations $\mathbf{d}_{\text{obs}} = [d_1^{\text{obs}}, d_2^{\text{obs}}, \dots, d_N^{\text{obs}}]^T$ can be seen as a single realization of \mathbf{d}^* . In other words, \mathbf{d}_{obs} is a fixed vector corresponding to actual measured values and \mathbf{d}^* is a stochastic vector representing uncertainty on those field observations. We will assume that positive and negative errors of equal magnitude are equally plausible and so take \mathbf{e} to have zero mean. We also choose a covariance matrix \mathbf{C}_d for \mathbf{e} . Following the Principle of Maximum Entropy (Jaynes 1983, 2003), the probability density function (PDF) that assumes the least additional information about \mathbf{e} under these conditions is a Gaussian probability density $p(\mathbf{e}|\mathbf{d}) = \mathcal{N}(\mathbf{e}|\mathbf{0}, \mathbf{C}_d)$ with covariance matrix \mathbf{C}_d and zero mean (*cf.* Bishop 2006). Our stochastic model

for the measurement process is thus given by

$$p(\mathbf{d}^*|\mathbf{d}) = \mathcal{N}(\mathbf{d}^*|\mathbf{d}, \mathbf{C}_d)$$

$$= \frac{1}{\sqrt{(2\pi)^N |\mathbf{C}_d|}} \exp\left(-\frac{1}{2}(\mathbf{d}^* - \mathbf{d})^T \mathbf{C}_d^{-1} (\mathbf{d}^* - \mathbf{d})\right), \quad (2)$$

where $p(\mathbf{d}^*|\mathbf{d})$ is the probability (density) for getting the measured value \mathbf{d}^* when the uncertain physical quantity being measured has the value \mathbf{d} . The PDF $p(\mathbf{d}^*|\mathbf{d})$ and the associated measurement covariance matrix \mathbf{C}_d depend of course on the nature of measurement and on the type of instrument used. A common model is to take independent observational errors (i.e. diagonal \mathbf{C}_d). However, for observations like InSAR or seismic data, off-diagonal components should be included in \mathbf{C}_d to allow correlation of measurement errors between neighbouring data samples (e.g. Lohman & Simons 2005; Fukahata & Wright 2008; Duputel *et al.* 2012a).

The second source of uncertainty corresponds to our imperfect knowledge of \mathbf{d} for a given source model \mathbf{m} , which comes from the prediction error due to imperfect forward modelling, also referred to as epistemic error. For earthquake source modelling problems, this component includes but is not limited to, lack of fidelity in the fault geometry, oversimplifications of the mechanical earth model and approximations made when calculating the Earth's response to an applied force.

Let $\mathbf{g}(\Psi, \mathbf{m})$ be a deterministic model for the forward predictions for a source model \mathbf{m} . In addition to the source model, the forward model depends on a set of uncertain properties parametrized by a vector Ψ that is not solved for (e.g. earth model elastic properties, fault geometry). We are uncertain about what value to take for the parameters Ψ . Suppose $\tilde{\Psi}$ denotes the most plausible value *a priori*. Then, for a given source model \mathbf{m} , we obtain the corresponding prediction $\mathbf{d}_{\text{pred}} = \mathbf{g}(\tilde{\Psi}, \mathbf{m})$. We define the uncertain prediction error by

$$\mathbf{e} = \mathbf{d} - \mathbf{d}_{\text{pred}} = \mathbf{d} - \mathbf{g}(\tilde{\Psi}, \mathbf{m}), \quad (3)$$

which is taken as a stochastic variable associated with a probability density $p(\mathbf{e}|\mathbf{m})$, that describes the uncertainty in the actual physical quantity \mathbf{d} (i.e. displacement), given \mathbf{d}_{pred} . Using a similar argument for \mathbf{e} as for \mathbf{e} above, we choose a maximum entropy distribution subject to a zero mean and a covariance matrix $\mathbf{C}_p(\mathbf{m})$ to get the Gaussian distribution $p(\mathbf{e}|\mathbf{m}) = \mathcal{N}(\mathbf{e}|\mathbf{0}, \mathbf{C}_p(\mathbf{m}))$. The corresponding stochastic forward model for the predictions is then given by the conditional Gaussian PDF

$$p(\mathbf{d}|\mathbf{m}) = \mathcal{N}[\mathbf{d}|\mathbf{g}(\tilde{\Psi}, \mathbf{m}), \mathbf{C}_p(\mathbf{m})] = \frac{1}{\sqrt{(2\pi)^N |\mathbf{C}_p(\mathbf{m})|}} \times \exp\left(-\frac{1}{2} [\mathbf{d} - \mathbf{g}(\tilde{\Psi}, \mathbf{m})]^T \mathbf{C}_p(\mathbf{m})^{-1} [\mathbf{d} - \mathbf{g}(\tilde{\Psi}, \mathbf{m})]\right). \quad (4)$$

Even though the prediction error is generally neglected (i.e. $\mathbf{C}_p = \mathbf{0}$), we know that its contribution can be comparable or even larger than measurement errors, in particular for large earthquakes. This can be easily understood if we consider, for example, a linear formulation of the forward problem $\mathbf{g}(\Psi, \mathbf{m}) = \mathbf{G}(\Psi) \cdot \mathbf{m}$. In this case, we can write

$$\mathbf{e} = [\mathbf{G}(\Psi) - \mathbf{G}(\tilde{\Psi})] \cdot \mathbf{m} = \boldsymbol{\Gamma}(\tilde{\Psi}, \Psi) \cdot \mathbf{m}, \quad (5)$$

where the matrix $\boldsymbol{\Gamma}$ describes the uncertainty in \mathbf{G} due to the uncertainty in Ψ . In this equation, the level of the prediction error \mathbf{e} modelled by \mathbf{C}_p scales with the magnitude of the source model

\mathbf{m} (this dependence is also discussed in Yagi & Fukahata 2011). The observational uncertainties, on the other hand, are independent of the model parameters and are essentially controlled by the nature and quality of the measurements. For large earthquakes, the contribution of \mathbf{C}_d is thus frequently negligible compared to \mathbf{C}_p .

At this point, we therefore have (1) a stochastic model $p(\mathbf{d}^*|\mathbf{d})$ associated with \mathbf{C}_d in eq. (2) describing the measurement uncertainty and (2) a stochastic forward model $p(\mathbf{d}|\mathbf{m})$ associated with \mathbf{C}_p in eq. (4) describing the prediction uncertainty. Using Bayesian source inversion, our goal here is to combine the available information from observations and prior information about the model parameters and forward modelling to construct a posterior distribution for the source model parameters. To do so, we use Bayes' theorem to get the posterior PDF $p(\mathbf{m}|\mathbf{d}_{\text{obs}})$ over the model space (Bayes 1763):

$$p(\mathbf{m}|\mathbf{d}_{\text{obs}}) = \kappa p(\mathbf{d}_{\text{obs}}|\mathbf{m}) p(\mathbf{m}), \quad (6)$$

where κ is a normalization constant and $p(\mathbf{d}_{\text{obs}}|\mathbf{m})$ is a likelihood function:

$$p(\mathbf{d}_{\text{obs}}|\mathbf{m}) = \int_{\mathfrak{D}_{\text{pred}}} p(\mathbf{d}_{\text{obs}}|\mathbf{d}) p(\mathbf{d}|\mathbf{m}) d\mathbf{d}. \quad (7)$$

Strictly speaking, $p(\mathbf{d}_{\text{obs}}|\mathbf{m})$ is a marginal or integrated likelihood in which \mathbf{d} has been marginalized out over the prediction space $\mathfrak{D}_{\text{pred}}$, which is the space of all conceivable forward model predictions. Eq. (6) states that the posterior probability density of \mathbf{m} given the measurements \mathbf{d}_{obs} is proportional to the product of a PDF $p(\mathbf{m})$ describing the prior information on \mathbf{m} and the likelihood function $p(\mathbf{d}_{\text{obs}}|\mathbf{m})$, which gives a measure of how well the model \mathbf{m} explains the data \mathbf{d}_{obs} . A similar result can be obtained using the concept of conjunction of states of information as introduced by Tarantola & Valette (1982). In eq. (7), $p(\mathbf{d}_{\text{obs}}|\mathbf{d})$ comes from substituting $\mathbf{d}^* = \mathbf{d}_{\text{obs}}$ in the probability model $p(\mathbf{d}^*|\mathbf{d})$. It describes the likelihood of having observed \mathbf{d}_{obs} if the actual displacement was \mathbf{d} . Using the stochastic models developed in eqs (2) and (4) in eqs (6) and (7), we can then show (*cf.* Appendix A)

$$p(\mathbf{m}|\mathbf{d}_{\text{obs}}) = \eta(\mathbf{m}) p(\mathbf{m}) \exp \left(-\frac{1}{2} [\mathbf{d}_{\text{obs}} - \mathbf{g}(\tilde{\Psi}, \mathbf{m})]^T \times \mathbf{C}_\chi(\mathbf{m})^{-1} [\mathbf{d}_{\text{obs}} - \mathbf{g}(\tilde{\Psi}, \mathbf{m})] \right), \quad (8)$$

where $\mathbf{C}_\chi(\mathbf{m})$ is the misfit covariance matrix defined as

$$\mathbf{C}_\chi(\mathbf{m}) = \mathbf{C}_d + \mathbf{C}_p(\mathbf{m}) \quad (9)$$

and $\eta(\mathbf{m})$ is a normalization factor:

$$\eta(\mathbf{m}) = \kappa (2\pi)^{-N/2} |\mathbf{C}_d|^{-1/2} |\mathbf{C}_p(\mathbf{m})|^{-1/2} |\mathbf{C}_d^{-1} + \mathbf{C}_p(\mathbf{m})^{-1}|^{-1/2}. \quad (10)$$

It is important to note that the covariance \mathbf{C}_χ plays a central role in the inversion process. First of all, \mathbf{C}_χ controls the shape of the posterior probability density $p(\mathbf{m}|\mathbf{d}_{\text{obs}})$ and therefore affects the solution of the inverse problem. Secondly, \mathbf{C}_χ is the only term in eq. (8) that describes the statistics of measurement (\mathbf{C}_d) and model prediction errors (\mathbf{C}_p). Among these two contributors, \mathbf{C}_d can easily be more readily taken into account because the statistics of observational uncertainties are generally well characterized. \mathbf{C}_p , on the other hand, is usually neglected even if its contribution can be larger than \mathbf{C}_d as discussed above. In this paper, we advocate improved modelling of the prediction-error uncertainty in any source inversion problem by developing a stochastic forward model using a covariance

matrix structure based on an explicit treatment of uncertainties in the predictions.

3 A STOCHASTIC MODEL FOR THE PREDICTION UNCERTAINTY

The development of a covariance matrix for the predictions (\mathbf{C}_p) is important regardless of the particular approach one uses to invert for source model parameters. Indeed, in most source inversion problems (e.g. Hartzell & Heaton 1983; Delouis *et al.* 2000; Ji *et al.* 2002; Simons *et al.* 2011; Minson *et al.* 2013, 2014), the discrepancies between data \mathbf{d}_{obs} and forward predictions $\mathbf{g}(\tilde{\Psi}, \mathbf{m})$ for a source model \mathbf{m} are quantified by defining a least-squares misfit function of the form

$$\chi(\mathbf{m}) = \frac{1}{2} [\mathbf{d}_{\text{obs}} - \mathbf{g}(\tilde{\Psi}, \mathbf{m})]^T \cdot \mathbf{C}_\chi^{-1} \cdot [\mathbf{d}_{\text{obs}} - \mathbf{g}(\tilde{\Psi}, \mathbf{m})]. \quad (11)$$

In a parameter optimization process, $\chi(\mathbf{m})$ is minimized while in a Bayesian formulation the likelihood function is given by $p(\mathbf{d}_{\text{obs}}|\mathbf{m}) = \eta(\mathbf{m}) \exp(-\chi(\mathbf{m}))$. Therefore, whatever the source estimation method, a central role is played by the misfit covariance matrix, $\mathbf{C}_\chi = \mathbf{C}_d + \mathbf{C}_p$. As we discussed previously, \mathbf{C}_p is the dominant term for large earthquakes and the construction of an improved prediction covariance matrix can lead to improved source imaging techniques. If one adopts a regularized least-squares approach for finite-fault models using a Tikhonov regularization (e.g. minimum moment, minimum roughness), then the particular choice of the penalty parameter depends on the effective information content of the data. This dependence on \mathbf{C}_χ is true regardless of whether one chooses the amount of damping by some L-curve approach, cross-validation or Bayesian model class selection. Similarly, if one chooses to adopt a fully Bayesian approach, then having the appropriate covariance matrix can control the extent to which one does or does not overfit the observations.

3.1 Prediction uncertainty due to inaccuracies in the forward model

The derivation proposed here is developing ideas proposed by Duputel *et al.* (2012a), who demonstrated that centroid location uncertainty in point-source moment tensor inversions can be accounted for by designing a prediction covariance matrix \mathbf{C}_p based on the relevant physics of the forward problem. In this study, we consider the effects of properties of the forward model which are not solved for but can significantly affect the predictions (e.g. Earth elastic properties, fault geometry).

Hereafter, we derive the statistics of the prediction uncertainty by assuming that $\mathbf{g}(\Psi, \mathbf{m})$ for given generic properties Ψ of the forward model is well approximated by linearized perturbations of our predictions $\mathbf{g}(\tilde{\Psi}, \mathbf{m})$ for the *a priori* set of parameters $\tilde{\Psi}$:

$$\mathbf{g}(\Psi, \mathbf{m}) \approx \mathbf{g}(\tilde{\Psi}, \mathbf{m}) + \mathbf{K}_\Psi(\tilde{\Psi}, \mathbf{m}) \cdot (\Psi - \tilde{\Psi}), \quad (12)$$

where the matrix $\mathbf{K}_\Psi(\tilde{\Psi}, \mathbf{m})$ is the so-called sensitivity kernel of the predictions with respect to Ψ :

$$(\mathbf{K}_\Psi)_{ij}(\tilde{\Psi}, \mathbf{m}) = \frac{\partial g_i}{\partial \Psi_j}(\tilde{\Psi}, \mathbf{m}). \quad (13)$$

Under the first-order approximation of eq. (12), we can write the prediction error ϵ as

$$\epsilon = \mathbf{g}(\Psi, \mathbf{m}) - \mathbf{g}(\tilde{\Psi}, \mathbf{m}) \approx \mathbf{K}_\Psi(\tilde{\Psi}, \mathbf{m}) \cdot \delta\Psi. \quad (14)$$

Using eq. (12) we can write Jacobian rule $p(\Psi) = p(\mathbf{d}|\mathbf{m}) \left| \frac{\partial \mathbf{d}}{\partial \Psi} \right|$, where $\left| \frac{\partial \mathbf{d}}{\partial \Psi} \right|$ is the Jacobian determinant of the transformation $\mathbf{d} = \mathbf{g}(\Psi)$ and we write the prediction covariance as

$$\begin{aligned} \mathbf{C}_p(\mathbf{m}) &= \int [\mathbf{g}(\Psi, \mathbf{m}) - \mathbf{g}(\tilde{\Psi}, \mathbf{m})] \\ &\quad \times [\mathbf{g}(\Psi, \mathbf{m}) - \mathbf{g}(\tilde{\Psi}, \mathbf{m})]^T p(\Psi) d\Psi, \end{aligned} \quad (15)$$

where $p(\Psi)$ is the prior probability density describing the uncertainty in the generic properties Ψ . We assume here that $p(\Psi)$ is a Gaussian distribution:

$$p(\Psi) = \mathcal{N}(\Psi | \tilde{\Psi}, \mathbf{C}_\Psi), \quad (16)$$

which corresponds to the least informative PDF that is adequate for given *a priori* parameters $\tilde{\Psi}$ and a covariance matrix \mathbf{C}_Ψ defined as

$$\mathbf{C}_\Psi = \int (\Psi - \tilde{\Psi})(\Psi - \tilde{\Psi})^T p(\Psi) d\Psi. \quad (17)$$

If more information is available about Ψ , one can of course choose another more informative form of $p(\Psi)$. By plugging eqs (14) and (17) into eq. (15), it follows that

$$\mathbf{C}_p = \mathbf{K}_\Psi \cdot \mathbf{C}_\Psi \cdot \mathbf{K}_\Psi^T, \quad (18)$$

where we drop the variables $\tilde{\Psi}$ and \mathbf{m} for clarity. Using the formulation developed above, we can do much better than predicting a set of observations for a given source model. We can now construct a probability distribution for the predictions $p(\mathbf{d}|\mathbf{m}) = \mathcal{N}[\mathbf{d}|\mathbf{g}(\tilde{\Psi}, \mathbf{m}), \mathbf{C}_p]$, that is, a stochastic forward model based on more of the physics of the problem and reflecting uncertainties in properties Ψ which are not inverted but can affect the predictions.

3.2 Accounting for inaccuracies in the earth model

Among the different sources of uncertainty, the approximate nature of the chosen earth model is of great interest as it is one of the largest contributors to forward modelling errors (Savage 1987; Hjörleifsdóttir & Ekström 2010; Yagi & Fukahata 2011). We explicitly treat this aspect in constructing a stochastic forward model for \mathbf{d} . In some extreme cases, an earth model $\tilde{\Omega}$ can be very different from the actual elastic structure and there will be no simple relationship between the corresponding predictions and the actual displacement values. In such situations, results of our inversion would be unreliable and we should focus our efforts on obtaining a more accurate earth model. However, in most applications, elastic models are reasonable approximations of the true underlying elastic structure of the Earth and we may still be able to solve the source inversion problem by designing an appropriate misfit covariance model, \mathbf{C}_x .

As in previous section, we can derive the statistics of the prediction uncertainty by assuming that $\mathbf{g}(\Omega, \mathbf{m})$ for given elastic parameters Ω is well approximated by linearized perturbations of our predictions $\mathbf{g}(\tilde{\Omega}, \mathbf{m})$ for the *a priori* earth model $\tilde{\Omega}$. The elastic parameters in Ω being strictly positive, we use the formulation described in Section 3.1 with $\Psi = \ln \Omega$. We therefore assume here that $p(\Omega)$ is a log-normal distribution which corresponds to the least-informative PDF (i.e. the maximum entropy PDF) that is adequate for a Jeffrey's parameter (Tarantola 2005):

$$p(\ln \Omega) = \mathcal{N}(\ln \Omega | \ln \tilde{\Omega}, \mathbf{C}_\Omega), \quad (19)$$

with $\ln \tilde{\Omega}$ and \mathbf{C}_Ω , respectively, the mean and covariance of $\ln \Omega$. This choice of a log-normal distribution is also justified by the fact that modern tomography techniques are often based on relative

model perturbations (e.g. $\delta \ln \Omega = \delta \Omega / \Omega$, Tromp *et al.* 2005). The prediction covariance matrix associated with such uncertainty in the earth model is then given by

$$\mathbf{C}_p = \mathbf{K}_\Omega \cdot \mathbf{C}_\Omega \cdot \mathbf{K}_\Omega^T, \quad (20)$$

where the matrix \mathbf{K}_Ω is the sensitivity kernel of the predictions with respect to the earth model parameters:

$$(\mathbf{K}_\Omega)_{ij}(\tilde{\Omega}, \mathbf{m}) = \frac{\partial g_i}{\partial \ln \Omega_j}(\tilde{\Omega}, \mathbf{m}). \quad (21)$$

In Section 4, we consider a simple 1-D case for which Ω_j represents the shear modulus μ_j in the j th layer of the tabular elastic model $\tilde{\Omega} = \tilde{\mu}$ used to compute the predictions $g_i(\tilde{\mu}, \mathbf{m})$. In the 3-D case, $\Omega_j = \mu_j$ can represent the shear modulus in the j th region of the earth model (*cf.* Appendix B).

3.3 Practical implementation in a Bayesian framework

In this study, we use a Bayesian sampling algorithm called Cascading Adaptive Transitional Metropolis In Parallel (CATMIP), which allows sampling in very high dimensional problems in a parallel computing framework (Minson *et al.* 2013). CATMIP combines the Metropolis algorithm with elements of simulated annealing and genetic algorithms to dynamically optimize the algorithms efficiency as it runs. As proposed initially by Beck & Au (2002) and Ching & Chen (2007), the CATMIP algorithm samples from a series of intermediate PDFs:

$$\begin{aligned} f(\mathbf{m}, \beta_i) &\propto p(\mathbf{m}) p(\mathbf{d}_{\text{obs}} | \mathbf{m})^\beta, \\ i &= 1, \dots, B \\ 0 &= \beta_0 < \beta_1 < \beta_2 < \dots < \beta_B = 1. \end{aligned} \quad (22)$$

In this procedure, we start at $\beta_0 = 0$ to sample the prior and slowly increase β_i through several transitional steps. When $\beta_i = \beta_B = 1$, we obtain an accurate sampling of the posterior probability density $p(\mathbf{m} | \mathbf{d}_{\text{obs}})$. As proposed in Ching & Chen (2007) and Beck & Zuev (2013), we optimize the transitional process by choosing each $\delta \beta_i = \beta_{i+1} - \beta_i$ adaptively rather than using a pre-set schedule for the sequence of β_i . More specifically, each $\delta \beta_i$ is chosen such that the effective sample size between $f(\mathbf{m}, \beta_i)$ and $f(\mathbf{m}, \beta_{i+1})$ is about 50 per cent (Beck & Zuev 2013). Between each transitional step, a large number of Markov chains run in parallel. Each chain is governed by the Metropolis algorithm in which the probability of acceptance of one candidate sample is determined by comparing the value of the intermediate PDF with that of the current sample (Minson *et al.* 2013).

Our derivation is consistent with ideas proposed initially by Tarantola & Valette (1982), who argued that modelling uncertainties can be incorporated into the inversion framework by adding a term to the data covariance matrix that represents the uncertainties in the physical theory (i.e. \mathbf{C}_p). However, we differ from Tarantola & Valette (1982) by recognizing that our prediction covariance matrix \mathbf{C}_p should also depend on the earthquake source model and is not just a constant matrix, that is, changing the magnitude and distribution of fault slip will change \mathbf{C}_p for a given elastic model. For practical implementation, there are different ways of dealing with the dependence of $\mathbf{C}_x = \mathbf{C}_d + \mathbf{C}_p$ upon the source model \mathbf{m} . For example, one can calculate $\mathbf{C}_p(\mathbf{m}_{\text{prior}})$ using an *a priori* source model, $\mathbf{m}_{\text{prior}}$, such as a centroid-moment-tensor solution or a preliminary finite-fault model and assume that \mathbf{C}_p is constant. In contrast, we propose here to update the prediction covariance during the

source inversion process. More precisely, in our implementation of CATMIP, the sample mean $\langle \mathbf{m} \rangle$ at each transitional step is used as a new model to re-compute \mathbf{C}_p . Therefore, we assume that \mathbf{C}_p does not vary significantly in the neighbourhood of $\langle \mathbf{m} \rangle$, which ensure that the likelihood term $p(\mathbf{d}_{\text{obs}} | \mathbf{m})$ in eq. (22) is Gaussian for a given value of β . For computational efficiency, the slip inversion being a linear problem $\mathbf{d} = \mathbf{G}\mathbf{m}$, we can pre-calculate the sensitivity kernels for each Green's functions in the matrix \mathbf{G}

$$(\mathbf{K}_\Omega^G)_{ijk} = \frac{\partial G_{ik}}{\partial \log \Omega_j}, \quad (23)$$

such that

$$\mathbf{K}_\Omega = \mathbf{K}_\Omega^G \cdot \langle \mathbf{m} \rangle. \quad (24)$$

In practice, this approach can be used for static and seismic data.

Although \mathbf{K}_Ω^G can be pre-computed, its calculation remains a challenging problem. We propose here to use the perturbation theory which has been extensively employed in seismic tomography through the Born approximation (e.g. Marquering *et al.* 1998; Tromp *et al.* 2005; Virieux & Operto 2009) and has been introduced for quasi-static problems by Du *et al.* (1994) and Cervelli *et al.* (2002). In the motivational example presented in Section 4, we use analytical solutions that are available in the quasi-static case for infinite strike-slip faults embedded in a layered earth model (Du *et al.* 1994). For non-infinite faults, one can increase the efficiency of the sensitivity kernel calculation by adopting an adjoint formulation. This approach allows a reduction in the computational cost when the number of stations is small compared to the number of elements and is popular in various fields such as 3-D seismic tomography (Tarantola 1984, 1988; Tromp *et al.* 2005), inverse problems in elasticity (Bonnet & Constantinescu 2005) and meteorological studies (Talagrand & Courtier 2007). To further increase the computational tractability of the sensitivity kernel calculations, we can also consider a limited number of tectonically parametrized regions where the uncertainties on elastic parameters are prescribed. Indeed, we are not interested in assigning variable uncertainties on a fine mesh but rather describing the earth model uncertainty in a limited number of tectonic regions (e.g. crust, mantle, etc.).

4 APPLICATION TO GEODETIC DATA: A MOTIVATIONAL EXAMPLE

In this synthetic application, we study the static surface displacements due to a vertical strike-slip fault and solve for the depth distribution of slip given uncertainties in the depth distribution of shear modulus (μ) in the elastic medium. With this purpose, we consider a simple model of an infinite 2-D strike-slip fault embedded in a shallow low compliance layer of thickness H overlying an elastic half-space (cf. red line on Figs 2b and d). We define μ_2 , the shear modulus in the half-space and μ_1 , the shear modulus in the shallow layer so that $\mu_2/\mu_1 = 1.4$. Given synthetic data at 100 observation points regularly sampled from the surface deformation of this 2-D model, we infer the depth distribution of slip assuming a homogeneous elastic half-space and accounting for the uncertainty in μ using the formulation of \mathbf{C}_p described in Section 3.2. For simplicity, we assume no uncertainty on the Poisson's ratio although this can easily be implemented using our formalism of \mathbf{C}_p . The 2-D calculation of \mathbf{C}_p , the fault parametrization as well as practical implications of using a non-constant prediction covariance structure are addressed in the following sections.

4.1 Calculation of \mathbf{C}_p in two dimensions

In this application example, we want to take into account the prediction error due to uncertainty in the 1-D shear modulus structure ($\Omega = \mu$). In this case, the prediction covariance \mathbf{C}_p defined in eq. (20) can be rewritten as

$$\mathbf{C}_p = \mathbf{K}_\mu \cdot \mathbf{C}_\mu \cdot \mathbf{K}_\mu^T. \quad (25)$$

From this equation, we know that in order to obtain \mathbf{C}_p , we need to estimate the shear modulus sensitivity kernel \mathbf{K}_μ and to choose an appropriate covariance \mathbf{C}_μ describing the uncertainty on μ . For practical implementation, we discretized the earth model into 50 small layers from depth of 0 to $5H$, where H is the thickness of the shallow layer. We then compute the sensitivity of the predictions with respect to the shear modulus in each layer using the first-order perturbations introduced initially by Du *et al.* (1994) for infinite strike-slip faults. The calculation of \mathbf{K}_μ in the quasi-static case is detailed in Appendix B.

In this simple implementation of \mathbf{C}_p , the covariance matrix \mathbf{C}_μ is used to describe the uncertainty and correlations of the shear modulus for each of the 50 layers used to discretize the earth model. Various covariance structures in \mathbf{C}_μ can be designed depending on the amount of information available about the earth model. Two different forms of \mathbf{C}_μ are presented in Figs 2(a) and (c). To illustrate the corresponding uncertainty on μ , Figs 2(b) and (d) show 1000 stochastic earth model realizations that are drawn for each form of \mathbf{C}_μ (cf. eq. 16). It should be noted that static predictions are only affected by gradients in elastic parameters and are not sensitive to absolute values in μ . Therefore, in this implementation, we take the half-space as the reference and allow the shear modulus to vary in the shallow layers. In Figs 2(a)–(b), we assume that the shallow layer thickness is known but that the shear modulus contrast with the homogeneous half-space is uncertain. In this case, we have a sharp transition in \mathbf{C}_μ between the shallow layer and the homogeneous half-space. In Figs 2(c)–(d), we consider the layer thickness as uncertain and we assume a smooth transition using a decaying exponential correlation function for depth larger than $0.8H$.

Figs 3(a) and (c) show the corresponding covariance matrices \mathbf{C}_p obtained for a simple uniform unit slip distribution between 0 to $0.9H$ where H is the thickness of the shallow layer. Figs 3(b) and (d) present 1000 stochastic prediction realizations for both versions of \mathbf{C}_p . Note that \mathbf{C}_p is not very different for the two forms of \mathbf{C}_μ , even though the prediction uncertainty for distant stations is slightly larger if we include uncertainty in the layer thickness. Several interesting features can be identified in the prediction covariance matrix structure. From the diagonal elements of \mathbf{C}_p , we note first an increase of the prediction uncertainty as one approaches the fault, in agreement with the idea proposed by Minson *et al.* (2013) that mismodelling error should be roughly proportional to the data amplitude. However, we also note a drop of prediction uncertainty for observation points very close to the fault, since they provide direct slip measurements that have little sensitivity to the shear modulus. The off-diagonal covariance components show a clear anticorrelation with values on the opposite side of the fault for the form of \mathbf{C}_μ considered here. If the predicted data happen to be anomalously large on one side, the prediction must also be anomalously large but of opposite sign on the other side of the fault. The prediction covariance \mathbf{C}_p thus provides essential information about data weighting and data correlation that should be taken into account in the inverse problem.

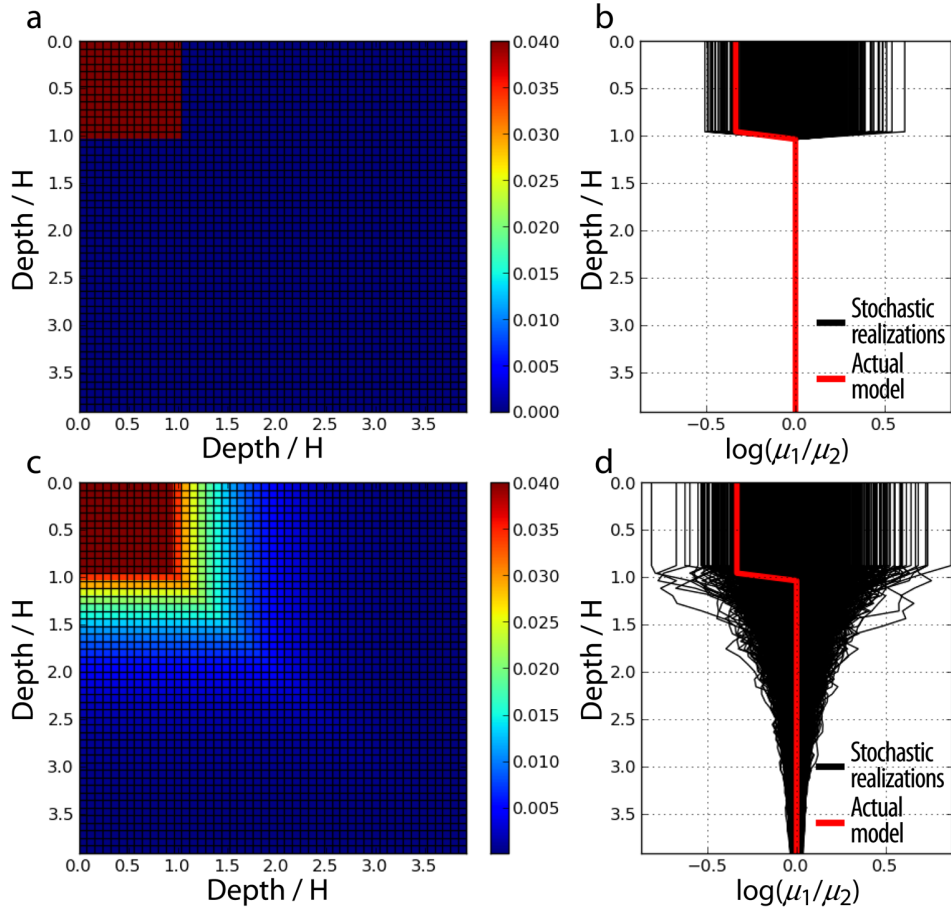


Figure 2. Uncertainty in the 1-D shear modulus structure μ . The shear modulus uncertainty is presented in (a)–(b) assuming a fixed thickness H for the shallow layer and in (c)–(d) considering the layer thickness as uncertain. For both cases, we present the shear modulus covariance matrix C_μ in (a) and (c). Using eq. (16) to sample for each form of C_μ , we show 1000 stochastic earth model realizations in (b) and (d), where individual stochastic realizations are plotted in black and the actual earth model is presented in red. We define μ_1 , the shear modulus in the shallow layers and μ_2 , the shear modulus in the half-space.

4.2 A side comment on fault parametrization

In this section, we investigate the model resolution in order to design a proper parametrization of the fault. We aim to derive a fault discretization that allows us to accurately reflect the slip distribution and account for the resolving power of available measurements. Furthermore, to allow a natural comparison between the inferred model and the true slip distribution, we need to understand the fundamental spatial resolution of the estimated slip model.

Fig. 4 shows the inversion results obtained for a target slip distribution with 1-m uniform slip (i.e. $\mathbf{m} = 1 \text{ m}$) at depths between 0 and $0.9H$. We use $p(\mathbf{m}) = \mathcal{U}(-0.3, 20)^M$ as the prior information on the slip parameters \mathbf{m} (i.e. a uniform probability distribution from -0.3 to 20 m in M -dimensions). As described above, the data computed for a layered half-space with $\mu_2/\mu_1 = 1.4$ (cf. red line in Fig. 2 d) is inverted using Green's functions for a homogeneous half-space including our formulation of C_p (using the shear modulus structure C_μ shown in Fig. 2c). The results obtained if we neglect C_p are presented in Fig. S1 of the Supporting Information and the advantages of including C_p in the inversion are discussed latter (see Section 4.3).

Histograms in Fig. 4(a) present the marginal PDFs obtained if the fault is discretized into 16 fault patches. Apart for the shallowest subfault, the shape of these marginals clearly suggests a multivariate Dirichlet distribution of slip over group of adjacent patches. An

N_p -dimensional Dirichlet distribution produces sets of N_p stochastic positive numbers that sum to a given constrained value (cf. Minson *et al.* 2013). The marginal of a Dirichlet distribution is a beta distribution of the form

$$\beta(m_i|1, N_p - 1) \propto (1 - m_i)^{N_p - 2}, \quad (26)$$

where we assumed unit concentration parameters (Bishop 2006). The best-fitting Beta distributions shown in black in Fig. 4(a) indicate that optimum values for N_p range between 2 and 4. This suggests that the sum of slip on $N_p \sim 3$ neighbouring patches can be resolved while it is poorly constrained on individual subfaults. Fig. 5 shows some model samples chosen randomly near the mean of the posterior distribution. For these models, the distribution of slip shows strong oscillations over adjacent patches while the average slip over group of subfaults are consistent with the target model. The best-fitting Dirichlet distributions along with this checker-boarding of neighbouring subfaults indicate that the slip can be well resolved over $N_p \sim 3$ neighbouring patches, that is, at a scale of about $0.2H$. Histograms in Fig. 4(b) present marginal PDFs similar to Fig. 4(a) with the fault discretized into 32 fault patches. In this case, the best-fitting Dirichlet distribution indicates checkerboarding over $N_p \sim 6$ patches which corresponds to a resolution scale of about $0.2H$, consistent with results obtained using the 16 patches discretization.

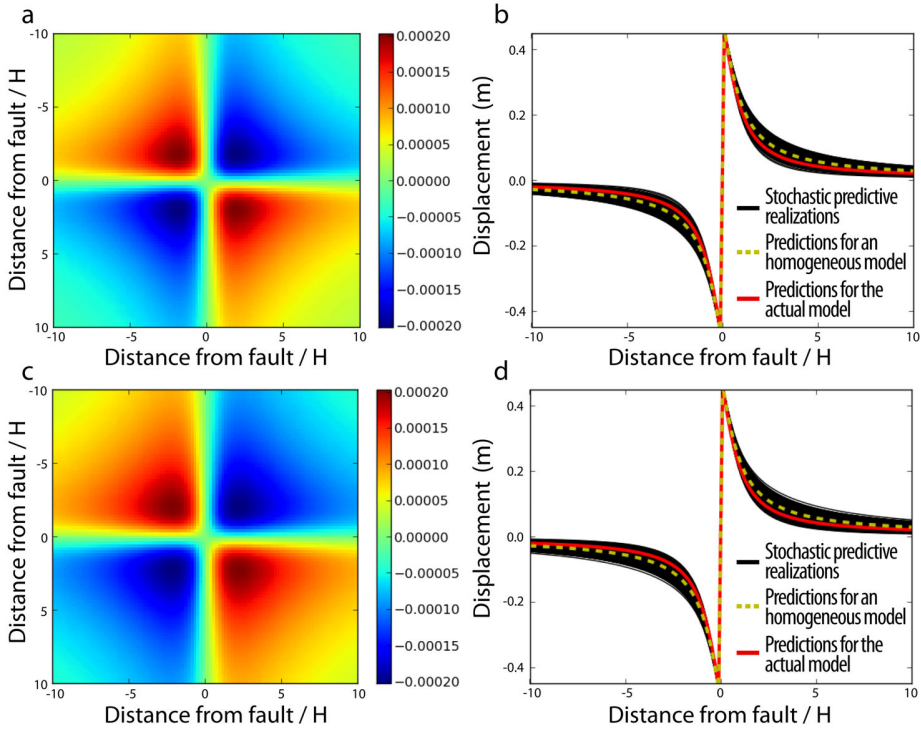


Figure 3. Prediction uncertainty in a 2-D quasi-static case. We assume a simple infinite strike-slip fault with unit slip from the free surface to $0.9H$, where H is the thickness of the shallow layer (*cf.* red line in Fig. 2). Panels (a) and (b) illustrate the prediction uncertainty statistics if we assume a fixed thickness for the shallow layer (*cf.* Figs 2a–b). Panels (c) and (d) present the predictive stochastic model obtained if we consider some uncertainty on the layer thickness (*cf.* Figs 2c–d). For both cases, we present the corresponding prediction covariance matrices in (a) and (c). For each stochastic model, we show 1000 stochastic predictions in (b) and (d) in black assuming a homogeneous half-space. The predicted data for the actual layered earth model is shown in red and the predictions for a homogeneous half-space are shown as yellow dashed lines.

There are several different possibilities to take into account this limited resolution. A first possibility is to increase the size of patches, therefore using a coarse fault discretization. This possibility has already been explored by Pritchard *et al.* (2002) and Barnhart & Lohman (2010) who proposed to use variable patch sizes depending on the resolution scale on the fault. On the other hand, one should assign small patch sizes to enhance the accuracy of the forward modelling in order to minimize parametrization errors due to the assumption of constant slip on elements that produces sharp discontinuities. A better practice is thus to use a discretization smaller than the actual resolution scale and eventually to filter the slip distribution *a posteriori* using a smoothing or averaging length comparable to the resolution scale. Therefore, we prefer here to use 16 fault patches and to account for the model resolution scale using local averaging rather than using coarse discretization. Fig. 4(c) shows marginal distributions of filtered model samples using an arithmetic mean over a sliding window of $N_p = 3$ patches. These results show a Gaussian-like distributions that are well centred around the target slip value (i.e. $\mathbf{m} = 1$ m), which confirms the possibility to resolve slip over three to four patches.

4.3 Comparison of inversion results with and without neglecting the prediction uncertainty

To assess the impact of including \mathbf{C}_p in the estimation process, we compare inversion results with and without neglecting the prediction uncertainty. We assume a non-uniform target slip distribution from 0 to $0.9H$ presented in Fig. 6(a). We compute the data for the

layered half-space presented in red in Fig 2(d) and add 5 mm of uncorrelated Gaussian observational noise. The resulting data vector is presented in red in Figs 6(d)–(f). Once again, the source inversion is performed assuming a homogeneous half-space. We therefore include the two classes of errors discussed in Section 2—errors on the measurements and in the predictions. As described before, we use a simple uniform prior $p(\mathbf{m}) = \mathcal{U}(-0.3, 20)^M$ on the slip distribution, a fault discretized into 16 patches, and a smoothing window over three patches. The measurement covariance matrix \mathbf{C}_d is diagonal with standard deviation of 5 mm. For the calculation of \mathbf{C}_p , we consider the first layer thickness as uncertain (i.e. \mathbf{C}_{μ} in Fig. 2c) and use a prediction covariance structure similar to the one presented in Fig. 2.

The comparison of the posterior model distribution mean with and without neglecting the prediction uncertainty are shown, respectively, on Figs 6(b) and (c). The corresponding 1-D and 2-D marginal posterior PDFs for each fault patch are also presented in Fig. 7 [each $p(m_i|\mathbf{d}_{\text{obs}})$] and Fig. 8 [each $p(m_i, m_j|\mathbf{d}_{\text{obs}})$] based on nearly 700 000 samples of the slip vector \mathbf{m} . We note significant discrepancies in the inversion results depending on whether the prediction covariance matrix \mathbf{C}_p is included or ignored. If \mathbf{C}_p is neglected, the mean of the distribution shown in Fig. 6(b) is very different from the target model in Fig. 6(a). Estimated slip values are larger than the target model for depths between 0.2 and $0.4H$ and significantly lower than the target slip value at larger depth. We note also that the uncertainty on the slip distribution is clearly underestimated: the marginal PDFs in Figs 7(a) and 8(lower left) show very narrow peaks at large depth that are clearly shifted with respect to the target slip values. On the other hand, if \mathbf{C}_p is included, we

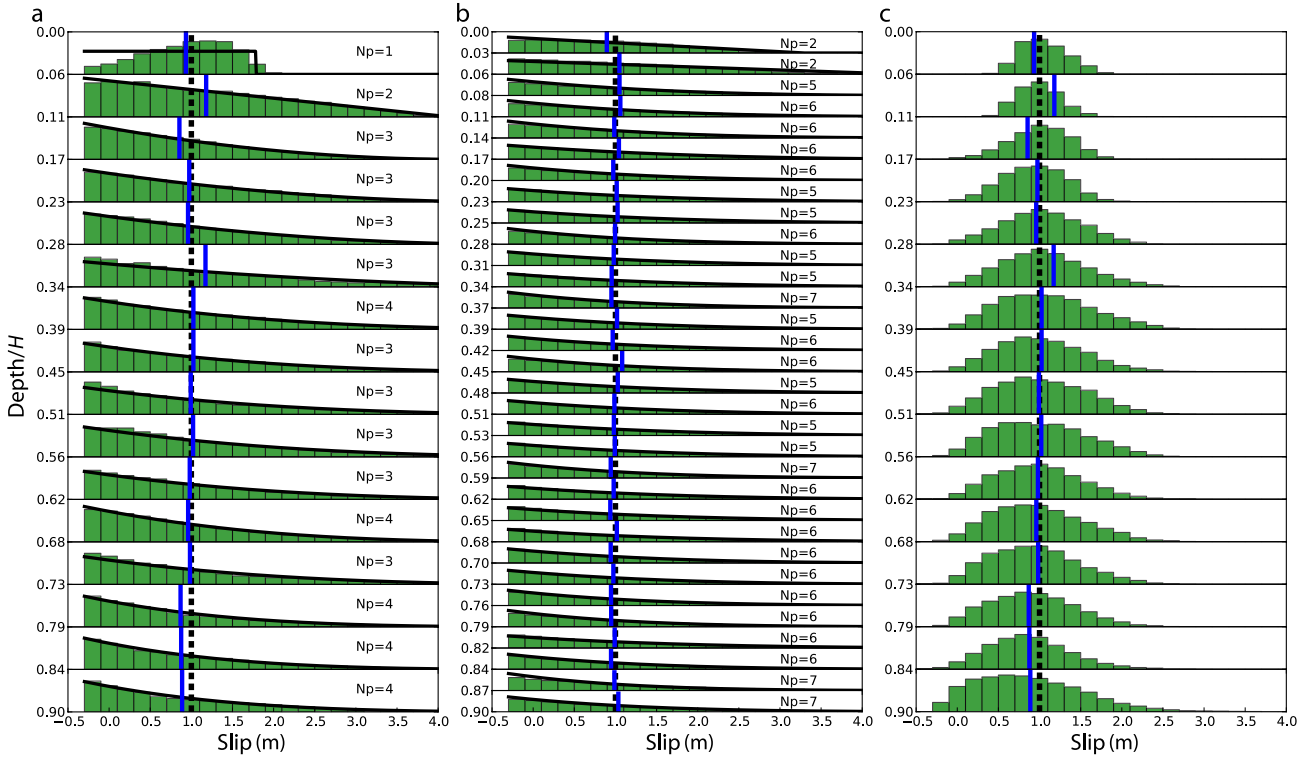


Figure 4. Source estimation for a constant unit slip distribution. Raw marginal PDFs for the slip in each fault patch are shown in (a) if the fault is discretized into 16 patches and in (b) if the fault is discretized into 32 patches. The target slip model is indicated as dashed black lines and the mean of the distribution is shown in blue. The number of parameters N_p of the best-fitting marginal Dirichlet distribution (black curves) is indicated for each patch. The marginal PDFs for 16 patches after using a moving average over three neighbouring patches is shown in (c).

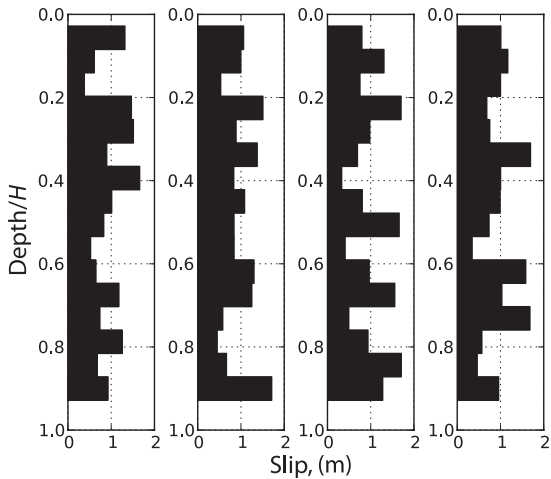


Figure 5. Examples of model samples chosen near the mean of the posterior distribution. The fault from 0 to $0.9H$ is discretized into 16 fault patches. The depicted models are the four samples closest to the mean of the posterior distribution in a CATMIP simulation of 8192 samples.

obtain much broader posterior distributions centred around a mean model that is in agreement with the target slip model. This increase of estimated posterior uncertainty is particularly visible on the 2-D marginal posterior PDFs in Fig. 8. In this figure, we also note a slight correlation between neighbouring patches at large depth (i.e. for patches P 5–P 16), which is certainly related to the averaging of slip on neighbouring patches as described in the previous section.

This correlation among adjacent patches will not affect inversion results as long as the slip distribution is relatively smooth as in Fig. 6(a). It can however be problematic if the target model includes short-scale variations of slip. To explore this possibility, Fig. 9 shows inversion results for a target model including an abrupt drop of 1 m in the slip distribution at depth $0.56H$ (*cf.* dashed black lines). As in the case of the smoother slip model in Fig. 7, the introduction of \mathbf{C}_p significantly improves the posterior model estimates. However, in Fig. 9(b), we note that the mean model (blue lines) is relatively smooth and does not reproduce the slip step at a depth of $0.56H$. The step in slip cannot be recovered because in this example we can only resolve features over a scale corresponding to three neighbouring patches (*cf.* Section 4.2). Consequently, the mean model shows better agreement with the filtered target model shown in white in Fig. 9(b), which corresponds to a three-neighbouring-patches moving average of the initial target model. In any case, note that both raw and filtered target models are within the error bounds defined by the posterior marginal distribution histograms. The two simple models presented here clearly illustrate the importance of using an accurate stochastic model for the prediction uncertainty in order to reliably infer the posterior distribution of source model parameters. Using our formulation for \mathbf{C}_p , we can obtain more realistic estimates of the posterior uncertainty but also improve the slip distribution model.

4.4 Dependence of prediction uncertainty upon the source model

An important finding of this work is the dependence of the prediction error upon the source model parameters \mathbf{m} . Two critical questions

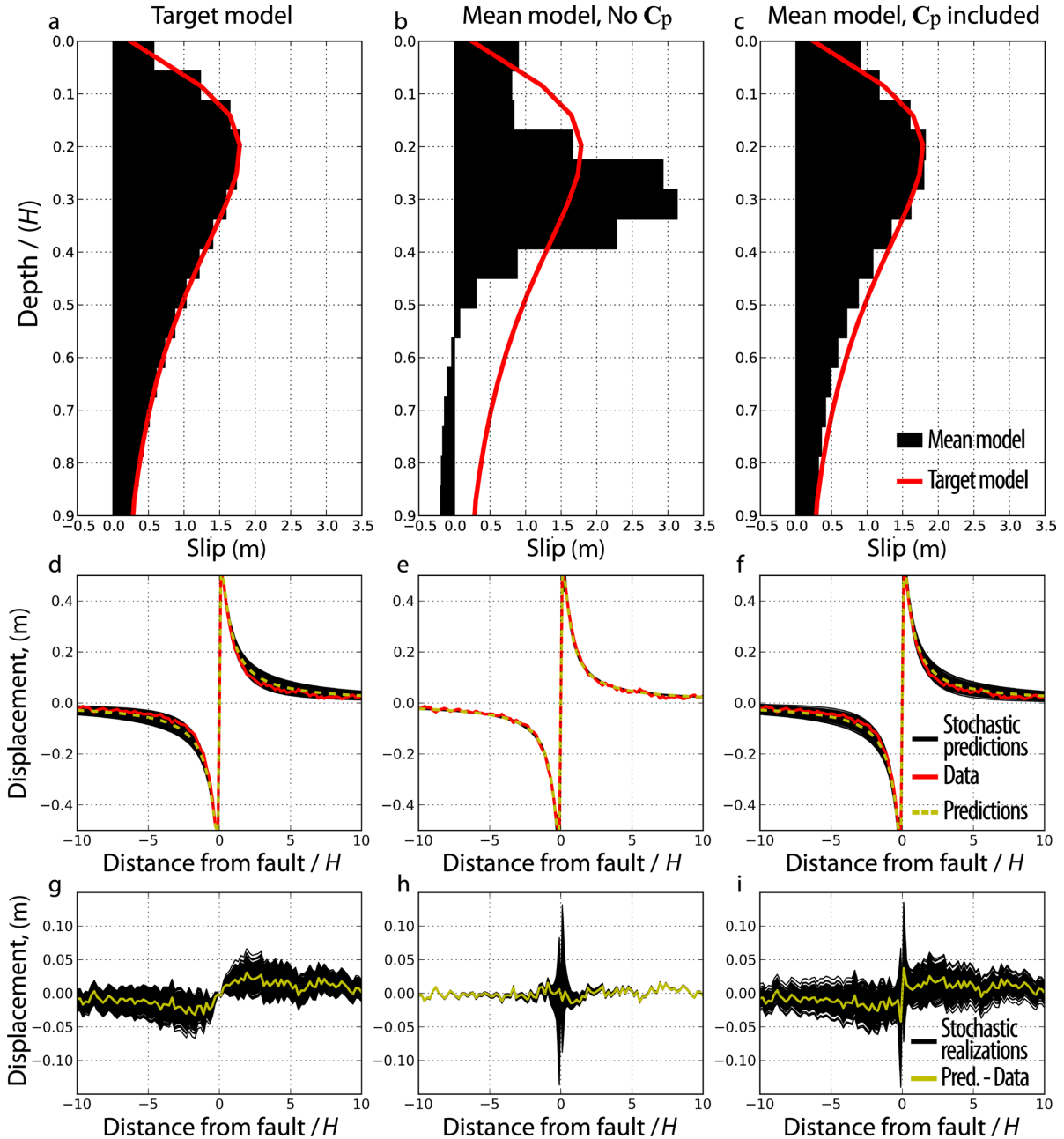


Figure 6. Comparison of inversion results with and without neglecting the prediction uncertainty. Panel (a) is the target slip model. The mean of the posterior distributions are shown in black (b) when the prediction uncertainty is neglected and (c) when C_p is included in the estimation process. The continuous red line corresponds to the target slip model. Comparisons between data and predictions for each model in a homogeneous half-space are shown in (d)–(f). The data are presented in red. The predictions shown in yellow are calculated for each model presented in black in (a)–(c). Black lines correspond to a set of 1000 stochastic realizations drawn from the posterior predictive PDF defined in eq. (27). The residuals between data and predictions are shown in (g)–(i). The yellow line is the difference between the data and the predictions presented, respectively, in red and yellow in (d)–(f). Black lines are the residuals between data and the 1000 stochastic predictions shown in (d)–(f).

need to be addressed. First, how is it possible to account for the coupling between C_p and the source model? Secondly, what is the variation of C_p as a function of \mathbf{m} ?

As discussed in Section 3.3, we propose here to account for the coupling between C_p and \mathbf{m} by updating the covariance at each transitional step (i.e. increase of β in eq. 22) using the mean of the

model distribution. The prediction uncertainty covariance matrix C_p is therefore considered here as a by-product of the inversion. We explored different possibilities to design C_p at $\beta_0 = 0$: (1) calculating C_p from the mean of the distribution (\mathbf{m}) at $\beta_0 = 0$, (2) computing C_p for a uniform unitary slip distribution as a function of depth, (3) calculating C_p from the solution of a prior source

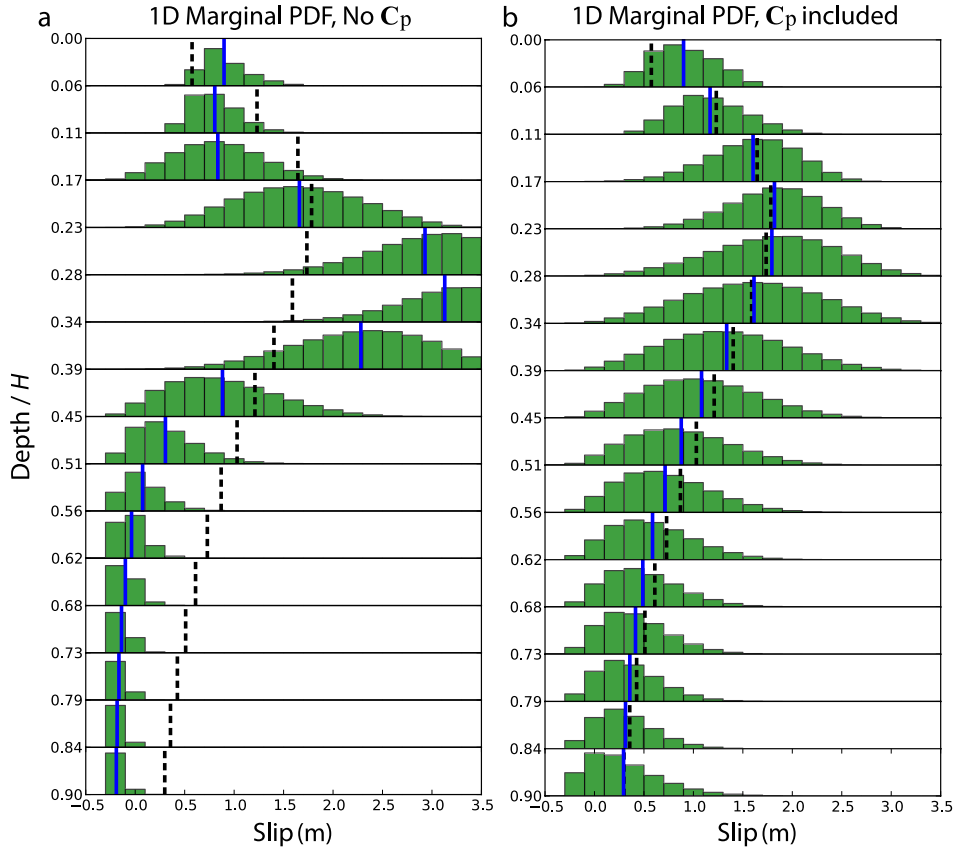


Figure 7. 1-D marginal posterior PDFs for each patch as a function of depth. The marginal probability density histograms are shown in green (a) when the prediction uncertainty is neglected and (b) when the prediction uncertainty is taken into account by including C_p in the inversion problem. The target slip model is indicated as dashed black lines and the mean of the distribution is shown in blue.

inversion in which C_p is neglected and (4) using a preliminary form of C_p whose diagonal elements are proportional to the observations as suggested by Minson *et al.* (2014). Fig. 10 presents the evolution of the prediction covariance in the sampling process using the mean of the distribution $\langle \mathbf{m} \rangle$ at $\beta_0 = 0$ (*cf.* Fig. 11). This evolution of C_p corresponds to the estimation process for the target model presented in Figs 6–8. Similar figures using approaches (2), (3) and (4) are shown in Figs S2–S10. For all four cases, we note that C_p converges properly to the covariance structure estimated from the target model and that the posterior distributions are almost identical. Less transitional steps are however necessary when using a diagonal C_p proportional to the observations at $\beta_0 = 0$ (*cf.* Figs S9 and S10).

The mean models used to compute C_p are presented in Fig. 11. The transitional process is clearly illustrated by the evolution of the model sample mean shown in this figure. The mean models at the first few transitional steps are largely controlled by the prior PDF [*i.e.* uniform probability distribution $p(\mathbf{m}) = \mathcal{U}(-0.3, 20)^M$] and then slowly converge to the target model as more weight is given to the likelihood (*i.e.* as β increases). The corresponding covariance matrix structures do not change significantly at each update although the overall magnitude of C_p is quite different for small and large values of β . Note that an additional sampling step is performed after reaching $\beta = 1$ in order to resample the posterior PDF with a prediction covariance estimated from the sample mean at $\beta_B = 1$. However, only minor differences are visible after the final update of C_p .

5 DISCUSSION

The previous synthetic application clearly illustrates the importance of incorporating inaccuracies of the earth model in the prediction uncertainty in source estimation problems. When neglecting C_p , the posterior mean model shows strong oscillations with a slip distribution that is overestimated between 0.2 and 0.4H and underestimated at larger depth. We observe similar features for a constant unit slip distribution in Fig. S1(b). Note that the negative slip at larger depth is due to the lower bound of the prior distribution $p(\mathbf{m}) = \mathcal{U}(-0.3, 20)^M$ used to obtain these results. Using strictly positive constraints leads to similar slip distributions as shown in Fig. S11. These oscillatory artefacts when C_p is neglected are clearly related to errors in the Green's functions that are calculated for an homogeneous half-space instead of a layered medium. To explain these artefacts, Fig. 12 shows the result of a simple linear least-square inversion without positivity constraints (*i.e.* a purely Gaussian case without prior information). In this example, we consider noise-free data but still use incorrect Green's functions (*i.e.* assuming an homogeneous half-space instead of the actual layered half-space with $\mu_2/\mu_1 = 1.4$). As shown in Fig. 12(a), if we assume shallow slip on a fault with large a depth extent, the inferred least-squares solution has strong artefacts at depth due to inaccuracies in the predictions based on a homogeneous elastic half-space. The model including C_p in Fig. 12(b) shows similar artefacts but has error bars indicating that deep slip cannot be resolved given the uncertainty in μ . The inferred slip model is actually identical to

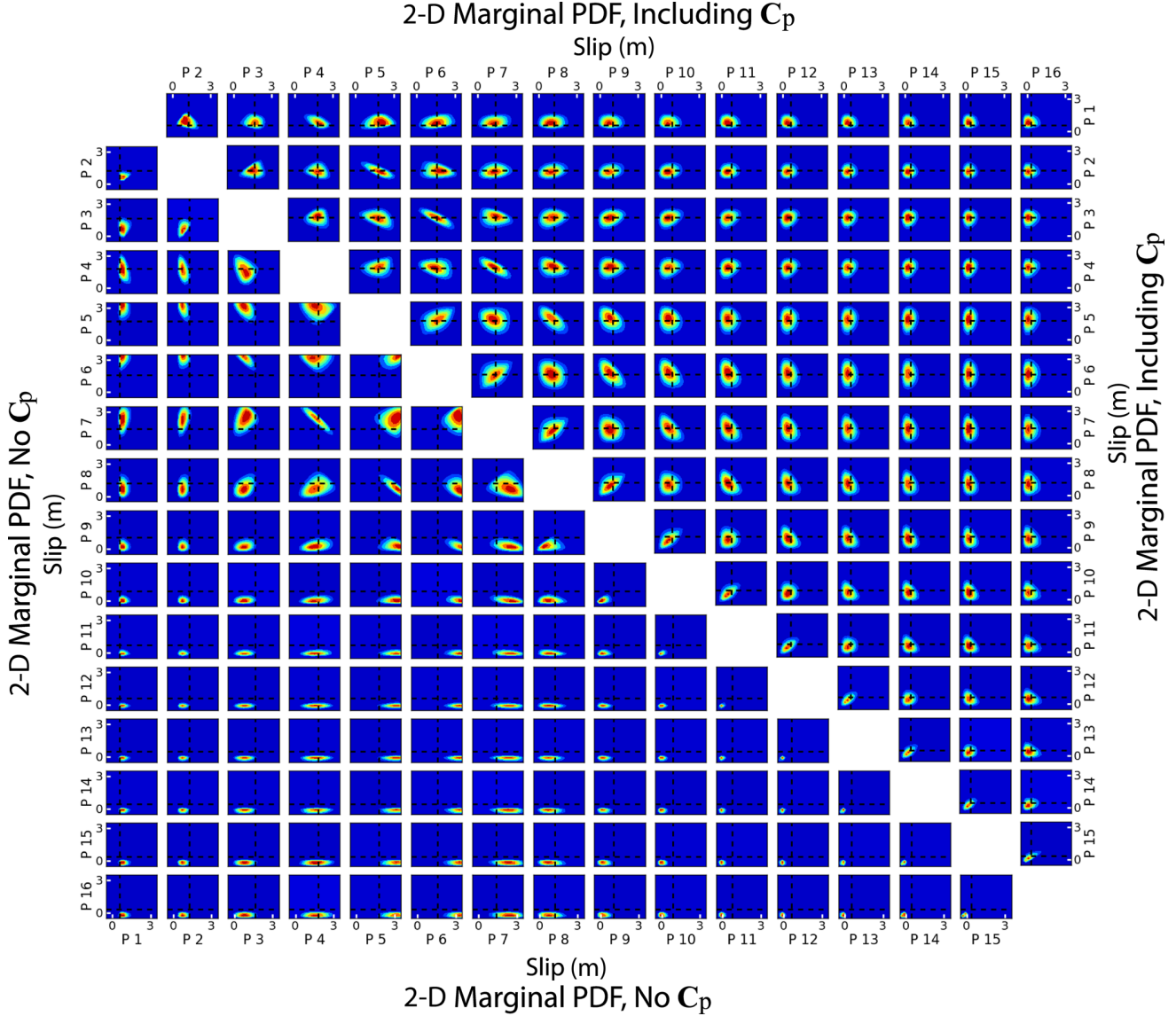


Figure 8. 2-D marginal posterior probability densities for all possible pairs of fault patches. Fault patches are numbered increasingly as a function of depth (e.g. P 16 is the deepest fault patch). The 2-D histograms are shown (bottom left) when C_p is neglected and (top right) when the prediction uncertainty is accounted for. Dashed black lines indicate the target slip value for each fault patch.

the series of dislocations derived by Savage (1987) and presented in Fig. 12(c). This slip distribution produces surface displacements that are exactly identical to the input target slip model in a layered half-space. Of course, in common source inversion practices, faults are parametrized with a limited depth extent and the prediction error cannot be perfectly mapped in the distribution of slip. Fig. 13 illustrates such case with a constant target slip model discretized in four slices down to $0.9H$. We note strong oscillations when C_p is neglected. Although there is no obvious analytical solution such as Savage (1987) in this case, these oscillations are clearly due to inaccuracies of half-space predictions since this is the only source of uncertainty considered here. On the other hand, the model including C_p is able to properly resolve the input target model since error in the Green's function cannot be perfectly reproduced by slip oscillations.

To get more insight on the improvement of inversion results using our formulation of C_p , we propose here to estimate the posterior

prediction uncertainty for the simple model presented in Fig. 6. To do so, we calculate the posterior predictive distribution $p(\mathbf{d}|\mathbf{d}_{\text{obs}})$ using the stochastic forward model $p(\mathbf{d}|\mathbf{m})$ in eq. (4) and the posterior model distribution $p(\mathbf{m}|\mathbf{d}_{\text{obs}})$ in eq. (8):

$$p(\mathbf{d}|\mathbf{d}_{\text{obs}}) = \int_{\mathcal{M}} p(\mathbf{d}|\mathbf{m}) p(\mathbf{m}|\mathbf{d}_{\text{obs}}) d\mathbf{m}. \quad (27)$$

This equation can be obtained directly from the total probability theorem (e.g. Bishop 2006) and describes the posterior variability on the predictions \mathbf{d} due to modelling error [i.e. $p(\mathbf{d}|\mathbf{m})$] and posterior uncertainty on the slip distribution [i.e. $p(\mathbf{m}|\mathbf{d}_{\text{obs}})$]. The PDF $p(\mathbf{d}|\mathbf{d}_{\text{obs}})$ can also be seen as the posterior information on the displacement field. This posterior predictive PDF is illustrated in black in Figs 6(e)–(f) by showing 1000 stochastic realizations drawn from $p(\mathbf{d}|\mathbf{d}_{\text{obs}})$. In Figs 6(h)–(i), we show the corresponding residuals after subtracting the data vector from each predictive realization. For comparison, Figs 6(d) and (g) also show the posterior predictive

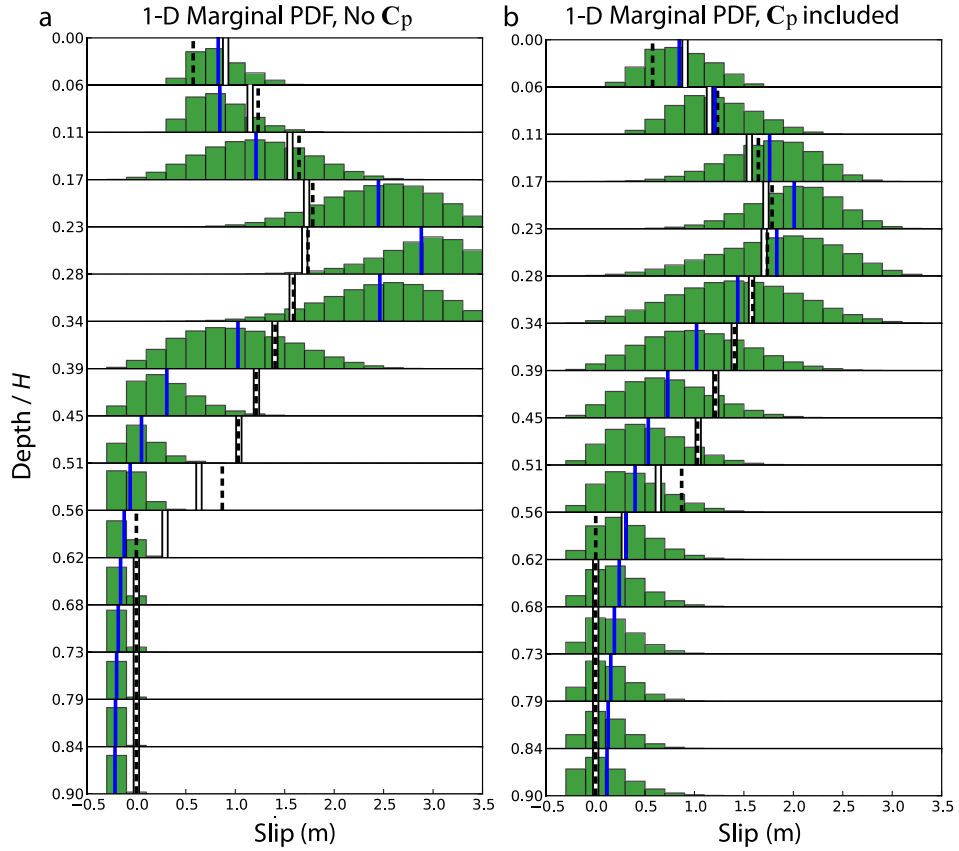


Figure 9. 1-D marginal posterior PDFs for a target model including a slip step of 1 m at $0.56H$. The marginal probability density histograms are shown in green (a) when the prediction uncertainty is neglected and (b) when the prediction uncertainty is taken into account by including C_p in the inversion problem. The mean of the posterior model distribution is shown in blue. The raw target slip model is indicated as dashed black lines and the locally averaged target slip model using a moving window over three adjacent patches is shown in white.

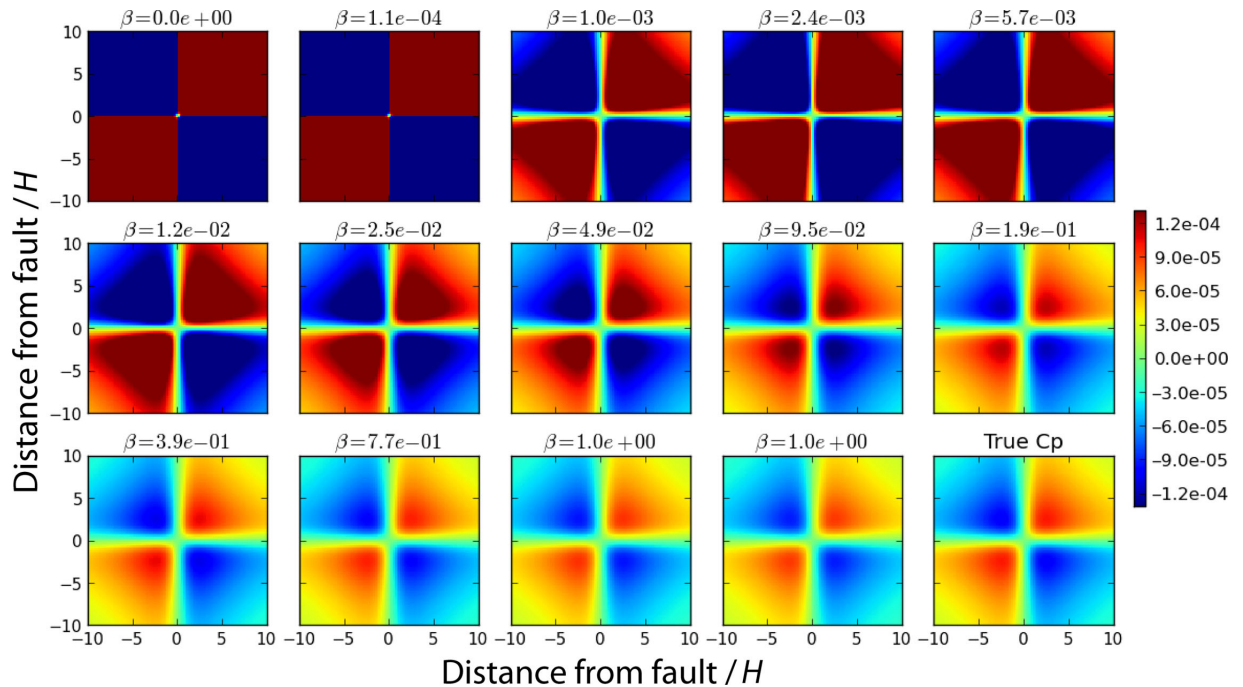


Figure 10. Evolution of the prediction covariance C_p at each transitional step. The values of β in eq. (22) are specified on top of each subfigure.

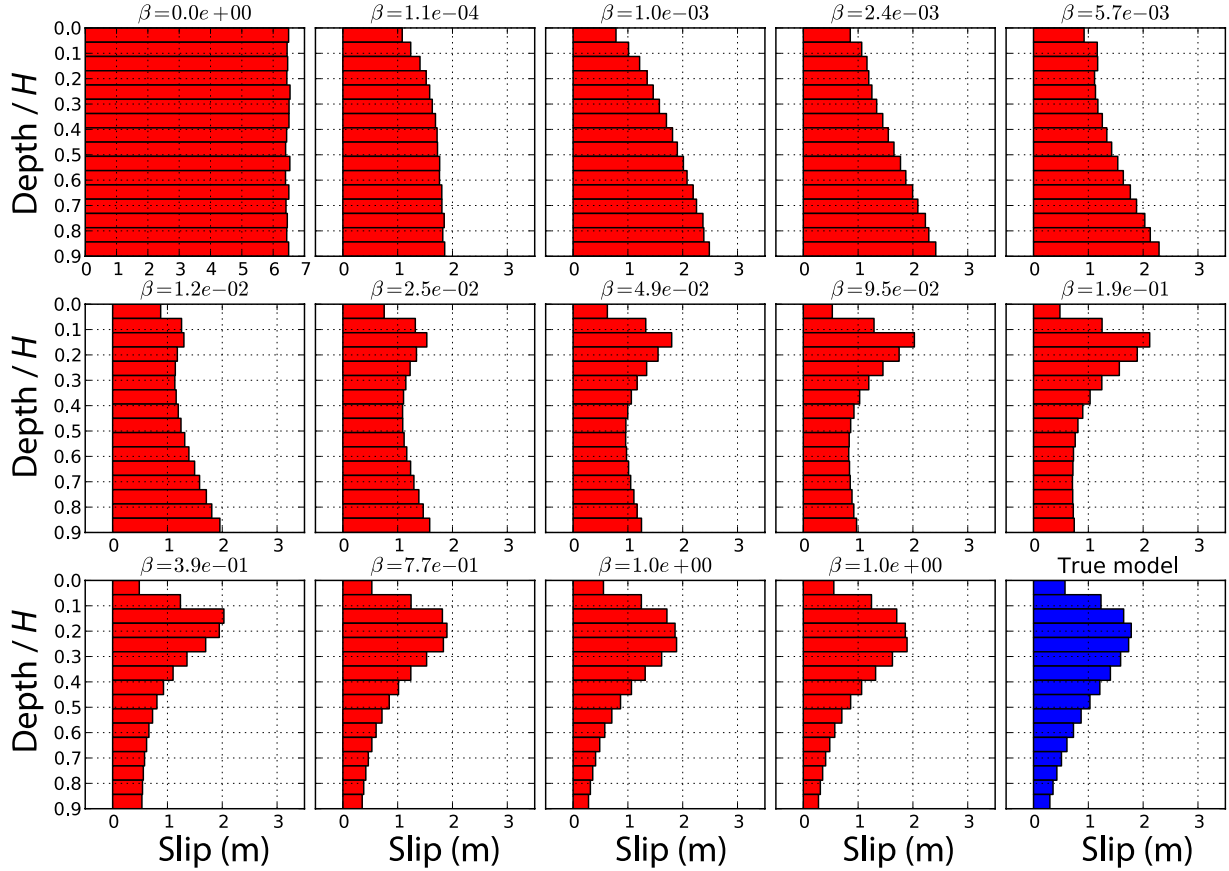


Figure 11. Slip models used for the calculation of the prediction covariance matrix \mathbf{C}_p . These slip models correspond to the mean of the model sample distributions at each transitional step. The values of β in eq. (22) are specified on top of each subfigures.

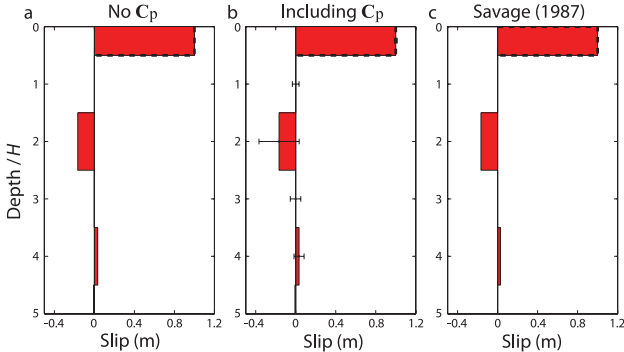


Figure 12. An illustration of the effects of prediction uncertainty on inversion results for an extend fault at depth. The target slip model, indicated as dashed black lines, is used to generate noise-free data in a layered half-space. Simple least-square inversion results for an extended fault in a homogeneous half-space are presented in (a) when \mathbf{C}_p is neglected and (b) when \mathbf{C}_p is included in the inversion. The calculation of \mathbf{C}_p used in (b) is based on the maximum *a posteriori* (MAP) slip model shown in (a). These two MAP models are very similar to the theoretically derived half-space equivalent slip distribution by Savage (1987) presented in (c).

PDF for the target slip model, assuming no uncertainty on the slip distribution (i.e. $p(\mathbf{m}|\mathbf{d}_{\text{obs}}) = \delta(\mathbf{m} - \mathbf{m}_{\text{true}})$ where \mathbf{m}_{true} is the target model). Figs 6(e) and (h) show the data fit if the prediction uncertainty is neglected [i.e. $p(\mathbf{d}|\mathbf{m}) = \delta(\mathbf{d} - \mathbf{g}(\mathbf{m}))$, where $\mathbf{g}(\mathbf{m})$ are the predictions for a homogeneous half-space]. In Figs 6(f) and (i), we

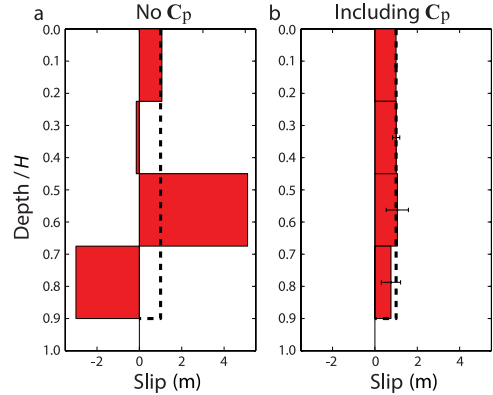


Figure 13. An illustration of the importance of the prediction covariance \mathbf{C}_p . The target slip model, indicated as dashed black lines, is used to generate noise-free data in a layered half-space. Simple least-square inversion results for an extended fault in a homogeneous half-space are presented in (a) when \mathbf{C}_p is neglected and (b) when \mathbf{C}_p is included in the inversion. The calculation of \mathbf{C}_p used in (b) is based on the maximum *a posteriori* slip model shown in (a).

use the stochastic forward model based on \mathbf{C}_p for the same $\mathbf{g}(\mathbf{m})$ (i.e. $p(\mathbf{d}|\mathbf{m}) = \mathcal{N}[\mathbf{d}|\mathbf{g}(\mathbf{m}), \mathbf{C}_p]$). The posterior predictive uncertainty is significantly larger if \mathbf{C}_p is taken into account. Even if the posterior variability of the source model is incorporated when \mathbf{C}_p is neglected, we note that the posterior predictive uncertainty is negligible

compared to the variability when \mathbf{C}_p is included. Moreover, when comparing data with predictions for a homogeneous half-space, the data misfit is clearly smaller if the prediction uncertainty is neglected. This small data residual is due to data overfitting resulting from the use of a deterministic forward model. By neglecting \mathbf{C}_p , too much information is conferred to imperfect forward predictions, leading to spurious posterior distributions which favour source models that closely explain observations. The differences between inversion results in Fig. 6(b) and the target model in Fig. 6(a) are thus certainly due to overfitting of observations using predictions for an inaccurate earth model (i.e. a homogeneous half-space instead of a layered medium). On the other hand, using a stochastic forward problem, we gain an extra flexibility by allowing some variability in the predictions, which allows us to select models having larger and correlated data residuals. Thus, the impact of including the prediction covariance \mathbf{C}_p is not just a better analysis of the posterior uncertainty. In fact, the use of \mathbf{C}_p also improves source parameter estimates by using physically based relative weights between measurements and by preventing overfitting of observations.

In this study, we have mainly focused on the impact of inaccuracies in the earth model, which significantly contribute to forward modelling errors. We recognize, however, that other contributors can have profound impact on the predictions. In particular, we know that approximation of the true source geometry by a fault surface $\tilde{\phi}$ based on prior information can be a major source of uncertainty in source estimation problems. A judicious approach is to incorporate ϕ into the source model parameters \mathbf{m} for which the data are inverted. However, this approach may be difficult to implement in practice since we would have to recalculate the Green's functions for each explored model, a computationally challenging prospect. Alternatively, if the imperfect fault surface is not grossly wrong, we can use our formulation of \mathbf{C}_p in order to account for the uncertainty in the fault geometry. One possibility is to design a \mathbf{C}_Ω that incorporates a high variability of elastic properties in a narrow zone around the fault. Another approach is to take into account a variability of ϕ in the inversion problem. The latter possibility is formulated in the following.

Let us define a parameter $\Psi = [\ln \Omega^T, \phi^T]^T$ incorporating all information about the earth model Ω and fault surface ϕ (which are assumed independent). As in Section 3.1, we assume that predictions $\mathbf{g}(\Psi, \mathbf{m})$ are modelled as first-order perturbations of our predictions $\mathbf{g}(\tilde{\Psi}, \mathbf{m})$. In this case, the prediction covariance can be written as

$$\mathbf{C}_p = \mathbf{K}_\Omega \cdot \mathbf{C}_\Omega \cdot \mathbf{K}_\Omega^T + \mathbf{K}_\phi \cdot \mathbf{C}_\phi \cdot \mathbf{K}_\phi^T. \quad (28)$$

The prediction uncertainty due to the fault geometry can therefore be included by augmenting the prediction covariance matrix with a new term $\mathbf{K}_\phi \cdot \mathbf{C}_\phi \cdot \mathbf{K}_\phi^T$, where \mathbf{C}_ϕ is the covariance matrix on fault geometry parameters and $\mathbf{K}_\phi(\tilde{\Psi}, \mathbf{m})$ is the corresponding sensitivity kernel

$$(\mathbf{K}_\phi)_{ij}(\tilde{\Psi}, \mathbf{m}) = \frac{\partial g_i}{\partial \phi_j}(\tilde{\Psi}, \mathbf{m}). \quad (29)$$

In this equation, the vector ϕ can, for example, include averages of dip and strike values over the entire (or portions of) the fault. This approach can be extended to other sources of modelling uncertainty and we should be able to define a gallery of prediction covariance matrices to be included in the source inversion problem. However, this formulation is not appropriate if prediction uncertainties are too large since there will be no simple relationship between the corresponding predictions $\mathbf{g}(\tilde{\Psi}, \mathbf{m})$ and $\mathbf{g}(\Psi, \mathbf{m})$. In such situations, the results of our inversion would be unreliable and more efforts

should be spent to improve forward modelling capabilities. The ultimate goal would be to allow for updating the uncertainty in all model parameters (i.e. \mathbf{m}, Ω, ϕ) by sampling from their posterior PDF but this requires greatly increasing the computational speed for the forward modelling, either by computer hardware and/or faster algorithms (e.g. building surrogate (meta-) models of the forward model using machine learning methods; Bishop 2006).

6 CONCLUSION

This study improves the modelling of the misfit covariance matrix as used in inversions for the distribution of slip on subsurface faults. The misfit covariance, \mathbf{C}_x , is a combination of the observational covariance matrix, \mathbf{C}_d , and the modelling covariance matrix, \mathbf{C}_p . The latter class of uncertainty is often entirely ignored even though prediction errors scale with the size of earthquakes and are thus generally larger than the observation uncertainty for large events. Furthermore, prediction errors can induce important correlation between the observation points that should be taken into account in source inversion problems. This work provides a general formalism to explicitly quantify the impact of uncertainties in our forward models and to account for such prediction error in source estimation problems. In particular, we describe a physically based stochastic model for the prediction uncertainty that allows for inaccuracies in the earth model by using sensitivity of the data predictions to first-order perturbations of elastic properties. Moreover, to account for the dependence of the prediction error upon the source model parameters \mathbf{m} , the covariance matrix \mathbf{C}_p is updated as the model evolves in the source inversion process. We also discuss the possibility to account for other sources of uncertainty such as imperfections in the fault geometry.

For a simple 2-D synthetic data inversion, we demonstrated the importance and feasibility of implementing \mathbf{C}_p in source inversion problems. The results indicate two main advantages of using an improved covariance matrix structure. First, it improves the posterior error description for the source model parameters. Secondly, it improves the source model characterization itself notably because using a more structured covariance matrix prevents overfitting of the observations. Although our implementation is based on a Bayesian formulation of the inversion problem, it should be noted that incorporating \mathbf{C}_p can be beneficial regardless of the particular inversion approach used. Indeed, the prediction covariance matrix offers a natural way to specify the relative information content found in different observations. Furthermore, if different data types are used, \mathbf{C}_p provides a physical basis for the relative weighting between disparate data sets.

The advances proposed here can thus enable production of the next generation of source models that are more resistant to overfitting of data, provide a physical basis for the relative weighting between disparate data sets, and include more realistic description of uncertainty in the inferred source model parameters. These improvements in the model prediction uncertainty require developing computationally tractable approaches to estimate the sensitivity of the predicted geodetic and seismic observations of large earthquakes to perturbations in material properties assumed in any given earth model. Much of the underlying theory and many of the tools already exist in the domain of seismic tomography and could thus be exploited to obtain more reliable images of the earthquake rupture phenomena. While this work is motivated by specific goals related to the study of large earthquakes, these techniques can also be applied to a broad range of inverse problems in geophysics and

earthquake engineering such as volcano monitoring and earthquake early warning.

ACKNOWLEDGEMENTS

We thank Bernard Valette and Yukitoshi Fukahata for their helpful reviews. We have benefited from discussions with Jean-Paul Ampuero, Jean Virieux, Romain Brossier, Victor Tsai, Romain Jolivet and Luis Rivera. MS acknowledges sabbatical support from the Univ. Joseph Fourier (Grenoble, France) during which this project started. PSA was supported by the Keck Institute of Space Studies Postdoctoral Fellowship. Our Bayesian sampling algorithm is based on the ALTAR implementation of CATMIP developed by Michael Aivasis and Hailiang Zhang. This work made use of the Matplotlib python library created by John D. Hunter. P. Agram was supported by the Keck Institute of Space Studies Postdoctoral Fellowship. This research was supported by the Southern California Earthquake Center. SCEC is funded by NSF Cooperative Agreement EAR-0529922 and USGS Cooperative Agreement 07HQAG0008. The SCEC contribution number for this paper is 1791. This work was partially supported by the National Science Foundation under Grant No. EAR-0941374.

REFERENCES

- Aki, K. & Richards, P., 2002. *Quantitative Seismology*, Freeman.
- Barnhart, W.D. & Lohman, R.B., 2010. Automated fault model discretization for inversions for coseismic slip distributions, *J. geophys. Res.*, **115**(B10), B10419, doi:10.1029/2010JB007545.
- Bayes, M., 1763. An essay towards solving a problem in the doctrine of chances by the late Rev. Mr. Bayes, F.R.S. communicated by Mr. Price, in a letter to John Canton, A.M.F.R.S., *Phil. Trans. R. Soc.*, **53**, 370–418.
- Beck, J.L. & Au, S.K., 2002. Bayesian updating of structural models and reliability using Markov chain Monte Carlo simulation, *J. Eng. Mech.*, **128**, 380–391.
- Beck, J.L. & Zuev, K.M., 2013. Asymptotically independent Markov sampling: a new Markov chain Monte Carlo scheme for Bayesian inference, *Int. J. Uncertainty Quantification*, **3**(5), 445–474.
- Bishop, C.M., 2006. *Pattern Recognition and Machine Learning*, Information Science and Statistics, Springer.
- Bonnet, M. & Constantinescu, A., 2005. Inverse problems in elasticity, *Inverse Probl.*, **21**(2), R1–R50.
- Bouchon, M., Toksoz, N.N., Karabulut, H., Bouin, M.-P., Dietrich, M., Aktar, M. & Edie, M., 2002. Space and time evolution of rupture and faulting during the 1999 Izmit (Turkey) earthquake, *Bull. seism. Soc. Am.*, **92**(1), 256–266.
- Cervelli, P., Segall, P., Amelung, F., Garbeil, H., Meertens, C., Owen, S., Miklius, A. & Lisowski, M., 2002. The 12 September 1999 Upper East Rift Zone dike intrusion at Kilauea Volcano, Hawaii, *J. geophys. Res.*, **107**(B7), ECV3 1–13.
- Ching, J. & Chen, Y.C., 2007. Transitional Markov chain Monte Carlo method for Bayesian model updating, model class selection, and model averaging, *J. Eng. Mech.*, **133**, 816–832.
- Dahlen, F.A. & Baig, A.M., 2002. Fréchet kernels for body-wave amplitudes, *Geophys. J. Int.*, **150**(2), 440–466.
- Dahlen, F.A. & Tromp, J., 1998. *Theoretical Global Seismology*, Princeton Univ. Press.
- Delouis, B., Lundgren, P., Salichon, J. & Giardini, D., 2000. Joint inversion of InSAR and teleseismic data for the slip history of the 1999 Izmit (Turkey) earthquake, *Geophys. Res. Lett.*, **27**(20), 3389–3392.
- Delouis, B., Giardini, D., Lundgren, P. & Salichon, J., 2002. Joint inversion of InSAR, GPS, teleseismic, and strong-motion data for the spatial and temporal distribution of earthquake slip: application to the 1999 Izmit mainshock, *Bull. seism. Soc. Am.*, **92**, 278–299.
- Du, Y., Segall, P. & Gao, H., 1994. Dislocations in inhomogeneous media via a moduli perturbation approach: general formulation and two-dimensional solutions, *J. geophys. Res.*, **99**(B7), 13 767–13 779.
- Duputel, Z., Rivera, L., Fukahata, Y. & Kanamori, H., 2012a. Uncertainty estimations for seismic source inversions, *Geophys. J. Int.*, **190**(2), 1243–1256.
- Duputel, Z., Rivera, L., Kanamori, H. & Hayes, G., 2012b. W phase source inversion for moderate to large earthquakes (1990–2010), *Geophys. J. Int.*, **189**(2), 1125–1147.
- Fukahata, Y. & Wright, T.J., 2008. A non-linear geodetic data inversion using ABIC for slip distribution on a fault with an unknown dip angle, *Geophys. J. Int.*, **173**(2), 353–364.
- Hartzell, S.H. & Heaton, T.H., 1983. Inversion of strong ground motion and teleseismic waveform data for the fault rupture history of the 1979 Imperial Valley, California, earthquake, *Bull. seism. Soc. Am.*, **73**(6), 1553–1583.
- Hernandez, B., Cotton, F. & Campillo, M., 1999. Contribution of radar interferometry to a two-step inversion of the kinematic process of the 1992 Landers earthquake, *J. geophys. Res.*, **104**(B6), 13 083–13 099.
- Hjörleifsdóttir, V. & Ekström, G., 2010. Effects of three-dimensional Earth structure on CMT earthquake parameters, *Phys. Earth planet. Inter.*, **179**, 178–190.
- Jaynes, E.T., 1983. *Papers on Probability, Statistics, and Statistical Physics*, Springer.
- Jaynes, E.T., 2003. *Probability Theory: The Logic of Science*, Cambridge Univ. Press.
- Ji, C., Wald, D.J. & Helmberger, D.V., 2002. Source description of the 1999 Hector Mine, California, earthquake, part I: wavelet domain inversion theory and resolution analysis, *Bull. seism. Soc. Am.*, **92**(4), 1192–1207.
- Kanamori, H. & Rivera, L., 2006. Energy partitioning during an earthquake, in *Radiated Energy and the Physics of Faulting*, Geophys. Monograph Series, pp. 3–13, American Geophysical Union.
- King, G., 2007. Earthquake seismology: 4.08—fault interaction, earthquake stress changes, and the evolution of seismicity, in *Treatise on Geophysics*, pp. 225–255, Elsevier.
- Komatitsch, D. & Villette, J.-P., 1998. The spectral element method: an efficient tool to simulate the seismic response of 2D and 3D geological structures, *Bull. seism. Soc. Am.*, **88**, 368–392.
- Lohman, R.B. & Simons, M., 2005. Some thoughts on the use of InSAR data to constrain models of surface deformation: noise structure and data downsampling, *Geochem. Geophys. Geosyst.*, **6**(1), Q01007, doi:10.1029/2004GC000841.
- Love, A.H.E., 1906. *A Treatise on the Mathematical Theory of Elasticity*, 2nd edn, Cambridge Univ. Press.
- Mai, M., 2012. Source inversion validation (SIV): current results & developments, in *Proceedings of the 2012 SCEC Source Inversion Validation Workshop*, Hilton Palm Springs Resort.
- Marquering, H., Nolet, G. & Dahlen, F.A., 1998. Three-dimensional waveform sensitivity kernels, *Geophys. J. R. astr. Soc.*, **132**(3), 521–534.
- Minson, S.E., Simons, M. & Beck, J.L., 2013. Bayesian inversion for finite fault earthquake source models I—theory and algorithm, *Geophys. J. Int.*, **194**(3), 1701–1726.
- Minson, S.E., Simons, M., Beck, J.L., Ortega, F., Jiang, J. & Owen, S.E., 2014. Bayesian inversion for finite fault earthquake source models II—The 2011 great Tohoku-oki, Japan earthquake, *Geophys. J. Int.*, submitted.
- Okada, Y., Kasahara, K., Hori, S. & Obara, K., 2004. Recent progress of seismic observation networks in Japan-Hi-net, F-net, K-NET and KiK-net, *Earth Planets Space*, **56**, 15–28.
- Pritchard, M.E., Simons, M., Rosen, P.A., Hensley, S. & Webb, F.H., 2002. Co-seismic slip from the 1995 July 30 Mw= 8.1 Antofagasta, Chile, earthquake as constrained by InSAR and GPS observations, *Geophys. J. Int.*, **150**(2), 362–376.
- Pritchard, M.E., Norabuena, E.O., Ji, C., Boroschek, R., Comte, D., Simons, M., Dixon, T.H. & Rosen, P.A., 2007. Geodetic, teleseismic, and strong motion constraints on slip from recent southern Peru subduction zone earthquakes, *J. geophys. Res.*, **112**(B3), B03307, doi:10.1029/2006JB004294.
- Rice, J.R. & Cocco, M., 2007. Seismic fault rheology and earthquake dynamics, in *Tectonic Faults: Agents of Change on a Dynamic Earth (Dahlem Workshop Reports)*, pp. 99–137, MIT Press.
- Savage, J.C., 1987. Effect of crustal layering upon dislocation modeling, *J. geophys. Res.*, **92**(B10), 10 595–10 600.

- Segall, P., 2010. *Earthquake and Volcano Deformation*, Princeton Univ. Press.
- Sekiguchi, H. & Iwata, T., 2002. Rupture process of the 1999 Kocaeli, Turkey, earthquake estimated from strong-motion waveforms, *Bull. seism. Soc. Am.*, **92**(1), 300–311.
- Simons, M. & Rosen, P.A., 2007. Interferometric synthetic aperture radar geodesy, in *Treatise on Geophysics*, pp. 391–446, Elsevier.
- Simons, M. *et al.*, 2011. The 2011 magnitude 9.0 Tohoku-Oki earthquake: mosaicking the megathrust from seconds to centuries, *Science*, **332**(6036), 1421–1425.
- Talagrand, O. & Courtier, P., 2007. Variational assimilation of meteorological observations with the adjoint vorticity equation. I: theory, *Q. J. R. Meteorol. Soc.*, **113**(478), 1311–1328.
- Tarantola, A., 1984. Inversion of seismic reflection data in the acoustic approximation, *Geophysics*, **49**(8), 1259–1266.
- Tarantola, A., 1988. Theoretical background for the inversion of seismic waveforms including elasticity and attenuation, *Pure appl. geophys.*, **128**(1–2), 365–399.
- Tarantola, A., 2005. *Inverse Problem Theory and Methods for Model Parameter Estimation*, SIAM.
- Tarantola, A. & Valette, B., 1982. Inverse problems = quest for information, *J. Geophys.*, **50**, 159–170.
- Tromp, J., Tape, C. & Liu, Q., 2005. Seismic tomography, adjoint methods, time reversal and banana-doughnut kernels, *Geophys. J. Int.*, **160**(1), 195–216.
- Virieux, J. & Operto, S., 2009. An overview of full-waveform inversion in exploration geophysics, *Geophysics*, **74**, WCC1–WCC26.
- Wald, D.J. & Heaton, T.H., 1994. Spatial and temporal distribution of slip for the 1992 Landers, California, earthquake, *Bull. seism. Soc. Am.*, **84**, 668–691.
- Williams, C.A., Aagaard, B. & Knepley, M.G., 2005. Development of software for studying earthquakes across multiple spatial and temporal scales by coupling quasi-static and dynamic simulations, *EOS, Trans. Am. geophys. Un.*, **86**, AGU abstract #S53A–1072.
- Yabuki, T. & Matsuzura, M., 1992. Geodetic data inversion using a Bayesian information criterion for spatial distribution of fault slip, *Geophys. J. Int.*, **109**, 363–375.
- Yagi, Y. & Fukahata, Y., 2011. Introduction of uncertainty of Green's function into waveform inversion for seismic source processes, *Geophys. J. Int.*, **186**(2), 711–720.
- Yagi, Y. & Kikuchi, M., 2000. Source rupture process of the Kocaeli, Turkey, earthquake of August 17, 1999, obtained by joint inversion of near-field data and teleseismic data, *Geophys. Res. Lett.*, **27**(13), 1969–1972.
- Yu, S.-B., Chen, H.-Y. & Kuo, L.-C., 1997. Velocity field of GPS stations in the Taiwan area, *Tectonophysics*, **274**, 41–59.

APPENDIX A: POSTERIOR PROBABILITY DENSITY FUNCTION (PDF) UNDER THE ASSUMPTION OF GAUSSIAN UNCERTAINTIES

Under the Gaussian assumption, we demonstrate that the posterior PDF is given by eq. (8) of the main text. We essentially follow the demonstration originally given by Tarantola & Valette (1982) in the more general case when C_p depends on \mathbf{m} . If $p(\mathbf{d}^*|\mathbf{d})$ and $p(\mathbf{d}|\mathbf{m})$ are assumed to be Gaussian PDFs as in eqs (2) and (4), the integrated likelihood in eq. (7) is proportional to the convolution between two Gaussians:

$$\begin{aligned} p(\mathbf{d}_{\text{obs}}|\mathbf{m}) = \nu(\mathbf{m}) \int_{\mathcal{D}_{\text{pred}}} \exp \left(-\frac{1}{2} \left\{ (\mathbf{d}_{\text{obs}} - \mathbf{d})^T \mathbf{C}_d^{-1} (\mathbf{d}_{\text{obs}} - \mathbf{d}) \right. \right. \\ \left. \left. + [\mathbf{d} - \mathbf{g}(\tilde{\Omega}, \mathbf{m})]^T \mathbf{C}_p(\mathbf{m})^{-1} [\mathbf{d} - \mathbf{g}(\tilde{\Omega}, \mathbf{m})] \right\} \right) d\mathbf{d}, \end{aligned} \quad (\text{A1})$$

where $\nu(\mathbf{m})$ is a normalization factor defined as

$$\nu(\mathbf{m}) = (2\pi)^{-N} |\mathbf{C}_d|^{-1/2} |\mathbf{C}_p(\mathbf{m})|^{-1/2}. \quad (\text{A2})$$

Eq. (A1) can be rearranged by separating quadratic terms from the linear terms

$$p(\mathbf{d}_{\text{obs}}|\mathbf{m}) = \nu \int_{\mathcal{D}_{\text{pred}}} \exp \left(-\frac{1}{2} (\mathbf{d}^T \mathbf{A} \mathbf{d} - 2 \mathbf{b}^T \mathbf{d} + c) \right) d\mathbf{d}, \quad (\text{A3})$$

where we define

$$\mathbf{A} = \mathbf{C}_d^{-1} + \mathbf{C}_p(\mathbf{m})^{-1}$$

$$\mathbf{b}^T = \mathbf{d}_{\text{obs}}^T \mathbf{C}_d^{-1} + \mathbf{g}(\tilde{\Omega}, \mathbf{m})^T \mathbf{C}_p(\mathbf{m})^{-1}$$

$$c = \mathbf{d}_{\text{obs}}^T \mathbf{C}_d^{-1} \mathbf{d}_{\text{obs}} + \mathbf{g}(\tilde{\Omega}, \mathbf{m})^T \mathbf{C}_p(\mathbf{m})^{-1} \mathbf{g}(\tilde{\Omega}, \mathbf{m}). \quad (\text{A4})$$

The matrix \mathbf{A} being positive definite, we can then show

$$\begin{aligned} p(\mathbf{d}_{\text{obs}}|\mathbf{m}) = \nu \exp \left(-\frac{1}{2} (c - \mathbf{b}^T \mathbf{A}^{-1} \mathbf{b}) \right) \\ \times \int_{\mathcal{D}_{\text{pred}}} \exp \left(-\frac{1}{2} (\mathbf{d} - \mathbf{A}^{-1} \mathbf{b})^T \mathbf{A} (\mathbf{d} - \mathbf{A}^{-1} \mathbf{b}) \right) d\mathbf{d}. \end{aligned} \quad (\text{A5})$$

The integral of the Gaussian in the right hand side being equal to $\sqrt{(2\pi)^N / |\mathbf{A}|}$, it follows that

$$p(\mathbf{d}_{\text{obs}}|\mathbf{m}) = \eta(\mathbf{m}) \exp \left(-\frac{1}{2} (c - \mathbf{b}^T \mathbf{A}^{-1} \mathbf{b}) \right) \quad (\text{A6})$$

where

$$\eta(\mathbf{m}) = (2\pi)^{-N/2} |\mathbf{C}_d|^{-1/2} |\mathbf{C}_p(\mathbf{m})|^{-1/2} |\mathbf{C}_d^{-1} + \mathbf{C}_p(\mathbf{m})^{-1}|^{-1/2}. \quad (\text{A7})$$

After substituting eqs (A4) into (A6) and using the following identities (Tarantola & Valette 1982)

$$\begin{aligned} [\mathbf{C}_d + \mathbf{C}_p(\mathbf{m})]^{-1} &= \mathbf{C}_d^{-1} - \mathbf{C}_d^{-1} [\mathbf{C}_d^{-1} + \mathbf{C}_p(\mathbf{m})^{-1}]^{-1} \mathbf{C}_d^{-1} \\ &= \mathbf{C}_p(\mathbf{m})^{-1} [\mathbf{C}_d^{-1} + \mathbf{C}_p(\mathbf{m})^{-1}]^{-1} \mathbf{C}_p(\mathbf{m})^{-1} \\ &= \mathbf{C}_p(\mathbf{m})^{-1} [\mathbf{C}_d^{-1} + \mathbf{C}_p(\mathbf{m})^{-1}]^{-1} \mathbf{C}_d^{-1} \end{aligned} \quad (\text{A8})$$

we then obtain

$$\begin{aligned} p(\mathbf{d}_{\text{obs}}|\mathbf{m}) = \eta(\mathbf{m}) \exp \left(-\frac{1}{2} [\mathbf{d}_{\text{obs}} - \mathbf{g}(\tilde{\Omega}, \mathbf{m})]^T \right. \\ \left. \times (\mathbf{C}_d + \mathbf{C}_p(\mathbf{m}))^{-1} [\mathbf{d}_{\text{obs}} - \mathbf{g}(\tilde{\Omega}, \mathbf{m})] \right), \end{aligned} \quad (\text{A9})$$

which demonstrates eq. (8) of Section 2.

APPENDIX B: SENSITIVITY KERNEL \mathbf{K}_μ IN THE QUASI-STATIC CASE FOR GENERAL 3-D PERTURBATIONS

We describe here the formulation of \mathbf{K}_μ for the case of a known source and a set of distributed receivers. We adopt a perturbation approach which has been extensively used in seismic (e.g. Dahlen & Baig 2002; Virieux & Operto 2009) and quasi-static problems (Du *et al.* 1994; Cervelli *et al.* 2002). Assuming that the earth model is characterized by the elastic stiffness tensor c_{ijkl} , for a given source field $f(x)$ and a set of boundary conditions, the predicted displacement field is described by the equation (Love 1906;

Segall 2010)

$$\frac{\partial}{\partial x_j} \left[c_{ijkl}(\mathbf{x}) \frac{\partial u_k}{\partial x_l}(\mathbf{x}) \right] + f_i(\mathbf{x}) = 0, \quad (\text{B1})$$

where the Einstein summation convention applies to repeated subscript indices. Introducing the Green's function $H_{ij}(\mathbf{x}, \mathbf{x}^s)$, the solution of this equation can be written in the integral form

$$u_i(\mathbf{x}) = \int_{V^s} H_{ij}(\mathbf{x}, \mathbf{x}^s) f_j(\mathbf{x}^s) d^3 \mathbf{x}^s, \quad (\text{B2})$$

where V^s is the volume of the source region. Let us now assume that a perturbation of the earth model

$$c_{ijkl}(\mathbf{x}) \rightarrow c_{ijkl}(\mathbf{x}) + \delta c_{ijkl}(\mathbf{x}) \quad (\text{B3})$$

leads to a perturbation of the predicted displacement field:

$$u_i(\mathbf{x}) \rightarrow u_i(\mathbf{x}) + \delta u_i(\mathbf{x}). \quad (\text{B4})$$

To derive the displacement sensitivity to the medium elastic properties, we insert eqs (B3)–(B4) into eq. (B1) and drop second-order terms:

$$\frac{\partial}{\partial x_j} \left[c_{ijkl}(\mathbf{x}) \frac{\partial \delta u_k}{\partial x_l}(\mathbf{x}) \right] + \delta f_i(\mathbf{x}) = 0, \quad (\text{B5})$$

where $\delta \mathbf{f}$ is defined as

$$\delta f_i(\mathbf{x}) = \frac{\partial}{\partial x_j} \left[\delta c_{ijkl}(\mathbf{x}) \frac{\partial u_k}{\partial x_l}(\mathbf{x}) \right]. \quad (\text{B6})$$

Note that this first-order perturbation equation is equivalent to the Born approximation in elastodynamics (Dahlen & Tromp 1998; Aki & Richards 2002) where $\delta \mathbf{f}$ is the secondary Born source. Since the solution of the eq. (B1) is given by eq. (B2), the solution for $\delta \mathbf{u}$ in eq. (B5) can be expressed as

$$\delta u_m(\mathbf{x}) = \int_V H_{mi}(\mathbf{x}, \mathbf{x}') \frac{\partial}{\partial x_j} \left[\delta c_{ijkl}(\mathbf{x}') \frac{\partial u_k}{\partial x_l}(\mathbf{x}') \right] d^3 \mathbf{x}', \quad (\text{B7})$$

where V denotes the earth model volume. After some manipulations using the divergence theorem, we obtain

$$\begin{aligned} \delta u_m(\mathbf{x}) = & - \int_V \frac{\partial H_{mi}(\mathbf{x}, \mathbf{x}')}{\partial x'_j} \frac{\partial u_k}{\partial x'_l}(\mathbf{x}') \delta c_{ijkl}(\mathbf{x}') d^3 \mathbf{x}' \\ & + \int_S H_{mi}(\mathbf{x}, \mathbf{x}') \delta c_{ijkl}(\mathbf{x}') \frac{\partial u_k}{\partial x'_l} n_j d^2 \mathbf{x}', \end{aligned} \quad (\text{B8})$$

where n_j is the normal to the Earth's surface. The second integral vanishes because of homogeneous boundary conditions. If we assume an isotropic medium, assuming only perturbations in the shear modulus (μ) while holding the Poisson's ratio constant, we can then write

$$\delta u_i(\mathbf{x}) = - \int_V \frac{\partial H_{ij}(\mathbf{x}, \mathbf{x}')}{\partial x'_k} \frac{\sigma_{jk}(\mathbf{x}')}{\mu(\mathbf{x}')} \delta \mu(\mathbf{x}') d^3 \mathbf{x}', \quad (\text{B9})$$

where $\sigma_{ij}(\mathbf{x}') = c_{ijkl}(\mathbf{x}') u_{kl}(\mathbf{x}')$. For practical implementation, we can discretize the elastic medium into a limited number of layers (as done in Section 4) or tectonically parametrized regions (e.g. crust, mantle). If we allow for piecewise variation of μ in such regions, we can then simplify eq. (B9) using again the divergence theorem to obtain the following 2-D surface integral (Du *et al.* 1994)

$$\delta u_i(\mathbf{x}) = - \sum_r \delta \ln \mu^r \int_{S^r} H_{ij}(\mathbf{x}, \mathbf{x}') \sigma_{jk}(\mathbf{x}') n_k^r(\mathbf{x}') d^2 \mathbf{x}', \quad (\text{B10})$$

where $n_k^r(\mathbf{x}')$ is the normal to the surface S^r delimiting the r th perturbed region. From this equation, we can directly extract the

shear modulus sensitivity kernel \mathbf{J}_μ of the predicted displacement field $\mathbf{u}(\mathbf{x})$ for the r th layer or tectonic region

$$(\mathbf{J}_\mu)_i^r(\mathbf{x}) = - \int_{S^r} H_{ij}(\mathbf{x}, \mathbf{x}') \sigma_{jk}(\mathbf{x}') n_k(\mathbf{x}') d^2 \mathbf{x}'. \quad (\text{B11})$$

Recognizing the fact that geodetic predictions (\mathbf{d}_{pred}) represent only a subset of the total predicted displacement field, we can write

$$\mathbf{d}_{\text{pred}} = \mathbf{R} \cdot \mathbf{u}, \quad (\text{B12})$$

where \mathbf{R} is a sampling operator acting on the complete displacement field $\mathbf{u}(\mathbf{x})$. Similarly, the integral form in eq. (B10) can be discretized to express the model prediction uncertainty (ϵ) as

$$\begin{aligned} \epsilon &= \mathbf{R} \cdot \delta \mathbf{u} \\ &= \mathbf{R} \cdot \mathbf{J}_\mu \cdot \delta \ln \mu. \end{aligned} \quad (\text{B13})$$

From the definition of ϵ in eq. (14) of Section 3.1, we can then write the sensitivity kernel as

$$\mathbf{K}_\mu = \mathbf{R} \cdot \mathbf{J}_\mu. \quad (\text{B14})$$

SUPPORTING INFORMATION

Additional Supporting Information may be found in the online version of this article :

Figure S1. Source estimation for a constant unit slip distribution if \mathbf{C}_p is neglected.

Figure S2. One-dimensional marginal posterior PDFs for each patch as a function of depth. The marginal probability density histograms are shown in green (a) when the prediction uncertainty is neglected and (b) when the prediction uncertainty is taken into account by including \mathbf{C}_p in the inversion problem. The target slip model is indicated as dashed black lines and mean of the distribution is shown in blue. The results in (b) are obtained using approach (2) described in Section 4.4 of the main text: \mathbf{C}_p is calculated at $\beta = 0$ assuming a uniform unitary slip distribution as a function of depth (*cf.* model shown in Fig. S4 for $\beta = 0$).

Figure S3. Evolution of the prediction covariance \mathbf{C}_p at each transitional step. The approach (3) described in Section 4.4 of the main text is used here: \mathbf{C}_p is calculated at $\beta = 0$ assuming a uniform unitary slip distribution as a function of depth (*cf.* model shown in Fig. S4 for $\beta = 0$).

Figure S4. Slip models used for the calculation of the prediction covariance \mathbf{C}_p . The approach (3) described in Section 4.4. of the main text is used here: the model used for the calculation of \mathbf{C}_p at $\beta = 0$ assuming a uniform unitary slip distribution as a function of depth (*cf.* model shown for $\beta = 0$).

Figure S5. One-dimensional marginal posterior PDFs for each patch as a function of depth. The marginal probability density histograms are shown in green (a) when the prediction uncertainty is neglected and (b) when the prediction uncertainty is taken into account by including \mathbf{C}_p in the inversion problem. The target slip model is indicated as dashed black lines and mean of the distribution is shown in blue. The results in (b) are obtained using approach (3) described in Section 4.4 of the main text: \mathbf{C}_p is calculated at $\beta = 0$ using the posterior mean model for which \mathbf{C}_p is neglected (*cf.* blue bars in (a) and Fig. S7).

Figure S6. Evolution of the prediction covariance \mathbf{C}_p at each transitional step. The approach (3) described in Section 4.4. of the main text is used here: \mathbf{C}_p is calculated at $\beta = 0$ using the posterior mean model for which \mathbf{C}_p was neglected (*cf.* Fig. S7 and blue bars in Fig. S5a).

Figure S7. Slip models used for the calculation of the prediction covariance \mathbf{C}_p . The approach (3) described in Section 4.4. of the main text is used here: the model used for the calculation of \mathbf{C}_p at $\beta = 0$ is the posterior mean model when \mathbf{C}_p is neglected (*cf.* blue bars in Fig. S5a).

Figure S8. One-dimensional marginal posterior PDFs for each patch as a function of depth. The marginal probability density histograms are shown in green (a) when the prediction uncertainty is neglected and (b) when the prediction uncertainty is taken into account by including \mathbf{C}_p in the inversion problem. The target slip model is indicated as dashed black lines and mean of the distribution is shown in blue. The results in (b) are obtained using approach (4) described in Section 4.4 of the main text: We use a preliminary form of \mathbf{C}_p whose diagonal elements are proportional to observations.

Figure S9. Evolution of the prediction covariance \mathbf{C}_p at each transitional step. At $\beta = 0$, we use a preliminary form of \mathbf{C}_p whose

diagonal elements are proportional to observations (*cf.* approach (4) described in Section 4.4 of the main text).

Figure S10. Slip models used for the calculation of the prediction covariance \mathbf{C}_p . We use a preliminary form of \mathbf{C}_p whose diagonal elements are proportional to observations (*cf.* approach (4) described in Section 4.4 of the main text).

Figure S11. Same as Fig. 7 in the main text but using strictly positive constraints with a prior $p(\mathbf{m}) = \mathcal{U}(0, 20)^M$ (<http://gji.oxfordjournals.org/lookup/suppl/doi:10.1093/gji/ggt517/-/DC1>).

Please note: Oxford University Press are not responsible for the content or functionality of any supporting materials supplied by the authors. Any queries (other than missing material) should be directed to the corresponding author for the article.

3.2 Modélisation bayésienne du séisme d’Iquique en 2014 ($M_W = 8.1$)

Nous utilisons ici l’approche développée dans la section 3.1 pour l’inversion cinématique du séisme d’Iquique en Avril 2014 (Chili, $M_W = 8.1$). Ce séisme de subduction a rompu une lacune sismique bien identifiée au nord du Chili qui a cassé précédemment en 1877. Nous utilisons une approche Bayésienne qui permet d’obtenir l’ensemble des modèles plausibles qui ajustent les observations disponibles (géodésiques, tsunami et sismologiques) et sont compatibles avec nos hypothèses *a priori*. Nous considérons un *a priori* très simple combinant la positivité du glissement et des paramètres cinématiques (vitesse de rupture, temps de montée) tout en évitant une régularisation non-physique du problème. Les résultats révèlent une zone de glissement très compacte (plus compacte que dans les modèles précédents) localisée en profondeur par rapport à la séquence de séismes pré-chocs qui ont précédé le choc principal. Le séisme d’Iquique ($M_W = 8.1$) et sa plus grande réplique ($M_W = 7.7$) n’ont rompu qu’un petit segment de la lacune sismique au nord du Chili, laissant la possibilité de futures grandes ruptures dans la région.

L’article proposé ci-dessous a été publié en 2015 dans *Geophysical Research Letters*. Ce travail a été effectué suite à mon recrutement à l’IPGS.



Geophysical Research Letters

RESEARCH LETTER

10.1002/2015GL065402

Key Points:

- A Bayesian ensemble of kinematic slip models is constructed using geodetic, tsunami and seismic data
- The earthquake involved a sharp slip zone, more compact than previously thought
- The main asperity is located downdip of the foreshock activity and updip of high-frequency sources

Supporting Information:

- Texts S1 and S2, Figures S1–S15, and Tables S1–S3

Correspondence to:

Z. Duputel,
zacharie.duputel@unistra.fr

Citation:

Duputel, Z., et al. (2015), The Iquique earthquake sequence of April 2014: Bayesian modeling accounting for prediction uncertainty, *Geophys. Res. Lett.*, 42, 7949–7957, doi:10.1002/2015GL065402.

Received 17 JUL 2015

Accepted 10 SEP 2015

Accepted article online 16 SEP 2015

Published online 3 OCT 2015

The Iquique earthquake sequence of April 2014: Bayesian modeling accounting for prediction uncertainty

Z. Duputel^{1,2}, J. Jiang², R. Jolivet^{2,3}, M. Simons², L. Rivera^{1,2}, J.-P. Ampuero², B. Riel², S. E. Owen⁴, A. W. Moore⁴, S. V. Samsonov⁵, F. Ortega Culaciati⁶, and S. E. Minson^{2,7}

¹Institut de Physique du Globe de Strasbourg, Université de Strasbourg/EOST, CNRS, Strasbourg, France, ²Seismological Laboratory, California Institute of Technology, Pasadena, California, USA, ³Now at Ecole Normale Supérieure, Department of Geosciences, PSL Research University, Paris, France, ⁴Jet Propulsion Laboratory, California Institute of Technology, Pasadena, California, USA, ⁵Canada Centre for Mapping and Earth Observation, Natural Resources Canada, Ottawa, Ontario, Canada, ⁶Departamento de Geofísica, Universidad de Chile, Santiago, Chile, ⁷Now at U.S. Geological Survey, Earthquake Science Center, Menlo Park, California, USA

Abstract The subduction zone in northern Chile is a well-identified seismic gap that last ruptured in 1877. On 1 April 2014, this region was struck by a large earthquake following a two week long series of foreshocks. This study combines a wide range of observations, including geodetic, tsunami, and seismic data, to produce a reliable kinematic slip model of the $M_w = 8.1$ main shock and a static slip model of the $M_w = 7.7$ aftershock. We use a novel Bayesian modeling approach that accounts for uncertainty in the Green's functions, both static and dynamic, while avoiding nonphysical regularization. The results reveal a sharp slip zone, more compact than previously thought, located downdip of the foreshock sequence and updip of high-frequency sources inferred by back-projection analysis. Both the main shock and the $M_w = 7.7$ aftershock did not rupture to the trench and left most of the seismic gap unbroken, leaving the possibility of a future large earthquake in the region.

1. Introduction

The largest historical seismic event reported in northern Chile is the great megathrust earthquake of 1877 with an estimated magnitude of 8.8 (cf, Figure 1) [Comte and Pardo, 1991; Lomnitz, 2004]. This event was preceded by the 1868 earthquake in southern Peru that ruptured southward into northern Chile (cf, Figure 1) [Dorbath et al., 1990]. The relative sizes of the 1868 and 1877 events are uncertain. Local tsunami wave heights suggest that the former event is smaller, with 14 m for the 1868 earthquake in Arica (located directly onshore of the rupture) and 21 m for the 1877 event in Mejillones (located south of the faulting area; [Abe, 1979]). On the other hand, far-field tsunami amplitudes in Hawaii and San Francisco are similar for the two earthquakes (around 5 m at Hilo for both events, 0.2 m and 0.3 m at San Francisco in 1868 and 1877, respectively; [Iida et al., 1967]) but are associated with less direct travel paths for the 1868 event, which suggest that this event may be larger than the 1877 earthquake. More recently, the 2001 $M_w = 8.4$ Arequipa earthquake partially reruptured the 1868 rupture zone and the 2007 $M_w = 7.7$ Tocopilla earthquake broke the southern downdip segment of the 1877 faulting area [Pritchard et al., 2006, 2007; Béjar-Pizarro et al., 2010]. The remaining unbroken ~600 km long region shown in Figure 1 may have accumulated about 9 m of slip deficit since 1868/1877 and has been identified as the North Chilean or Iquique seismic gap [Kelleher, 1972; Nishenko, 1991; Metois et al., 2013]. Although very little is known about previous historical events, large earthquakes in northern Chile were reported in 1615 and 1768 and in southern Peru in 1604 and 1784, corresponding to an average recurrence interval of about 130 years over the entire gap.

On 1 April 2014, northern Chile experienced a great earthquake which ruptured the central portion of the 1868/1877 seismic gap (23:46:45 UTC, epicenter 19.572°S, 70.908°W [National Seismological Center of Chile (CSN)]). This event was preceded by an intense foreshock sequence [Brodsky and Lay, 2014] and followed by a large $M_w = 7.7$ aftershock. W phase inversion [Duputel et al., 2012] was performed for the $M_w = 8.1$ main shock and $M_w = 7.7$ aftershock (Figure S1, available in the supporting information). The point source solutions shown in Figure 1 are similar to those found in the Global Centroid Moment Tensor (GCMT) catalog. Several coseismic slip models have been proposed for the main shock using teleseismic observations [Yagi et al., 2014;

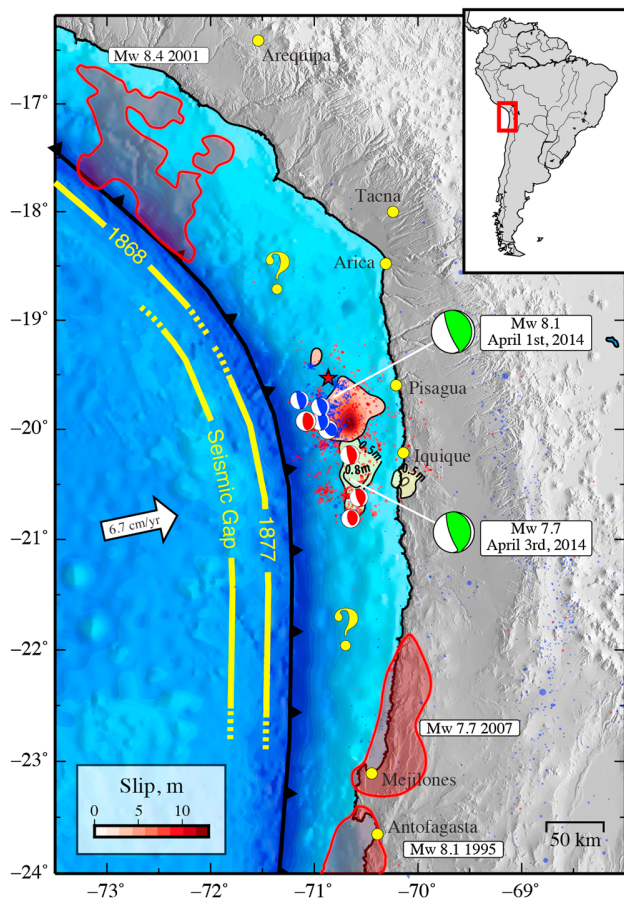


Figure 1. The 2014 Iquique earthquake sequence. Green focal mechanisms are W-phase solutions for the $M_w = 8.2$ main shock and $M_w = 7.7$ aftershock. Yellow lines indicate the supposed rupture zones for the 1868 and 1877 earthquakes [Comte and Pardo, 1991]. Red contours are area of ruptures of the 1995 $M_w = 8.1$ Antofagasta, the 2001 $M_w = 8.4$ Arequipa, and the 2007 $M_w = 7.7$ Tocopilla earthquakes [Pritchard et al., 2006, 2007; Béjar-Pizarro et al., 2010]. Black contours and red color scale indicate the preferred coseismic slip model of the main shock. Yellow filled areas present the posterior slip model obtained for the $M_w = 7.7$ aftershock. Blue and red focal mechanisms are respectively GCMT solutions for foreshocks and aftershock of $M_w > 6$ (1 January 2014 to 4 February 2014 and 1 April 2014 to 9 April 2014). Blue and red circles are respectively foreshocks and aftershocks of magnitude $4 < M < 6$ from the CSN catalog (1 January 2014 to 4 February 2014 and 1 April 2014 to 9 April 2014).

Ruiz et al., 2014], GPS static data, tsunami records [An et al., 2014], or a combination of these observations [Hayes et al., 2014; Schurr et al., 2014; Gusman et al., 2015; Lay et al., 2014; Liu et al., 2015]. These models show similar first-order features but also significant differences such as the amplitude, extent, location, and up-dip limit of the primary slip zone (cf., Figure S2). Such discrepancies complicate the interpretation of the Iquique sequence in the context of the entire earthquake cycle and limit any quantitative conclusion on the reduction of the accumulated slip deficit. These discrepancies also blur the relations between coseismic slip, high-frequency radiation, and foreshock activity [Meng et al., 2015].

Going forward, we need a robust coseismic slip model to understand its spatial relationship to interseismic, preseismic, and postseismic slip, which will provide better insights into the mechanical behavior of the megathrust. With this purpose we combine a wide range of observations including interferometric synthetic aperture radar (InSAR), static GPS, tsunami, tide gauges, high-rate GPS, and strong motion data. The 2014 Iquique earthquake is investigated using an innovative Bayesian approach accounting for uncertainty in the Green's functions. Our goal is not only to obtain a trustworthy slip distribution but also to produce realistic estimates of uncertainty, which can impact our interpretation of the rupture process. We are currently working on Bayesian modeling of interseismic and postseismic deformation, which is left to a future publication.

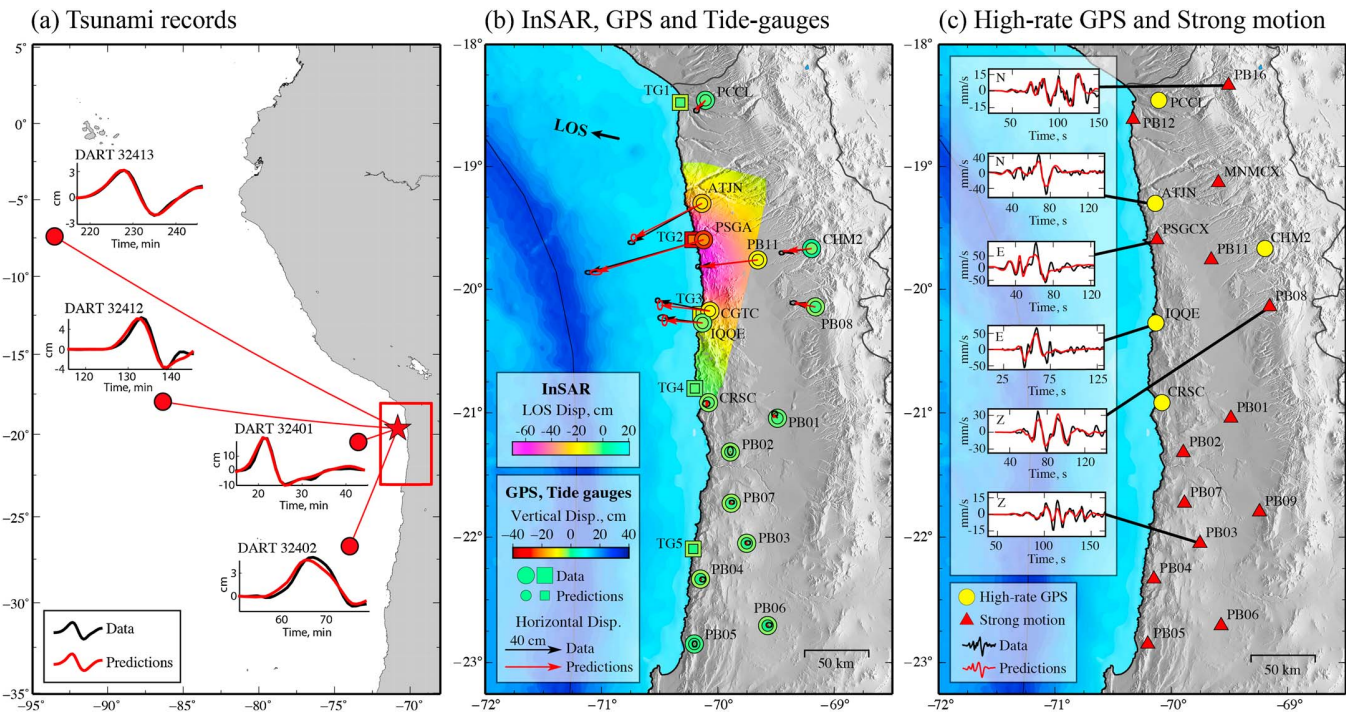


Figure 2. Geodetic, tsunami, and seismic observations. Observations are shown in black and predictions for the posterior mean model in Figure 3b are shown in red. (a) Tsunami waveforms. Red star is the Iquique main shock epicenter and red circles indicate the location of DART stations. Red box indicates the region covered in Figures 2b and 2c. (b) Geodetic data. Vectors indicate observed and predicted horizontal GPS displacements with their associated 1σ data and prediction error ellipses. Colored circles and squares are observed (outer circles/squares) and predicted (inner circles/squares) vertical displacements from GPS and tide gauges, respectively. Dark arrows indicate line of sight direction (LOS) from the satellite to the ground. (c) High-rate GPS and strong motion data. Examples of observed waveforms (black lines) and the corresponding predictions (red lines) are presented.

2. Observations and Probabilistic Analysis

Exploiting the many different data types available in Chile, we gathered one of the most comprehensive data set to date for the 2014 Iquique earthquake (Figure 2). For joint static-kinematic modeling of the main shock, we use RADARSAT-2 InSAR data and GPS data from a network operated by the California Institute of Technology (Caltech), École Normale Supérieure (ENS), Geo Forschungs Zentrum (GFZ), and Universidad de Chile (DGF). We also measured vertical coseismic offsets using five coastal tide gauges close to the main shock epicentral area (data provided by the Servicio Hidrográfico y Oceanográfico de la Armada - SHOA). In addition, we use far-field tsunami records from Deep-ocean Assessment and Reporting of Tsunamis (DART) buoys 32401, 32402, 32412, and 32413 (cf., Figure 2). To constrain the rupture kinematics, we include near-field high-rate GPS (hrGPS) as well as strong motion data from the IPSC network [Witze, 2014]. We also conduct static slip modeling of the $M_w = 7.7$ aftershock using GPS, tide gauges, and tsunami data. As specified in the supporting information, we use this model to remove the aftershock signal from InSAR data before inverting the $M_w = 8.1$ main shock. Further details on data processing and modeling of the aftershock can be found in the supporting information.

Our model adopts a curved fault geometry that accounts for dip variation of the slab interface as a function of depth (cf., supporting information and Figure S5). On each fault patch we solve for the along-strike and along-dip components of slip as well as the rise time and rupture velocity. We also solve for epicenter coordinates. Each point on the fault is allowed to rupture only once during the earthquake, assuming a prescribed triangular source time function. The inversion includes additional “nuisance” parameters to account for InSAR residual orbital errors (i.e., a linear function of range and azimuth).

The inversion accounts for uncertainty in the Green’s functions while also avoiding nonphysical spatial smoothing over the slip distribution. We use a Bayesian approach to derive the posterior probability density function, $p(\mathbf{m}|\mathbf{d})$, describing the full ensemble of plausible slip models, \mathbf{m} , that explain observations, \mathbf{d} , and agree with a priori assumptions, $p(\mathbf{m})$. As detailed in the supporting information, prior assumptions are

as follows: (1) no back slip in excess of 1 m and a maximum slip of 20 m, (2) a centered Gaussian prior on the strike-slip component with a standard deviation of 3 m, and (3) broad uniform prior probability density functions (PDFs) for the slip duration and rupture velocity (Figure S7). We do not use any spatial smoothing or norm damping that might bias slip inversion results [Causse et al., 2010]. We have also developed a realistic error model combining measurement uncertainties and prediction errors due to Earth model inaccuracies (cf., supporting information). We use the stochastic forward model approach of Duputel et al. [2014] to map uncertainties in the elastic parameters into the static and kinematic predictions. Based on previous tomographic models of the region [Legrand et al., 2007; Lüth, 2000; Husen et al., 1999], we calculate the Green's functions for a reference 1-D elastic structure and estimate the error on those Green's functions assuming 5% to 20% uncertainty (cf., supporting information and Figure S6). As noted by Jolivet et al. [2015], ignoring the prediction error leads to biased results and overoptimistic uncertainties on the estimated slip distribution. To our knowledge, it is the first time that epistemic uncertainties in kinematic predictions are estimated using such a physically based approach. This study assumes that static (\mathbf{d}_s) and kinematic (\mathbf{d}_k) data sets are independent. If we think in the frequency domain, the physical independence between \mathbf{d}_s and \mathbf{d}_k is supported by the fact that kinematic data is band-passed (i.e., static displacements are removed from kinematic data). Under this assumption, data and prediction covariances still include off-diagonal components describing spatial and temporal correlations due to prediction uncertainties. The independence of \mathbf{d}_s and \mathbf{d}_k also enables a progressive integration of information from static and kinematic data sets.

As described in Minson et al. [2013], we employ a two-step approach in which we first sample for the static slip distribution

$$p(\mathbf{m}_s|\mathbf{d}_s) \propto p(\mathbf{d}_s|\mathbf{m}_s) p(\mathbf{m}_s) \quad (1)$$

where \mathbf{d}_s represents InSAR, GPS, tide gauges, and tsunami data, and \mathbf{m}_s is the vector of static slip (i.e., final, integrated slip) and nuisance parameters. Solving first for $p(\mathbf{m}_s|\mathbf{d}_s)$ allows us to shrink the sampled space before addressing the full joint kinematic rupture model

$$p(\mathbf{m}|\mathbf{d}) = p(\mathbf{m}_s, \mathbf{m}_k|\mathbf{d}_s, \mathbf{d}_k) \quad (2)$$

$$\propto p(\mathbf{d}_k|\mathbf{m}_s, \mathbf{m}_k) p(\mathbf{m}_s|\mathbf{d}_s) p(\mathbf{m}_k) \quad (3)$$

where \mathbf{d}_k includes hrGPS and strong motion data and \mathbf{m}_k is the vector of kinematic parameters consisting of slip duration, rupture velocity, and epicenter coordinates.

Sampling $p(\mathbf{m}|\mathbf{d})$ in a high-dimensional space is computationally challenging and has long been intractable for kinematic finite-fault source inversions. As the volume of the model space grows exponentially with its dimensionality, we have to generate a large number of samples and perform a large number of forward evaluations, a phenomenon often referred to as the *curse of dimensionality* [Bellman, 1961]. To tackle this problem, we use the AITar algorithm, a parallel Markov Chain Monte Carlo (MCMC) sampler named in honor of Albert Tarantola, which exploits novel massively parallel computational approaches using Graphic Processing Units (GPUs). AITar is based on the Cascading Adaptive Transitional Metropolis In Parallel (CATMIP) algorithm [Minson et al., 2013] and includes the approach of Duputel et al. [2014] to account for prediction uncertainties.

3. Rupture Process of the April 2014 Earthquake Sequence

3.1. Joint Static-Kinematic Modeling of the $M_w = 8.1$ Main Shock

For the main shock, we sample the high-dimensional model space with a large number of samples (~16 billion models, using 140,000 MCMC chains, the computation takes around 24 h using 90 GPUs). Figure 3 shows the mean of the posterior model ensemble and the associated uncertainty after static inversion and joint kinematic-static inversion. Comparisons between observations and predictions from the mean of the posterior model ensemble presented in Figures 2 and S8–S11 indicate good agreement for geodetic, tsunami, and seismic data.

Both static-only and joint kinematic models (Figure 3) show a primary slip zone located south of the hypocenter with a small amount of slip at shallow depth. Due to rupture time information provided by hrGPS and strong motion data, the final slip model appears sharper than the one based only on geodetic and tsunami data. The seismic moment is estimated as 1.6×10^{21} N m ($M_w = 8.1$), in agreement with our W phase solution.

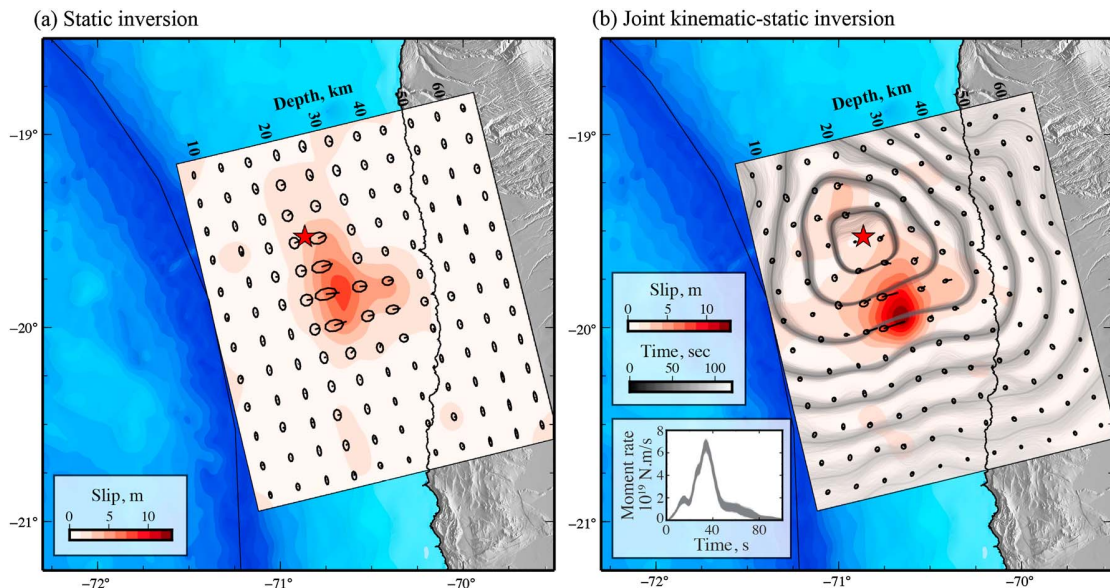


Figure 3. Probabilistic slip model obtained for the 2014 Iquique earthquake. The mean of the posterior PDF is shown (a) after static inversion and (b) after joint kinematic-static inversion. Red colors indicate slip amplitude. Arrows and their associated 95% error ellipses indicate the slip direction and uncertainty. Red star is the inverted hypocenter location. Gray lines are a posterior set of 1000 rupture fronts shown every 10 s. Bottom left inset shows the posterior ensemble of moment rate functions.

The inverted hypocenter, indicated by the red star, is consistent with the CSN hypocenter and about 15 km north of the USGS hypocenter (cf., Figure S12). Model uncertainties in Figure 3b show that the rupture front is well constrained between the hypocenter and the main asperity but poorly resolved in late stages of the rupture associated with low slip amplitudes. These late stages also show significant rupture complexity in back-projection imaging [Meng et al., 2015], including rerupturing episodes that cannot be represented by the source parameterization adopted here. We also present the posterior ensemble of moment rate functions in the bottom left inset of Figure 3b. As reported previously [e.g., Lay et al., 2014], there is a ~20 s interval of low moment rate at the onset of this event, corresponding to the period of time when slip propagates from the hypocenter to the primary asperity. This very slow initiation is then followed by a rapid increase of the moment rate up to 6.8×10^{19} N m/s around 35 s after the origin time.

The absence of shallow slip in our models differs from results of Schurr et al. [2014], Yagi et al. [2014], and Liu et al. [2015] based on seismic and geodetic data but are somewhat similar to the results of An et al. [2014] and Gusman et al. [2015], which have incorporated tsunami observations in their analysis. To assess the relative influence of each data set on different parts of the slip model, we use the sensitivity $\mathbf{S}(\mathcal{D})$, defined as

$$\mathbf{S}(\mathcal{D}) = \text{diag} \left(\mathbf{G}^t(\mathcal{D}) \cdot \mathbf{C}_\chi^{-1}(\mathcal{D}) \cdot \mathbf{G}(\mathcal{D}) \right) \quad (4)$$

where $\mathbf{G}(\mathcal{D})$ and $\mathbf{C}_\chi(\mathcal{D})$ are, respectively, the Green's function for the dip slip component and covariance matrix for a given data set \mathcal{D} (i.e., geodetic, tsunami or seismic data). The sensitivity plots in Figure S13 clearly show that shallow slip is well constrained by tsunami data in contrast to other data sets. Increasing the amount of slip at shallow depth produces early tsunami arrivals which are not consistent with observed waveforms. On the other hand, previous finite-fault models shown in Figure S2 depict significant slip in the downdip part of the megathrust compared to our results. As mentioned by Hayes et al. [2014] (cf., extended data Figure 3), downdip slip does not match InSAR data that favor slip concentrated farther away from the coast. This is also consistent with Figure S13d, showing that the downdip part is well constrained by geodetic data.

After joint inversion the near-field geodetic, tsunami, and seismic data resolve a compact slip zone located ~40 km south of the hypocenter, with maximum slip above 10 m. As shown in Figure S2, this primary slip region is more compact and has larger slip amplitude than most previously published results [e.g., Schurr et al., 2014; Lay et al., 2014; An et al., 2014; Yagi et al., 2014; Gusman et al., 2015]. This difference is probably due to the imposed spatial smoothing in previous slip models, which is absent in our approach. Moreover,

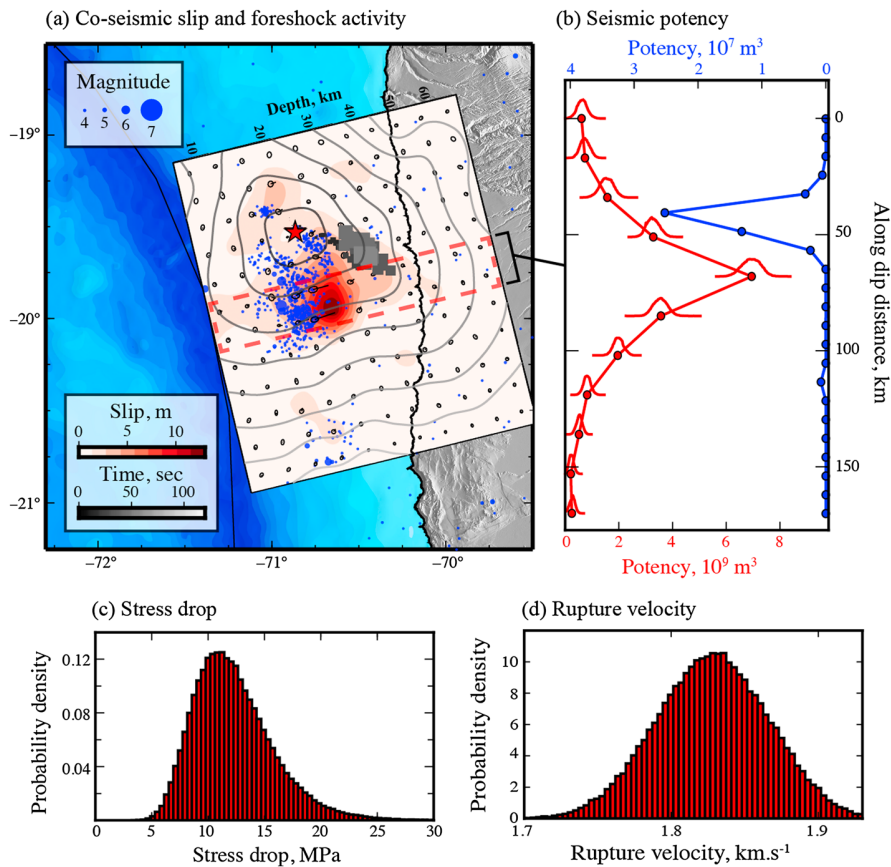


Figure 4. Spatiotemporal distribution of coseismic slip. (a) Comparison of the foreshock activity with the posterior slip model shown in Figure 3b. Gray squares are the high-frequency back projection results of Meng *et al.* [2015] scaled by beamforming amplitude. Blue circles indicate foreshock epicenters from the CSN catalog scaled by magnitude. The rectangular area marked with red dashed lines indicates the profile used for seismic potency estimates in Figure 4b. (b) Distribution of seismic potency as a function of the along-dip distance from the trench. Red histograms and red line show the seismic potency profile estimated from our probabilistic model. Blue line shows the cumulative seismic potency of foreshocks in distance bins. (c) Posterior PDF of the average stress drop. (d) Posterior PDF of the average rupture velocity between the hypocenter and the primary slip zone located ~ 40 km south of the hypocenter.

additional data sets included in our analysis ensure better constraints in the inversion process. Results of Liu *et al.* [2015] and geodetic fault modeling by Hayes *et al.* [2014] also depict a compact main shock rupture but these models involve shallow slip, which is inconsistent with tsunami observations (as discussed above). The average slip for subfaults with moment at least 15% of the peak subfault moment is about 5 m. The posterior PDF of average stress drop ($\Delta\sigma$) obtained by calculating the coseismic change in shear traction at the center of each fault patch is shown in Figure 4c (cf., supporting information). This measurement is consistent with the energy-based averaging of stress drop proposed by Noda *et al.* [2013]. Although the posterior uncertainty on $\Delta\sigma$ is relatively large, the average value of 10 MPa suggests a more compact source than a 3 MPa global average [Allmann and Shearer, 2009]. However, for heterogeneous stress drop distribution, we expect that measurements of Allmann and Shearer [2009] for a circular crack model underestimates our energy-based averaging of $\Delta\sigma$ [cf., Noda *et al.*, 2013].

3.2. Static Modeling of the $M_w = 7.7$ Aftershock

The 3 April 2014 $M_w = 7.7$ aftershock is modeled using Altar in order to draw ~ 1 billion models out of the posterior PDF. The mean and variability of this posterior ensemble of models are presented in Figures 1 and S14. Comparison between observations and predictions for GPS, tide gauges, and tsunami data is shown in Figures S14a and S14b.

Most of the $M_w = 7.7$ aftershock slip is located at depth larger than 20 km. As for the main shock, tsunami data is useful to constrain the absence of slip close to the trench. The aftershock is associated with two main

slip asperities near the south easternmost extent of the $M_w = 8.2$ rupture. This feature is consistent with the slip model of *Liu et al.* [2015] and the two groups of high-frequency sources reported by *Meng et al.* [2015].

Although our model matches geodetic and tsunami observations reasonably well, posterior slip uncertainty is quite large (cf., Figure S14), which prevents more detailed interpretation of the rupture process. Incorporating kinematic data to improve model resolution is left to a future study.

4. Discussion and Conclusion

The $M_w = 8.1$ Iquique earthquake shows an unusual initiation phase with very small moment rate in the first 20 s. As shown in Figure 4a, this initial phase occurred in a region where a relatively large number of foreshocks occurred. The southward rupture propagated initially with a low-average velocity (~ 1.8 km/s, Figures 4d and S15) and concentrated at the edge of a large slip patch that ruptured subsequently. The foreshock activity is also concentrated in the updip periphery of this main asperity. Figure 4b illustrates this by juxtaposing the distribution of seismic potency from our probabilistic coseismic models (in red) and the cumulative seismic potency of foreshocks (in blue). As discussed previously [*Lay et al.*, 2014; *Meng et al.*, 2015], the foreshock activity may be driven by an extended slow slip event, similar to one inferred to have preceded the 2011 $M_w = 9$ Tohoku-oki earthquake [*Kato et al.*, 2012].

The initial slow rise of the moment rate function and the low rupture speed between the hypocenter and the main asperity suggest that the area around the hypocenter is associated with low stress level and high fracture energy. This interpretation is consistent with a precursory slow slip event which might have kept a low stress level in this region. The clear separation between foreshocks and coseismic slip suggests that this possible slow slip transient occurred updip of the main rupture zone and in the area where the main shock rupture was triggered. *Bouchon et al.* [2013] recently suggested that nearly 70% of large interplate earthquakes are preceded by foreshock sequences, possibly triggered by slow slip events. A preseismic transient detected on GPS stations near Pisagua has been conjectured [*Ruiz et al.*, 2014], but it may be associated mainly with the cumulative coseismic displacement of the foreshocks [*Schurr et al.*, 2014]. The amplitude of any purported preseismic creep may simply be too small to be detected by GPS stations. An alternative interpretation can be the cascade triggering of neighboring earthquakes due to static stress transfer and/or the drive of afterslip, ultimately leading to the triggering of the main shock [*Helmstetter and Sornette*, 2003].

The fast rupture speed corridor along the downdip edge of the main asperity coincides nicely with back-projection results of *Meng et al.* [2015], shown by the gray squares in Figure 4a. This distribution of high-frequency sources along the edge of the primary slip zone was observed for several previous earthquakes [*Meng et al.*, 2011; *Lay et al.*, 2012] and might be related to the presence of deep asperities [*Huang et al.*, 2012]. The back-projection showed repeated rupture along that corridor with initial rupture times that are consistent with those inferred here. These late high-frequency rupture episodes may have been induced by the relatively late rupture of the main slip asperity. However, this interpretation is uncertain because our source inversion procedure does not explicitly solve for episodes of rerupture.

Our results indicate a very localized main shock rupture with large slip, suggesting the possibility of nearly complete stress drop in a small portion of the North Chilean seismic gap. The compactness of the source differs from previously published smoothed slip models for which the main shock only reduced part of the accumulated slip deficit in the ruptured region [e.g., *Schurr et al.*, 2014; *Yagi et al.*, 2014]. Even though the April 2014 main shock involved large coseismic slip, it only ruptured a relatively small area ($\sim 100 \times 50$ km) and has not released most of the interseismic strain accumulated since the 1868 and 1877 events. The fact that the rupture did not propagate further south might be related to the presence of a region of low interseismic coupling identified by several studies [*Metois et al.*, 2013; *Schurr et al.*, 2014; *Li et al.*, 2015], which could behave as a barrier to earthquake slip propagation. With a northern extent close to the southern end of the main shock rupture, the $M_w = 7.7$ aftershock partially ruptured the segment south of this low coupled barrier. As suggested by *Hayes et al.* [2014], this region was probably loaded by the main shock and the first 27 h of aftershocks. The physical relationship between the $M_w = 7.7$ aftershock and the main shock need to be further explored with improved resolution of the aftershock model and the development of a reliable postseismic model.

Our modeling results clearly show that the $M_w = 8.1$ main shock and the $M_w = 7.7$ aftershock did not rupture up to the trench. This lack of shallow slip is similar to that inferred for 1995 Antofagasta and 2007 Tocopilla

earthquakes [Pritchard *et al.*, 2006; Béjar-Pizarro *et al.*, 2010; Motagh *et al.*, 2010]. It is not obvious whether the shallow part of the megathrust interface is seismogenic. Recent geodetic studies lead to diverging conclusions about the degree of interseismic coupling at depth shallower than 30 km [Chlieh *et al.*, 2011; Béjar-Pizarro *et al.*, 2013; Schurr *et al.*, 2014; Metois *et al.*, 2013; Li *et al.*, 2015]. Using land-based geodetic data, it is very difficult to infer locking properties far offshore: because of limited resolution, small differences in modeling and smoothing approaches may result in very different coupling models. On the other hand, seafloor deformation observations off the coast of Peru suggest strong coupling at shallow depth [Gagnon *et al.*, 2005]. Whether the shallow portions of the seismic gap are coupled or not, failure in a single large event is certainly possible, as seems to have occurred in the 1868 and 1877 events. During such events, shallow slip could be encouraged by strong dynamic effects or favorable fault weakening properties [e.g., Kozdon and Dunham, 2013; Noda and Lapusta, 2013], a scenario similar to what was observed in Japan during the 2011 Tohoku-oki earthquake. As in many subduction zones, improved inland and seafloor observational networks as well as tools allowing proper posterior uncertainty estimates are necessary to better understand the relative role of seismic and aseismic processes in present day deformation.

Acknowledgments

This research was supported by the Initiative d'Excellence (IDEX) funding framework (Université de Strasbourg), the Institut National des Sciences de l'Univers (INSU) and the CNRS international program for scientific cooperation (PICS). Part of this work was carried out at the Jet Propulsion Laboratory, California Institute of Technology (CALTECH), under a contract with the National Aeronautics and Space Administration. This research was also supported by the Southern California Earthquake Center (SCEC, funded by NSF Cooperative agreement EAR-0529922 and USGS Cooperative agreement 07HQAG0008). Some GPUs used for this research were donated by the NVIDIA Corporation. This work uses data operated by CALTECH, Ecole normale supérieure (ENS), Geo Forschungs Zentrum (GFZ) Universidad de Chile, Servicio Hidrográfico y Oceanográfico de la Armada (SHOA), and the Canadian Space Agency. The slip contours of the Tocopilla earthquake were provided by M. Béjar-Pizarro. This study contributed from fruitful discussions with H. Kanamori, O. Lengliné, L. Meng, and B. Gombert. We thank the Editor, E. Evans (USGS reviewer), W. Thatcher (USGS reviewer), J. Loveless (GRL reviewer), and an anonymous GRL reviewer for their constructive comments, which helped improve this manuscript.

The Editor thanks John Loveless and an anonymous reviewer for their assistance in evaluating this paper.

References

- Abe, K. (1979), Size of great earthquakes of 1837–1974 inferred from tsunami data, *J. Geophys. Res.*, **84**, 1561–1568.
- Allmann, B. P., and P. M. Shearer (2009), Global variations of stress drop for moderate to large earthquakes, *J. Geophys. Res.*, **114**, B01310, doi:10.1029/2008JB005821.
- An, C., I. Sepúlveda, and P. L. F. Liu (2014), Tsunami source and its validation of the 2014 Iquique, Chile, earthquake, *Geophys. Res. Lett.*, **41**, 3988–3994, doi:10.1002/2014GL060567.
- Béjar-Pizarro, M., *et al.* (2010), Asperities and barriers on the seismogenic zone in North Chile: State-of-the-art after the 2007 M_w 7.7 Tocopilla earthquake inferred by GPS and InSAR data, *Geophys. J. Int.*, **183**(1), 390–406.
- Béjar-Pizarro, M., A. Socquet, R. Armijo, D. Carrizo, J. Genrich, and M. Simons (2013), Andean structural control on interseismic coupling in the North Chile subduction zone, *Nat. Geosci.*, **6**(6), 462–467.
- Bellman, R. (1961), *Adaptive Control Processes: A Guided Tour*, Princeton Univ. Press Princeton, N. J.
- Bouchon, M., V. Durand, D. Marsan, H. Karabulut, and J. Schmittbuhl (2013), The long precursory phase of most large interplate earthquakes, *Nat. Geosci.*, **6**(4), 299–302.
- Brodsky, E. E., and T. Lay (2014), Recognizing foreshocks from the 1 April 2014 Chile earthquake, *Science*, **344**(6185), 700–702.
- Causse, M., F. Cotton, and P. M. Mai (2010), Constraining the roughness degree of slip heterogeneity, *J. Geophys. Res.*, **115**, B05304, doi:10.1029/2009JB006747.
- Chlieh, M., H. Perfettini, H. Tavera, J.-P. Avouac, D. Remy, J.-M. Nocquet, F. Rolandone, F. Bondoux, G. Gabalda, and S. Bonvalot (2011), Interseismic coupling and seismic potential along the Central Andes subduction zone, *J. Geophys. Res.*, **116**, B12405, doi:10.1029/2010JB008166.
- Comte, D., and M. Pardo (1991), Reappraisal of great historical earthquakes in the northern Chile and southern Peru seismic gaps, *Nat. Hazards*, **4**(1), 23–44.
- Dorbat, L., A. Cisternas, and C. Dorbat (1990), Assessment of the size of large and great historical earthquakes in Peru, *Bull. Seismol. Soc. Am.*, **80**(3), 551–576.
- Duputel, Z., L. Rivera, H. Kanamori, and G. Hayes (2012), W phase source inversion for moderate to large earthquakes (1990–2010), *Geophys. J. Int.*, **189**(2), 1125–1147.
- Duputel, Z., P. S. Agram, M. Simons, S. E. Minson, and J. L. Beck (2014), Accounting for prediction uncertainty when inferring subsurface fault slip, *Geophys. J. Int.*, **197**(1), 464–482.
- Gagnon, K., C. D. Chadwell, and E. Norabuena (2005), Measuring the onset of locking in the Peru–Chile trench with GPS and acoustic measurements, *Nature*, **434**(7030), 205–208.
- Gusman, A. R., S. Murotani, K. Satake, M. Heidarzadeh, E. Gunawan, S. Watada, and B. Schurr (2015), Fault slip distribution of the 2014 Iquique, Chile, earthquake estimated from ocean-wide tsunami waveforms and GPS data, *Geophys. Res. Lett.*, **42**, 1053–1060, doi:10.1002/2014GL062604.
- Hayes, G. P., M. W. Herman, W. D. Barnhart, K. P. Furlong, S. Riquelme, H. M. Benz, E. Bergman, S. Barrientos, P. S. Earle, and S. Samsonov (2014), Continuing megathrust earthquake potential in Chile after the 2014 Iquique earthquake, *Nature*, **512**(7514), 295–298.
- Helmstetter, A., and D. Sornette (2003), Foreshocks explained by cascades of triggered seismicity, *J. Geophys. Res.*, **108**(B10), 2457, doi:10.1029/2003JB002409.
- Huang, Y., L. Meng, and J.-P. Ampuero (2012), A dynamic model of the frequency-dependent rupture process of the 2011 Tohoku-Oki earthquake, *Earth Planets Space*, **64**(12), 1061–1066.
- Husen, S., E. Kissling, E. Flueh, and G. Asch (1999), Accurate hypocentre determination in the seismogenic zone of the subducting Nazca Plate in northern Chile using a combined on-/offshore network, *Geophys. J. Int.*, **138**(3), 687–701.
- Iida, K., D. C. Cox, and G. Pararas-Carayannis (1967), Preliminary catalog of tsunamis occurring in the Pacific ocean, Data Rep. 5, HIG-67-10, Hawaii Inst. of Geophys., Univ. Hawaii, Honolulu, Hawaii.
- Jolivet, R., M. Simons, P. S. Agram, Z. Duputel, and Z. K. Shen (2015), Aseismic slip and seismogenic coupling along the central San Andreas Fault, *Geophys. Res. Lett.*, **42**, 297–306, doi:10.1002/2014GL062222.
- Kato, A., K. Obara, T. Igashiki, H. Tsuruoka, S. Nakagawa, and N. Hirata (2012), Propagation of slow slip leading up to the 2011 M_w 9.0 Tohoku-Oki earthquake, *Science*, **335**(6069), 705–708.
- Kelleher, J. A. (1972), Rupture zones of large South American earthquakes and some predictions, *J. Geophys. Res.*, **77**(11), 2087–2103.
- Kozdon, J. E., and E. M. Dunham (2013), Rupture to the trench: Dynamic rupture simulations of the 11 March 2011 Tohoku Earthquake, *Bull. Seismol. Soc. Am.*, **103**(2B), 1275–1289.
- Lay, T., H. Kanamori, C. J. Ammon, K. D. Koper, A. R. Hutko, L. Ye, H. Yue, and T. M. Rushing (2012), Depth-varying rupture properties of subduction zone megathrust faults, *J. Geophys. Res.*, **117**, B04311, doi:10.1029/2011JB009133.
- Lay, T., H. Yue, E. E. Brodsky, and C. An (2014), The 1 April 2014 Iquique, Chile, M_w 8.1 earthquake rupture sequence, *Geophys. Res. Lett.*, **41**, 3818–3825, doi:10.1002/2014GL060238.

- Legrand, D., B. Delouis, L. Dorbath, C. David, J. Campos, L. Marquéz, J. Thompson, and D. Comte (2007), Source parameters of the $M_w = 6.3$ Aroma crustal earthquake of July 24, 2001 (northern Chile), and its aftershock sequence, *J. South Amer. Earth Sci.*, 24(1), 58–68.
- Li, S., M. Moreno, J. Bedford, M. Rosenau, and O. Oncken (2015), Revisiting viscoelastic effects on interseismic deformation and locking degree: A case study of the Peru-North Chile subduction zone, *J. Geophys. Res. Solid Earth*, 120, 4522–4538, doi:10.1002/2015JB011903.
- Liu, C., Y. Zheng, R. Wang, and X. Xiong (2015), Kinematic rupture process of the 2014 Chile M_w 8.1 earthquake constrained by strong-motion, GPS static offsets and teleseismic data, *Geophys. J. Int.*, 202(2), 1137–1145.
- Lomnitz, C. (2004), Major earthquakes of Chile: A historical survey, 1535–1960, *Seismol. Res. Lett.*, 75(3), 368–378.
- Lüth, S. (2000), Results of wide-angle investigations and crustal structure along a traverse across the central Andes at 21 degrees south, PhD thesis, Berliner Geowissenschaftliche Abhandlungen, Inst. of Geol., Geophys. and Geoinformatics, Free Univ. of Berlin, Berlin.
- Meng, L., A. Inbal, and J.-P. Ampuero (2011), A window into the complexity of the dynamic rupture of the 2011 M_w 9 Tohoku-Oki earthquake, *Geophys. Res. Lett.*, 38, L00G07, doi:10.1029/2011GL048118.
- Meng, L., H. Huang, R. Bürgmann, J.-P. Ampuero, and A. Strader (2015), Dual megathrust slip behaviors of the 2014 Iquique earthquake sequence, *Earth Planet. Sci. Lett.*, 411, 177–187.
- Metois, M., A. Socquet, C. Vigny, D. Carrizo, S. Peyrat, A. Delorme, E. Maureira, M. C. Valderas-Bermejo, and I. Ortega (2013), Revisiting the North Chile seismic gap segmentation using GPS-derived interseismic coupling, *Geophys. J. Int.*, 194(3), 1283–1294.
- Minson, S. E., M. Simons, and J. L. Beck (2013), Bayesian inversion for finite fault earthquake source models I—Theory and algorithm, *Geophys. J. Int.*, 194(3), 1701–1726.
- Motagh, M., B. Schurr, J. Anderssohn, B. Cailleau, T. R. Walter, R. Wang, and J.-P. Villotte (2010), Subduction earthquake deformation associated with 14 November 2007, M_w 7.8 Tocopilla earthquake in Chile: Results from InSAR and aftershocks, *Tectonophysics*, 490(1-2), 60–68.
- Nishenko, S. P. (1991), Circum-Pacific seismic potential: 1989–1999, *Pure Appl. Geophys.*, 135(2), 169–259.
- Noda, H., and N. Lapusta (2013), Stable creeping fault segments can become destructive as a result of dynamic weakening, *Nature*, 7433, 518–521.
- Noda, H., N. Lapusta, and H. Kanamori (2013), Comparison of average stress drop measures for ruptures with heterogeneous stress change and implications for earthquake physics, *Geophys. J. Int.*, 193(3), 1691–1712.
- Pritchard, M. E., C. Ji, and M. Simons (2006), Distribution of slip from 11 $M_w > 6$ earthquakes in the northern Chile subduction zone, *J. Geophys. Res.*, 111, B10302, doi:10.1029/2005JB004013.
- Pritchard, M. E., E. O. Norabuena, C. Ji, R. Boroschek, D. Comte, M. Simons, T. H. Dixon, and P. A. Rosen (2007), Geodetic, teleseismic, and strong motion constraints on slip from recent southern Peru subduction zone earthquakes, *J. Geophys. Res.*, 112, B03307, doi:10.1029/2006JB004294.
- Ruiz, S., M. Metois, A. Fuenzalida, J. Ruiz, F. Leyton, R. Grandin, C. Vigny, R. Madariaga, and J. Campos (2014), Intense foreshocks and a slow slip event preceded the 2014 Iquique M_w 8.1 earthquake, *Science*, 345(6201), 1165–1169.
- Schurr, B., et al. (2014), Gradual unlocking of plate boundary controlled initiation of the 2014 Iquique earthquake, *Nature*, 512(7514), 299–302.
- Witze, A. (2014), Chile quake defies expectations, *Nature*, 508(7497), 440–441.
- Yagi, Y., R. Okuwaki, B. Enescu, S. Hirano, Y. Yamagami, S. Endo, and T. Komoro (2014), Rupture process of the 2014 Iquique Chile Earthquake in relation with the foreshock activity, *Geophys. Res. Lett.*, 41, 4201–4206, doi:10.1002/2014GL060274.

3.3 Exploration bayésienne du glissement et de l'endommagement co-sismique lors du séisme Landers en 1992 ($M_W = 7.3$)

La non-unicité des modèles de glissement est un problème connu en géophysique. Pour de nombreux séismes, plusieurs modèles permettent d'expliquer les observations de façon similaire. Le séisme de Landers en 1992 (USA, $M_W = 7.3$) illustre bien ce problème. Les modèles existants montrent des différences notables en particulier concernant la quantité de glissement à faible profondeur. Dans cette partie, nous estimons l'ensemble des modèles plausibles permettant d'expliquer les observations géodésiques de surface. En utilisant des données haute-résolution à proximité de la faille, nous évaluons les propriétés de la zone endommagée et son impact sur le glissement à faible profondeur. Une partie du déficit de glissement observé à faible profondeur pour le séisme de Landers semble expliquée par la réduction du module de cisaillement à proximité de la faille. Cette hétérogénéité de structure n'est généralement pas prise en compte dans les modèles de glissement.

L'article ci-dessous a été publié en 2018 dans *Geophysical Journal International*. Ce travail a été effectué dans le cadre du doctorat de Baptiste Gombert (thèse soutenue en Mars 2018).

Revisiting the 1992 Landers earthquake: a Bayesian exploration of co-seismic slip and off-fault damage

B. Gombert,¹ Z. Duputel,¹ R. Jolivet,² C. Doubre,¹ L. Rivera¹ and M. Simons³

¹*Institut de Physique du Globe de Strasbourg, UMR7516, Université de Strasbourg, EOST/CNRS, Strasbourg, France. E-mail: gombert@unistra.fr*

²*Laboratoire de géologie, Département de Géosciences, École Normale Supérieure, PSL Research University, CNRS UMR, Paris, France*

³*Seismological Laboratory, Geological and Planetary Sciences, California Institute of Technology, Pasadena, CA, USA*

Accepted 2017 October 17. Received 2017 October 16; in original form 2017 May 23

SUMMARY

Existing models for the distribution of subsurface fault slip associated with the 1992 Landers, CA, earthquake ($M_w = 7.3$) show significant dissimilarities. In particular, they exhibit different amounts of slip at shallow depths (<5 km). These discrepancies can be primarily attributed to the ill-posed nature of the slip inversion problem and to the use of physically unjustifiable smoothing or regularization constraints. In this study, we propose a new coseismic model obtained from the joint inversion of multiple observations in a relatively unregularized and fully Bayesian framework. We use a comprehensive data set including GPS, terrestrial geodesy, multiple SAR interferograms and co-seismic offsets from correlation of aerial images. These observations provide dense coverage of both near- and far-field deformation. To limit the impact of modelling uncertainties, we develop a 3-D fault geometry designed from field observations, co-seismic offsets and the distribution of aftershocks. In addition, we account for uncertainty in the assumed elastic structure used to compute the Green's functions. Our solution includes the ensemble of all plausible models that are consistent with our prior information and fit the available observations within data and prediction uncertainties. Using near-fault high-resolution ground deformation measurements and the density of aftershocks, we investigate the properties of the damage zone and its impact on the inferred slip at depth. We attribute a part of the inferred slip deficit at shallow depth to our models not including the impact of a damage zone associated with a reduction of shear modulus in the vicinity of the fault.

Key words: Inverse theory; Probability distributions; Earthquake source observations; Fractures, faults, and high strain deformation zones.

1 INTRODUCTION

Following the 1979 Imperial Valley earthquake more than three decades ago (Olson & Apsel 1982; Hartzell & Heaton 1983), finite-fault source models have been routinely constructed after most significant earthquakes. Despite the increasing volume and quality of available geodetic and seismological data, we still observe a significant variability in inferred subsurface fault slip for a given event. Estimating the distribution of fault slip from surface deformation is fundamentally an ill-posed inverse problem with different models that can fit the data equally well. Therefore, different finite-fault models for the same earthquake often display significant dissimilarities. Over the past decade, there have been considerable efforts in the seismological community to study this problem and characterize the variability of the models (e.g. Mai *et al.* 2016). Furthermore, data and forward predictions are imperfect and the corresponding uncertainties are often difficult to account for. A standard approach to overcome the non-uniqueness of the solution relies on Tikhonov

regularization (e.g. Hansen 1998) involving minimization of first or second order spatial derivatives of the slip model to enforce smoothness of the slip distribution. However, various regularization strategies can affect the solution. The impact of different approaches to regularization, coupled with the lack of consideration of model uncertainties, can hamper our ability to draw clear conclusions about earthquake source processes.

Due to the availability of a comprehensive data set, many finite-fault models have been published for the 1992 $M_w = 7.3$ Landers earthquake (e.g. Murray *et al.* 1993; Cohee & Beroza 1994; Freymueller *et al.* 1994; Hudnut *et al.* 1994; Wald & Heaton 1994; Cotton & Campillo 1995; Fialko 2004b; Xu *et al.* 2016). Common patterns emerge in the inferred slip distributions including the fact that most of the slip occurred in the central section of the rupture (i.e. the Homestead Valley Fault). However, there are also clear inconsistencies. In particular, published studies have inferred shallow slip to vary between 30 per cent and 112 per cent of the slip inferred at 7 km depth. Since there is no indication of large inter- or

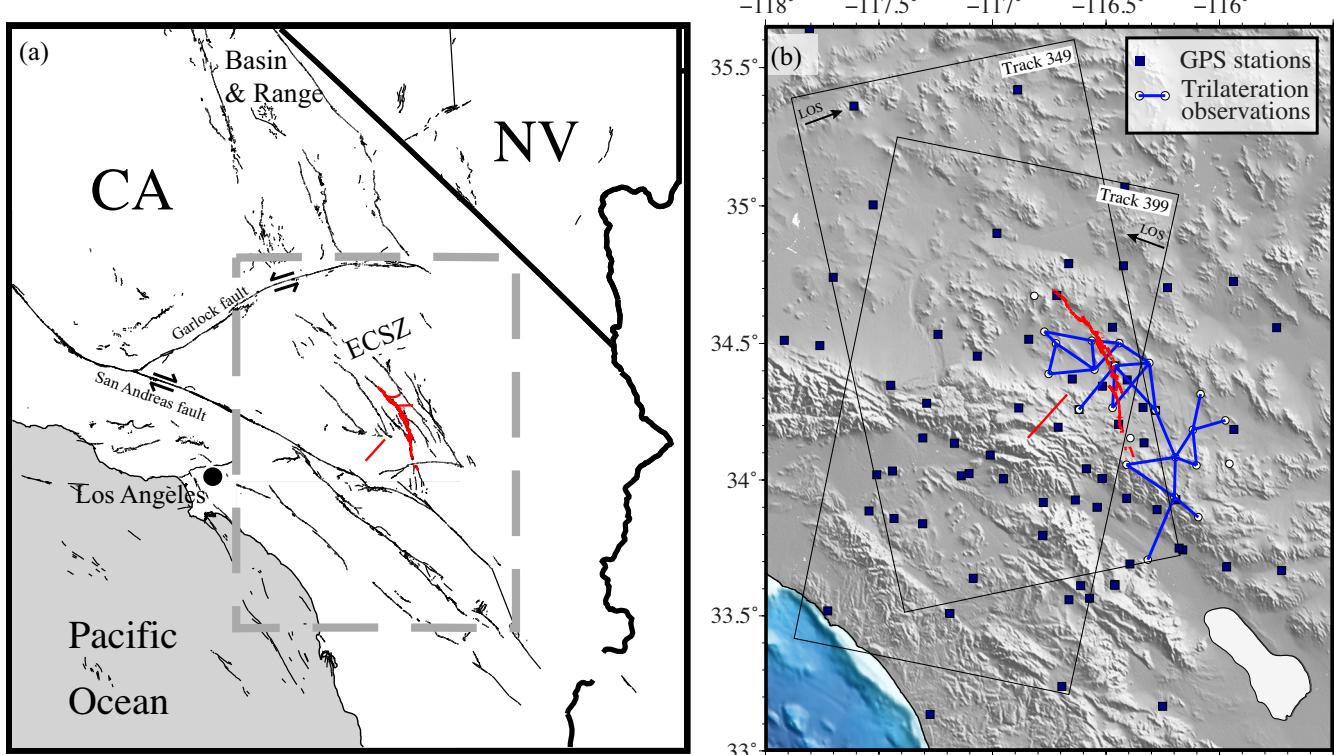


Figure 1. General overview of the area. (a) Tectonic context of Southern California. The dashed grey rectangle shows the extent of (b). The Landers earthquake surface rupture is plotted in red. The faults involved are part of the Eastern California Shear Zone (ECSZ). (b) Far-field observations used in this study. The thin black rectangles illustrate the InSAR track footprints. The ascending interferogram (Track 349) covers the time span between 26 May and 30 June 1992 and the descending interferogram (Track 399) between 24 April and 7 August. Topography is from the Space Radar Topographic Mission (SRTM) database.

post-seismic slip at shallow depth (Shen *et al.* 1994; Savage & Svare 1997; Fialko 2004a), the amount of the potential shallow coseismic slip deficit has an impact on seismic risk assessment as this suggests that part of the accumulated strain is not released by the earthquake (Simons *et al.* 2002; Fialko *et al.* 2005). Simons *et al.* (2002) and Kaneko & Fialko (2011) suggested that such deficits might be an artefact due to inelastic response of the medium in the vicinity of the fault. Inelasticity would bias slip models where observations at short distances are modelled assuming elastic Green's functions. An apparent shallow slip deficit could also be caused by smoothing constraints and sparseness of near-fault data (Simons *et al.* 2002; Xu *et al.* 2016). Finally, unaccounted heterogeneities in the crust elastic properties can also result in a biased slip distribution at depth (Barbot *et al.* 2008). One way to evaluate these hypotheses is to derive all the models consistent with the available data without arbitrary regularization of the inverse problem and explore the potential mechanisms statistically.

We perform a Bayesian exploration of the 1992 Landers rupture to evaluate the population of plausible slip models given geodetic data and forward problem uncertainties. Our approach is exempt from any smoothing and allows us to assess the extent of any purported shallow slip deficit as constrained by available geodetic data. Using near-fault data, we also investigate the impact of lateral heterogeneities on the inferred slip distribution at depth.

2 DATA OVERVIEW

We use a large geodetic data set composed of GPS measurements at 82 sites, 23 trilateration measurements, 2 SAR interferograms and

14 optical correlation images. This combination of data provides good coverage in both the near- and far-fields.

2.1 GPS and trilateration data

We use 3-component observations from 82 GPS stations scattered across southern California (Hudnut *et al.* 1994) with a few stations in the vicinity of the fault (Figs 1 and 2). Observations of the vertical component of displacement are associated with significantly larger uncertainties than the horizontal components. In addition, a trilateration network covers the southern part of the rupture (Figs 1 and 2). We invert directly the horizontal relative line-length changes provided by Murray *et al.* (1993) instead of the pre-inverted displacement vectors of the trilateration stations. The GPS and trilateration data include up to a few months of inter-seismic and post-seismic deformation. However, the associated post-seismic displacements measured by GPS are expected to be less than ~ 10 cm, which is substantially smaller than the ~ 8 m of co-seismic displacement observed near the earthquake rupture. (Murray *et al.* 1993; Peltzer *et al.* 1998).

2.2 InSAR data

We use two SAR interferograms computed from pre- and post-earthquake acquisitions on both ascending and descending tracks of the ERS satellite (Fig. 1b). Interferograms are computed using the ROI_PAC software (Rosen *et al.* 2004). We downsample the unwrapped interferograms using a recursive quad-tree algorithm (Simons *et al.* 2002; Lohman & Simons 2005) to reduce the

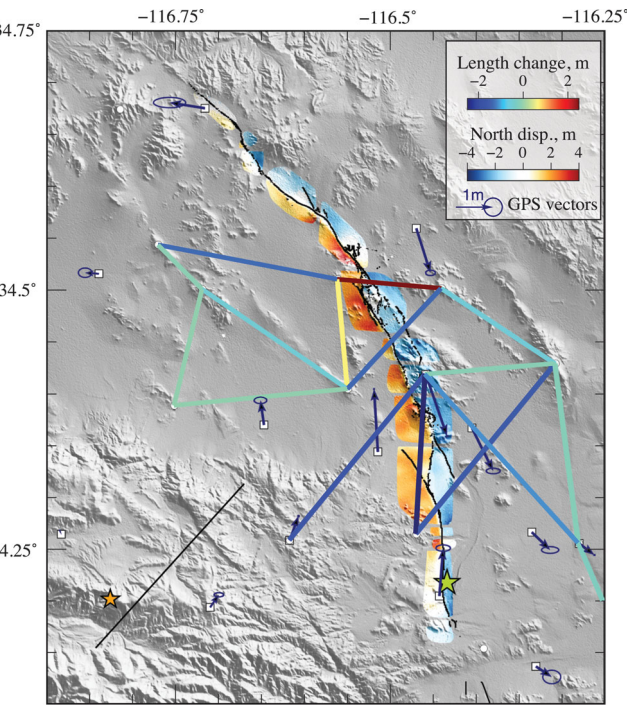


Figure 2. Near-field observations. Lines are coloured according to length changes in the trilateration network. The optical correlation mosaic is plotted around the fault trace from Sieh *et al.* (1993). Main shock and Big Bear aftershock ($M_w = 6.5$) hypocentres from the Southern California Earthquake Center are indicated with a green and an orange star, respectively.

number of observation points. The final downsampled ascending and descending interferograms contain 730 and 663 pixels, respectively. Downsampled observations, predictions, and residuals are shown in Supporting Information Fig. S1. Using the procedure described by Jolivet *et al.* (2014) for each InSAR scene, we estimate an empirical data covariance function, which statistically represents atmospheric noise. We find standard deviations of 3.5 cm and 0.9 cm for the descending and ascending tracks, respectively. The correlation length is 11 km for both images. Covariance functions are shown in Supporting Information Fig. S2. While the second image of the interferogram on the ascending track was acquired only 2 d after the main shock, the interferogram on the descending track includes more than one month of post-seismic deformation.

2.3 Optical correlation images

We use optical correlation images of the ground displacement from Ayoub *et al.* (2009). Maps of ground displacement are made using 14 pairs of aerial photographs acquired before and after the earthquake. Cross-correlation is performed to derive horizontal co-seismic displacements in the vicinity of the fault. Pre-earthquake photographs were acquired during the summer 1989 while post-earthquake were acquired during the autumn 1995. The footprint of each pair is slightly less than $10 \times 10 \text{ km}^2$ and the data set covers almost the entire surface rupture of the fault (Figs 2 and 7a). Because of their near-field coverage, optical data can finely constrain shallow slip in our models. However, as pointed out by Kaneko & Fialko (2011), near-fault observations may include inelastic effects that can bias slip estimates assuming linear elasticity. To avoid such artefact, we remove any near-fault pixels within 300 m of the fault. This cut-off length is in agreement with measurements by Milliner *et al.* (2015) showing that off-fault deformation is generally limited to a nar-

row zone around the fault (with an average half-width smaller than 80 m). Removing data in the vicinity of the fault also reduces the impact of modelling errors due to fault parametrization. Indeed, the assumption of constant slip in fault patches and the discretization of the fault trace (every ~ 1.5 km) induce artefacts in the predicted deformation field very close to the fault (see Supporting Information text T1 and Fig. S3). In addition, using the same technique as for InSAR data in Section 2.2, each image is downsampled and data covariance is estimated using empirical covariograms. The resulting standard deviation is typically around 30 cm and the correlation length ranges from 300 m to 1 km. Most of the post-seismic deformation is included in the timespan separating the two acquisitions (Fialko 2004a). However, as mentioned by Milliner *et al.* (2015), the detection threshold of optical image correlation is about 10 cm, suggesting that ~ 15 cm of near-field post-seismic deformation lie in the uncertainties of the measurement.

3 PROBABILISTIC SLIP INVERSION

3.1 Model parametrization

While most previous studies used relatively simplified linear geometries, our fault parametrization shown in Fig. 3 consists of nine segments following the surface rupture trace. The three main segments are the Johnson Valley, Homestead Valley, and Emerson and Camp Rock faults (Sieh *et al.* 1993). Those three segments are linked by two small junctions and completed by the small Galaxy Lake Fault in the northern part of the rupture. In addition, we parametrize two antithetic faults on the eastern side of the Emerson segment. These two faults were not directly mapped by Sieh *et al.* (1993) but have been previously incorporated as linear segments by Fialko (2004b) from the distribution of aftershocks. In the present study, the northern antithetic segment is refined as a curved fault from the detailed analysis of InSAR ground deformation profiles along with the Hauksson *et al.* (2012) relocated earthquake catalogue (see Fig. 3). Finally, we use an additional fault corresponding to the $M_w = 6.5$ Big Bear aftershock, which orientation is derived from the Hauksson *et al.* (2012) catalogue. Consistent with Fialko (2004b), faults segments are assumed to be vertical and to extend down to 15 km. Although this depth is roughly in agreement with the maximum depth of aftershock, we cannot exclude a more complex geometry at depth as often reported when multiple fault segments interact (Segall & Pollard 1980). To evaluate the effect of such complexities, we propose an alternative geometry in which shallow parallel branches merge on a single deeper segment. This geometry is similar to a flower structure that can be observed in some strike-slip faults (e.g. Zingone *et al.* 2015).

For both assumed fault geometries, each segment is discretized in four rows of subfaults extending down to 1.5 km, 4.5 km, 9.0 km, and 15.0 km depth. The size of each subfault is designed to have an acceptable resolution at depth (resolution $R \geq 0.8$ as defined in the Supporting Information for the strike-slip component, see Supporting Information Fig. S4). This strategy ensures small posterior model uncertainty but more importantly, it enables good convergence of the Bayesian sampling algorithm used for the inversion.

3.2 Bayesian sampling

We use a Bayesian approach to obtain the full posterior probability density function (PDF) of the slip distribution given the observations and uncertainties. According to the Bayes–Laplace theorem, we

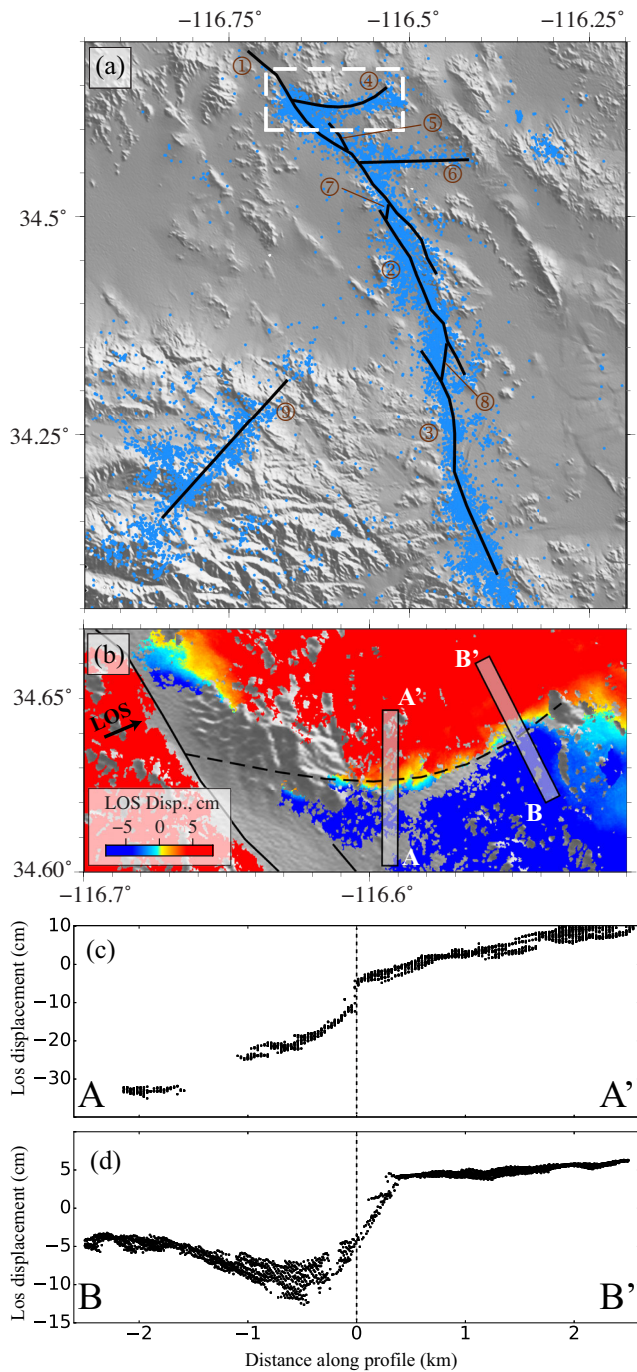


Figure 3. (a) Surface trace of the parametrized fault segments. Each segment is plotted as a thick black line. 1. Emerson and Camp Rock Faults, 2. Homestead Valley Fault, 3. Johnson Valley Fault, 4. Northern conjugate Fault, 5. Galway Lake Fault, 6. Southern conjugated Fault, 7. Emerson-Homestead Valley junction, 8. Kickapoo Fault, 9. Big Bear Fault. Blue dots represent aftershock locations from Hauksson *et al.* (2012). Dashed white rectangle shows the extent of (b). (b) Surface trace of the northern conjugate segment (dashed line). Rectangles show the position of the profiles shown in (c) and (d). Background colour represents the InSAR ascending track LOS displacement pattern. (c,d) InSAR data profiles A-A' and B-B'

write the posterior PDF as:

$$p(\mathbf{m}|\mathbf{d}_{\text{obs}}) \propto p(\mathbf{m}) \exp \left[-\frac{1}{2} (\mathbf{d}_{\text{obs}} - \mathbf{G}\mathbf{m})^T \mathbf{C}_x^{-1} (\mathbf{d}_{\text{obs}} - \mathbf{G}\mathbf{m}) \right] \quad (1)$$

where \mathbf{m} is the model vector, $p(\mathbf{m})$ is the prior distribution, \mathbf{d}_{obs} is the data vector, \mathbf{G} is the Green functions matrix, and \mathbf{C}_x is the misfit covariance describing both data and forward prediction uncertainties. We compute the Green's functions for a semi-infinite stratified elastic medium using the EDKS software (Zhu & Rivera 2002)

To sample the model space we use AlTar, a parallel Markov Chain Monte Carlo (MCMC) algorithm based on the CATMIP formalism (Minson *et al.* 2013). Using multiple MCMC chains in parallel, Al-Tar initially samples the prior PDF, $p(\mathbf{m})$, and then slowly increases the information brought by the data until it samples the posterior PDF. The implementation benefits from the use of high efficiency Graphic Processing Units (GPUs), allowing us to run more than 500 000 chains in parallel. Our final solution consists of an ensemble of models that are statistically distributed according to the posterior PDF. No spatial smoothing constraint is used in this procedure. We adopt different priors for the two different slip directions. The strike-slip component prior is a uniform PDF between -1 m and 30 m, hence promoting right-lateral faulting. The dip-slip prior is a Gaussian PDF centred on 0 m with a standard deviation of 5 m.

3.3 Model prediction uncertainties

Accounting for uncertainties in our forward predictions uncertainties is crucial since they correspond to one of the largest sources of variability between published slip models. Moreover, these uncertainties are important in our Bayesian framework as we do not use smoothing regularization. The model prediction uncertainties are described by the matrix \mathbf{C}_p , which is added to the observation uncertainties matrix \mathbf{C}_d to obtain the misfit covariance:

$$\mathbf{C}_x = \mathbf{C}_d + \mathbf{C}_p. \quad (2)$$

We build \mathbf{C}_p using the approach of Duputel *et al.* (2014) to account for uncertainties in the elastic model used to compute the Green's functions. The layered elastic model used in this study is derived from the Southern California Earthquake Center 3-D velocity model (Kohler *et al.* 2003). Uncertainties on the elastic parameters are inferred by comparing different models in the source region along with the distribution of 3-D velocity models from Kohler *et al.* (2003), as shown in Supporting Information Fig. S5.

3.4 Probabilistic slip model

Using our Bayesian framework, we generate 500 000 models representing our posterior information on slip distribution given available geodetic data. To interpret this ensemble, we need to extract a representative model and the corresponding uncertainties. In Fig. 4, we show the posterior mean model (i.e. the average of all sampled models) along with 95 per cent confidence ellipses. A more detailed view is available in Supporting Information Fig. S6. The posterior mean model is a common choice as the Bayesian approach encourages one to think in terms of an ensemble solution instead of one single model. However, as shown in Supporting Information Fig. S7, other models can also be depicted such as the maximum a posteriori model (i.e. the mode of the posterior distribution) or the best fitting model (i.e. the sample in our population having the maximum posterior value). In our case, the maximum a posteriori model is insignificantly different to the posterior mean model since most

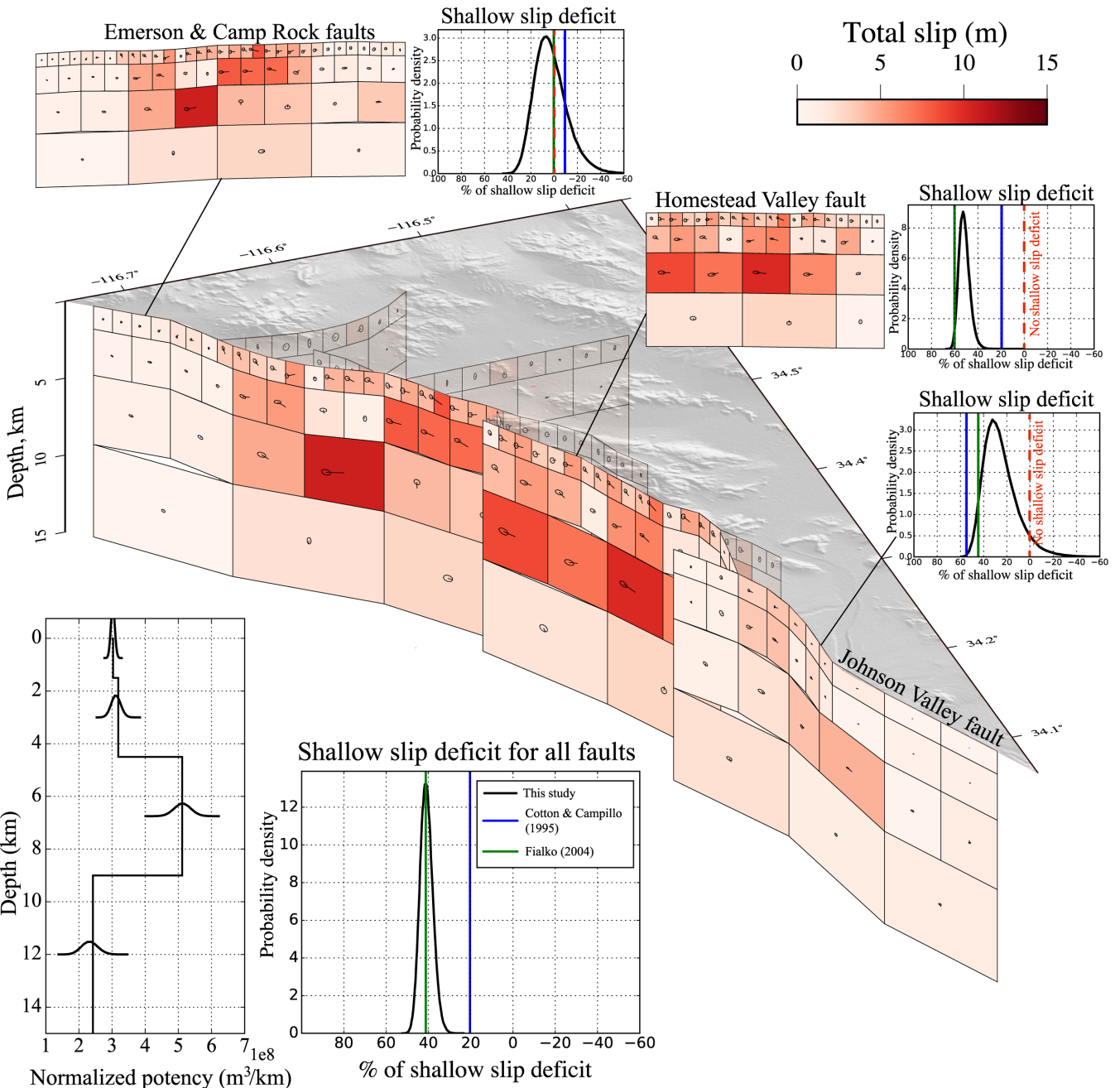


Figure 4. Posterior mean co-seismic slip model. The colour of each subfault patch indicates the slip amplitude. Arrows and their associated 95 per cent confidence ellipse indicate the slip direction and uncertainty. The bottom left inset shows the potency normalized by patch row width as a function of depth. PDFs of shallow slip deficit (SSD) are presented for the entire fault system and for individual fault segments. Vertical lines on the same plots indicate the SSD of two published models (Cotton & Campillo 1995; Fialko 2004b).

marginal PDFs are nearly Gaussians (*cf.* Supporting Information text T2).

The results in Fig. 4 are based on vertical fault segments. They can be compared with the solution in Supporting Information Fig. S8 obtained assuming a more complicated flower parametrization introduced in Section 3.1. Despite different fault dips, the inferred slip distributions are fairly similar in both geometries, showing the lack of sensitivity to the parametrization at depth. Although posterior PDFs of both geometries generally overlap in fault patches with large slip, we still observe significant differences as shown in Supporting Information Fig. S8. This suggests that modelling uncertainties included in C_p are still underestimated as we only in-

corporate Earth model uncertainties and neglect errors in the fault parametrization. In the following, we focus on the results obtained using vertical fault segments.

As expected, we observe predominately strike-slip motion along the entire fault system. Most of the slip concentrates along the central and northern parts of the rupture, with a peak amplitude of ~ 11 m. These features are to first order comparable to previous results, although published models have lower peak slip amplitudes (e.g. Cohee & Beroza 1994; Fialko 2004b; Xu *et al.* 2016). This difference is probably due to smoothing imposed in previous studies that decreases the maximum slip amplitude. The two small junctions (shown in Supporting Information Fig. S6) show relatively

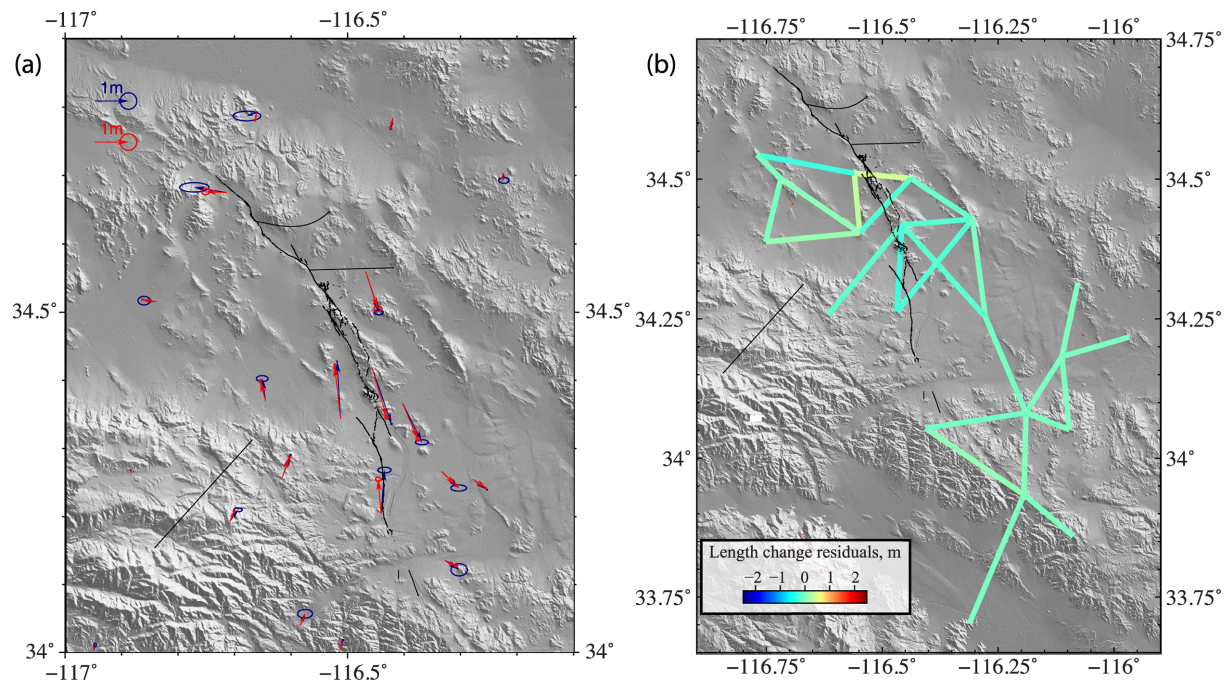


Figure 5. Model performance for GPS and trilateration data. (a) GPS observations (blue) and predictions (red) with their 1σ error ellipses. (b) Length changes residuals for the posterior mean model.

large slip at depth, although they are associated with significant posterior uncertainties. In addition, these estimates are associated with significant along-dip correlation of slip amplitudes (*cf.* Supporting Information Fig. S9).

The model predictions reproduce the observations reasonably well. The performance of the models for GPS and trilateration data is presented in Fig. 5 with associated posterior uncertainties. Posterior mean InSAR predictions and residuals are shown in Fig. 6 in high-resolution, and decimated in Supporting Information Fig. S1. In high-resolution, we observe some moderate residuals in the vicinity of the fault, mainly due to the finiteness of the fault patches. Some larger wavelength residuals are visible on the southern part of the descending track. We suspect that this signal originates from post-seismic deformation (Fialko 2004a) as the second pass of this track is 5 weeks after the main shock. Finally, our model explains reasonably well the optical correlation images despite large uncertainties associated with this data set (Fig. 7). We also computed an equivalent moment tensor and centroid location and tested it against long period seismological observations (details are provided in Supporting Information text T3 and Figs S10–S12).

3.5 Shallow slip deficit

A shallow slip deficit is commonly observed for large strike-slip earthquakes (Simons *et al.* 2002; Fialko *et al.* 2005). Although, in a simple linear elastic model, a uniform slip distribution at depth is expected when averaged over many seismic cycles (Tse & Rice 1986), this deficit does not seem to be recovered by either inter-seismic creep or post-seismic deformation (Fialko 2004a). Some exceptions with no detectable shallow slip deficit have nonetheless been documented such as the 2013 $M_w = 7.7$ Balochistan earthquakes (Jolivet *et al.* 2014; Vallage *et al.* 2015).

Although a shallow slip deficit is observed in most published models of the Landers earthquake, there is a large variability in the actual amount of shallow slip deficit between different inversion

results. To investigate this, we compute the normalized potency as a function of depth:

$$P_k = \frac{\sum_i \Delta u_{ik} \times A_{ik}}{w_k} \quad (3)$$

where Δu_{ik} is the slip inferred in a patch of area A_{ik} and width w_k located in the k th row and at an along-strike position i . This formulation allows us to avoid any bias due to the increase of patch size with depth. As shown in Fig. 4, we find a maximum potency on the 3rd row of patches (*i.e.* between 4.5 and 9 km depth, consistent with Simons *et al.* (2002)) that is nearly 1.7 times larger than surface estimates (*i.e.* at depth between 0 and 1.5 km). To highlight this for individual fault segments, we define the percentage of shallow slip deficit (SSD) as:

$$\text{SSD} = 100 \left(\frac{P_{k=3} - P_{k=1}}{P_{k=3}} \right). \quad (4)$$

According to this definition, $\text{SSD} > 0$ indicates some amount of shallow slip deficit while $\text{SSD} \leq 0$ means that potency is equal or larger at the surface than at depth (*i.e.* no shallow slip deficit). The posterior distribution of SSD is shown in Fig. 4 for the three main fault segments and the overall rupture. Results and probability estimates are also summarized in Table 1.

Although the overall rupture depicts a shallow slip deficit of about 41 per cent, we find different behaviours for different fault segments. We observe the smallest deficit along the Emerson and Camp Rock segment where the probability of shallow slip deficit is only 62%. The Johnson Valley fault is more likely to present a shallow deficit, but the SSD is relatively moderate ($\text{SSD} \sim 25$ per cent). The largest deficit is measured for the Homestead Valley fault where the mean SSD is 52 per cent with a probability close to 1 that the deficit is larger than 25 per cent. The remaining fault segments are either too small, with too large uncertainties or did not slip enough to contribute significantly to the overall rupture estimate.

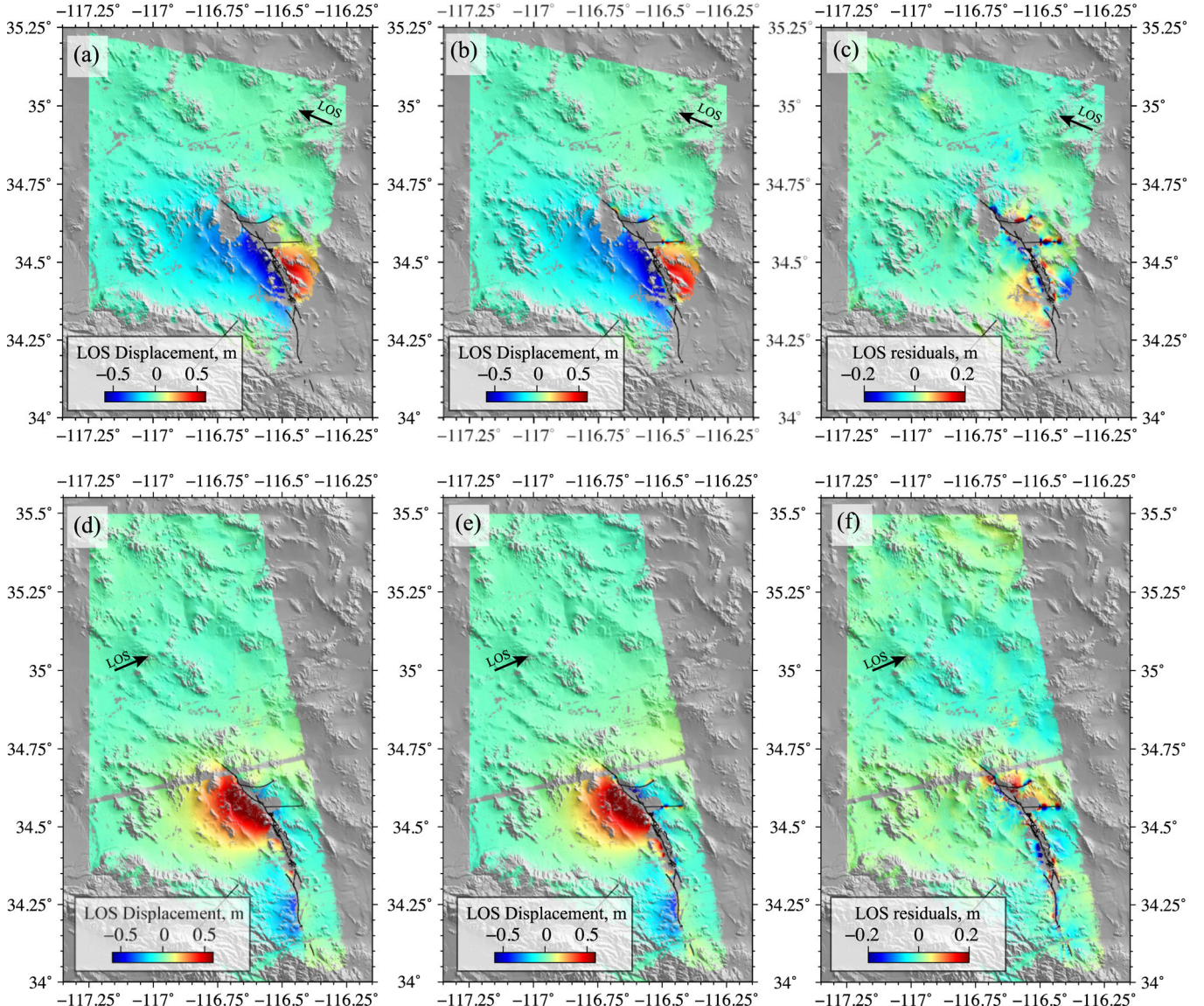


Figure 6. Model performance for InSAR. (a, d) InSAR observations. (b, e) Predictions for the posterior mean model. (c, f) InSAR residuals of the descending (top) and ascending (bottom) tracks.

4 DISCUSSION

As pointed out in Section 1, previously published models differ, in particular regarding the amount of shallow slip deficit. A detailed comparison between our solution and previous models is provided in Fig. 4 and Supporting Information Fig. S13. The SSD values for previously published models extend from 70 per cent (i.e. a large shallow slip deficit) to −12 per cent (shallow slip exceeds slip at 7 km depth). Our slip deficit is thus smaller than some models (e.g. Zeng & Anderson 2000) but larger than others (e.g. Cohee & Beroza 1994; Wald & Heaton 1994; Cotton & Campillo 1995; Hernandez *et al.* 1999). Overall, there is a fairly good agreement with the model of Fialko (2004b) which closely matches our estimate of slip deficit. Unlike most of these previous models, our inversion includes near-field optical images which give a solid constraint on slip along the shallow part of the fault, hence improving our estimates of SSD. This is presented in Supporting Information Fig. S14 showing slip posterior uncertainties obtained with and without incorporating optical images, illustrating their significance in our inversion.

To assess the impact of smoothing constraints on the shallow slip deficit, we also performed damped least squares inversions incorporating a second-order Tikhonov regularization minimizing the roughness of the slip model \mathbf{m}_{est} (Segall & Harris 1987; Ortega 2013):

$$\mathbf{m}_{\text{est}}(\epsilon) = (\mathbf{G}^T \mathbf{C}_\chi^{-1} \mathbf{G} + (\epsilon \nabla^2)^2)^{-1} \mathbf{G}^T \mathbf{C}_\chi \mathbf{d}_{\text{obs}} \quad (5)$$

where ∇^2 is the Laplacian operator defined on fault slip surface coordinates, and ϵ is the damping parameter. As shown in Supporting Information Figs S15(c)–(h), the larger the damping ϵ , the smoother the solution. Supporting Information Fig. S15(a) shows that shallow slip deficit values vary widely as a function of ϵ , from 13 per cent to 57 per cent. Unsurprisingly, models with little regularization (e.g. $\epsilon \sim 0.1$) are quite consistent with our Bayesian solution, including in terms of shallow slip deficit. The choice of ϵ is to a large extent arbitrary. However, we still note large variations of the SSD by selecting a few models localized around the corner of the L-curve (Supporting Information

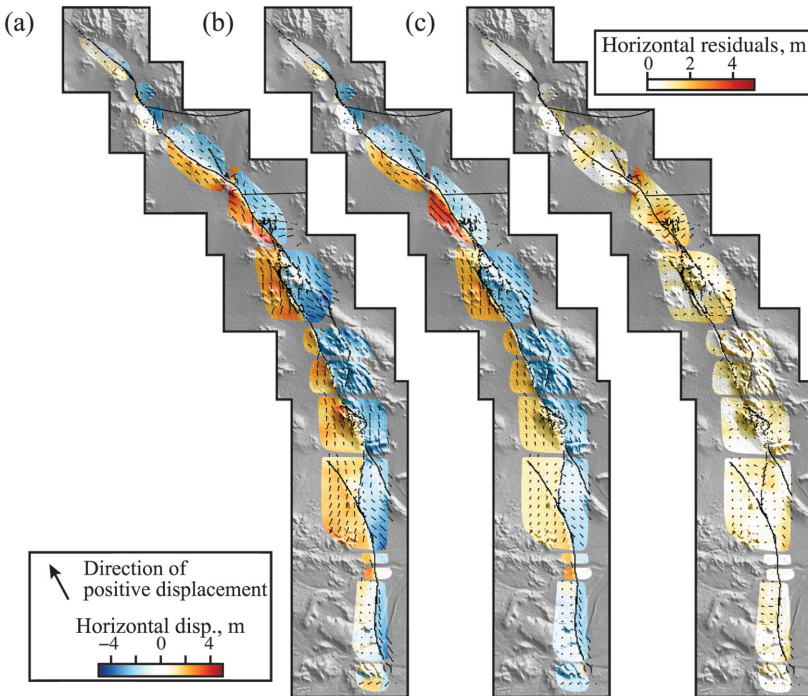


Figure 7. Model performance for optical image correlation data. (a) Observations. (b) Predictions for the posterior mean model. (c) Residuals. Positive displacements are towards the northwest (see arrow in the legend).

Table 1. Shallow slip deficit estimated for different fault segments and for the whole rupture. A zero or negative SSD means that there is no deficit. An SSD value of 50 per cent means that there is twice more slip at depth than at the surface.

Fault segment	Mean SSD	95 per cent conf. interval	Probability than SSD is greater or equal than...		
			0 per cent	25 per cent	50 per cent
Emerson and Camp Rock	2.6 per cent	-25.1 per cent to 33.5 per cent	62 per cent	3.1 per cent	0 per cent
Johnson Valley	25.4 per cent	-3.8 per cent to 57.6 per cent	94 per cent	58.2 per cent	<1 per cent
Homestead Valley	51.7 per cent	42.7 per cent to 61.9 per cent	100 per cent	97.0 per cent	67.5 per cent
All faults combined	40.9 per cent	35.2 per cent to 47.3 per cent	100 per cent	99.9 per cent	<1 per cent
All faults combined taking into account a compliant zone	29.6 per cent	14.32 per cent to 46.4 per cent	99.6 per cent	75.8 per cent	<1 per cent

Fig. S15b). Such a strong dependence on ϵ complicates any interpretation of the results of smoothed models in terms of shallow slip deficit. Of course, other factors can possibly impact the inferred slip distribution such as the choice of fault geometry or the data sets included in the inversion. As shown in Supporting Information Table S2, we do not see any clear direct relationship between used data sets and the inferred SSD. For example, both Fialko (2004b) and Xu *et al.* (2016) used observations similar to ours but with different estimates of the SSD. Such variability does not seem to be explained by the assumed fault parametrization since both studies used a complex geometry similar to the one we use (*cf.* Supporting Information Table S2). Another example is Cohee & Beroza (1994) and Zeng & Anderson (2000) that are based on similar fault planes and data sets but with different SSD estimates. Inversion results can be affected by other parameters such as fault discretization, data weighting, and elastic structure (whose uncertainty is accounted for in the present study). A better understanding of the variability of previous models would require extensive tests using different geometries, data sets, and weighting schemes, which is beyond the scope of this study.

Different artefacts affecting co-seismic slip models are often proposed to explain the shallow slip deficit inferred for large strike-slip earthquakes. One of them is the inelastic strain in the vicinity of the fault that is usually unaccounted in finite-fault inversions (e.g. Simons *et al.* 2002; Fialko *et al.* 2005). Such inelastic response can indeed bias slip inversions that are based on elastic Green's functions and artificially decrease the amount of slip at shallow depth (Kaneko & Fialko 2011). However, as reported by Milliner *et al.* (2015), inelastic strain for the 1992 Landers earthquake is limited to a relatively narrow region around the fault (e.g. within ~ 65 m of the fault trace in Fig. 8c). To avoid any strong bias due to our elastic assumption and reduce modelling errors due to fault discretization at shallow depth, we have removed displacement data within a minimum distance of 300 m from the fault trace (see Section 2.3). This procedure is roughly equivalent to localizing the inelastic contribution of the strain field onto an idealized fault plane (Dahlen & Tromp 1998). Although removing near-fault pixels should reduce artefacts due to inelastic effects, unaccounted lateral heterogeneities due to accumulated damage around the fault can also have a significant impact on surface deformation patterns and by extension on the inverted slip distribution (Barbot *et al.* 2008).

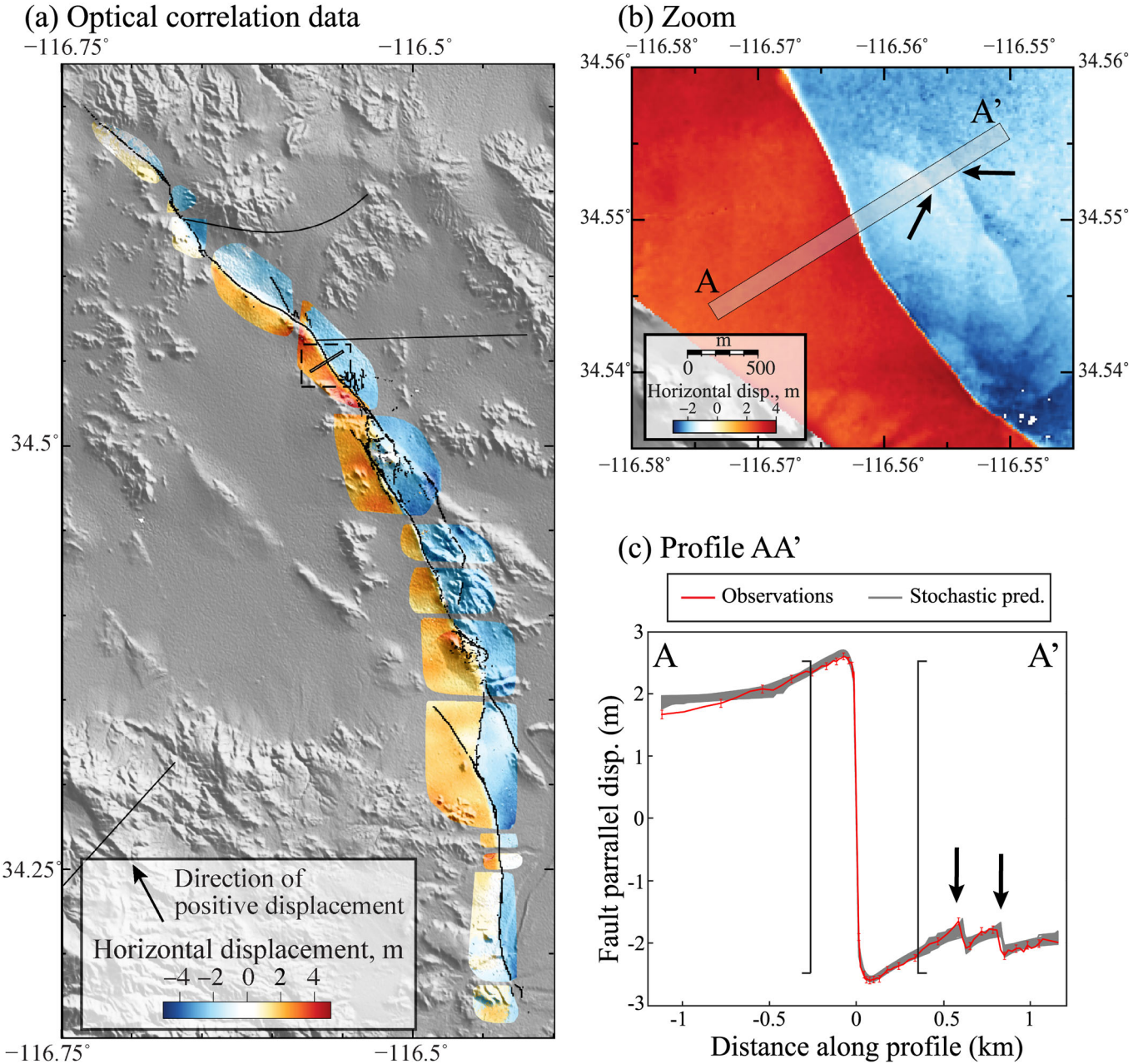


Figure 8. Modelling of near-field deformation data. (a) Overall view of optical correlation data. The profile shown in (c) is localized with a black line. (b) Close up view of near-field data. Grey rectangle indicate the location of the profile shown in (c). (c) Comparison between observed displacement (in red) and the stochastic predictions (in grey). Black arrows labelled F1 and F2 in (b) and (c) highlight two small secondary ruptures visible in the data. These small ruptures are incorporated in our modelling approach assuming two vertical dislocations. Data inside the black brackets are not used in the inversion of the full 3-D slip distribution presented in Fig. 4 to reduce the impact of inelastic effects in the vicinity of the main rupture.

The fault zone is often regarded as a highly deformed core surrounded by a more or less broad damage zone of reduced stiffness (e.g. Chester *et al.* 1993; Ben-Zion & Sammis 2003; Dor *et al.* 2006; Mitchell & Faulkner 2009). The damage zone consists of cracks and microfractures in the host rock and can be associated with secondary faults reducing the elastic strain released on the main rupture interface (Chester & Chester 1998; Dieterich & Smith 2009). Such secondary cracks have been reported around the Landers fault system (McGill & Rubin 1999). An example is given in Fig. 8, showing two secondary ruptures (labelled F1 and F2) visible in optical correlation images near the Emerson Valley fault. Such off-

fault ruptures are not accounted for in our slip model presented in Fig. 4.

To investigate the properties of the damage zone and secondary ruptures, we analyse a profile across the fault using simple vertical elastic screw dislocations embedded in a compliant fault zone (Segall 2010). Using a Metropolis algorithm, we invert for the slip distribution on each fault, a compliant zone half-width and an effective shear modulus contrast μ_1/μ_0 (where μ_1 is the shear modulus of the fault zone while μ_0 is the modulus of the surrounding crust). The compliant zone half-width and shear modulus ratio being typical Jeffreys parameters (Tarantola 2005), they are sampled in the

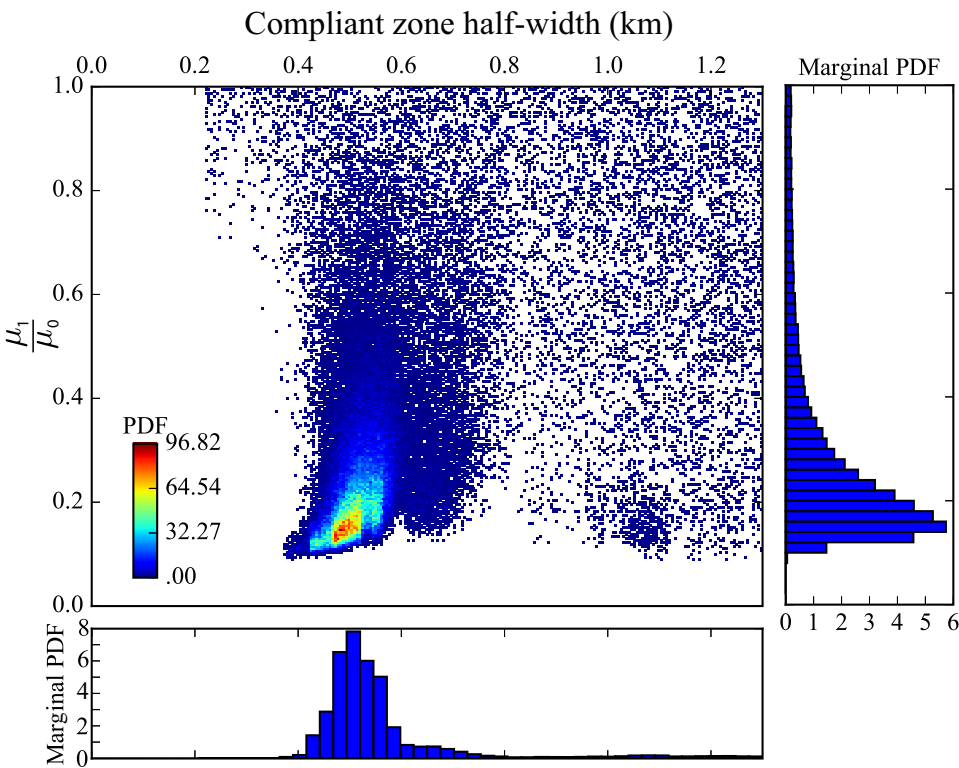


Figure 9. Posterior joint probability distribution of the compliant zone half-width and shear modulus ratio. Dots are model samples that are coloured according to the PDF value. Blue histograms are marginal PDFs for both parameters.

logarithmic domain. To avoid any effect of off-fault inelasticity, we remove the data within 65 m of the fault, which is consistent with fault-width measurements by Milliner *et al.* (2015) at this location. The results presented in Fig. 8(c) indicate very shallow secondary ruptures with 32 ± 8 cm and 36 ± 5 cm of slip down to 84 ± 30 m and 180 ± 40 m respectively for faults F1 and F2. Although such slip amplitudes are not negligible, these off-fault dislocations are relatively shallow and thus represent only 3.3 per cent of the total seismic slip inferred from the surface down to 0.5 km. Of course, these measurements are only valid locally since the properties of secondary faults might vary significantly along the main rupture (Lewis & Ben-Zion 2010; Milliner *et al.* 2015; Thomas *et al.* 2017).

The results shown in Fig. 9 highlight the existence of a ~ 1.1 km wide compliant zone around this part of the fault. Although there is some correlation between the compliant zone width and rigidity, our solution indicates that shear modulus can be reduced by as much as a factor ~ 5 within the damage zone (i.e. a shear modulus ratio of ~ 0.2). This estimate is consistent with measurements from guided seismic waves (Li *et al.* 1994, 2007; Peng *et al.* 2003) that indicate shear modulus ratios between 0.1 and 0.4, corresponding to 80 per cent of our models. On the other hand, these studies suggest relatively small damage zone widths of a few hundred meters, which is narrower than our estimates.

Using the aftershock catalogue of Hauksson *et al.* (2012), we compare our estimates with the distribution of seismicity around the main fault, which is another indicator of distributed damage in the host rock (Amitrano 2006; Powers & Jordan 2010). As shown in Fig. 10(a), we select two profiles across the main rupture surrounding the southern antithetic fault to avoid any bias due to events located on this segment. Following Powers & Jordan (2010), we

compute the horizontal density $v(x)$ of seismicity where x is the fault normal distance, and assume a power law decay of the form

$$v(x) = v_0 \left(1 + \frac{x^2}{d^2}\right)^{-\gamma/2} \quad (6)$$

where v_0 is the aftershock density at $x = 0$, d is the damage zone half-width and γ is the asymptotic roll-off of the seismicity away from the fault. Using a Metropolis inversion scheme, we then sample v_0 , d , and γ given the seismicity density, $v(x)$. Comparison between observations and stochastic predictions are shown in Fig. 10(b) and the full posterior PDFs for the 3 parameters are shown in Supporting Information Fig. S16. Although the posterior mean damage-zone half-width $d \sim 800$ m is larger than what is inferred from optical images ($d \sim 570$ m), an inversion with a fixed $d = 570$ m also explains the data reasonably well (cf. Fig. 10b).

To estimate the impact of the damage zone on the inverted slip distribution, we also invert the fault-parallel displacement profile of Fig. 8(c) without a compliant zone and after removing the data within 300 m of the fault (i.e. the same way it is done in our main slip inversion). The posterior PDFs of shallow slip and stochastic predictions with and without accounting for the damage zone are shown in Fig. 11. Although far field deformation is well-predicted in both inversions, predictions neglecting a compliant zone fail to reproduce near-fault observations and underestimate slip at shallow depth. On average, accounting for the compliant zone increases shallow slip by a factor of 1.2. On the other hand, neglecting lateral shear modulus heterogeneities will systematically lead to smaller slip (with a probability of 98 per cent). To roughly estimate the effect of the damage zone, we can empirically correct the surface mean slip of the Landers rupture by factors drawn from posterior PDFs with and without accounting for the compliant zone. Results

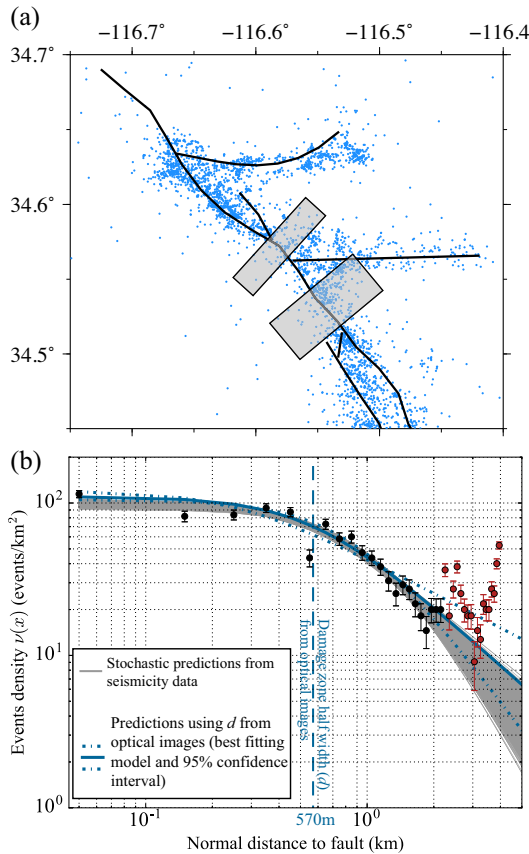


Figure 10. Distribution of seismicity across the fault. (a) Our parametrized fault trace is indicated with thick black lines. Blue dots are aftershock epicentres from Hauksson *et al.* (2012). Grey rectangles illustrate the location of profiles used for the seismicity density analysis. (b) Seismicity density as a function of fault normal distance. Densities are computed over the two stacked profiles using 100 m wide distance bins. Black circles are resulting event density measurements used in the power-law inversion. Red circles are observations not included in the inversion since they correspond to events located at distance larger than ~ 2 km that may be partly linked to the southern antithetic fault segment. The 1σ error bars were obtained by computing the standard deviation of density in each bin from 1000 random catalogues generated according to event location uncertainties.

presented in Fig. 12 and Table 1, indicate that this significantly reduces the overall shallow slip deficit from 41 per cent to 27 per cent. These results should, however, be considered with caution, as the damage behaviour can vary significantly along the fault (Lewis & Ben-Zion 2010). We tried to conduct similar experiments in other locations on the fault but did not obtain reliable constraints on the compliant zone parameters (see e.g. Supporting Information Figs S17 and S18). Even if damage properties can widely vary along the fault, such structures will necessarily impact slip estimated at shallow depth, thereby reducing the inferred shallow deficit.

5 CONCLUSION

We used an extensive geodetic data set, careful uncertainty estimates and a realistic fault geometry to produce a stochastic finite-fault model of the Landers earthquake. Our Bayesian approach to the inversion has two main advantages: (1) the solution is not biased by any kind of smoothing and (2) posterior parameter uncertainties are available and provide valuable information on the validity of the

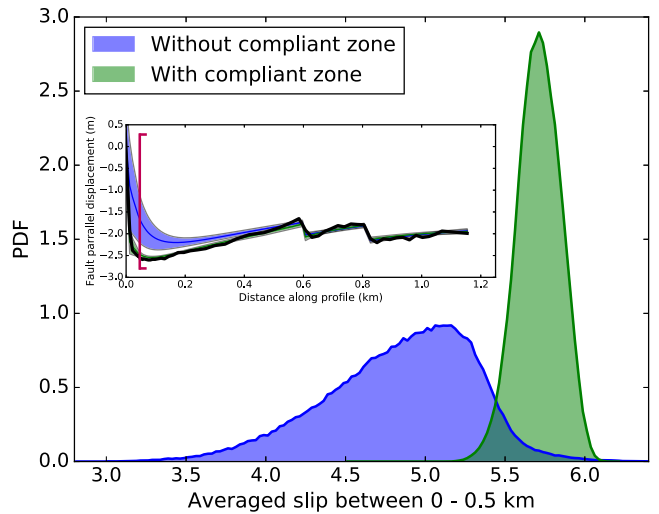


Figure 11. Comparison between shallow slip posterior PDFs assuming an homogeneous half-space (in blue) and accounting for a damage zone of reduced stiffness (in green). The inset shows stochastic predictions for both inversions. Observations are plotted as a thin black line. Blue results are inferred without the data inside the brackets in Fig. 8(c) and green results without the data inside the red brackets at ± 65 m

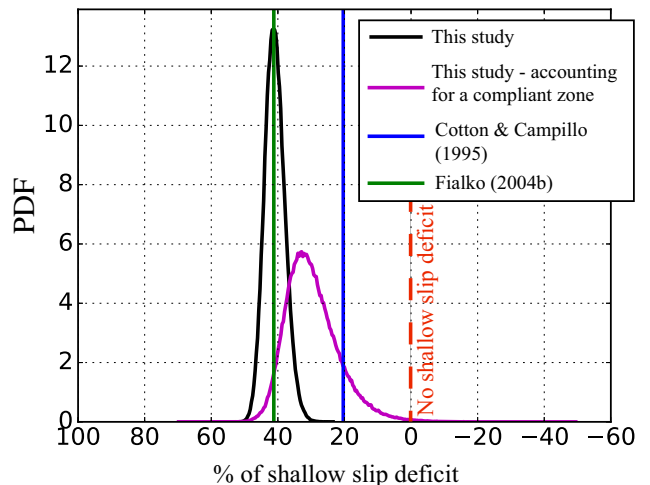


Figure 12. Overall shallow slip deficit (SSD). The black PDF indicate the SSD for the overall rupture presented in Fig. 4. The purple PDF is the SSD corrected from the effect of the damage zone with reduced stiffness. Blue and green vertical lines are the SSD for two published models (Cotton & Campillo 1995; Fialko 2004b).

model. The predictions from our solution agree well with various observations.

Consistent with previous studies, our solution indicates a substantial shallow slip deficit that is particularly pronounced for the Homestead Valley Fault. We argue that part of this deficit results from unmodelled lateral heterogeneities in shear modulus, corresponding to a damage zone surrounding the fault. Using high resolution optical correlation images, we highlight a ~ 1 km wide damage zone on the Emerson Valley Fault responsible for an apparent reduction in shallow slip by a factor ~ 1.2 . Our results also show the presence of secondary ruptures with significant slip amplitudes at shallow depth. By reducing the elastic strain on the main fault, these features also contribute to the apparent slip deficit budget.

Although we do not include data in the immediate vicinity of the fault where inelastic behaviour is commonly observed, we cannot

rule out that some wide plastic deformation is included in our inversion and participates in the observed deficit. Following the same procedure, other near-field displacement data of large strike-slip earthquakes could provide new insights on fault zone properties and their link to co-seismic slip distribution.

ACKNOWLEDGEMENTS

We are grateful to J.P. Avouac and F. Ayoub for providing the optical images correlation observations. We also thank Y. Fialko for sending us his co-seismic slip model. This study contributed from fruitful discussions with Sarah Minson, Lijun Zhu, Michael Aivazis and Gilles Peltzer. Some GPUs used for this research were donated by the NVIDIA Corporation. This work was supported by the Initiative d'Excellence (IDEX) funding framework (Université de Strasbourg) and the CNRS PICS program (Zacharie Duputel). This work was also funded by NSF grant 1447107 awarded to Mark Simons. We thank the Editor, Martin Mai, and two anonymous reviewers for their constructive comments, which helped improve this manuscript.

REFERENCES

- Amitrano, D., 2006. Rupture by damage accumulation in rocks, *Int. J. Fract.*, **139**(3), 369–381.
- Ayoub, F., Leprince, S. & Avouac, J.-P., 2009. Co-registration and correlation of aerial photographs for ground deformation measurements, *ISPRS J. Photogramm. Remote Sens.*, **64**(6), 551–560.
- Barbot, S., Fialko, Y. & Sandwell, D., 2008. Effect of a compliant fault zone on the inferred earthquake slip distribution, *J. geophys. Res.*, **113**(B6), B06404, doi:10.1029/2007JB005256.
- Ben-Zion, Y. & Sammis, C.G., 2003. Characterization of fault zones, in *Seismic Motion, Lithospheric Structures, Earthquake and Volcanic Sources: The Keiiti Aki Volume*, pp. 677–715, Springer.
- Chester, F.M. & Chester, J.S., 1998. Ultracataclasite structure and friction processes of the Punchbowl fault, San Andreas system, California, *Tectonophysics*, **295**(1), 199–221.
- Chester, F.M., Evans, J.P. & Biegel, R.L., 1993. Internal structure and weakening mechanisms of the San Andreas fault, *J. geophys. Res.*, **98**(B1), 771–786.
- Cohee, B.P. & Beroza, G.C., 1994. Slip distribution of the 1992 Landers earthquake and its implications for earthquake source mechanics, *Bull. seism. Soc. Am.*, **84**(3), 692–712.
- Cotton, F. & Campillo, M., 1995. Frequency domain inversion of strong motions: application to the 1992 Landers earthquake, *J. geophys. Res.*, **100**(B3), 3961–3975.
- Dahlen, F. & Tromp, J., 1998. *Theoretical Global Seismology*, Princeton University Press.
- Dieterich, J.H. & Smith, D.E., 2009. Nonplanar faults: Mechanics of slip and off-fault damage, *Pure appl. Geophys.*, **166**(10–11), 1799–1815.
- Dor, O., Ben-Zion, Y., Rockwell, T.K. & Brune, J., 2006. Pulverized rocks in the Mojave section of the San Andreas Fault Zone, *Earth planet. Sci. Lett.*, **245**(3), 642–654.
- Duputel, Z., Agram, P.S., Simons, M., Minson, S.E. & Beck, J.L., 2014. Accounting for prediction uncertainty when inferring subsurface fault slip, *Geophys. J. Int.*, **197**(1), 464–482.
- Fialko, Y., 2004a. Evidence of fluid-filled upper crust from observations of postseismic deformation due to the 1992 Mw 7.3 Landers earthquake, *J. geophys. Res.*, **109**(B8), B08401, doi:10.1029/2004JB002985.
- Fialko, Y., 2004b. Probing the mechanical properties of seismically active crust with space geodesy: study of the coseismic deformation due to the 1992 M_w 7.3 Landers (southern California) earthquake, *J. geophys. Res.*, **109**(B3), B03307, doi:10.1029/2003JB002756.
- Fialko, Y., Sandwell, D., Simons, M. & Rosen, P., 2005. Three-dimensional deformation caused by the Bam, Iran, earthquake and the origin of shallow slip deficit, *Nature*, **435**(7040), 295–299.
- Freymueller, J., King, N. & Segall, P., 1994. The co-seismic slip distribution of the Landers earthquake, *Bull. seism. Soc. Am.*, **84**(3), 646–659.
- Hansen, P.C., 1998. *Rank-deficient and Discrete Ill-posed Problems: Numerical Aspects of Linear Inversion*, SIAM.
- Hartzell, S.H. & Heaton, T.H., 1983. Inversion of strong ground motion and telesismic waveform data for the fault rupture history of the 1979 Imperial Valley, California, earthquake, *Bull. seism. Soc. Am.*, **73**(6A), 1553–1583.
- Hauksson, E., Yang, W. & Shearer, P.M., 2012. Waveform relocated earthquake catalog for southern California (1981 to June 2011), *Bull. seism. Soc. Am.*, **102**(5), 2239–2244.
- Hernandez, B., Cotton, F. & Campillo, M., 1999. Contribution of radar interferometry to a two-step inversion of the kinematic process of the 1992 Landers earthquake, *J. geophys. Res.*, **104**(B6), 13 083–13 099.
- Hudnut, K.W. et al., 1994. Co-seismic displacements of the 1992 Landers earthquake sequence, *Bull. seism. Soc. Am.*, **84**(3), 625–645.
- Jolivet, R. et al., 2014. The 2013 Mw 7.7 Balochistan earthquake: seismic potential of an accretionary wedge, *Bull. seism. Soc. Am.*, **104**(2), 1020–1030.
- Kaneko, Y. & Fialko, Y., 2011. Shallow slip deficit due to large strike-slip earthquakes in dynamic rupture simulations with elasto-plastic off-fault response, *Geophys. J. Int.*, **186**(3), 1389–1403.
- Kohler, M., Magistrale, H. & Clayton, R., 2003. Mantle heterogeneities and the SCEC reference three-dimensional seismic velocity model version 3, *Bull. seism. Soc. Am.*, **93**(2), 757–774.
- Lewis, M.A. & Ben-Zion, Y., 2010. Diversity of fault zone damage and trapping structures in the Parkfield section of the San Andreas Fault from comprehensive analysis of near fault seismograms, *Geophys. J. Int.*, **183**(3), 1579–1595.
- Li, H., Zhu, L. & Yang, H., 2007. High-resolution structures of the Landers fault zone inferred from aftershock waveform data, *Geophys. J. Int.*, **171**(3), 1295–1307.
- Li, Y.-G., Vidale, J.E., Aki, K., Marone, C.J. & Lee, W.H., 1994. Fine structure of the Landers fault zone: segmentation and the rupture process, *Science*, **265**, 367–367.
- Lohman, R.B. & Simons, M., 2005. Some thoughts on the use of InSAR data to constrain models of surface deformation: Noise structure and data downsampling, *Geochem. Geophys. Geosyst.*, **6**(1), Q01007, doi:10.1029/2004GC000841.
- Mai, P.M. et al., 2016. The earthquake-source inversion validation (SIV) project, *Seismol. Res. Lett.*, **87**(3), 690–708.
- McGill, S.F. & Rubin, C.M., 1999. Surficial slip distribution on the central Emerson fault during the June 28, 1992, Landers earthquake, California, *J. geophys. Res.*, **104**(B3), 4811–4833.
- Milliner, C.W., Dolan, J.F., Hollingsworth, J., Leprince, S., Ayoub, F. & Sammis, C.G., 2015. Quantifying near-field and off-fault deformation patterns of the 1992 Mw 7.3 Landers earthquake, *Geochem. Geophys. Geosyst.*, **16**(5), 1577–1598.
- Minson, S., Simons, M. & Beck, J., 2013. Bayesian inversion for finite fault earthquake source models I—Theory and algorithm, *Geophys. J. Int.*, **194**(3), 1701–1726.
- Mitchell, T. & Faulkner, D., 2009. The nature and origin of off-fault damage surrounding strike-slip fault zones with a wide range of displacements: a field study from the Atacama fault system, northern Chile, *J. Struct. Geol.*, **31**(8), 802–816.
- Murray, M., Savage, J., Lisowski, M. & Gross, W., 1993. Coseismic displacements: 1992 Landers, California, earthquake, *Geophys. Res. Lett.*, **20**(7), 623–626.
- Olson, A.H. & Apsel, R.J., 1982. Finite faults and inverse theory with applications to the 1979 Imperial Valley earthquake, *Bull. seism. Soc. Am.*, **72**(6A), 1969–2001.
- Ortega, F., 2013. Aseismic Deformation in Subduction Megathrusts: Central Andes and North-East Japan, *PhD thesis*, California Institute of Technology.
- Peltzer, G., Rosen, P., Rogez, F. & Hudnut, K., 1998. Poroelastic rebound along the Landers 1992 earthquake surface rupture, *J. geophys. Res.*, **103**(B12), 30 131–30 145.
- Peng, Z., Ben-Zion, Y., Michael, A.J. & Zhu, L., 2003. Quantitative analysis of seismic fault zone waves in the rupture zone of the 1992 Landers,

- California, earthquake: evidence for a shallow trapping structure, *Geophys. J. Int.*, **155**(3), 1021–1041.
- Powers, P.M. & Jordan, T.H., 2010. Distribution of seismicity across strike-slip faults in California, *J. geophys. Res.*, **115**(B5), B05305, doi:10.1029/2008JB006234.
- Rosen, P.A., Hensley, S., Peltzer, G. & Simons, M., 2004. Updated repeat orbit interferometry package released, *EOS, Trans. Am. geophys. Un.*, **85**(5), 47.
- Savage, J.C. & Svart, J.L., 1997. Postseismic deformation associated with the 1992 $M_w=7.3$ Landers earthquake, southern California, *J. geophys. Res.*, **102**(B4), 7565–7577.
- Segall, P., 2010. *Earthquake and Volcano Deformation*, Princeton University Press.
- Segall, P. & Harris, R., 1987. Earthquake deformation cycle on the San Andreas Fault near Parkfield, California, *J. geophys. Res.*, **92**(B10), 10 511–10 525.
- Segall, P. & Pollard, D., 1980. Mechanics of discontinuous faults, *J. geophys. Res.*, **85**(B8), 4337–4350.
- Shen, Z.-K., Jackson, D.D., Feng, Y., Cline, M., Kim, M., Fang, P. & Bock, Y., 1994. Postseismic deformation following the Landers earthquake, California, 28 June 1992, *Bull. seism. Soc. Am.*, **84**(3), 780–791.
- Sieh, K. et al., 1993. Near-field investigations of the Landers earthquake sequence, April to July 1992, *Science*, **260**, 171–176.
- Simons, M., Fialko, Y. & Rivera, L., 2002. Coseismic deformation from the 1999 $M_w 7.1$ Hector Mine, California, earthquake as inferred from InSAR and GPS observations, *Bull. seism. Soc. Am.*, **92**(4), 1390–1402.
- Tarantola, A., 2005. *Inverse Problem Theory and Methods for Model Parameter Estimation*, SIAM.
- Thomas, M.Y., Bhat, H.S. & Klinger, Y., 2017. Effect of Brittle Off-Fault Damage on Earthquake Rupture Dynamics, in *Fault Zone Dynamic Processes: Evolution of Fault Properties During Seismic Rupture*, vol. 227, p. 255, eds Thomas, M. Y., Mitchell, T. M. & Bhat, H. S., John Wiley & Sons, Inc.
- Tse, S.T. & Rice, J.R., 1986. Crustal earthquake instability in relation to the depth variation of frictional slip properties, *J. geophys. Res.*, **91**(B9), 9452–9472.
- Vallage, A., Klinger, Y., Grandin, R., Bhat, H. & Pierrot-Deseilligny, M., 2015. Inelastic surface deformation during the 2013 $M_w 7.7$ Balochistan, Pakistan, earthquake, *Geology*, **43**(12), 1079–1082.
- Wald, D.J. & Heaton, T.H., 1994. Spatial and temporal distribution of slip for the 1992 Landers, California, earthquake, *Bull. seism. Soc. Am.*, **84**(3), 668–691.
- Xu, X., Tong, X., Sandwell, D.T., Milliner, C.W., Dolan, J.F., Hollingsworth, J., Leprince, S. & Ayoub, F., 2016. Refining the shallow slip deficit, *Geophys. J. Int.*, **204**(3), 1867–1886.
- Zeng, Y. & Anderson, J., 2000. Evaluation of numerical procedures for simulating near-fault long-period ground motions using Zeng method, Report 2000/01 to the PEER Utilities Program, available at <http://peer.berkeley.edu>.
- Zhu, L. & Rivera, L.A., 2002. A note on the dynamic and static displacements from a point source in multilayered media, *Geophys. J. Int.*, **148**(3), 619–627.
- Zigone, D., Ben-Zion, Y., Campillo, M. & Roux, P., 2015. Seismic tomography of the Southern California plate boundary region from noise-based Rayleigh and Love waves, *Pure appl. Geophys.*, **172**(5), 1007–1032.

SUPPORTING INFORMATION

Supplementary data are available at [GJI](#) online.

Supporting text T1: Modelling errors due to fault parameterization

Supporting Text T2: Maximum a posteriori model

Supporting text T3: Model prediction for long period seismological data

Figure S1. Decimated InSAR images. (a, d) Decimated InSAR observations used in the inversion. (b, e) Predictions for the posterior

mean model. (c, f) InSAR residuals of the descending (top) and ascending (bottom) tracks.

Figure S2. Empirical covariance functions for the InSAR observations: 1D empirical covariance functions and the associated best-fit exponential function for the descending (left) and ascending (right) tracks. For each image, we compute the empirical covariance as a function of the distance between pixels and then fit an exponential function to these covariances (Jolivet et al., 2012). This exponential function is then used to build the data covariance matrix used in the inversion.

Figure S3. Effect of geometry on forward modelling. (a) Forward model predictions for the one of the optical images mosaic imposing 4.1 m of slip on a shallow fault with 300 m long patches. (b) same as (a) but with a broader geometry (1.5 km-long patches). (c) and (d) Difference between (a) and (b).

Figure S4. Problem resolution. For each slip component, we compute the Resolution matrix as $R = C_m G^T (GC_m G^T + C_\chi)^{-1} G \cdot C_m$ is a diagonal matrix constructed from our model a priori distribution standard deviation. The diagonal values are plotted on the fault. The closer to 1, the better is the resolution of the parameter.

Figure S5. Different models variability of the P-wave, S-wave, and density as a function of depth in the Landers area. Grey lines are model values of the 3D Community Velocity Model (CVM, Kohler et al. 2003) available at <http://scseedc.caltech.edu/research-tools/3d-velocity.html> (last accessed January 2016). The dashed black line represents the averaged CVM value for this area. A layered version used in this study for Green's function [GF] calculations is plotted as a solid black line. Models from Cotton & Campillo (1993), Wald & Heaton (1994), Hauksson (1993), and Jones and Helberger (1998) are plotted as solid green, dashed green, red, and blue lines, respectively. Grey histograms are the probability density function representing our confidence level on the elastic properties, as used to build the model prediction error. Histograms are derived from the averaged CVM assuming a Gaussian distribution.

Figure S6. Posterior mean co-seismic slip model. The color of each subfault patch indicates the slip amplitude. Arrows and their associated 95% confidence ellipse indicate the slip direction and uncertainty.

Figure S7. Comparison between posterior mean, maximum a posteriori and best fitting models. (a) Maximum a posteriori coseismic slip model. It is built by considering the maximum of each marginal PDF (cf., supporting text T2). The 10 patches where the slip is the most important are labelled in purple. (b) Best-fitting model sample. This model represents the sample in our population having the maximum posterior value (cf., supporting text T2). The colour of each subfault patch indicates the slip amplitude. Arrows and their associated 95% confidence ellipse indicate the slip direction and uncertainty. (c) Boxplot of the strike-slip within the 10 patches labelled in (a). Horizontal red lines show posterior mean values (Figure 5 in main text). Horizontal blue lines show the maximum a posteriori model (a), and horizontal green lines show the best fitting sample (b). Notice that the best fitting sample is a poor estimate of the MAP

Figure S8. The subfigure at the centre is the posterior mean coseismic slip models for an alternative “flower” geometry. The colour of each subfault patch indicates the slip amplitude. Arrows and their associated 95% confidence ellipse indicate the slip direction and uncertainty. The patches that slip the most in the vertical geometry are numbered from 1 to 10. We show the PDF of SSD as a black line on the bottom-right insert. The magenta line illustrates the SSD value when corrected from a compliant zone. On the same plots are

represented the SSD for two published models, Cotton & Campillo (1995) and Fialko (2004b). The histograms on the sides show the strikeslip PDF of the 10 patches that are labelled on the finite-fault model for both the vertical and flower geometries. The percentage of which the two PDFs overlap is given on the top-left corner of each histograms.

Figure S9. Posterior covariance of two along-dip patches of the Homestead Valley segment and the Homestead Valley Camp Rock segments junction. (a) Homestead Valley and (b) Homestead Valley Camp Rock junction posterior mean coseismic slip. In each one of the two segments, the across-patch correlation is computed for the two coloured patches. (c) Joint posterior PDF of the strike-slip component of the two coloured patches in (a), also labelled 1 and 2. (d) Same as (c), but for the two coloured patches in (b) (labelled 3 and 4). For both (c) and (d), dots are model samples that are coloured according to the PDF value. Blue histograms are marginal PDFs for both parameters.

Figure S10. Red dots indicate the posterior ensemble of centroid locations derived from our solution. The red focal mechanism is the moment tensor computed from our posterior mean model. The blue and yellow focal mechanisms come from the Global CMT (Ekström et al., 2012) and W-Phase (Duputel et al. 2012) catalogues, respectively.

Figure S11. Broadband seismograms (black line) and synthetics computed from the posterior mean model moment tensor (red line) are plotted for 5 stations along with their locations. On each map, the blue star and the red dot indicate the hypocenter and station locations, respectively. For each trace is indicated the station azimuth φ and epicentral distance Δ .

Figure S12. Figure S9 continued. Broadband seismograms (black line) and synthetics computed from the posterior mean model moment tensor (red line) are plotted for 5 stations along with their locations. On each map, the blue star and the red dot indicate the hypocenter and station locations, respectively. For each trace is indicated the station azimuth φ and epicentral distance Δ .

Figure S13. Comparison of SSD values. The thick black line is the probability density of SSD values for this study. Vertical coloured lines represent the SSD values of 6 published models.

Figure S14. Posterior slip uncertainties for (a) the solution obtained by inverting all datasets and (b) the solution obtained by inverting all the datasets minus the optical correlation mosaic.

Figure S15. Impact of smoothing constraints on the shallow slip deficit (SSD). (a) SSD value of models obtained by a least-square inversion as a function of the damping parameter ϵ (see equation 5 in the main text). Red dots indicate the models shown in (c) to (g). The horizontal dashed line marks the mean SSD value of our stochastic solution, and the grey shaded area represent the $1-\sigma$ deviation. (b) L-curve of the regularized models. Dots colour indicates the damping value. The red rectangle shows the extent of the top-right inset. The position of the models (c-h) is indicated with their damping value. (c)-(h) Least-square models for six different damping values.

Figure S16. Results of the Metropolis sampling of the aftershock density profile parameters v_0 , d and γ . 1D plots are posterior marginal PDFs and 2D plots are posterior joint PDFs. On the 2D histograms dots are model samples that are coloured according to the PDF value. Hot colours indicate region of high-probability.

Figure S17. Modeling of Near-field deformation data. (a) Localization of the profiles in the optical correlation observations. (b) Close up view of near-field data. Grey rectangle indicate the location of the inverted profile. (c) Comparison between observed displacement (in red) and the stochastic predictions (in grey). Data inside the black brackets are not used in the inversion of the full 3D slip distribution presented in Figure 6 of the main manuscript.

Figure S18. Posterior joint probability distribution of the compliant zone half-width and shear modulus ratio for the profile presented in Figure S12. Dots are model samples that are coloured according to the PDF value. Blue histograms are marginal PDFs for both parameters. Red lines are the prior information used in the sampling.

Table S1. Source parameters for 3 solutions. Wphase (Duputel et al., 2012), Global CMT (Ekström, 2012), and this study.

Table S2. Summary of fault geometries and datasets used in this study and in previously published models, and associated SSD values. In the InSAR column, the number in parentheses is the number of interferograms used.

Please note: Oxford University Press is not responsible for the content or functionality of any supporting materials supplied by the authors. Any queries (other than missing material) should be directed to the corresponding author for the paper.

3.4 Budget de déformation le long de la subduction équatorienne

Pendant longtemps, notre vision des failles consistait en l'existence de segments de faille bloqués persistants au cours du temps et rompant répétitivement lors de séismes dits caractéristiques (Shimazaki and Nakata, 1980 ; Schwartz and Coppersmith, 1984). La subduction équatorienne est un contre-exemple remarquable montrant une séquence de séismes beaucoup plus complexe que suggéré par ce paradigme. La séquence a débuté en 1906 avec un grand séisme de magnitude $M_W = 8.6$ qui a rompu l'interface de subduction sur une distance d'environ 500 km. La même région a ensuite été remobilisée par une série de séismes plus petits en 1942, 1958, 1979, 1998 et en 2016. Etant donné le regroupement temporel entre ces différents événements, il a été suggéré que le moment cumulé généré co-sismiquement dans cette région excédait le déficit de moment accumulé depuis 1906 (Nocquet et al., 2017). Un tel excès remet en question les modèles simplistes considérant que les tremblements de terre réinitialisent la contrainte élastique accumulée entre les séismes dans des aspérités bloquées. Cette conclusion repose cependant sur des modèles co-sismiques et inter-sismiques associés à de fortes incertitudes qui ne sont généralement pas quantifiées. Dans l'étude présentée ci-dessous, nous produisons un modèle cinématique du séisme de Pedernales en 2016 ainsi qu'un modèle du couplage de l'interface de subduction. Notre analyse montre qu'un excès de moment co-sismique ne peut être démontré que si les séismes de Pedernales en 1942 et 2016 sont co-localisés. En relachant cette hypothèse, nous montrons que cette conclusion n'est plus possible étant donné les incertitudes estimées *a posteriori*. Nos résultats montrent également que cette région est associée à un couplage extrêmement hétérogène, avec des aspérités co-localisées aux grands séismes dans la région. Cette variabilité spatiale et l'histoire sismique complexe de la région démontre l'existence de fortes hétérogénéités dans les propriétés frictionnelles de l'interface de subduction équatorienne.

L'article proposé ci-dessous a été publié en 2018 dans *Earth and Planetary Science Letters*. Ce travail a été effectué dans le cadre du doctorat de Baptiste Gombert (thèse soutenue en Mars 2018).



Strain budget of the Ecuador–Colombia subduction zone: A stochastic view



B. Gombert^{a,*}, Z. Duputel^a, R. Jolivet^b, M. Simons^c, J. Jiang^d, C. Liang^e, E.J. Fielding^e, L. Rivera^a

^a Institut de Physique du Globe de Strasbourg, UMR7516, Université de Strasbourg, EOST/CNRS, France

^b Laboratoire de géologie, Département de Géosciences, École Normale Supérieure, PSL Research University, CNRS UMR 8538, Paris, France

^c Seismological Laboratory, Geological and Planetary Sciences, California Institute of Technology, Pasadena, CA, USA

^d Institute of Geophysics and Planetary Physics, University of California, San Diego, La Jolla, CA, USA

^e Jet Propulsion Laboratory, California Institute of Technology, Pasadena, CA, USA

ARTICLE INFO

Article history:

Received 6 April 2018

Received in revised form 15 June 2018

Accepted 29 June 2018

Available online 20 July 2018

Editor: J.-P. Avouac

Keywords:

Ecuador–Colombia subduction zone

strain budget

bayesian inversion

kinematic source model

geodetic coupling model

ABSTRACT

The 2016 Pedernales earthquake ($M_W = 7.8$) ruptured a portion of the Colombia–Ecuador subduction interface where several large historical earthquakes have been documented since the great 1906 earthquake ($M = 8.6$). Considering all significant ruptures that occurred in the region, it has been suggested that the cumulative moment generated co-seismically along this part of the subduction over the last century exceeds the moment deficit accumulated inter-seismically since 1906. Such an excess challenges simple models with earthquakes resetting the elastic strain accumulated inter-seismically in locked asperities. These inferences are however associated with large uncertainties that are generally unknown. The impact of spatial smoothing constraints on co-seismic and inter-seismic models also prevents any robust assessment of the strain budget. We propose a Bayesian kinematic slip model of the 2016 Pedernales earthquake using the most comprehensive dataset to date including InSAR and GPS offsets, tsunami waveforms, and kinematic records from high-rate GPS and strong-motion. In addition, we use inter-seismic geodetic velocities to produce a probabilistic inter-seismic coupling model of the subduction interface. Our stochastic co-seismic and inter-seismic solutions include the ensemble of all plausible models consistent with our prior information and that fit the observations within uncertainties. The analysis of these model ensembles indicates that an excess of co-seismic moment during the 1906–2016 period is likely in Central Ecuador only if we assume that 1942 and 2016 earthquakes are collocated. If this assumption is relaxed, we show that this conclusion no longer holds given uncertainties in co- and inter-seismic processes. The comparison of 1942 and 2016 teleseismic records reveals large uncertainties in the location of the 1942 event, hampering our ability to draw strong conclusions on the unbalanced moment budget in the region. Our results also show a heterogeneous coupling of the subduction interface that coincides with two slip asperities in our co-seismic model for the 2016 Pedernales earthquake and with the location of historical ruptures in 1958, 1979 and 1998. The spatial variability in coupling and complexity in earthquake history suggest strong heterogeneities in frictional properties of the subduction megathrust.

© 2018 Elsevier B.V. All rights reserved.

1. Introduction

A long standing question is the existence of persistent fault segments remaining locked in the inter-seismic period and failing suddenly during earthquakes while the surrounding interface creeps continuously. This conceptual model predicts so-called “character-

istic” earthquakes repeatedly rupturing the same locked fault segments with either periodic, time-predictable or slip-predictable behaviors (Shimazaki and Nakata, 1980; Schwartz and Coppersmith, 1984). This paradigm is contradicted by an increasing number of observations showing that the same fault area can break entirely in a single large earthquake ($M_W > 8.5$) but also in a series of smaller ruptures. A remarkable example of such behavior is the Colombia–Ecuador subduction zone that experienced a complex sequence of earthquakes since the beginning of the 20th century (see Fig. 1). In 1906, the great $M_W = 8.6$ earthquake ruptured a $\sim 500\text{-km}$ -

* Corresponding author.

E-mail address: gombert@unistra.fr (B. Gombert).

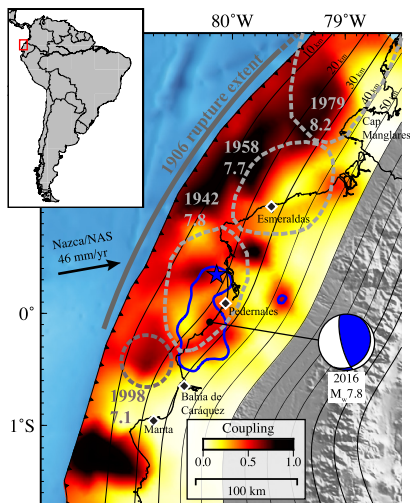


Fig. 1. Interseismic coupling and historical earthquakes. The color scale indicates the geodetic coupling of the subduction interface obtained from inter-seismic GPS velocities (cf. section 2). Blue line and blue star are respectively the 2 m isocontours of co-seismic slip and hypocenter obtained for the 2016 Pedernales earthquake (cf. section 3). Grey dashed lines show the approximate extent of the 1942, 1958, 1979, and 1998 events (Kanamori and McNally, 1982; Chlieh et al., 2014). The location of these previous ruptures is still debated, and some alternative plausible locations are shown in Fig. 10 and S9. The thick gray line shows the along-strike extent of the 1906 $M_W = 8.6$ earthquake. The focal mechanism of the 2016 Pedernales earthquake is presented in blue. Thin black lines are isocontours of the slab depth. The line with the adjacent black triangles shows the location of the trench. The black arrow illustrates the convergence direction of the Nazca plate toward the North Andean Silver plate (NAS, Chlieh et al., 2014). (For interpretation of the colors in the figure(s), the reader is referred to the web version of this article.)

long segment of the subduction interface (Gutenberg and Richter, 1949; Ye et al., 2016). Several decades later, the same area was re-ruptured by a series of smaller $M_W \leq 8.2$ events in 1942, 1958, 1979 and 1998 (Kanamori and McNally, 1982; Beck and Ruff, 1984; Mendoza and Dewey, 1984; Chlieh et al., 2014). In April 2016, the region in the vicinity of the 1942 Ecuador event was again ruptured by the $M_W = 7.8$ Pedernales earthquake (Ye et al., 2016; He et al., 2017; Nocquet et al., 2017; Yi et al., 2018). Such variability among successive ruptures is also observed in other regions like Japan and Sumatra where recent $M_W \sim 9$ megathrust earthquakes ruptured large fault segments that previously experienced a series of smaller events (Simons et al., 2011; Lay, 2015).

In addition to such spatial variability among successive ruptures, major earthquakes in the Colombia–Ecuador subduction zone seem to be clustered in time. Specifically, it has been recently suggested that the seismic moment of the 1942, 1958 and 1979 earthquakes exceeds the deficit accumulated since 1906 and that the 2016 Pedernales event may be associated with more fault slip than the deficit accumulated since the 1942 earthquake (Nocquet et al., 2017). Similar observations are reported in other regions, for example in 1797 and 1833 earthquakes in Sumatra (Sieh et al., 2008), 1812 and 1857 earthquakes in California (Jacoby et al., 1988; Heaton, 1990), and for the 2003 $M_W = 7.6$ and 2013 $M_W = 7.8$ Scotia sea earthquakes (Vallée and Satriano, 2014). Such spatial and temporal clustering can be caused by spatial variations of fault coupling associated with heterogeneous frictional properties (Kaneko et al., 2010). Moreover, there can be fluctuations in the patterns of inter-seismic fault coupling before large earthquakes (Perfettini and Avouac, 2004; Mavrommatis et al., 2014; Yokota and Koketsu, 2015) or during the post-seismic response of nearby large earthquakes (Heki and Mitsui, 2013; Melnick et al., 2017).

Although the existence of an anomalously large co-seismic slip associated with a supercycle behavior is plausible, other studies suggest that the seismic moment of the 2016 Pedernales earth-

quake is actually consistent with the strain accumulated in the region since the 1942 and 1906 earthquakes (e.g., Ye et al., 2016; Yoshimoto et al., 2017; Yi et al., 2018). These contrasting statements partly result from the ill-posed nature of inter- and co-seismic slip inversions used to evaluate the strain budget along the megathrust. Such inferences are affected by the lack of resolution near the trench during the inter-seismic period but also by non-physics-based smoothing constraints used to regularize slip inversions. In addition, inter- and co-seismic estimates usually do not incorporate rigorous uncertainties (or very often, no uncertainty at all), which complicates a quantitative assessment of the overall strain budget. Strain budget analyses also suffer from the lack of information about past earthquakes (Yi et al., 2018). Incorrect considerations on the size and position of historical events can strongly affect the conclusion on the strain state of the plate boundary.

We propose a probabilistic exploration of the Colombia–Ecuador earthquake sequence, fully accounting for uncertainties, including measurement errors, modeling errors, but also uncertainties in the location or magnitude of past events. Using a Bayesian framework, we explore both the inter-seismic geodetic coupling of the subduction interface and the co-seismic slip distribution of the $M_W = 7.8$ Pedernales earthquake. These estimates do not rely on any spatial smoothing and provide full posterior probability distributions describing the ensemble of plausible models that fit the observations and are consistent with simple prior constraints (e.g., slip positivity in the direction of convergence).

2. Geodetic coupling

2.1. Stochastic inter-seismic modeling

We first compute a stochastic model of geodetic coupling along the Ecuadorian subduction interface. We use inter-seismic GPS velocities computed by Chlieh et al. (2014) and Nocquet et al. (2014) from 29 stations installed in Ecuador and Colombia and measured from 1994 to 2012 (Mothes et al., 2018; Mora-Páez et al., 2018). Considering that more than 20 years separate the 1979 earthquake and the first GPS measurements, it is unlikely that they are significantly affected by post-seismic deformation. The 1998 earthquake having a smaller magnitude, its impact on the data is also probably minimal. The fault geometry is based on a 3D surface following the Slab1.0 interface and discretized in triangles (cf. Fig. S1 in the electronic supplements). Using a back-slip approach (Savage, 1983), we invert for the inter-seismic slip rate along the direction of convergence between Nazca and North Andean Silver (NAS) plates at each of the triangle knots assuming a barycentric interpolation scheme within the triangles. This approach avoids unphysical slip discontinuities associated with traditional parameterizations based on sub-faults with piecewise constant slip (Ortega Culaciati, 2013).

In our Bayesian inversion framework, the solution is the posterior ensemble of all plausible inter-seismic slip rate models ($\mathbf{m}_{\mathcal{I}}$) that fit the GPS data ($\mathbf{d}_{\mathcal{I}}$) and that are consistent with our prior hypotheses. This solution does not rely on any smoothing regularization and is based on a simple uniform prior for the inter-seismic slip-rate that writes $p(\mathbf{m}_{\mathcal{I}}) = \mathcal{U}(-0.05 \cdot V_p, 1.05 \cdot V_p)^M$ where V_p is the plate rate and M is the number of triangle knots (260 knots). We thus restrict our posterior PDF to models in which slip on the fault aligns with the direction of plate motion. Following Bayes' theorem, the posterior PDF is given by

$$p(\mathbf{m}_{\mathcal{I}} | \mathbf{d}_{\mathcal{I}}) \propto p(\mathbf{m}_{\mathcal{I}}) \exp \left[-\frac{1}{2} (\mathbf{d}_{\mathcal{I}} - \mathbf{G}_{\mathcal{I}} \mathbf{m}_{\mathcal{I}})^T \mathbf{C}_{\mathcal{I}}^{-1} (\mathbf{d}_{\mathcal{I}} - \mathbf{G}_{\mathcal{I}} \mathbf{m}_{\mathcal{I}}) \right] \quad (1)$$

where $\mathbf{G}_{\mathcal{I}}$ is the Green's function matrix and $\mathbf{C}_{\mathcal{I}}$ is the misfit covariance matrix combining observational errors and prediction

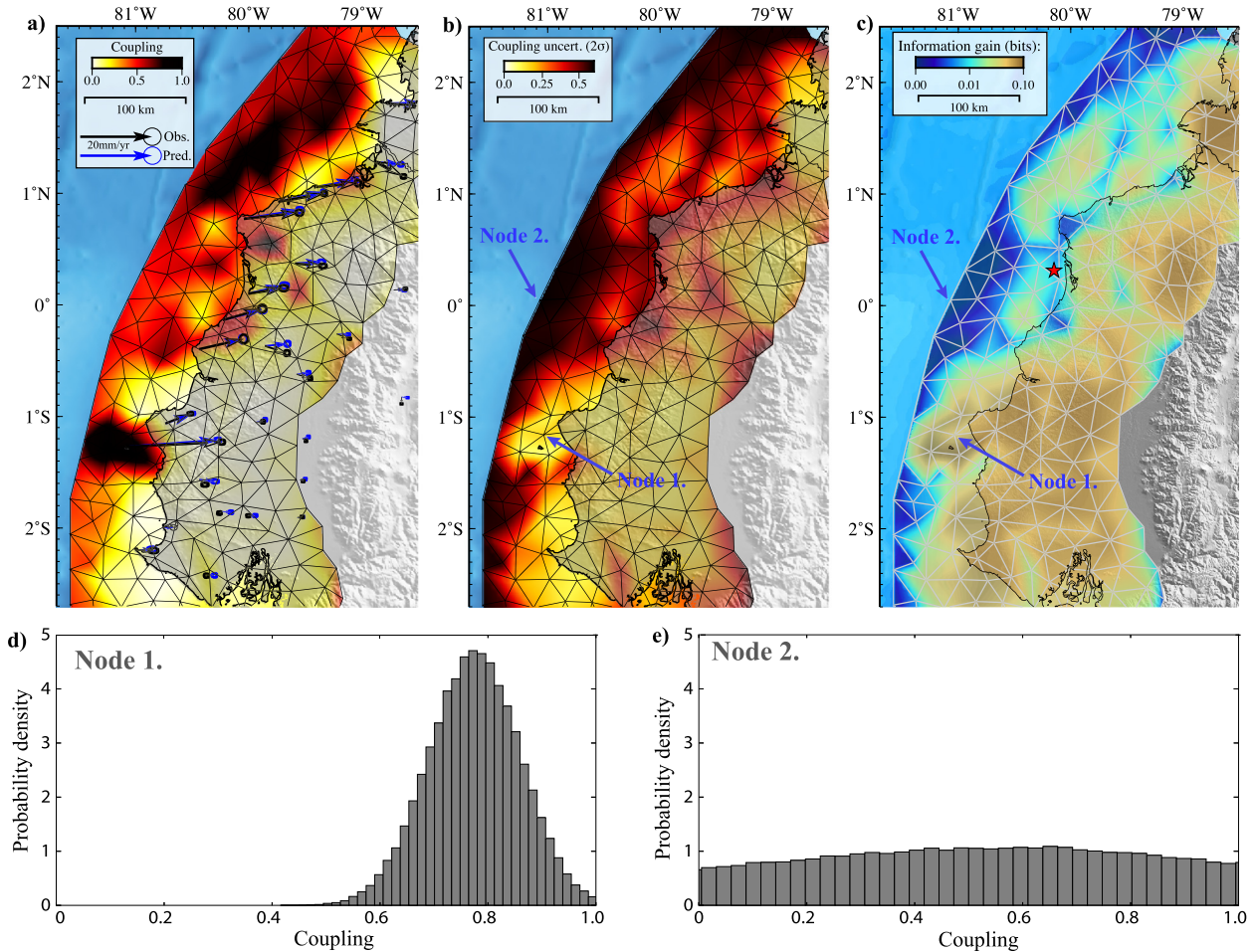


Fig. 2. Interseismic coupling of the Ecuadorian subduction margin. a) Posterior mean coupling model. Thin black lines represent the fault parametrization. Coupling values are inverted at each triangle knot. Interseismic GPS displacement and model predictions are plotted as black and blue arrows, respectively. b) 2σ uncertainties of the coupling model. c) Kullback–Leibler divergence between the posterior and prior PDFs of coupling. Higher values indicate regions where the gain of information of the posterior PDF is significant relative to the prior distribution. d) and e) Marginal probability densities for the two nodes pointed out in b) and c).

uncertainties. Green's functions are computed for a semi-infinite stratified elastic medium derived from regional velocity models shown in Fig. S2 (Béthoux et al., 2011; Vallee et al., 2013; Nocquet et al., 2017). We account for prediction uncertainties due to inaccuracies in this layered model using the approach of Duputel et al. (2012, 2014). The uncertainty on the elastic structure, presented as grey histograms in Fig. S2, is estimated by comparing previously published models in the region.

We sample the posterior PDF $p(\mathbf{m}_{\mathcal{I}} | \mathbf{d}_{\mathcal{I}})$ using Altar, a parallel Markov Chain Monte Carlo (MCMC) algorithm following the CATMIP algorithm (Minson et al., 2013). More details on the application of Altar to investigate inter-seismic deformations can be found in Jolivet et al. (2015b) and Klein et al. (2017). The resulting posterior ensemble of slip-rate models in eq. (1) is then converted into stochastic coupling maps (\mathbf{m}_C) using $\mathbf{m}_C = 1 - \mathbf{m}_{\mathcal{I}}/V_p$.

2.2. Geodetic coupling results

Using our Bayesian framework, we generate 160 000 models corresponding to the posterior information on geodetic coupling given measured inter-seismic velocities. We find that this number is large enough to converge toward the posterior probability density. Representing the ensemble of posterior models is challenging for multidimensional problems such as those addressed in this study. To represent an ensemble solution, a common choice is to compute the posterior mean (i.e., the average of all model samples). The posterior mean coupling model is shown in Fig. 1

and Fig. 2a along with the associated 2σ posterior uncertainties in Fig. 2b. The posterior median model available in Fig. S3 is very similar to the posterior mean, confirming that most marginal PDFs are nearly Gaussians. The variability of the model population composing the solution is shown in supplementary movie M1.

Several features in our solution can be observed in previously published geodetic coupling models (e.g., Nocquet et al., 2014; Chlieh et al., 2014). In the South, there is a very clear high-coupling area offshore the Manta peninsula. This inter-seismically highly coupled region has been previously associated with transient slow-slip events (Vallee et al., 2013; Nocquet et al., 2014). As shown in Fig. 2a and Fig. 2e, this area is associated with small model uncertainties probably because a GPS station is located on La Plata Island, right above the coupled asperity. This coupled patch is bounded to the north by a low-coupling corridor that might have acted as a creeping barrier for the 1906, 1942, 1998 and 2016 earthquakes (cf. Fig. 1; Chlieh et al., 2014).

North of Bahía de Caráquez, we infer multiple patches of high geodetic coupling. Other coupled patches can be identified offshore of Bahía de Caráquez, North and South of Pedernales, and far offshore Esmeraldas. To first order, such heterogeneity is consistent with the “unsmoothed” solution of Chlieh et al. (2014). This is unsurprising since our modeling approach is not affected by any prior-induced spatial smoothing. The high coupling asperity directly offshore of Bahía de Caráquez probably ruptured individually during the 1998 $M_W = 7.2$ earthquake while the coupled

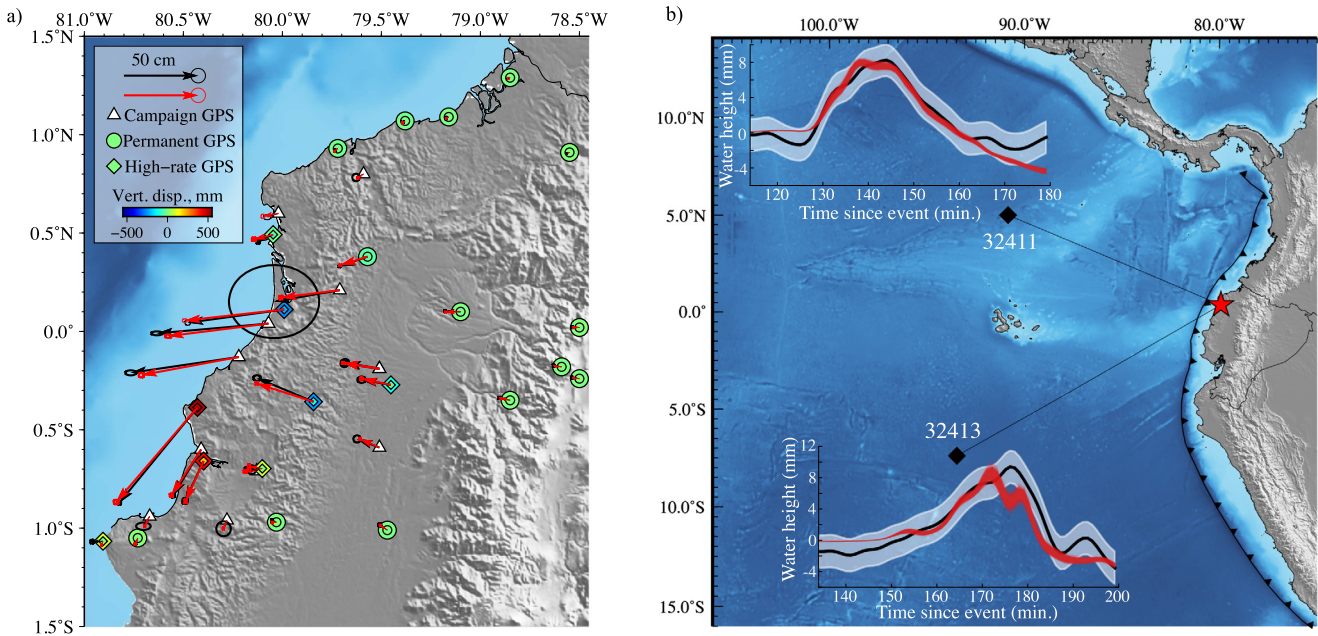


Fig. 3. GPS and tsunami observations used in this study. **a)** GPS data and model predictions. Black and red arrows show observed and predicted GPS horizontal displacements along with their 95%-confidence ellipses (representing observational and prediction uncertainties, respectively). For the permanent and High-rate GPS, the symbol color represents the vertical displacement. The outer symbol is the observation while the inner symbol is the mean model prediction. **b)** Observed and predicted tsunami waveforms. The red star defines the event epicenter while black diamonds are the locations of the two DART buoys that recorded the tsunami. For each of them, the amplitude of the first arrival is plotted as a thick black line. The surrounding shaded area marks the 2σ confidence interval. Stochastic forward model predictions are plotted in red.

areas closer to Pedernales could have failed during the 1942 and 2016 earthquake (Fig. 1). On the other hand, the large region of high coupling between Esmeraldas and Cap Manglares could be involved in the 1958 and 1979 ruptures (cf. Fig. 1).

However, we observe larger model uncertainties in this northern part due to the lack of offshore measurements (Fig. 2b). This is quite clear in Fig. 2e showing that marginal PDFs close to the trench are nearly uniform. Coupling uncertainties are also illustrated in the supplementary movie M1 showing that large variations in our model ensemble can fit the GPS observations equally well. To quantify the robustness of our coupling map, we calculate the information gain from prior to posterior marginal PDFs using the Kullback-Leibler divergence, defined as:

$$D_{KL}^i = \int p(m_C^i | \mathbf{d}_C) \log_2 \frac{p(m_C^i)}{p(m_C^i | \mathbf{d}_C)} dm_C^i \quad (2)$$

where m_C^i is the coupling sampled in i -th knot of the triangular mesh. The resulting map shown in Fig. 2c, indicates how much information is gained from the data in different regions of the model. It illustrates the difficulty to infer coupling properties close to the trench using land-based geodetic data. Still, the information gain remains significant within 30–40 km of the coast, and even sometimes almost up to the trench (e.g., offshore of the Manta peninsula and between Esmeraldas and Cap Manglares). This suggests that aforementioned asperities are reliable features of our solution. To evaluate the impact of the mesh size on our solution, we have conducted an inversion using a coarser fault discretization (cf. Fig. S4). Because the heterogeneities visible in Fig. 2 are also present for that coarse parameterization, we choose the finer one to get a better spatial resolution.

3. Rupture process of the 2016 Pedernales earthquake

3.1. Data overview

We use several geodetic datasets covering both near-field and far-field static displacements (cf. Fig. 3a). We gather GPS data from

12 campaign stations and 14 permanent stations with daily solutions (CGPS; Mothes et al., 2018), and 8 high-rate stations (HRGPS; Alvarado et al., 2018). Static offsets from campaign and permanent stations are provided by Nocquet et al. (2017). We estimate our own static displacements from HRGPS by measuring co-seismic offsets from the position before and after the event. We use 1σ errors provided by Nocquet et al. (2017) for the campaign and CGPS and estimate uncertainties for HRGPS offsets from the standard deviation measured in 20 seconds pre- and post-event time windows. Vertical components of campaign GPS are not used in the inversion as they show large uncertainties. In addition, we use three interferograms derived from ALOS-2 wide-swath descending acquisitions, from ALOS-2 strip-map ascending acquisitions and from Sentinel 1 descending acquisitions (cf. Fig. 4). Unwrapped interferograms are downsampled using a quad-tree algorithm (cf. Fig. S5; Lohman and Simons, 2005). We estimate uncertainties related to atmospheric noise by estimating empirical covariance functions for each interferogram (Jolivet et al., 2012, 2015a). Estimated parameters are summarized in Table S1 and covariance functions are available in Fig. S6.

Three nearby DART buoys (Deep-ocean Assessment and Reporting of Tsunamis) recorded the tsunami generated by this event. Unfortunately, the waveform recorded by the closest station (D32067) is unusable for modeling because of multiple data gaps and contamination by seismic waves. We use tsunami waveforms recorded at DART stations D32413 and D32411 (cf. Fig. 3b), as they provide important constraints on the up-dip part of the rupture. To remove tidal signals and reduce high-frequency noise, we band-pass filter the waveforms between 8 min and 3 hours using a third order Butterworth filter. We derive observational uncertainties from standard deviations computed in 140 and 100 min windows before the first arrivals respectively for buoys D32413 and D32411.

We also include near-field seismic waveforms recorded by 10 strong-motion accelerometers and 8 HRGPS stations (cf. Figs. 5 and 6; Alvarado et al., 2018). We integrate the accelerometric data

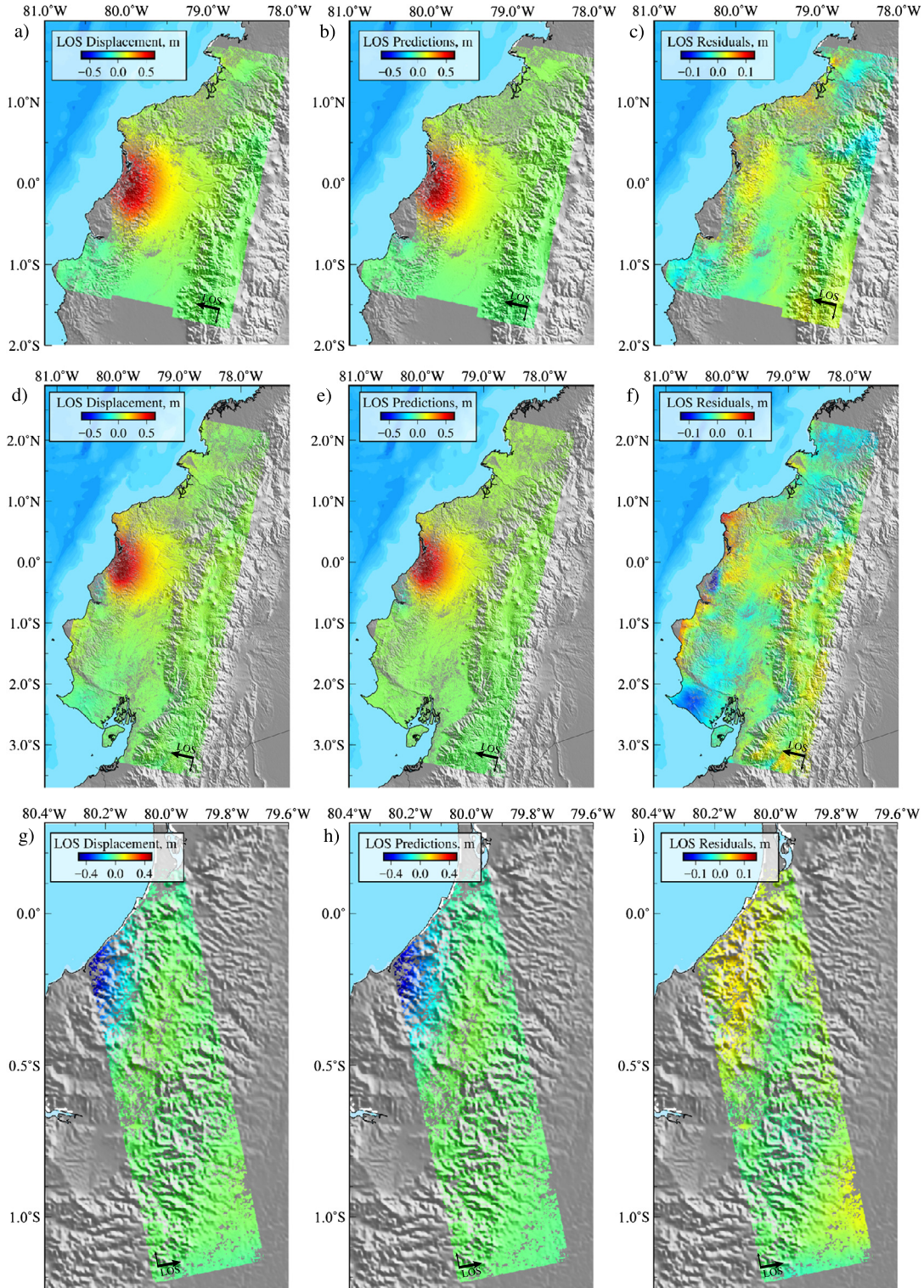


Fig. 4. Model performance for InSAR. (a, d, g) InSAR observations. (b, e, h) Predictions for the posterior mean model. (c, f, i) Residuals of the Sentinel (top row), descending ALOS-2 wide-swath (middle row), and ascending ALOS-2 strip-map (bottom row) interferograms. Decimated observations, predictions, and residuals are shown in Fig. S5.

twice and downsample them to 1 sps to match the HRGPS sampling rate. Waveforms are bandpass filtered between 0.015 Hz and 0.08 Hz, except for a few noisy records for which we increased the lower corner frequency to 0.037 Hz (Table S2). Waveforms are inverted in a 150 s-long time window starting from the origin time of the mainshock (23:58:36 UTC).

3.2. Stochastic co-seismic modeling

Our kinematic modeling of the 2016 Pedernales earthquake is based on a non-planar fault geometry in which the dip varies from 10° to 27° between 10 and 50 km depth, following the bending of the Slab1.0 model (cf. Fig. S7; Hayes et al., 2012). The fault

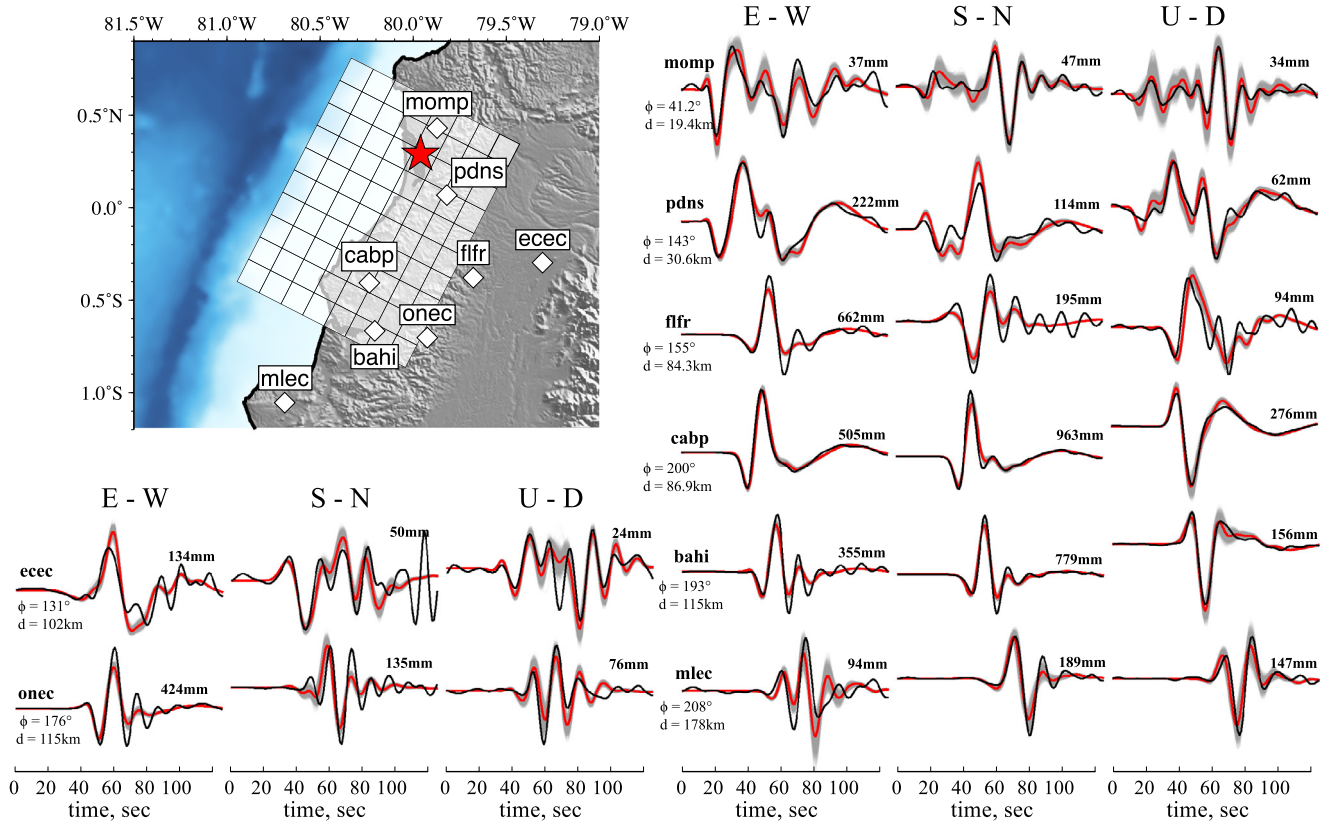


Fig. 5. High-rate GPS observations and model predictions. The white diamonds on the top-left map indicate the position of the stations. The red star marks the inverted epicenter location. White rectangles are the fault parametrization. The East, North, and vertical components of each station are plotted around the map. For each waveform, the bold number indicates its maximum amplitude. The station azimuth Φ and distance d to the epicenter are also given. The black line is the recorded waveform. The gray lines are the stochastic predictions for our posterior model. The red line is the mean of the stochastic predictions.

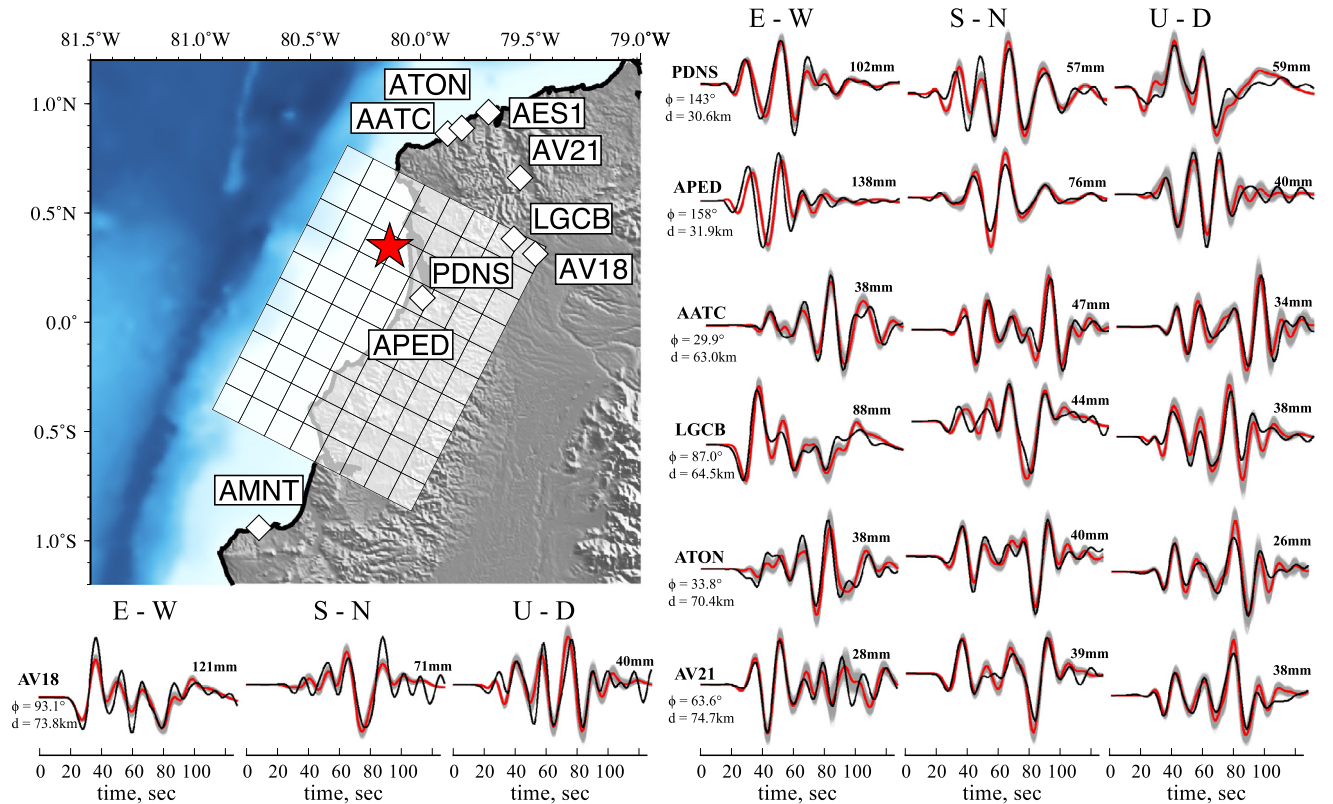


Fig. 6. Strong-motion observations and model predictions. Same as Fig. 5. We show only the stations where three components are available. The remaining 5 waveforms from 3 additional stations and the associated model predictions are shown in Fig. S8.

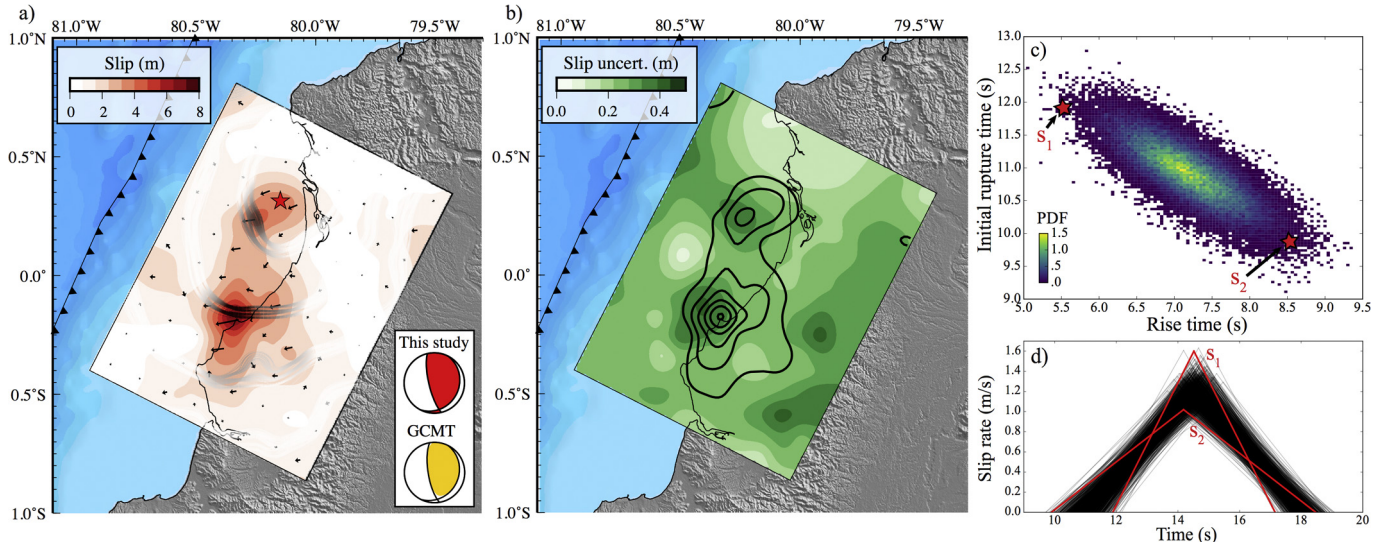


Fig. 7. Final co-seismic slip distribution. **a)** The color and arrows on the fault plane indicate the amplitude and direction of slip, respectively. Gray-scale lines are stochastic rupture fronts inferred from our model population plotted at 10 s, 20 s, and 30 s. The darker the lines, the larger the slip at that location. The red star marks the hypocenter location. **b)** Slip uncertainty. The color on the fault represents the absolute slip uncertainties. Black contour lines show the co-seismic slip every 1 m, starting from 2 m. **c)** Marginal probability distribution of rise time and initial rupture time in the first slip asperity (located close to the hypocenter). **d)** Posterior ensemble of source time functions at the same location of the fault. The source time functions labeled s_1 and s_2 in (d) correspond to rupture initiation times and rise times that are indicated with red stars in (c).

is discretized in 15×15 km patches in which we sample static (\mathbf{m}_S) and kinematic (\mathbf{m}_K) model parameters. The static model vector \mathbf{m}_S includes two components of static slip in each patch (i.e., the final integrated slip) and extra nuisance parameters to account for InSAR orbital errors (i.e., 3 parameters per interferogram to model a linear function of range and azimuth). The two components of static slip are U_{\parallel} , aligned with the direction of convergence between Nazca and NAS plates, and U_{\perp} , which is perpendicular to U_{\parallel} . The vector of kinematic parameters \mathbf{m}_K includes rupture velocity and rise time in each patch, along with hypocenter coordinates (i.e., the point of rupture initiation). Each point on the fault is only allowed to rupture once during the earthquake and we prescribe a triangular slip velocity function.

Following the approach of Minson et al. (2013), we first solve the final static slip distribution (i.e., \mathbf{m}_S) given available static observations (\mathbf{d}_S), i.e., InSAR, GPS offsets and tsunami data. Using AlTar, we thus sample the posterior distribution:

$$\begin{aligned} p(\mathbf{m}_S | \mathbf{d}_S) & \propto p(\mathbf{m}_S) p(\mathbf{d}_S | \mathbf{m}_S) \\ & \propto p(\mathbf{m}_S) \exp \left[-\frac{1}{2} (\mathbf{d}_S - \mathbf{G}_S \mathbf{m}_S)^T \mathbf{C}_S^{-1} (\mathbf{d}_S - \mathbf{G}_S \mathbf{m}_S) \right] \end{aligned} \quad (3)$$

where \mathbf{G}_S is the matrix including Green's functions that are computed using the same layered elastic medium than the one used for the inter-seismic coupling model (cf. section 2). Tsunami waveforms are simulated using COMCOT (Liu et al., 1998) assuming a time step of 1 sec and a 30-arc second GEBCO (General Bathymetric Chart of the Oceans) bathymetry. (Weatherall et al., 2015). As in eq. (1), the misfit covariance \mathbf{C}_S describes observational errors and prediction uncertainties due to inaccuracies of the assumed elastic structure (Duputel et al., 2012, 2014). As we want to promote a dominant thrust motion while allowing local variations of the slip direction, the prior PDF $p(\mathbf{m}_S)$ includes uniform prior $\mathcal{U}(-1 \text{ m}, 15 \text{ m})$ along the direction of convergence (U_{\parallel}) and Gaussian prior $\mathcal{N}(0, 0.5 \text{ m})$ in the perpendicular direction (U_{\perp}).

In a second step, we address the full joint inversion problem by incorporating kinematic observations \mathbf{d}_K . HRGPS and strong motion data provide information on kinematic parameters \mathbf{m}_K and

bring additional constraints on \mathbf{m}_S . The posterior PDF is then given by Minson et al. (2013):

$$\begin{aligned} p(\mathbf{m}_S, \mathbf{m}_K | \mathbf{d}_S, \mathbf{d}_K) & \propto p(\mathbf{m}_K) p(\mathbf{m}_S | \mathbf{d}_S) p(\mathbf{d}_K | \mathbf{m}_S, \mathbf{m}_K) \\ & \propto p(\mathbf{m}_K) p(\mathbf{m}_S | \mathbf{d}_S) \\ & \times \exp \left[-\frac{1}{2} (\mathbf{d}_K - \mathbf{g}_K(\mathbf{m}_S, \mathbf{m}_K))^T \mathbf{C}_K^{-1} (\mathbf{d}_K - \mathbf{g}_K(\mathbf{m}_S, \mathbf{m}_K)) \right] \end{aligned} \quad (4)$$

where $\mathbf{g}_K(\mathbf{m}_S, \mathbf{m}_K)$ is the (non-linear) forward predictions for HRGPS and strong motion waveforms that are based on the Herrmann (2013) implementation of the discrete wave-number method (Bouchon and Aki, 1977). As in eq. (3), \mathbf{C}_K is the misfit covariance describing measurement errors and predictions uncertainties due to Earth model inaccuracies. The prior $p(\mathbf{m}_K)$ is a combination of uniform priors $\mathcal{U}(1 \text{ s}, 12 \text{ s})$ and $\mathcal{U}(1 \text{ km/s}, 4 \text{ km/s})$ for rise-time and rupture velocity and a Gaussian PDF $\mathcal{N}(\mathbf{x}_h, \sigma = 5 \text{ km})$ for the hypocenter coordinates (\mathbf{x}_h).

3.3. Co-seismic modeling results

The Pedernales rupture is mainly unidirectional with a significant southward directivity (see posterior mean model in Fig. 7, cumulative slip snapshots in Fig. 8, and supplementary movie M2; Ye et al., 2016; Nocquet et al., 2017; Yi et al., 2018). The inverted hypocenter (0.31°N , -80.15°W , depth = 19.6 km; indicated by the red star in Fig. 7), is consistent with estimates from the Instituto Geofísico de la Escuela Politécnica Nacional (0.35°N , -80.16°W , depth = 17.0 km; <http://www.igepn.edu.ec>). Our solution depicts two large slip asperities separated by ~ 50 km that coincides roughly with two high-coupling zones north and south of the equator in Fig. 1 and supplementary movie M1. The first asperity is located close to the epicenter and fails within 15 s after the origin time (Fig. 8). The second slip asperity ruptures about 10 s later and contributes to more than 60% of the total seismic moment. The rupture directivity and the location of the southernmost asperity, with slip up to 8 m below the coastline, can probably ex-

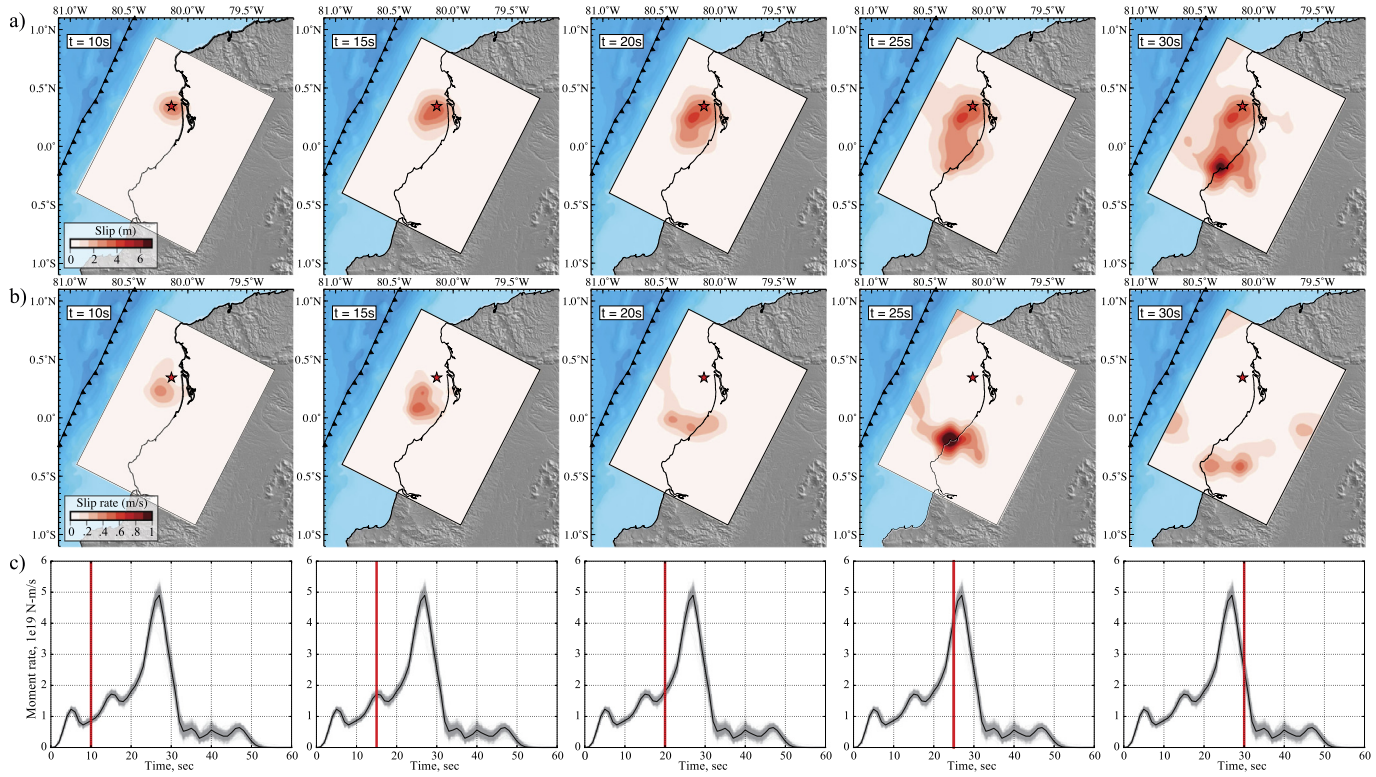


Fig. 8. Temporal evolution of co-seismic slip. **a)** Cumulative slip on the fault 10 s, 15 s, 20 s, 25 s, and 30 s after the origin time. The red color-scale indicates slip amplitude. The red star marks the epicenter location. **b)** Evolution of slip rate on the fault. **c)** Source time function (STF) of the event. Grey lines are stochastic STFs inferred from our model population while the black curve represents the posterior mean STF. Vertical red lines indicate the temporal position of each one of the snapshots.

plain the large damages that have been reported south of the city of Pedernales (Nocquet et al., 2017).

Posterior model uncertainties indicate that we have good constraints on slip amplitude through the fault plane (Fig. 7b and supplementary movie M3). Moreover, stochastic rupture fronts presented in Fig. 7a show that rupture initiation times are well resolved in large slip areas. There is however a tradeoff between rupture initiation times and rise times as illustrated in Fig. 7c-d. This is because our seismic observations are mostly sensitive on sub-fault centroid times rather than on rupture times and rise times, resulting in a negative correlation with a -1 slope between the two later parameters.

The southward directivity is clearly visible on HRGPS and strong motion data that show large ground motion amplitudes south of the rupture. This is well captured by our stochastic model predictions (Figs. 5 and 6). Some discrepancies are visible in the late arrivals, which are probably due to unaccounted 3D heterogeneities. Geodetic measurements provide good constraints on the static slip pattern, with large static displacements observed above the large slip asperity in the south. Our solution is able to predict GPS measurements (Fig. 3a) and InSAR data, with small residuals for Sentinel and ALOS-2 data (Fig. 4). We notice larger misfits for the ALOS-2 descending track, probably due to atmospheric noise since this interferogram is associated with significant spatially-correlated observational noise (cf. Fig. S6). Our solution also provides satisfactory fit to tsunami waveforms despite their relatively small amplitude (<1 cm, Fig. 3b). These tsunami observations are important since they clearly show the absence of slip in the shallow portion of the fault (shallow slip would produce large amplitude waves arriving too early at DART stations). This is also reported by Ye et al. (2016) that conducted trial and error teleseismic inversions, progressively removing shallow rows of patches to match the onset of tsunami signals.

4. Strain budget along the Colombia–Ecuador subduction zone

The Colombia–Ecuador subduction zone provides an outstanding opportunity to study the behavior of a megathrust fault over multiple earthquake cycles. As mentioned above, before the 2016 Pedernales earthquake, the subduction interface experienced a sequence of megathrust ruptures that started with a large $M_W = 8.6$ event in 1906 followed by a series of smaller earthquakes in 1942, 1958, 1979 and 1998. Because these events seem to cluster in time, it has been suggested that strain released by most recent earthquakes exceeds the deformation that accumulated inter-seismically since 1906 (Nocquet et al., 2017; Yi et al., 2018).

The strain budget along the megathrust can be investigated by comparing the co-seismic moment generated by earthquakes with the moment deficit accumulated during previous inter-seismic periods. We define the moment deficit accumulated over an inter-seismic time-span T over an area A of a fault as:

$$M_0^{deficit} = T V_p \iint_A \mu(\mathbf{x}) m_C(\mathbf{x}) d\mathbf{x} \quad (5)$$

where V_p is the long-term convergence rate, $\mu(\mathbf{x})$ is the shear modulus along the subduction interface and $m_C(\mathbf{x})$ is the coupling model introduced in section 2. Using such approach, Nocquet et al. (2017) propose that the co-seismic moment of the 1942 and 2016 earthquakes are much larger than the deficit accumulated since the 1906 earthquake (by a factor of 3 to 5 times for the 1942 event and 1.3 to 1.6 times for 2016). This seems also true for northern segments and in particular for the 1958 earthquake that has a seismic moment 1.5 to 1.8 times larger than the moment deficit estimated from the modeling of geodetic coupling. As discussed by Nocquet et al. (2017) and Yi et al. (2018), these estimates remain questionable given uncertainties on co-seismic slip and inter-seismic coupling.

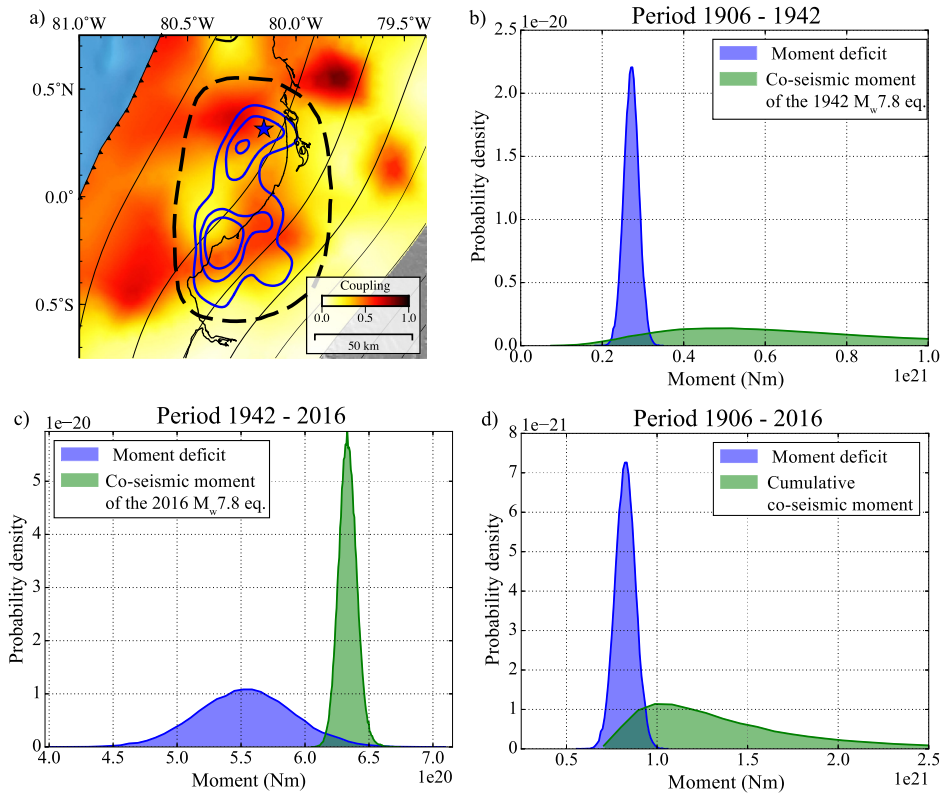


Fig. 9. Comparison of co-seismic moment and moment deficit. **a)** The background color represents the coupling posterior mean model. The blue star shows the hypocentre location. Blue lines are the 2 m, 3 m, and 4 m co-seismic slip isocontours. The black dashed line delimits the area where the co-seismic moment and moment deficit are computed. **b)** Probability densities of the co-seismic moment released by the 1942 earthquake and the moment deficit accumulated between 1906 and 1942 within the dashed ellipse shown in a). **c)** Probability densities of the co-seismic moment released by the 2016 earthquake and the moment deficit accumulated between 1942 and 2016. **d)** Probability densities of the co-seismic moment released by the sum of the 1942 and 2016 events, and of the moment deficit during the 1906–2016 period.

Hereafter, we use our stochastic co-seismic and inter-seismic solutions to fully account for posterior uncertainties and address the strain budget probabilistically. We assume a magnitude of $M_W = 7.8 \pm 0.2$ for the 1942 earthquake (Swenson and Beck, 1996; Ye et al., 2016). We compare the probability distributions of seismic moment generated by the 1942 and 2016 earthquakes with the moment deficit accumulated since 1906 (Fig. 9). Assuming the two events are co-located, maximum a posteriori models indicate that the seismic moment for the 1942 and 2016 events are larger than the accumulated deficit by a factor of 2.0 and 1.2, respectively. Taken together for the 1906–2016 period, the moment generated co-seismically is 1.3 times larger than the moment deficit accumulated inter-seismically. Those estimates are subject to considerable uncertainties reflected by the overlap between the PDFs (Fig. 9). Although this overlap is not negligible, there is a relatively small probability of about 5% to have a moment deficit larger or equal than the cumulative seismic moment of the 1942 and 2016 earthquakes. In this scenario, an excess of co-seismic moment since 1906 is likely given available observations.

This conclusion only holds if the 2016 rupture largely overlaps with the 1942 earthquake, whose location is still debated. In particular, Yi et al. (2018) suggests that the 1942 earthquake occurred at shallower depth than the 2016 rupture from the comparison of macroseismic maps of 1942 and 1958 events (Swenson and Beck, 1996). Therefore we test the alternative hypothesis suggesting that the 1942 earthquake occurred between lat 0.5°S – 0.5°N at a depth shallower than 40 km (Nocquet et al., 2017). Fig. 10a, b shows that the negative moment balance no longer holds. In this case, the probability of having a deficit equivalent or larger than the co-seismic moment is larger than 70%. Fig. 10c, d shows that this remains true if we further restrain the location of the 1942

event to be located up-dip of the 2016 earthquake (as proposed by Yi et al., 2018).

We conducted a similar analysis for the 1958 northern Ecuador earthquake, assuming a magnitude $M_W = 7.6 \pm 0.2$ (according to Ye et al., 2016). Maximum a posteriori models in Fig. S9b show that the seismic moment generated by the 1958 earthquake is quite similar to the accumulated deficit between 1906 and 1958. This contradicts with Nocquet et al. (2017) that estimated that the 1958 earthquake had a seismic moment exceeding by 50% to 180% the moment accumulated inter-seismically. In our case, we clearly see that the PDF of the moment deficit falls within uncertainties of the 1958 co-seismic moment. As shown in Fig. S9, this still holds if we assume different location for the 1958 earthquake, which discards the negative moment balance issue reported for 1942 and 2016 earthquakes.

5. Discussion and conclusion

We develop stochastic models of the inter-seismic slip-rate along the Colombia–Ecuador subduction and of the 2016 Pederales earthquake, which provide new constraints on uncertainties of inter- and co-seismic slip processes. Our results are to first order consistent with some previously published models (e.g., Nocquet et al., 2017; Chlieh et al., 2014). In particular, our coupling model presented in Fig. 2 is similar to the “unsmoothed” model of Chlieh et al. (2014) since it is not affected by smoothing regularization. Our solution clearly depicts a heterogeneous coupling of the subduction interface (cf. Fig. 2). The heterogeneity of fault coupling properties seems to be a common feature to many subduction zones (Avouac, 2015), but is often blurred because of poor spatial resolution and smoothing constraints used in the inversion. Despite large uncertainties due to the lack of geodetic observations far offshore, all

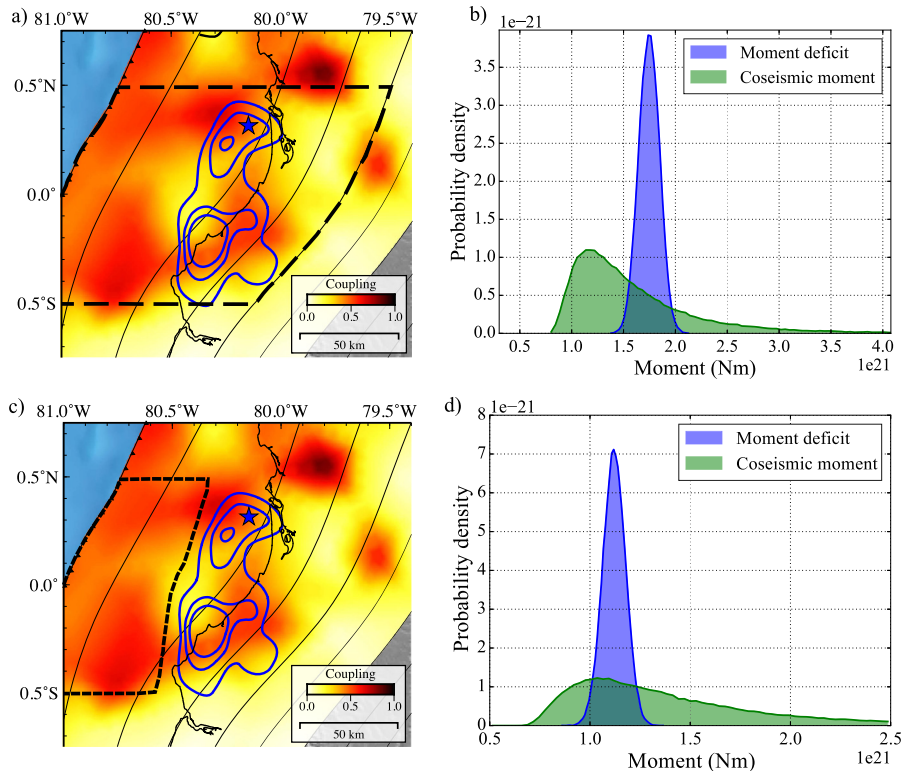


Fig. 10. Comparison of co-seismic moment and moment deficit considering the 1942 event happened at a different location. **a)** Same as Fig. 9a. The black dashed line delimits the area between 0.5°S and 0.5°N where the co-seismic moment and moment deficit are computed. **b)** Probability densities of the co-seismic moment and moment deficit in the 1906–2016 period. The co-seismic moment is the sum of the 1942 and 2016 events moment. **c)** Same as a), but the dashed black area shows where the 1942 earthquake could have been located. **d)** Probability densities of the co-seismic moment and moment deficit. The co-seismic moment is the sum of the 1942 and 2016 events moment. The moment deficit is the sum of the moment deficits computed in the updip section (shown in c)) for the 1942–2016 period and in the downdip section (ellipse in 9a) for the 1906–2016 period.

models in our posterior ensemble show a large spatial heterogeneity (cf. supplementary movie M1).

Such heterogeneity roughly correlates with the spatial complexity of the 2016 earthquake revealed by our co-seismic solution. Our results indicate a unidirectional rupture towards the South with two large slip zones that coincide with two high-coupling asperities in the inter-seismic solution (cf. Fig. 1). We evaluate the possibility that the seismic moment generated by the 1942 and 2016 earthquakes is larger than the moment deficit accumulated since the great 1906 earthquake (as suggested by Nocquet et al., 2017). Our analyses show that this conclusion only holds if we assume that there is a large overlap between the 1942 and 2016 ruptures. If this particular assumption is loosened, results indicate that such an unbalanced moment budget is no longer required by observations. North of the Pedernales rupture, we also show that the seismic moment of the 1958 earthquake is not necessarily larger than the deficit accumulated since 1906 given uncertainties in co- and inter-seismic processes. The question therefore entirely lies within the accuracy of the location and extent of historical earthquakes.

One of the previously mentioned argument favoring an overlap between 1942 and 2016 earthquakes comes from the analysis of teleseismic waveforms recorded at a similar location for both events (see details in supplementary text T1). Ye et al. (2016) showed that 1942 and 2016 waveforms at the station DBN (De Bilt, Netherlands) present significant dissimilarities. Fig. S10 shows that such discrepancies can be explained by differences in the hypocenter location with the same slip distribution for both events (as previously suggested by Nocquet et al., 2017). However, the shape of the observed teleseismic P-wave is mostly controlled by the relative location between the hypocenter and the main slip asperities

(i.e., by the corresponding apparent moment-rate function). In fact, Fig. S10c shows that the 1942 DBN waveform could be explained equally well if we assume that the 1942 rupture occurred updip of the 2016 earthquake as suggested by focal depth and macroseismic maps of the 1942 event (Yi et al., 2018). In this scenario, there is a probability of $\sim 70\%$ to have a balanced moment budget since 1906 (i.e., a moment deficit that is larger or equal to the seismic moment of 1942 and 2016 events). On the contrary, if there is a large overlap between both earthquakes, our results show that there is a 95% probability that the moment generated by 1942 and 2016 ruptures is larger than the moment deficit accumulated since 1906. In this case such an unbalanced moment budget can possibly be explained by temporal variations in strain accumulation, which have been observed for example before and after the 2011 $M_W = 9.0$ Tohoku earthquake (e.g., Mavrommatis et al., 2014; Heki and Mitsui, 2013) and after the 2010 Maule earthquake (Melnick et al., 2017; Loveless, 2017). Alternatively, Nocquet et al. (2017) propose a “supercycle” model where the apparent excess of co-seismic moment results from the fact that the 1906 and 1942 earthquakes did not release all of the accumulated strain along the megathrust. This is consistent with the modeling of historic tsunami records suggesting that the 1906 earthquake mainly ruptured the shallow part of the subduction without involving much slip close to the 2016 Pedernales event (Yoshimoto et al., 2017). However, these estimates might be biased by the poor sensitivity of tsunami data to deep slip, which can explain the relatively low magnitude of their resulting model ($M_W = 8.4$). The fact that the surface wave magnitude $M_s = 8.6$ is otherwise consistent with M_W also suggests that the 1906 earthquake is not a typical “tsunami” earthquake and is therefore probably not associated with a predominantly shallow rupture (Kanamori, 1972).

The complex behavior of the Colombia–Ecuador subduction can be related to the large heterogeneity revealed by our coupling solution, which suggests significant spatial variability of fault frictional properties (Fig. 1) Such frictional heterogeneities could result from spatial variations in rheology, fluid pore pressure (e.g., Avouac, 2015) or fault roughness associated with the subduction of topographic features such as ridges, fracture zones, and seamounts (Collot et al., 2017; Graindorge, 2004). As shown for example by Kaneko et al. (2010), such frictional heterogeneity can produce earthquakes of different sizes re-rupturing the same fault region at short time intervals. Complex earthquake sequences may also be promoted by partial stress drop of past events that produces significant stress heterogeneity along the fault (Cochard and Madariaga, 1996). The fact that large earthquakes (like the 1906 event) are rapidly followed by sequences of smaller ruptures (e.g., in 1942, 1958, 1979, 1998 and 2016) can then be understood if static stress drop of the smaller events is small compared to the increase of dynamic stresses at rupture fronts (Heaton, 1990; Melgar and Hayes, 2017).

As instrumental observations accumulate, there is a growing record of large earthquakes that break portions of faults that experienced previously documented large ruptures. These earthquakes continuously provide new observations suggesting complex earthquake sequences with substantial spatial and temporal variability among successive ruptures of the same fault system. As shown here, the study of long-term earthquake sequences and the associated strain budget still relies on many assumptions and are affected by large uncertainties. To address the seismogenic behavior of active faults, we need to quantify how large observational and modeling uncertainties are and how much information we have gained in comparison to our preconceptions. Inaccuracies on historical earthquakes size and position can be substantial and also need to be properly considered. Such quantitative analysis is essential to understand how strain accumulates inter-seismically and is released by earthquakes, thereby improving seismic hazard assessment along subduction zones.

Acknowledgement

The ALOS-2 original data are copyright JAXA and provided under JAXA RA4 PI Project P1372002. The Copernicus Sentinel-1 data were provided by the European Space Agency (ESA). Contains modified Copernicus data 2016, processed by ESA and NASA/JPL. We thank the Instituto Geofísico de la Escuela Politécnica Nacional (IG-EPN Ecuador) and the IRD for making available the static GPS, high-rate GPS and accelerometers data used in this study. Aside from the data from the IG-EPN and IRD networks, the data set also includes accelerometer data from OCP and GPS data from the Instituto Geográfico Militar (IGM) and Servicio Geológico Colombiano, Proyecto GeoRED from Colombia, that we also thank. The waveform of the 1942 earthquake used on this study was provided by Lingling Ye and Hiroo Kanamori. This project has received funding from the Agence Nationale de la Recherche (ANR-17-ERC3-0010), the European Union's Horizon 2020 research and innovation program (grant agreement 758210), and the CNRS international program for scientific co-operation (PICS). This research was also supported by the NASA Earth Surface and Interior focus area and performed at the Jet Propulsion Laboratory, California Institute of Technology, under a contract with the National Aeronautics and Space Administration. We thank the Editor, Jean-Philippe Avouac, and two anonymous reviewers for their constructive comments, which helped improve this manuscript.

Appendix A. Supplementary material

Supplementary material related to this article can be found online at <https://doi.org/10.1016/j.epsl.2018.06.046>.

References

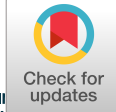
- Alvarado, A., Ruiz, M., Mothes, P., Yepes, H., Segovia, M., Vaca, M., Ramos, C., Enríquez, W., Ponce, G., Jarrín, P., et al., 2018. Seismic, volcanic, and geodetic networks in Ecuador: building capacity for monitoring and research. *Seismol. Res. Lett.* 89 (2A), 432–439.
- Avouac, J.-P., 2015. From geodetic imaging of seismic and aseismic fault slip to dynamic modeling of the seismic cycle. *Annu. Rev. Earth Planet. Sci.* 43 (1), 233–271.
- Beck, S.L., Ruff, L.J., 1984. The rupture process of the Great 1979 Colombia Earthquake – evidence for the asperity model. *J. Geophys. Res.* 89 (NB11), 9281–9291.
- Béthoux, N., Segovia, M., Alvarez, V., Collot, J.-Y., Charvis, P., Gailler, A., Monfret, T., 2011. Seismological study of the central Ecuadorian margin: evidence of upper plate deformation. *J. South Am. Earth Sci.* 31 (1), 139–152.
- Bouchon, M., Aki, K., 1977. Discrete wave-number representation of seismic-source wave fields. *Bull. Seismol. Soc. Am.* 67 (2), 259–277.
- Chlieh, M., Mothes, P., Nocquet, J.-M., Jarrín, P., Charvis, P., Cisneros, D., Font, Y., Collot, J.-Y., Villegas-Lanza, J.-C., Rolandone, F., et al., 2014. Distribution of discrete seismic asperities and aseismic slip along the Ecuadorian megathrust. *Earth Planet. Sci. Lett.* 400, 292–301.
- Cochard, A., Madariaga, R., 1996. Complexity of seismicity due to highly rate-dependent friction. *J. Geophys. Res., Solid Earth* (1978–2012) 101 (B11), 25321–25336.
- Collot, J.-Y., Sanclemente, E., Nocquet, J.-M., Leprêtre, A., Ribodetti, A., Jarrin, P., Chlieh, M., Graindorge, D., Charvis, P., 2017. Subducted oceanic relief locks the shallow megathrust in central Ecuador. *J. Geophys. Res., Solid Earth* 122 (5), 3286–3305. 2016JB013849.
- Duputel, Z., Agram, P.S., Simons, M., Minson, S.E., Beck, J.L., 2014. Accounting for prediction uncertainty when inferring subsurface fault slip. *Geophys. J. Int.* 197 (1), 464–482.
- Duputel, Z., Rivera, L., Fukahata, Y., Kanamori, H., 2012. Uncertainty estimations for seismic source inversions. *Geophys. J. Int.* 190 (2), 1243–1256.
- Graindorge, D., 2004. Deep structures of the Ecuador convergent margin and the Carnegie Ridge, possible consequence on great earthquakes recurrence interval. *Geophys. Res. Lett.* 31 (4), L04603.
- Gutenberg, B., Richter, C.F., 1949. *Seismicity of the Earth and Associated Phenomena*. Princeton University Press, Princeton, New Jersey.
- Hayes, G.P., Wald, D.J., Johnson, R.L., 2012. Slab1.0: a three-dimensional model of global subduction zone geometries. *J. Geophys. Res., Solid Earth* 117 (B1).
- He, P., Hetland, E.A., Wang, Q., Ding, K., Wen, Y., Zou, R., 2017. Coseismic slip in the 2016 Mw 7.8 Ecuador earthquake imaged from Sentinel-1A radar interferometry. *Seismol. Res. Lett.* 88 (2A), 277–286.
- Heaton, T.H., 1990. Evidence for and implications of self-healing pulses of slip in earthquake rupture. *Phys. Earth Planet. Inter.* 64 (1), 1–20.
- Heki, K., Mitsui, Y., 2013. Accelerated pacific plate subduction following interplate thrust earthquakes at the Japan trench. *Earth Planet. Sci. Lett.* 363, 44–49.
- Herrmann, R.B., 2013. Computer programs in seismology: an evolving tool for instruction and research. *Seismol. Res. Lett.* 84 (6), 1081–1088.
- Jacoby, G.C., Sheppard, P.R., Sieh, K.E., 1988. Irregular recurrence of large earthquakes along the San Andreas fault: evidence from trees. *Science* 241 (4862), 196–199.
- Jolivet, R., Candela, T., Lasserre, C., Renard, F., Klinger, Y., Doin, M.-P., 2015a. The burst-like behavior of aseismic slip on a rough fault: the creeping section of the Haiyuan fault, China. *Bull. Seismol. Soc. Am.* 105 (1), 480–488.
- Jolivet, R., Lasserre, C., Doin, M.-P., Guillaso, S., Peltzer, G., Dailu, R., Sun, J., Shen, Z.-K., Xu, X., 2012. Shallow creep on the Haiyuan fault (Gansu, China) revealed by SAR interferometry. *J. Geophys. Res., Solid Earth* 117 (B6).
- Jolivet, R., Simons, M., Agram, P., Duputel, Z., Shen, Z.-K., 2015b. Aseismic slip and seismogenic coupling along the central San Andreas Fault. *Geophys. Res. Lett.* 42 (2), 297–306.
- Kanamori, H., 1972. Mechanism of tsunami earthquakes. *Phys. Earth Planet. Inter.* 6, 356–359.
- Kanamori, H., McNally, K.C., 1982. Variable rupture mode of the subduction zone along the Ecuador–Colombia coast. *Bull. Seismol. Soc. Am.* 72 (4), 1241–1253.
- Kaneko, Y., Avouac, J.-P., Lapusta, N., 2010. Towards inferring earthquake patterns from geodetic observations of interseismic coupling. *Nat. Geosci.* 3 (5), ngeo843–369.
- Klein, E., Duputel, Z., Masson, F., Yavasoglu, H., Agram, P., 2017. Aseismic slip and seismogenic coupling in the Marmara Sea: what can we learn from onland geodesy? *Geophys. Res. Lett.* 44 (7), 3100–3108.
- Lay, T., 2015. The surge of great earthquakes from 2004 to 2014. *Earth Planet. Sci. Lett.* 409, 133–146.
- Liu, P.L.F., Woo, S.-B., Cho, Y.-S., 1998. *Computer Programs for Tsunami Propagation and Inundation*. Cornell University, USA.

- Lohman, R.B., Simons, M., 2005. Some thoughts on the use of InSAR data to constrain models of surface deformation: noise structure and data downsampling. *Geochem. Geophys. Geosyst.* 6 (1), Q01007.
- Loveless, J.P., 2017. Super-interseismic periods: redefining earthquake recurrence. *Geophys. Res. Lett.* 44 (3), 1329–1332.
- Mavrommatis, A.P., Segall, P., Johnson, K.M., 2014. A decadal-scale deformation transient prior to the 2011 Mw 9.0 Tohoku-oki earthquake. *Geophys. Res. Lett.* 41 (13), 4486–4494.
- Melgar, D., Hayes, G.P., 2017. Systematic observations of the slip pulse properties of large earthquake ruptures. *Geophys. Res. Lett.* 44 (19), 9691–9698.
- Melnick, D., Moreno, M., Quinteros, J., Baez, J.C., Deng, Z., Li, S., Oncken, O., 2017. The super-interseismic phase of the megathrust earthquake cycle in Chile. *Geophys. Res. Lett.* 44 (2), 784–791.
- Mendoza, C., Dewey, J.W., 1984. Seismicity associated with the great Colombia-Ecuador earthquakes of 1942, 1958, and 1979 – implications for barrier models of earthquake rupture. *Bull. Seismol. Soc. Am.* 74 (2), 577–593.
- Minson, S., Simons, M., Beck, J., 2013. Bayesian inversion for finite fault earthquake source models I—theory and algorithm. *Geophys. J. Int.* 194 (3), 1701–1726.
- Mora-Páez, H., Peláez-Gaviria, J.-R., Diederix, H., Bohórquez-Orozco, O., Cardona-Piedrahita, L., Corchuelo-Cuervo, Y., Ramírez-Cadena, J., Díaz-Mila, F., 2018. Space geodesy infrastructure in Colombia for geodynamics research. *Seismol. Res. Lett.* 89 (2A), 446–451.
- Mothes, P.A., Rolandone, F., Nocquet, J.-M., Jarrin, P.A., Alvarado, A.P., Ruiz, M.C., Cisneros, D., Páez, H.M., Segovia, M., 2018. Monitoring the earthquake cycle in the northern Andes from the Ecuadorian cGPS network. *Seismol. Res. Lett.* 89 (2A), 534–541.
- Nocquet, J.M., Jarrin, P., Vallée, M., Mothes, P.A., Grandin, R., Rolandone, F., Delouis, B., Yépes, H., Font, Y., Fuentes, D., Regnier, M., Laurendeau, A., Cisneros, D., Hernandez, S., Sladen, A., Singauch, J.C., Mora, H., Gomez, J., Montes, L., Charvis, P., 2017. Supercycle at the Ecuadorian subduction zone revealed after the 2016 Pedernales earthquake. *Nat. Geosci.* 10 (2), 145–149.
- Nocquet, J.M., Villegas-Lanza, J.C., Chlieh, M., Mothes, P.A., Rolandone, F., Jarrin, P., Cisneros, D., Alvarado, A., Audin, L., Bondoux, F., Martin, X., Font, Y., Regnier, M., Vallée, M., Tran, T., Beauval, C., Mendoza, J.M.M., Martinez, W., Tavera, H., Yépes, H., 2014. Motion of continental slivers and creeping subduction in the northern Andes. *Nat. Geosci.* 7 (4), 287–291.
- Ortega Culaciati, F.H., 2013. Aseismic Deformation in Subduction Megathrusts: Central Andes and North-East Japan. PhD thesis. California Institute of Technology, Pasadena, CA, USA.
- Perfettini, H., Avouac, J.P., 2004. Stress transfer and strain rate variations during the seismic cycle. *J. Geophys. Res., Solid Earth* 109 (B6).
- Savage, J., 1983. A dislocation model of strain accumulation and release at a subduction zone. *J. Geophys. Res., Solid Earth* 88 (B6), 4984–4996.
- Schwartz, D.P., Coppersmith, K.J., 1984. Fault behavior and characteristic earthquakes: examples from the Wasatch and San Andreas Fault Zones. *J. Geophys. Res., Solid Earth* (1978–2012) 89 (B7), 5681–5698.
- Shimazaki, K., Nakata, T., 1980. Time-predictable recurrence model for large earthquakes. *Geophys. Res. Lett.* 7 (4), 279–282.
- Sieh, K., Natawidjaja, D.H., Meltzner, A.J., Shen, C.C., Cheng, H., Li, K.S., Suwargadi, B.W., Galetzka, J., Philibosian, B., Edwards, R.L., 2008. Earthquake supercycles inferred from sea-level changes recorded in the corals of West Sumatra. *Science* 322 (5908), 1674–1678.
- Simons, M., Minson, S.E., Sladen, A., Ortega, F., Jiang, J., Owen, S.E., Meng, L., Ampuero, J.-P., Wei, S., Chu, R., Helmberger, D.V., Kanamori, H., Hetland, E., Moore, A.W., Webb, F.H., 2011. The 2011 magnitude 9.0 Tohoku-Oki earthquake: mosaicking the megathrust from seconds to centuries. *Science* 332 (6036), 1421–1425.
- Swenson, J.L., Beck, S.L., 1996. Historical 1942 Ecuador and 1942 Peru subduction earthquakes and earthquake cycles along Colombia-Ecuador and Peru subduction segments. *Pure Appl. Geophys.* 146 (1), 67–101.
- Vallee, M., Nocquet, J.-M., Battaglia, J., Font, Y., Segovia, M., Regnier, M., Mothes, P., Jarrin, P., Cisneros, D., Vaca, S., et al., 2013. Intense interface seismicity triggered by a shallow slow slip event in the Central Ecuador subduction zone. *J. Geophys. Res., Solid Earth* 118 (6), 2965–2981.
- Vallée, M., Satriano, C., 2014. Ten year recurrence time between two major earthquakes affecting the same fault segment. *Geophys. Res. Lett.* 41 (7), 2312–2318.
- Weatherall, P., Marks, K., Jakobsson, M., Schmitt, T., Tani, S., Arndt, J.E., Rovere, M., Chayes, D., Ferrini, V., Wigley, R., 2015. A new digital bathymetric model of the world's oceans. *Earth Space Sci.* 2 (8), 331–345.
- Ye, L., Kanamori, H., Avouac, J.-P., Li, L., Cheung, K.F., Lay, T., 2016. The 16 April 2016, MW7.8 (MS7.5) Ecuador earthquake: a quasi-repeat of the 1942 MS7.5 earthquake and partial re-rupture of the 1906 MS8.6 Colombia-Ecuador earthquake. *Earth Planet. Sci. Lett.* 454 (Suppl. C), 248–258.
- Yi, L., Xu, C., Wen, Y., Zhang, X., Jiang, G., 2018. Rupture process of the 2016 Mw 7.8 Ecuador earthquake from joint inversion of InSAR data and teleseismic P waveforms. *Tectonophysics* 722, 163–174.
- Yokota, Y., Koketsu, K., 2015. A very long-term transient event preceding the 2011 Tohoku earthquake. *Nat. Commun.* 6, 5934.
- Yoshimoto, M., Kumagai, H., Acero, W., Ponce, G., Vásconez, F., Arrais, S., Ruiz, M., Alvarado, A., Pedraza García, P., Dionicio, V., Chamorro, O., Maeda, Y., Nakano, M., 2017. Depth-dependent rupture mode along the Ecuador-Colombia subduction zone. *Geophys. Res. Lett.* 84 (5), 1561–2210.

3.5 La source impulsive du séisme d'Ezgeleh en 2017 ($M_W = 7.3$)

Lors d'une rupture de type fissure (c-à-d, "crack-like rupture" en anglais), le glissement croît à mesure que la rupture se propage. D'après ce modèle, le glissement à un point donné de la faille ne s'arrête que lorsque l'information sur l'arrêt de rupture est reçue. Lors d'une rupture en pulse, le glissement se produit dans une zone étroite entre le front de rupture et le front de cicatrisation. D'un point de vue cinématique, la différence entre ces deux modèles réside donc dans le temps de montée (la durée locale de glissement) qui est comparable à la durée totale de rupture pour une fissure alors qu'elle est beaucoup plus courte pour un pulse de glissement. Comme indiqué à la fin du chapitre 1, l'existence de ruptures en pulse a des implications importantes sur la mécanique des failles. Ces ruptures impliquant des contraintes dynamiques importantes au niveau du front de rupture, elles sont plus difficiles à arrêter et peuvent ainsi se propager dans des régions ayant rompu récemment (comme observé en Équateur dans la section précédente). Alors qu'une majorité d'observations suggère que les séismes se produisent sous la forme de pulses de glissement, l'impulsivité de la rupture est souvent "gommée" par les contraintes de lissages utilisées pour régulariser la solution. Dans cette partie, nous présentons un modèle cinématique pour le séisme d'Ezgeleh en 2017 (Iran, $M_W = 7.3$) en combinant des données interférométriques et accélérométriques. L'incorporation de ces données en champ proche révèle que la rupture se transforme très rapidement en un pulse de glissement étroit par rapport à la taille de la zone de glissement. Cette rupture impulsive montre une forte directivité vers le sud qui semble expliquer la répartition des dégâts constatés dans la région épicentrale.

L'étude présentée ci-dessous a été publiée en 2019 dans *Geophysical Research Letters*. Ce travail a été effectué dans le cadre du doctorat de Baptiste Gombert (thèse soutenue en Mars 2018).



Geophysical Research Letters

RESEARCH LETTER

10.1029/2018GL081794

Key Points:

- The Ezgeleh earthquake ruptured a flat thrust fault in the Zagros fold and thrust belt
- Kinematic slip modeling reveals a highly impulsive source with southward directivity, possibly causing the large damage in the area
- The direction of coseismic slip suggests a strain partitioning between thrust and unmapped strike-slip faults

Supporting Information:

- Supporting Information S1
- Movie S1
- Movie S2

Correspondence to:

B. Gombert,
 baptiste.gombert@earth.ox.ac.uk

Citation:

Gombert, B., Duputel, Z., Shabani, E., Rivera, L., Jolivet, R., & Hollingsworth, J. (2019). Impulsive source of the 2017 $M_W = 7.3$ Ezgeleh, Iran, earthquake. *Geophysical Research Letters*, 46, 5207–5216.
<https://doi.org/10.1029/2018GL081794>

Received 21 DEC 2018

Accepted 30 APR 2019

Accepted article online 8 MAY 2019

Published online 29 MAY 2019

Impulsive Source of the 2017 $M_W = 7.3$ Ezgeleh, Iran, Earthquake

B. Gombert^{1,2} , Z. Duputel² , E. Shabani³ , L. Rivera² , R. Jolivet⁴ , and J. Hollingsworth⁵

¹Department of Earth Sciences, University of Oxford, Oxford, UK, ²Institut de Physique du Globe de Strasbourg, UMR7516, Université de Strasbourg, EOST/CNRS, Strasbourg, France, ³Department of Seismology, Institute of Geophysics, University of Tehran, Tehran, Iran, ⁴Laboratoire de géologie, Département de Géosciences, École Normale Supérieure, PSL Research University, CNRS UMR 8538, Paris, France, ⁵ISTerre/CNRS, UMR5275, Université Grenoble Alpes, Grenoble, France

Abstract On 12 November 2017, a $M_W = 7.3$ earthquake struck near the Iranian town of Ezgeleh, at the Iran-Iraq border. This event was located within the Zagros fold and thrust belt which delimits the continental collision between the Arabian and Eurasian Plates. Despite a high seismic risk, the seismogenic behavior of the complex network of active faults is not well documented in this area due to the long recurrence interval of large earthquakes. In this study, we jointly invert interferometric synthetic aperture radar and near-field strong motions to infer a kinematic slip model of the rupture. The incorporation of these near-field observations enables a fine resolution of the kinematic rupture process. It reveals an impulsive seismic source with a strong southward rupture directivity, consistent with significant damage south of the epicenter. We also show that the slip direction does not match plate convergence, implying that some of the accumulated strain must be partitioned onto other faults.

Plain Language Summary Iran is a very seismically active region. However, the 2017 Ezgeleh earthquake of magnitude 7.3 occurred in a region where large earthquakes have not been documented for several centuries. Our knowledge of fault locations, geometries, and seismic behaviors is therefore limited in this region. We use near-field seismological and satellite geodetic data to retrieve the spatial and temporal distribution of slip occurring on the fault during the Ezgeleh earthquake. We show that the high slip rate and Southward directivity of the rupture may have worsened the damage south of the epicenter. We also observe that tectonic motion is partitioned between different types of faults. Although the Ezgeleh earthquake did release a significant part of that strain, other seismogenic faults in the region could represent an important hazard for the nearby population.

1. Introduction

On 12 November 2017, the Iranian province of Kermanshah and the Iraqi Kurdistan were shaken by a severe $M_W = 7.3$ earthquake located south of the border. It caused the death of ~630 people and considerable damage, in particular in the Iranian city of Sarpol-e Zahab (cf. Figure 1). The earthquake triggered numerous landslides and rock falls, including a massive 4×1 -km landslide in Kermanshah (Miyajima et al., 2018).

The hypocenter is located within the Zagros Mountains near the Iranian town of Ezgeleh, a tectonically active region that accommodates crustal shortening (e.g., Berberian & King, 1981) resulting from the collision between the Arabian Plate and the Eurasian Plate. About a third to a half of current convergence is accommodated within the Zagros belt (Vernant et al., 2004). The belt hosts many moderate earthquakes ($M = 5–6$) with depths ranging from 4 to 20 km, although this range is debated (e.g., Niazi et al., 1978; Nissen et al., 2011; Talebian & Jackson, 2004). Our knowledge of the regional seismotectonics is further complicated by the very rare occurrence of coseismic surface rupture (Talebian & Jackson, 2004; Walker et al., 2005).

The Ezgeleh earthquake occurred at the transition between the Lorestan Arc in the southeast and the Kirkuk Embayment (KE) in the northwest (cf. Figure 1). The area is covered by an 8- to 13-km-thick sedimentary cover heavily folded into numerous anticlines (e.g., Alavi, 2007; Falcon, 1969). Sediments are crossed by many thrust faults that flatten within the basement (Sadeghi & Yassaghi, 2016; Tavani et al., 2018). As

©2019. The Authors.

This is an open access article under the terms of the Creative Commons Attribution-NonCommercial-NoDerivs License, which permits use and distribution in any medium, provided the original work is properly cited, the use is non-commercial and no modifications or adaptations are made.

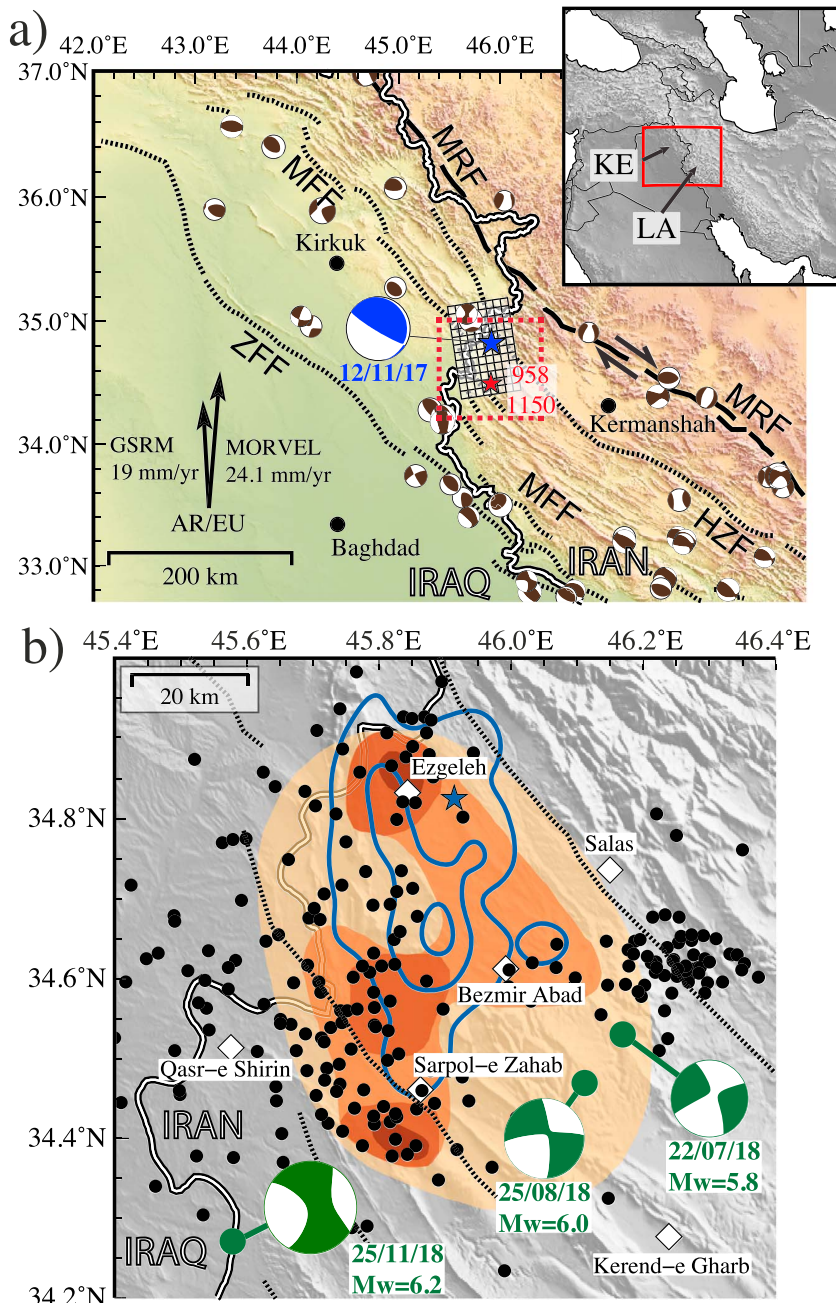


Figure 1. Regional seismotectonic context and damage associated with the 2017 Ezgeleh earthquake. (a) The blue star marks the epicenter location, and the squares represent the fault parametrization. The blue beachball is the moment tensor estimated in this study, and the brown moment tensors are regional seismicity from the Global CMT catalog (Ekström et al., 2012). The red star shows the approximate location of two historical earthquakes. The dashed black line is the Main Recent Fault (MRF), and dotted lines are supposed locations of regional blind faults (MFF = Mountain Flexure Fault; HZF = High Zagros Fault; ZFF = Zagros Foredeep Fault; Berberian, 1995). Arrows indicate the convergence of the Arabian plate (AR) with respect to stable Eurasia (EU) from the GSRRM v2.1 (Kreemer et al., 2014) and MORVEL (DeMets et al., 2010) models, computed with the UNAVCO Plate Motion Calculator. LA = Lorestan Arc. KE = Kirkuk Embayment. The red dashed square indicates the position of (b). (b) Black dots are aftershocks located by the International Institute of Earthquake Engineering and Seismology of Iran. Focal mechanisms from the Global CMT catalog of three large aftershocks are shown in green. Brown colors indicate the level of damage based on a compilation of destruction rate and landslide activity interpolated from field surveys conducted by the Geological Survey of Iran (GSI, 2017). The darker the color, the more intense the damage. Blue lines are the 1.5-m coseismic slip contour. CMT = centroid moment tensor.

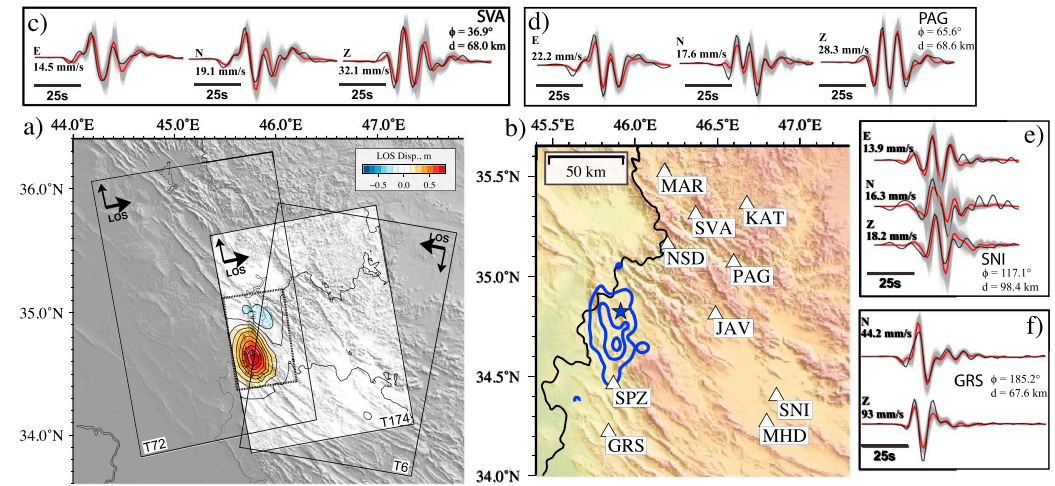


Figure 2. Observations used in the inversion. (a) Unwrapped Sentinel-1A interferograms showing surface displacement in Line Of Sight (LOS) direction (Track 174). The footprint of one additional ascending and descending tracks are also shown. Data, predictions, and model performance of the three interferograms are available in Figures S1 and S2. (b) Location of strong-motion records (white triangles). (c–f) Waveforms of four selected stations around the epicenter. For each waveform, the bold number indicates its maximum amplitude. ϕ and d are station azimuth and distance to epicenter, respectively. The black line is the recorded waveform, gray lines are stochastic predictions for our posterior model, and the red line is the mean of stochastic predictions. Remaining waveforms are shown in Figure S3.

expected from the lack of surface ruptures and fault scarps, most of these faults are blind, hence the difficulty to infer their geometry. In this region, plate convergence is roughly north-south (cf. Figure 1) with a rate between 19 (Kreemer et al., 2014) and 24 mm/year (DeMets et al., 2010). Slip is partitioned between thrust faults at the front of the belt, such as the Mountain Front Fault, the High Zagros Fault, the Zagros Foredeep Fault, and the Main Recent Fault, a right lateral strike-slip fault located at the back of the belt (cf. Figure 1; Berberian, 1995). This part of the Zagros belt hosts moderate seismicity, but the last significant earthquakes ($5.9 \lesssim M \lesssim 6.4$) to strike the area happened in 958 and 1150 (Ambraseys & Melville, 2005). Therefore, our understanding of the regional seismotectonic setting is obscured by the undersampled seismic cycle and the absence of ground geodesy. The 2017 Ezgeleh earthquake highlighted the seismic hazard in this portion of the Zagros belt. Its analysis hence provides a unique opportunity to enrich our understanding of the region and the associated seismic hazard. In addition, the availability of near-field strong-motion records offers the possibility to closely study the propagation of the rupture on the fault.

In this study, we propose a stochastic analysis of the 2017 earthquake source process. We use a Bayesian framework to infer a population of coseismic slip models that fit available observations. While currently available studies were either limited to the static final distribution of slip on the fault (Barnhart et al., 2018; He et al., 2018; Vajedian et al., 2018; Wanpeng et al., 2018; Yang et al., 2018) or used far-field teleseismic data (Chen et al., 2018; Nissen et al., 2019), we jointly invert interferometric synthetic aperture radar (InSAR) and near-field strong-motion data which provide a better resolution (Anderson, 2003) to propose a kinematic description of the earthquake source. We use a layered velocity model that is routinely used to locate earthquakes by the Iranian Seismological Center, which ensures modeling is performed to the best of our knowledge (supporting information Table S1).

2. Inversion of Coseismic Slip

2.1. Observations

Due to the remote location of the event, the only available geodetic data come from InSAR. We use three synthetic aperture radar interferograms computed from acquisition by the Sentinel-1 satellite, along two ascending and one descending tracks (Figures 2a, S1, and S2). We use the ISCE software with precise orbits and Shuttle Radar Topography Mission Digital Elevation Model (DEM) to compute the coseismic interferograms (Rosen et al., 2012). The coherence of the radar phase is excellent, likely due to the arid conditions of this region. Acquisition dates are available in Table S2. We measure up to 80 cm of ground displacement toward the satellite in the ascending tracks, suggesting uplift and/or displacement toward the southwest.

The number of data points in the unwrapped interferograms is reduced using a recursive quad tree algorithm (cf., Figure S1; Lohman & Simons, 2005). We estimate uncertainties due to tropospheric perturbations in the phase by estimating empirical covariance functions for each interferogram (Jolivet et al., 2014). Estimated covariance parameters are summarized in Table S2.

We include near-field seismic waveforms recorded by 10 strong-motion accelerometers from the Iran Strong Motion Network to constrain the temporal evolution of slip during the earthquake rupture. Although located only on one side of the rupture, all stations are within 102 km of the epicenter (cf. Figure 2b). Details on strong motion data processing are given in supporting information Text S1 (Ide, 2007; Lee & Lahr, 1972). The east component of the two stations located south of the rupture (SPZ and GRS) was not used due to the poor quality of the record. We integrate accelerometric data to recover ground velocity, downsampled to 1 sps. Waveforms are bandpass filtered between 7 and 50 s using a fourth-order Butterworth band-pass filter, then windowed around the first arrivals.

2.2. Estimation of the Fault Plane

The two nodal planes of the global centroid moment tensor mechanism (Ekström et al., 2005) are either a shallow northeast dipping plane (351° strike and 11° dip) or a nearly vertical plane (121° strike and 83° dip). We conduct a grid search on fault geometry parameters for each nodal plane. The goal is to discriminate between the two planes and to find the optimal fault geometry to limit forward modeling errors.

We grid search the fault location and its strike and dip angles by inverting the InSAR displacement to find the geometry that better explains the observations. For each tested geometry, slip is inverted on 96 subfault patches using a simple least squares technique. More details on the method are given in supporting information Text S2 (Tarantola, 2005). We find that even the best subvertical plane has a root-mean-square 6 times larger than the shallow-dipping plane (cf. Figures S4 and S5). Although the subvertical plane is compatible with a back thrust fault that may exist in the region (Tavani et al., 2018) or with the reactivation of steep normal faults (Jackson, 1980), the shallow-dipping plane is in better agreement with receiver functions analysis (Paul et al., 2010) and the tectonic setting (e.g., Berberian, 1995; Vergés et al., 2011). Our optimal plane (351° strike, 14° dip, 13-km depth) agrees well with other studies using a similar grid search approach (Barnhart et al., 2018; Wanpeng et al., 2018). In the following, we will consider that the Ezgeleh earthquake occurred on our optimum shallow dipping plane.

2.3. Coseismic Slip Modeling

We use fault parameters inferred in section 2.2 to construct a planar fault and divide it into 96 subfault patches, each with a dimension of $7 \times 7 \text{ km}^2$. Patch size was determined through trial and error to limit correlation between slip on neighboring parts of the fault. Source model parameters include total final slip, rupture velocity, and rise time for each patch along with hypocenter location. We define \mathbf{m}_s the vector including the two components of static slip (i.e., final integrated slip), and \mathbf{m}_k the vector of kinematic parameters describing the temporal evolution of slip.

We solve the problem in a Bayesian framework using AlTar, a Markov chain Monte Carlo algorithm based on the algorithm described by Minson et al. (2013). It samples the full posterior probability distribution of the models that fit observations and are consistent with prior information. The strength of our solution is that it does not rely on any spatial smoothing and provides accurate estimates of the posterior slip uncertainty. We sample the posterior probability density $p(\mathbf{m}_s, \mathbf{m}_k | \mathbf{d}_s, \mathbf{d}_k)$ given by

$$p(\mathbf{m}_s, \mathbf{m}_k | \mathbf{d}_s, \mathbf{d}_k) \propto p(\mathbf{m}_k) p(\mathbf{m}_s) p(\mathbf{d}_s | \mathbf{m}_s) p(\mathbf{d}_k | \mathbf{m}_s, \mathbf{m}_k) \quad (1)$$

where \mathbf{d}_s and \mathbf{d}_k are the InSAR and strong-motion observations, respectively. The prior PDFs $p(\mathbf{m}_s)$ and $p(\mathbf{m}_k)$ are mostly uniform distributions designed to prevent some model features such as back slip. They are described in detail in Table S3. For further details on the method, the reader can refer to supporting information Text S3 (Duputel et al., 2014; Herrmann, 2013; Minson et al., 2013) and Gombert et al. (2018).

3. Results

In the first seconds following the hypocentral time, slip propagates in every direction around the hypocenter (cf. Figure 3 and supporting information Movie S1). Approximately 5 s after origin, the rupture almost only propagates toward the south. The largest slip rate occurs roughly after 6 s, 20 km south of the epicenter. We observe a strong directivity toward the south, consistent with a shorter, higher amplitude signal at stations

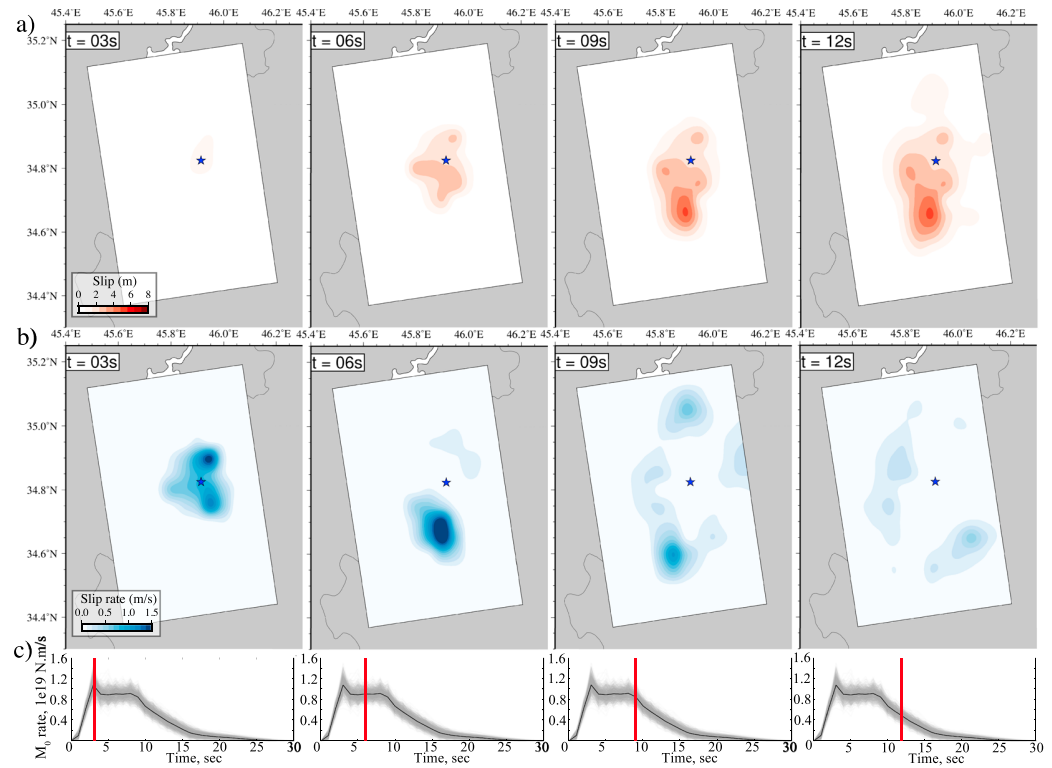


Figure 3. Temporal evolution of coseismic slip. (a) Cumulative slip on the fault 3, 6, 9, and 12 s after the origin time. The red color scale indicates slip amplitude. (b) Evolution of slip rate on the fault. (c) Source time function (STF) of the event. Gray lines are stochastic STFs inferred from our model population, while the black curve represents the posterior mean STF. Vertical red lines indicate the time of each snapshot.

SPZ and GRS compared to stations located in the north (cf. Figures 2 and S3). In addition, we infer a large slip rate on the fault. As shown in Figures 4d, 4e, and S6, slip rate increases up to more than 3 m/s where the slip is maximum. The slip rate functions of two fault patches presented here show the fast increase in slip rate associated with a short rise time ≤ 5 s, defining a sharp slip pulse (Heaton, 1990). Although larger than the values usually reported in kinematic slip models (usually ranging from 0.1 to 1 m/s), our slip rate estimates for this event are compatible with well-documented earthquakes (e.g., Cirella et al., 2012; Minson et al., 2014). The fast slip rate of the fault is reflected in the moment rate function shown in Figure 3c. To obtain the moment rate function, we first calculate the scalar moment function, $M_0(t)$, by summing the moment tensor function of each subfault and using the definition of the scalar moment from Dahlen and Tromp (1998). The moment rate function is then obtained using the time derivative of $M_0(t)$. As shown in Figure 3c, 90% of the moment was released within the first 14 s of the rupture, depicting an overall impulsive earthquake. The mean rupture speed along strike is 3.0 ± 0.25 km/s (Figure S7), which is $\sim 0.9V_s$ at that depth.

The posterior mean model of the final cumulative slip is shown in Figure 4a. At first order, this solution is in agreement with previously published static models (Barnhart et al., 2018; Wanpeng et al., 2018). We infer a ~ 50 -km-long and ~ 30 -km-wide rupture, with a peak slip of 5.5 ± 0.5 m. One difference arises as previous models proposed that two distinct asperities ruptured during the earthquake. Our posterior mean model does not show a clearly distinct rupture area in the north, closer to the hypocenter. However, roughly 20% of the models in our solution present such a feature (see supporting information Movie S2). This indicates that it is in the realm of possibilities but available observations cannot entirely resolve it. The slip direction is constant along most of the fault, with a $131.5^\circ \pm 0.8^\circ$ rake corresponding to a motion toward the southwest. The inferred focal mechanism is therefore consistent with long-period moment tensor inversions.

Our Bayesian framework allows us to directly infer the posterior uncertainties associated with the model parameters. Slip uncertainties are represented in Figure 4a by the 95% confidence ellipses. In addition,

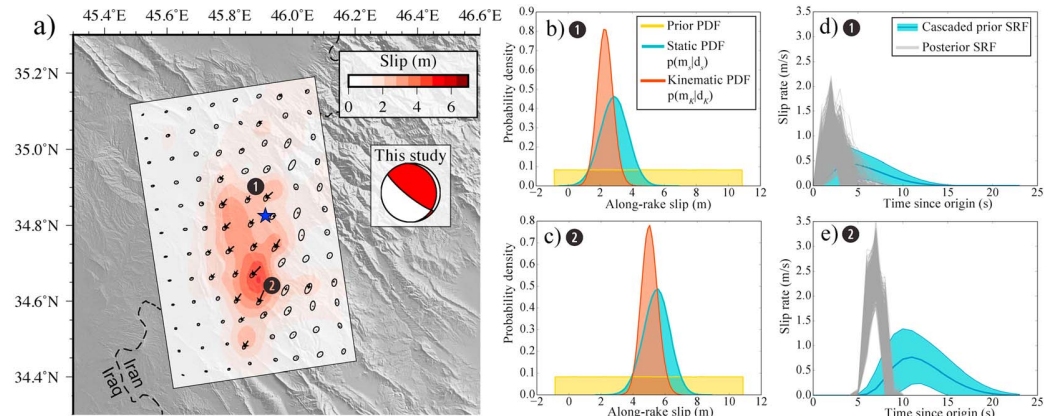


Figure 4. Final coseismic slip distribution. (a) Color and arrows on the fault plane indicate amplitude and direction of slip, respectively. Ellipses represent the 95% posterior uncertainty. Results presented in subfigures (b–e) are obtained for patches labeled 1 and 2. The background topography comes from the Shuttle Radar Topography Mission (Farr et al., 2007). (b, c) Prior, posterior static PDF, and posterior kinematic PDF of along-rake slip in patches 1 and 2. (d, e) Slip rate evolution in patches 1 and 2. The blue line is the mean prior slip rate function (SRF) used in the sampling, surrounded by 1σ uncertainties. Posterior SRFs in gray are from 1000 models randomly selected from our solution.

terior marginal distributions after the static and kinematic inversions of the along-rake slip of two fault patches are shown in Figures 4b and 4c. Unsurprisingly, the inclusion of kinematic observations reduces the posterior uncertainties of those parameters. On the highest slipping patch for instance, the 1σ posterior uncertainty decreases from 0.82 to 0.52 m. Over the fault, we observe a rather low posterior uncertainty at shallow and intermediate depths, where slip is located. At depths larger than 15 km, uncertainties become more significant. However, the inspection of each model composing the solution reveals a good consistency in the slip distribution, with nonetheless a larger variability in the northern part of the rupture (cf. supporting information Movie S2). This is confirmed by our analysis of the model ensemble revealing that data provide more information where the fault experienced large slip (cf. supporting information Text S4 and Figure S8).

As shown in Figures S1, S2, and S9, model predictions fit Sentinel-1A observations very well. Residuals are small over the three tracks, and they are consistent with the amplitude of 5–7 days of postseismic signal (~ 10 cm; Barnhart et al., 2018). Stochastic model predictions of the strong-motion data are shown in Figures 2 and S3. Overall, our solution can explain the observations with a good accuracy. Posterior model predictions of stations KAT, SNI, and MHD suffer from larger uncertainties, likely explained by their greater distance from the hypocenter.

4. Discussion

As suggested by previous studies (Barnhart et al., 2018; He et al., 2018; Wanpeng et al., 2018), the Ezgeleh earthquake likely occurred on the Mountain Flexure Fault (sometimes referred to as Main Front Fault, noted MFF in Figure 1). Along the major part of the Zagros belt, the MFF follows a NW-SE axis with a $\sim 120^\circ$ azimuth and is aligned with many topographic features (visible on the DEM in Figure 4). However, the strike of the fault differs by about 50° with the topography orientation at the location of the earthquake. This discrepancy is explained by a major bend in the MFF at this location as it transitions between the Lorestan Arc in the south and the KE in the north (e.g., Koshnaw et al., 2017; Vergés et al., 2011). Interestingly, the fault bend between the Lorestan Arc and KE corresponds to the northern bound of the rupture (Figure 3). This geometry change possibly stopped the rupture propagation, as suggested by numerical models (Aochi et al., 2000). The rupture may also have been halted by the 8- to 10-km-thick sediment cover, whose depth roughly corresponds to the up-dip limit of slip. Although poorly constrained, these boundaries could nonetheless help to better assess the probable size for future large events in the region, a valuable element in seismic hazard assessment (e.g., Hetényi et al., 2016).

These sediments are heavily folded in the forearc basin and host many large anticlines (e.g., Casciello et al., 2009; Kent, 2010). These folds are evidence for thin-skin shortening occurring within the belt (Koshnaw

et al., 2017). However, the slip of the 2017 earthquake occurred at larger depth, between 10 and 15 km. This deeper coseismic deformation suggests that thick-skin shortening is also happening in this part of the Zagros range (Nissen et al., 2011; Vergés et al., 2011). The slip direction of the Ezgeleh earthquake on the MFF is nearly perpendicular to the alignment of the topographic features mentioned above (cf. Figure 4a), creating a maximum 65 cm of uplift and 33 cm of subsidence across the belt (cf. Figure S10). Despite the relatively large depth of the Ezgeleh earthquake, such coseismic deformation may thus contribute to the growth of the Zagros topography. Afterslip might also contribute, although it seems to occur on a shallow dipping decollement at the front of the mountain range (Barnhart et al., 2018).

An interesting feature of the Ezgeleh earthquake is the discrepancy between the coseismic slip direction and the current plate motion. Both the GSRM v2.1 model (Kreemer et al., 2014) and the MORVEL model (DeMets et al., 2010) predict a nearly N-S plate convergence (see Figure 1), while the overall coseismic slip vector is oriented on a S 30°W axis (see Figure 4).

This difference suggests that strain partitioning is occurring in this part of the Zagros belt, with a partial decoupling between the thrust and right lateral strike-slip motion (McCaffrey, 1992; Platt, 1993). Strain partitioning in the Lurestan Arc and the KE has been proposed before based on the analysis of regional focal mechanisms (Talebian & Jackson, 2004). The Main Recent Fault (MRF; see Figure 1) is a major NW-SE, 800-km-long right lateral strike-slip fault which accommodates some of the strain (Tchalenko & Braud, 1974). It hosted several large earthquakes and has an ~50-km horizontal offset (Talebian & Jackson, 2002). However, other structures may be accommodating the strike-slip component of the convergence. Between July and November 2018, three significant aftershocks with respective magnitudes of $M_W = 5.8$, $M_W = 6.0$, and $M_W = 6.2$ occurred south of the mainshock epicenter (cf. Figure 1b). These events present a right lateral strike-slip focal mechanism but are located more than 100 km west of the MRF. They could have ruptured the Khanaqin fault, a N-S strike-slip structure marking the boundary between the Lurestan Arc and the KE (e.g., Blanc et al., 2003; Berberian, 1995; Hessami et al., 2001). However, there is very limited evidence that the Khanaqin fault is actually a strike-slip fault. As a matter of fact, a recent study by Tavani et al. (2018) using reconstruction of seismic profiles proposed that the Khanaqin fault is a back thrust structure accommodating the SW-NE motion. Therefore, undetected strike-slip faults may be accommodating some of the strike-slip deformation closer to the forearc than the MRF. Throughout the Zagros, the MRF is known to accommodate a major component of the northward motion via strain partitioning (Talebian & Jackson, 2002). However, not all the regional shear is accommodated solely on the MRF, especially along its northwest limit, where strike-slip faulting becomes increasingly distributed (Copley & Jackson, 2006). The additional contribution from other less known active structures in this region therefore poses an important uncharacterized seismic risk for local populations.

While the rupture directivity imaged here is visible in published slip models (Chen et al., 2018; Nissen et al., 2019), the sharpness of the slip pulse in these studies is blurred by their use of far-field data and smoothing constraints. The good spatial and temporal resolution of our kinematic slip model enabled by the use of near-field observations reveals interesting features. Figures 3 and S6 show that the rupture starts as a growing crack that rapidly transitions into a pulse with a rise time of about 4 s. This crack-pulse transition occurs within the first 4 s and less than 7 km from the hypocenter, therefore away from the rupture boundaries. Day (1982) proposed that if the slip rate is controlled by the fault geometry the rise time should be $T_R = 0.5 \times W/V_R$, with W the fault width and V_R the rupture velocity. However, we infer T_R values systematically higher than inverted rise times (Figure S11). This pulse-like behavior is therefore unlikely to result from healing phases emanating from the along-dip finiteness of the fault. A rapid crack-pulse transition is in agreement with early observations by Heaton (1990) and later studies (e.g., Beroza & Mikumo, 1996; Meier et al., 2016; Wang et al., 2019). Such a pulse may result from a number of mechanisms such as frictional self-healing, fault strength or stress heterogeneities, bimaterial effects, and wave reflections within low-velocity fault zones (e.g., Andrews & Ben-Zion, 1997; Huang & Ampuero, 2011; Perrin et al., 1995). After this early transition from a growing crack, the rupture continues its journey along strike as a decaying pulse toward the north and a strong growing pulse toward the south.

This strong southward propagating pulse seems to have a significant impact in the distribution of damage and landslides triggered by the earthquake. The Ezgeleh earthquake induced extensive destructions of dwellings in Iraqi Kurdistan, but mostly in the Iranian province of Kermanshah. Figure 1b shows the intensity of damage created by the mainshock. It is obtained from field observations conducted by the Inter-

national Institute of Earthquake Engineering and Seismology of Iran. Reported macroseismic intensities are also shown in Figure S12. Damage intensity roughly follows the surface projection of the slip distribution, but larger damage was reported in the south. In addition to building damage, many rockfalls and landslides occurred south of the rupture and up to 125 km from the centroid, including a large 4-km-long and 1-km-wide landslide (Miyajima et al., 2018). These observations may however be biased by the difficulty to report such phenomena on the Iraqi side of the border. Many different factors can also largely influence the effects of an earthquake, like soil nature or mountain slopes. In addition to rupture directivity, studies have suggested that the strong impulsiveness of the source can intensify low-frequency ground shaking, particularly damaging to buildings (Melgar & Hayes, 2017; Somerville & Graves, 2003). The large slip rate and short rise time of the southward propagating pulse may therefore have exacerbated the damage observed southwest of the Ezgeleb earthquake.

5. Conclusion

The 2017 Ezgeleb earthquake breaks a long hiatus on strong events affecting the Zagros thrust and fold belt in the Kermanshah province. The joint inversion of InSAR and near-field strong-motion observations reveals a predominantly thrust motion on a near-horizontal blind crustal fault. We also infer a highly impulsive source propagating toward the south. These kinematic properties may have played a role in the numerous slope instabilities and in the important damage that affected Iranian cities.

Furthermore, the misalignment between the plate convergence and the slip direction provide additional hints for a strain partitioning in this part of the Zagros belt between thrust motion on flat crustal faults and right lateral strike slip. As suggested by late aftershocks, unmapped dextral faults could be accommodating part of that shear strain and therefore represent an important seismic risk for nearby populations.

Acknowledgments

This project has received funding from the European Research Council (ERC) under the European Union's Horizon 2020 research and innovation program under grant agreements 758210 and 805256. This work also received financial support from Agence Nationale de la Recherche (project ANR-17-ERC3-0010). The Copernicus Sentinel-1 data were provided by the European Space Agency (ESA). Seismological observations belong to the Iran Strong Motion Network (<https://ismn.bhrc.ac.ir/en>). We acknowledge the Geological Survey of Iran (Seismotectonics and Seismology group) for making available their preliminary report (in Persian). It can be obtained upon request to info@gsi.ir. The AlTar algorithm used for the inversion was developed by the Seismological Laboratory at Caltech and was provided by Mark Simons. We thank the Editor, Gavin Hayes, and two anonymous reviewers for their constructive comments which helped improve this manuscript.

References

- Alavi, M. (2007). Structures of the Zagros fold-thrust belt in Iran. *American Journal of Science*, 307(9), 1064–1095.
- Ambraseys, N. N., & Melville, C. P. (2005). *A history of Persian earthquakes*. Cambridge, UK: Cambridge University Press.
- Anderson, J. G. (2003). Strong-motion seismology. *International Geophysics Series*, 81(B), 937–966.
- Andrews, D. J., & Ben-Zion, Y. (1997). Wrinkle-like slip pulse on a fault between different materials. *Journal of Geophysical Research*, 102(B1), 553–571.
- Aochi, H., Fukuyama, E., & Matsura, M. (2000). Spontaneous rupture propagation on a non-planar fault in 3-D elastic medium. *Pure and Applied Geophysics*, 157(11–12), 2003–2027.
- Barnhart, W. D., Brengman, C. M. J., Li, S., & Peterson, K. E. (2018). Ramp-flat basement structures of the Zagros Mountains inferred from co-seismic slip and afterslip of the 2017 M_w 7.3 Darbandikhan, Iran/Iraq earthquake. *Earth and Planetary Science Letters*, 496, 96–107.
- Berberian, M. (1995). Master blind thrust faults hidden under the Zagros folds: Active basement tectonics and surface morphotectonics. *Tectonophysics*, 241(3–4), 193–224.
- Berberian, M., & King, G. C. P. (1981). Towards a paleogeography and tectonic evolution of Iran. *Canadian Journal of Earth Sciences*, 18(2), 210–265.
- Beroza, G. C., & Mikumo, T. (1996). Short slip duration in dynamic rupture in the presence of heterogeneous fault properties. *Journal of Geophysical Research*, 101(B10), 22,449–22,460.
- Blanc, E.-P., Allen, M. B., Inger, S., & Hassani, H. (2003). Structural styles in the Zagros simple folded zone, Iran. *Journal of the Geological Society*, 160(3), 401–412.
- Casciello, E., Vergés, J., Saura, E., Casini, G., Fernández, N., Blanc, E., et al. (2009). Fold patterns and multilayer rheology of the Lurestan Province, Zagros simply folded belt (Iran). *Journal of the Geological Society*, 166(5), 947–959.
- Chen, K., Xu, W., Mai, P. M., Gao, H., Zhang, L., & Ding, X. (2018). The 2017 M_w 7.3 Sarpol Zahab earthquake, Iran: A compact blind shallow-dipping thrust event in the mountain front fault basement. *Tectonophysics*, 747, 108–114.
- Cirella, A., Piatanesi, A., Tinti, E., Chini, M., & Cocco, M. (2012). Complexity of the rupture process during the 2009 L'Aquila, Italy, earthquake. *Geophysical Journal International*, 190(1), 607–621.
- Copley, A., & Jackson, J. (2006). Active tectonics of the Turkish-Iranian plateau. *Tectonics*, 25, TC6006. <https://doi.org/10.1029/2005TC001906>
- Dahlen, F. A., & Tromp, J. (1998). *Theoretical global seismology*. Princeton, NJ: Princeton University Press.
- Day, S. M. (1982). Three-dimensional finite difference simulation of fault dynamics: Rectangular faults with fixed rupture velocity. *Bulletin of the Seismological Society of America*, 72(3), 705–727.
- DeMets, C., Gordon, R. G., & Argus, D. F. (2010). Geologically current plate motions. *Geophysical Journal International*, 181(1), 1–80.
- Duputel, Z., Agram, P. S., Simons, M., Minson, S. E., & Beck, J. L. (2014). Accounting for prediction uncertainty when inferring subsurface fault slip. *Geophysical Journal International*, 197(1), 464–482.
- Ekström, G., Dziewonski, A. M., Maternovskaya, N. N., & Nettles, M. (2005). Global seismicity of 2003: Centroid–moment-tensor solutions for 1087 earthquakes. *Physics of the Earth and Planetary Interiors*, 148(2–4), 327–351.
- Ekström, G., Nettles, M., & Dziewonski, A. M. (2012). The global CMT project 2004–2010: Centroid-moment tensors for 13,017 earthquakes, 200–201, 1–9.
- Falcon, N. L. (1969). Problems of the relationship between surface structure and deep displacements illustrated by the Zagros Range. *Geological Society, London, Special Publications*, 3(1), 9–21.
- Farr, T. G., Rosen, P. A., Caro, E., Crippen, R., Duren, R., Hensley, S., et al. (2007). The shuttle radar topography mission. *Reviews of Geophysics*, 45, RG2004. <https://doi.org/10.1029/2005RG000183>

- GSI (2017). Preliminary report on geological features of the Ezgaleh-Kermanshah earthquake (M 7.3), November 12, 2017, West Iran. GSI preliminary report number: 17-01, ver.03.
- Gombert, B., Duputel, Z., Jolivet, R., Simons, M., Jiang, J., Liang, C., et al. (2018). Strain budget of the Ecuador–Colombia subduction zone: A stochastic view. *Earth and Planetary Science Letters*, 498, 288–299.
- He, P., Wen, Y., Xu, C., & Chen, Y. (2018). High-quality three-dimensional displacement fields from new-generation SAR imagery: Application to the 2017 Ezgaleh, Iran, earthquake. *Journal of Geodesy*, 93, 573–591.
- Heaton, T. H. (1990). Evidence for and implications of self-healing pulses of slip in earthquake rupture. *Physics of the Earth and Planetary Interiors*, 64(1), 1–20.
- Herrmann, R. B. (2013). Computer programs in seismology: An evolving tool for instruction and research. *Seismological Research Letters*, 84(6), 1081–1088.
- Hessami, K., Koyi, H., & Talbot, C. J. (2001). The significance of strike-slip faulting in the basement of the Zagros fold and thrust belt. *Journal of petroleum Geology*, 24(1), 5–28.
- Hétényi, G., Cattin, R., Berthet, T., Le Moigne, N., Chophel, J., Lechmann, S., et al. (2016). Segmentation of the Himalayas as revealed by arc-parallel gravity anomalies. *Scientific reports*, 6, 33866.
- Huang, Y., & Ampuero, J.-P. (2011). Pulse-like ruptures induced by low-velocity fault zones. *Journal of Geophysical Research*, 116, B12307. <https://doi.org/10.1029/2011JB008684>
- Ide, S. (2007). Slip inversion, *Treatise on geophysics* (Vol. 4, pp. 193–224). Amsterdam: Elsevier.
- Jackson, J. (1980). Reactivation of basement faults and crustal shortening in orogenic belts. *Nature*, 283(5745), 343–346.
- Jolivet, R., Duputel, Z., Riel, B., Simons, M., Rivera, L., Minson, S., et al. (2014). The 2013 M_w 7.7 Balochistan earthquake: Seismic potential of an accretionary wedge. *Bulletin of the Seismological Society of America*, 104(2), 1020–1030.
- Kent, W. N. (2010). Structures of the Kirkuk Embayment, northern Iraq: Foreland structures or Zagros Fold Belt structures. *GeoArabia*, 15(4), 147–188.
- Koshnaw, R. I., Horton, B. K., Stockli, D. F., Barber, D. E., Tamar-Agha, M. Y., & Kendall, J. J. (2017). Neogene shortening and exhumation of the Zagros fold-thrust belt and foreland basin in the Kurdistan region of northern Iraq. *Tectonophysics*, 694, 332–355.
- Kreemer, C., Blewitt, G., & Klein, E. C. (2014). A geodetic plate motion and Global Strain Rate Model. *Geochemistry, Geophysics, Geosystems*, 15, 3849–3889. <https://doi.org/10.1002/2014GC005407>
- Lee, W. H. K., & Lahr, J. C. (1972). HYPO71: A computer program for determining hypocenter, magnitude, and first motion pattern of local earthquakes. US Geological Survey.
- Lohman, R. B., & Simons, M. (2005). Some thoughts on the use of InSAR data to constrain models of surface deformation: Noise structure and data downsampling. *Geochemistry, Geophysics, Geosystems*, 6, Q01007. <https://doi.org/10.1029/2004GC000841>
- McCaffrey, R. (1992). Oblique plate convergence, slip vectors, and forearc deformation. *Journal of Geophysical Research*, 97(B6), 8905–8915.
- Meier, M.-A., Heaton, T., & Clinton, J. (2016). Evidence for universal earthquake rupture initiation behavior. *Geophysical Research Letters*, 43, 7991–7996. <https://doi.org/10.1002/2016GL070081>
- Melgar, D., & Hayes, G. P. (2017). Systematic observations of the slip pulse properties of large earthquake ruptures. *Geophysical Research Letters*, 44, 9691–9698. <https://doi.org/10.1002/2017GL074916>
- Minson, S., Simons, M., & Beck, J. (2013). Bayesian inversion for finite fault earthquake source models I—Theory and algorithm. *Geophysical Journal International*, 194(3), 1701–1726.
- Minson, S., Simons, M., Beck, J., Ortega, F., Jiang, J., Owen, S., et al. (2014). Bayesian inversion for finite fault earthquake source models—II: The 2011 great Tohoku-oki, Japan earthquake. *Geophysical Journal International*, 198(2), 922–940.
- Miyajima, M., Fallahi, A., Ikemoto, T., Samaei, M., Karimzadeh, S., Setiawan, H., et al. (2018). Site investigation of the Sarpole-Zahab earthquake, M_w 7.3 in SW Iran of November 12, 2017. JSCE Journal of Disaster, FactSheet: FS2018-E-0002.
- Niazi, M., Asudeh, I., Ballard, G., Jackson, J., King, G., & McKenzie, D. (1978). The depth of seismicity in the Kermanshah region of the Zagros Mountains (Iran). *Earth and Planetary Science Letters*, 40(2), 270–274.
- Nissen, E., Ghods, A., Karasözen, E., Elliott, J. R., Barnhart, W. D., Bergman, E. A., et al. (2019). The 12 November 2017 M_w 7.3 Ezgaleh–Sarpolzahab (Iran) earthquake and active tectonics of the Lurestan arc. *Journal of Geophysical Research: Solid Earth*.
- Nissen, E., Tatar, M., Jackson, J. A., & Allen, M. B. (2011). New views on earthquake faulting in the Zagros fold-and-thrust belt of Iran. *Geophysical Journal International*, 186(3), 928–944.
- Paul, A., Hatzfeld, D., Kaviani, A., Tatar, M., & Péquegnat, C. (2010). Seismic imaging of the lithospheric structure of the Zagros Mountain belt (Iran). *Geological Society, London, Special Publications*, 330(1), 5–18.
- Perrin, G., Rice, J. R., & Zheng, G. (1995). Self-healing slip pulse on a frictional surface. *Journal of the Mechanics and Physics of Solids*, 43(9), 1461–1495.
- Platt, J. (1993). Mechanics of oblique convergence. *Journal of Geophysical Research*, 98(B9), 16,239–16,256.
- Rosen, P. A., Gurrola, E., Sacco, G. F., & Zebker, H. (2012). The InSAR scientific computing environment. In *VDE, 2012. EUSAR. 9th European Conference on Synthetic Aperture Radar* (pp. 730–733).
- Sadeghi, S., & Yassaghi, A. (2016). Spatial evolution of Zagros collision zone in Kurdistan, NW Iran: Constraints on Arabia–Eurasia oblique convergence. *Solid Earth*, 7(2), 659–659.
- Somerville, P., & Graves, R. (2003). Characterization of earthquake strong ground motion. Landslide tsunamis: Recent findings and research directions, Springer pp. 1811–1828.
- Talebian, M., & Jackson, J. (2002). Offset on the Main Recent Fault of NW Iran and implications for the late Cenozoic tectonics of the Arabia–Eurasia collision zone. *Geophysical Journal International*, 150(2), 422–439.
- Talebian, M., & Jackson, J. (2004). A reappraisal of earthquake focal mechanisms and active shortening in the Zagros Mountains of Iran. *Geophysical Journal International*, 156(3), 506–526.
- Tarantola, A. (2005). Inverse problem theory and methods for model parameter estimation. Siam 89.
- Tavani, S., Parente, M., Puzone, F., Corradetti, A., Gharabeigli, G., Valinejad, M., et al. (2018). The seismogenic fault system of the 2017 M_w 7.3 Iran–Iraq earthquake: Constraints from surface and subsurface data, cross-section balancing, and restoration. *Solid Earth*, 9(3), 821.
- Tchalenko, J., & Braud, J. (1974). Seismicity and structure of the Zagros (Iran): The Main Recent Fault between 33 and 35°N. *Philosophical Transactions of the Royal Society A*, 277(1262), 1–25.
- Vajedian, S., Motagh, M., Mousavi, Z., Motaghi, K., Fielding, E., Akbari, B., et al. (2018). Coseismic deformation field of the M_w 7.3 12 November 2017 Sarpol-e Zahab (Iran) earthquake: A decoupling horizon in the northern Zagros Mountains inferred from InSAR observations. *Remote Sensing*, 10(10), 1589.
- Vergés, J., Saura, E., Casciello, E., Fernandez, M., Villaseñor, A., Jiménez-Munt, I., & García-Castellanos, D. (2011). Crustal-scale cross-sections across the NW Zagros belt: Implications for the Arabian margin reconstruction. *Geological Magazine*, 148(5–6), 739–761.

- Vernant, P., Nilforoushan, F., Hatzfeld, D., Abbassi, M., Vigny, C., Masson, F., et al. (2004). Present-day crustal deformation and plate kinematics in the Middle East constrained by GPS measurements in Iran and northern Oman. *Geophysical Journal International*, 157(1), 381–398.
- Walker, R. T., Andalibi, M., Gheitanchi, M., Jackson, J., Karegar, S., & Priestley, K. (2005). Seismological and field observations from the 1990 November 6 Furg (Hormozgan) earthquake: A rare case of surface rupture in the Zagros Mountains of Iran. *Geophysical Journal International*, 163(2), 567–579.
- Wang, Y., Day, S. M., & Denolle, M. A. (2019). Geometric controls on pulse-like rupture in a dynamic model of the 2015 Gorkha earthquake. *Journal of Geophysical Research: Solid Earth*, 124, 1544–1568. <https://doi.org/10.1029/2018JB016602>
- Wanpeng, F., Sergey, S., Rafael, A., Ali, Y., Junhua, L., Qiang, Q., et al. (2018). Geodetic constraints of the 2017 $M_{\text{W}}7.3$ Sarpol Zahab, Iran earthquake and its implications on the structure and mechanics of the north-west Zagros thrust-fold belt. *Geophysical Research Letters*, 45, 6853–6861. <https://doi.org/10.1029/2018GL078577>
- Yang, Y.-H., Hu, J.-C., Yassaghi, A., Tsai, M.-C., Zare, M., Chen, Q., et al. (2018). Midcrustal Thrusting and Vertical Deformation Partitioning Constraint by 2017 $M_{\text{W}}7.3$ Sarpol Zahab earthquake in Zagros Mountain belt, Iran. *Seismological Research Letters*, 89(6), 2204–2213.

3.6 Perspectives

Dans ce chapitre, nous avons montré comment une prise en compte réaliste des incertitudes peut nous aider à répondre à différentes questions sur le comportement des failles actives. Concernant le séisme de Landers en 1992, nous avons montré qu'une partie du déficit de glissement superficiel observé pour les séismes décrochants pouvait s'expliquer par la présence d'une zone endommagée à proximité de la faille. En combinant différentes données en Équateur, nous avons évalué la plausibilité d'un excédent de glissement co-sismique par rapport au déficit de glissement accumulé depuis le dernier mégaséisme dans la région. Dans le cas du séisme d'Ezgeleh en 2017, nos observations montrent l'existence d'une rupture sous la forme d'un pulse de glissement fortement directif pouvant expliquer la répartition des dégâts constatés dans la région épicentrale.

Bien que les études présentées dans ce chapitre se focalisent principalement sur le glissement co-sismique et le couplage inter-sismique, les mêmes approches peuvent être employées pour explorer d'autres phases du cycle sismique. Ci-dessous nous présentons deux études récentes qui s'intéressent cette fois aux déformations transitoires associées aux séismes lents et à l'initiation des tremblements de terre. Ces travaux font partie de projets en cours dans le cadre de l'ANR S5 (porteur : J.-M. Nocquet) et de l'ERC PRESEISMIC (porteur : Z. Duputel).

3.6.1 Détection de séismes lents potentiellement récurrents au Chili

Bien que le Chili soit une région tectoniquement très active, très peu de séismes lents y ont été observés. Certains glissements lents ont été détectés avant l'occurrence des séismes d'Iquique en 2014 ($M_W = 8.1$, voir section 3.2) et de Valparaiso en 2017 ($M_W = 6.0$, voir section 3.6.2). Cependant, la proportion de glissement asismique pendant ces phases d'initiation reste débattue, une partie non-négligeable des déplacements GPS pouvant être induits par les séismes pré-chocs. En dehors de ces deux événements, aucun séisme lent récurrent n'a été observé, contrairement à la plupart des autres zones de subduction. Leur détection est notamment compliquée par le fait que certaines régions du Chili sont faiblement équipées en stations GPS permanentes. Jusqu'à présent, il n'était donc pas possible de déterminer si des séismes lents n'étaient pas détectés ou s'ils étaient simplement absents au Chili.

Pour pallier au déficit de stations GPS permanentes, nous avons analysé plus de 15 ans de données GPS de campagne dans le cadre du post-doctorat de Emilie Klein. Ce travail a mis en évidence un déplacement centimétrique cohérent entre 2014 et 2016 dans la région d'Atacama, confirmé par les stations GPS permanentes installées dans la région. L'inversion Bayésienne de ces données montre que ces observations peuvent être expliquées par un séisme lent profond d'une magnitude $M_W = 6.9$ sur une durée supérieure à 1 an. L'analyse d'une station GPS permanente installée depuis 2002 indique que des événements similaires semblent s'être produits en 2005 et en 2009, ce qui pourrait correspondre à une récurrence de 4 à 5 ans. Ces résultats sont présentés en annexe A.5 dans un article publié à *Geophysical Research Letters*.

Etant donné la possible récurrence de ces séismes lents, il est apparu nécessaire de mieux instrumenter la région d'Atacama pour améliorer notre caractérisation du phénomène. En collaboration avec l'ENS Paris, GéoAzur, l'IPGP et l'Université du Chili (dans le cadre du projet

ANR S5 et de l'ERC PRESEISMIC), nous avons donc déployé un réseau de stations GPS permanentes et de sismomètres large bande autour de Copiapó.

3.6.2 Glissement sismique et asismique lors de la préparation de grands séismes.

Bien qu'il soit établi que certains séismes soient précédés de petits évènements pré-chocs, les points de vue divergent sur l'initiation des tremblements de terre (Mignan, 2014). Certains modèles suggèrent que ces séismes précurseurs pourraient être déclenchés par une phase d'initiation asismique, au cours de laquelle la faille glisse lentement avant d'accélérer pour aboutir à la rupture sismique proprement dite (Dodge et al., 1996 ; Bouchon et al., 2011 ; Kato et al., 2016). D'autres modèles suggèrent plutôt une cascade aléatoire de séismes pré-chocs menant de façon hasardeuse au choc principal (Helmstetter and Sornette, 2003 ; Marzocchi and Zhuang, 2011 ; Ellsworth and Bulut, 2018). La différence entre ces deux interprétations réside principalement dans le partitionnement entre déformations sismiques et asismiques pendant la phase de préparation des grandes ruptures sismiques. La disponibilité de données sismologiques et géodésiques à proximité des failles actives est une occasion sans précédent pour explorer la genèse des tremblements de terre. Mon projet ERC débuté en 2019 consiste à combiner ces observations pour mieux comprendre l'évolution temporelle et le partitionnement entre glissement sismique et asismique pendant la phase d'initiation des ruptures sismiques.

Dans une étude récemment publiée dans *Geophysical Research Letters*, nous présentons des premiers résultats obtenus dans le cas de la séquence de Valparaiso en 2017 (en libre accès à l'URL : <https://doi.org/10.1029/2020GL091916>). Ce travail a été effectué dans le cadre du doctorat d'Emmanuel Caballero (en cours) et du post-doctorat d'Agnès Chouvet (jusqu'en Aout 2019). Cette analyse montre qu'une partie importante de la déformation observée en surface avant le choc principal est associée à un pré-glissement asismique de l'interface de subduction (Caballero et al., 2020). Un autre travail publié récemment dans le même journal s'intéresse aux séquences de séismes pré-chocs en Californie du sud (Moutote et al., 2020). Cette étude effectuée dans le cadre du doctorat de Luc Moutote (en cours) est accessible à l'URL : <https://doi.org/10.1029/2020GL091757>. Dans ce travail, nous ré-évaluons des études récentes qui suggèrent que les chocs principaux en Californie du sud sont souvent précédés par une activité sismique anormalement élevée (Trugman and Ross, 2019 ; van den Ende and Ampuero, 2020). Bien qu'ils reposent sur un catalogue de sismicité très complet, les travaux de Trugman and Ross (2019) et van den Ende and Ampuero (2020) négligent les interactions entre séismes. Dans notre étude, nous analysons le même catalogue en considérant un modèle ETAS qui restitue plus fidèlement l'amasement temporel de la sismicité. Nos résultats montrent que moins de 10% des chocs principaux en Californie du Sud sont précédés par une sismicité anormalement élevée. Cela suggère que les observations de séismes pré-chocs peuvent généralement être expliquées par une sismicité de fond et par des cascades d'évènements, même lorsque nous disposons de catalogues très complets. Pour mieux comprendre la préparation des grands séismes, il semble nécessaire de combiner l'analyse de la sismicité pré-choc avec d'autres observations en champ proche (tel que les données GNSS ou inclinométriques).

Sismicité volcanique

4.1 Différences entre sismicité volcanique et sismicité tectonique

Il est difficile de savoir exactement combien de volcans sont actuellement actifs sur Terre. En considérant les éruptions au cours des 10 000 dernières années, on considère généralement qu'il y a environ 1 500 volcans potentiellement actifs dont une cinquantaine entrent en éruption chaque année (cf., Figure 15). Ce nombre est certainement sous-estimé car il ne prend pas en compte la plupart des éruptions sous-marines. Comme les failles actives, les volcans sont des systèmes dynamiques sujet à des variations importantes de contraintes et produisant une sismicité caractéristique. Comme pour les systèmes tectoniques, on peut définir les régions associées à un aléa volcanique important et effectuer des prédictions à long-terme plus ou moins précises. Les éruptions volcaniques sont également précédées par des précurseurs bien identifiés qui permettent généralement de prédire l'occurrence d'éruptions à court terme (voir par exemple Roult et al., 2012 ; Shapiro et al., 2017). De telles prédictions restent impossibles pour les séismes tectoniques bien que les observations précédant certains grands séismes soient parfois similaires aux précurseurs pré-éruptifs (augmentation du taux de sismicité, migration de séismes, déformations pré-sismiques ; Kato et al., 2012 ; Bouchon et al., 2013 ; Socquet et al., 2017).

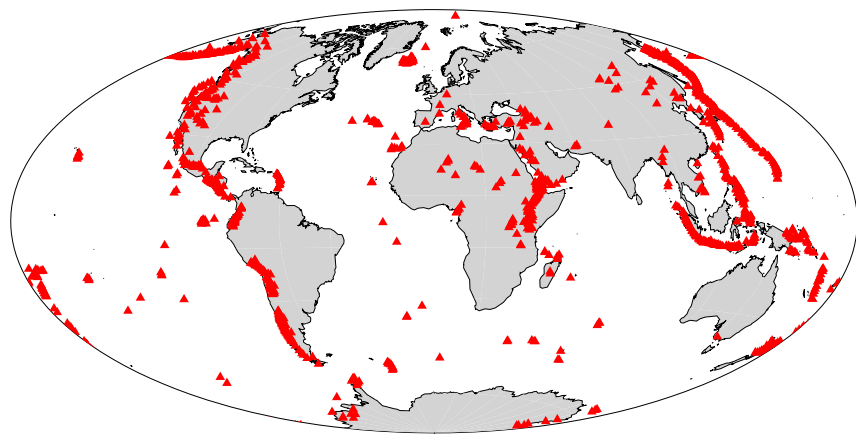


FIG. 15 – Volcans actifs sur Terre. La carte représente les 1 428 volcans connus étant entrés en éruption au cours de l'Holocène. Dans cette liste, 562 volcans ont connu des éruptions historiques (il y a moins de 5 000 ans) et environ 50 volcans entrent en éruption chaque année (Smithsonian Institution, 2013).

Comme illustré sur la Figure 16, les volcans sont associés à une sismicité extrêmement diverse qui est beaucoup plus variée que celle habituellement observée autour des failles (Kawakatsu and Yamamoto, 2007). Il est courant d'observer une combinaison de séismes volcano-tectoniques, de signaux basse-fréquence et de trémors volcaniques au cours d'un seul épisode éruptif. Cette di-

versité reflète la complexité des sources volcaniques ainsi que l'extrême hétérogénéité structurale des volcans. Notre compréhension des mécanismes de génération des séismes volcaniques reste encore très limitée. De façon générale, l'activité sismique des volcans trouve son origine dans les interactions dynamiques entre la terre solide, le gaz et les fluides (magma ou fluides hydrothermaux) au voisinage de conduits géométriquement complexes (Chouet and Matoza, 2013). Il est possible de classifier les signaux volcano-sismiques en deux grandes catégories basées sur notre compréhension des processus sources associés (Chouet, 1996). La première famille est associée aux signaux pour lesquelles la phase fluide joue un rôle essentiel dans la génération d'ondes élastiques. Les trémors volcaniques, la sismicité basse fréquence et très longue période sont souvent considérés comme des manifestations de tels processus. La deuxième famille d'événements correspond à des ruptures cassantes associées à des processus purement élastiques. Cette famille inclut notamment les événements volcano-tectoniques qui correspondent à des séismes "classiques" en cisaillement mais déclenchés par les perturbations de contraintes induites par le transport magmatique. Cette classification reste cependant schématique au vu de la complexité dynamique des volcans. Ces deux catégories peuvent être vues comme des manifestations extrêmes d'une variété plus continue de signaux (Neuberg et al., 2000). Ainsi par exemple, les séismes hybrides sont souvent considérés comme des ruptures cisallantes impliquant la résonance d'un conduit magmatique (Lahr et al., 1994), bien que certaines études semblent pouvoir expliquer ces observations sans impliquer une résonance fluide (Harrington and Brodsky, 2007). De façon similaire, on peut penser que les fluides jouent un rôle important dans la génération de certains événements volcano-tectoniques, par exemple en réduisant la contrainte normale effective de failles déjà chargées (White and McCausland, 2016 ; Coulon et al., 2017).

Ce chapitre se focalise sur l'activité du Piton de la Fournaise qui est également marquée par une grande diversité de signaux sismiques. On s'intéressera d'abord aux séismes volcano-tectoniques qui sont souvent utilisés pour le suivi de l'activité volcanique. Alors que ces événements sont considérés comme des ruptures cisallantes conventionnelles, le lien entre le transport magmatique et l'occurrence de ces séismes reste encore évasif. Ces événements sont alternative-ment interprétés comme des marqueurs directs du chemin emprunté par le magma (Grandin et al., 2011), comme un endommagement distribué dans l'édifice causé par une surpression du réservoir magmatique (Carrier et al., 2015) ou comme l'activation de structures pré-existantes déjà proches de la rupture (Rubin and Gillard, 1998). Au Piton de la Fournaise, on explorera en particulier la sismicité associée à une phase de réalimentation profonde du réservoir magmatique superficiel et la sismicité pré-éruptive qui a marqué l'activité du volcan entre 2014 et 2018. On s'intéressera ensuite à la source des signaux très longue période observés lors de l'effondrement de la caldeira sommitale au Piton de la Fournaise en 2007. Les sources volcaniques sont conventionnellement décrites au moyen d'un tenseur moment sismique qui permet de modéliser des ruptures cisallantes et différentes sources volumiques (ouverture ou fermeture de fissures, implissons, explosions, etc.). Les processus volcaniques impliquant souvent un transfert de masse, la modélisation des sources volcaniques nécessite la considération de forces simples en plus d'un tenseur moment sismique. Un exemple remarquable est l'éruption du Mont St Helens en 1980 qui a combiné un effondrement de flanc majeur représenté par une force horizontale (Kanamori and Given, 1982) et une série d'explosions volcaniques correspondant à la superposition d'une

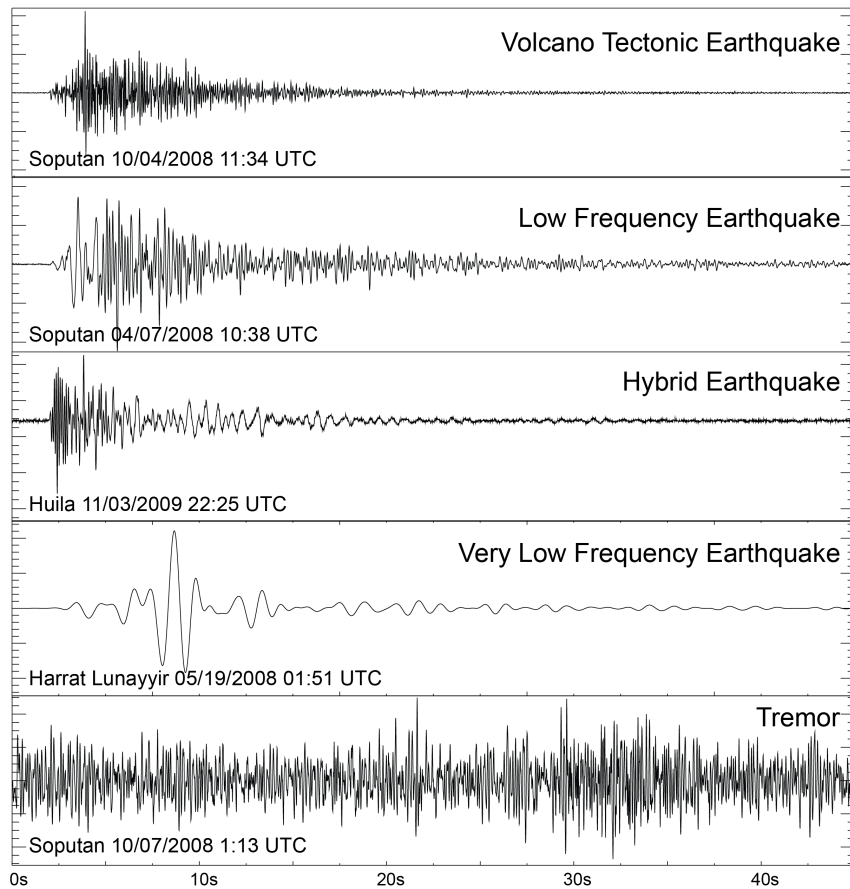


FIG. 16 – **Exemples de signaux volcano-sismiques communs.** Le séisme volcano-tectonique, le séisme basse fréquence et le trémor volcanique ont été enregistrés sur le volcan Soputanpatepangan (Indonésie). Le séisme Hybride provient du volcan Nevado del Huila (Colombie). Le séisme très longue période a été enregistré au Harrat Lunayyir (Arabie saoudite). Figure modifiée d’après Zoback et al. (2013).

source isotropique et d'une force verticale (Kanamori et al., 1984). Dans le contexte d'un effondrement de caldeira, on s'intéressera donc à l'importance du déchargement et du recharge de l'édifice volcanique induite par l'affaissement de la colonne de roche au dessus du réservoir magmatique.

4.2 Réalimentation profonde du réservoir magmatique superficiel au Piton de la Fournaise

Notre compréhension du lien entre le transport magmatique et l'occurrence de séismes est souvent limitée par la difficulté à détecter des événements dans un environnement volcanique. La variété des signaux enregistrés sur les volcans et le faible rapport signal sur bruit associé aux événements volcaniques compliquent souvent la détection et la localisation de la sismicité. Par ailleurs, les événements volcano-tectoniques sont généralement regroupés en essaims très actifs qui compliquent l'identification individuelle de chaque séisme. Dans l'étude présentée ci-dessous, nous proposons d'améliorer le niveau de détection des événements volcano-tectoniques au Piton de la Fournaise en utilisant une approche de "comparaison à modèle" (template matching). Cette

approche consiste à utiliser la signature d'évènements déjà catalogués comme des modèles de signaux à détecter. Pour chacun de ces modèles, on estime la fonction de corrélation entre les enregistrements continus et les formes d'ondes modèles à différentes stations. Ces fonctions de corrélations sont ensuite moyennées après correction des différences de temps de trajet entre les stations considérées. Les détections sont finalement effectuées lorsque cette fonction de corrélation moyenne indique un coefficient de corrélation important pour un modèle de séisme donné. Cette approche est appliquée au Piton de la Fournaise entre Juin 2014 et Novembre 2015. Les évènements détectés sont ensuite relocalisés par double différence après mesure des délais P et S inter-évenement. Les séismes localisés à faible profondeur (au dessus du niveau de la mer) définissent un anneau de sismicité au dessus de la chambre magmatique superficielle. Ces évènements sont vraisemblablement localisés sur une faille annulaire héritée des effondrements successifs de la partie sommitale du Piton de la Fournaise. Nos détections mettent également à jour un grand nombre de séismes profonds (entre 1 et 8 km sous le niveau de la mer) qui migrent vers la surface en 2015. Cette migration profonde est suivie de l'occurrence de séismes superficiels menant à une éruption 20 jours plus tard. Ces observations suggèrent un transfert de magma profond vers le réservoir sommital du Piton de la Fournaise. Cette réalimentation profonde marque le début d'une nouvelle phase d'activité du Piton de la Fournaise qui avait connu une phase relativement calme depuis 2010. Le volcan est depuis revenu à une phase extrêmement active avec plus de 3 éruptions par an en moyenne.

L'article proposé ci-dessous a été publié en 2016 dans *Geophysical Research Letters*. Ce travail a été effectué suite à mon recrutement à l'IPGS et a notamment été supporté par un projet INSU en 2016.



Geophysical Research Letters

RESEARCH LETTER

10.1002/2016GL068383

Key Points:

- A large number of volcano-tectonic earthquakes are detected and relocated using a template matching approach
- Relocated seismicity outlines a persistent ring-shaped structure at shallow depth and a vertically elongated complex at larger depths
- Magma transfer from a deep source is evidenced by a large number of upward migrating earthquakes moving toward a shallow reservoir

Supporting Information:

- Supporting Information S1
- Data Set S1

Correspondence to:

O. Lengliné,
lengline@unistra.fr

Citation:

Lengliné, O., Z. Duputel, and V. Ferrazzini (2016), Uncovering the hidden signature of a magmatic recharge at Piton de la Fournaise volcano using small earthquakes, *Geophys. Res. Lett.*, 43, 4255–4262, doi:10.1002/2016GL068383.

Received 23 FEB 2016

Accepted 29 MAR 2016

Accepted article online 4 APR 2016

Published online 7 MAY 2016

Uncovering the hidden signature of a magmatic recharge at Piton de la Fournaise volcano using small earthquakes

O. Lengliné¹, Z. Duputel¹, and V. Ferrazzini²

¹IPGS-EOST, Université de Strasbourg/CNRS, Strasbourg, France, ²Observatoire Volcanologique du Piton de la Fournaise, Institut de Physique du Globe de Paris, La Réunion, France

Abstract We apply a template matching method to detect and locate preeruptive earthquakes at Piton de la Fournaise volcano in 2014 and 2015. This approach enabled the detection of many events and unveiled persistent seismicity features through multiple eruptions. Shallow earthquakes define a ring-shaped structure beneath the main crater. The repetitive occurrence of events along this structure suggests that it corresponds to a preexisting zone of weakness within the edifice. We also show evidence of deep magma transfer in 2015. More than 5000 deep earthquakes define an upward migration immediately followed by the occurrence of shallow events leading to an eruption 20 days later. This suggests the creation of a hydraulic connection between the lower part of the volcanic system and a magma reservoir located near sea level. We can envisage that such replenishments of the shallow reservoir occurred in the past but were undetected because of limited deep earthquake detections.

1. Introduction

Eruptions at basaltic volcanoes are often preceded by abundant seismic activity [e.g., Collombet *et al.*, 2003]. This activity serves as one of the indicators of an impending eruption [e.g., Schmid *et al.*, 2012]. Beyond the usefulness of seismicity rate monitoring as a short-term eruption precursor at active volcanoes, earthquakes can also help to understand volcano dynamics. Volcano-tectonic (VT) earthquakes represent brittle failures within the volcanic edifice [McNutt and Roman, 2015]. While these events are related to stress perturbations caused by intruding magma bodies, a clear link between the stress source and the occurrence of these earthquakes is still elusive. These events are either interpreted as a direct marker of the magma pathway [e.g., Grandin *et al.*, 2011], as distributed damage within the volcanic edifice caused by the magma chamber pressure source [e.g., Carrier *et al.*, 2015] or as result of the activation of preexisting structures already near to failure [e.g., Rubin and Gillard, 1998]. This poses a challenge for the interpretation of preeruptive seismicity as an indicator of magma dynamics within the volcanic edifice.

A typical limitation to decipher the actual link between the magma feeding system and the occurrence of VT events is the lack of precise observations of these latter events. Volcanoes are associated with various seismic signals (e.g., long-period events, tremor, and rockfalls), which might mask the signature of VT events if they occur at the same time. The complexity of the seismic signals, combined with the low signal-to-noise ratio for small events, results in difficulties for both the detection and precise location of VT earthquakes. Furthermore, VT events often occur in very active swarm episodes that render the identification of each separate event difficult. In these circumstances, it is usually not possible to detect and locate earthquakes accurately during preeruptive crises.

In recent years, several innovative techniques have been applied to detect and characterize the various seismic signals. These techniques have revealed tectonic seismicity in unprecedented detail, which has led to the identification of new types of seismic phenomena. In particular, Shelly *et al.* [2006] showed that non-volcanic tremors occurring in subduction zones are composed of swarms of low-frequency earthquakes. These previously unnoticed events were detected by using a template matching approach, where continuous seismic data streams are correlated with known seismic signals included in a template database. This processing method leads to the recovery of signals within noisy data. Similar template matching approaches were used to unveil previously undetected low magnitude earthquakes [e.g., Gibbons and Ringdal, 2006] or

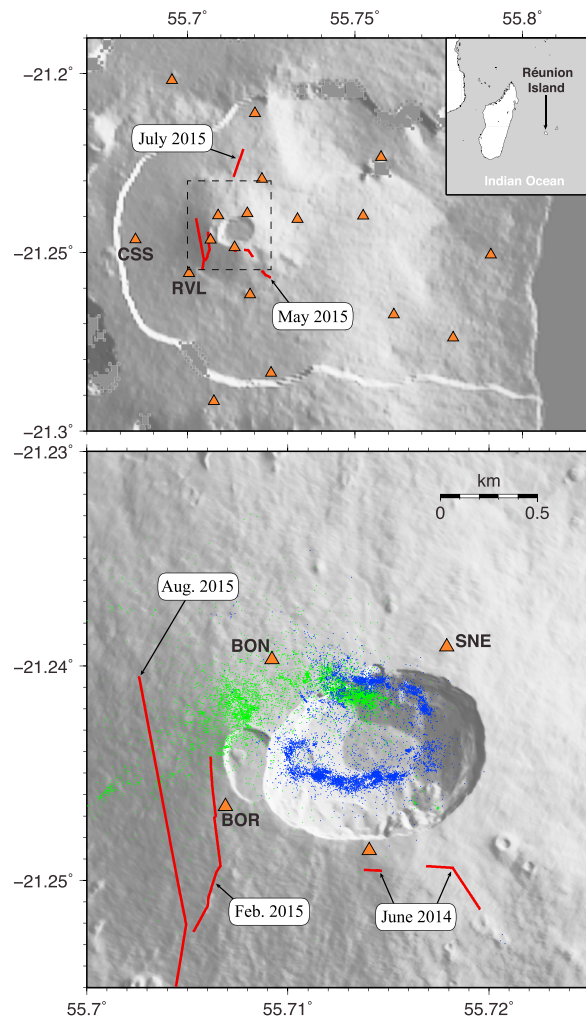


Figure 1. Volcano-tectonic setting. (top) Global map of the Piton de la Fournaise volcanic edifice. Orange triangles indicate seismic stations used in this study. Code names are indicated for stations used for event detection. The eruptive fissures of the five studied eruptions are indicated by red lines. (bottom) Same as Figure 1 (top) with the position of all relocated shallow earthquakes (blue dots) and deep events (green dots).

to uncover uncataloged seismic events following large earthquakes [e.g., *Peng and Zhao, 2009; Lengléné et al., 2012; Shimojo et al., 2014*].

Volcanic seismicity therefore appears as a perfect candidate for the application of this template matching technique. The recent application of this approach on Ontake volcano, Japan, revealed 30 times more events than those listed in original JMA catalog [*Zhang and Wen, 2015*]. The template matching approach can also be coupled with a relocation algorithm [e.g., *Waldbauer and Ellsworth, 2000*], such that newly detected events are then relocated relative to each other. Because of the high similarity between events, precise cross-correlation time delays can be estimated to obtain accurate relocation. *Shelly et al. [2013a, 2013b]* used such an approach to evidence migrations of seismicity that were previously undetected at Mount Rainier and Yellowstone (USA) volcanoes.

We use the template matching approach to detect events that occurred during recent eruptive unrests at Piton de la Fournaise volcano (Réunion Island, France) from June 2014 to November 2015 (see Figures 1 and S1 and Table S1 in the supporting information). Réunion Island is located in the Indian Ocean, east of Madagascar. Our approach reveals many more events than those included in the original catalog. Relocation of these newly detected events expose the structure of the volcano and highlight how the system evolves over time, in unprecedented detail. We notably resolve an upward migration of the seismicity that is interpreted

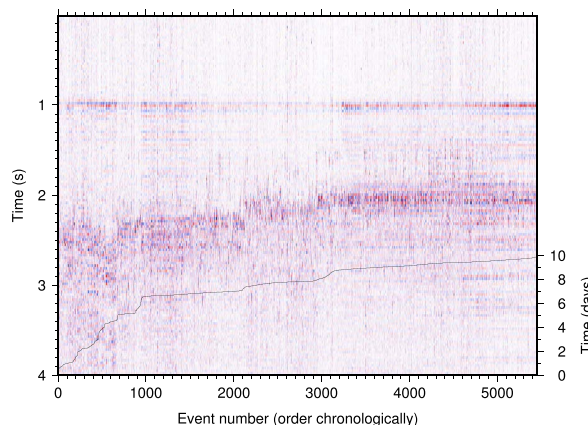


Figure 2. Vertical records at stations CSS for relocated deep events between 16 April 2015 and 25 April 2015. All waveforms are bandpass filtered between 8 and 32 Hz and normalized by their maximum amplitude. Events are ordered sequentially and are aligned on the P wave arrival. We can clearly see the S wave arrival drifting from 2.5 s for the first events to less than 2 s for the last events of the sequence. This diminution of the $S-P$ arrival time attests a progressive migration of events in the direction of the station (mostly corresponding to an upward movement). The black line shows the date of occurrence of events (in days) relative to the first event of the sequence.

matching approach to shed new light on the nature of the volcanic seismicity at Piton de la Fournaise. The template database is built using all located events listed in the catalog during the 2014 and 2015 preeruptive seismic crises. For each template event, we extract a 5.12 s long signal starting 1 s before the P wave pick for all stations and on all three components. These templates are separated in two groups: (1) 680 shallow events located above sea level and (2) 73 deep events located below sea level. Waveforms are filtered in the 5–25 Hz and 8–32 Hz passband, respectively, for shallow and deep events (see Figure S3).

The earthquake detection is done using a selection of channels maximizing the signal-to-noise ratio for each group of events. For shallow events, we use the vertical components of the three summit stations (BOR, BON, and SNE). For deep events, we select the three components of CSS and RVL (cf. Figure 1). At each time step (0.01 s), we compute correlation coefficients between template waveforms and continuous records. For a given template, we obtain traces of correlation coefficients at all selected channels. We apply a maximum filter over a duration of ± 0.1 s and shift the correlation signal by correcting for the travel time differences between stations. We then stack the shifted correlation coefficients of all the different channels. The maximum filter allows coherent stacking even if there is a small travel time difference between the template and the detected event (i.e., if the two events are not perfectly collocated). We then set a correlation coefficient threshold to 0.4 and consider as possible detections all time windows where this threshold is exceeded. In the case where multiple templates are associated with a common detection, we simply consider one detection associated with the template giving the highest correlation coefficient. For each newly detected event, we finally extract the three component waveforms (5.12 s long) at all stations where a P wave pick was available in the template event. This method results in the detection of 8011 shallow earthquakes and 8049 deep events, corresponding to ~ 10 times more shallow events and ~ 100 times more deep events than those listed in the original catalog. A majority of the detected deep events occurred within weeks before the May 2015 eruption. Waveforms of such deep events are presented in Figure 2.

For all detected events and available channels, we compute travel time delays from cross correlation by extracting 1.28 s long time windows around the P and S wave arrivals on the vertical and the two horizontal components, respectively. On average, we extract 11 stations for P waves and 10 stations for S waves for each detected earthquake. We use a second-order polynomial fit around the maximum of the cross-correlation function to obtain subsample time delay estimates. We retain all computed time delays associated with a correlation coefficient greater than 0.7. Travel time delays are then used to infer the relative locations of

as a deep magma pulse recharging a shallow reservoir near sea level. This replenishment is followed by an eruption 20 days later.

2. Methods

We use continuous data recorded by 18 broadband stations of the Observatoire Volcanologique du Piton de la Fournaise (OVPF, Figure 1). All these stations are recording continuously at 100 Hz and have three components. We focus our analysis on five recent preeruptive episodes that produced abundant seismicity (listed in Table S1). A relatively small number of earthquakes were originally included in the location catalog (see Figure S1 in the supporting information). This is notably due to the fact that during periods of high seismicity rate only a small fraction of the automatically detected events can be manually picked and located. In order to detect and locate new events, we employ a template

all detected events. Deep and shallow events are relocated separately since the large interevent distance between these two groups results in significant dissimilarities between waveforms (Figure 4). All newly detected events and those originally present in the catalog are all relocated together using the HypoDD software [Waldhauser and Ellsworth, 2000; Waldhauser, 2001]. For shallow events, ray parameters are computed from a homogeneous medium (straight rays). The velocity of this homogeneous medium is taken from the shallowest layer of the velocity model of the volcano: 3.5 km s^{-1} . For deep events we considered a 1-D velocity model [Battaglia et al., 2005]. During the inversion process we weight similarly P and S wave travel time delays and progressively reject outliers. Events without enough links with other earthquakes are discarded at each iteration. We are able to relocate 7857 shallow events out of the 8011 detections and 6548 earthquakes out of 8049 detected events.

3. Results

The relocation of shallow events delineates a ring-shaped structure with a mean radius of 300 m located below the summit crater and about 700 m above sea level. The shape of this shallow structure is well constrained by relative time delay measurements, but its absolute position is uncertain as it mostly depends on the initial location of template events. Most events on this shallow structure are triggered along two east-west trending streaks (Figure 1). These two features were previously noticed by Sapin et al. [1996] and Massin et al. [2011] who interpreted them as two subvertical planes dipping toward the center of the main crater. Our results rather suggest that the vertical extent of hypocenters is much more limited and mainly results from location uncertainties. Based on earthquake relocations, we find that the seismic cloud collapses within ± 50 m of a best fitting plane (see Figure S2 in the supporting information).

Based on the spatiotemporal distribution of shallow events, we also reveal the rapid migration of earthquakes preceding several eruptions (see Figure S3 in the supporting information). Immediately before June 2014 and May 2015, the seismicity rapidly migrated along the southern cluster toward the west with a velocity of about 1.7 km h^{-1} . Such feature is also observed before February 2015 but at much lower speed (66 m h^{-1}), with a migration lasting for the entire preeruptive episode. Other migrations are visible during preeruptive swarms but are not immediately followed by an eruption. On the other hand, such temporal evolution is not visible before July 2015 and August 2015 eruptions.

All relocated deep events (below sea level) are concentrated in a small area extending mainly to the west of the two summit craters. Their location defines several structures organized in a vertically elongated complex (Figures 1 and 3). It is possible that the depth extent of seismicity partly results from uncertainties due to the trade-off between depth variation and the origin time difference of events. However, Figure 2 points out that earthquakes are progressively triggered with a diminution of the $S-P$ arrival time at station CSS, located directly above these deep clusters. This shows not only that the vertical extent of seismicity is real but also that earthquakes migrate toward shallower depth with time (Figure 2). These deep earthquakes are migrating from 7.5 km to 1.5 km below sea level with longitude increasing as depth decreases. The location of these deep events coincides with the locations of the preeruptive earthquake migration identified before the 1998 eruption [Battaglia et al., 2005]. Our relocations highlight a seismically quiescent zone between sea level and a depth of 1.5 km in which no earthquakes are located. The thickness of this aseismic area is not very well constrained, as it is based on the comparison of two relocated data sets (deep events and shallow events) that we process independently (see previous section). It is however in agreement with previous observations based on the seismicity at the same location [e.g., Nercissian et al., 1996].

More than 80% of relocated deep events occurred between 16 and 25 April 2015. This seismicity starts at a depth of about 6 km on 16 April and seems to propagate both toward deeper and shallower depths relative to the initial location (Figure 3). The downward migration does not last more than a few days and most of the activity continues to progress upward. The seismicity reaches a depth of 2 km on 25 of April 2015 and remains active at that depth. This deep activity is then accompanied by the triggering of shallow event swarms preceding the 17 May 2015 eruption.

Although no magnitudes are computed for new detected earthquakes, they likely have lower magnitudes than the template events since they were not included in the original catalog. The largest deep template event in the catalog has a duration magnitude $M_D = 1.3$. By computing the relative amplitude between newly detected events and template events, we find that all new earthquakes (except one) have smaller amplitude,

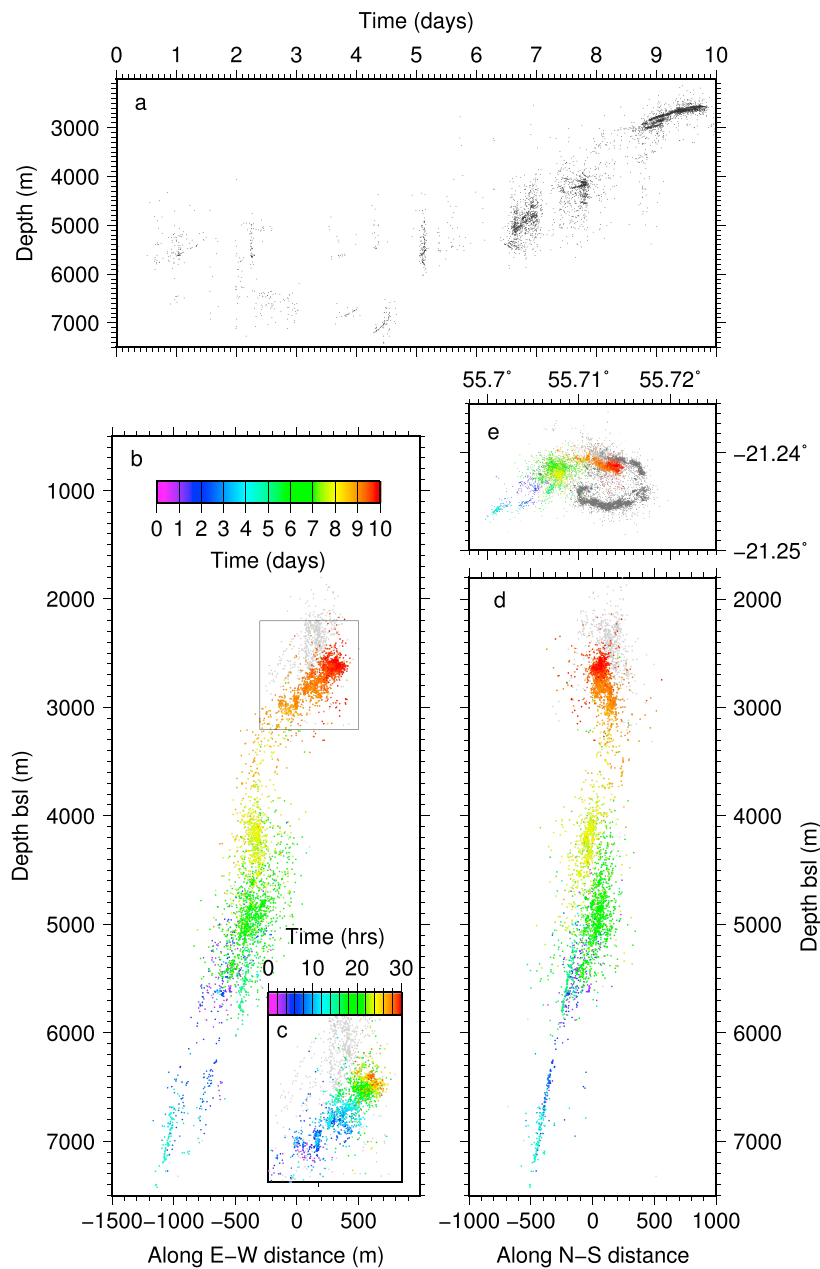


Figure 3. Spatiotemporal distribution of seismicity. (a) Depth of seismicity as a function of time during the first 10 days of the deep seismic crisis in April 2015. The black dots represent the location of earthquakes, and the origin time is taken as 16 April 2015. The eruption started on 17 May 2015. (b) E-W and (d) N-S cross sections of the deep seismicity. The gray dots refer to the location of all deep seismic events, while colors indicate the occurrence times of those events that occurred in the first 10 days. (c) Zoom in time and space on the shallower cluster (cf. square in Figure 3b). (e) Map view of the deep seismicity migration. The gray dots correspond to relocated shallow earthquakes (plotted for reference).

which suggests that most of them have $M < 1.3$. This contrasts with the migration of seismicity resolved in 1998 where the magnitude of about 700 deep events out of a total of 3100 ranged between 1.5 and 2.2.

The vertical migration speed during this sequence is of the order of 350 m per day, which is roughly 10 times slower than the one identified preceding the 1998 eruption of the Piton de la Fournaise [Battaglia et al., 2005]. Our observations also suggest that the distribution of deep events is not continuous but rather clusters at some depth intervals where intense swarms are progressively activated. The migration speed of events within these clusters is similar to the overall upward migration observed over the entire deep seismic crisis.

In the last 2 days, a west dipping bended swarm is activated between 3 km and 2 km below sea level. The migration within this cluster is not purely vertical, the events being also progressively triggered toward east (Figure 3c). The deep earthquakes occurring outside this migration sequence take place during several episodes mainly on 1, 5, and 13 May 2015 and during the last week of July 2015. During these episodes the deep seismicity is restricted to a limited depth interval between 1.5 km and 2.5 km below sea level with no apparent sign of migration.

4. Discussion and Conclusion

Our results show that the shallow preeruptive seismicity at Piton de la Fournaise occurs on some tightly clustered structures, while other areas of the volcanic edifice, including the neighborhood of the hypothetical magma pathways, remain quiet. During all of the five analyzed preeruptive periods, shallow events cluster on a persistent ring-shaped structure. The southern edge of this ring-shaped structure is associated with westward migrations of earthquakes before June 2014, February 2015, and May 2015 eruption. Since very few events are located above and below this structure, any identification of dyke propagation based on seismicity remains speculative. This could be related to our detection method, since events that are very different from templates can be difficult to recover. For example, it is possible that mode I earthquakes produced at the tip of a propagating dike are too small to be confidently picked from surface stations and thus cannot be included in the template database [Rubin and Gillard, 1998].

The shallow seismicity ring probably outlines preexisting zones of weakness that are triggered by static stress changes due to overpressurization of the magma chamber or dike intrusions in the volcanic edifice (probably either by shear stress increase across faults or decreased normal stress). It might correspond to a ring fault hosting repetitive collapses of the summit crater [e.g., Staudacher, 2010]. Such ring faults are documented in other volcanic areas [e.g., Mori and McKee, 1987], some of them being associated with migration of seismicity [Prejean et al., 2003] or with large earthquake ruptures [Nettles and Ekström, 1998]. On the other hand, events being located in a very limited depth range (± 50 m around a east dipping plane), we cannot totally rule out the possibility that seismicity is triggered on a single slowly slipping plane. Such slow slip process has been observed on other volcanoes [Cervelli et al., 2002; Segall et al., 2006] and might involve a subhorizontal detachment such as observed during the April 2007 Piton de la Fournaise eruption [Got et al., 2013; Chaput et al., 2014; Froger et al., 2015]. To better understand the physical process driving the shallow seismicity, we are currently working on inferring focal mechanisms of shallow earthquakes. This analysis is left to a future study.

Similarly, the coincident location of upward migrating deep seismicity before March 1998 and May 2015 eruptions suggests that deep events certainly occur on persistent structures that have a low frictional strength and are near to failure. These structures might be seismically activated, as the stress source associated with an ascending magma pulse is moving through the edifice. As static stress perturbations decays rapidly with distance, the triggered activity is certainly clustered around the moving magma body but does not necessarily represent its horizontal extent. Such interpretation is consistent with the analysis of geodetic data showing an acceleration of the edifice inflation rate starting in mid-April 2015 (i.e., when the deep seismicity starts) [Peltier et al., 2016]. The simultaneous increase of the $\text{CO}_2/\text{H}_2\text{O}$ ratio in summit fumaroles also suggests enrichment in deep and likely hot fluids associated with such magma upwelling [Peltier et al., 2016]. The deep seismicity migration therefore suggests the transfer of magma from a deeper source toward a shallow reservoir. This shallow magma chamber probably corresponds to the 1.5 km thick zone below sea level where no earthquakes are detected. This location agrees with the low velocity anomaly exposed by previous tomographic studies [e.g., Nercissian et al., 1996; Prôno et al., 2009] and with the source of deformation inverted from geodetic data for various eruptions [Peltier et al., 2007, 2008, 2009, 2016]. Furthermore, the end of deep earthquake migration on 25 April 2015 is almost immediately followed by the triggering of a shallow event swarm (within half a day, Figure 4), which clearly suggests hydraulic connection across the magma chamber. The delay between the time the magma enters this reservoir on 25 April and the onset of the eruption on 17 May probably corresponds to the buildup of a sufficient pressure in order to propagate magma up to the surface.

Interestingly, we also observe the occurrence of deep events (around 2 km below sea level) following swarms of shallow earthquakes (see Figure 4 on 29 April, 13 May, 28 July, and 21 August 2015). In all these cases the onset of deep seismicity immediately follows an arrest of shallow seismic activity. A possible explanation is the difficulty of detecting deep earthquakes when shallow ones occur because they dominate the seismic

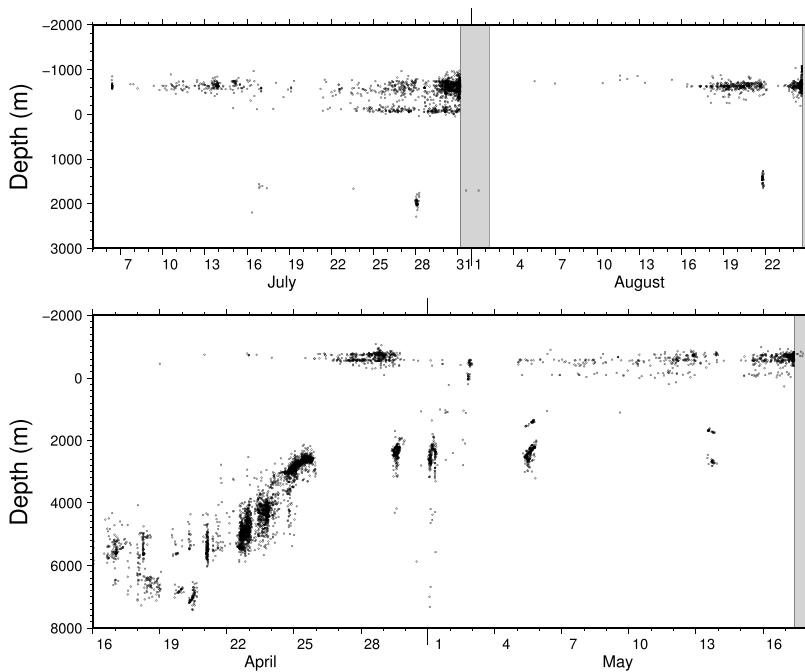


Figure 4. Evolution of earthquake depths in April–August 2015. Earthquake (black dots) depth during the preeruptive sequences of eruptions of (bottom) April–May and (top) July–August 2015. Relocated earthquakes with less than 10 travel times in total are not represented. Gray areas indicate eruption time periods.

signal. However, this possibility is unlikely as deep and shallow events are detected on two different sets of stations where they produced respectively the largest signal-to-noise ratio. These oscillations in event depths are thus probably related to variations in the position of the stress source.

Our analysis enabled the identification and location of many more events than originally included in the catalog. The template matching method is an efficient approach to recover small events when visual identification of the seismic signals and of the arrival times is difficult. In particular, it is noteworthy to realize that only 27 deep earthquakes were initially present in the catalog in April 2015, while several thousands of upward migrating events were detected in this study. We can envisage that migrations from a deep magma source, such as the one presented here, could have occurred in the past but were undetected because only a few earthquakes could be identified and located. A notable exception is the preeruptive seismicity preceding the 1998 eruption, which produced events large enough to be readily identified [Battaglia et al., 2005]. One could speculate that such unnoticed deep magma transfers could provide an explanation for the occurrences of the many eruptive episodes of the Piton de la Fournaise volcano since 1998. This method could also be used to better understand preeruptive behavior at volcanoes worldwide.

Acknowledgments

We thank Patrice Boissier, Julia Cantarano, Jean-Luc Got, Robin Matoza, Aline Peltier, Benoit Taisne, Michel Tas, and Nicolas Villeneuve for helpful discussions. We thank two anonymous reviewers for suggestions. We thank Mike Heap for grammatical assistance. Data are available through the eida.ipgp.fr arclink server and at the OVPF upon request. This research was supported by the Initiative d'Excellence (IDEX) funding framework (Université de Strasbourg) and the CNRS-INSU Tellus-ALEAS program. Figures were made with the GMT software [Wessel and Smith, 1998].

References

- Battaglia, J., V. Ferrazzini, T. Staudacher, K. Aki, and J.-L. Cheminée (2005), Pre-eruptive migration of earthquakes at the Piton de la Fournaise volcano (Réunion Island), *Geophys. J. Int.*, **161**(2), 549–558.
- Carrier, A., J.-L. Got, A. Peltier, V. Ferrazzini, T. Staudacher, P. Kowalski, and P. Boissier (2015), A damage model for volcanic edifices: Implications for edifice strength, magma pressure, and eruptive processes, *J. Geophys. Res. Solid Earth*, **120**, 567–583, doi:10.1002/2014JB011485.
- Cervelli, P., P. Segall, K. Johnson, M. Lisowski, and A. Miklius (2002), Sudden aseismic fault slip on the south flank of Kilauea volcano, *Nature*, **415**(6875), 1014–1018.
- Chaput, M., V. Pinel, V. Famin, L. Michon, and J. L. Froger (2014), Cointrusive shear displacement by sill intrusion in a detachment: A numerical approach, *Geophys. Res. Lett.*, **41**, 1937–1943, doi:10.1002/2013GL058813.
- Collombet, M., J.-R. Grasso, and V. Ferrazzini (2003), Seismicity rate before eruptions on Piton de la Fournaise volcano: Implications for eruption dynamics, *Geophys. Res. Lett.*, **30**, 2099, doi:10.1029/2003GL017494.
- Froger, J. L., V. Famin, V. Cayol, A. Augier, L. Michon, and J.-F. Lénat (2015), Time-dependent displacements during and after the April 2007 eruption of Piton de la Fournaise, revealed by interferometric data, *J. Volcanol. Geotherm. Res.*, **296**, 55–68.
- Gibbons, S. J., and F. Ringdal (2006), The detection of low magnitude seismic events using array-based waveform correlation, *Geophys. J. Int.*, **165**(1), 149–166.

- Got, J.-L., A. Peltier, T. Staudacher, P. Kowalski, and P. Boissier (2013), Edifice strength and magma transfer modulation at Piton de la Fournaise volcano, *J. Geophys. Res. Solid Earth*, **118**, 5040–5057, doi:10.1002/jgrb.50350.
- Grandin, R., et al. (2011), Seismicity during lateral dike propagation: Insights from new data in the recent Manda Hararo–Dabbahu rifting episode (Afar, Ethiopia), *Geochem. Geophys. Geosyst.*, **12**, Q0AB08, doi:10.1029/2010GC003434.
- Lenglîné, O., B. Enescu, Z. Peng, and K. Shiomi (2012), Decay and expansion of the early aftershock activity following the 2011, M_w 9.0 Tohoku earthquake, *Geophys. Res. Lett.*, **39**, L18309, doi:10.1029/2012GL052797.
- Massin, F., V. Ferrazzini, P. Bachélery, A. Nercessian, Z. Duputel, and T. Staudacher (2011), Structures and evolution of the plumbing system of Piton de la Fournaise volcano inferred from clustering of 2007 eruptive cycle seismicity, *J. Volcanol. Geotherm. Res.*, **202**(1), 96–106.
- McNutt, S. R., and D. C. Roman (2015), Chapter 59—Volcanic seismicity, in *The Encyclopedia of Volcanoes (Second Edition)*, 2nd ed., edited by H. Sigurdsson, pp. 1011–1034, Academic Press, Amsterdam, doi:10.1016/B978-0-12-385938-9.00059-6.
- Mori, J., and C. McKee (1987), Outward-dipping ring-fault structure at rabaul caldera as shown by earthquake locations, *Science*, **235**(4785), 193–195.
- Nercessian, A., A. Hirn, J.-C. Lépine, and M. Sapin (1996), Internal structure of Piton de la Fournaise volcano from seismic wave propagation and earthquake distribution, *J. Volcanol. Geotherm. Res.*, **70**(3), 123–143.
- Nettles, M., and G. Ekström (1998), Faulting mechanism of anomalous earthquakes near Bárdarbunga Volcano, Iceland, *J. Geophys. Res.*, **103**(B8), 17,973–17,983.
- Peltier, A., T. Staudacher, and P. Bachélery (2007), Constraints on magma transfers and structures involved in the 2003 activity at Piton de La Fournaise from displacement data, *J. Geophys. Res.*, **112**, B03207, doi:10.1029/2006JB004379.
- Peltier, A., V. Famin, P. Bachélery, V. Cayol, Y. Fukushima, and T. Staudacher (2008), Cyclic magma storages and transfers at Piton de La Fournaise volcano (La Réunion hotspot) inferred from deformation and geochemical data, *Earth Planet. Sci. Lett.*, **270**(3), 180–188.
- Peltier, A., P. Bachélery, and T. Staudacher (2009), Magma transport and storage at Piton de La Fournaise (La Réunion) between 1972 and 2007: A review of geophysical and geochemical data, *J. Volcanol. Geotherm. Res.*, **184**(1), 93–108.
- Peltier, A., F. Beauducel, N. Villeneuve, V. Ferrazzini, A. Di Muro, A. Aiuppa, A. Derrien, K. Jourde, and B. Taisne (2016), Deep fluid transfer evidenced by surface deformation during the 2014–2015 unrest at Piton de la Fournaise volcano, *J. Volcanol. Geotherm. Res.*, doi:10.1016/j.volgeores.2016.04.03.
- Peng, Z., and P. Zhao (2009), Migration of early aftershocks following the 2004 Parkfield earthquake, *Nat. Geosci.*, **2**(12), 877–881.
- Prejean, S., A. Stork, W. Ellsworth, D. Hill, and B. Julian (2003), High precision earthquake locations reveal seismogenic structure beneath Mammoth Mountain, California, *Geophys. Res. Lett.*, **30**, 2247, doi:10.1029/2003GL018334.
- Prôno, E., J. Battaglia, V. Monteiller, J.-L. Got, and V. Ferrazzini (2009), P-wave velocity structure of Piton de la Fournaise volcano deduced from seismic data recorded between 1996 and 1999, *J. Volcanol. Geotherm. Res.*, **184**(1), 49–62.
- Rubin, A. M., and D. Gillard (1998), Dike-induced earthquakes: Theoretical considerations, *J. Geophys. Res.*, **103**(B5), 10,017–10,030.
- Sapin, M., A. Hirn, J.-C. Lépine, and A. Nercessian (1996), Stress, failure and fluid flow deduced from earthquakes accompanying eruptions at Piton de la Fournaise volcano, *J. Volcanol. Geotherm. Res.*, **70**(3), 145–167.
- Schmid, A., J. Grasso, D. Clarke, V. Ferrazzini, P. Bachélery, and T. Staudacher (2012), Eruption forerunners from multiparameter monitoring and application for eruptions time predictability (Piton de la Fournaise), *J. Geophys. Res.*, **117**, B11203, doi:10.1029/2012JB009167.
- Segall, P., E. K. Desmarais, D. Shelly, A. Miklius, and P. Cervelli (2006), Earthquakes triggered by silent slip events on Kilauea volcano, Hawaii, *Nature*, **442**(7098), 71–74.
- Shelly, D. R., G. C. Beroza, S. Ide, and S. Nakamura (2006), Low-frequency earthquakes in Shikoku, Japan, and their relationship to episodic tremor and slip, *Nature*, **442**(7099), 188–191.
- Shelly, D. R., S. C. Moran, and W. A. Thelen (2013a), Evidence for fluid-triggered slip in the 2009 Mount Rainier, Washington earthquake swarm, *Geophys. Res. Lett.*, **40**, 1506–1512, doi:10.1002/grl.50354.
- Shelly, D. R., D. P. Hill, F. Massin, J. Farrell, R. B. Smith, and T. Taira (2013b), A fluid-driven earthquake swarm on the margin of the Yellowstone caldera, *J. Geophys. Res. Solid Earth*, **118**, 4872–4886, doi:10.1002/jgrb.50362.
- Shimojo, K., B. Enescu, Y. Yagi, and T. Takeda (2014), Fluid-driven seismicity activation in northern Nagano region after the 2011 M9.0 Tohoku-oki earthquake, *Geophys. Res. Lett.*, **41**, 7524–7531, doi:10.1002/2014GL061763.
- Staudacher, T. (2010), Field observations of the 2008 summit eruption at Piton de la Fournaise (Île de La Réunion) and implications for the 2007 Dolomieu collapse, *J. Volcanol. Geotherm. Res.*, **191**(1), 60–68.
- Waldhauser, F. (2001), HypoDD—A program to compute double-difference hypocenter locations, *U.S.G.S. Open File Rep.*, 01–113.
- Waldhauser, F., and W. L. Ellsworth (2000), A double-difference earthquake location algorithm: Method and application to the northern Hayward fault, California, *Bull. Seismol. Soc. Am.*, **90**(6), 1353–1368.
- Wessel, P., and W. H. Smith (1998), New, improved version of generic mapping tools released, *Eos Trans. AGU*, **79**(47), 579–579.
- Zhang, M., and L. Wen (2015), Earthquake characteristics before eruptions of Japan's Ontake volcano in 2007 and 2014, *Geophys. Res. Lett.*, **42**, 6982–6988, doi:10.1002/2015GL065165.

4.3 Caractéristiques spatiotemporelles du transport magmatique superficiel au Piton de la Fournaise

Il est souvent difficile de relier la sismicité observée à une source de pression magmatique en migration. Dans certaines circonstances, une intrusion magmatique peut même se produire de façon asismique (voir par exemple Aki and Koyanagi, 1981 ; Wright et al., 2006). L'occurrence de séismes suffisamment grands pour être enregistrés correspond vraisemblablement à la rupture de structures pré-existantes à proximité du magma en migration. Par ailleurs, l'étape finale de l'ascension du magma est généralement accompagnée par une activité sismique très faible comprenant principalement des évènements de faible magnitude difficiles à localiser individuellement. Cette observation est liée au faible niveau de contrainte à faible profondeur qui favorise la nucléation de petits séismes qui ne peuvent pas être localisés avec des méthodes conventionnelles (Taisne et al., 2011 ; De Barros et al., 2013). Comme les volcans basaltiques sont généralement associés à des chambres magmatiques superficielles, la dernière phase des intrusions magmatiques vers la surface est difficile à caractériser, limitant une possible prédiction de l'activité éruptive en surface. Dans l'étude proposée ci-dessous, nous appliquons l'approche de détection et de relocalisation présentée dans la partie précédente pour caractériser la sismicité pré-éruptive de 13 éruptions entre juin 2014 et Juillet 2018 au Piton de la Fournaise. Cette sismicité pré-éruptive est principalement localisée sur la structure annulaire révélée dans la partie précédente. Nous observons que seule une portion de cette structure est activée avant chaque éruption, fournissant une indication sur la direction de l'intrusion magmatique. Par ailleurs, nous montrons que le délai entre le début de la crise sismique pré-éruptive et le début de l'éruption est proportionnel à la distance entre le site éruptif et le cone sommital. Ces observations démontrent que le début de l'intrusion fournit déjà une information sur la localisation du futur site éruptif.

L'article proposé ci-dessous a été publié en 2019 dans *Geophysical Research Letters*. Ce travail a été effectué suite à mon recrutement à l'IPGS et a été supporté par l'appel d'offre interne à l'IPGS et mon projet ERC.



Geophysical Research Letters

RESEARCH LETTER

10.1029/2018GL080895

Key Points:

- We use a template matching technique to detect and relocate earthquakes during the 13 last eruptive unrests at Piton de la Fournaise volcano
- Almost all detected events are located on a ring-shaped structure, corresponding to an area of weakness in the upper edifice of the volcano
- The location and timing of pre-eruptive seismic swarms on this ring-shaped structure bring information on the future eruptive site

Supporting Information:

- Supporting Information S1

Correspondence to:

Z. Duputel,
zacharie.duputel@unistra.fr

Citation:

Duputel, Z., Lengliné, O., & Ferrazzini, V. (2019). Constraining spatiotemporal characteristics of magma migration at Piton de la Fournaise volcano from pre-eruptive seismicity. *Geophysical Research Letters*, 46, 119–127.
<https://doi.org/10.1029/2018GL080895>

Received 13 OCT 2018

Accepted 13 DEC 2018

Accepted article online 21 DEC 2018

Published online 5 JAN 2019

Constraining Spatiotemporal Characteristics of Magma Migration at Piton De La Fournaise Volcano From Pre-eruptive Seismicity

Z. Duputel¹ , O. Lengliné¹ , and V. Ferrazzini² ¹Institut de Physique du Globe de Strasbourg, UMR7516, EOST, CNRS, Université de Strasbourg, Strasbourg, France,²Observatoire Volcanologique du Piton de la Fournaise, Institut de Physique du Globe de Paris, Sorbonne Paris Cité, CNRS, La Plaine des Cafres, Université Paris Diderot, Paris, France

Abstract Volcano-tectonic seismicity has been recorded for decades on various volcanoes and is linked with the magma transport and reservoir pressurization. Yet earthquakes often appear broadly distributed such that magma movement is difficult to infer from its analysis. We explore the seismicity that occurred before eruptions at Piton de la Fournaise in the last 5 years. Using template matching and relocation techniques, we produce a refined image of the summit seismicity, demonstrating that most earthquakes are located on a ring structure. However, only a portion of this structure is activated before each eruption, which provides an indication as to the direction of the future eruptive site. Furthermore, we show that the delay between the pre-eruptive swarm and the eruption onset is proportional to the distance of the eruptive fissures relative to the summit cone. This reveals that the beginning of the intrusion already bears information regarding the future eruption location.

Plain Language Summary Earthquakes on volcanoes are usually related to the ascent of magma in the edifice and can therefore provide information concerning an impending eruption. Yet on many occasions, it is not easy to relate the recorded seismicity to the propagation of magma in the volcano. In this study, we detect and locate earthquakes that occurred before 13 eruptions at Piton de la Fournaise, a hawaiian-type volcano located on La Réunion island in the Indian Ocean. We demonstrate that a detailed analysis of the seismicity occurring when the magma starts its ascent can bring important information regarding the future eruption location.

1. Introduction

One goal of volcano monitoring is to provide reliable information concerning an impending eruption. With this purpose, one generally relies on the detection of anomalous signals that could reflect magma intrusions within the edifice. A major challenge is the difficulty in interpreting the different observations that are recorded during the pre-eruptive phase. Volcano-tectonic events are often considered to signal dynamic shear failure within the edifice. It is envisioned that a migrating magma pressure source can locally create high-stress concentrations that ultimately result in material failure and microearthquakes. Such a relation between the propagation of a magma-filled dike and the occurrence of earthquakes has been documented on several occasions (e.g., Battaglia et al., 2005; Einarsson & Brandsdóttir, 1980; Grandin et al., 2011; Rubin et al., 1998; Sigmundsson et al., 2015). However, it is often not easy to relate the recorded seismicity to a moving magma source. In certain circumstances, a dike can even intrude the volcanic edifice with no detectable earthquakes (e.g., Aki & Koyanagi, 1981; Wright et al., 2006). Indeed, as noted by Rubin and Gillard (1998), the occurrence of earthquakes large enough to be detected most likely corresponds to the failure of pre-existing weak structures within the edifice in the vicinity of the propagating crack but not necessarily the exact tip of the dike. Furthermore, the final stage of the magma ascent is often accompanied by very low seismic activity only comprising low-amplitude events that are difficult to track and locate (Eibl et al., 2017; Taisne et al., 2011; Zecevic et al., 2013). This is because the low stresses at shallow depth only permit very small earthquakes that cannot be easily detected and located. In addition, upper parts of volcanic edifices are usually highly heterogeneous, which can prevent long faults to develop. Therefore, as shallow magma chambers are usually found on basaltic

©2018. The Authors.

This is an open access article under the terms of the Creative Commons Attribution-NonCommercial-NoDerivs License, which permits use and distribution in any medium, provided the original work is properly cited, the use is non-commercial and no modifications or adaptations are made.

Table 1
Date, Time, Duration, and Location of the Analyzed Eruptions

Date	Time	Duration	Location
20/06/2014	21:35	19 hr	Summit area
04/02/2015	07:00	11.5 days	Summit area
17/05/2015	09:45	13.3 days	Southeast flank
31/07/2015	05:20	2.1 days	North flank
24/08/2015	14:50	58.3 days	Southwest flank
26/05/2016	04:05	26 hr	South flank
11/09/2016	04:41	6.8 days	North flank
31/01/2017	15:40	27.0 days	South flank
17/05/2017	16:10 ^a	4.0 days	North flank
13/07/2017	20:50	45.1 days	South flank
03/04/2018	06:40	17 hr	North flank
27/04/2018	19:50	34.6 days	Southwest flank
12/07/2018	23:30	19 hr	Northwest flank

Note. Eruptive fissures are mapped in Figures 1, 2, and S3.

^aOnly gas and no magma was associated with the eruption on 17/5/2017.

volcanoes, the last stage of magma propagation between such reservoirs and the surface is difficult to track. It thus limits our ability to make predictions of the future surface eruptive activity based on seismicity recording.

In this study, we focus on the Piton de la Fournaise volcano located on La Réunion island in the Indian Ocean. This frequently active (i.e., 13 eruptions between June 2014 and July 2018; Table 1) basaltic volcano represents an excellent field laboratory that is monitored by a dense network of geodetic and seismological stations (see Figure 1; Brenguier et al., 2012; Staudacher & Peltier, 2016). Being able to predict the location of a future eruption is of great interest at the Piton de la Fournaise. Indeed, a major concern are distal flank eruptions close to inhabited areas outside of the Enclos Fouqué caldera. In addition, as the volcano is a popular tourist attraction (with over 350,000 visitors per year; Harris et al., 2017), the prediction of eruptive fissure location is important to plan the evacuation of visitors hiking into the caldera. Eruptions are generally preceded by an intense shallow seismic crisis lasting a few hours (Roult et al., 2012), which originates from a persistent structure located below the volcano summit around sea level (Lengliné et al., 2016; Sapin et al., 1996). Some shallow events are occasionally captured in the latter stage of the crisis, but they are usually difficult to locate (e.g., De Barros et al., 2013; Taisne et al., 2011). In fact, most events located before eruptions remain confined below the central cone and do not track the last stage of magma movement. Here we use a template

matching technique to detect and relocate seismic events during the 13 last eruptive unrests at Piton de la Fournaise volcano. We show that a careful analysis of the pre-eruptive seismicity provides clear indications as to the location of an oncoming eruption.

2. Data and Methods

Earthquake detection is conducted using a template matching procedure following the same approach described in Lengliné et al. (2016). This detection process has been directly implemented at the Piton de la Fournaise Volcano Observatory to provide an automated detection of any seismic events. Each day, we build a template earthquake catalog from the last 1,000 events manually located in the shallow part of the volcano. Among these 1,000 template candidates, we only select events that have a depth uncertainty lower than 340 m and be located above sea level in the Enclos Fouqué caldera. We then scan the previous 24 hr of continuous seismic data to detect events that match at least one of the events in this template list. The earthquake detection is performed using the vertical components of at least three stations near the central cone (BOR, BON, SNE, FJS, RVL, or CSS). All traces are filtered between 5 and 25 Hz. For each template, we compute correlation coefficients for each time step (0.01 s) on all selected channels. We then apply a maximum filter over a duration of ± 0.1 s and stack the correlation traces after applying a travel time correction. We consider all time windows where the average correlation over the last three traces is larger than 0.45 as possible detections. In the case when multiple templates lead to a common detection, we only consider the detection associated with the template that produced the highest correlation coefficient with the continuous data stream. Once detection times have been obtained, we extract the waveforms at all of the stations in the Piton de la Fournaise Volcano Observatory network for each newly detected event based on the template travel times. This results in a total set of 16,246 events between June 2014 and July 2018. This compares to the 1,635 events that are listed in the original catalog for the same time period. Almost all of these events occur during the seismic crises that precede the eruptions listed in Table 1.

In order to obtain the precise location of each event, we use a double-difference relative location algorithm (Waldhauser, 2000). We first compute *P* and *S* wave differential travel times for all pairs of detected events on 1.28-s-long windows based on the maximum of the cross-correlation function. The differential travel times of *P* wave are computed on vertical components, whereas the differential travel times of *S* waves are obtained on both horizontal components. Following Carrier and Got (2014), we apply an a priori Cauchy distribution with $\sigma_0 = 0.1$ s to this cross-correlation function in order to mitigate the contamination of outliers in the data set. We discard travel time delays when the correlation coefficient multiplied by the a priori function is lower than 50%. All events are finally relocated together which results in a final set of 15,598 relocated events. We use a simple homogeneous velocity model for the relocation with a *P* wave velocity of 3.0 km/s and a V_p/V_s

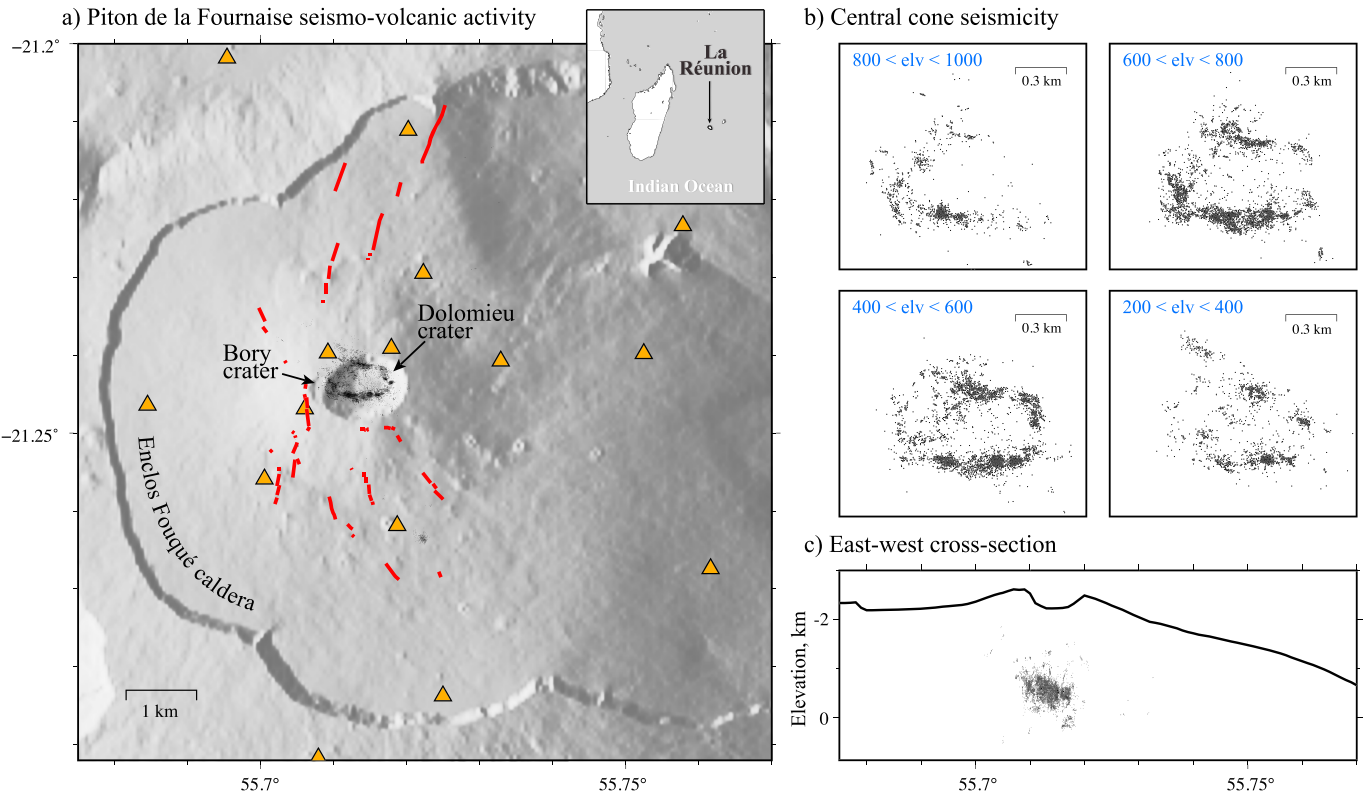


Figure 1. Relocated earthquake catalog, eruptive fissures and seismic stations. (a) Map view of the 15,598 relocated earthquakes (black circles) and volcanic fissures of eruptions between June 2014 and July 2018 (red lines). Orange triangles indicate seismic stations of the Piton de la Fournaise observatory. (b) Map view of relocated earthquakes in four different depth intervals ("elv" stands for elevation above sea level in meters). (c) Projection of relocated events onto an east-west cross section. Topography at latitude -21.45° is shown for reference. We observe in (b) and (c) that deeper seismicity focuses on the east, while shallower events are mostly located on the west. The overall structure has an eastward dipping angle of $\sim 20^{\circ}$.

ratio of 1.73. We also account for the station elevations when computing raypaths. Events that are discarded during the relocation process correspond to earthquakes that have too few links with other events to be adequately relocated.

3. Results

The entire set of relocated earthquakes is presented in Figure 1. We observe that almost all events focus on a ring structure located below the summit of the volcano between a depth of 200 m and 1 km above sea level. This structure was already evidenced by Lengliné et al. (2016) using data from the 2014 and 2015 eruptions. Its location is considered to correspond to a zone of weakness or stress concentration at the roof of the magma reservoir (located around sea level according to previous studies; Lénat et al., 2012; Peltier et al., 2005). Our updated relocated catalog seems to show more details than previous studies (e.g., Lengliné et al., 2016; Sapin et al., 1996): we notice secondary seismicity alignments inside the main ring structure such as a N45° lineation that is clearly visible to the northwest of the Dolomieu crater in Figure 1b. This structure certainly corresponds to a ring fault system hosting repetitive collapses of the volcano summit (e.g., Staudacher, 2010). Alignments of seismicity inside the main ring structure might outline secondary faults or weak structures associated with the different collapsed areas that affected Dolomieu and Bory summit craters in the past (Michon et al., 2013). Earthquake swarms that occur on the ring structure before each eruption seem to have distinct locations. Indeed, the correlation matrix highlighting the similarity of the recorded signals shows that events are mostly correlated with earthquakes belonging to the same pre-eruptive swarm (cf., Figure S1 in the supporting information). One consequence of this poor correlation among seismic swarms is that most earthquakes are detected shortly before or after their template events (cf., Figure S2).

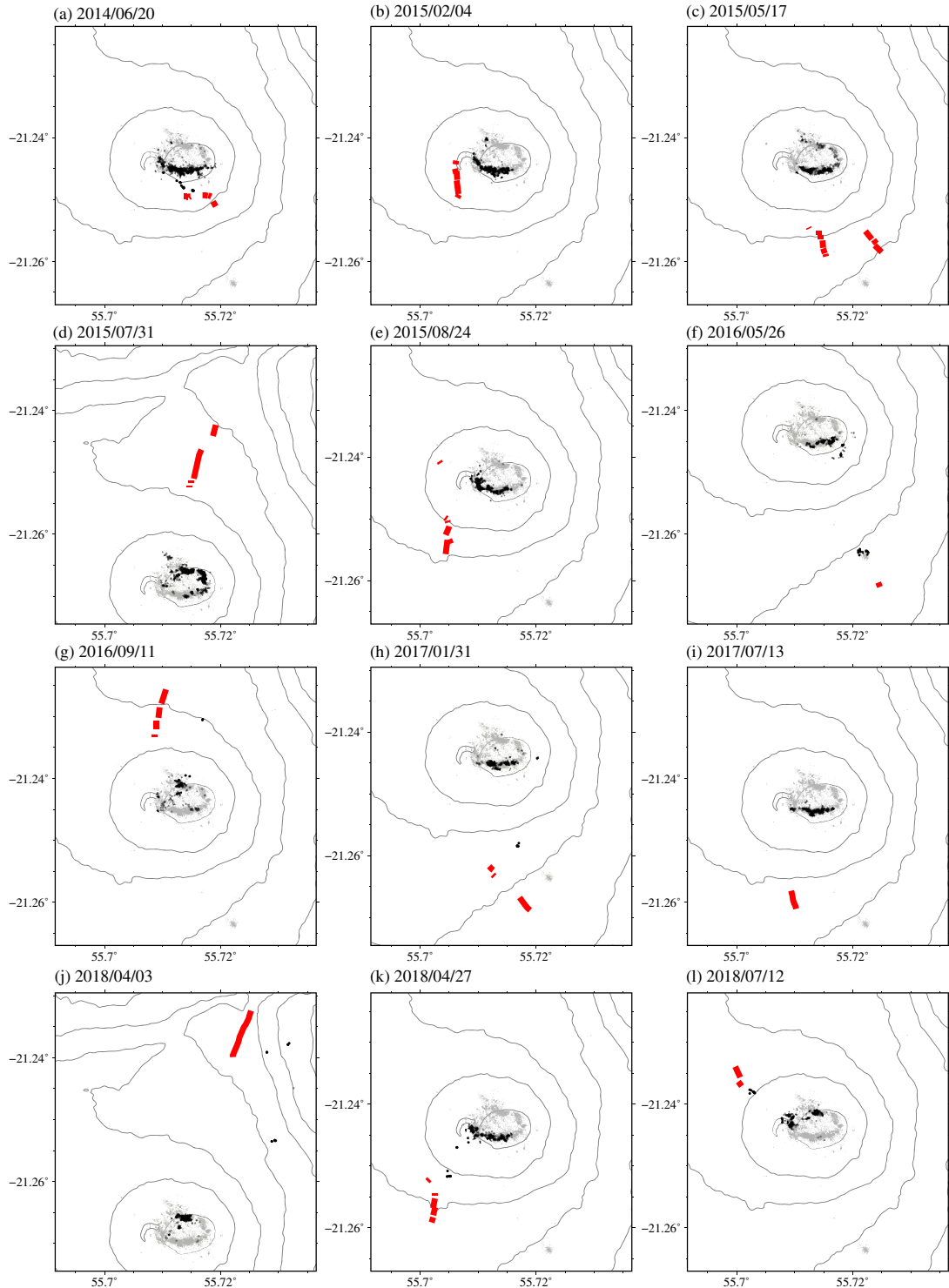


Figure 2. (a–l) Location of earthquakes and eruptive fissures. Each map presents the seismic crisis preceding an eruption (cf., date indicated on top of each subfigure). The location of eruptive fissures is indicated in red. Black circles represent the seismic events that occurred within 24 hr before the eruption. Gray circles represent the entire set of relocated seismic events. Fissure locations are based on visual inspections from field investigations with GPS tracking and photogrammetry. The same map is presented in Figure S3 for the eruption of 17/5/2017 that was only associated with gas emissions (no lava was ejected from the fissure). We also compare the azimuthal distribution of earthquakes and eruptive fissures in Figure S4.

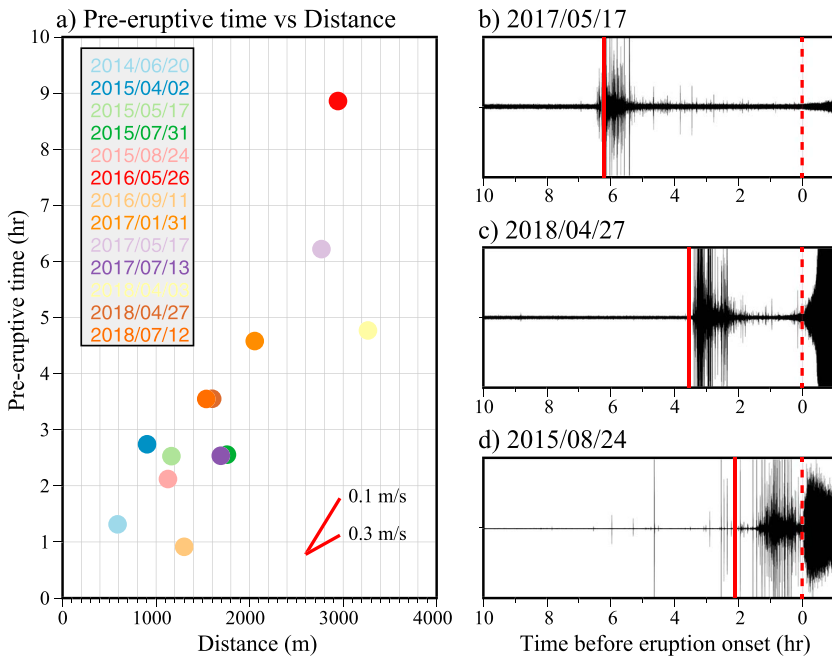


Figure 3. Time evolution of pre-eruptive seismic crises. (a) Pre-eruptive swarm time delay as a function of distance between earthquakes and eruptive fissures. The pre-eruptive time corresponds to the time difference between the swarm onset and the eruption onset. (b–d) Examples of continuous seismograms on the vertical component recorded before three eruptions at station BOR, located on the southwest rim of the Bory crater (cf., Figure 1). The continuous red line refers to the seismic crisis onset. The dashed red line at time 0 indicates the start of the eruption.

To analyze the pre-eruptive activity, we focus on events that occurred within 24 hr before each of the 13 eruptions that occurred between 2014 and 2018 (see Table 1). Eruptions at Piton de la Fournaise are typically preceded by a seismic crisis a few hours before the eruption onset. We report in Figure 2 the location of earthquakes preceding each eruption along with the corresponding eruptive fissures. For all eruptions, we readily observe that only a portion of the ring structure is activated during the pre-eruptive seismic crisis. Furthermore, we clearly see that the activated portion of the ring provides a good indication of the future eruptive fissure location. More specifically, the azimuth of the eruptive site relative to the summit area can be extrapolated from the location of earthquakes on the main ring structure. We can see in Figures 2, S3, and S4 that we have a perfect match for all 13 analyzed eruptions. It suggests that, although individual events do not allow us to track the magma propagation all the way up to the surface, there is a clear link between earthquake locations on the ring structure and the existence of a moving magma body.

To investigate how the pre-eruptive seismicity is connected to the mass magma transport within the edifice, we measure the timing of the seismic crises relative to the eruption onsets. Pre-eruptive seismic crises are conspicuous on the seismograms presented in Figure 3: eruptions are systematically preceded by a significant increase of seismicity for a duration that varies significantly between each eruption (from a few tens of minutes to more than 8 hr). We can also note that the earthquake rate drops before the onset of the eruptions. As mentioned before, this suggests that the ultimate propagation of the magma up to the eruptive site is mostly aseismic, which makes it difficult to track using earthquakes. Some events can still be detected during this phase (see Figure 2), but they are difficult to locate because they are usually visible only at a few stations (e.g., De Barros et al., 2013; Taisne et al., 2011). We can however investigate if there is any relationship between the timing of the seismic swarms and the location of the eruptive sites. Figure 3 shows the pre-eruptive time delay of the seismic swarms as a function of their distance to the eruption sites. Pre-eruptive time delays correspond to the time difference between the beginning of the seismic crisis and the eruption onset. They are computed using a simple approach, considering that the seismic crisis starts when the earthquake rate reaches a threshold of 150 events per hour. The distance to the eruption site is defined as the shortest distance between earthquakes occurring at the beginning of the seismic crisis and the eruptive fissures. There is a clear correlation between the time delay and the distance of the seismic swarms to the eruption sites. This simply

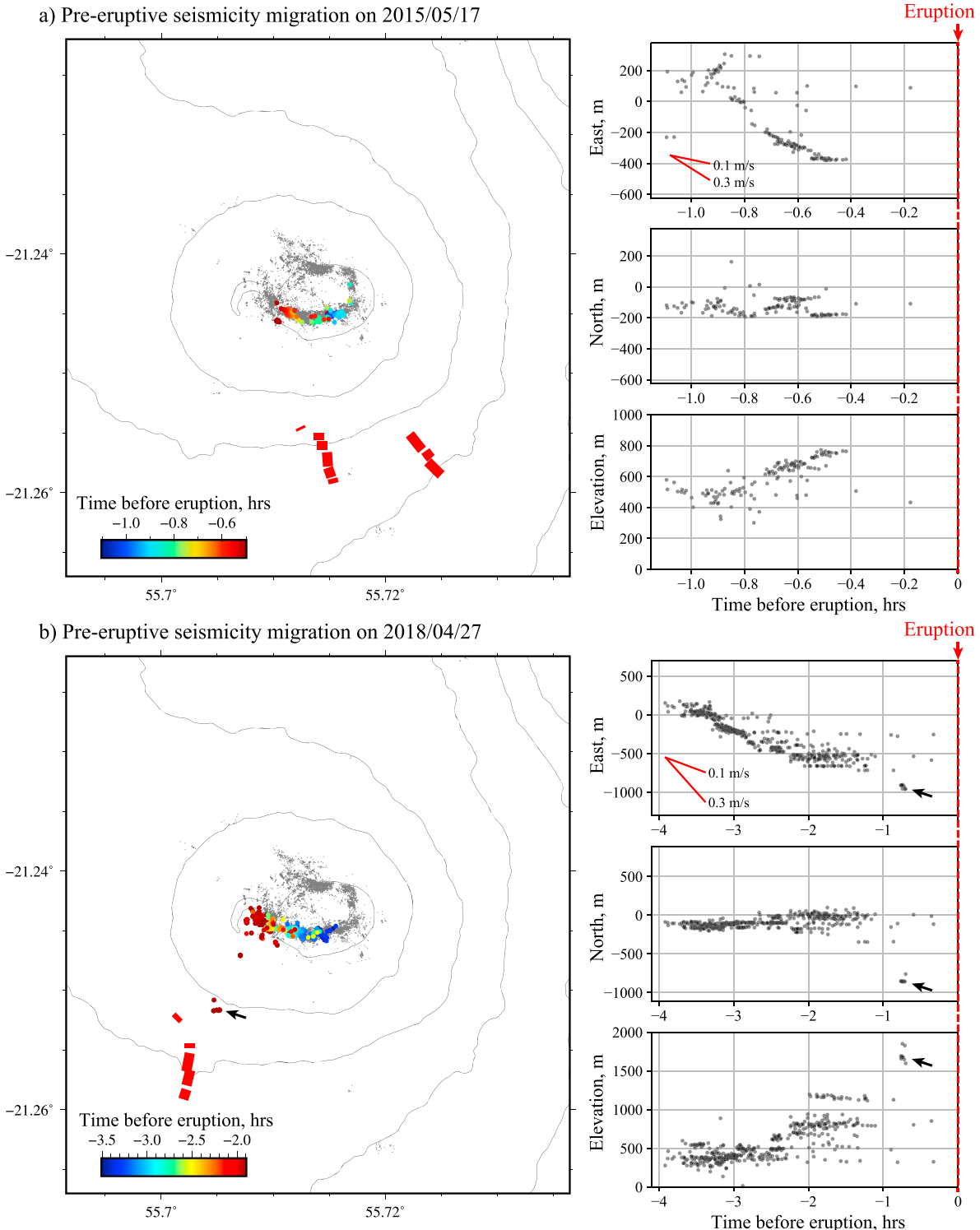


Figure 4. Pre-eruptive earthquake migrations. (a) Migration observed before the 17/5/2015 eruption. (b) Migration observed before the eruption on 27/4/2018. Earthquakes are color coded as a function of time before eruption in the map showed on the left. Subfigures on the right depict earthquake coordinates as a function of time. Black arrows in (b) indicate a shallow cluster of seismicity that occurred close to eruptive fissures about 40 min before the eruption on 27/4/2018. Similar maps are presented in Figure S3 of the supporting information for the 11 other eruptions analyzed in this study.

indicates that an eruption occurring at a large distance from the magma reservoir will also occur at a large delay after the onset of the seismic crisis. This is consistent with previous studies showing that longer seismic crisis are usually associated with eruptions at larger distances from the summit (Aki & Ferrazzini, 2000; Peltier et al., 2005; Roult et al., 2012). A rough linear fit on the observed scaling allows us to constrain a migration speed for the magma of the order of 0.1 m/s.

4. Discussion

Seismicity is not always a straightforward indicator of magma propagation. Although volcano-tectonic earthquakes can sometimes be interpreted as a direct marker of dike pathways (e.g., Rubin et al., 1998; Sigmundsson et al., 2015), it can also correspond to distributed damage caused by pressure variations in the magma reservoir (Carrier et al., 2015) or alternatively as the result of pre-existing suitably oriented structures already near to failure (Rubin & Gillard, 1998). At Piton de la Fournaise, almost all pre-eruptive seismicity is focused on the same ~20° eastward dipping ring-shaped cluster below the summit and above a shallow magma reservoir located around sea level (see Figure 1; Peltier et al., 2009). This cluster certainly represents an area of weakness outlining the piston structure associated with the repetitive formation of pit craters and caldera collapses in the volcano summit (Lénat et al., 2012; Michon et al., 2013). This interpretation seems consistent with the existence of a shallow low-density fractured column beneath the central cone that has been inferred from gravity measurements (Gailler et al., 2009). Such a weakened zone that is prone to failure can facilitate the propagation of magma intrusions. These intrusions can in turn maintain damages within the edifice due to the associated stress changes and induced hydrothermal alteration (Heap et al., 2015; Mordensky et al., 2018; Pola et al., 2012; Wyering et al., 2014).

Although pre-eruptive swarms occur consistently on the main ring structure, our results show a clear correlation between earthquake locations and the azimuth of eruptive sites relative to the central cone (Figure 2). In addition, the delay between the seismic crisis and the eruption onset correlates relatively well with the distance of the eruption fissure relative to the magma chamber (Figure 3). To gain further insights into this pre-eruptive activity, we also investigate the evolution of earthquake locations during each eruptive unrest. Interestingly, we notice a systematic migration of the earthquake activity during the seismic crises (Figures 4 and S5). These seismicity migrations correspond primarily to an east to west propagation at a speed of the order of 0.1 m/s. Westward propagations are usually associated with an upward seismicity migration at a similar speed (see right subplots in Figure 4). This earthquake migration speed is consistent with the overall magma migration velocity inferred in section 3. Although the horizontal direction of earthquake migrations is sometimes consistent with eruptive fissure locations (e.g., Figure 4b), the evolution of seismicity is often not in agreement with the final location of the eruption site (e.g., Figure 4a where eruptive fissures are located at the southeast of a westward migrating swarm).

A simple interpretation of these results is that the observed seismicity responds to blade-like dike intrusions propagating vertically from the roof of the magma reservoir. We can suppose that only the weakened part of the edifice located close to the intruding dike will be activated seismically. The upward seismicity migration from east to west could then be attributed to the eastward dip of the ring structure. Indeed, because of this structure geometry, an upward migrating stress source will cause the failure of events located more and more to the west. Once this intruding dike has inflated vertically, its lateral propagation direction is mostly controlled by its location relative to the volcano summit (i.e., the stress field created by the topography) and the existence of preferential intrusion paths (e.g., rift zones; Michon et al., 2015). This interpretation is consistent with the analysis of geodetic time series that evidenced two phases of dike propagation: first, a vertical migration when the magma leaves the reservoir and then a lateral migration in the direction of the eruptive site (Peltier et al., 2005, 2007).

Our findings suggest that a careful analysis of the seismicity during the onset of a magma intrusion provides direct information on the future eruption location. More specifically, at a given time after the beginning of a seismic crisis, we can predict the azimuth and minimum distance of the eruptive site relative to the summit area. After a seismically active phase at the beginning of the intrusion, the magma propagates almost aseismically up to the surface. Although seismicity is very low after the seismic crisis, a few events can still be detected during this second phase. This is illustrated in Figure 4b where a shallow seismicity cluster is activated close to the final eruptive site 40 min before the eruption (cf., black arrow in Figure 4b). Our tests show that including more stations away from the central cone does not allow to increase the number of detections

at shallow depth. This is mainly due to the limited number of templates located out of the ring structure. Shallow events are difficult to locate because they are usually observed only at a few stations with small signal-to-noise ratio (hence, they cannot be used as templates in our detection and relocation procedure). The development of a dedicated approach tracking the location of such shallow microearthquakes is of major interest at Piton de la Fournaise, where the prediction of the location of an eruption is important to plan rescue and evacuation operations. Some approaches have been proposed to get approximate locations based on time-averaged seismic amplitudes or amplitude ratios (De Barros et al., 2013; Taisne et al., 2011). Beyond the implications for monitoring purposes, the development of new approaches enabling accurate localization of individual induced microearthquakes is important to improve our understanding of the dynamics of magma propagation.

Acknowledgments

This project was supported by the IPGS internal call for projects and the CNRS-INSU Tellus-ALEAS program. This project has also received funding from the European Research Council (ERC, under the European Union's Horizon 2020 research and innovation programme under grant agreement 805256) and from Agence Nationale de la Recherche (project ANR-17-ERC3-0010). We thank Patrice Boissier, Aline Peltier, Benoit Taisne, and Michael Heap for helpful discussions. Michel Tas is additionally thanked for grammatical assistance. We thank the Editor, Rebecca Carey, and two anonymous reviewers for their constructive comments, which helped improve this manuscript. The data used in this study were acquired by the Volcanological and Seismological Observatory of Piton de la Fournaise (OVPF-IPGP) and are accessible via the VOLOBSIS Portal at <http://volobisis.ipgp.fr>. Figures were made with the GMT software (Wessel & Smith, 2006)

References

- Aki, K., & Ferrazzini, V. (2000). Seismic monitoring and modeling of an active volcano for prediction (vol 105, pg 16,617, 2000). *Journal of Geophysical Research*, 105(B10), 23,763–23,763.
- Aki, K., & Koyanagi, R. (1981). Deep volcanic tremor and magma ascent mechanism under Kilauea, Hawaii. *Journal of Geophysical Research*, 86(B8), 7095–7109.
- Battaglia, J., Ferrazzini, V., Staudacher, T., Aki, K., & Cheminée, J.-L. (2005). Pre-eruptive migration of earthquakes at the Piton de la Fournaise volcano (Réunion Island). *Geophysical Journal International*, 161(2), 549–558.
- Brenguier, F., Kowalski, P., Staudacher, T., Ferrazzini, V., Lauret, F., Boissier, P., et al. (2012). First results from the undervolc high resolution seismic and GPS network deployed on Piton de la Fournaise Volcano. *Seismological Research Letters*, 83(1), 97–102.
- Carrier, A., & Got, J. L. (2014). A maximum a posteriori probability time-delay estimation for seismic signals. *Geophysical Journal International*, 198(3), 1543–1553.
- Carrier, A., Got, J.-L., Peltier, A., Ferrazzini, V., Staudacher, T., Kowalski, P., & Boissier, P. (2015). A damage model for volcanic edifices: Implications for edifice strength, magma pressure, and eruptive processes. *Journal of Geophysical Research: Solid Earth*, 120, 567–583. <https://doi.org/10.1002/2014JB011485>
- De Barros, L., Bean, C. J., Zecevic, M., Brenguier, F., & Peltier, A. (2013). Eruptive fracture location forecasts from high-frequency events on Piton de la Fournaise Volcano. *Geophysical Research Letters*, 40, 4599–4603. <https://doi.org/10.1002/grl.50890>
- Eibl, E. P., Bean, C. J., Vogfjörd, K. S., Ying, Y., Lokmer, I., Möllhoff, M., et al. (2017). Tremor-rich shallow dyke formation followed by silent magma flow at Bárðarbunga in Iceland. *Nature Geoscience*, 10(4), 299.
- Einarsson, P., & Brändsdóttir, B. (1980). Seismological evidence for lateral magma intrusion during the July 1978 deflation of the Krafla Volcano in NE-Iceland. *Journal of Geophysics*, 47, 160–165.
- Gailler, L.-S., Lénat, J.-F., Lambert, M., Levieux, G., Villeneuve, N., & Froger, J. L. (2009). Gravity structure of Piton de la Fournaise volcano and inferred mass transfer during the 2007 crisis. *Journal of Volcanology and Geothermal Research*, 184(1-2), 31–48.
- Grandin, R., Jacques, E., Nercessian, A., Ayele, A., Doubre, C., Socquet, A., et al. (2011). Seismicity during lateral dike propagation: Insights from new data in the recent Manda Hararo-Dabbahu rifting episode (Afar, Ethiopia). *Geochemistry, Geophysics, Geosystems*, 12, Q0AB08. <https://doi.org/10.1029/2010GC003434>
- Harris, A. J. L., Villeneuve, N., Di Muro, A., Ferrazzini, V., Peltier, A., Coppola, D., et al. (2017). Effusive crises at Piton de la Fournaise 2014–2015: A review of a multi-national response model. *Journal of Applied Volcanology*, 6(1), 11.
- Heap, M. J., Kennedy, B. M., Pernin, N., Jacquemard, L., Baud, P., Farquharson, J. I., et al. (2015). Mechanical behaviour and failure modes in the Whakaari (White Island volcano) hydrothermal system, New Zealand. *Journal of Volcanology and Geothermal Research*, 295, 26–42.
- Lénat, J.-F., Bacheler, P., & Merle, O. (2012). Anatomy of Piton de la Fournaise volcano (La réunion, Indian Ocean). *Bull Volcanol*, 74(9), 1945–1961.
- Lengliné, O., Duputel, Z., & Ferrazzini, V. (2016). Uncovering the hidden signature of a magmatic recharge at Piton de la Fournaise volcano using small earthquakes. *Geophysical Research Letters*, 43, 4255–4262. <https://doi.org/10.1002/2016GL068383>
- Michon, L., Di Muro, A., Villeneuve, N., Saint-Marc, C., Fadda, P., & Manta, F. (2013). Explosive activity of the summit cone of Piton de la Fournaise volcano (La réunion island): A historical and geological review. *Journal of Volcanology and Geothermal Research*, 264, 117–133.
- Michon, L., Ferrazzini, V., Di Muro, A., Villeneuve, N., & Famin, V. (2015). Rift zones and magma plumbing system of Piton de la Fournaise volcano: How do they differ from Hawaii and Etna? *Journal of Volcanology and Geothermal Research*, 303, 112–129.
- Mordensky, S., Villeneuve, M., Kennedy, B., Heap, M., Gravley, D., Farquharson, J., & Reuschlé, T. (2018). Physical and mechanical property relationships of a shallow intrusion and volcanic host rock, Pinnacle Ridge, Mt. Ruapehu, New Zealand. *Journal of Volcanology and Geothermal Research*, 359, 1–20.
- Peltier, A., Ferrazzini, V., Staudacher, T., & Bacheler, P. (2005). Imaging the dynamics of dyke propagation prior to the 2000–2003 flank eruptions at Piton de La Fournaise, Reunion Island. *Geophysical Research Letters*, 32, L22302. <https://doi.org/10.1029/2005GL023720>
- Peltier, A., Staudacher, T., & Bacheler, P. (2007). Constraints on magma transfers and structures involved in the 2003 activity at Piton de La Fournaise from displacement data. *Journal of Geophysical Research*, 112, B03207. <https://doi.org/10.1029/2006JB004379>
- Peltier, A., Staudacher, T., Bacheler, P., & Cayol, V. (2009). Formation of the April 2007 Caldera collapse at Piton de La Fournaise volcano: Insights from GPS data. *Journal of Volcanology and Geothermal Research*, 184(1), 152–163.
- Pola, A., Crosta, G., Fusi, N., Barberini, V., & Norini, G. (2012). Influence of alteration on physical properties of volcanic rocks. *Tectonophysics*, 566, 67–86.
- Roult, G., Peltier, A., Taisne, B., Staudacher, T., Ferrazzini, V., & Di Muro, A. (2012). A new comprehensive classification of the Piton de la Fournaise activity spanning the 1985–2010 period. Search and analysis of short-term precursors from a broad-band seismological station. *Journal of Volcanology and Geothermal Research*, 241–242, 78–104.
- Rubin, A. M., & Gillard, D. (1998). Dike-induced earthquakes: Theoretical considerations. *Journal of Geophysical Research*, 103(B5), 10,017–10,030.
- Rubin, A. M., Gillard, D., & Got, J.-L. (1998). A reinterpretation of seismicity associated with the January 1983 dike intrusion at Kilauea Volcano, Hawaii. *Journal of Geophysical Research*, 103(B5), 10,003–10,015.
- Sapin, M., Hirn, A., Lépine, J.-C., & Nercessian, A. (1996). Stress, failure and fluid flow deduced from earthquakes accompanying eruptions at Piton de la Fournaise volcano. *Journal of Volcanology and Geothermal Research*, 70(3-4), 145–167.

- Sigmundsson, F., Hooper, A., Hreinsdóttir, S., Vogfjörd, K. S., Ófeigsson, B. G., Heimisson, E. R., et al. (2015). Segmented lateral dyke growth in a rifting event at Bárðarbunga volcanic system, Iceland. *Nature*, 517(7533), 191.
- Staudacher, T. (2010). Field observations of the 2008 summit eruption at Piton de la Fournaise (Île de La réunion) and implications for the 2007 Dolomieu collapse. *Journal of Volcanology and Geothermal Research*, 191(1-2), 60–68.
- Staudacher, T., & Peltier, A. (2016). Ground deformation at Piton De La Fournaise, a review from 20 years of GNSS monitoring, *Active Volcanoes of the Southwest Indian Ocean* pp. 251–269. Berlin, Heidelberg: Springer.
- Taisne, B., Brenguier, F., Shapiro, N. M., & Ferrazzini, V. (2011). Imaging the dynamics of magma propagation using radiated seismic intensity. *Geophysical Research Letters*, 38, L04304. <https://doi.org/10.1029/2010GL046068>
- Waldhauser, F. (2000). A Double-Difference earthquake location algorithm: Method and application to the Northern Hayward Fault, California. *Bulletin of the Seismological Society of America*, 90(6), 1353–1368.
- Wessel, P., & Smith, W. H. F. (2006). New, improved version of generic mapping tools released,. *Eos, Transactions American Geophysical Union*, 79(47), 579–579.
- Wright, T. J., Ebinger, C., Biggs, J., Ayele, A., Yirgu, G., Keir, D., & Stork, A. (2006). Magma-maintained rift segmentation at continental rupture in the 2005 Afar dyking episode. *Nature*, 442(7100), 291–294.
- Wyering, L. D., Villeneuve, M. C., Wallis, I. C., Siratovich, P. A., Kennedy, B. M., Gravley, D. M., & Cant, J. L. (2014). Mechanical and physical properties of hydrothermally altered rocks, Taupo Volcanic Zone, New Zealand. *Journal of Volcanology and Geothermal Research*, 288, 76–93.
- Zecevic, M., De Barros, L., Bean, C. J., O'Brien, G. S., & Brenguier, F. (2013). Investigating the source characteristics of long-period (LP) seismic events recorded on Piton de la Fournaise volcano, La réunion. *Journal of Volcanology and Geothermal Research*, 258, 1–11.

4.4 Mécanisme à la source de l'effondrement de caldeira en 2007 au Piton de la Fournaise

L'activité explosive et les effondrements à l'origine de la formation des caldeira sommitales représente un aléa volcanique majeur sur un volcan effusif actif tel que le Piton de la Fournaise (Michon et al., 2013). Les effondrements de caldeira se manifestent généralement sous la forme d'une série d'incrément de subsidence associés à l'émission de signaux sismiques très longue période équivalents à des magnitudes autour de $M_W = 5$. Ces évènements impliquent différents processus de source comme l'activation de failles annulaires et la contraction de réservoirs magmatiques. Ces mécanismes sont généralement modélisés au moyen d'un tenseur moment sismique, qui aboutit à des modèles de types CLVD (compensated-linear-vector-dipoles Shuler et al., 2013b). Cette représentation de source néglige cependant l'effet du décharge et du rechargement de l'édifice par l'effondrement de la colonne de roche surplombant le réservoir magmatique (Kumagai et al., 2001). Dans l'étude présentée ci-dessous, nous analysons les signaux très longue période observés lors de l'effondrement de caldeira dans la partie sommitale du Piton de la Fournaise en 2007. L'analyse de la source des signaux indique un mécanisme de type piston avec une fissure en effondrement (i.e., "collapsing crack") correspondant à la contraction du réservoir magmatique et une force verticale représentant l'effondrement de la colonne de roche surplombant le réservoir. Nos résultats ont également démontré que la taille de l'effondrement principal était largement sous-estimé dans les précédentes analyses de la source (Fontaine et al., 2019). Comme reporté précédemment, nous observons des évènements VLP précurseurs qui précèdent l'activité de surface. La forme d'onde de ces précurseurs est cependant assez différente des évènements principaux ce qui suggère un mécanisme à la source différent. Nous montrons par ailleurs que la dynamique de l'effondrement est principalement contrôlée par le flux de magma sortant de la chambre magmatique. De façon similaire à l'effondrement du Kīlauea en 2018, on observe une réduction de l'intervalle entre les incrément de subsidence qui résulte de l'accélération du flux de magma sortant et de l'affaiblissement de l'édifice suite aux effondrements successifs.

L'article présenté ci-dessous a été publié en 2019 dans *Earth and Planetary Science Letters*. Ce travail a été effectué suite à mon recrutement à l'IPGS et a été supporté en partie par mon projet ERC.



The 2007 caldera collapse of Piton de la Fournaise volcano: Source process from very-long-period seismic signals

Zacharie Duputel*, Luis Rivera

Institut de Physique du Globe de Strasbourg, UMR7516, Université de Strasbourg/EOST, CNRS, Strasbourg, France



ARTICLE INFO

Article history:

Received 13 May 2019

Received in revised form 19 August 2019

Accepted 22 August 2019

Available online 16 September 2019

Editor: M. Ishii

Keywords:

caldera collapse

magma reservoir processes

Piton de la Fournaise

single force source

surface waves

ABSTRACT

In April 2007, Piton de la Fournaise volcano experienced its largest caldera collapse in at least 300 yr. This event consisted of a series of 48 subsidence increments characterized by very-long-period (VLP) seismic signals equivalent to M_w 4.4 to 5.4. Source analysis of VLP events suggests a piston-like mechanism with a collapsing crack source corresponding to the contraction of the magma reservoir and a single force representing the collapse of the above rock column. We show that the collapse dynamics is primarily controlled by magma withdrawal from the reservoir, which was likely in a bubbly state at the time of the event. Similar to the 2018 Kilauea collapse, we observe a reduction of the time-interval between successive subsidence increments, which results from the acceleration of magma withdrawal and a progressive weakening of the edifice at the beginning of the sequence.

© 2019 The Author(s). Published by Elsevier B.V. This is an open access article under the CC BY license (<http://creativecommons.org/licenses/by/4.0/>).

1. Introduction

Although caldera collapses are frequent in the evolution of basaltic systems, they have been monitored at only a few volcanoes worldwide (e.g., Kumagai et al., 2001; Michon et al., 2007; Neal et al., 2019). Such collapses usually consist of a quasi-periodic series of discrete subsidence events manifested by tilt steps and very long period (VLP) signals (e.g., Fontaine et al., 2014; Kumagai et al., 2001). While the initiation mechanisms of such phenomena remains largely enigmatic, they generally involve a lateral magma withdrawal from a subsurface reservoir through low elevation vents. Observations indicate a complex feedback process between summit collapses and the dynamics of the eruptive vent. While magma outflow from a sub-surface reservoir is usually associated with summit deflations (e.g., Epp et al., 1983), collapses can also act as a mechanism to push the magma out of the chamber. Effusive surges and short-term edifice inflations following summit collapses suggest a piston-like mechanism, in which the depressurized magma chamber is regularly repressurized by the subsiding rock column (Kumagai et al., 2001; Michon et al., 2011; Neal et al., 2019).

Caldera collapses involve different source processes like dip-slip motion on ring faults and the contraction of magma reservoirs. These mechanisms are often modeled using moment tensor parameters, whose inversion on volcanoes usually yields vertical

compensated-linear-vector-dipoles (CLVD) representing ring faulting (e.g., Shuler et al., 2013) or tensile crack sources associated with the pressurization of magma reservoirs (Kumagai et al., 2001; Mildon et al., 2016). Such a moment tensor representation, however, ignores the effects of the detached mass that can be significant during gravity-driven caldera collapses. As far as the excitation of long period seismic waves is concerned, the descending collapse rock column induces unloading and loading of the volcanic edifice that can be modeled with a single force (e.g., Takei and Kumazawa, 1994). Because volcanoes involve mass advection processes generating forces on the Earth, the modeling of volcanic sources commonly requires the consideration of single forces in addition to moment tensor components (Nakano et al., 2003; Chouet and Matouza, 2013). A remarkable example is the 1980 Mount St. Helens eruption (USA), which combined a massive landslide represented by a horizontal single force (Kanamori and Given, 1982) and a series of volcanic explosions corresponding to the superposition of an isotropic source and a vertical force (Kanamori et al., 1984). Other examples of volcanic phenomena inducing single forces are dome collapses (e.g., Uhira et al., 1994) or magma movements in the edifice (e.g., Chouet et al., 2010).

In this study, we focus on the April 2007 collapse that affected the summit area of Piton de la Fournaise volcano located on La Réunion island (cf., Fig. 1). Although numerous collapses have occurred in the summit area since the 18th century, the 2007 event is the largest collapse reported at Piton de la Fournaise (Michon et al., 2013). It followed a particularly active period with 4 eruptions in 10 months (Peltier et al., 2009) that ended in a lateral

* Corresponding author.

E-mail address: zacharie.duputel@unistra.fr (Z. Duputel).

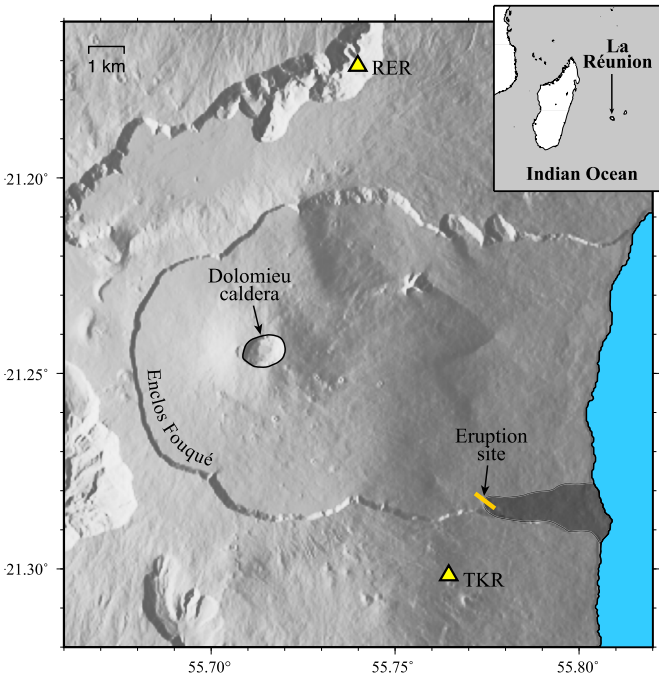


Fig. 1. Location of the Piton de la Fournaise volcano. The April 2007 collapse occurred in the Dolomieu crater located at the summit of the Piton de la Fournaise central cone. The eruptive fissure of April 2007 is indicated with an orange line and the corresponding lava flow is outlined in dark grey. Yellow triangles indicate the location of stations RER and TKR used in the present study. (For interpretation of the colors in the figure(s), the reader is referred to the web version of this article.)

low-altitude eruption with exceptionally high flow rate and a large volume of ejected lava (Staudacher et al., 2009). Early geodetic co-eruptive measurements show a significant deflation of the volcano before the collapse (Peltier et al., 2009; Fontaine et al., 2014; Froger et al., 2015), suggesting that the low-altitude eruption induced a sudden depressurization of the magma reservoir that ultimately resulted in the collapse of the rock column below the summit (Michon et al., 2007). This major failure within the edifice was accompanied by a sudden decrease of seismic velocities in the summit area (Duputel et al., 2009) and an exponentially decaying post-eruptive deflation of the central cone (Froger et al., 2015).

The surface collapse activity started on April 5 at 20:48 UTC with an earthquake of magnitude $M \sim 5$ that could be observed at teleseismic distances (Fig. 2 and Supplementary Fig. S1). This event was followed by more than 40 smaller collapses that occurred quasi-periodically until mid April 2007 (Michon et al., 2011; Fontaine et al., 2014). Each collapse was characterized by inflationary tilt steps and VLP signals (cf., supplementary Fig. S2; Fontaine et al., 2014). It was also accompanied by an intense microseismic activity below the volcano summit (Massin et al., 2011). The collapse resulted into a depression of ~ 330 m of the Dolomieu summit crater with a total volume similar to the bulk volume of emitted lava ($\sim 10^8$ m 3 ; Michon et al., 2007; Urai et al., 2007; Staudacher et al., 2009). Although numerous studies have focused on geodetic deformation, seismicity and velocity variations associated with this activity (Peltier et al., 2009; Froger et al., 2015; Brenguier et al., 2008; Massin et al., 2011; Got et al., 2013), only a limited number of studies focused on the actual source mechanism of the VLP signals generated by collapse events (e.g., Fontaine et al., 2019). In this study, we thus combine near-field observations at the Geoscope station RER (8.5 km from the volcano summit) and surface waves observed at 25 teleseismic stations to investigate the source of collapse events that affected Piton de la Fournaise in April 2017. To mitigate any bias due to the effect of lateral heterogeneities on teleseismic surface waves, our analysis accounts for

3D heterogeneities using the spectral element approach. We then explore different source representations to constrain the different source processes involved during the April 2007 caldera collapse.

2. Seismological observations and waveform simulations

We select 25 teleseismic broadband stations for which the VLP signal generated by the main collapse event is clearly visible. The resulting dataset has an azimuthal gap of 30° and is composed of stations within 90° of epicentral distances. Seismic waveforms are deconvolved to velocity and band-pass filtered between 50 s and 100 s. Periods shorter than 50 s are filtered out to mitigate the effect of short-scale structural heterogeneities that are not resolved in global 3D velocity models. The 100 s corner period reduces the effect of long-period noise, in particular for stations in Indian ocean southern islands and Antarctica (removing those stations would result in an azimuthal gap exceeding 130°). In the 50–100 s period range, the observed seismograms are dominated by fundamental mode surface waves for which a significant fraction of the energy stays near the free surface where lateral structural heterogeneities are significant at global scale (e.g., due to oceans and continents). To account for such strong lateral variations, we conduct 3-D spectral-element simulations to compute the Green's functions used for source characterization (Komatsch and Tromp, 1999). We assume a global 3-D Earth model composed of S40RTS (Ritsema et al., 2011) and Crust2.0 (Bassin et al., 2000). In addition to 3-D variations of wave speeds and density, our simulations include the effect of ellipticity, topography, bathymetry, oceans and self-gravitation.

We complement teleseismic records with near-field observations at the Geoscope station RER, located 8.5 km away from the Piton de la Fournaise summit area. Given its proximity to the source, the RER station provides direct information on the overall duration and centroid time of the source. It is modeled using Herrmann (2013) implementation of the wavenumber integration method for the local velocity model used at the Piton de la Fournaise Volcano Observatory (OVPF; model derived from Battaglia et al., 2005). We only use the vertical component seismogram and do not incorporate horizontal channels that are significantly contaminated by tilt signals (Fontaine et al., 2014). Before inversion, the seismogram is deconvolved to velocity and band-pass filtered in the period range of 5–100 s. The resulting waveform consists of a long-period signal with a relatively simple sinusoid pulse with a duration of ~ 17 s (see Supplementary Fig. S2a).

3. Source mechanism of the main collapse event on April 5, 2007

As mentioned above, the April 2007 collapse can possibly involve different source processes that can be modeled at long period by a moment tensor source (e.g., slip on a ring fault, contraction of a magma reservoir) or by a single force (e.g., unloading and loading of the volcanic edifice by the detaching rock column). In the following, we confront these different source representations to the seismological observations of the main VLP event on April 5 at 20:48 UTC.

3.1. Moment tensor inversion

We employ a strategy similar to Duputel et al. (2016) where centroid moment tensor (CMT) parameters are inverted for using surface waves in a 3-D Earth model. The parameters to be determined are the 6 elements of the seismic moment tensor as well as the centroid location and source duration. Although we have tested different centroid locations, our tests show a very limited sensitivity of long period seismic waves to the source location at the

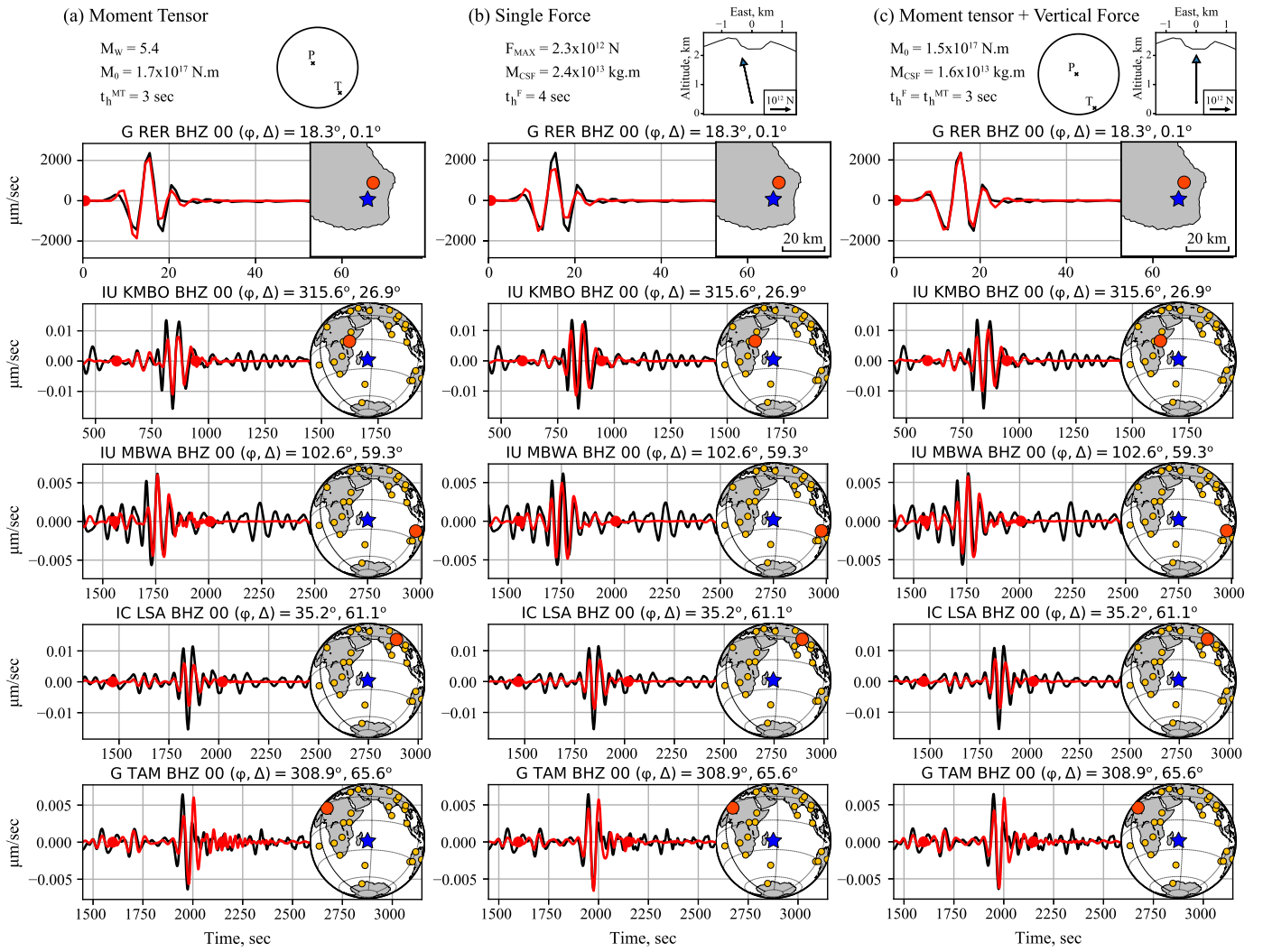


Fig. 2. Different source representations tested for the main caldera collapse on April 5, 2007. Source models are presented on top for (a) the moment tensor inversion, (b) the single force inversion and (c) the joint moment tensor and force solution. t_h^{MT} and t_h^F are respectively the moment-tensor and force half-durations. M_w is the moment magnitude, M_0 is the scalar seismic moment, F_{MAX} is the maximum force and M_{CSF} is the CSF value (cf., Kawakatsu, 1989). Comparison between data (black) and synthetic (red) traces are shown for representative stations. The part of the waveform used for source inversion is delimited by red dots. The blue star in right insets indicate the source location. Yellow circles show the distribution of stations used for the inversion while the red circle indicate the location of the station whose waveform is presented. The station azimuth (ϕ) and epicentral distance (Δ) is indicated on top of each seismic trace.

100 m scale of the Piton de la Fournaise summit area. We therefore fix the centroid below the Dolomieu summit crater ($21.244^\circ S$, $55.714^\circ E$) and only grid-search for the best point-source depth (from 0.5 km to 3.5 km). The centroid time and duration are also estimated using a simple grid-search strategy assuming an isosceles triangular moment rate function (MRF). Our preferred CMT solution for the main April 2007 collapse is presented in Fig. 2a and Fig. 3a. The optimum centroid time is 20:48:49 UTC and the source half-duration is 3 s (cf., Supplementary Fig. S3). We find a best point-source depth 2 km below the free surface (i.e. ~ 500 m above sea level). This estimate is however subject to large uncertainties as waveform fits are similar if we change the source depth.

Although estimated posterior uncertainties are relatively small, results suggest a large negative correlation between isotropic and vertical compensated linear vector dipole (CLVD) components (cf., Supplementary Table S1). To explore the contribution of the isotropic component to fit the data, we conduct an inversion assuming the trace of the moment tensor to be zero (i.e., the deviatoric moment tensor). Results in the Supplementary Fig. S4 show that such source cannot fit data properly (in particular at the near-field station RER), therefore confirming that an isotropic

component is necessary to explain available observations. To further assess what mechanism is requested by our observations, we estimate the minimum RMS misfit associated with every type of moment tensor source (cf., Supplementary Text S1). The resulting source-type diagram in Fig. 3b allows us to estimate what type of moment tensor source is consistent with the observed waveforms (Ford et al., 2010). Results suggest that the main collapse is consistent with a vertical closing crack, in agreement with the values and orientation of the principal axes in Fig. 3a. The source-type diagram in Fig. 3b also reveals uncertainty on the double-couple component of the source, which results from poor constraints on $M_{r\theta}$ and $M_{r\phi}$, due to the small amplitudes of the associated excitation kernels (see Table S1; Kanamori and Given, 1981).

Our moment tensor model is qualitatively similar to the moment tensor solution of Fontaine et al. (2019). However, the small scalar moment ($M_0 = 1.5 \times 10^{16}$ N.m), negative centroid time-delay (-4 s), very long duration (20 s) and large depth (5 km) reported by Fontaine et al. (2019) is inconsistent with both near- and far-field observations. Fig. S17 indicates that waveform predictions from such source model are significantly smaller than observations by about 1 order of magnitude, which likely results from a

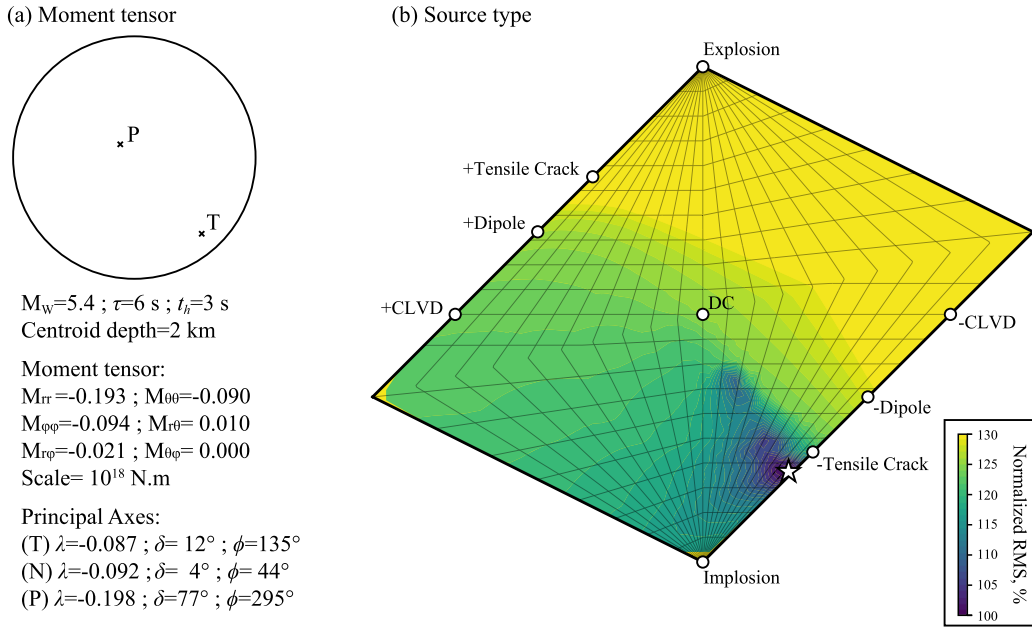


Fig. 3. Moment tensor solution for the main Piton de la Fournaise caldera collapse on April 5, 2007. (a) Preferred moment tensor solution. The half-duration $t_h = 3$ s and the centroid time-shift is $\tau = 6$ s with respect to 20:48:43 UTC. λ , δ and ϕ indicate respectively the eigenvalue, plunge and azimuth angles of the principal axes. Moment tensor components and eigenvalues are scaled by a factor of 10^{18} N.m. (b) Source type plot showing the Normalized RMS misfit corresponding to different types of moment tensor sources (see Supplementary Text S1). The optimum solution presented in (a) is indicated by a white star. The corresponding waveform fits are presented in Fig. 2a and S16.

bug in their inversion procedure (Hejrani and Fontaine, personal communication). Beyond this scaling issue, additional differences could potentially be attributed to the use of a spherical model (PREM) and the fact that RER was not incorporated in their inversion.

3.2. Single force inversion

To investigate possible effects due to the unloading and loading of the collapsing rock column, we also perform a centroid single force (CSF) inversion using an approach similar to Kawakatsu (1989). At long period, the effect of a detached mass can be modeled by a single time-varying force (e.g., Kanamori and Given, 1982; Ekström and Stark, 2013). To represent the effect of the descending mass acceleration and deceleration, we assume a sinusoidal source time history such that the final integral of the force equal to zero (e.g., Kawakatsu, 1989). We invert for the 3 components of the peak force vector along with the source timing and duration.

Results in Fig. 4 indicates a predominantly vertical force vector that is consistent with the downward motion of the rock column (i.e., the initial upward orientation of the force is in the opposite direction of the accelerating rock mass). In agreement with the moment tensor inversion, we obtain a centroid time at 20:48:49 UTC and a half-duration of 4 s (cf., Supplementary Fig. S3b). As far as the overall fit is concerned, the CSF solution in Fig. 2b seems to fit the data as well as the moment tensor model shown in Fig. 2a. The posterior correlation matrix presented in Supplementary Table S2 do not show significant correlations between the different components of the inverted peak force vector. If we constrain the force vector to be purely vertical, we do not notice a significant deterioration of the waveform fit (cf., Supplementary Fig. S5), which indicates that the small south-west component of the force in Fig. 4a is not required to fit the data. This is consistent with the fact that horizontal force components are associated with larger uncertainties (cf., Table S2).

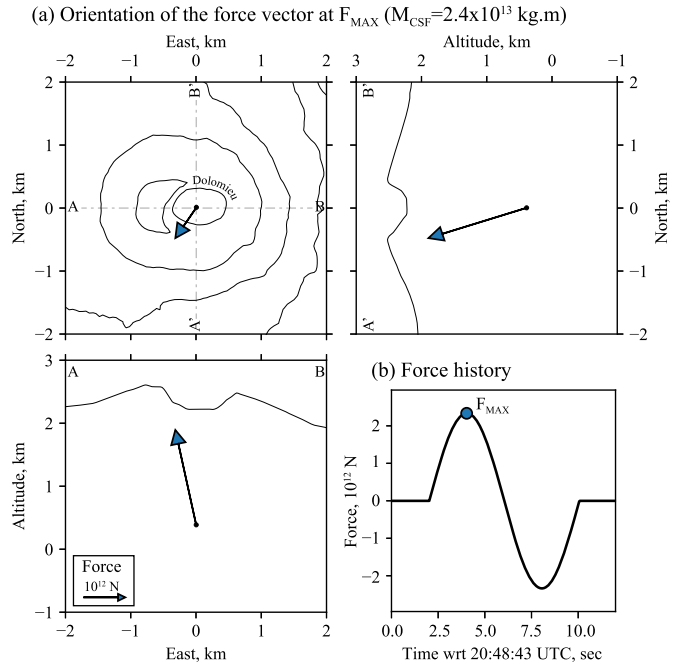


Fig. 4. Single force solution for the main Piton de la Fournaise caldera collapse on April 5, 2007. (a) Initial orientation of the peak force vector (i.e., at F_{MAX}). Force scale is indicated on the lower left panel. (b) Force time-history. The blue dot labeled F_{MAX} indicate the time when the force is maximum (i.e., the initial peak force). Waveform fit is presented in Fig. 2b and S18.

3.3. Joint inversion of moment tensor and force

We also conduct a joint inversion of moment tensor and force parameters. Given our limited sensitivity to the centroid depth and the force horizontal components, we assume a vertical force and fix the source 2 km below the free surface. We thus invert for the 6 elements of the moment tensor, the maximum force amplitude along with their centroid times and durations. The solution pre-

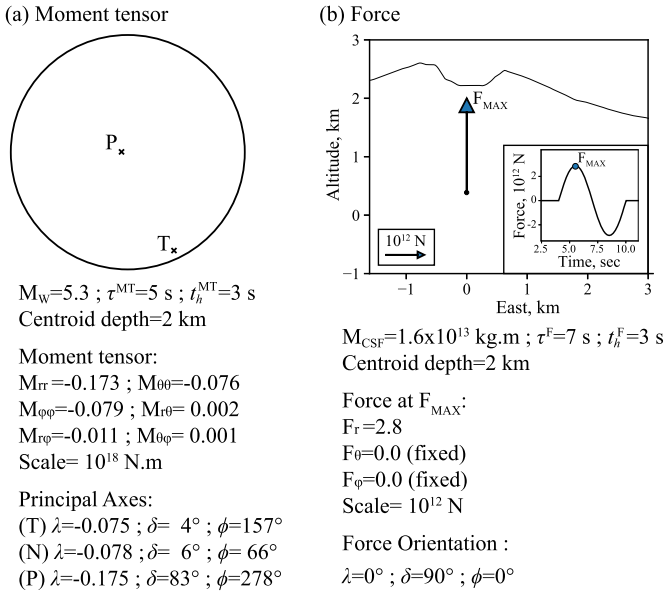


Fig. 5. Joint Moment Tensor and Force solution for the main Piton de la Fournaise caldera collapse on April 5. (a) Moment tensor parameters. (b) Force parameters. t_h^M and t_h^F denote the half-duration of the moment tensor and force source, respectively. The centroid time-shift of the moment tensor (τ^{MT}) and force (τ^F) are defined with respect to 20:48:43 UTC. λ , δ and ϕ indicate respectively the eigenvalue or force, plunge and azimuth angles of the principal axes. The lower right inset in (b) indicate the force time history. The blue dot labeled F_{MAX} indicate the time when the force is maximum (i.e., the initial peak force). Waveform fit is presented in Fig. 2c and S19.

sented in Fig. 2c and Fig. 5 is obtained for a half-duration of 3 s for both single force and moment tensor sources (consistently with CMT and CSF solutions presented above).

The inverted focal mechanism in Fig. 5a is consistent with a vertically closing crack and is very similar to the one obtained in Fig. 3. The force source in Fig. 5b is consistent with a downward moving rock column as the single force model in Fig. 4. Optimum centroid times indicate that the closing crack source occurs ~ 2 s before the upward force is applied. However, this delay remains small compared to the sampling rate of the seismological data (1 sample per second). The retrieved peak force amplitude is correlated with the moment tensor parameters (e.g., with the vertical CLVD component; cf., Supplementary Table S3). As in Table S1, we also notice a large negative correlation between isotropic and vertical CLVD components. Despite these tradeoffs, Fig. 2 shows that this joint model yields to a better waveform fit at the near-field station RER compared to moment tensor and single force sources presented before.

4. VLP precursors and smaller collapse events

Although smaller collapses that followed the April 5 event are not visible at teleseismic distances, the associated VLP events are well recorded at the RER Geoscope station (e.g., Fontaine et al., 2014; Fontaine et al., 2019). To obtain a catalog of these smaller VLP events, we use the ObsPy implementation of the STA/LTA algorithm on the vertical component of RER between April 5 and April 14, 2007. We use a short time average (STA) window of 20 s and a long time average of 400 s with thresholds of 3.4 and 3.0 for on and off trigger times. This detection procedure results into a catalog of 48 collapse events (including the main collapse) that are listed in Supplementary Table S4. As shown in Fig. 7, the main collapse event was also preceded by several VLP events. This is consistent with Fontaine et al. (2019) that reported 4 VLP events accompanied by tilt steps within 20 h before the main collapse.

Although the small amplitude of these events complicates any automated STA/LTA detection procedure, we can visually identify at least 7 VLP precursors on Fig. 7 that seem coincident with tilt changes reported by Fontaine et al. (2014) (see Tables S9–S11).

As for the main collapse event, the smaller collapses manifest as relatively simple long-period waveforms. Supplementary Fig. S2a shows that waveforms generated by the successive collapses have a similar shape, indicating that these events correspond to similar source mechanisms. We therefore fix the source geometry according to CMT and CSF models obtained for the main event and investigate smaller collapses by only inverting the source depth, timing, duration and size (i.e., seismic moment or force magnitude). Results are summarized in Supplementary Tables S4–S6. The magnitudes of smaller events ranges from 4.4 to 5.0 and their half-duration from 3 s to 7 s. Waveform fits presented in the Supplementary Figs. S6–S10 show that joint moment tensor and force models usually perform better than single moment tensor or force sources. This is not surprising given that the joint model incorporates more parameters than the other source models.

As shown in Fig. S2b, VLP precursors are also relatively similar to the main collapse event, even if they appear to have a longer duration. As described before, we investigate the source of these VLP precursors assuming a similar source geometry as the main event. Results in Tables S9–S11 and Fig. S11 suggest that the joint moment tensor and force source is more appropriate to fit the observations. In this case, the observed differences with the main collapse event is attributed to a larger time-difference between the CMT and CSF sources. However, this remains quite uncertain as the analysis is based on waveforms recorded at a single station.

5. Discussion and conclusion

In this study, we investigate the caldera collapse that affected the summit of Piton de la Fournaise in 2007. The surface collapse activity started on April 5 with a $M_w \sim 5.4$ VLP event visible at teleseismic distances. This main event was then followed by 47 smaller collapses with similar source mechanisms. Using a moment tensor parameterization, the source of the main collapse is best represented by a vertically closing crack (cf., Fig. 3). Our results show that ring-faulting is not the dominant source mechanism as a CLVD source is unable to fit the observed VLP signals (Fig. S4; Shuler et al., 2013). Using a single force representation, the inversion yields an initially upwards vertical force that is consistent with the downward displacement of the rock column above the magma reservoir. This single force model fits the observations as well as a moment tensor source even if it relies on fewer model parameters (cf., Fig. 2a–b). Model selection using log model evidence (LME), Akaike (AIC) and Bayesian (BIC) information criteria thus favor the simpler force model over a moment tensor description (see Supplementary Text S2 and Table S7). The joint inversion of force and moment tensor parameters suggests the combination of an initially upward vertical force and a closing crack. Despite its larger number of parameters, LME, AIC and BIC criteria favor this joint model over previous source parameterization because it is more consistent with observations (especially at the near-field station RER, see Table S7). The combination of a moment tensor and a force also results in better waveform fits and lower AIC and BIC values for smaller VLP events that followed the main collapse (see Supplementary Fig. S6–S10 and Table S8). Although the joint model seems to be the most appropriate according to LME, AIC and BIC criteria, it is important to note that this solution is derived from noisy data and is affected by tradeoffs between source parameters. In the following the different source representations will be taken into account to evaluate the dependance of estimated quantities on the assumed parameterization.

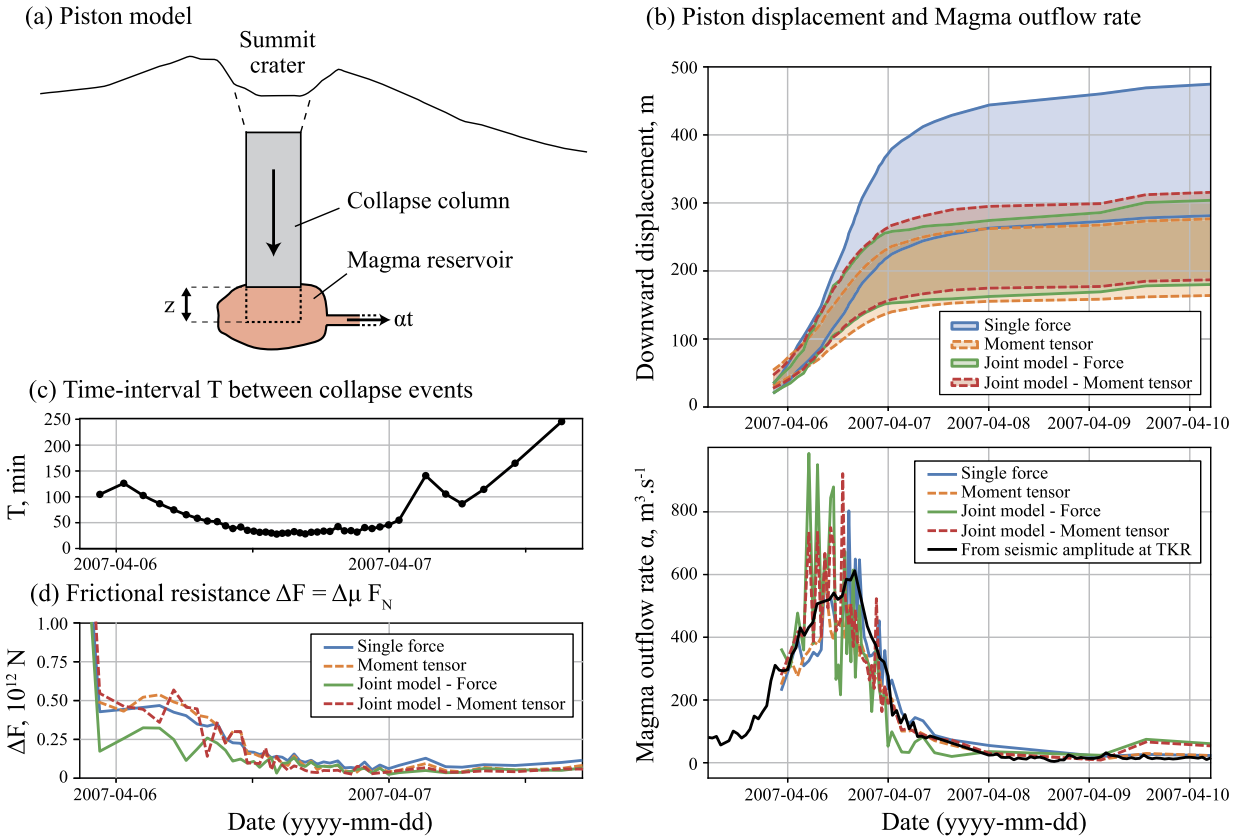


Fig. 6. Piston source model. (a) A schematic diagram of the source model used to explain very-long-period signals observed at Piton de la Fournaise. (b) Piston downward displacement (z) and magma outflow rate (α). The full time evolution of the cumulative displacement between April 5 and April 14 is shown in the Supplementary Fig. S12. (c) Time-interval between successive collapse events in our catalog. (d) Frictional resistance $\Delta F = \Delta\mu F_N$, corresponding to the difference between static and dynamic friction (see Supplementary Text S5). The different colors in (b) and (d) correspond to the different source models obtained in sections 3 and 4. The upper and lower bound estimates of Δz in (b) correspond respectively to $\rho = 1.6 \text{ g cm}^{-3}$ and $\rho = 2.7 \text{ g cm}^{-3}$. The estimates of α and ΔF are based on $\rho = 2.7 \text{ g cm}^{-3}$ for the single force model and $\rho = 1.6 \text{ g cm}^{-3}$ for the other models (see main text). The black line shown in the bottom subfigure of (b) corresponds to the magma extrusion rate estimated from seismic amplitudes observed at station TKR (see main text and Supplementary Text S3).

A simple interpretation of the results presented above is that the collapsing crack source corresponds to the vertical contraction of the magma reservoir while the vertical force represents the resulting collapse of the overlying fractured rock column. This interpretation seems consistent with our joint source models showing that the closing crack source usually occurs before the vertical force is applied to the edifice (cf., Fig. 4 and Table S6). The combination of a collapsing crack and a single force has been already inferred to explain long-period signals observed on volcanoes (e.g., Nakano et al., 2003) in particular during caldera collapses (e.g., Kikuchi et al., 2001). Moreover, previous seismological and geodetic studies have shown that closing crack sources can correspond to magma chamber deflations during a caldera collapse (e.g., Riel et al., 2015; Mildon et al., 2016). The use of a single force has also been suggested to represent a subsiding caldera block (Kumagai et al., 2001).

Assuming a simple piston cylinder to represent the subsiding caldera block as illustrated in Fig. 6a, we can use the different source models discussed above to estimate the downward displacement of the collapsing rock column (cf., Supplementary Text S3). We assume a piston diameter of 450 m consistently with Urai et al. (2007), Michon et al. (2011) and Fontaine et al. (2019). The piston extends vertically from the roof of the magma reservoir (at an elevation of ~ 300 m; Peltier et al., 2008; Duputel et al., 2019) to ~ 1700 m above sea level at the upper limit of CLVD and normal faulting events observed during the collapse sequence (Massin et al., 2011). For each model, we compute a lower-bound estimate of downward displacement for a density

$\rho = 2.7 \text{ g cm}^{-3}$ (taken from the velocity model used at OVPF) and an upper-bound using $\rho = 1.6 \text{ g cm}^{-3}$ (according to the gravity study of Gailler et al., 2009). Moment tensor crack estimates use Lamé parameters $\lambda = 6-11 \text{ GPa}$ and $\mu = 8-13 \text{ GPa}$ corresponding to the aforementioned values of ρ along with P and S wave speeds derived from local velocity models (Battaglia et al., 2005; Mordret et al., 2015). The results shown in Fig. 6b and Fig. S12 indicate a total piston displacement ranging from $z \sim 190$ m to $z \sim 635$ m depending on the source model and the value of ρ . The 450 m estimate proposed by Michon et al. (2011) fall in the middle of this range. Interestingly, our joint source model produces consistent piston displacement estimates whether they are derived from moment tensor or force parameters. In this case, we estimate a total displacement $z \sim 330$ m assuming $\rho = 1.6 \text{ g cm}^{-3}$, in agreement with direct observations reporting a depression depth of ~ 330 m in the Dolomieu crater (Michon et al., 2007; Urai et al., 2007). The single force model is associated with larger estimates (i.e., $z \sim 370-635$ m) that are also consistent with field observations if we assume a denser piston cylinder. The moment tensor estimates $z \sim 220-370$ m are also consistent with the observed final depth of the caldera. As shown in Fig. S12, the evolution of the piston displacement is globally consistent with Fontaine et al. (2019) that estimated a final depth of 340 m. For simplicity, we will now assume $\rho = 1.6 \text{ g cm}^{-3}$ for the moment tensor and joint model and $\rho = 2.7 \text{ g cm}^{-3}$ for the single force model.

The above estimates of vertical displacement can be used to evaluate the volume change of the magma reservoir after each collapse. Dividing this volumetric change by the time-delay T

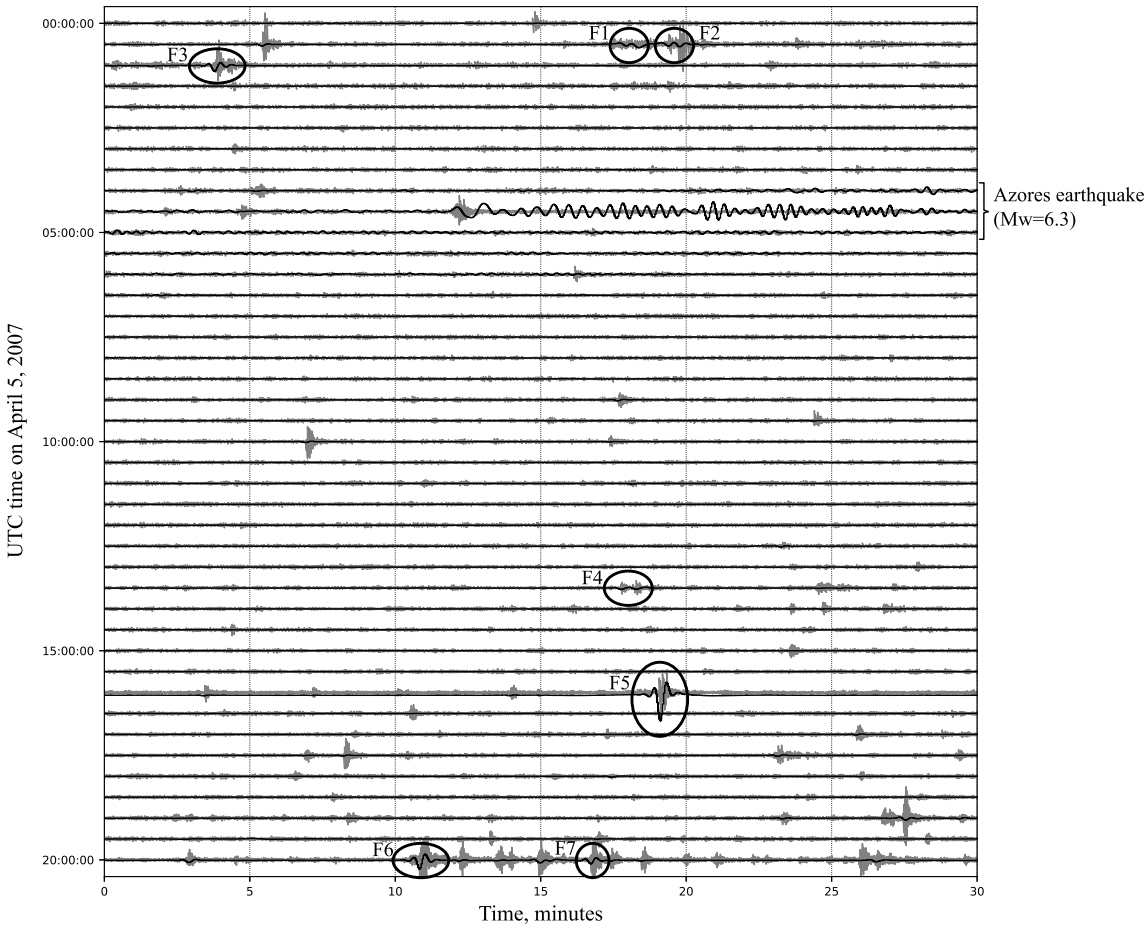


Fig. 7. Seismic velocity record at RER station on 5 April 2007 before the main collapse event at 20:48:43 UTC. Gray lines represent raw, unfiltered BHZ data. Black lines are the seismograms filtered in the 20–200 s passband. Ellipses indicate VLP precursors (listed in Tables S9–S11 of the online supplementary). Events F1–F2, F3, F4 and F5 correspond respectively to events E2, E3, E4 and E5 reported by Fontaine et al. (2019). Events F6–F7 are coincident with a tilt step that occurred a few minutes before the main collapse (e.g., Fontaine et al., 2014).

since the previous collapse, we obtain a volumetric change rate $\alpha = \Delta z S/T$ (where Δz is the downward displacement increment and S is the cross-sectional area at the base of the piston). This volumetric change rate shown in Fig. 6b can be compared directly to the magma outflow rate. It has been showed that the high-frequency ground motion velocity amplitude near the eruption site has similar evolution to the emission rate during the April 2007 eruption (Staudacher et al., 2009; Coppola et al., 2009; Michon et al., 2011). Using the approach of Hibert et al. (2015), we therefore estimate the magma outflow rate from continuous records at station TKR, located close to eruptive fissure (see Supplementary Text S4). The estimated lava extrusion rate shown in black in Fig. 6b is consistent with volumetric change rates estimated from our VLP catalog. This confirms that the 2007 Piton de la Fournaise collapse is primarily controlled by lateral magma withdrawal from the shallow reservoir. Our magma outflow estimates are lower than preliminary volumetric change rates obtained empirically by Michon et al. (2011) from seismic acceleration at the RER station reaching up to $1000 \text{ m}^3 \text{s}^{-1}$. On the other hand, our average emission rate of $61 \text{ m}^3 \text{s}^{-1}$ is roughly consistent with field observations of Staudacher et al. (2009) that reported an overall mean lava outflow of $52 \text{ m}^3 \text{s}^{-1}$ (estimated from the volume of the lava field and the duration of the eruption) and peak rate larger than $200 \text{ m}^3 \text{s}^{-1}$ on April 6 (a lower bound estimate due to hidden flow within lava tubes). Such emission rates are exceptionally large compared to classical emission rates of Piton de la Fournaise (Hibert et al., 2015) and are of the same order as effusion rates

observed on other volcanoes when the caldera collapse influenced the emission rate (e.g., Gudmundsson et al., 2016).

As reported for other caldera collapses (e.g., Shuler et al., 2013), the duration of individual collapse events are significantly longer than what is typically observed for earthquakes of similar sizes. Our duration estimates ranges from 6 s to 14 s, while standard scaling laws for earthquakes (e.g., Duputel et al., 2013) predict durations ranging from 0.6 to 2 s for $M_w = 4$ and $M_w = 5$ events, respectively (cf., Supplementary Tables S4–S6). In addition, the source duration of VLP events does not seem to scale with their size. This clearly suggests that the underlying physical mechanism is not the same as earthquakes that are commonly observed on tectonic fault systems. Using a simple piston spring-block model (Kumagai et al., 2001), the duration of collapse events is controlled by the geometry of the subsiding caldera block but also by the properties of the magma reservoir. In this model, the weight of the collapsing piston is balanced by friction on the surrounding ring fault and by pressure in the magma reservoir. When the magma reservoir depressurization exceeds static friction, the piston moves down into the chamber which suddenly increases its internal pressure and generate VLP signals. Assuming that the inter-event time-delay T is large compared to the duration of individual collapses, we can write (see Supplementary Text S5):

$$t_h = \frac{\pi}{2} \sqrt{\frac{\rho V_0 h}{\kappa S}} \quad (1)$$

where t_h is the piston source half-duration, V_0 is the initial volume of the magma reservoir and κ is the bulk modulus of the magma. Using geodetic estimates of the magma chamber volume (Peltier et al., 2008), we can interpret our estimates of t_h for each collapse to evaluate κ . Despite the large uncertainties, results shown in Fig. S13 typically ranges from $\kappa = 10^8$ Pa to $\kappa = 10^{10}$ Pa, which indicates that the magma in the reservoir was in a bubbly state during the caldera collapse (Huppert and Woods, 2002). The increase of source durations observed from April 6 to April 7 in Tables S4–S6 suggests a reduction of the magma bulk modulus implying that the magma becomes more bubbly. This might correspond to the exsolution of gas following the depressurization of the chamber when a significant increase in the magma outflow rate is estimated (cf., Fig. 6b). Such interpretation seems consistent with field observations indicating a dramatic increase in the height of lava fountains to more than 200 m simultaneous with the reduction of κ and the increase of magma extrusion rate (Staudacher et al., 2009). The magma bulk modulus might also be impacted by a possible input of deep magma (as suggested by Fontaine et al., 2019). Such variation of the magma bulk modulus due to the influx of gas-rich magma has been proposed during the 2000 Miyake-jima collapse by Michon et al. (2011).

An interesting aspect of the 2007 Piton de la Fournaise collapse is the evolution of the time-interval T between successive collapse increments shown in Fig. 6c. As reported previously (e.g., Michon et al., 2007), T gradually decreases from about 2 h at the beginning of the collapse to ~30 min on April 6 at 12:00 GMT and then increases again until the end of the collapse. As detailed in text S5, the time-interval in our piston spring-block model can be expressed as:

$$T = \frac{2\Delta\mu F_n V_0}{\alpha\kappa S} \quad (2)$$

where $\Delta\mu$ is the difference between static (μ_S) and dynamic (μ_D) friction coefficients and F_n is the effective normal force exerted on the ring-fault delimiting the piston cylinder. Although the decrease of κ due to the exsolution of gas will tend to increase the time-interval between collapse events, the estimated variations of κ seems to have a moderate effect on T (as also inferred by Michon et al., 2011). On the other hand, we see in Fig. S14 that the variations of T can be partly explained by the increase of the magma outflow rate α . As noted by Stix and Kobayashi (2008) and Michon et al. (2011), the variations of time-interval are also controlled by changes in frictional resistance (i.e., $\Delta\mu F_n$ in eq. (2)). Fig. 6d shows the evolution of $\Delta F = \Delta\mu F_n$ estimated from collapse event durations and vertical displacements (see eq. (23) of the Supplementary Text S5). Fig. S15 shows that similar estimates of $\Delta\mu F_n$ can be obtained if we use the time-interval T and magma outflow α from seismic amplitudes (see eq. (25) of the Supplementary Text S5). These results suggest that the initial evolution of T can be explained by a decrease of the friction parameter $\Delta\mu F_n$ at the beginning of the collapse. Consistently with Michon et al. (2011), our results also indicate that larger values of T at the end of the sequence corresponds to an increase of $\Delta\mu F_n$ during the last collapse events (see Fig. S15). As proposed by Michon et al. (2011), such a transitory decrease of frictional resistance might correspond to the reduction of the effective normal force F_n caused by upward migrations of hydrothermal fluids. Such weakening could also be caused by frictional melting or the activation of magma pockets intruding in the ring-fault system. Recent observations of exhumed caldera faults suggest that frictional melting play a critical role in caldera collapses (e.g., Han et al., 2019). Moreover, seismicity and field observations at Piton de la Fournaise show that the ring-fault system is a preferential path of magma intrusions (e.g., Staudacher, 2010;

Duputel et al., 2019). Both interpretations seem plausible given satellite observations showing a ring-shaped thermal anomaly in the Dolomieu crater during summit subsidence and the existence of small lava flows emitted from the edge of the collapsed piston on April 6 (Urai et al., 2007).

As mentioned above, the surface collapse activity was preceded by a series of VLP precursors visible in Fig. 7. As suggested by (Fontaine et al., 2019), these events might correspond to deep collapses at depth before the onset of the surface subsidence. Such precursory VLP activity has also been observed before the 2000 Miyake-jima caldera formation (Kobayashi et al., 2012). These precursors have a longer duration than the VLP signal of the main collapse event (cf., Fig. S2b). Assuming the same source geometry, this could be explained by a larger centroid time difference between the vertical contraction of the magma reservoir and the resulting collapse of the overlying fractured column. Such larger time difference could potentially result from the fact that most of the piston remains locked during the early stage of the sequence. After the main collapse, the piston falls down more easily while the frictional resistance is reduced as shown in Fig. 6d. To a smaller extent, we notice some differences between the main collapse and the following smaller collapses in Fig. S2a. There are also discrepancies in VLP signals emitted at the end of the collapse sequence (e.g., Fig. S8–S10). These discrepancies can be explained by differences in focal depth and centroid time (cf., Table S4–S6) that can possibly be linked with the weakening of the edifice. However, such interpretations remain uncertain given our limited sensitivity to depth and the availability of a single broadband station to characterize small VLP events before and after the main collapse.

The 2007 Piton de la Fournaise summit subsidence outlines the hazard caused by caldera collapses on basaltic volcanoes. In this context, a parameter of primary importance is the critical volume fraction of evacuated magma to trigger the collapse. According to the volume change derived after the main collapse, this critical volume fraction is only a few percent (between 1% and 4% of the shallow magma reservoir volume). This corresponds to critical underpressures in the magma chamber ranging from -5 to -70 MPa, which is in rough agreement with geodetic estimates (ranging from -5 to -10 MPa; Peltier et al., 2009; Got et al., 2013). Previous estimates by (Michon et al., 2011) yielded a larger critical volume fraction of 8.2% corresponding to larger critical underpressures (from -45 MPa to -150 MPa). It is interesting to notice that the 2007 Piton de la Fournaise collapse has characteristics that are similar to other basaltic caldera forming eruptions. The 1968 Fernandina, 2000 Miyakejima and 2018 Kilauea collapses are characterized by quasi-periodic series of incremental subsidence events manifested by tilt steps and VLP signals similar to what is observed at Piton de la Fournaise. These events are also driven by magma withdrawal from shallow reservoirs through low-elevation eruptive vents. For both Fernandina and Kilauea, the time interval T between successive collapses follows an evolution that is quite similar to what is observed at Piton de la Fournaise (Stix and Kobayashi, 2008; Michon et al., 2011; Neal et al., 2019). Despite these similarities, there are also significant differences. For example, the total duration of the whole caldera collapse ranges from about 2 days at Piton de la Fournaise to more than 3 months at Kilauea. Some of these discrepancies can possibly be explained by differences in the summit caldera block geometry, reservoir volume, edifice strength, magma properties and lava extrusion rates. The relative importance of these different parameters are still poorly constrained given the challenging circumstances in which such collapses have been observed. New near-field seismogeodetic observations of the recent Kilauea summit subsidence therefore appear promising to better understand the mechanisms at the origin of caldera collapses.

Acknowledgements

This project was supported by the IPGS internal call for projects. This project has also received funding from the European Research Council (ERC, under the European Union's Horizon 2020 research and innovation programme under grant agreement No. 805256) and from Agence Nationale de la Recherche (project ANR-17-ERC3-0010). We thank Olivier Lengliné, Dimitri Zigone and Michael Heap for helpful discussions. Michel Tas is additionally thanked for grammatical assistance. This study incorporates data acquired by the Piton de la Fournaise Volcano Observatory (OVPF - IPGP) accessible via the VOLOBSIS Portal at <http://volobisis.ipgp.fr>. We also use seismic data from GEOSCOPE (G), IRIS/IDA (II), IRIS/USGS (IU), Pacific21 (PS), Australian National Seismograph Network (AU), New China Digital Seismograph Network (IC) and Northeast Tibet Plateau experiment (Z1). We wish to thank the network and station operators for their commitment to collect high-quality seismic data. We thank the editor, Miaki Ishii, one anonymous reviewer and Laurent Michon for their constructive comments, which helped improve this manuscript.

Appendix A. Supplementary material

Supplementary material related to this article can be found online at <https://doi.org/10.1016/j.epsl.2019.115786>.

References

- Bassin, C., Laske, G., Masters, G., 2000. The current limits of resolution for surface wave tomography in North America. *Eos Trans. AGU* 81.
- Battaglia, J., Ferrazzini, V., Staudacher, T., Aki, K., Cheminée, J.L., 2005. Pre-eruptive migration of earthquakes at the Piton de la Fournaise volcano (Réunion Island). *Geophys. J. Int.* 161, 549–558.
- Brenguier, F., Shapiro, N.M., Campillo, M., Ferrazzini, V., Duputel, Z., Coutant, O., Nercessian, A., 2008. Towards forecasting volcanic eruptions using seismic noise. *Nat. Geosci.* 1, 126–130.
- Chouet, B.A., Matoza, R.S., 2013. A multi-decadal view of seismic methods for detecting precursors of magma movement and eruption. *J. Volcanol. Geotherm. Res.* 252, 108–175.
- Chouet, B.A., Dawson, P.B., James, M.R., Lane, S.J., 2010. Seismic source mechanism of degassing bursts at Kilauea Volcano, Hawaii: results from waveform inversion in the 10–50 s band. *J. Geophys. Res.* 115, 716.
- Coppola, D., Piscopo, D., Staudacher, T., Cigolini, C., 2009. Lava discharge rate and effusive pattern at Piton de la Fournaise from MODIS data. *J. Volcanol. Geotherm. Res.* 184, 174–192.
- Duputel, Z., Ferrazzini, V., Brenguier, F., Shapiro, N., Campillo, M., Nercessian, A., 2009. Real time monitoring of relative velocity changes using ambient seismic noise at the Piton de la Fournaise volcano (La Réunion) from January 2006 to June 2007. *J. Volcanol. Geotherm. Res.* 184, 164–173.
- Duputel, Z., Tsai, V.C., Rivera, L., Kanamori, H., 2013. Using centroid time-delays to characterize source durations and identify earthquakes with unique characteristics. *Earth Planet. Sci. Lett.* 374, 92–100.
- Duputel, Z., Vergne, J., Rivera, L., Wittlinger, G., Farra, V., Hetényi, G., 2016. The 2015 Gorkha earthquake: a large event illuminating the Main Himalayan Thrust fault. *Geophys. Res. Lett.* 43, 2517–2525.
- Duputel, Z., Lengliné, O., Ferrazzini, V., 2019. Constraining spatiotemporal characteristics of magma migration at Piton De La Fournaise volcano from pre-eruptive seismicity. *Geophys. Res. Lett.* 46, 119–127.
- Ekström, G., Stark, C.P., 2013. Simple scaling of catastrophic landslide dynamics. *Science* 339, 1416–1419.
- Epp, D., Decker, R.W., Okamura, A.T., 1983. Relation of summit deformation to East Rift Zone eruptions on Kilauea Volcano, Hawaii. *Geophys. Res. Lett.* 10, 493–496.
- Fontaine, F.R., Roult, G., Michon, L., Barruol, G., Di Muro, A., 2014. The 2007 eruptions and caldera collapse of the Piton de la Fournaise volcano (La Réunion Island) from tilt analysis at a single very broadband seismic station. *Geophys. Res. Lett.* 41, 2803–2811.
- Fontaine, F.R., Roult, G., Hejraní, B., Michon, L., Ferrazzini, V., Barruol, G., Tkalcic, H., Di Muro, A., Peltier, A., Reymond, D., Staudacher, T., Massin, F., 2019. Very- and ultra-long-period seismic signals prior to and during caldera formation on La Réunion Island. *Sci. Rep.* 9, 8068.
- Ford, S.R., Dreger, D.S., Walter, W.R., 2010. Network sensitivity solutions for regional moment-tensor inversions. *Bull. Seismol. Soc. Am.* 100, 1962–1970.
- Froger, J.L., Famin, V., Cayol, V., Augier, A., Michon, L., Lénat, J.F., 2015. Time-dependent displacements during and after the April 2007 eruption of Piton de la Fournaise, revealed by interferometric data. *J. Volcanol. Geotherm. Res.* 296, 55–68.
- Gailler, L.S., Lénat, J.F., Lambert, M., Levieux, G., Villeneuve, N., Froger, J.L., 2009. Gravity structure of Piton de la Fournaise volcano and inferred mass transfer during the 2007 crisis. *J. Volcanol. Geotherm. Res.* 184, 31–48.
- Got, J.L., Peltier, A., Staudacher, T., Kowalski, P., Boissier, P., 2013. Edifice strength and magma transfer modulation at Piton de la Fournaise volcano. *J. Geophys. Res.* 118, 5040–5057.
- Gudmundsson, M.T., Jonsdóttir, K., Hooper, A., Holohan, E.P., Halldórsson, S.A., Ófeigsson, B.G., Cesca, S., Vogfjord, K.S., Sigmundsson, F., Hognadóttir, T., Einarsdóttir, S., Bagnardi, M., Parks, M.M., Hjörleifsdóttir, V., Palsson, F., Walter, T.R., Schöpfer, M.P.J., Heimann, A., Reynolds, H.I., Dumont, S., Bali, E., Gudfinnsson, G.H., Dahm, T., Roberts, M.J., Hensch, M., Belart, J.M.C., Spaans, K., Jakobsson, S., Gudmundsson, G.B., Fridrikssdóttir, H.M., Drouin, V., Dürig, T., Áðalgeirsðóttir, G., Riishuus, M.S., Pedersen, G.B.M., van Boeckel, T., Oddsson, B., Pfeffer, M.A., Barsotti, S., Bergsson, B., Donovan, A., Burton, M.R., Aiuppa, A., 2016. Gradual caldera collapse at Bárðarbunga volcano, Iceland, regulated by lateral magma outflow. *Science* 353, aaf8988.
- Han, R., Kim, J.S., Kim, C.M., Hirose, T., Jeong, J.O., Jeong, G.Y., 2019. Dynamic weakening of ring faults and catastrophic caldera collapses. *Geology* 47, 107–110.
- Herrmann, R.B., 2013. Computer programs in seismology: an evolving tool for instruction and research. *Seismol. Res. Lett.* 84, 1081–1088.
- Hibert, C., Mangeney, A., Polacci, M., Muro, A.D., Vergniolle, S., Ferrazzini, V., Peltier, A., Taisne, B., Burton, M., Dewez, T., Grandjean, G., Dupont, A., Staudacher, T., Brenguier, F., Kowalski, P., Boissier, P., Catherine, P., Lauret, F., 2015. Toward continuous quantification of lava extrusion rate: Results from the multidisciplinary analysis of the 2 January 2010 eruption of Piton de la Fournaise volcano, La Réunion. *J. Geophys. Res., Solid Earth* 120, 3026–3047.
- Huppert, H.E., Woods, A.W., 2002. The role of volatiles in magma chamber dynamics. *Nature* 420, 493–495.
- Kanamori, H., Given, J.W., 1981. Use of long-period surface waves for rapid determination of earthquake-source parameters. *Phys. Earth Planet. Inter.* 27, 8–31.
- Kanamori, H., Given, J.W., 1982. Analysis of long-period seismic waves excited by the May 18, 1980, eruption of Mount St. Helens – a terrestrial monopole. *J. Geophys. Res., Solid Earth* 87, 5422–5432.
- Kanamori, H., Given, J.W., Lay, T., 1984. Analysis of seismic body waves excited by the Mount St. Helens eruption of May 18, 1980. *J. Geophys. Res., Solid Earth* (1978–2012) 89, 1856–1866.
- Kawakatsu, H., 1989. Centroid single force inversion of seismic waves generated by landslides. *J. Geophys. Res., Solid Earth* 94, 12363–12374.
- Kikuchi, M., Yamanaka, Y., Koketsu, K., 2001. Source process of the long-period seismic pulses associated with the 2000 eruption of Miyake-jima volcano, and its implications. *J. Geogr.* 110, 204–216.
- Kobayashi, T., Ohminato, T., Ida, Y., Fujita, E., 2012. Intermittent inflations recorded by broadband seismometers prior to caldera formation at Miyake-jima volcano in 2000. *Earth Planet. Sci. Lett.* 357–358, 145–151.
- Komatitsch, D., Tromp, J., 1999. Introduction to the spectral element method for three-dimensional seismic wave propagation. *Geophys. J. Int.* 139, 806–822.
- Kumagai, H., Ohminato, T., Nakano, M., Ooi, M., Kubo, A., Inoue, H., Oikawa, J., 2001. Very-long-period seismic signals and caldera formation at Miyake Island, Japan. *Science* 293, 687–690.
- Massin, F., Ferrazzini, V., Bachelery, P., Nercessian, A., Duputel, Z., Staudacher, T., 2011. Structures and evolution of the plumbing system of Piton de la Fournaise volcano inferred from clustering of 2007 eruptive cycle seismicity. *J. Volcanol. Geotherm. Res.* 202, 96–106.
- Michon, L., Staudacher, T., Ferrazzini, V., Bachelery, P., Marti, J., 2007. April 2007 collapse of Piton de la Fournaise: a new example of caldera formation. *Geophys. Res. Lett.* 34.
- Michon, L., Massin, F., Famin, V., Ferrazzini, V., Roult, G., 2011. Basaltic calderas: collapse dynamics, edifice deformation, and variations of magma withdrawal. *J. Geophys. Res., Solid Earth* 116, 8485.
- Michon, L., Di Muro, A., Villeneuve, N., Saint-Marc, C., Fadda, P., Manta, F., 2013. Explosive activity of the summit cone of Piton de la Fournaise volcano (La Réunion island): a historical and geological review. *J. Volcanol. Geotherm. Res.* 264, 117–133.
- Mildon, Z.K., Pugh, D.J., Tarasewicz, J., White, R.S., Brandsdóttir, B., 2016. Closing crack earthquakes within the Krafla caldera, North Iceland. *Geophys. J. Int.* 207, 1137–1141.
- Mordret, A., Rivet, D., Landès, M., Shapiro, N.M., 2015. Three-dimensional shear velocity anisotropic model of Piton de la Fournaise Volcano (La Réunion Island) from ambient seismic noise. *J. Geophys. Res., Solid Earth* 120, 406–427.
- Nakano, M., Kumagai, H., Chouet, B.A., 2003. Source mechanism of long-period events at Kusatsu-Shirane Volcano, Japan, inferred from waveform inversion of the effective excitation functions. *J. Volcanol. Geotherm. Res.* 122, 149–164.
- Neal, C.A., Brantley, S.R., Antolik, L., Babb, J.L., Burgess, M., Calles, K., Cappos, M., Chang, J.C., Conway, S., Desmither, L., Dotray, P., Elias, T., Fukunaga, P., Fuke, S., Johanson, I.A., Kamibayashi, K., Kaauahikaua, J., Lee, R.L., Pekalib, S., Miklius, A., Million, W., Moniz, C.J., Nadeau, P.A., Okubo, P., Parcheta, C., Patrick, M.R., Shiro, B., Swanson, D.A., Tollett, W., Trusdell, F., Younger, E.F., Zoeller, M.H.,

- Montgomery-Brown, E.K., Anderson, K.R., Poland, M.P., Ball, J.L., Bard, J., Coombs, M., Dietterich, H.R., Kern, C., Thelen, W.A., Cervelli, P.F., Orr, T., Houghton, B.F., Ganseddi, C., Hazlett, R., Lundgren, P., Diefenbach, A.K., Lerner, A.H., Waite, G., Kelly, P., Clors, L., Werner, C., Mulliken, K., Fisher, G., Damby, D., 2019. The 2018 rift eruption and summit collapse of Kilauea Volcano. *Science* 363, 367.
- Peltier, A., Famin, V., Bachelery, P., Cayol, V., Fukushima, Y., Staudacher, T., 2008. Cyclic magma storages and transfers at Piton de La Fournaise volcano (La Reunion hotspot) inferred from deformation and geochemical data. *Earth Planet. Sci. Lett.* 270, 180–188.
- Peltier, A., Staudacher, T., Bachelery, P., Cayol, V., 2009. Formation of the April 2007 caldera collapse at Piton de La Fournaise volcano: insights from GPS data. *J. Volcanol. Geotherm. Res.* 184, 152–163.
- Riel, B., Milillo, P., Simons, M., Lundgren, P., Kanamori, H., Samsonov, S., 2015. The collapse of Bardarbunga caldera, Iceland. *Geophys. J. Int.* 202, 446–453.
- Ritsema, J., Deuss, A., van Heijst, H.J., Woodhouse, J.H., 2011. S4ORTS: a degree-40 shear-velocity model for the mantle from new Rayleigh wave dispersion, teleseismic traveltimes and normal-mode splitting function measurements. *Geophys. J. Int.* 184, 1223–1236.
- Shuler, A., Ekström, G., Nettles, M., 2013. Physical mechanisms for vertical-CLVD earthquakes at active volcanoes. *J. Geophys. Res., Solid Earth* 118, 1569–1586.
- Staudacher, T., 2010. Field observations of the 2008 summit eruption at Piton de la Fournaise (Ile de La Réunion) and implications for the 2007 Dolomieu collapse. *J. Volcanol. Geotherm. Res.* 191, 60–68.
- Staudacher, T., Ferrazzini, V., Peltier, A., Kowalski, P., Boissier, P., Catherine, P., Lauret, F., Massin, F., 2009. The April 2007 eruption and the Dolomieu crater collapse, two major events at Piton de la Fournaise (La Reunion Island, Indian Ocean). *J. Volcanol. Geotherm. Res.* 184, 126–137.
- Stix, J., Kobayashi, T., 2008. Magma dynamics and collapse mechanisms during four historic caldera-forming events. *J. Geophys. Res., Solid Earth* 113.
- Takei, Y., Kumazawa, M., 1994. Why have the single force and torque been excluded from seismic source models? *Geophys. J. Int.* 118, 20–30.
- Uhira, K., Yamasato, H., Takeo, M., 1994. Source mechanism of seismic waves excited by pyroclastic flows observed at Unzen volcano, Japan. *J. Geophys. Res.* 99, 17757–17773.
- Urai, M., Geshi, N., Staudacher, T., 2007. Size and volume evaluation of the caldera collapse on Piton de la Fournaise volcano during the April 2007 eruption using ASTER stereo imagery. *Geophys. Res. Lett.* 34.

4.5 Perspectives

Dans ce chapitre, nous avons montré comment les observations sismologiques peuvent être utiles pour mieux comprendre la dynamique des volcans. Nous avons ainsi montré comment le suivi détaillé de la sismicité volcano-tectonique peut nous permettre de déterminer les caractéristiques spatiotemporelles du transport magmatique profond et superficiel au Piton de la Fournaise. En analysant les formes d'ondes enregistrées lors de l'effondrement de Caldeira en 2007 au Piton de la Fournaise, nous avons également étudié la dynamique de ce type de phénomène.

4.5.1 Caractérisation des mécanismes à la source des séismes volcaniques

Même si les séismes volcano-tectoniques (VT) sont généralement interprétés comme des ruptures cisaillantes "classiques" déclenchées par l'activité volcanique, la relation entre ces séismes et la migration de magma reste encore mal comprise. Comme on l'a vu dans ce chapitre, la sismicité superficielle au Piton de la Fournaise est principalement focalisée sur un système annulaire, correspondant vraisemblablement à une structure déjà prête à rompre. La caractérisation des mécanismes aux foyers paraît être une information importante pour mieux comprendre l'origine de cette sismicité. Cependant, ce travail est souvent compliqué par la faible amplitude des signaux, la complexité structurale des volcans et le grand nombre d'événements observés pendant les phases d'intrusion magmatiques. L'incertitude sur la localisation de la sismicité peut également être problématique lorsque l'on considère des stations proches situées à des altitudes similaires aux séismes. Différentes approches existent aujourd'hui pour prendre en compte ces incertitudes et analyser les mécanismes d'un grand nombre de micro-séismes (voir par exemple Shelly et al., 2016 ; Pugh et al., 2016b,a ; Pugh and White, 2018).

La détermination des mécanismes aux foyers sur différents volcans montre que les événements VT détectés pendant les intrusions magmatiques ne sont généralement pas associés à des sources non double-couples, suggérant que l'ouverture des dikes se fait principalement de façon asismique (Ágústsdóttir et al., 2016). Dans la thèse de Catalina Morales et dans un article en cours de préparation, nous montrons que la composante non double-couple de certains séismes observés lors de l'intrusion magmatique de Mai 2018 au large Mayotte ne pouvait pas correspondre à l'ouverture de dikes. En considérant une large gamme d'ouvertures possibles (0.5 – 10 m), la composante non double-couple et la durée de ces événements correspondent en effet à des vitesses de migration du magma irréalistes (290 – 2000 m/s). Ces composantes non double-couples correspondent plus vraisemblablement à une contamination des modèles de source par la structure superficielle encore mal connue dans la région. Les observations semblent donc indiquer que les séismes VT correspondent principalement à l'activation de fractures ou de failles à proximité de l'extrémité des dikes (Rubin and Gillard, 1998). Pour certaines intrusions, on observe des séismes avec des mécanismes quasiment opposés bien qu'ils soient regroupés spatialement (White et al., 2011). Si des failles pré-existantes sont orientées favorablement, elles seront en effet activées de façon opposée de part et d'autre de l'extrémité du dike (Ágústsdóttir et al., 2016). Comme proposé par White et al. (2011), un mécanisme alternatif pour expliquer ces observations est la rupture de "bouchons" solidifiés sur les parois du conduit magmatique.

Alors que les séismes VT sont associés à une source connue (rupture cisaillante), les événements longue-période (LP) sont causés par des processus fluides encore mal contraints. La théorie la plus répandue est que ces événements sont produits par la résonance de cavités remplies de fluide (Chouet and Matoza, 2013), mais les mécanismes d'excitation cette résonance restent encore débattus (pour un récapitulatif, voir Chouet and Matoza, 2013). Dans le cas de volcans andésitiques, la sismicité LP pourrait par exemple être associée à des ruptures fragiles entre le magma visqueux et l'encaissant. Dans le contexte de volcans basaltiques, Julian (1994) suggère que les séismes LP pourraient correspondre à la résonance de conduits magmatiques excités par des perturbations de pressions induites par une modification de l'écoulement fluide ou par des séismes au voisinage du conduit. D'autres études proposent que les séismes LP superficiels correspondent à la résonance de fissures remplies de fluide hydrothermal activées par la remontée de magma (voir par exemple Kumagai et al., 2005 ; Zecevic et al., 2013). La densification des réseaux d'observation volcanologiques permet aujourd'hui de disposer d'un plus grand nombre de capteurs en champ proche. Cette amélioration des réseaux permanents couplée au déploiement de réseaux denses est une bonne occasion pour améliorer notre compréhension des mécanismes d'excitation de la sismicité LP.

4.5.2 Suivi du transport magmatique à partir de la sismicité

Comme discuté précédemment, la sismicité VT pendant les phases intrusives correspond vraisemblablement à la rupture de failles pré-existantes au voisinage de l'extrémité des dikes. Les séismes fournissent donc une information importante pour contraindre la migration du magma au sein des édifices volcaniques (Segall et al., 2013 ; Ágústsdóttir et al., 2019). L'intrusion de 1977 au Krafla (Islande) est particulièrement intéressante à cet égard. Lors de cet évènement, un essaim de séismes en migration a atteint un champ géothermique simultanément à l'intersection d'un forage géothermique par un dike, produisant alors une petite éruption (Brandsdóttir and Einarsson, 1979 ; Larsen et al., 1979). Cet épisode est une confirmation directe de l'utilité de la sismicité pour suivre la propagation des dikes.

Dans l'article présenté en annexe A.6, nous effectuons un suivi de l'intrusion magmatique de mai 2018 au Kīlauea. Cette intrusion a conduit à une éruption majeure avec un volume émis supérieur à 0.8 km^3 . Cet évènement volcanique est associé au déclenchement d'un séisme de magnitude $M_W = 7.2$ sur le flanc sud du volcan et à l'effondrement de la Caldeira sommitale (Neal et al., 2019). En particulier, nous avons souhaité savoir si les observations de la propagation du dike pouvaient nous aider à contraindre un modèle physique et nous informer sur l'initiation de la séquence éruptive de 2018. Pour ce faire, nous avons détecté et localisé plus de 6000 séismes pendant l'intrusion magmatique dans la zone de rift du Kīlauea. En utilisant la localisation des événements ainsi que les amplitudes sismiques en champ proche, nous avons pu suivre en détail la propagation du dike sur plus de 20 km. Ces observations sont cohérentes avec le modèle logarithmique proposé par Grossman-Ponemon et al. (2020) pour décrire la propagation d'un dike alimenté par un réservoir magmatique. D'après les données inclinométriques à proximité du cratère Pu'u'ō'ō, ce modèle est également en accord avec la décroissance de pression dans le réservoir magmatique. Ce travail encourage le suivi d'intrusions magmatiques combinant observations géophysiques et modèles physiques.

4.5.3 Analyse comparative des effondrements de Caldeira basaltiques

Bien que les effondrements de caldeira soient relativement fréquents dans l'histoire des volcans basaltiques (Michon et al., 2013), ce type de phénomène n'a été observé que sur un faible nombre de volcans à l'échelle globale. Les exemples les plus récents sont les effondrements du Miyakejima en 2000, du Piton de la Fournaise en 2007, du Bárðarbunga en 2014 et du Kīlauea en 2018 (Kumagai et al., 2001 ; Michon et al., 2007 ; Gudmundsson et al., 2016 ; Neal et al., 2019).

Les observations géophysiques indiquent qu'il existe de nombreuses similitudes entre les effondrement de Caldeira sur différents volcans. Ainsi par exemple, un comportement caractéristique est la nature incrémentale de ces effondrements. Ces phénomènes sont également associés à de grandes intrusions distales souvent associées à une éruption à basse altitude avec des volumes éruptés très importants. Malgré ces points communs, il existe également des différences majeures. Alors qu'au Kīlauea et au Piton de la Fournaise, les observations indiquent principalement une série quasi-périodique d'effondrements soudains (cf., section 4.4), la subsidence de la caldeira du Bárðarbunga s'est fait de façon plus continue (asismique) avec quelques événements ponctuels. La durée totale de l'effondrement est également significativement différente d'une caldeira à l'autre. Le gros de l'effondrement s'est fait en 2 jours au Piton de la Fournaise alors que le même phénomène a duré 40 jours au Miyakejima et plus de 3 mois au Kīlauea.

Le temps T entre deux événements de subsidence semble être un paramètre clé qui révèle la dynamique de l'effondrement. Au Piton de la Fournaise et au Kīlauea, T a d'abord diminué puis ré-augmenté. Au Miyakejima, T a montré une évolution plus erratique mais semble avoir augmenté en fin d'effondrement. Au premier ordre, ces différences peuvent être associées des variations géométriques et rhéologiques (géométrie du piston et du réservoir magmatique, propriétés du magma, débit de magma sortant, résistance frictionnelle à la descente du Piston ; Stix and Kobayashi, 2008 ; Michon et al., 2011). La géométrie de la faille annulaire a également un impact important sur la déformation et les formes d'ondes enregistrées autour du volcan (Segall et al., 2019 ; Shuler et al., 2013a). Pendant longtemps, notre compréhension des effondrement de caldeira souffrait de l'absence de données géophysiques en champ proche. Les exemples les plus récents ont bénéficié d'une amélioration significative de la couverture instrumentale qui peut nous permettre de mieux contraindre l'importance relative des différents paramètres contrôlant la dynamique de ces phénomènes. Il semble également intéressant d'explorer les mécanismes à la source des effondrement récents pour éclairer les événements qui n'ont pas pu être enregistrés avec autant de détails dans le passé.

4.5.4 Sismicité au nord de l'Île de la Réunion : origine tectonique ou processus magmatique ?

Le récent essaim de sismicité au large de Mayotte a montré la nécessité de surveiller les zones volcaniques même lorsqu'elles sont inactives depuis longtemps. C'est le cas au nord de l'île de la Réunion qui est associée à une sismicité soutenue depuis plusieurs années.

L'île de la Réunion est composée de deux massifs volcaniques juxtaposés : Le Piton des Neiges et le Piton de la Fournaise. Au nord de l'île, le Piton des Neiges est inactif depuis environ 12 000 ans (Deniel et al., 1992). Bien que l'activité volcanique soit actuellement focalisée sur le massif

du Piton de la Fournaise, cette région Nord-Est est associée à une sismicité importante (voir Figure 17). En dehors des périodes de crises sismiques pré-éruptives au le Piton de la Fournaise, la majorité de la sismicité de l'île est focalisée en profondeur à proximité de Saint Denis (le chef-lieu de l'île, agglomération comprenant plus de 200 000 habitants). La plupart des séismes ressentis avec des magnitude $M > 2$ dans l'île proviennent de cet essaim. Cette sismicité étant mal contrainte par le réseau actuel, de nombreuses questions restent en suspens : Quelle est la distribution spatiale et temporelle de ces séismes ? Quelle est la variation temporelle du taux de sismicité ? Ces évènements sont-ils d'origine tectonique ou volcanique ?

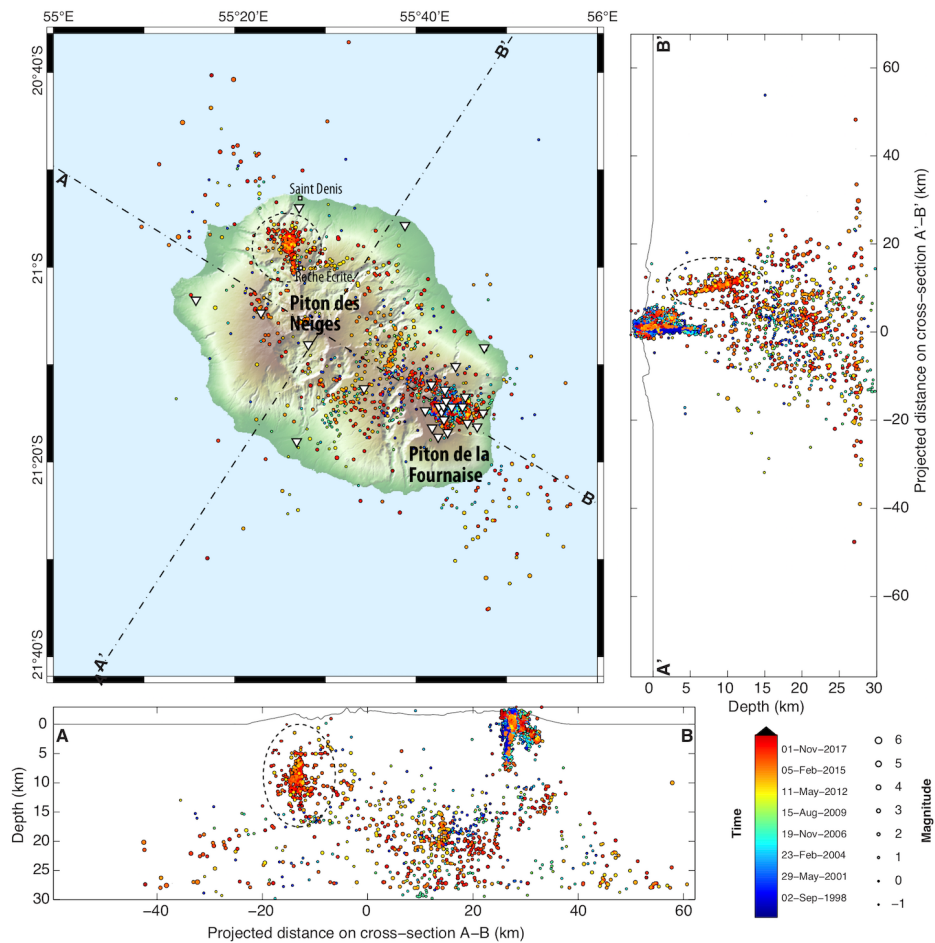


FIG. 17 – Localisations hypocentrales de l’Observatoire Volcanologique du Piton de la Fournaise (OVPF) depuis 1998. Les points représentent la localisation des séismes (colorés en fonction de leur temps origine). L’ensemble de la sismicité est projeté sur des coupes en bas et à droite correspondant aux profils A-B et A'-B' indiqués sur la carte. On observe une forte activité sismique dans le nord de l’île depuis 2013 (voir ellipses en pointillé). Les stations large-bande de l’OVPF sont indiquées par des triangles blancs.

Pour répondre à ces questions, nous avons commencé à densifier le réseau en 2020 (en collaboration avec l’OVPF et grâce à un financement INSU ALEAS). Nous avons également intégré les données du réseau temporaire ZF installé pour effectuer le suivi du transport de sédiments dans la Rivière des Pluies (Fontaine et al., 2016). Des analyses préliminaires via des approches de “template matching” et de relocalisation semblent indiquer une sismicité soutenue focalisée sur un plan à pendage vers le nord-est entre 5 et 20 km de profondeur. Michon et al. (2015) interprète

cet essaim comme l'extension Nord d'une zone de rift orientée N120° causée par une extension Nord-Est - Sud-Ouest. Cette interprétation semble en désaccord avec la détermination des mécanismes qui indiquent un glissement inverse. Ce type de faille inverse qui semble affecter une épaisseur importante de la croûte océanique a déjà été observé au Kīlauea. Ces observations ont précédemment été interprétées comme résultant de la charge de l'édifice volcanique qui pourrait être suffisamment importante pour rompre la croûte océanique (Got et al., 2008). Les nouvelles données en cours d'acquisition vont permettre l'amélioration des localisations de séismes mais aussi la construction d'un modèle tomographique local. Ces contraintes sismologiques pourront alimenter des modèles mécaniques pour tester l'interprétation de Got et al. (2008) au nord de La Réunion. De façon complémentaire, le taux de sismicité pourra être comparé à l'évolution temporelle de la signature chimique de l'activité magmatique profonde au niveau de la Rivière de pluies (analysée de façon hebdomadaire dans le cadre du site d'observation ERORUN de l'OSU-Réunion).

Bibliographie

- B. T. Aagaard, M. G. Knepley, and C. A. Williams. A domain decomposition approach to implementing fault slip in finite-element models of quasi-static and dynamic crustal deformation. *J. Geophys. Res. : Solid Earth*, 118(6) :3059–3079, 2013. doi : 10.1002/jgrb.50217.
- T. Ágústsdóttir, J. Woods, T. Greenfield, R. G. Green, R. S. White, T. Winder, B. Brandsdóttir, S. Steinþórsson, and H. Soosalu. Strike-slip faulting during the 2014 Bárðarbunga-Holuhraun dike intrusion, central Iceland. *Geophys. Res. Lett.*, 43(4) :1495–1503, 2016. doi : 10.1002/2015GL067423.
- T. Ágústsdóttir, T. Winder, J. Woods, R. S. White, T. Greenfield, and B. Brandsdóttir. Intense Seismicity During the 2014–2015 Bárðarbunga-Holuhraun Rifting Event, Iceland, Reveals the Nature of Dike-Induced Earthquakes and Caldera Collapse Mechanisms. *J. Geophys. Res. : Solid Earth*, 124(8) :8331–8357, 2019. doi : 10.1029/2018JB016010.
- K. Aki and R. Koyanagi. Deep volcanic tremor and magma ascent mechanism under Kilauea, Hawaii. *J. Geophys. Res.*, 86(B8) :7095–7109, 1981. doi : 10.1029/JB086iB08p07095.
- K. Aki and P. G. Richards. *Quantitative Seismology*. University Science Books, Sausalito, CA, 2nd edition, 2002. ISBN 0935702962.
- S. Allgeyer and P. Cummins. Numerical tsunami simulation including elastic loading and sea-water density stratification. *Geophys. Res. Lett.*, 41(7) :2368–2375, 2014. doi : 10.1002/2014GL059348.
- B. P. Allmann and P. M. Shearer. Global variations of stress drop for moderate to large earthquakes. *J. Geophys. Res.*, 114(B1) :B01310, 2009. doi : 10.1029/2008JB005821.
- J.-P. Avouac. From Geodetic Imaging of Seismic and Aseismic Fault Slip to Dynamic Modeling of the Seismic Cycle. *Annual Review of Earth and Planetary Sciences*, Vol 43, 43 :233–271, 2015. doi : 10.1146/annurev-earth-060614-105302.
- J.-P. Avouac, F. Ayoub, S. Wei, J.-P. Ampuero, L. Meng, S. Leprince, R. Jolivet, Z. Duputel, and D. Helmberger. The 2013, Mw 7.7 Balochistan earthquake, energetic strike-slip reactivation of a thrust fault. *Earth Planet. Sci. Lett.*, 391(0) :128–134, 2014. doi : 10.1016/j.epsl.2014.01.036.
- F. Ayoub, S. Leprince, and J.-P. Avouac. Co-registration and correlation of aerial photographs for ground deformation measurements. *ISPRS J. Photogramm. Remote Sens.*, 64(6) :551–560, 2009. doi : 10.1016/j.isprsjprs.2009.03.005.
- H. Bao, J.-P. Ampuero, L. Meng, E. J. Fielding, C. Liang, C. W. D. Milliner, T. Feng, and H. Huang. Early and persistent supershear rupture of the 2018 magnitude 7.5 Palu earthquake. *Nature Geosci.*, 12(3) :200–205, 2019.

- J. Bedford, M. Moreno, J. C. Baez, D. Lange, F. Tilmann, M. Rosenau, O. Heidbach, O. Oncken, M. Bartsch, A. Rietbrock, A. Tassara, M. Bevis, and C. Vigny. A high-resolution, time-variable afterslip model for the 2010 Maule $M_w = 8.8$, Chile megathrust earthquake. *Earth Planet. Sci. Lett.*, 383 :26–36, 2013. doi : 10.1016/j.epsl.2013.09.020.
- C. M. Bishop. *Pattern Recognition and Machine Learning*. Information Science and Statistics. Springer, New York, 2006. ISBN 0387310738.
- G. Blewitt. GPS and Space-Based Geodetic Methods. In *Treatise on Geophysics*, pages 307–338. Elsevier, 2015. ISBN 9780444538031. doi : 10.1016/B978-0-444-53802-4.00060-9.
- M. Bouchon. Teleseismic body wave radiation from a seismic source in a layered medium. *Geophys. J. Int.*, 47(3) :515–530, 1976. doi : 10.1111/j.1365-246X.1976.tb07099.x.
- M. Bouchon. A simple method to calculate Green’s functions for elastic layered media. *Bull. Seism. Soc. Am.*, 71(4) :959–971, 1981.
- M. Bouchon. The state of stress on some faults of the San Andreas System as inferred from near-field strong motion data. *J. Geophys. Res.*, 102(B6) :11731–11744, 1997. doi : 10.1029/97JB00623.
- M. Bouchon and H. Karabulut. The Aftershock Signature of Supershear Earthquakes. *Science*, 2008.
- M. Bouchon, N. N. Toksoz, H. Karabulut, M.-P. Bouin, M. Dietrich, M. Aktar, and M. Edie. Space and Time Evolution of Rupture and Faulting during the 1999 Izmit (Turkey) Earthquake. *Bull. Seism. Soc. Am.*, 92(1) :256–266, 2002. doi : 10.1785/0120000845.
- M. Bouchon, H. Karabulut, M. Aktar, S. Ozalaybey, J. Schmittbuhl, and M. P. Bouin. Extended Nucleation of the 1999 $M_w 7.6$ Izmit Earthquake. *Science*, 331(6019) :877–880, 2011. doi : 10.1126/science.1197341.
- M. Bouchon, V. Durand, D. Marsan, H. Karabulut, and J. Schmittbuhl. The long precursory phase of most large interplate earthquakes. *Nature Geosci.*, 6(4) :299–302, 2013. doi : 10.1038/Ngeo1770.
- B. Brandsdóttir and P. Einarsson. Seismic activity associated with the September 1977 deflation of the Krafla central volcano in northeastern Iceland. *J. Volc. Geoth. Res.*, 6(3-4) :197–212, 1979. doi : 10.1016/0377-0273(79)90001-5.
- R. Bürgmann and D. Chadwell. Seafloor Geodesy. *Annual Review of Earth and Planetary Sciences*, Vol 43, 42(1) :509–534, 2014. doi : 10.1146/annurev-earth-060313-054953.
- E. Caballero, A. Chouimet, Z. Duputel, J. Jara, C. Twardzik, and R. Jolivet. Seismic and aseismic fault slip during the initiation phase of the 2017 $M_w=6.9$ Valparaiso earthquake. *Submitted to Geophys. Res. Lett.*, 2020. doi : 10.1002/essoar.10505421.1.
- A. Carrier, J.-L. Got, A. Peltier, V. Ferrazzini, T. Staudacher, P. Kowalski, and P. Boissier. A damage model for volcanic edifices : Implications for edifice strength, magma pressure, and

- eruptive processes. *J. Geophys. Res. : Solid Earth*, 120(1) :567–583, 2015. doi : 10.1002/2014JB011485.
- M. Causse, F. Cotton, and P. M. Mai. Constraining the roughness degree of slip heterogeneity. *J. Geophys. Res.*, 115(B5) :B05304, 2010. doi : 10.1029/2009JB006747.
- C. D. Chadwell, J. A. Hildebrand, F. N. Spiess, J. L. Morton, W. R. Normark, and C. A. Reiss. No spreading across the Southern Juan de Fuca Ridge axial cleft during 1994–1996. *Geophys. Res. Lett.*, 26(16) :2525–2528, 1999. doi : 10.1029/1999GL900570.
- B. A. Chouet. Long-period volcano seismicity : its source and use in eruption forecasting. *Nature*, 380(6572) :309–316, 1996. doi : 10.1038/380309a0.
- B. A. Chouet and R. S. Matoza. A multi-decadal view of seismic methods for detecting precursors of magma movement and eruption. *J. Volc. Geoth. Res.*, 252 :108–175, 2013.
- A. Chouvet, M. Vallée, M. Causse, and F. Courboulex. Global catalog of earthquake rupture velocities shows anticorrelation between stress drop and rupture velocity. *Tectonophysics*, 733 :148–158, 2018. doi : 10.1016/j.tecto.2017.11.005.
- A. Cochard and R. Madariaga. Dynamic faulting under rate-dependent friction. *Pure appl. geophys.*, 142(3) :419–445, 1994. doi : 10.1007/BF00876049.
- S. Colombelli, A. Zollo, G. Festa, and M. Picozzi. Evidence for a difference in rupture initiation between small and large earthquakes. *Nature Communications*, 5 :4089, 2014. doi : 10.1038/ncomms4958.
- F. Cotton and M. Campillo. Frequency domain inversion of strong motions : Application to the 1992 Landers earthquake. *J. Geophys. Res.*, 100 :3961, 1995. doi : 10.1029/94JB02121.
- C. A. Coulon, P. A. Hsieh, R. White, J. B. Lowenstern, and S. E. Ingebritsen. Causes of distal volcano-tectonic seismicity inferred from hydrothermal modeling. *J. Volc. Geoth. Res.*, 345 :98–108, 2017. doi : 10.1016/j.jvolgeores.2017.07.011.
- F. A. Dahlen and J. Tromp. *Theoretical Global Seismology*. Princeton University press, 1998.
- S. M. Day. Three-dimensional finite difference simulation of fault dynamics : Rectangular faults with fixed rupture velocity. *Bull. Seism. Soc. Am.*, 72(3) :705–727, 1982.
- L. De Barros, C. J. Bean, M. Zecevic, F. Brenguier, and A. Peltier. Eruptive fracture location forecasts from high-frequency events on Piton de la Fournaise Volcano. *Geophys. Res. Lett.*, 40(17) :4599–4603, 2013. doi : 10.1002/grl.50890.
- B. Delouis, D. Giardini, P. Lundgren, and J. Salichon. Joint Inversion of InSAR, GPS, Teleseismic, and Strong-Motion Data for the Spatial and Temporal Distribution of Earthquake Slip : Application to the 1999 Izmit Mainshock. *Bull. Seism. Soc. Am.*, 92 :278–299, 2002. doi : 10.1785/0120000806.

- B. Delouis, J.-M. Nocquet, and M. Vallée. Slip distribution of the February 27, 2010 Mw = 8.8 Maule Earthquake, central Chile, from static and high-rate GPS, InSAR, and broadband teleseismic data. *Geophys. Res. Lett.*, 37(17) :L17305–, 2010. doi : 10.1029/2010GL043899.
- C. Deniel, G. Kieffer, and J. Lecointre. New ^{230}Th - ^{238}U and ^{14}C age determinations from Piton des Neiges volcano, Reunion — A revised chronology for the Differentiated Series. *J. Volc. Geoth. Res.*, 51(3) :253–267, 1992. doi : 10.1016/0377-0273(92)90126-X.
- J. Dettmer, R. Benavente, P. R. Cummins, and M. Cambridge. Trans-dimensional finite-fault inversion. *Geophys. J. Int.*, 199(2) :735–751, 2014. doi : 10.1093/gji/ggu280.
- D. A. Dodge, G. C. Beroza, and W. L. Ellsworth. Detailed observations of California fore-shock sequences : Implications for the earthquake initiation process. *Journal of Geophysical Research : Solid Earth (1978–2012)*, 101(B10) :22371–22392, 1996. doi : 10.1029/96JB02269.
- M.-P. Doin, C. Lasserre, G. Peltzer, O. Cavalie, and C. Doubre. Corrections of stratified tropospheric delays in SAR interferometry : Validation with global atmospheric models. *Journal of Applied Geophysics*, 69(1) :35–50, 2009. doi : 10.1016/j.jappgeo.2009.03.010.
- Z. Duputel and L. Rivera. Long-period analysis of the 2016 Kaikoura earthquake. *Phys. Earth Planet. Inter.*, 265 :62–66, 2017. doi : 10.1016/j.pepi.2017.02.004.
- Z. Duputel, L. Rivera, H. Kanamori, G. P. Hayes, B. Hirshorn, and S. Weinstein. Real-time W Phase inversion during the 2011 Off the Pacific Coast of Tohoku Earthquake. *Earth Planets Space*, 63 :535–539, 2011.
- Z. Duputel, H. Kanamori, V. C. Tsai, and L. Rivera. The 2012 Sumatra great earthquake sequence. *Earth Planet. Sci. Lett.*, 351-352 :247–257, 2012a.
- Z. Duputel, L. Rivera, Y. Fukahata, and H. Kanamori. Uncertainty estimations for seismic source inversions. *Geophys. J. R. astr. Soc.*, 190(2) :1243–1256, 2012b.
- Z. Duputel, L. Rivera, H. Kanamori, and G. Hayes. W phase source inversion for moderate to large earthquakes (1990–2010). *Geophys. J. Int.*, 189(2) :1125–1147, 2012c. doi : 10.1111/j.1365-246X.2012.05419.x.
- Z. Duputel, P. S. Agram, M. Simons, S. E. Minson, and J. L. Beck. Accounting for prediction uncertainty when inferring subsurface fault slip. *Geophys. J. Int.*, 197(1) :464–482, 2014. doi : 10.1093/gji/ggt517.
- Z. Duputel, J. Jiang, R. Jolivet, M. Simons, L. Rivera, Ampuero, B. Riel, S. E. Owen, A. W. Moore, S. V. Samsonov, F. O. Culaciati, and S. E. Minson. The Iquique earthquake sequence of April 2014 : Bayesian modeling accounting for prediction uncertainty. *Geophys. Res. Lett.*, 42(19) :7949–7957, 2015. doi : 10.1002/2015GL065402.
- Z. Duputel, J. Vergne, L. Rivera, G. Wittlinger, V. Farra, and G. Hetényi. The 2015 Gorkha earthquake : A large event illuminating the Main Himalayan Thrust fault. 43(6) :2517–2525, 2016. doi : 10.1002/2016GL068083.

- A. M. Dziewonski, T. A. Chou, and J. H. Woodhouse. Determination of earthquake source parameters from waveform data for studies of global and regional seismicity. *J. Geophys. Res.*, 86 :2825–2852, 1981.
- G. Ekström and A. M. Dziewonski. Centroid-moment tensor solutions for 35 earthquakes in Western North America (1977-1983). *Bull. Seism. Soc. Am.*, 1985.
- G. Ekström, M. Nettles, and A. M. Dziewonski. The global CMT project 2004–2010 : Centroid-moment tensors for 13,017 earthquakes. *Phys. Earth Planet. Inter.*, 200-201 :1–9, 2012. doi : 10.1016/j.pepi.2012.04.002.
- W. L. Ellsworth and F. Bulut. Nucleation of the 1999 Izmit earthquake by a triggered cascade of foreshocks. *Nature Geosci.*, 11(7) :531–+, 2018. doi : 10.1038/s41561-018-0145-1.
- F. R. Fontaine, A. Gonzalez, A. Burtin, G. Barruol, A. Recking, J. L. Join, and E. Delcher. Monitoring the Transport of Sediment During Tropical Cyclones From High-frequency Seismic Noise in Two Rivers of La Réunion Island. *AGU Fall Meeting, San Francisco*, pages S43A–2793, 2016.
- F. R. Fontaine, G. Roult, B. Hejrani, L. Michon, V. Ferrazzini, G. Barruol, H. Tkalčić, A. Di Muro, A. Peltier, D. Reymond, T. Staudacher, and F. Massin. Very- and ultra-long-period seismic signals prior to and during caldera formation on La Réunion Island. *Scientific Reports*, 9(1) :8068, 2019. doi : 10.1038/s41598-019-44439-1.
- A. Frankel. Rupture Process of the M 7.9 Denali Fault, Alaska, Earthquake : Subevents, Directivity, and Scaling of High-Frequency Ground Motions. *Bull. Seism. Soc. Am.*, 94(6B) : S234–S255, 2004. doi : 10.1785/0120040612"><meta.
- R. J. Geller. Scaling relations for earthquake source parameters and magnitudes. *Bull. Seism. Soc. Am.*, 66(5) :1501–1523, 1976.
- B. Gombert. *Vers une nouvelle génération de modèles de glissements co-sismiques : analyse stochastique et approche multi-données*. PhD thesis, Université de Strasbourg, 2018.
- B. Gombert, Z. Duputel, R. Jolivet, C. Doubre, L. Rivera, and M. Simons. Revisiting the 1992 Landers earthquake : a Bayesian exploration of co-seismic slip and off-fault damage. *Geophys. J. Int.*, 212(2) :839–852, 2018a. doi : 10.1093/gji/ggx455.
- B. Gombert, Z. Duputel, R. Jolivet, M. Simons, J. Jiang, C. Liang, E. J. Fielding, and L. Rivera. Strain budget of the Ecuador-Colombia subduction zone : A stochastic view. *Earth Planet. Sci. Lett.*, 498 :288–299, 2018b. doi : 10.1016/j.epsl.2018.06.046.
- B. Gombert, Z. Duputel, E. Shabani, L. Rivera, R. Jolivet, and J. Hollingsworth. Impulsive Source of the 2017 MW=7.3 Ezgeleh, Iran, Earthquake. *Geophys. Res. Lett.*, 46(10) :5207–5216, 2019. doi : 10.1029/2018GL081794.
- J.-L. Got, V. Monteiller, J. Monteux, R. Hassani, and P. Okubo. Deformation and rupture of the oceanic crust may control growth of Hawaiian volcanoes. *Nature*, 451(7177) :453–456, 2008. doi : 10.1038/nature06481.

- R. Grandin, E. Jacques, A. Nercessian, A. Ayele, C. Doubre, A. Socquet, D. Keir, M. Kassim, A. Lemarchand, and G. King. Seismicity during lateral dike propagation : Insights from new data in the recent Manda Hararo–Dabbahu rifting episode (Afar, Ethiopia). *Geochim. Geophys. Geosyst.*, 12(4) :1–24, 2011. doi : 10.1029/2010GC003434.
- R. Grandin, M. Vallée, C. Satriano, R. Lacassin, Y. Klinger, M. Simoes, and L. Bollinger. Rupture process of the Mw7.9 2015 Gorkha earthquake (Nepal) : Insights into Himalayan megathrust segmentation. 42(20) :8373–8382, 2015. doi : 10.1002/2015GL066044.
- B. E. Grossman-Ponemon, E. R. Heimisson, A. J. Lew, and P. Segall. Logarithmic Growth of Dikes From a Depressurizing Magma Chamber. *Geophys. Res. Lett.*, 47(4) :e2019GL086230, 2020. doi : 10.1029/2019GL086230.
- M. Guatteri and P. Spudich. What can strong-motion data tell us about slip-weakening fault-friction laws ? *Bull. Seism. Soc. Am.*, 90(1) :98–116, 2000.
- M. T. Gudmundsson, K. Jónsdóttir, A. Hooper, E. P. Holohan, S. A. Halldórsson, B. G. Ofeigsson, S. Cesca, K. S. Vogfjord, F. Sigmundsson, T. Hognadóttir, P. Einarsson, O. Sigmarsdóttir, A. H. Jarosch, K. Jónasson, E. Magnusson, S. Hreinsdóttir, M. Bagnardi, M. M. Parks, V. Hjörleifsdóttir, F. Palsson, T. R. Walter, M. P. J. Schöpfer, S. Heimann, H. I. Reynolds, S. Dumont, E. Bali, G. H. Gudfinnsson, T. Dahm, M. J. Roberts, M. Hensch, J. M. C. Belart, K. Spaans, S. Jakobsson, G. B. Gudmundsson, H. M. Fridriksdóttir, V. Drouin, T. Dürrig, G. Aðalgeirsdóttir, M. S. Riishuus, G. B. M. Pedersen, T. van Boekel, B. Oddsson, M. A. Pfeffer, S. Barsotti, B. Bergsson, A. Donovan, M. R. Burton, and A. Aiuppa. Gradual caldera collapse at Bárdarbunga volcano, Iceland, regulated by lateral magma outflow. *Science*, 353 (6296) :aaaf8988, 2016. doi : 10.1126/science.aaaf8988.
- R. M. Harrington and E. E. Brodsky. Volcanic hybrid earthquakes that are brittle-failure events. *Geophys. Res. Lett.*, 34(6), 2007. doi : 10.1029/2006GL028714.
- S. H. Hartzell. Earthquake aftershocks as Green’s functions. *Geophys. Res. Lett.*, 5(1) :1–4, 1978. doi : 10.1029/GL005i001p00001.
- S. H. Hartzell and T. H. Heaton. Inversion of strong ground motion and teleseismic waveform data for the fault rupture history of the 1979 Imperial Valley, California, earthquake. *Bull. Seism. Soc. Am.*, 73(6) :1553–1583, 1983.
- T. H. Heaton. Evidence for and implications of self-healing pulses of slip in earthquake rupture. *Phys. Earth Planet. Inter.*, 64(1) :1–20, 1990. doi : 10.1016/0031-9201(90)90002-F.
- H. Hébert. On the use of satellite altimetry to infer the earthquake rupture characteristics : Application to the 2004 Sumatra event. 172(2) :707–714, 2008. doi : 10.1111/j.1365-246X.2007.03669.x.
- A. Helmstetter and D. Sornette. Foreshocks explained by cascades of triggered seismicity. *J. Geophys. Res. : Solid Earth*, 108(B10), 2003. doi : 10.1029/2003JB002409.

- B. Hernandez, F. Cotton, and M. Campillo. Contribution of radar interferometry to a two-step inversion of the kinematic process of the 1992 Landers earthquake. *J. Geophys. Res.*, 104 (B6) :13083–13099, 1999. doi : 10.1029/1999JB900078.
- R. B. Herrmann. Computer Programs in Seismology : An Evolving Tool for Instruction and Research. *Seismol. Res. Lett.*, 84(6) :1081–1088, 2013. doi : 10.1785/0220110096.
- V. Hjörleifsdóttir, H. Kanamori, and J. Tromp. Modeling 3-D wave propagation and finite slip for the 1998 Balleny Islands earthquake. *J. Geophys. Res.*, 114 :B03301, 2009.
- Y. Huang and J.-P. Ampuero. Pulse-like ruptures induced by low-velocity fault zones. *Journal of Geophysical Research : Solid Earth (1978–2012)*, 116(B12) :B04301, 2011. doi : 10.1029/2011JB008684.
- Y. Huang, L. Meng, and J.-P. Ampuero. A dynamic model of the frequency-dependent rupture process of the 2011 Tohoku-Oki earthquake. *Earth Planets Space*, 64(12) :1061–1066, 2012. doi : 10.5047/eps.2012.05.011.
- S. Ide. Slip Inversion. *Treatise on Geophysics*, 4 :193–223, 2007. doi : 10.1016/B978-044452748-6.00068-7.
- D. Inazu and T. Saito. Simulation of distant tsunami propagation with a radial loading deformation effect. *Earth Planets Space*, 65(8) :835–842, 2013. doi : 10.5047/eps.2013.03.010.
- E. T. Jaynes. *Probability Theory : The Logic of Science*. Cambridge university press, New York, 2003.
- C. Ji, D. J. Wald, and D. V. Helmberger. Source Description of the 1999 Hector Mine, California, Earthquake, Part I : Wavelet Domain Inversion Theory and Resolution Analysis. *Bull. Seism. Soc. Am.*, 92(4) :1192–1207, 2002. doi : 10.1785/0120000916.
- K. M. Johnson, J. Fukuda, and P. Segall. Challenging the rate-state asperity model : Afterslip following the 2011 M9 Tohoku-oki, Japan, earthquake. *Geophys. Res. Lett.*, 39(20) :L20302, 2012. doi : 10.1029/2012GL052901.
- R. Jolivet, R. Grandin, C. Lasserre, M.-P. Doin, and G. Peltzer. Systematic InSAR tropospheric phase delay corrections from global meteorological reanalysis data. *Geophys. Res. Lett.*, 38 (17) :L17311, 2011. doi : 10.1029/2011GL048757.
- R. Jolivet, M. Simons, P. S. Agram, Z. Duputel, and Z. K. Shen. Aseismic slip and seismogenic coupling along the central San Andreas Fault. 42(2) :297–306, 2015. doi : 10.1002/2014GL062222.
- B. R. Julian. Volcanic tremor : Nonlinear excitation by fluid flow. *Journal of Geophysical Research : Solid Earth (1978–2012)*, 99(B6) :11859–11877, 1994. doi : 10.1029/93JB03129.
- H. Kanamori. W phase. *Geophys. Res. Lett.*, 20(16) :1691–1694, 1993.
- H. Kanamori and D. L. Anderson. Theoretical basis of some empirical relations in seismology. 65 :1073–1095, 1975.

- H. Kanamori and E. E. Brodsky. The physics of earthquakes. *Reports on Progress in Physics*, 67(8) :1429–1496, 2004. doi : 10.1088/0034-4885/67/8/R03.
- H. Kanamori and J. W. Given. Analysis of long-period seismic waves excited by the May 18, 1980, eruption of Mount St. Helens- A terrestrial monopole. 87(B7) :5422–5432, 1982.
- H. Kanamori and L. Rivera. Energy Partitioning During an Earthquake. In *Radiated Energy and the Physics of Faulting, Geophys. Monogr. Ser.*, pages 3–13. American Geophysical Union, Washington D. C., 2006. ISBN 9781118666272. doi : 10.1029/170GM03.
- H. Kanamori and L. Rivera. Source inversion of W phase : speeding up seismic tsunami warning. *Geophys. J. Int.*, 175(1) :222–238, 2008. doi : 10.1111/j.1365-246X.2008.03887.x.
- H. Kanamori, J. W. Given, and T. Lay. Analysis of seismic body waves excited by the Mount St. Helens eruption of May 18, 1980. *Journal of Geophysical Research : Solid Earth (1978–2012)*, 89(B3) :1856–1866, 1984. doi : 10.1029/JB089iB03p01856.
- H. Kanamori, D. L. Anderson, and T. H. Heaton. Frictional Melting During the Rupture of the 1994 Bolivian Earthquake. *Science*, 279(5352) :839–842, 1998. doi : 10.1126/science.279.5352.839.
- Y. Kaneko, J.-P. Avouac, and N. Lapusta. Towards inferring earthquake patterns from geodetic observations of interseismic coupling. *Nature Geosci.*, 3(5) :ngeo843–369, 2010. doi : 10.1038/ngeo843.
- A. Kato, K. Obara, T. Igarashi, H. Tsuruoka, S. Nakagawa, and N. Hirata. Propagation of Slow Slip Leading Up to the 2011 Mw 9.0 Tohoku-Oki Earthquake. *Science*, 335(6069) :705–708, 2012. doi : 10.1126/science.1215141.
- A. Kato, J. Fukuda, T. Kumazawa, and S. Nakagawa. Accelerated nucleation of the 2014 Iquique, Chile Mw 8.2 Earthquake. *Scientific Reports*, 6 :24792, 2016. doi : 10.1038/srep24792.
- H. Kawakatsu and M. Yamamoto. 4.13 - Volcano Seismology. In G. Schubert, editor, *Treatise on Geophysics*, pages 389–420. Elsevier, Amsterdam, 2007. ISBN 978-0-444-52748-6. doi : 10.1016/B978-044452748-6.00073-0.
- M. Kikuchi and H. Kanamori. Inversion of complex body waves—III. *Bull. Seism. Soc. Am.*, 81 (6) :2335, 1991.
- E. Klein, C. Vigny, L. Fleitout, R. Grandin, R. Jolivet, E. Rivera, and M. Metois. A comprehensive analysis of the Illapel 2015 Mw8.3 earthquake from GPS and InSAR data. *Earth Planet. Sci. Lett.*, 469 :123–134, 2017. doi : 10.1016/j.epsl.2017.04.010.
- D. Komatitsch and J. Tromp. Introduction to the spectral element method for three-dimensional seismic wave propagation. *Geophys. J. Int.*, 139(3) :806–822, 1999. doi : 10.1046/j.1365-246x.1999.00967.x.
- D. Komatitsch and J. Tromp. Spectral-element simulations of global seismic wave propagation—II. Three-dimensional models, oceans, rotation and self-gravitation. 150(1) :303–318, 2002. doi : 10.1046/j.1365-246X.2002.01716.x.

- H. Kumagai, T. Ohminato, M. Nakano, M. Ooi, A. Kubo, H. Inoue, and J. Oikawa. Very-Long-Period Seismic Signals and Caldera Formation at Miyake Island, Japan. *Science*, 293(5530) : 687–690, 2001. doi : 10.1126/science.1062136.
- H. Kumagai, B. A. Chouet, and P. B. Dawson. Source process of a long-period event at Kilauea volcano, Hawaii. *Geophys. J. Int.*, 161(1) :243–254, 2005. doi : 10.1111/j.1365-246X.2005.02502.x.
- J. C. Lahr, B. A. Chouet, C. D. Stephens, J. A. Power, and R. A. Page. Earthquake classification, location, and error analysis in a volcanic environment : implications for the magmatic system of the 1989–1990 eruptions at redoubt volcano, Alaska. *J. Volc. Geoth. Res.*, 62(1) :137–151, 1994. doi : 10.1016/0377-0273(94)90031-0.
- G. Larsen, K. Grönvold, and S. Thorarinsson. Volcanic eruption through a geothermal borehole at Námafjall, Iceland. *Nature*, 278(5706) :707–710, 1979. doi : 10.1038/278707a0.
- K. M. Larson, P. Bodin, and J. Gomberg. Using 1-Hz GPS data to measure deformations caused by the Denali fault earthquake. *Science*, 300(5624) :1421–1424, 2003. doi : 10.1126/science.1084531.
- C. L. Lawson and R. J. Hanson. *Solving Least Squares Problems*, volume 15. Siam, Philadelphia, 1995.
- T. Lay. The surge of great earthquakes from 2004 to 2014. *Earth Planet. Sci. Lett.*, 409 :133–146, 2015. doi : 10.1016/j.epsl.2014.10.047.
- T. Lay and H. Kanamori. *An Asperity Model of Large Earthquake Sequences*. American Geophysical Union, 1981. ISBN 9781118665749. doi : 10.1029/ME004p0579.
- T. Lay and H. Kanamori. Insights from the great 2011 Japan earthquake. *Physics today*, 64 (12) :33–39, 2011. doi : doi:10.1063/PT.3.1361.
- T. Lay, H. Kanamori, C. J. Ammon, K. D. Koper, A. R. Hutko, L. Ye, H. Yue, and T. M. Rushing. Depth-varying rupture properties of subduction zone megathrust faults. *J. Geophys. Res.*, 117 (B4) :B04311, 2012. doi : 10.1029/2011JB009133.
- T. Lay, Z. Duputel, L. Ye, and H. Kanamori. The December 7, 2012 Japan Trench intraplate doublet (Mw 7.2, 7.1) and interactions between near-trench intraplate thrust and normal 2 faulting 3. *Phys. Earth Planet. Inter.*, 220 :73–78, 2013.
- C. Liang and E. J. Fielding. Measuring Azimuth Deformation With L-Band ALOS-2 ScanSAR Interferometry. *IEEE Trans. Geosci. Remote Sensing*, 55(5) :2725–2738, 2017. doi : 10.1109/TGRS.2017.2653186.
- P. L. F. Liu, S.-B. Woo, and Y.-S. Cho. Computer Programs for Tsunami Propagation and Inundation. Cornell University, USA, 1998.
- R. Madariaga. High-frequency radiation from crack (stress drop) models of earthquake faulting. *Geophys. J. R. astr. Soc.*, 51(3) :625–651, 1977. doi : 10.1111/j.1365-246X.1977.tb04211.x.

- M. Mai. Source Inversion Validation (SIV) : Current Results & Developments. In *2012 SCEC Source Inversion Validation Workshop*, 2012.
- L. Mansinha and D. E. Smylie. The displacement fields of inclined faults. *Bull. Seism. Soc. Am.*, 61(5) :1433–1440, 1971. doi : 10.1029/JZ072i018p04731.
- W. Marzocchi and J. Zhuang. Statistics between mainshocks and foreshocks in Italy and Southern California. *Geophys. Res. Lett.*, 38(9) :–n/a, 2011. doi : 10.1029/2011GL047165.
- D. Massonnet, M. Rossi, C. Carmona, F. Adragna, G. Peltzer, K. Feigl, and T. Rabaute. The displacement field of the Landers earthquake mapped by radar interferometry. *Nature*, 364 : 138–142, 1993. doi : 10.1038/364138a0.
- M. A. Meier, T. H. Heaton, and J. Clinton. Evidence for universal earthquake rupture initiation behavior. *Geophys. Res. Lett.*, 43(15) :7991–7996, 2016. doi : 10.1002/2016GL070081.
- M. A. Meier, Ampuero, and T. H. Heaton. The hidden simplicity of subduction megathrust earthquakes. *Science*, 357(6357) :1277–1281, 2017. doi : 10.1126/science.aan5643.
- D. Melgar and G. P. Hayes. Systematic Observations of the Slip Pulse Properties of Large Earthquake Ruptures. *Geophys. Res. Lett.*, 44(19) :9691–9698, 2017. doi : 10.1002/2017GL074916.
- A. Meltzer, R. Rudnick, P. Zeitler, A. Levander, G. Humphreys, K. Karlstrom, G. Ekström, R. Carlson, T. Dixon, M. Gurnis, P. M. Shearer, and R. van der Hilst. USArray initiative. *GSA today*, 1999.
- L. Meng, J.-P. Ampuero, J. Stock, Z. Duputel, Y. Luo, and V. C. Tsai. An earthquake in a maze : compressional rupture branching in a weakened oceanic lithosphere during the April 11 2012 M8.6 Sumatra earthquake. 2012.
- R. Michel, J.-P. Avouac, and J. Taboury. Measuring ground displacements from SAR amplitude images : Application to the Landers Earthquake. *Geophys. Res. Lett.*, 26(7) :875–878, 1999. doi : 10.1029/1999GL900138.
- L. Michon, T. Staudacher, V. Ferrazzini, P. Bachelery, and J. Marti. April 2007 collapse of Piton de la Fournaise : A new example of caldera formation. *Geophys. Res. Lett.*, 34(21), 2007. doi : 10.1029/2007GL031248.
- L. Michon, F. Massin, V. Famin, V. Ferrazzini, and G. Roult. Basaltic calderas : Collapse dynamics, edifice deformation, and variations of magma withdrawal. *Journal of Geophysical Research : Solid Earth (1978–2012)*, 116(B3) :8485, 2011. doi : 10.1029/2010JB007636.
- L. Michon, A. Di Muro, N. Villeneuve, C. Saint-Marc, P. Fadda, and F. Manta. Explosive activity of the summit cone of Piton de la Fournaise volcano (La Réunion island) : A historical and geological review. *J. Volc. Geoth. Res.*, 264 :117–133, 2013. doi : 10.1016/j.jvolgeores.2013.06.012.
- L. Michon, V. Ferrazzini, A. Di Muro, N. Villeneuve, and V. Famin. Rift zones and magma plumbing system of Piton de la Fournaise volcano : How do they differ from Hawaii and Etna ? *J. Volc. Geoth. Res.*, 303 :112–129, 2015. doi : 10.1016/j.jvolgeores.2015.07.031.

- A. Mignan. The debate on the prognostic value of earthquake foreshocks : A meta-analysis. *Scientific Reports*, 4(1) :4099–5, 2014. doi : 10.1038/srep04099.
- S. E. Minson, M. Simons, and J. L. Beck. Bayesian inversion for finite fault earthquake source models I—theory and algorithm. 194(3) :1701–1726, 2013. doi : 10.1093/gji/ggt180.
- L. Moutote, D. Marsan, O. Lengliné, and Z. Duputel. Low significance of foreshock activity in Southern California. *Submitted to Geophys. Res. Lett.*, 2020. doi : 10.31223/X5130R.
- C. A. Neal, S. R. Brantley, L. Antolik, J. L. Babb, M. Burgess, K. Calles, M. Cappos, J. C. Chang, S. Conway, L. Desmither, P. Dotray, T. Elias, P. Fukunaga, S. Fuke, I. A. Johanson, K. Kamibayashi, J. kauahikaua, R. L. Lee, S. Pekalib, A. Miklius, W. Million, C. J. Moniz, P. A. Nadeau, P. Okubo, C. Parcheta, M. R. Patrick, B. Shiro, D. A. Swanson, W. Tollett, F. Trusdell, E. F. Younger, M. H. Zoeller, E. K. Montgomery-Brown, K. R. Anderson, M. P. Poland, J. L. Ball, J. Bard, M. Coombs, H. R. Dietterich, C. Kern, W. A. Thelen, P. F. Cervelli, T. Orr, B. F. Houghton, C. Ganseddi, R. Hazlett, P. Lundgren, A. K. Diefenbach, A. H. Lerner, G. Waite, P. Kelly, L. Clors, C. Werner, K. Mulliken, G. Fisher, and D. Damby. The 2018 rift eruption and summit collapse of Kilauea Volcano. *Science*, 363(6425) :367–+, 2019. doi : 10.1126/science.aav7046.
- J. Neuberg, R. Luckett, B. Baptie, and K. Olsen. Models of tremor and low-frequency earthquake swarms on Montserrat. *J. Volc. Geoth. Res.*, 101(1) :83–104, 2000. doi : 10.1016/S0377-0273(00)00169-4.
- C. G. Newhall. 4.12 - Volcanology 101 for Seismologists. In G. Schubert, editor, *Treatise on Geophysics*, pages 351–388. Elsevier, Amsterdam, 2007. ISBN 978-0-444-52748-6. doi : 10.1016/B978-044452748-6.00072-9.
- J. M. Nocquet, P. Jarrin, M. Vallée, P. A. Mothes, R. Grandin, F. Rolandone, B. Delouis, H. Yepes, Y. Font, D. Fuentes, M. Regnier, A. Laurendeau, D. Cisneros, S. Hernandez, J. C. Singauch, H. Mora, J. Gomez, L. Montes, and P. Charvis. Supercycle at the Ecuadorian subduction zone revealed after the 2016 Pedernales earthquake. *Nature Geosci.*, 10(2) :145–149, 2017. doi : 10.1038/ngeo2864.
- H. Noda, N. Lapusta, and H. Kanamori. Comparison of average stress drop measures for ruptures with heterogeneous stress change and implications for earthquake physics. *Geophys. J. Int.*, 193(3) :1691–1712, 2013. doi : 10.1093/gji/ggt074.
- Y. Okada. Surface deformation due to shear and tensile faults in a half-space. *Bull. Seism. Soc. Am.*, 75 :1135–1154, 1985.
- Y. Okada. Internal deformation due to shear and tensile faults in a half-space. *Bull. Seism. Soc. Am.*, 82 :1018–1040, 1992.
- A. H. Olson and J. G. Anderson. Implications of frequency-domain inversion of earthquake ground motions for resolving the space-time dependence of slip on an extended fault. *Geophys. J. Int.*, 94(3) :443–455, 1988. doi : 10.1111/j.1365-246X.1988.tb02267.x”, ”keywords”: [”frequency-domain.

- A. H. Olson and R. J. Apsel. Finite Faults and Inverse-Theory with Applications to the 1979 Imperial-Valley Earthquake. *Bull. Seism. Soc. Am.*, 72(6) :1969–2001, 1982.
- S. Peyrat, K. Olsen, and R. Madariaga. Dynamic modeling of the 1992 Landers earthquake. *Journal of Geophysical Research : Solid Earth (1978–2012)*, 106(B11) :26467–26482, 2001. doi : 10.1029/2001JB000205.
- A. Piatanesi, E. Tinti, M. Cocco, and E. Fukuyama. The dependence of traction evolution on the earthquake source time function adopted in kinematic rupture models. *Geophys. Res. Lett.*, 31(4), 2004. doi : 10.1029/2003GL019225.
- M. E. Pritchard, E. O. Norabuena, C. Ji, R. Boroschek, D. Comte, M. Simons, T. H. Dixon, and P. A. Rosen. Geodetic, teleseismic, and strong motion constraints on slip from recent southern Peru subduction zone earthquakes. *J. Geophys. Res.*, 112(B3) :B03307, 2007.
- D. J. Pugh and R. S. White. MTfit : A Bayesian Approach to Seismic Moment Tensor Inversion. *Seismol. Res. Lett.*, 89(4) :1507–1513, 2018. doi : 10.1785/0220170273.
- D. J. Pugh, R. S. White, and P. A. F. Christie. A Bayesian method for microseismic source inversion. *Geophys. J. Int.*, 206(2) :1009–1038, 2016a. doi : 10.1093/gji/ggw186.
- D. J. Pugh, R. S. White, and P. A. F. Christie. Automatic Bayesian polarity determination. *Geophys. J. Int.*, 206(1) :275–291, 2016b. doi : 10.1093/gji/ggw146.
- T. Ragon and M. Simons. Accounting for uncertain fault geometry in earthquake source inversions – I : theory and simplified application. *Geophys. J. Int.*, 214(2) :1174–1190, 2018.
- J. Renou, M. Vallée, and P. Dublanchet. How Does Seismic Rupture Accelerate ? Observational Insights From Earthquake Source Time Functions. *J. Geophys. Res. : Solid Earth*, 124(8) :8942–8952, 2019. doi : 10.1029/2019JB018045.
- S. Riquelme, M. Medina, F. Bravo, S. Barrientos, J. Campos, and A. Cisternas. W-Phase Real-Time Implementation and Network Expansion from 2012 to 2017 : The Experience in Chile. *Seismol. Res. Lett.*, 89(6) :2237–2248, 2018. doi : 10.1785/0220180146"><meta.
- L. Rivera and H. Kanamori. Representations of the radiated energy in earthquakes. *Geophys. J. Int.*, 162(1) :148–155, 2005. doi : 10.1111/j.1365-246X.2005.02648.x.
- P. Romanet, H. S. Bhat, R. Jolivet, and R. Madariaga. Fast and Slow Slip Events Emerge Due to Fault Geometrical Complexity. *Geophys. Res. Lett.*, 45(10) :4809–4819, 2018. doi : 10.1029/2018GL077579.
- G. Roult, A. Peltier, B. Taisne, T. Staudacher, V. Ferrazzini, and A. Di Muro. A new comprehensive classification of the Piton de la Fournaise activity spanning the 1985–2010 period. Search and analysis of short-term precursors from a broad-band seismological station. *J. Volc. Geoth. Res.*, 241-242 :78–104, 2012. doi : 10.1016/j.jvolgeores.2012.06.012.
- A. M. Rubin and D. Gillard. Dike-induced earthquakes : Theoretical considerations. *J. Geophys. Res.*, 103(B5) :10017–10030, 1998. doi : 10.1029/97JB03514.

- K. Satake. 4.17 - Tsunamis. In *Treatise on Geophysics*, pages 483–511. Elsevier, Amsterdam, 2007. ISBN 978-0-387-75888-6. doi : doi:10.1016/B978-044452748-6.00078-X.
- T. Sato. Seismic radiation from circular cracks growing at variable rupture velocity. *Bull. Seism. Soc. Am.*, 84(4) :1199–1215, 1994.
- C. H. Scholz. Earthquakes and friction laws. *Nature*, 391(6662) :37–42, 1998. doi : 10.1038/34097.
- D. P. Schwartz and K. J. Coppersmith. Fault behavior and characteristic earthquakes : Examples from the Wasatch and San Andreas Fault Zones. *Journal of Geophysical Research : Solid Earth (1978–2012)*, 89(B7) :5681–5698, 1984. doi : 10.1029/JB089iB07p05681.
- P. Segall and R. Harris. Earthquake deformation cycle on the San Andreas Fault near Parkfield, California. *Journal of Geophysical Research : Solid Earth (1978–2012)*, 92(B10) :10511–10525, 1987. doi : 10.1029/JB092iB10p10511.
- P. Segall, A. L. Llenos, S. H. Yun, A. M. Bradley, and E. M. Syracuse. Time-dependent dike propagation from joint inversion of seismicity and deformation data. *J. Geophys. Res. : Solid Earth*, 118(11) :5785–5804, 2013. doi : 10.1002/2013JB010251.
- P. Segall, K. R. Anderson, I. Johanson, and A. Miklius. Mechanics of Inflationary Deformation During Caldera Collapse : Evidence From the 2018 Kilauea Eruption. *Geophys. Res. Lett.*, 46 (21) :11782–11789, 2019. doi : 10.1029/2019GL084689.
- H. Sekiguchi and T. Iwata. Rupture Process of the 1999 Kocaeli, Turkey, Earthquake Estimated from Strong-Motion Waveforms. *Bull. Seism. Soc. Am.*, 92(1) :300–311, 2002. doi : 10.1785/0120000811.
- N. M. Shapiro, D. V. Droznin, S. Y. Droznina, S. L. Senyukov, A. A. Gusev, and E. I. Gordeev. Deep and shallow long-period volcanic seismicity linked by fluid-pressure transfer. *Nature Geosci.*, 10(6) :442–445, 2017. doi : 10.1038/NGEO2952.
- D. R. Shelly, J. L. Hardebeck, W. L. Ellsworth, and D. P. Hill. A new strategy for earthquake focal mechanisms using waveform-correlation-derived relative polarities and cluster analysis : Application to the 2014 Long Valley Caldera earthquake swarm. *J. Geophys. Res. : Solid Earth*, 121(12) :8622–8641, 2016. doi : 10.1002/2016JB013437.
- K. Shimazaki and T. Nakata. Time-predictable recurrence model for large earthquakes. *Geophys. Res. Lett.*, 7(4) :279–282, 1980. doi : 10.1029/GL007i004p00279.
- A. Shuler, G. Ekström, and M. Nettles. Physical mechanisms for vertical-CLVD earthquakes at active volcanoes. *J. Geophys. Res. : Solid Earth*, 118(4) :1569–1586, 2013a. doi : 10.1002/jgrb.50131.
- A. Shuler, M. Nettles, and G. Ekström. Global observation of vertical-CLVD earthquakes at active volcanoes. *J. Geophys. Res. : Solid Earth*, 118(1) :138–164, 2013b. doi : 10.1029/2012JB009721.

- P. G. Silver and T. H. Jordan. Optimal estimation of scalar seismic moment. *Geophys. J. Int.*, 70(3) :755–787, 1982. doi : 10.1111/j.1365-246X.1982.tb05982.x.
- M. Simons and P. A. Rosen. 3.12 - Interferometric Synthetic Aperture Radar Geodesy. In *Treatise on Geophysics*. Elsevier, Amsterdam, 2007.
- M. Simons, Y. Fialko, and L. Rivera. Coseismic Deformation from the 1999 Mw 7.1 Hector Mine, California, Earthquake as Inferred from InSAR and GPS Observations. *Bull. Seism. Soc. Am.*, 92 :1390–1402, 2002.
- M. Simons, S. E. Minson, F. Ortega, J. Jiang, S. E. Owen, L. Meng, J.-P. Ampuero, S. Wei, R. Chu, D. V. Helmberger, H. Kanamori, E. Hetland, A. W. Moore, and F. H. Webb. The 2011 Magnitude 9.0 Tohoku-Oki Earthquake : Mosaicking the Megathrust from Seconds to Centuries. *Science*, 332(6036) :1421–1425, 2011. doi : 10.1126/science.1206731.
- Smithsonian Institution. Volcanoes of the World, v. 4.3.4. Global Volcanism Program, 2013.
- A. Socquet, J. P. Valdes, J. Jara, F. Cotton, A. Walpersdorf, N. Cotte, S. Specht, F. Ortega-Culaciati, D. Carrizo, and E. Norabuena. An 8 month slow slip event triggers progressive nucleation of the 2014 Chile megathrust. *Geophys. Res. Lett.*, 44(9) :4046–4053, 2017. doi : 10.1002/2017GL073023.
- A. Socquet, J. Hollingsworth, E. Pathier, and M. Bouchon. Evidence of supershear during the 2018 magnitude 7.5 Palu earthquake from space geodesy. *Nature Geosci.*, 12(3) :192–199, 2019. doi : 10.1038/s41561-018-0296-0.
- F. N. Spiess. Acoustic techniques for Marine Geodesy. *Marine Geodesy*, 4(1) :13–27, 1980. doi : 10.1080/15210608009379369.
- P. Spudich and M. Guatteri. The effect of bandwidth limitations on the inference of earthquake slip-weakening distance from seismograms. *Bull. Seism. Soc. Am.*, 94(6) :2028–2036, 2004.
- J. Stix and T. Kobayashi. Magma dynamics and collapse mechanisms during four historic caldera-forming events. *Journal of Geophysical Research : Solid Earth (1978–2012)*, 113(B9), 2008. doi : 10.1029/2007JB005073.
- B. Taisne, F. Brenguier, N. M. Shapiro, and V. Ferrazzini. Imaging the dynamics of magma propagation using radiated seismic intensity. *Geophys. Res. Lett.*, 38(4) :L04304, 2011. doi : 10.1029/2010GL046068.
- A. Tarantola. *Inverse Problem Theory and Methods for Model Parameter Estimation*. SIAM, Philadelphia, 2005.
- A. Tarantola and B. Valette. Inverse problems = quest for information. *J. Geophys.*, 50 :159–170, 1982.
- M. Y. Thomas, J.-P. Avouac, J. Champenois, J.-C. Lee, and L.-C. Kuo. Spatiotemporal evolution of seismic and aseismic slip on the Longitudinal Valley Fault, Taiwan. *J. Geophys. Res. : Solid Earth*, 119(6) :5114–5139, 2014. doi : 10.1002/2013JB010603.

- M. Y. Thomas, H. S. Bhat, and Y. Klinger. Effect of Brittle Off-Fault Damage on Earthquake Rupture Dynamics. In *Fault Zone Dynamic Processes*, pages 255–280. John Wiley & Sons, Inc., Hoboken, NJ, USA, 2017. ISBN 9781119156888. doi : 10.1002/9781119156895.ch14.
- E. Tinti, E. Fukuyama, A. Piatanesi, and M. Cocco. A Kinematic Source-Time Function Compatible with Earthquake Dynamics. *Bull. Seism. Soc. Am.*, 95(4) :1211–1223, 2005a. doi : 10.1785/0120040177.
- E. Tinti, P. Spudich, and M. Cocco. Earthquake fracture energy inferred from kinematic rupture models on extended faults. *J. Geophys. Res. : Solid Earth*, 110(B12), 2005b. doi : 10.1029/2005JB003644.
- D. T. Trugman and Z. E. Ross. Pervasive Foreshock Activity Across Southern California. *Geophys. Res. Lett.*, 46(15) :8772–8781, 2019. doi : 10.1029/2019GL083725.
- V. C. Tsai, J.-P. Ampuero, H. Kanamori, and D. J. Stevenson. Estimating the effect of Earth elasticity and variable water density on tsunami speeds. *Geophys. Res. Lett.*, 40(3) :492–496, 2013. doi : 10.1002/grl.50147.
- C. Twardzik, M. Vergnolle, and A. Avallone. Unravelling the contribution of early postseismic deformation using sub-daily GNSS positioning. *Scientific Reports*, 9(1) :1–12, 2019. doi : 10.1038/s41598-019-39038-z.
- A. Vallage, Y. Klinger, R. Lacassin, A. Delorme, and M. P. Deseilligny. Geological structures control on earthquake ruptures : The Mw7.7, 2013, Balochistan earthquake, Pakistan. *Geophys. Res. Lett.*, 43(19) :10,155–10,163, 2016. doi : 10.1002/2016GL070418.
- M. Vallée and C. Satriano. Ten year recurrence time between two major earthquakes affecting the same fault segment. *Geophys. Res. Lett.*, 41(7) :2312–2318, 2014. doi : 10.1002/2014GL059465.
- M. Vallée, J. Charléty, A. M. G. Ferreira, B. Delouis, and J. Vergoz. SCARDEC : a new technique for the rapid determination of seismic moment magnitude, focal mechanism and source time functions for large earthquakes using body-wave deconvolution. *Geophys. J. R. astr. Soc.*, 184 (1) :338–358, 2011. doi : 10.1111/j.1365-246X.2010.04836.x.
- M. P. A. van den Ende and Ampuero. On the Statistical Significance of Foreshock Sequences in Southern California. *Geophys. Res. Lett.*, 47(3) :e2019GL086224, 2020. doi : 10.1029/2019GL086224.
- A. Venkataraman and H. Kanamori. Effect of directivity on estimates of radiated seismic energy. *J. Geophys. Res.*, 109(B4) :1265, 2004. doi : 10.1029/2003JB002548.
- C. Vigny, A. Socquet, S. Peyrat, J.-C. Ruegg, M. Metois, R. Madariaga, S. Morvan, M. Lancieri, R. Lacassin, J. Campos, D. Carrizo, M. Béjar-Pizarro, S. Barrientos, R. Armijo, C. Aranda, M. C. Valderas-Bermejo, I. Ortega, F. Bondoux, S. Baize, H. Lyon-Caen, A. Pavez, J. P. Villette, M. Bevis, B. Brooks, R. Smalley, H. Parra, J. C. Baez, M. Blanco, S. Cimbaro, and E. Kendrick. The 2010 Mw 8.8 Maule Megathrust Earthquake of Central Chile, Monitored by GPS. *Science*, 332(6036) :1417–1421, 2011. doi : 10.1126/science.1204132.

- D. J. Wald and T. H. Heaton. Spatial and temporal distribution of slip for the 1992 Landers, California, earthquake. *Bull. Seism. Soc. Am.*, 84 :668–691, 1994.
- T. Wang, S. Wei, X. Shi, Q. Qiu, L. Li, D. Peng, R. J. Weldon, and S. Barbot. The 2016 Kaikoura earthquake : Simultaneous rupture of the subduction interface and overlying faults. *Earth Planet. Sci. Lett.*, 482 :44–51, 2018. doi : 10.1016/j.epsl.2017.10.056.
- S. Wei, D. Helmberger, Z. Zhan, and R. Graves. Rupture complexity of the Mw 8.3 sea of okhotsk earthquake : Rapid triggering of complementary earthquakes ? *Geophys. Res. Lett.*, 40(19) :5034–5039, 2013. doi : 10.1002/grl.50977.
- R. White and W. McCausland. Volcano-tectonic earthquakes : A new tool for estimating intrusive volumes and forecasting eruptions. *J. Volc. Geoth. Res.*, 309 :139–155, 2016. doi : 10.1016/j.jvolgeores.2015.10.020.
- R. S. White, J. Drew, H. R. Martens, J. Key, H. Soosalu, and S. S. Jakobsdottir. Dynamics of dyke intrusion in the mid-crust of Iceland. *Earth Planet. Sci. Lett.*, 304(3-4) :300–312, 2011. doi : 10.1016/j.epsl.2011.02.038.
- T. J. Wright, C. Ebinger, J. Biggs, A. Ayele, G. Yirgu, D. Keir, and A. Stork. Magma-maintained rift segmentation at continental rupture in the 2005 Afar dyking episode. *Nature*, 442(7100) :291–294, 2006. doi : 10.1038/nature04978.
- Y. Yagi and M. Kikuchi. Source rupture process of the Kocaeli, Turkey, earthquake of August 17, 1999, obtained by joint inversion of near-field data and teleseismic data. *Geophys. Res. Lett.*, 27(13) :1969–1972, 2000. doi : 10.1029/1999GL011208.
- E. H. Yoffe. LXXV. The moving griffith crack. *London Edinburgh Dublin Philosoph. Mag. J. Sci.*, 42(330) :739–750, 1951. doi : 10.1080/14786445108561302.
- Y. Yokota and T. Ishikawa. Shallow slow slip events along the Nankai Trough detected by GNSS-A. *Science Advances*, 6(3) :eaay5786, 2020. doi : 10.1126/sciadv.aay5786.
- M. Zecevic, L. De Barros, C. J. Bean, G. S. O'Brien, and F. Brenguier. Investigating the source characteristics of long-period (LP) seismic events recorded on Piton de la Fournaise volcano, La Réunion. *J. Volc. Geoth. Res.*, 258 :1–11, 2013. doi : 10.1016/j.jvolgeores.2013.04.009.
- Y. Zeng, J. G. Anderson, and G. Yu. A composite source model for computing realistic synthetic strong ground motions. *Geophys. Res. Lett.*, 21(8) :725–728, 1994. doi : 10.1029/94GL00367.
- Z. Zhan, D. V. Helmberger, H. Kanamori, and P. M. Shearer. Supershear rupture in a Mw 6.7 aftershock of the 2013 Sea of Okhotsk earthquake. *Science*, 345(6193) :204–207, 2014. doi : 10.1126/science.1252717.
- X. Zhao, Z. Duputel, and Z. Yao. Regional W-Phase Source Inversion for Moderate to Large Earthquakes in China and Neighboring Areas. *J. Geophys. Res. : Solid Earth*, 122(12) :10,052–10,068, 2017. doi : 10.1002/2017JB014950.

BIBLIOGRAPHIE

- L. Zhu and L. A. Rivera. A note on the dynamic and static displacements from a point source in multilayered media. *Geophys. J. Int.*, 148(3) :619–627, 2002. doi : 10.1046/j.1365-246X.2002.01610.x.
- M. L. Zoback, E. Geist, J. Pallister, D. P. Hill, S. Young, and W. McCausland. Advances in natural hazard science and assessment, 1963–2013. In M. E. Bickford, editor, *The Impact of the Geological Sciences on Society*, pages 81–154. Geological Society of America, 2013. ISBN 9780813725017.
- J. F. Zumberge, M. B. Heflin, D. C. Jefferson, M. M. Watkins, and F. H. Webb. Precise point positioning for the efficient and robust analysis of GPS data from large networks. *J. Geophys. Res. : Solid Earth*, 102(B3) :5005–5017, 1997. doi : 10.1029/96JB03860.

Annexes

A.1 Curriculum Vitae

Zacharie Duputel

Sismologue, Chargé de Recherche au CNRS

Institut de Physique du Globe de Strasbourg
5 Rue René Descartes
67084 Strasbourg Cedex

Tel : +333 68 85 00 39

Email : zacharie.duputel@unistra.fr

Page-web : <https://zduputel.github.io>

Formation et carrière

2014 - Chargé de Recherche CNRS

Institut de Physique du Globe de Strasbourg - EOST, France.

2012 - 2013 Post-doctorat

California Institute of Technology - Seismological Laboratory, Pasadena, CA, USA.

2008 - 2011 Doctorat en Géophysique

Institut de Physique du Globe de Strasbourg - EOST, Université de Strasbourg, France.

2004 - 2008 École d'ingénieur en Géophysique

Ecole et Observatoire des Sciences de la Terre (EOST), Strasbourg, France.

2002 - 2004 DEUG en Géophysique

Université de La Réunion, Saint Denis, France.

Encadrement et enseignement

2014 - 2021 Encadrement de 5 projets de recherche (M1/2A d'école), 4 stages de master (M2), 3 thèses de doctorat et 3 post-doctorats.

2015 Cours sur l'inversion du glissement à l'école d'été JIG (niveau doctorat)

2014 - 2020 Participations ponctuelles aux cours de Recherche en géophysique (1A école), Méthodes inverses (1A école), Déformation et Géodésie (M2).

Administration de la recherche

2018 - Membre de la commission observatoire de l'UMS830

2018 - 2020 Membre élu du conseil de laboratoire de l'IPGS

2018 - Membre de la commission recherche de l'EOST

2016 - Membre du comité INSU CT3-ALEAS

2015 - Membre de la commission informatique de l'IPGS

Bibliométrie

41 publications, 1851 citations, h-index = 22 (SCOPUS)

Projets financés

2014 - 2020 Porteur de 12 projets financés pour un montant total d'environ 3 millions d'euros (dont 1 928 500 euros en tant que porteur principal). Financements : ERC starting grant, ANR, IdEx UNISTRA, INSU CT3 et appel d'offre interne au laboratoire.

Participation à des jurys de thèse et comités de sélection

2018 **Rapporteur** - M. Frietsch, Department of Earth Sciences, University College London, Londres, UK.
2018 **Rapporteur** - M. Halló, Faculté de Math et Physique, Université Charles de Prague, République tchèque.
2018 **Comité de sélection MCF** - Géodynamique et études des intérieurs planétaires. Paris Diderot/Institut de Physique du Globe de Paris, Paris, France
2018 **Examinateur** - A. Chouquet, Institut de Physique du Globe de Paris, Paris, France.
2016 **Rapporteur** - R. Benavente, Australian National University, Camberra, Australie.
2016 **Examinateur** - A. Vallage, Institut de Physique du Globe de Paris, Paris, France.

Prix et distinctions

2019 - 2023 ERC Starting Grant - Projet PRESEISMIC
2020 Top downloaded paper 2018-2019 - Geophys. Res. Lett.
2015 Outstanding reviewer award - Geophys. J. Int.
2012 Prix Le Monde de la Recherche Universitaire - Mention spéciale Google
2012 Prix de thèse de l'Université de Strasbourg

A.2 Activités d'enseignement et d'encadrement

En tant que chargé de recherche au CNRS, mon activité d'enseignement concerne principalement la formation à la recherche. Je participe ainsi régulièrement à l'encadrement de stagiaires à l'École et Observatoire des Sciences de la Terre (EOST) principalement pour les projets de recherche en 2ème année d'école et pour les stages de Master 2. J'encadre également plusieurs doctorants rattachés à l'école doctorale Sciences de la Terre et Environnement (ED413). Je participe par ailleurs à plusieurs cours. Ces cours contribuent en particulier à assurer une continuité entre la recherche effectuée en laboratoire et l'enseignement dispensé à l'EOST. Les étudiants encadrés et les cours dispensés depuis 2014 sont listés ci-dessous. Au delà de la formation à la recherche, j'ai également supervisé ou co-supervisé l'encadrement de plusieurs post-doctorants.

Doctorants encadrés

- 2020 - 2023 Luc Moutote - Ecole doctorale STE
Projet : Séquences de séismes préchocs : cascades aléatoires ou déclencheur asismique ?
- 2019 - 2022 Emmanuel Caballero Levya - Ecole doctorale STE
Projet : Inversion de la source sismique - incertitude sur le modèle élastique.
- 2016 - 2020 Catalina Morales - Ecole doctorale STE
Projet : Détermination de la source des séismes - Prise en compte de la structure 3D.
- 2015 - 2018 Baptiste Gombert - Ecole doctorale STE
Projet : Exploration Bayésienne du glissement sur les failles.

Encadrement de stages étudiants (niveau M1/M2)

- 2020 - 2021 Lise Firode - Master 2 parcours d'excellence à l'EOST
Projet : Détection par la méthode des sous-espaces - Application à la sismicité de La Réunion.
- 2019 - 2020 Luc Moutotte - Master 2 Physique de la Terre
Projet : Analyse des séquences de séismes pré-chocs en californie du sud.
- 2018 - 2019 Juliette Cresseaux - Master 2 parcours d'excellence à l'EOST
Projet : Détection et relocalisation de séismes volcano-tectoniques au Kamchatka.
- 2018 - 2019 Juliette Cresseaux - Projet de recherche en 2ème année à l'EOST
Projet : Lien entre sismicité profonde et superficielle le long de la subduction andine.

BIBLIOGRAPHIE

- 2016 - 2018 Anaika Charles - Projet de recherche en 2ème année à l'EOST
Projet : Relocalisation de séismes volcano-tectoniques au Piton de la Fournaise.
- 2016 - 2017 Alexandre Longelin - Master 2 parcours d'excellence à l'EOST
Projet : Suivi temporel du glissement le long d'une faille à l'aide de données GPS.
- 2016 - 2017 Vanina Gentet - Projet de recherche en 2ème année à l'EOST
Projet : Étude de la sismicité sous le flanc Est du Piton de la Fournaise.
- 2015 - 2016 Mathilde Wimez - Projet de recherche en 2ème année à l'EOST
Projet : Calcul de mécanismes au foyer au Piton de la Fournaise.
- 2014 - 2015 Julia Cantarano - Projet de recherche en 2ème année à l'EOST
Projet : Analyse de la crise sismique pré-éruptive de juin 2014 au Piton de la Fournaise.

Écoles d'été, formations et cours

- 2016 - 2020 Cours Déformation et Géodésie (niveau M2) - EOST
Cours sur l'inversion du glissement.
- 2016 - 2019 Cours Recherche en géophysique (niveau 1A école d'ingénieurs) - EOST
Introduction générale concernant la recherche sur les grands séismes.
- 2015 - 2020 Formation sur le calcul intensif par le mésocentre de l'Unistra (niveau doctorat)
Organisation de la formation.
- 2015 École d'été "Joint Inversion in Geophysics" à Barcelonnette (niveau doctorat)
Cours sur l'inversion probabiliste du glissement.
- 2015 Cours Méthodes inverses (niveau 1A école d'ingénieurs) - EOST
Cours sur les méthodes d'échantillonnage de type Monte Carlo.
- 2014 GE162 : Seismology - CALTECH
Cours sur le tenseur moment sismique.

Post-doctorants supervisés

- 2018 - 2019 Cédric Twardzik - post-doctorant
Projet : Caractérisation de l'évolution spatio-temporelle de séismes lents.
- 2018 - 2019 Agnès Chouinet - post-doctorante
Projet : Étude de la phase d'initiation du séisme de Valparaiso en 2017 ($M_w=6.9$).
- 2016 - 2017 Emilie Klein - post-doctorante
Projet : Couplage sur la faille nord-anatolienne ; Séismes lents au Chili.

A.3 Liste des publications

2021

41. O. Lengliné, Z. Duputel and P. G. Okubo. Tracking dike propagation leading to the 2018 Kilauea eruption. *Earth Planet. Sci. Lett.*, v. 553, pp. 116653.

2020

40. C. Morales-Yáñez, Z. Duputel and L. Rivera. Impact of 3D Earth structure on W-phase CMT parameters. *Geophys. J. Int.*, v. 223, pp. 1432-1445.

39. R. Jolivet, M. Simons, **Z. Duputel**, J.-A. Olive, H. Bhat and Q. Bletery. Interseismic loading of subduction megathrust drives long term uplift in northern Chile. *Geophys. Res. Lett.*, v. 47, pp. e2019GL085377.

38. S. Schippkus, H. Hausmann, **Z. Duputel**, G. Bokelmann, AlpArray Working Group. The Alland earthquake series in Eastern Austria : Evidence for oblique basement reactivation, 2019. *Austr. J. Earth Sci.*, v. 112, pp. 182-194.

2019

37. **Z. Duputel** and L. Rivera. The 2007 Caldera Collapse of Piton de la Fournaise Volcano : Source Process from Very-Long-Period Seismic Signals. Accepted for publication in *Earth Planet. Sci. Lett.*

36. B. Gombert, **Z. Duputel**, E. Shabani, L. Rivera, R. Jolivet and J. Hollingsworth, 2019. The impulsive source of the 2017 (MW =7.3) Ezgeleh, Iran, earthquake. *Geophys. Res. Lett.*, v. 46, pp. 5207-5216.

35. **Z. Duputel**, O. Lengliné and V. Ferrazzini, 2019. Probing magma migration in the upper edifice of Piton de la Fournaise volcano using small triggered earthquakes. *Geophys. Res. Lett.*, v. 46, pp. 119-127.

2018

34. E. Klein, **Z. Duputel**, D. Zigone, C. Vigny, J.-P. Boy, C. Doubre and G. Meneses, 2018. Deep transient slow slip detected by survey GPS in the region of Atacama, Chile. *Geophys. Res. Lett.*, v. 45, pp. 12263-12273.

33. B. Gombert, **Z. Duputel**, R. Jolivet, M. Simons, C. Liang, E. J. Fielding and L. Rivera, 2018. Strain budget of the Ecuador-Colombia subduction zone : a stochastic view. *Earth Planet Sci. Lett.*, v. 498, pp. 288-299.

32. B. Gombert, **Z. Duputel**, R. Jolivet, C. Doubre, L. Rivera and M. Simons, 2018. Revisiting the 1992 Landers earthquake : a Bayesian exploration of co-seismic slip and off-fault damage. *Geophys. J. Int.*, v. 212, pp. 839–852.

2017

31. X. Zhao, **Z. Duputel** and Z. Yao, 2017. Regional W-phase source inversion for moderate to large earthquakes in China and neighboring areas. *J. Geophys. Res.*, v. 122, pp. 10052-10068.
30. E. Klein, **Z. Duputel**, F. Masson, H. Yavasoglu and P. Agram, 2017. Aseismic slip and seismogenic coupling in the Marmara Sea : What can we learn from onland Geodesy ? *Geophys. Res. Lett.*, v. 44, pp. 3100-3108.
29. **Z. Duputel** and L. Rivera, 2017. Long-period analysis of the 2016 Kaikoura earthquake. *Phys. Earth Planet. Int.*, v. 265, pp. 62-66.
- 28 H. Yue, M. Simonsa, **Z. Duputel**, J. Jiang, E. Fielding, C. Liang, S. Owen, A. Moore, B. Riel, J.-P. Ampuero, S. V. Samsonov, 2017. Depth varying rupture properties during the 2015 Mw 7.8 Gorkha (Nepal) earthquake. *Tectonophysics*, v. 714-715, pp. 44-54.

2016

27. L. Ye, T. Lay, H. Kanamori **Z. Duputel**, 2016. Diverse Rupture Processes in the 2015 Peru Deep Earthquake Doublet, 2016. *Science Advances*, v. 2, e1600581.
26. O. Lengliné, **Z. Duputel**, V. Ferrazzini, 2016. The 2015 Gorkha earthquake : Uncovering the signature of a deep magmatic recharge at Piton de la Fournaise volcano using small earthquakes., *Geophys. Res. Lett.* v. 43, pp. 4255-4252.
25. **Z. Duputel**, J. Vergne, L. Rivera, G. Wittlinger, G. Hetényi, 2016. The 2015 Gorkha earthquake : A large event illuminating the Main Himalayan Thrust fault. *Geophys. Res. Lett.*, v.43, pp. 2517–2525.

2015

24. **Z. Duputel**, J. Jiang, R. Jolivet, M. Simons, L. Rivera, J.-P. Ampuero, B. Riel, S. E. Owens, A. W. Moore, S. V. Samsonov, F. Ortega-Culaciati, S. E. Minson, 2015. The Iquique earthquake sequence of April 2014 : Bayesian modeling accounting for prediction uncertainty. *Geophys. Res. Lett.*, v. 42, iss. 19, pp. 7949-7957.
23. R. Jolivet, M. Simons, P. S. Agram, **Z. Duputel**, Z.-K. Shen, 2015. Aseismic slip and seismogenic coupling along the central San Andreas Fault, *Geophysical Research Letters*, v. 42, pp. 1-10

2014

22. C. Zaroli, J.-J. Lévêque, B. Schuberth, **Z. Duputel**, G. Nolet, 2014. Global S-wave tomography using receiver pairs : An alternative to get rid of earthquake mislocation. *Geophys. J. Int.*, v. 199, p. 1043-1057

21. R. Jolivet, **Z. Duputel**, B. Riel, M. Simons, L. Rivera, S. E. Minson, H. Zhang, M. Aivazis, F. Ayoub, S. Leprince, S. Samsonov, M. Motagh, E. Fielding, 2014. The 2013 M7.7 Balochistan earthquake : Seismic potential of an accretionary wedge. *Bull. Seism. Soc. Am.*, v. 104, p. 1020-1030.
20. J.-P. Avouac, F. Ayoub, S. Wei, J.-P. Ampuero, L. Meng, S. Leprince, R. Jolivet, **Z. Duputel**, D. Helmberger, 2014. The 2013, Mw 7.7 Balochistan earthquake, energetic strike-slip reactivation of a thrust fault, *Earth Planet Sci. Lett.*, v. 391, p. 128-134.

19. **Z. Duputel**, P. S. Agram, M. Simons, S. E. Minson, J.L. Beck, 2014. Accounting for prediction uncertainty when inferring subsurface fault slip. *Geophys. J. Int.*, v. 197, p. 464-482.

2013

18. **Z. Duputel**, V. C. Tsai, L. Rivera, H. Kanamori, 2013. Using centroid time-delays to characterize source durations and identify earthquakes with unique characteristics, *Earth Planet Sci. Lett.*, v. 375, p. 92-100.
17. T. Lay, **Z. Duputel**, L. Ye, H. Kanamori, 2013. The December 7, 2012 Japan Trench intraplate doublet (Mw 7.2, 7.1) and interactions between near-trench intraplate thrust and normal faulting, *Phys. Earth Planet. Inter.*, v. 220, p. 73-78.
16. F.-C. Lin, V. C. Tsai, B. Schmandt, **Z. Duputel**, Z. Zhan, 2013. Extracting seismic core phases with array interferometry, *Geophys. Res. Lett.*, v. 40, p. 1.

2012

15. D. Wang, N. C. Becker, D. Walsh, G. J. Fryer, S. A. Weinstein, C. S. McCreery, V. Sardina, V. Hsu, B. F. Hirshorn., G. P. Hayes, **Z. Duputel**, L. Rivera, H. Kanamori, K. K. Koyanagi, B. Shiro, 2012. Real-time Forecasting of the April 11, 2012 Sumatra Tsunami. *Geophysical Research Letters*, v. 39, L19601.
14. Z. Zhan, D. Helmberger, M. Simons, H. Kanamori, W. Wu, N. Cubas, **Z. Duputel**, J.-P. Avouac, R. Chu, V.C. Tsai, K.W. Hudnut, S. Ni, E. Hetland, F.H. Ortega Culaciati, 2012. Earthquakes with anomalously steep dip in the source region of the 2011 Tohoku-Oki earthquake and possible explanations. *Earth and Planetary Science Letters*, v. 353-354, p. 121-133.
13. **Z. Duputel**, H. Kanamori, V.C. Tsai, L. Rivera, L. Meng, J.-P. Ampuero, J. Stock, 2012c. The 2012 Sumatra great earthquake sequence. *Earth and Planetary Science Letters*, v. 351-352, p. 247-257.
12. L. Meng, J.-P. Ampuero, J. Stock, **Z. Duputel**, Y. Luo, V.C. Tsai, 2012. An earthquake in a maze : compressional rupture branching in a weakened oceanic lithosphere during the April 11 2012 M8.6 Sumatra earthquake. *Science*, v. 337, no 6095, p. 724-726.

11. **Z. Duputel**, L. Rivera, Y. Fukahata, H. Kanamori, 2012b. Uncertainty estimations for seismic source inversions. *Geophysical Journal International*, v. 190, iss. 2, p. 1243-1256.
10. **Z. Duputel**, L. Rivera, H. Kanamori, G. Hayes, 2012a. W-phase fast source inversion for moderate to large earthquakes ($M_w \geq 6.5$, 1990 - 2010). *Geophysical Journal International*, v. 189, iss. 2, p. 1125-1147.
9. S. Barde-Cabusson , A. Finizola, A. Peltier, M. Chaput, N. Taquet, S. Dumont, **Z. Duputel**, A. Guy A., L. Mathieu, S. Saumet, F. Sorbadère, M. Vieille, 2012. Structural control of collapse events inferred by self-potential mapping on the Piton de la Fournaise volcano (La Réunion Island). *J. Volcanol. Geotherm. Res.*, v. 209-210, p. 9-18.

2011

8. V.C. Tsai, G.P. Hayes, **Z. Duputel**, 2011. Constraints on the Long-Period Moment-Dip Tradeoff for the Tohoku Earthquake, *Geophysical Research Letters*, v. 38, L00G17.
7. **Z. Duputel**, L. Rivera, H. Kanamori, G.P. Hayes, B. Hirsorn and S. Weinstein 2011. Real-time W Phase inversions during the 2011 Tohoku-oki earthquake, *Earth, Planets and Space*, v. 63, no. 7, p. 535-539.
6. F. Massin, V. Ferrazzini, P. Bachèlery, A. Nercessian, **Z. Duputel**, T. Staudacher, 2011. Structures and evolution of the plumbing system of Piton de la Fournaise volcano inferred from clustering of 2007 eruptive cycle seismicity. *Journal of Volcanology and Geothermal Research*, v. 202, iss. 1-2, p. 96-106.

2010

5. **Z. Duputel**, M. Cara, L. Rivera, G. Herquel, 2010. Improving the analysis and inversion of multimode Rayleigh-wave dispersion by using group-delay time information observed on arrays of high-frequency sensors, *Geophysics*, v. 75, iss. 2, R13.

2009

4. A. Mordret, A.D. Jolly, **Z. Duputel**, N. Fournier, 2009. Monitoring of phreatic eruptions using Interferometry on Retrieved Cross-Correlation Function from Ambient Seismic Noise : Results from Mt Ruapehu, New Zealand. *Journal of Volcanology and Geothermal Research*, v. 191, iss. 1-2, p. 46-59.
3. S. Barde Cabusson, G. Levieux, J.F. Lénat, A. Finizola, A. Revil, M. Chaput, S. Dumont, **Z. Duputel**, A. Guy, L. Mathieu, S. Saumet, F. Sorbadère, M. Vieille, 2009. Transient self-potential anomalies associated with recent lava flows at Piton de la Fournaise volcano (Réunion Island, Indian Ocean). *Journal of Volcanology and Geothermal Research*, v. 187, p. 164-173.

2. **Z. Duputel**, V. Ferrazzini, F. Brenguier, N.M. Shapiro, M. Campillo, A. Nercessian, 2009. Real time monitoring of relative velocity changes using ambient seismic noise at the Piton de la Fournaise volcano (La Réunion) from January 2006 to June 2007. *Journal of Volcanology and Geothermal Research*, v. 184, iss. 1-2, p. 164-173.

2007

1. F. Brenguier, N.M. Shapiro, M.Campillo, V. Ferrazzini, **Z. Duputel**, O. Coutant, A. Nercessian, 2008. Towards forecasting volcanic eruptions using seismic noise. *Nature Geoscience*, v. 1, iss. 2, p. 126-130.

A.4 Participation au montage de projets

Depuis 2014, j'ai participé au montage de 12 projets de recherche financés pour un montant total d'environ 3 millions d'euros. J'ai contribué en tant que porteur principal pour 6 de ces projets dont un projet ERC starting grant. Les projets financés auxquels j'ai participé sont listés ci-dessous.

Année 2020	Projet INSU CT3 (CNRS) Titre : Sismicité sous le Nord de l'île de la Réunion : origine tectonique ou processus magmatique ? PI : O. Lengliné ; Budget : 6 000 euros
2019 - 2023	Projet ERC - Starting grant PRESEISMIC : Exploring the nucleation of large earthquakes PI : Z. Duputel ; Budget : 1 500 000 euros
2019 - 2021	Projet ANR S5 : Synchronous Slow Slip & Seismic Swarm PI : J.-M. Nocquet ; Budget : 430 000 euros
Année 2019	Projet INSU CT3 COP2020 : Slow Slip Trigger. PI : C. Vigny ; Budget : 10 800 euros
Année 2018	Projet interne IPGS Détection automatique et relocalisation d'évènements volcano-tectoniques au Piton de la Fournaise. PI : Z. Duputel ; Budget : 4 500 euros
2018 - 2019	Projet ANT Tremplin-ERC (T-ERC) PISCO : Probabilistic investigation of fault slip and coupling over the earthquake cycle PI : Z. Duputel ; Budget : 150 000 euros
2016 - 2019	Projet IdEx "Recherche doctorale" (Université de Strasbourg) Titre : Earthquake source characterization : accounting for 3D structure. PIs : L. Rivera / Z. Duputel ; Budget : 100 000 euros
Année 2016	Projet INSU CT3 Titre : Détection, relocalisation et classification automatique d'événements sismiques appliquées au Piton de la Fournaise. PI : O. Lengliné ; Budget : 7 500 euros

- 2015 - 2017 Projet International de Collaboration scientifique (PICS, CNRS)
Titre : Utilisation de méthodes Bayésiennes pour l'étude des grands séismes.
PIs : Z. Duputel / M. Simons (Caltech) ; Budget : 18 000 euros
- 2015 - 2019 Projet ANR
Titre : ALPARRAY-FR : Voir et comprendre les Alpes en 3D, de la croûte au manteau.
PI : A. Paul ; Budget : 620 000 euros
- 2014 - 2016 Projet IdEx "attractivité" (Université de Strasbourg)
Titre : Bringing a bayesian perspective to large dimensional problems in geo-physics and astrophysics.
PI : Z. Duputel ; Budget : 150 000 euros
- Année 2014 Projet INSU CT3 (CNRS)
Titre : Toward a new generation of source models incorporating realistic uncertainty estimates.
PI : Z. Duputel ; Budget : 6 000 euros

A.5 Détection de séismes lents profonds dans la région de l'Atacama au Chili

L'article proposé ci-dessous a été publié en 2019 dans *Geophysical Research Letters*.



Geophysical Research Letters

RESEARCH LETTER

10.1029/2018GL080613

Key Points:

- We detected a transient signal that occurred between 2014 and 2016 in Central North Chile using sGPS data
- We rejected any nontectonic source such as instrumental or hydrological processes
- These observations confirmed by cGPS are explained by slow slip events in the transition zone of the megathrust

Supporting Information:

- Supporting Information S1
- Movie S1

Correspondence to:

E. Klein,
klein@geologie.ens.fr

Citation:

Klein, E., Duputel, Z., Zigone, D., Vigny, C., Boy, J.-P., Doubre, C., & Meneses, G. (2018). Deep transient slow slip detected by survey GPS in the region of Atacama, Chile. *Geophysical Research Letters*, 45, 12,263–12,273.
<https://doi.org/10.1029/2018GL080613>

Received 24 SEP 2018

Accepted 11 NOV 2018

Accepted article online 15 NOV 2018

Published online 26 NOV 2018

Deep Transient Slow Slip Detected by Survey GPS in the Region of Atacama, Chile

E. Klein^{1,2,3} , Z. Duputel¹ , D. Zigone¹ , C. Vigny² , J.-P. Boy¹ , C. Doubre¹ , and G. Meneses²

¹Institut de Physique du Globe de Strasbourg; UMR 7516, Université de Strasbourg/EOST, CNRS, Strasbourg, France,

²Laboratoire de géologie, Département de Géosciences, ENS, CNRS, UMR 8538, PSL Research University, Paris, France,

³Now at Institute of Geophysics and Planetary Physics, Scripps Institution of Oceanography, University of California, San Diego, California, USA

Abstract We detected a long-term transient deformation signal between 2014 and 2016 in the Atacama region (Chile) using survey Global Positioning System (GPS) observations. Over an ~150 km along-strike region, survey GPS measurements in 2014 and 2016 deviate significantly from the interseismic trend estimated using previous observations. This deviation from steady state deformation is spatially coherent and reveals a horizontal westward diverging motion of several centimeters, along with a significant uplift. It is confirmed by continuous measurements of recently installed GPS stations. We discard instrumental, hydrological, oceanic, or atmospheric loading effects and show that the transient is likely due to deep slow slip in the transition zone of the subduction interface (~40- to 60-km depth). In addition, daily observations recorded by a continuous GPS station operating between 2002 and 2015 highlight similar transient signals in 2005 and 2009, suggesting a recurrent pattern.

Plain Language Summary The dense development of Global Positioning System (GPS) networks along plate boundaries worldwide has allowed us to observe different fault behaviors: long-term deformation over decades to centuries or the motion generated by major earthquakes. We also observe slow slip events, occurring over weeks to months, creating significant motion without generating seismic waves. These events are observed on most subduction zones on Earth, repeating regularly. Usually occurring at depth larger than 40 km, they are often associated with long-lasting low amplitudes seismic vibrations. Although the Chilean subduction zone is one of the most active on Earth, no such slow event has yet been observed. Using survey GPS observations since 2010 in the region of Atacama (Central North Chile), completed by continuous observations, we have detected a transient signal between 2014 and 2016. After investigating all possible sources, we demonstrate that a deep slow slip event is the most likely origin. Despite a quite sparse seismic network in this region, the seismic observations show an unusual long-lasting low amplitudes seismic activity. Going further, the observations recorded by a GPS station operational since 2002 shows similar signals in 2009 and 2005, highlighting a recurrent pattern of slow slip events in the Atacama region.

1. Introduction

Thanks to the development of Global Positioning System (GPS) networks along plate boundaries in the last 25 years, slow slip events (SSEs) have been detected within the brittle-ductile transition region of various subduction zone interfaces: Japan, Cascadia, Mexico, Costa Rica, New Zealand, Alaska, among others (see Beroza & Ide, 2011; Peng & Gomberg, 2010; Schwartz & Rokosky, 2007, for reviews). These SSEs are characterized by slow aseismic fault creep and are often associated with seismicity on the form of nonvolcanic tremor activity (e.g., Miller et al., 2002; Obara, 2002; Payero et al., 2008; Rogers & Dragert, 2003) and low-frequency earthquakes (e.g., Frank et al., 2013; Hirose & Obara, 2005; Shelly et al., 2007). Although SSEs have been extensively studied over the last decade, physical mechanisms controlling slow slip remain quite elusive (Ikari et al., 2013; Leeman et al., 2016; Romanet et al., 2018; Segall et al., 2010). The influence of SSEs on the seismic cycle and their impact in terms of seismic hazard are also not yet fully understood. Slow slip seems to be closely related to earthquakes as several observations suggest that SSEs may have happened just before or after large seismic events (Kato et al., 2012; Radiguet et al., 2016; Ruiz et al., 2014; Wallace et al., 2017; Zigone et al., 2012).

©2018. The Authors.

This is an open access article under the terms of the Creative Commons Attribution-NonCommercial-NoDerivs License, which permits use and distribution in any medium, provided the original work is properly cited, the use is non-commercial and no modifications or adaptations are made.

On the other hand, some SSEs occur quasiperiodically independently of large earthquakes (Rogers & Dragert, 2003; Wallace et al., 2016). Although the Chilean megathrust is one of the most active, with three megathrust earthquakes of $M_w \geq 8$ over the last decade (Illapel 2015, Iquique 2014, Maule 2010, Ruiz et al., 2016, 2014, Vigny et al., 2011), it is one of the only subduction zone where recurrent deep SSEs have not been observed yet. Until recently, the poor coverage of continuous GPS over this 4,000-km-long plate boundary prevented our ability to determine if SSEs occur in the region. In recent years, two aseismic events were observed on the shallow part of the interface (<40 km), both associated with low to moderate seismic activity, and were followed by a significant earthquake: a few weeks to a month-long slip event preceding the 2014 $M_w = 8.1$ Iquique earthquake (Ruiz et al., 2014; Socquet et al., 2017) and a few days-long slip event associated with the 2017 $M_w = 6.9$ Valparaíso earthquake (Ruiz et al., 2017).

Despite the poor continuous GPS instrumentation, decadal-scale interseismic deformation has been intensely monitored thanks to the deployment and yearly measurements of several dense survey GPS (sGPS) networks overlying the plate interface, in the regions of South Central Chile (Moreno et al., 2010; Ruegg et al., 2009), Coquimbo (Khazaradze & Klotz, 2003; Klotz et al., 2001; Métois et al., 2012; Vigny et al., 2009), Atacama (Klein et al., 2018; Métois et al., 2014), and North Chile (Kendrick et al., 2003; Klotz et al., 1999; Métois et al., 2013). The coupling pattern constrained by the resulting interseismic velocity field highlights a heterogeneous segmentation, alternating between coupled segments where megathrust earthquakes are likely to occur and Low Coupling Zones (LCZ), which might act as seismic barriers (Métois et al., 2016).

The region of Atacama ($29\text{--}25^\circ\text{S}$) possesses somewhat different characteristics compared to the rest of the subduction zone. Seismic activity on the shallower part of the interface (<30 km) is quite low (Métois et al., 2016) with the exception of the occurrence of regular swarms offshore Caldera (27°S in 1973, 1979, 2006; Holtkamp et al., 2011; Figure 1a). A clear gap in seismicity is also visible at depths greater than 40 km compared to adjacent regions (Figure 1a). Historical seismicity reports two events of $M_w \geq 8.5$ (1819, 1922), both characterized by complex rupture sequences (Willis, 1929). In this region, a sGPS network was installed starting in 2010 and measured yearly to estimate the steady state velocity field and derive the coupling ratio on the megathrust interface (Figure 1a and Figure S1 in the supporting information). The two highly coupled Atacama and Chañaral segments are separated by the Baranquilla LCZ (Klein et al., 2018; Métois et al., 2014), where the aforementioned swarm events occurred (Métois et al., 2016; Figures 1a and 1b; 28°S). However, in a region ~ 150 km long centered on Copiapó and Caldera (Figure 1), GPS measurements made in 2015 and 2016 deviate from the steady state interseismic trend (Figure 2a). Estimating the static offset from available survey data reveals a spatially coherent pattern of displacements with centimeter-level amplitude. This transient deformation is also consistent with the observations made by the few continuous stations in the area (Figures 1b and 2b), which discard any instrumental errors related to the sGPS processing.

In this study, we investigate the possible origins of this transient signal that can be associated with tectonic or nontectonic sources. In particular, we assess potential effects due to hydrological, oceanic, or atmospheric sources and we investigate if this signal corresponds to episodic aseismic slip.

2. GPS Observations

2.1. Survey GPS Observations

The survey network in Atacama was first installed and measured in 2010, right after the $M_w = 8.8$ Maule earthquake (Métois et al., 2014). Annual surveys have been conducted ever since, jointly with the northward extension of the network in Taltal (Klein et al., 2018). The Central Andes GPS Project (Brooks et al., 2003) and South America Geodynamic Activities (Klotz et al., 2001) GPS marks in the area were remeasured at the same time to gather a data set of almost 70 survey points, measured at least 3 times and up to 7 times (see Table S1 and Klein et al., 2018, for more details about the network and measurements). The sGPS data set is augmented by observations from recently installed cGPS stations operated by the *Centro Sismológico Nacional de Chile* (CSN; Báez et al., 2018), together with a selection of well-distributed permanent stations across the South American continent (International GPS Service; Beutler et al., 1999), (*Red Argentina de Monitoreo Satelital Continuo*; Piñón et al., 2018), and *Rede Brasileira de Monitoramento Contínuo* networks. This data set is processed using a differential approach (GAMIT/GLOBK software), following methods outlined in Herring et al. (2010a, 2010b) and with the same approach used by previous studies in Central North Chile (Klein et al., 2018; Métois et al., 2016; Vigny et al., 2009). Position time series are estimated by combining daily solutions using global sites to define the reference frame in GLOBK because of postseismic deformation following the Maule earthquake which affects many reference stations on the South American continent (Klein et al., 2016).

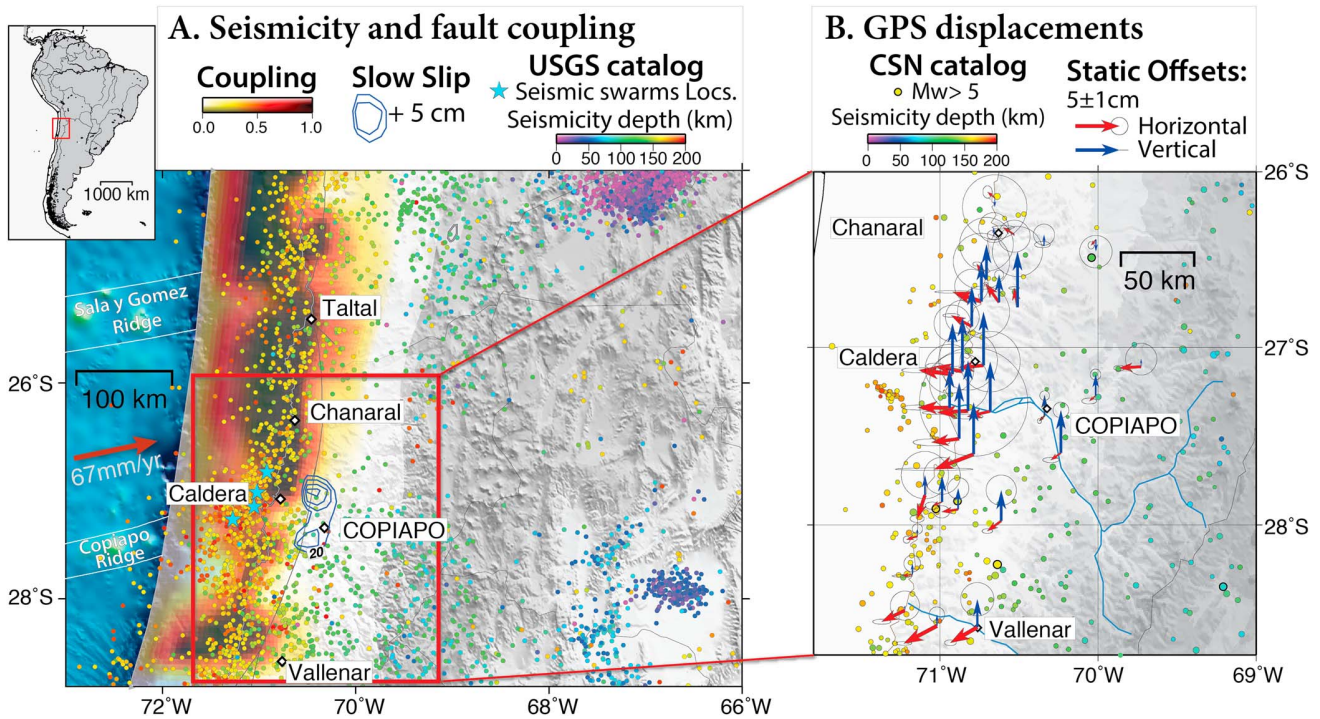


Figure 1. Seismotectonic context. (a) Coupling model and seismicity in the study region. Circles represent earthquake locations from the United States Geological Survey (USGS) catalog (1973–2017) that are colored as function of depth. Blue stars depict locations of seismic swarms in 1973, 1979, 2006, (Holtkamp et al., 2011) and 2015. The red color map shows the coupling model from Klein et al. (2018) obtained using interseismic velocities (see Figure S1). White lines represent main bathymetric features of the Nazca plate (Álvarez et al., 2015). Our preferred SSE slip model is represented with blue contour lines (+5 cm). Inset: Location of the study zone in South America. (b) Static horizontal (red) and vertical (blue) offsets estimated from sGPS time series. Seismicity from the CSN catalog (2014.5–2016) is represented as function of depth (same color scale as in a). SSE = slow slip event; sGPS = survey GPS; CSN = Centro Sismológico Nacional de Chile; GPS = Global Positioning System.

After 7 years of yearly sGPS observations in a very localized area of the Atacama region, the 2016 position deviates significantly from the interseismic trend, both in horizontal and vertical (Figures 2a and S2). While the effect on the horizontal components is significantly smaller, we also observe a similar deviation in the vertical trend in 2015.

We estimate the deviation between the 2016 position predicted by the 2010–2014 trend and the 2016 measured position. The resulting static offsets show a very coherent pattern over an ~150-km region, on both horizontal and vertical components. Horizontal displacement vectors are diverging: northwestward north of Caldera and southwestward south of Caldera (Figure 1b). Vertical offsets are showing a centimeter-level uplift with amplitudes clearly above the noise level, while the interseismic regime is characterized by subsidence (Figure 2a, Up). The northern boundary of this transient signal is marked by a lack of measurable deviation from the 2010–2014 interseismic trend at the latitude of Chañaral (Figure 1b), while the southern one is more difficult to define, due to the coseismic and postseismic deformations associated with the 2015 Illapel earthquake.

Because of such a spatial coherency of the signal, we exclude both instrumental errors during the data acquisition (equipment issues or artificial signal due to the change of equipment; see Table S1) or random errors in the processing parameterization. Furthermore, we rule out any issue in the definition of the reference frame, which would result in a systematic error over the whole area processed and not only in this region.

2.2. Continuous GPS Observations

Until 2015, the Atacama region had poor coverage of cGPS instruments with only one station installed in 2002 in Copiapo (COPO), which was decommissioned in 2015. A few months before COPO was decommissioned, two new nearby stations (BN03 and UDAT) were installed by the CSN. Two other stations were installed at the same period, TAM3 located about 25 km southeast of COPO and LLCH 120 km southwest of COPO (Figure 2c).

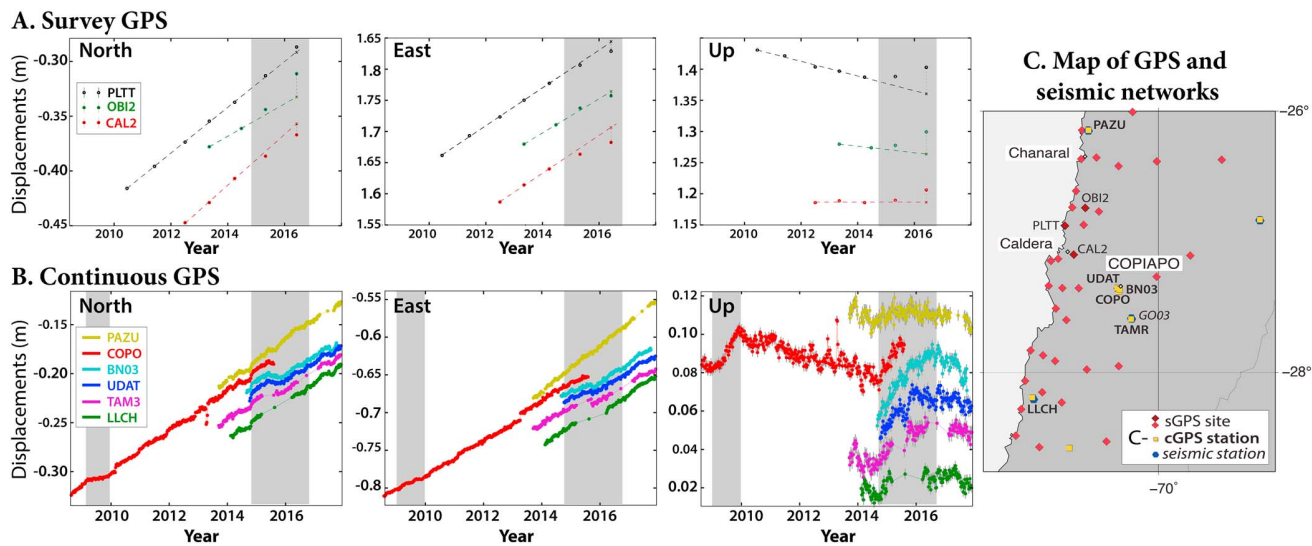


Figure 2. Survey and continuous GPS time series. (a) sGPS annual time series and (b) cGPS weekly time series (downsampled from University of Nevada, Reno (UNR) daily time series). Time series are ordered by latitude of sites and are represented in ITRF08 (Altamimi et al., 2012). Duration of the 2010 and 2014 transients is depicted by gray areas. (c) Location of GPS sites and seismic stations. Detrended time series are presented in Figure S2 of the supporting information. GPS = Global Positioning System.

To confirm that the signal extracted from survey mode data does not artificially result from our differential processing, we investigate the time series of CSN cGPS stations provided by the Nevada Geodetic Laboratory, University of Nevada, Reno (UNR), (Figure 2b) and processed following a different processing strategy (PPP, for more details see <http://geodesy.unr.edu/gps/ngl.acn.txt>).

All the stations in the region of Copiapó show a clear transient signal starting in mid-2014 that is visible on vertical and horizontal components (Figures 3a and S3). The cGPS station LLCH located south of the region also shows such a signal but with a smaller amplitude, in agreement with the amplitude decrease observed by nearby campaign measurements. Similar to sGPS observations at the latitude of Chañaral (26.4° S), no clear transient displacement is detected on the time series of the station PAZU located 140 km north of Copiapó (Figure 2b). Most of stations shown in Figure 2b have been installed shortly before (PAZU, TAM3, and LLCH) or during (BN03 and UDAT) the transient signal, while COPO was decommissioned before the conclusion of the event. To avoid any inconsistent amplitudes due to such temporal incoherences, we do not estimate any static offset from the cGPS observations. Although sGPS offsets are probably underestimated because they were measured before the end of the transient, they span a common time period and can therefore be used together to constrain a slip model representing that time period. Figure S4 shows that sGPS and cGPS solutions are consistent, which confirms the existence of a transient signal. In the time series of COPO which started in 2002, we observe a similar transient signal in 2009 with a shorter duration but comparable amplitude (Figure 3). We also observe a transient uplift in 2004/2005 with comparable amplitude, although the time series at that time is much noisier. It is difficult to estimate the exact duration of this transient, in the absence of data from the earlier period. Deviations in the horizontal components are also visible during the same time period (Figure S3). Unfortunately, COPO was the only permanent station in operation in the region until 2015 and the survey network was installed starting in 2010.

3. Assessment of Hydrological, Oceanic, and Atmospheric Loading Effects

In 2015, a very strong El Niño event was responsible for large rainfalls in Central North Chile. Smaller rainfalls occurred in May 2010 (probably also related to the strong El Niño event that year) and May 2014 (Figure 3b). Such events could generate variations of hydrostatic pore pressure in underlying aquifer, which could be measurable by GPS (e.g., Silverii et al., 2016). To assess if such effects could explain the observed transient, we gathered rainfall data set in Atacama, in particular at meteorological stations in the city of Copiapó (between 2002 and 2014 from Valdés-Pineda et al., 2018, and from global weather website between 2009 and present day). Significant rainfalls have occurred several months before and after the beginning of the transient (in 2014

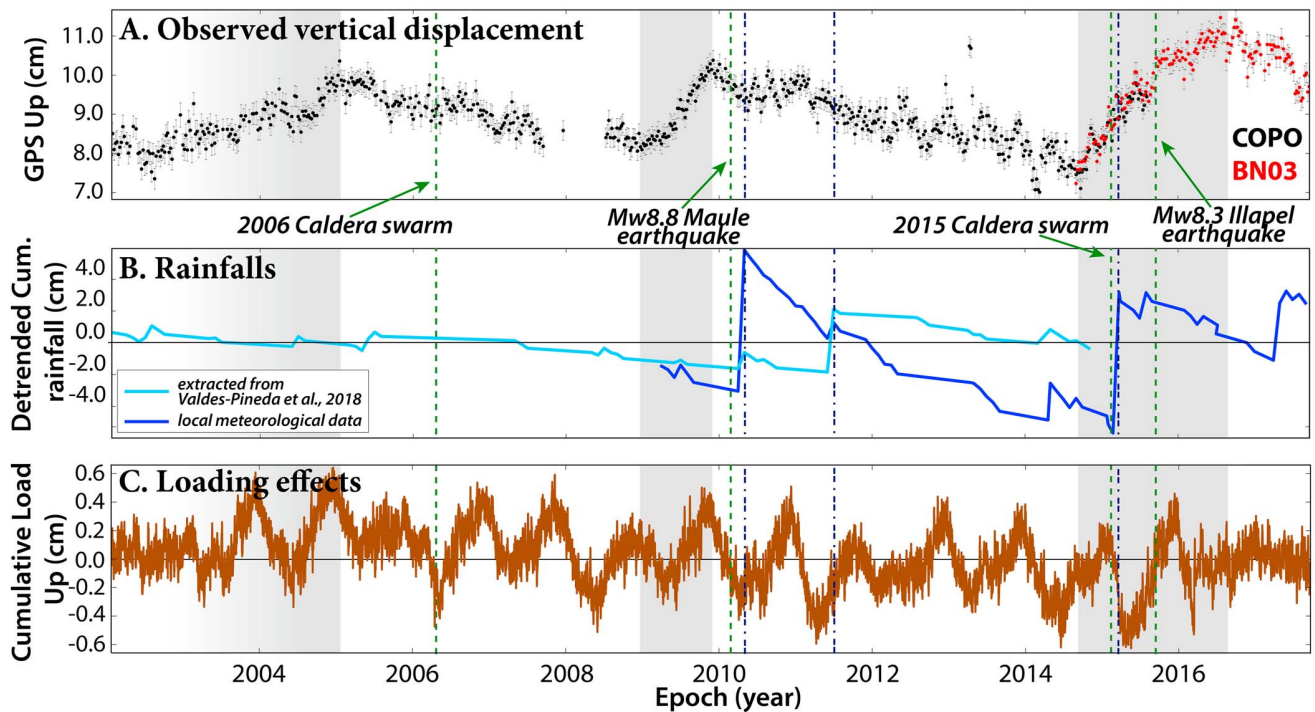


Figure 3. Comparison between observed vertical displacements, rainfalls, and displacements caused by hydrological, oceanic, and atmospheric loads. (a) Weekly vertical time series of COPO (black) and BN03 (red) represented in ITRF08. (b) Detrended cumulative rainfall time series (between 2002 and 2014 from Valdés-Pineda et al., 2018, local meteorological data between 2009 and present day). (c) Cumulative loads (Estimating the Circulation and Climate of the Ocean, European Centre for Medium Range Forecasts Re-Analysis Interim, and GRACE Mascons products) at COPO station. Green dashed lines correspond to the 2006 and 2015 swarms in Caldera, the 2010 M_w 8.8 Maule, and 2015 M_w 8.3 Illapel earthquakes, blue dashed lines to dates of major rainfalls. Duration of visible transient events is indicated by gray areas. COPO = Copiapó; GPS = Global Positioning System; GRACE = Gravity Recovery And Climate Experiment.

and 2015), but no clear temporal correlation is visible (Figures 3a and 3b). Moreover, any hydrological load should produce subsidence (e.g., Borsa et al., 2014; Wahr et al., 2013) while uplift is observed in 2014–2016.

Going further, we calculate the elastic response due to nontidal oceanic, atmospheric, and hydrological loading effects at our GPS sites (see, e.g., Petrov & Boy, 2004, for more details). Loading predictions are computed, respectively, using the Estimating the Circulation and Climate of the Ocean modeled ocean bottom pressure (ECCO, run kf080h; Wunsch et al., 2009), European Centre for Medium Range Forecasts Weather Re-Analysis Interim surface pressure (ECMWF ERA-interim; Dee et al., 2011), and Global Land Data Assimilation System/Noah v1 snow, soil moisture, and canopy water (GLDAS/Noah v1, Rodell et al., 2004). We also derive surface displacements due to hydrological loading from the National Aeronautics and Space Administration/Goddard Space Flight Center 1° iterated global mascons (NASA/GSFC, updates from Luthcke et al., 2013). Cumulative vertical displacements due to environmental loading contributions predict a vertical signal of less than 1 cm, without any marked transient signal in 2005, 2009, and 2015 (Figures 3c and S5 for the different contributions on the three components). We are therefore confident that the signal measured by GPS is not due to any nontectonic sources such as atmospheric, oceanic, or hydrological loads.

4. Evaluation of Seismotectonic Source

4.1. Postseismic Deformation Following the 2015 M_w = 8.3 Illapel Earthquake

Megathrust earthquakes often trigger continental scale postseismic deformation (e.g., following the 2011 Tohoku earthquake or the 2010 M_w = 8.8 Maule earthquake; Klein et al., 2016; Sun et al., 2015; Trubienko et al., 2014). As the Atacama region is located only ~500 km north of the rupture zone of the 2015 Illapel earthquake (Klein et al., 2017; Ruiz et al., 2016), postseismic deformation following this event could potentially affect the area where we detect the transient. Nevertheless, this M_w = 8.3 earthquake was significantly smaller than the Maule earthquake, consequently triggering significantly smaller postseismic deformation. In addition, postseismic deformation at such distances from the rupture zone is most likely due to viscoelastic relaxation in the asthenosphere, therefore generating a very long wavelength horizontal surface

motion pointing toward the coseismic rupture zone, that is, southwestward (Klein et al., 2016). The short-scale divergent pattern shown in Figure 1b at the latitude of Copiapo (27.5° S) is thus not consistent with such broad-scale postseismic deformation. However, the southward horizontal motion observed around Vallenar (28° S) could possibly correspond to the postseismic signal of the 2015 Illapel earthquake. These two regions are separated by smaller displacements around 28.2° S, which clearly delineates two zones affected by distinct deformation sources.

4.2. Aseismic Slip on the Interface

After ruling out any strong postseismic signal in the region, an obvious tectonic source able to generate such a spatially coherent transient deformation is aseismic slip along the subduction interface. As presented in section 1, this area is characterized by relatively little seismic activity at depth larger than 40 km (Figure 1a). In addition, no significant earthquake in the Atacama region, able to induce such a deformation, occurred when the 2014 transient started. In the following, we use a Bayesian approach to explore how such slip at the interface can explain our observations.

4.2.1. Bayesian Modeling Strategy

We build a fault geometry with triangular patches based on the finite element mesh designed in Klein et al. (2016, 2017) from Slab1.0 (Hayes et al., 2012) between 28° and 26° S down to 70-km depth.

The forward problem is defined as $\mathbf{d} = \mathbf{G}\mathbf{m}$ with \mathbf{d} , the vector containing GPS offsets, and \mathbf{m} the slip model parameters. We assume a pure along-dip faulting, and Green functions \mathbf{G} are calculated at each node of the fault plane, assuming a homogeneous elastic half-space (Okada, 1985). The model space is explored using AlTar, a parallel Monte Carlo approach (Duputel et al., 2015; Jolivet et al., 2015; Minson et al., 2013) to derive the posterior probability density function (PDF) of the model \mathbf{m} given available observations \mathbf{d}_{obs}

$$p(\mathbf{m}|\mathbf{d}_{\text{obs}}) \propto p(\mathbf{m}) \exp\left(-\frac{1}{2}(\mathbf{d}_{\text{obs}} - \mathbf{G}\mathbf{m})^T \mathbf{C}_d^{-1} (\mathbf{d}_{\text{obs}} - \mathbf{G}\mathbf{m})\right) \quad (1)$$

\mathbf{C}_d is the covariance matrix describing observational uncertainties. $p(\mathbf{m})$ is the prior PDF, defined as centered truncated Gaussian with a standard deviation of 25 cm bounded between -1 cm (small back slip is allowed to ensure correct sampling near zero) and 50 cm (Figure S6).

4.2.2. Results

Given large uncertainties (± 2 cm) on vertical displacements, we first develop a solution based only on horizontal components. The resulting posterior mean slip distribution is presented in (Figure 4a). This distribution depicts significant slip between 40- and 60-km depth with a peak slip larger than 50 cm. This deep slip patch is associated with a geodetic moment of $2.93 \cdot 10^{19}$ N.m ($M_w = 6.9$; see M_w PDF in Figure 4 and Text S1). As shown in Figure 4c, this solution reproduces the observed horizontal displacements and also the vertical ones not included in the inversion. Because displacements extracted from sGPS observations are associated with significant uncertainties (about 1 cm in horizontal, Figure 1b), there are significant posterior uncertainties on the slip distribution, of the order of 10 cm (Figure 4b and blue slip PDFs in Figure 4a). Both the posterior mode model (representing the maximum of each parameter marginal PDF) and the median model are presented in Figure S7 together with Movie S1 showing more than a thousand model realizations from the space of possible solutions. The variability of the slip at shallow depths reflects high uncertainties in this part of the model. Nonetheless, the deep patch of slip remains quite stable, especially at 27° S on almost every model.

We also conducted an inversion using both horizontal and vertical observations. The posterior mean slip distribution shown in Figure S8 presents a slightly smaller slip amplitude with an equivalent geodetic moment of $2.72 \cdot 10^{19}$ N.m. In particular, approximately 15 cm of slip is needed to fit the data in the southern part of the fault (27.5° S), while more than 25 cm is required for the horizontal displacement based model. Nevertheless, the overall slip distribution is consistent for both models, with similar amplitudes in the main slip area (PDFs in Figure 4a). As expected, integrating more observations results in slightly smaller posterior slip uncertainties on the deep patch (Figure 4a, red PDFs, and Figure S8). Finally, we tested a model with broader priors, producing similar spatial slip distribution, M_w , and data fit (Figure S9). Therefore, we are confident that the overall pattern of slow slip distribution is fairly well defined.

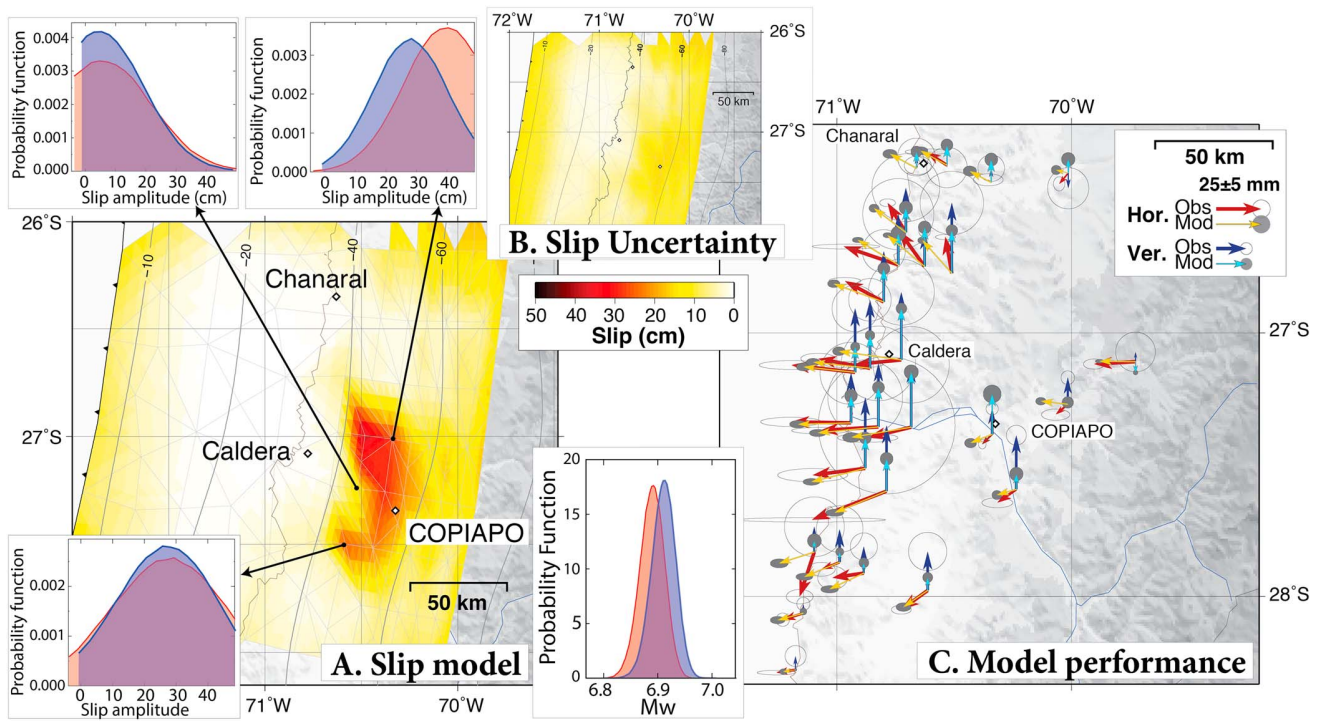


Figure 4. Bayesian modeling of deep aseismic slip. (a) Mean posterior slip distribution (color scale in centimeters). Insets show posterior marginal probability density functions (in blue) at three different locations of the subduction interface, indicated by arrows. Red probability density functions depict the model inverted with both horizontal and vertical components (cf., Figure S8b) 1 σ posterior slip uncertainties represented with the same color scale as the slip distribution. (c) Predicted horizontal (yellow) and vertical (light blue) offsets and their associated 2 σ uncertainties (filled gray ellipses) compared to measured horizontal (dark red) and vertical (dark blue) displacements.

5. Discussion and Conclusions

In this study, we report observations of a transient deformation signal, initially detected by the sGPS network, on the Atacama region along the Chilean subduction zone. We interpret this signal as a deep aseismic slip event on the subduction interface.

We carefully verified that observed GPS deviations cannot be explained by any nontectonic sources. Because the transient is revealed by both sGPS and cGPS observations which were processed independently, any instrumental errors are very unlikely. We also eliminated any oceanic, hydrological, or atmospheric sources. Although sGPS alone does not allow to accurately constrain the temporal evolution of this event, the compilation of cGPS time series in the region shows that this event started in September 2014 and lasted until mid-2016 (i.e., duration longer than 1 year).

Using a Bayesian modeling approach, we demonstrate that deep slow slip along the subduction interface can explain the observed GPS deviations. The event released a scalar moment equivalent to a $M_w = 6.9$, and its long duration (more than a year) is consistent with the duration versus magnitude scaling laws for slow earthquakes proposed by Ide et al. (2007). The inversion places the SSE downdip of the seismogenic zone (between 40- and 60-km depths; Figure 1a) in the so-called transition zone, which is commonly observed for SSEs in other subduction zones (Obara & Kato, 2016; Rolandone et al., 2018; Schwartz & Rokosky, 2007). This deep SSE in Atacama differs from the recently reported aseismic events in Chile on the shallower part of the interface preceding the occurrence of large earthquakes (Ruiz et al., 2017; Socquet et al., 2017).

Because of the sparse regional seismic network, it is difficult to discern nonvolcanic tremor activity, which is commonly observed in many subduction zones during SSEs (e.g., Cascadia, Mexico, and Japan; Obara, 2002; 2011; Payero et al., 2008; Rogers & Dragert, 2003; Zigone et al., 2012). Only one seismological station is available in the vicinity of the 2014–2016 SSE (GO03; Figure 2c). Some bursts of energy of a few decibels above the average could indicate tremor activities (for more details about the methodology, see Text S3; Husker et al., 2010; Kostoglodov et al., 2010; and Figure S10), but it is unclear whether such signal is tectonic or is associated

with random fluctuations of high-frequency noise. Additional seismic stations in the region would be necessary to further investigate the occurrence of the nonvolcanic tremor and its relationship with the deep slow slip deduced from GPS data.

Another interesting aspect is the possible interaction between SSE and repeated occurrences of seismic swarms offshore Caldera over the last 50 years (in 1973, 1979, and 2006; Holtkamp et al., 2011; and in 2015, CSN catalog, Figure 1b). Seismic swarms are often accompanied by significant magnitude earthquakes ($M_w \geq 6.5$ in 2006; Ducret, 2013; Figure S3) and can be markers of aseismic slip on the interface (e.g., Ruiz et al., 2017). Our tests (presented in Text S2 and Figure S11) show that the observed GPS transient is most likely not associated with seismic or aseismic slip in the area of the March 2015 swarm that occurred at shallow depth (~20 km). In particular, shallow slip on the interface produces subsidence inland rather than uplift. Nonetheless, an indirect link between the deep transient event and the seismic swarms offshore Caldera should be more thoroughly investigated in the future.

Two additional transient signals observed on the COPO time series (Figure 3) suggest that similar SSEs might have occurred in 2005 and 2009. Based on this single cGPS station, the 2009 event seems to last for about 12 months, while the 2005 event is probably shorter (although it is hard to precisely define its beginning). Such recurrence is similar to long-term SSEs reported in southwest Japan, New Zealand, and Mexico (Hirose & Obara, 2005; Radiguet et al., 2012; Wallace & Beavan, 2010), which typically occur every 3–4 years with a scalar moment equivalent to a $M_w = 7$.

To our knowledge, this is the first observation of potentially recurrent deep SSEs reported in Chile. It raises key questions regarding the stress release mechanism along this segment of the Chilean subduction zone and potential interactions between slow slip asperities in the transition zone and megathrust asperities at seismogenic depths.

The shallower part of the interface is characterized by high coupling down to 40 km on the Atacama and Chañaral segments. These two segments are separated by a low coupled portion, the Baranquilla LCZ, which is located at the same latitude as the SSE reported in this study (27°S; Klein et al., 2018; Métois et al., 2013). Note that 2016 measurements have been excluded from the later interseismic model in order to capture the coupling of the subduction interface between SSEs. The modeled slow slip therefore lies below the coupled seismogenic zone with two main slip asperities that seems to be separated by a narrow creeping area (Figure 1a). The comparison of mean slip deficit in the SSE area with the slip inferred from this study is not entirely conclusive. The coupling ratio appears too low at these depths to accumulate in 4 years the 15 cm of slip released by the 2015 SSE (i.e., assuming that the 2009 SSE released all of the previously accumulated stress). However, both the coupling and the slow slip models are associated with significant uncertainties at such depths and the PDF of both models show a significant overlap (Figure S12). While we cannot completely rule out a small contamination of Klein et al.'s (2018) coupling model by measurements at the onset of the SSE in 2015, the above conclusion seems also consistent with the coupling values reported in models constrained before 2014 (Métois et al., 2013, 2016). Although it is difficult to conclude from a single GPS station, the difference in duration between the 2009 and 2014 transients could suggest that both events are different and therefore possibly not perfectly colocated. It could also suggest that the 2009 event did not release all of the previously accumulated stress where the 2015 SSE occurred. In any case, the interplay between interface locking and SSE in this region needs further investigation based on future observations.

The occurrence of deep SSEs also has impact in terms of seismic hazard. In particular, aseismic slip in the transition zone can potentially trigger earthquakes in the seismogenic zone. A similar mechanism has recently been proposed in Mexico where the 2014 SSE is believed to have triggered the $M_w = 7.3$ Papanoa earthquake by either increasing the static stress in the coupled region or by helping the weakening of the earthquake hypocentral area (Radiguet et al., 2016). The occurrence of transient aseismic slip in Chile can thus potentially influence the seismic cycle by changing the stress level in the seismogenic zone, which may advance or delay the occurrence of the next earthquake in the region.

Given the limited amount of observations available until recently, it is obvious that denser deployments of geodetic and seismic instruments are necessary to better capture the behavior of the megathrust in the Atacama region. The launch of new Synthetic Aperture Radar satellite constellations such as the Sentinel-1 mission can also help to monitor and detect transient deformations in sparsely instrumented regions (e.g., Rousset et al., 2016). Such improvements of our observational capabilities also open up new opportunities to

investigate the potential impact of deep SSEs on the shallower part of the interface in Atacama where the last major event occurred almost a century ago.

Acknowledgments

This work was performed in the frame of the French-Chilean LiA *Montessus de Ballore* with financial support of Agence Nationale de la Recherche (projects ANR-2012-BS06-004 and ANR-17-ERC3-0010), the European Research Council (ERC) under the European Union's Horizon 2020 research and innovation programme (grant agreement: 805256), and the Marie Curie Initial Training Network *Zooming in between plates* (ITN FP7 grant agreement 604713). We are also thankful to the Institut National des Sciences de l'Univers (INSU-CNRS) and the Réseau Sismologique & Géodésique Français (RESIF, as part of the *Investissements d'Avenir* program, ANR-11-EQPX-0040, and the French Ministry of Ecology, Sustainable Development and Energy) for providing the geodetic instruments for all campaigns. We would like to warmly thank all CSN staff, for their precious help for the fieldwork. We thank Mark Simons (CalTech) for providing the Altair code used in this study. The authors would also like to sincerely thank Sergio Ruiz (University of Chile), Francesca Silveri, Adrian Borsa (IGPP, SIO), Romain Jolivet, and Sabrina Speich (ENS, Paris) for fruitful discussions. We would like to thank the reviewers for thorough reviews of this manuscript. We are particularly grateful to Laura Wallace for her very thorough and constructive comments that helped us to really improve this study. We also sincerely thank Dara Goldberg who helped us improve the English language usage of the manuscript. All the figures have been made using Generic Mapping Tools GMT (Wessel et al., 2013) using topography from ETOPO5. Data availability: Solutions of continuous GPS data collected by CSN cGPS stations are available through the UNR website (<http://geodesy.unr.edu/>). Interseismic survey measurements used here have been published previously (Klein et al., 2018), and additional measurements are available upon request. Seismic data collected are available through the Incorporated Research Institutions for Seismology (IRIS) Data Management Center.

References

- Altamimi, Z., Métivier, L., & Collilieux, X. (2012). ITRF2008 plate motion model. *Journal of Geophysical Research*, 117, B07402. <https://doi.org/10.1029/2011JB008930>
- Álvarez, O., Giménez, M., Folguera, A., Spagnotto, S., Bustos, E., Baez, W., & Braatenberg, C. (2015). New evidence about the subduction of the Copiapo ridge beneath South America, and its connection with the Chilean-Pampean flat slab, tracked by satellite GOCE and EGM2008 models. *Journal of Geodynamics*, 91, 65–88.
- Báez, J., Leyton, F., Troncoso, C., del Campo, F., Bevis, M., Vigny, C., et al. (2018). The Chilean GNSS network: Current status and progress toward early warning applications, vol. 89, pp. 1546–1554.
- Beroza, G. C., & Ide, S. (2011). Slow earthquakes and nonvolcanic tremor. *Annual Review of Earth and Planetary Sciences*, 39, 271–296.
- Beutler, G., Rothacher, M., Schaer, S., Springer, T., Kouba, J., & Neilan, R. (1999). The International GPS Service (IGS): An interdisciplinary service in support of Earth sciences. *Advances in Space Research*, 23(4), 631–653.
- Borsa, A. A., Agnew, D. C., & Cayan, D. R. (2014). Ongoing drought-induced uplift in the western United States. *Science*, 345(6204), 1587–1590.
- Brooks, B. A., Bevis, M., Smalley, R., Kendrick, E., Manceda, R., Lauria, E., et al. (2003). Crustal motion in the southern Andes (26°–36°S): Do the Andes behave like a microplate? *Geochemistry, Geophysics, Geosystems*, 4(10), 1085. <https://doi.org/10.1029/2003GC000505>
- Dee, D. P., Uppala, S., Simmons, A., Berrisford, P., Poli, P., Kobayashi, S., et al. (2011). The ERA-Interim reanalysis: Configuration and performance of the data assimilation system. *Quarterly Journal of the Royal Meteorological Society*, 137(656), 553–597.
- Ducret, G. (2013). Mesure De Déformation Par Interférométrie Radar: Développements Méthodologiques Et Applications à La Subduction Chilienne (Ph.D Thesis), Laboratoire de Géologie, Ecole Normale Supérieure de Paris.
- Duputel, Z., Jiang, J., Jolivet, R., Simons, M., Rivera, L., Ampuero, J.-P., et al. (2015). The Iquique earthquake sequence of April 2014: Bayesian modeling accounting for prediction uncertainty. *Geophysical Research Letters*, 42, 7949–7957. <https://doi.org/10.1002/2015GL065402>
- Frank, W. B., Shapiro, N. M., Kostoglodov, V., Husker, A. L., Campillo, M., Payero, J. S., & Prieto, G. A. (2013). Low-frequency earthquakes in the Mexican Sweet Spot. *Geophysical Research Letters*, 40, 2661–2666. <https://doi.org/10.1002/grl.50561>
- Hayes, G. P., Wald, D. J., & Johnson, R. L. (2012). Slab1.0: A three-dimensional model of global subduction zone geometries. *Journal of Geophysical Research*, 117, B01302. <https://doi.org/10.1029/2011JB008524>
- Herring, T., King, R., & McClusky, S. C. (2010a). GAMIT : GPS Analysis at MIT, release 10.4.
- Herring, T., King, R., & McClusky, S. C. (2010b). GLOBK : Global Kalman filter VLBI and GPS analysis program release 10.4.
- Hirose, H., & Obara, K. (2005). Repeating short-and long-term slow slip events with deep tremor activity around the Bungo channel region, southwest Japan. *Earth, planets and space*, 57(10), 961–972.
- Holtkamp, S. G., Pritchard, M. E., & Lohman, R. B. (2011). Earthquake swarms in South America. *Geophysical Journal International*, 187(1), 128–146. <https://doi.org/10.1111/j.1365-246x.2010.05137.x>
- Husker, A., Peyrat, S., Shapiro, N., & Kostoglodov, V. (2010). Automatic non-volcanic tremor detection in the mexican subduction zone. *Geofísica Internacional*, 49(1), 17–25.
- Ide, S., Beroza, G. C., Shelly, D. R., & Uchide, T. (2007). A scaling law for slow earthquakes. *Nature*, 447(7140), 76–79.
- Ikari, M. J., Marone, C., Saffer, D. M., & Kopf, A. J. (2013). Slip weakening as a mechanism for slow earthquakes. *Nature Geoscience*, 6(6), 468–472.
- Jolivet, R., Simons, M., Agram, P., Duputel, Z., & Shen, Z.-K. (2015). Aseismic slip and seismogenic coupling along the central San Andreas Fault. *Geophysical Research Letters*, 42, 297–306. <https://doi.org/10.1002/2014GL062222>
- Kato, A., Obara, K., Igarashi, T., Tsuruoka, H., Nakagawa, S., & Hirata, N. (2012). Propagation of slow slip leading up to the 2011 Mw 9.0 Tohoku-Oki earthquake. *Science*, 335(6069), 705–708.
- Kendrick, E., Bevis, M., Smalley, R., Brooks, B., Vargas, R. B., Lauria, E., & Fortes, L. P. S. (2003). The Nazca–South America Euler vector and its rate of change. *Journal of South American Earth Sciences*, 16(2), 125–131.
- Khazaradze, G., & Klotz, J. (2003). Short-and long-term effects of GPS measured crustal deformation rates along the south central Andes. *Journal of Geophysical Research*, 108(B6), 2289. <https://doi.org/10.1029/2002JB001879>
- Klein, E., Fleitout, L., Vigny, C., & Garaud, J. (2016). Afterslip and viscoelastic relaxation model inferred from the large scale postseismic deformation following the 2010 Mw 8.8 Maule earthquake (Chile). *Geophysical Journal International*, 205(3), 1455–1472. <https://doi.org/10.1093/gji/ggw086>
- Klein, E., Métois, M., Meneses, G., Vigny, C., & Delorme, A. (2018). Bridging the gap between North and Central Chile: Insight from new GPS data on coupling complexities and the Andean sliver motion. *Geophysical Journal International*, 213(3), 1924–1933.
- Klein, E., Vigny, C., Fleitout, L., Grandin, R., Jolivet, R., Rivera, E., & Métois, M. (2017). A comprehensive analysis of the 2015 Mw 8.3 Illapel earthquake from GPS and inSAR data. *Physics of the Earth and Planetary Interiors*, 469, 123–134.
- Klotz, J., Angermann, D., Michel, G., Porth, R., Reigber, C., Reinking, J., et al. (1999). GPS-derived deformation of the Central Andes including the 1995 Antofagasta $M_w = 8.0$ earthquake. *Pure and Applied Geophysics*, 154, 709–730.
- Klotz, J., Khazaradze, G., Angermann, D., Reigber, C., Perdomo, R., & Cifuentes, O. (2001). Earthquake cycle dominates contemporary crustal deformation in central and southern Andes. *Earth and Planetary Science Letters*, 193(3), 437–446.
- Kostoglodov, V., Husker, A., Shapiro, N. M., Payero, J. S., Campillo, M., Cotte, N., & Clayton, R. (2010). The 2006 slow slip event and nonvolcanic tremor in the Mexican subduction zone. *Geophysical Research Letters*, 37, L24301. <https://doi.org/10.1029/2010GL045424>
- Leeman, J. R., Saffer, D. M., Scuderi, M. M., & Marone, C. (2016). Laboratory observations of slow earthquakes and the spectrum of tectonic fault slip modes. *Nature Communications*, 7, 11104.
- Luthcke, S. B., Sabaka, T., Loomis, B., Arendt, A., McCarthy, J., & Camp, J. (2013). Antarctica, Greenland and Gulf of Alaska land-ice evolution from an iterated GRACE global mascon solution. *Journal of Glaciology*, 59(216), 613–631.
- Métois, M., Socquet, A., Vigny, C., Carrizo, D., Peyrat, S., Delorme, A., et al. (2013). Revisiting the north Chile seismic gap segmentation using GPS-derived interseismic coupling. *Geophysical Journal International*, 194(3), 1283–1294. <https://doi.org/10.1093/gji/ggt183>
- Métois, M., Vigny, C., & Socquet, A. (2012). Interseismic coupling, segmentation and mechanical behavior of the central Chile subduction zone. *Journal of Geophysical Research*, 117, B03406. <https://doi.org/10.1029/2011JB008736>
- Métois, M., Vigny, C., & Socquet, A. (2016). Interseismic coupling, megathrust earthquakes and seismic swarms along the Chilean subduction zone (38°–18°S). *Pure and Applied Geophysics*, 173(5), 1431–1449.

- Métois, M., Vigny, C., Socquet, A., Delorme, A., Morvan, S., Ortega, I., & Valderas-Bermejo, C.-M. (2014). GPS-Derived interseismic coupling on the subduction and seismic hazards in the Atacama region, Chile. *Geophysical Journal International*, 196(2), 644–655. <https://doi.org/10.1093/gji/ggt418>
- Miller, M. M., Melbourne, T., Johnson, D. J., & Sumner, W. Q. (2002). Periodic slow earthquakes from the Cascadia subduction zone. *Science*, 295(5564), 2423–2423.
- Minson, S., Simons, M., & Beck, J. (2013). Bayesian inversion for finite fault earthquake source models I—Theory and algorithm. *Geophysical Journal International*, 194, 1701–1726.
- Moreno, M., Rosenau, M., & Oncken, O. (2010). 2010 Maule earthquake slip correlates with pre-seismic locking of Andean subduction zone. *Nature*, 467(7312), 198–202. <https://doi.org/10.1038/nature09349>
- Obara, K. (2002). Nonvolcanic deep tremor associated with subduction in southwest Japan. *Science*, 296(5573), 1679–1681.
- Obara, K. (2011). Characteristics and interactions between non-volcanic tremor and related slow earthquakes in the Nankai subduction zone, southwest Japan. *Journal of Geodynamics*, 52(3-4), 229–248.
- Obara, K., & Kato, A. (2016). Connecting slow earthquakes to huge earthquakes. *Science*, 353(6296), 253–257.
- Okada, Y. (1985). Surface deformation due to shear and tensile faults in a half-space. *Bulletin of the seismological society of America*, 75(4), 1135–1154.
- Payero, J. S., Kostoglodov, V., Shapiro, N., Mikumo, T., Iglesias, A., Pérez-Campos, X., & Clayton, R. W. (2008). Nonvolcanic tremor observed in the Mexican subduction zone. *Geophysical Research Letters*, 35, L07305. <https://doi.org/10.1029/2007GL032877>
- Peng, Z., & Gomberg, J. (2010). An integrated perspective of the continuum between earthquakes and slow-slip phenomena. *Nature Geoscience*, 3(9), 599.
- Petrov, L., & Boy, J.-P. (2004). Study of the atmospheric pressure loading signal in very long baseline interferometry observations. *Journal of Geophysical Research*, 109, B03405. <https://doi.org/10.1029/2003JB002500>
- Piñón, D. A., Gómez, D. D., Smalley, Jr. R., Cimbaro, S. R., Lauría, E. A., & Bevis, M. G. (2018). The history, state, and future of the Argentine continuous satellite monitoring network and its contributions to geodesy in Latin America. *Seismological Research Letters*, 89(2A), 475–482.
- Radiguet, M., Cotton, F., Vergnolle, M., Campillo, M., Walpersdorf, A., Cotte, N., & Kostoglodov, V. (2012). Slow slip events and strain accumulation in the Guerrero gap, Mexico. *Journal of Geophysical Research*, 117, B04305. <https://doi.org/10.1029/2011JB008801>
- Radiguet, M., Perfettini, H., Cotte, N., Gualandi, A., Valette, B., Kostoglodov, V., et al. (2016). Triggering of the 2014 Mw 7.3 Papanoa earthquake by a slow slip event in Guerrero, Mexico. *Nature Geoscience*, 9(11), 829.
- Rodell, M., Houser, P., Jambor, U., Gottschalck, J., Mitchell, K., Meng, C., et al. (2004). The global land data assimilation system. *Bulletin of the American Meteorological Society*, 85(3), 381–394.
- Rogers, G., & Dragert, H. (2003). Episodic tremor and slip on the Cascadia subduction zone: The chatter of silent slip. *Science*, 300(5627), 1942–1943.
- Rolandone, F., Nocquet, J.-M., Mothes, P. A., Jarrin, P., Vallée, M., Cubas, N., et al. (2018). Areas prone to slow slip events impede earthquake rupture propagation and promote afterslip. *Science Advances*, 4(1), eaao6596.
- Romanet, P., Bhat, H. S., Jolivet, R., & Madariaga, R. (2018). Fast and slow slip events emerge due to fault geometrical complexity. *Geophysical Research Letters*, 45, 4809–4819. <https://doi.org/10.1029/2018GL077579>
- Rousset, B., Jolivet, R., Simons, M., Lasserre, C., Riel, B., Millillo, P., et al. (2016). An aseismic slip transient on the North Anatolian Fault. *Geophysical Research Letters*, 43, 3254–3262. <https://doi.org/10.1002/2016GL068250>
- Ruegg, J.-C., Rudloff, A., Vigny, C., Madariaga, R., de Chabalier, J., Campos, J., et al. (2009). Interseismic strain accumulation measured by GPS in the seismic gap between Constitución and Concepción in Chile. *Physics of the Earth and Planetary Interiors*, 175(1–2), 78–85.
- Ruiz, S., Aden-Antoniow, F., Baez, J., Otarola, C., Potin, B., DelCampo, F., et al. (2017). Nucleation phase and dynamic inversion of the Mw 6.9 Valparaíso 2017 earthquake in Central Chile. *Geophysical Research Letters*, 44, 10,290–10,297. <https://doi.org/10.1002/2017GL075675>
- Ruiz, S., Klein, E., del Campo, F., Rivera, E., Poli, P., Metois, M., et al. (2016). The seismic sequence of the 16 September 2015 Mw 8.3 Illapel, Chile, earthquake. *Seismological Research Letters*, 87(4), 789–799.
- Ruiz, S., Metois, M., Fuenzalida, A., Ruiz, J., Leyton, F., Grandin, R., et al. (2014). Intense foreshocks and a slow slip event preceded the 2014 Iquique Mw 8.1 earthquake. *Science*, 345(6201), 1165–1169.
- Schwartz, S. Y., & Rokosky, J. M. (2007). Slow slip events and seismic tremor at circum-Pacific subduction zones. *Reviews of Geophysics*, 45, RG3004. <https://doi.org/10.1029/2006RG000208>
- Segall, P., Rubin, A. M., Bradley, A. M., & Rice, J. R. (2010). Dilatant strengthening as a mechanism for slow slip events. *Journal of Geophysical Research*, 115, B12305. <https://doi.org/10.1029/2010JB007449>
- Shelly, D. R., Beroza, G. C., & Ide, S. (2007). Non-volcanic tremor and low-frequency earthquake swarms. *Nature*, 446(7133), 305.
- Silverii, F., D'Agostino, N., Métois, M., Fiorillo, F., & Ventafridda, G. (2016). Transient deformation of karst aquifers due to seasonal and multiyear groundwater variations observed by GPS in southern Apennines (Italy). *Journal of Geophysical Research: Solid Earth*, 121, 8315–8337. <https://doi.org/10.1002/2016JB013361>
- Socquet, A., Valdes, J. P., Jara, J., Cotton, F., Walpersdorf, A., Cotte, N., et al. (2017). An 8 month slow slip event triggers progressive nucleation of the 2014 Chile megathrust. *Geophysical Research Letters*, 44, 4046–4053. <https://doi.org/10.1002/2017GL073023>
- Sun, T., Wang, K., Linuma, T., Hino, R., He, J., Fujimoto, H., et al. (2015). Prevalence of viscoelastic relaxation after the 2011 Tohoku-Oki earthquake. *Nature*, 514, 84–87. <https://doi.org/10.1038/nature13778>
- Trubienko, O., Garaud, J.-D., & Fleitout, L. (2014). Models of postseismic deformation after megaearthquakes: The role of various rheological and geometrical parameters of the subduction zone. *Solid Earth Discussions*, 6(1), 427–466. <https://doi.org/10.5194/se-6-427-2014>
- Valdés-Pineda, R., Canón, J., & Valdés, J. B. (2018). Multi-decadal 40- to 60-year cycles of precipitation variability in Chile (South America) and their relationship to the AMO and PDO signals. *Journal of Hydrology*, 556, 1153–1170. <https://doi.org/10.1016/j.jhydrol.2017.01.031>
- Vigny, C., Rudloff, A., Ruegg, J. C., Madariaga, R., Campos, J., & Alvarez, M. (2009). Upper plate deformation measured by GPS in the Coquimbo Gap, Chile. *Physics of the Earth and Planetary Interiors*, 175(1), 86–95.
- Vigny, C., Socquet, A., Peyrat, S., Ruegg, J.-C., Metois, M., Madariaga, R., et al. (2011). The 2010 Mw 8.8 Maule megathrust earthquake of central Chile, monitored by GPS. *Science*, 332(6036), 1417–1421. <https://doi.org/10.1126/science.1204132>
- Wahr, J., Khan, S. A., Dam, T., Liu, L., Angel, J. H., Broeke, M. R., & Meertens, C. M. (2013). The use of GPS horizontals for loading studies, with applications to northern California and southeast Greenland. *Journal of Geophysical Research: Solid Earth*, 118, 1795–1806. <https://doi.org/10.1002/jgrb.50104>
- Wallace, L. M., & Beavan, J. (2010). Diverse slow slip behavior at the Hikurangi subduction margin, New Zealand. *Journal of Geophysical Research*, 115, B12402. <https://doi.org/10.1029/2010JB007717>
- Wallace, L. M., Kaneko, Y., Hreinsdóttir, S., Hamling, I., Peng, Z., Bartlow, N., et al. (2017). Large-scale dynamic triggering of shallow slow slip enhanced by overlying sedimentary wedge. *Nature Geoscience*, 10(10), 765–770.

- Wallace, L. M., Webb, S. C., Ito, Y., Mochizuki, K., Hino, R., Henrys, S., et al. (2016). Slow slip near the trench at the Hikurangi subduction zone, New Zealand. *Science*, 352(6286), 701–704.
- Wessel, P., Smith, W. H. F., Scharroo, R., Luis, J., & Wobbe, F. (2013). Generic Mapping Tools: Improved version released. *Eos, Transactions American Geophysical Union*, 94(45), 409–410. <https://doi.org/10.1002/2013EO450001>
- Willis, B. (1929). *Studies in comparative seismology: Earthquake conditions in Chile*. Washington: Carnegie Institution of Washington.
- Wunsch, C., Heimbach, P., Ponte, R. M., Fukumori, I., & Members, E.-G. C. (2009). The global general circulation of the ocean estimated by the ECCO-consortium. *Oceanography*, 22(2), 88–103.
- Zigone, D., Rivet, D., Radiguet, M., Campillo, M., Voisin, C., Cotte, N., et al. (2012). Triggering of tremors and slow slip event in Guerrero, Mexico, by the 2010 Mw 8.8 Maule, Chile, earthquake. *Journal of Geophysical Research*, 117, B09304. <https://doi.org/10.1029/2012JB009160>

A.6 Suivi de la propagation du dike à l'origine de l'éruption de mai 2018 au Kīlauea

L'article proposé ci-dessous sera publié en 2021 dans *Earth and Planetary Science Letters*.



Tracking dike propagation leading to the 2018 Kīlauea eruption

Olivier Lengliné ^{a,*}, Zacharie Duputel ^a, P.G. Okubo ^b



^a Institut de Physique du Globe de Strasbourg, UMR7516, Université de Strasbourg/EOST, CNRS, Strasbourg, France

^b Department of Earth Sciences, School of Ocean and Earth Science and Technology, University of Hawaii at Manoa, Honolulu, HI 96822, USA

ARTICLE INFO

Article history:

Received 25 May 2020

Received in revised form 14 October 2020

Accepted 28 October 2020

Available online 9 November 2020

Editor: R. Bendick

Keywords:

Kīlauea volcano

seismicity

dike dynamics

ABSTRACT

In May 2018, a major eruption occurred in the lower East Rift Zone of the Kīlauea volcano. The eruption started with the collapse of the Pu'u 'Ō'ō crater followed by a large downrift dike intrusion for more than 20 km in a well instrumented region. This large volcanic event is a rare opportunity to infer the dynamics of magma transfer that is often difficult to capture. In this study, we use seismological records to infer the migration of the dike. We detect, pick and locate more than 6000 earthquakes during the course of the magma intrusion. Using these locations together with near-field seismic amplitudes, we can precisely reconstruct the progression of the dike over time. We show that this migration is consistent with a logarithmic model of dike growth connected to a feeding magma chamber. The decrease of pressure inside the reservoir is also consistent with the dike propagation model derived from our observations. This work encourages real time monitoring of magma intrusions from the combination of seismological data and physical models.

© 2020 The Authors. Published by Elsevier B.V. This is an open access article under the CC BY license (<http://creativecommons.org/licenses/by/4.0/>).

1. Introduction

Lateral dike intrusions are ubiquitous features of basaltic volcanoes (Walker and Sigurdsson, 2000). These horizontal migrations usually occur after vertical ascent of magma under a central vent or within a complex plumbing network (Rivalta et al., 2015; Townsend et al., 2017). For example at Piton de la Fournaise volcano, magma tracked by earthquake locations and geodetic signals, is first transferred vertically before propagating into the rift zones where eruptive vents are formed (e.g. Smitarello et al., 2019; Duputel et al., 2019). This last stage of lateral magma migration before eruptions is thus of interest in order to assess the location of the future eruptive site.

As hydraulic fractures, volcanic dikes are geometrically controlled by the direction of the least principal stress (Gudmundsson, 2002), but the extent and timing of intrusions remain difficult to predict (Segall, 2013). Dike propagation is mainly governed by rock strength and the driving pressure at the crack tip, which is the difference between the least compressive stress and magma pressure within the dike (Rubin, 1995). Real-time *in situ* assessment of the dike driving pressure is unfeasible. One has to rely on models to explain the propagation of dikes and predict their future behavior. Constraints on these models can be derived from analog experiments (e.g., Maccaferri et al., 2019) or from the tracking

of intrusions using seismological and geodetic signals. Such observations have been made on several occasions for example in Afar (Grandin et al., 2010, 2011) or in Iceland (Sigmundsson et al., 2015; Woods et al., 2019). At Kīlauea volcano, magma intrusions in the rift zones are frequently captured by seismic and geodetic instruments (Owen et al., 2000; Montgomery-Brown et al., 2010; Lundgren et al., 2013). In most cases, we observe that seismicity migrates and delineates the advance of the dike (Brandsdóttir and Einarsson, 1979). Earthquake migration speed is usually high at the beginning of the intrusion and then decays with time before stopping. This behavior is generally interpreted as the consequence of the decrease in the driving pressure resulting from the progressive drainage of the feeding magma reservoir (Rivalta, 2010). Such interpretation is in agreement with geodetic signals (tiltmeter or GPS) that exhibit a deflationary trend where the magma originates. In some cases, outflow of the magma reservoir is barely visible while the dike propagates over a long distance. This observation can be explained by the low compressibility of rock that will force the magma in the reservoir to decompress considerably (Rivalta and Segall, 2008). Several models have been proposed to explain lateral dike propagations. These models usually rely on several hypotheses to derive analytical predictions of dike dynamics (Rubin, 1995; Rivalta, 2010; Pinel et al., 2017; Grossman-Ponemon et al., 2019). With the improvement of computing capabilities, an increasing number of physical processes and couplings are taken into account. Models generally include fluid mechanics associated with magma within the dike, coupled with linear elastic fracture mechanics governing the dike propagation. Some studies include a

* Corresponding author.

E-mail address: lengline@unistra.fr (O. Lengliné).

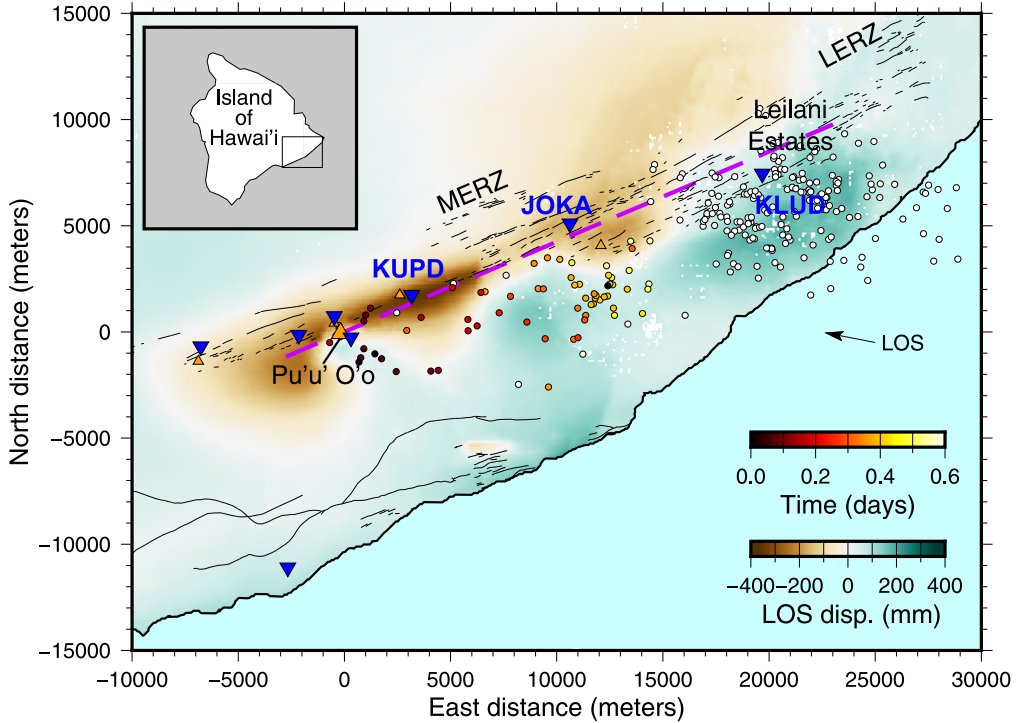


Fig. 1. May 2018 Dike propagation in the Middle East Rift Zone (MERZ) of the Kilauea volcano. Circles are earthquake locations from the HVO catalog that occurred during the dike intrusion (circle colors indicate time relative to the 1st of May 2018). The assumed dike geometry is depicted with a purple dashed line. Background colors correspond to an unwrapped Sentinel-1 interferogram showing surface displacement in Line Of Sight (LOS) direction. Black lines show mapped cracks and fissures and black triangles are vents from Trusdell et al. (2005). Seismic stations used in this study are blue triangles. The map on the upper left corner show the studied location. (For interpretation of the colors in the figure(s), the reader is referred to the web version of this article.)

connection between the dike and a filled magma reservoir. In general, all of these models are limited to 2 dimensions.

Well documented dike propagations are essential to assess the validity of numerical models. However, as magma usually propagate away from the volcano summit, dikes often reach areas where the monitoring network is less dense, providing poorer constraints on the intrusion dynamics. Dike propagation can also occur aseismically. At Piton de la Fournaise volcano for example, lateral migrations take place at very shallow depth such that only weak seismic signals are produced and most of the migration is aseismic (Duputel et al., 2019). In other cases, long-range dike propagation is well monitored, but is complicated by multiple structures activated during the intrusion that are difficult to model properly (Woods et al., 2019).

In this study, we focus on the dike intrusion of May 2018 that propagated in the Middle East Rift Zone (MERZ) of Kilauea volcano (Fig. 1). This intrusion is connected to the collapse of Pu'u 'O'o crater floor which occurred during a period of high pressurization of the Kilauea's magmatic system as noticed from the high lava lake level at the summit of the volcano (Neal et al., 2019). The downrift propagation of the dike was detected by the occurrence of earthquakes and associated deformation. The dike eventually created the first eruptive fissures in Leilani Estates subdivision, about 20 km downrift from Pu'u 'O'o crater, at 03:00 UTC on May 4. This intrusion led to one of the largest effusive eruptions in the recent history of Kilauea with a large eruptive volume of 0.8 km^3 (Neal et al., 2019). This major volcanic event was accompanied by the triggering of a $M_W = 7.2$ earthquake on the south flank of the volcano (Chen et al., 2019) and a large summit caldera collapse (Segall et al., 2019; Tepp et al., 2020) similar to what has been observed in 2007 at Piton de la Fournaise (Duputel and Rivera, 2019). We are particularly interested in testing if observations of the dike propagating in the MERZ can help to constrain a physical model and highlight the early stages of the 2018 eruptive sequence at

Kilauea volcano. To closely track the magma migration, we need to improve our temporal and spatial resolution by detecting and locating as many events as possible during the diking episode. Given the sparsity of the seismic network in the area and the small size of dike-triggered events, earthquake signals are not clearly visible at most stations. Fortunately, one station is located right on the dike path, at the center of the intrusion segment. We therefore use this station to increase the number of dike-induced event detections and recorded more than 6300 events. The relatively simple and long-range propagation of the dike (around 20 km) also facilitates inferences on the intrusion dynamics. Our observations are interpreted in the context of a previously proposed model of dike growth.

2. Template matching detections

To carry out our analysis, we start by selecting earthquakes in the Hawaii Volcano Observatory (HVO) catalog that occurred approximately at the time of the initial 2018 dike intrusion. This catalog contains 280 events located in the vicinity of the MERZ between 2018-04-29 (0 h UTC) and 2018-05-04 (21 h UTC). This time span starts with the first sign of activity in the MERZ and ends before the occurrence of a $M_W = 5.7$ earthquake in the south flank of the volcano. It encompasses the collapse of the Pu'u 'O'o crater and the opening of the first eruptive fissure in the Lower East Rift Zone (LERZ). As shown in Fig. 1, most earthquakes occur on the 1st of May and show an apparent migration from the Pu'u 'O'o crater towards the North-East in about a day (Shiro et al., 2018). Seismic events are then located close to the Leilani estates.

We assume a dike intrusion starting at Pu'u 'O'o crater with an azimuth of 67° . This simple geometry is consistent both with the alignments of fissures and craters along the MERZ and the observed descending Interferometric Synthetic Aperture Radar image captured by the sentinel 1 satellite between 2018/04/23 and

2018/05/05 (see Fig. 1). It is also very close to the dike geometry of Chen et al. (2019) derived from observed deformations. Fig. 1 shows that most events in the initial catalog are located south of the rift zone. Such apparent shift of event locations has been previously noted by Hansen et al. (2004) and attributed to a systematic bias mainly resulting from poor station coverage in the south flank of Kīlauea volcano. Here we take advantage of one station (JOKA) located very close to the dike pathway to mitigate this potential location bias in our results.

In this study, we employ a template matching approach in order to detect possible missed events in the original catalog during the lateral propagation of the dike. This strategy follows similar studies performed in other volcanic environments (Shelly and Hill, 2011; Lengliné et al., 2016; Duputel et al., 2019; Shelly and Thelen, 2019). We use as templates, all events reported in the initial HVO catalog and shown in Fig. 1, but in order to possibly filter events that took place in the south flank of the volcano, we only select earthquakes with a depth shallower than 5 km. Indeed, it is likely that a dike in the rift zone can trigger events usually occurring at larger depth within the south flank Dieterich et al. (2000). So while we focus on rift zone events, the whole process of this dike intrusion episode might be more complex with activation of structures in the south flank of the volcano. The template signals are filtered between 2 and 20 Hz using a time-window of 5.12 s starting 1 s before the P-wave arrival. These templates are used to detect new events in continuous records for the 3 components of the JOKA station and the vertical component of KUPD or KLUD depending on whether a P-wave pick is available. This choice is mostly motivated by the proximity of those recording sites to the dike path as the signal to noise ratio decreases rapidly with the epicentral distance. For each time step (0.01 s) and each station, we compute the correlation coefficient between the template waveform and the continuous signal. The average correlation coefficient is then computed on 4 channels after shifting each trace according to the associated P-wave travel time. This results into an average correlation function for each template over the investigated time period. New detections are finally obtained when the average correlation function exceeds a threshold value that is computed each day from a fixed probability of false detection. This probability is estimated by computing the average correlation coefficients between continuous records and a reversed version of the template signals (both time and polarity reversed). The resulting values represent the correlation coefficients of a noise signal preserving the time-bandwidth product of the template event and processed in the same way (using the same passband filter, same network geometry, etc.). From this population of correlation coefficients, we can then derive a correlation threshold by imposing a given probability of false detection. Here we fixed this probability of false detection to 10^{-1} per day per template. For the 280 templates in the HVO catalog, we thus expect 168 false detections in total between 2018-04-29 and 2018-05-04. This analysis results into the detection of 6327 events (see Fig. 2). From this new catalog, we extract the waveform signal of each detection at all stations for which a P-wave pick is available for the template associated with each detection.

From the visual inspection of detected waveforms at station JOKA (see Fig. 2), we can already deduce some rough information on the position of dike-induced earthquakes. Indeed, the S-P times decrease from events 300 to 1000 and increase after event 1500 up to a maximum for events 3000 to 4000. After event 4000, a lower S-P time is observed and seems constant for the rest of the events. This observation is consistent with a dike propagating eastward from the west of JOKA site, passing nearby the station and then moving away to the east. The minimum S-P time delay observed at station JOKA is typically around 0.6 s. This indicates a minimum distance to the station of ~ 3300 m assuming $V_P = 4000$ m.s $^{-1}$

derived from the model of Klein (1981) and setting $V_S = V_P/\sqrt{3}$. As the dike trace inferred from geodetic measurements is typically around 1 km from the station (Chen et al., 2019), this suggests a depth estimate of the events the closest to the station around 3 km. The S-P time delay observed at the onset of the migration is around 2.2 s and increase up to the same value after passing the station. We can also observe that a lot of the latest events have a delay typically of the order of 1.5 s. This gives us distances to station JOKA of 12 km and 8 km respectively for these two sets of time delays supposing the same velocity model. If we impose the same depth of 3 km for these events we get epicentral distances of 11.1 km and 8.1 km, placing the first events around the Pu'u 'Ō'ō crater and the last events, associated with the propagation, at the location where the first ground cracks were reported, so in agreement with geological observations. We also observe that events after event 4000 are then located around the same location and are not at the dike front. At that time, based on the location of the farthest seismic events, the dike tip is at least 3 km farther downrift.

3. Location of dike-induced earthquakes

3.1. Distance to station JOKA

In order to get first-order constraints on the location of newly detected earthquakes, we use signals recorded by the three components of station JOKA to estimate variations in raypath distance from S-P travel time delays. Considering that the event separation distance is small compared to the epicentral distance to the recording site, the differential P-wave, ΔT_P^{ij} and S-wave, ΔT_S^{ij} , travel time between two events, i and j , can be written as

$$\Delta T_c^{ij} = T_c^j - T_c^i = \Delta r_c^{ij} / V_c \quad (1)$$

where the index c refers either to P or S, T_c^j is the travel time for event j , V_c is the velocity and Δr_c^{ij} is the difference of raypath distance for wave c between event i and j . We assume that P- and S-wave raypaths are similar such that $\Delta r_P^{ij} = \Delta r_S^{ij} = \Delta r^{ij}$. Thus, we can write

$$\Delta T_S^{ij} - \Delta T_P^{ij} = \Delta r^{ij} / V_S - \Delta r^{ij} / V_P \quad (2)$$

$$= \Delta r^{ij} \left(\frac{V_P - V_S}{V_P V_S} \right) \quad (3)$$

$$= (r^j - r^i) \left(\frac{V_P - V_S}{V_P V_S} \right) \quad (4)$$

where r^i is the distance of event i to station JOKA. Using this technique, we can thus estimate the distance of each event to the station.

We compute differential travel times for P- and S-waves measured by cross-correlation for all pairs of events. Differential travel times are estimated for P-waves in a window of 1.10 s encompassing the P-wave arrival. The S-wave arrival is computed from the P-wave travel time assuming $V_P/V_S = 1.73$ (where V_P and V_S denote P- and S-wave velocities). We measure S-wave travel time differences in a window starting 0.5 s before the S-wave arrival and ending 2 s later (see Fig. 2). We only keep event pairs with a cross-correlation larger than 0.6 in P- and S-wave windows and with travel time difference smaller than 0.15 s. If both East and North components provide measurements that meet the required threshold, we only keep the delay associated with the highest correlation coefficient.

We set up an inverse problem to find the distances r^i for each event based on the multiple differential travel time measured for all possible pairs of events. We set \mathbf{m} the parameter vector that

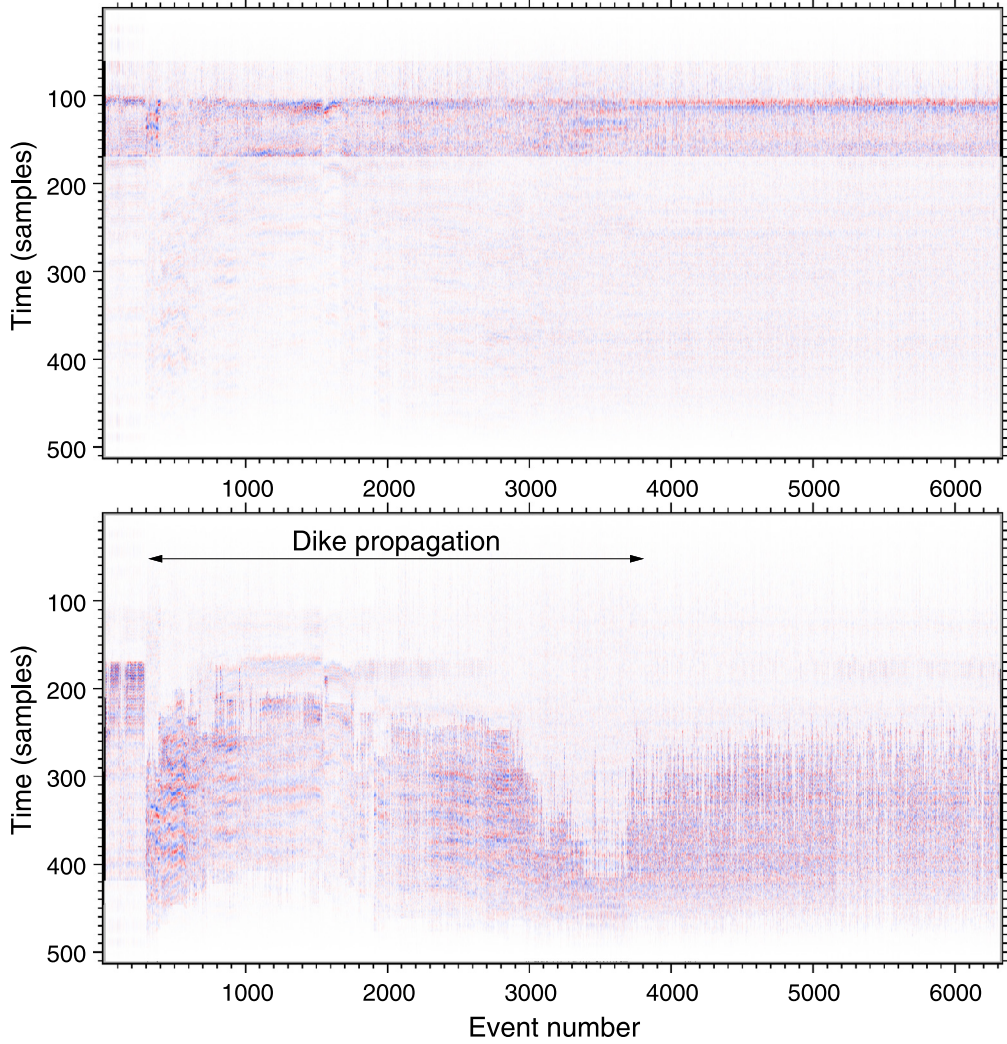


Fig. 2. Detected events at station JOKA. Top figure, vertical component records. Each row indicates the signal of a different event starting 1 s before the P-wave pick. The vertical axis denotes time in samples (sampling step is 0.01 s). Colors shows the normalized amplitude of each seismogram filtered between 2 and 20 Hz. The window used for computing the P-wave delays are shown unaltered while the other parts of the seismogram are transparent. Bottom figure shows records at the same station on the horizontal (East) component. In that case, only the S-wave window is shown with non-transparent colors.

contains the distances to station JOKA for all events (i.e., r_i). Our data vector, \mathbf{d} is given by the differential travel time measurements $\Delta T_S^{ij} - \Delta T_P^{ij}$ for all pair of events. The forward problem in Eq. (4) can then be rewritten as

$$\mathbf{d} = \mathbf{G}\mathbf{m} \quad (5)$$

where \mathbf{G} is a matrix that only contains two non zero values for each row that are $\pm \frac{v_p - v_s}{V_p V_s}$. Uncertainty on the data vector \mathbf{d} are described by a diagonal covariance matrix \mathbf{C}_d whose elements are given by $\frac{1}{2} \frac{(1-CC)^2}{(CC)^2}$ where CC is the average correlation coefficient measure for P and S delay times. We assume a Gaussian *a priori* information with a mean prior model $\mathbf{m}_{\text{prior}}$ corresponding to the distance from station JOKA obtained using initial locations in the HVO catalog. Given the poorly constrained depths in the HVO catalog, we set the depth for all events at 3 km as determined in the previous section. This is consistent with the relocation results of Rubin et al. (1998), showing that all events recorded during the 1983 intrusion in Kilauea's rift zone are located close to the dike path at about 3 to 4 km depth. The *a priori* distance uncertainties are set to 5 km for all events. The distances from station JOKA are obtained by solving the linear least square problem defined in

Eq. (5). The maximum *a posteriori* model is given by (Tarantola, 2005):

$$\tilde{\mathbf{m}} = \left(\mathbf{G}^t \mathbf{C}_d^{-1} \mathbf{G} + \mathbf{C}_m^{-1} \right)^{-1} \left(\mathbf{G}^t \mathbf{C}_d^{-1} \mathbf{d} + \mathbf{C}_m^{-1} \mathbf{m}_{\text{prior}} \right), \quad (6)$$

where \mathbf{C}_m is the diagonal *a priori* covariance matrix that contains the initial uncertainties on the distance from JOKA. *A posteriori* uncertainties, $\tilde{\sigma}_m$, are also estimated on the inferred parameters as the square root elements of the diagonal of the posterior covariance matrix $\tilde{\mathbf{C}}_m = \left(\mathbf{G}^t \mathbf{C}_d^{-1} \mathbf{G} + \mathbf{C}_m^{-1} \right)^{-1}$. Results on Fig. 3 confirm what has been inferred above from S-P time delays (cf., Section 2 and Fig. 2). The seismicity migration associated with the eastward dike propagation is evident from event 500 to event 3500. Earthquakes are first getting closer to JOKA station down to a minimum distance of 3.5 km. Events are then moving away, in agreement with an overall dike propagation to the East of JOKA. We also observe that some events located close to the station that appears continuously over the whole investigated period. This might reflect the fact that there exists an area near the recording site that has permanent weak structures, close to equilibrium that are activated by slight changes of stress. This might also reflects the increase sensibility of our detection method to events located close by the recording site.

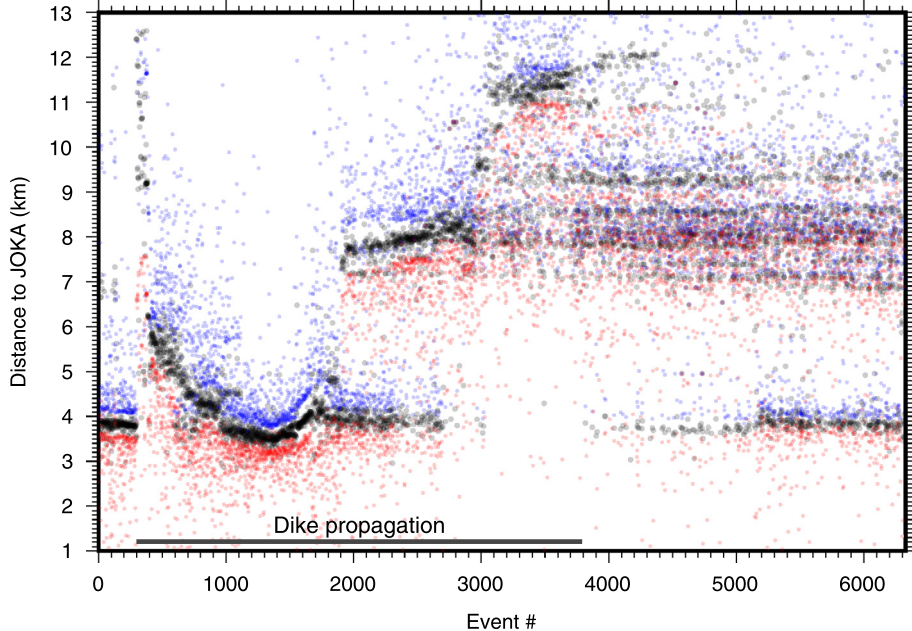


Fig. 3. Inverted distance to station JOKA obtained from differential travel time, ΔT_α^{ij} (black circles) as a function of the event number. The blue and red circles indicate the $\pm 2\sigma$ distance uncertainty for each earthquake.

3.2. Earthquake localization from P-wave travel-time differences

In this section, we estimate absolute earthquake locations by taking advantage of the fact that each detected event has been recorded by at least another station than JOKA (cf., Section 2). With this purpose we have to pick the P-wave arrival time for all detected events. This is realized by using a kurtosis approach. This technique simply detects changes in the distribution of seismic amplitudes at the arrival of the seismic wave. To optimize the results, for each detected waveform, we first apply a band-pass filter between 2 and 20 Hz and remove the mean of the vertical trace. The kurtosis is then computed as

$$F(t) = \frac{\tilde{x}_4(t)}{|\tilde{x}_2(t)|^2} \quad (7)$$

where t is time and $\tilde{x}_k(t)$ is the k -th order moment of the waveform $x(t)$ computed in a sliding window including N data samples. The kurtosis function $F(t)$ will show peaks when there is a change of the statistical content of the waveform, which is commonly used to detect P-wave onsets (Lang et al., 2014). As detected earthquakes should be spatially located in the vicinity of their associated template events, their P-wave travel times must also be similar to their respective templates. As an *a priori* information for each detection, we therefore give higher weights to peaks in $F(t)$ that are close to the template P-wave pick. More specifically, the weight is defined as

$$w(t - t_{\text{prior}}) = \exp(-0.1(t - t_{\text{prior}})^2) \quad (8)$$

where t_{prior} is the template P-wave arrival time. For each detection, the P-wave arrival is then picked at the maximum of the function

$$F_w(t) = F(t)w(t - t_{\text{prior}}), \quad (9)$$

where F is computed in an interval of 0.5 s around t_{prior} . Following Baillard et al. (2014), we have tested various combinations of window sizes N and filtering parameters. By comparing the results of the above procedure for several signals, we found that more

robust picking was achieved taking $N = 20$ samples (0.2 s) and filtering the waveforms in the 2–20 Hz frequency passband.

Based on the resulting catalog of P-wave arrivals, we then locate each earthquake individually using differences of P-wave arrival times at all available pair of stations. Using this differential approach, we do not have to estimate the event origin time. It also has the advantage of correcting any systematic bias in our picking procedure (e.g., due to bandpass filtering). We use a grid-search approach to find the optimum location for each event. We consider a 2D grid of horizontal locations to be explored and set the depth of all events to 3 km (consistently with results in Section 2). For a given event, the posterior probability distribution of the earthquake location \mathbf{x} is defined as (Tarantola, 2005)

$$p(\mathbf{x}|\mathbf{dt}_{\text{obs}}) \propto p(\mathbf{dt}_{\text{obs}}|\mathbf{x}) p(\mathbf{x}) \quad (10)$$

where $p(\mathbf{dt}_{\text{obs}}|\mathbf{x})$ is the likelihood function describing the ability of a location \mathbf{x} to fit the observed P-wave differential travel-times \mathbf{dt}_{obs} . In this equation, $p(\mathbf{x})$ is our *a priori* information on the event location.

To mitigate the impact of outliers, we employ a L1 norm misfit function, corresponding to a Laplacian distribution for the data likelihood:

$$p(\mathbf{dt}_{\text{obs}}|\mathbf{x}) = \prod_j \frac{1}{2\sigma_{dt}^j} \exp\left(-\frac{|dt^j(\mathbf{x}) - dt_{\text{obs}}^j|}{\sigma_{dt}^j}\right) \quad (11)$$

where $dt^j(\mathbf{x})$ and dt_{obs}^j are the predicted and observed differential travel times for the j -th pair of stations (in average an we have 5 P-wave picks by event and thus 10 pairs). σ_{dt}^j corresponds to an uncertainty on dt_{obs}^j . Based on visual inspections for several waveforms, we set the picking uncertainty to $0.5/\sqrt{\max(F)}$, where F is the maximum amplitude of the kurtosis function in Eq. (7). The differential travel time uncertainty σ_{dt}^j is then derived by summing up the variances of the corresponding P-wave picks. The *a priori* distribution is defined as:

$$p(\mathbf{x}) = p_\perp(\mathbf{x})p_r(\mathbf{x}) \quad (12)$$

where $p_{\perp}(\mathbf{x})$ and $p_r(\mathbf{x})$ are two distributions that are described below. The first term written as

$$p_{\perp}(\mathbf{x}) = \frac{1}{\sqrt{2\pi}} \exp\left(-\frac{d_{\perp}^2(\mathbf{x})}{2}\right) \quad (13)$$

penalizes event locations \mathbf{x} at a large horizontal distance d_{\perp} (here in km) from the rift zone (idealized as a dashed purple line in Fig. 1). The second term $p_r(\mathbf{x})$ is defined as

$$p_r(\mathbf{x}) = \frac{1}{2\sigma_r} \exp\left(-\frac{|r(\mathbf{x}) - r_{\text{prior}}|}{\sigma_r}\right). \quad (14)$$

This is a Laplace prior on the distance r from station JOKA (see Eq. (4)). The distribution is centered on r_{prior} corresponding to the maximum *a posteriori* distance in Eq. (6) with a scale parameter σ_r corresponding to the associated posterior variance (see Section 3.1).

The localization procedure is illustrated in Fig. 4 for an event located between stations JOKA and KUPD. For that example, we show the posterior distribution $p(\mathbf{x}|\mathbf{dt}_{\text{obs}})$ along with the data likelihood $p(\mathbf{dt}_{\text{obs}}|\mathbf{x})$ and the prior distribution $p(\mathbf{x})$ defined in Eq. (10)–(14). For each event, the optimum location is defined from the maximum *a posteriori* (i.e., the location maximizing $p(\mathbf{x}|\mathbf{dt}_{\text{obs}})$ shown in Fig. 4a). P-wave differential travel-times provide good constraints on the event location along the dike. However, as shown by the data likelihood in Fig. 4b) and assuming that the location cannot be too far from the rift zone (Fig. 4c), we still end up with relatively tight constraints on the event location.

Fig. 5 shows the resulting localization results projected along the rift zone as a function of time. There is a clear migration of earthquakes propagating from the Pu'u 'O'o crater at time t_0 on 1 May 2018 around 01h30 UTC and ending up around Leilani Estates after a bit less than 2 days.

The migration can be well approximated by a function of the form proposed by Grossman-Ponemon et al. (2019) for lateral dike migration fed by an over-pressurized magma reservoir, setting the distance along dike propagation as d_{\parallel} ,

$$d_{\parallel}(t) = a \log(1 + (t - t_0)/\tau) \quad (15)$$

where a and τ are constants and t is the time since the start of the migration. Although there are some uncertainties on these parameters depending on the choice of the events used to define the migration front, setting $a = 8.2$ km and $\tau = 0.11$ day is in good agreement with the observed seismicity (cf., Blue line in Fig. 5). These results are validated in the next section using seismic amplitudes to track the propagating dike.

4. Tracking dike from seismic amplitudes

We follow the method presented by Battaglia and Aki (2003) and later improved by Taisne et al. (2011) that exploits recorded seismic amplitudes as an indicator of the proximity of the seismic source to the recording sites. Given that both intrinsic attenuation and geometrical spreading attenuate seismic waves with distance, the seismic amplitudes measured at different seismic stations can be used to locate earthquakes. Such a method has been shown to be well adapted to track dike intrusion in various volcanic environments (Taisne et al., 2011; Caudron et al., 2015, 2018). One

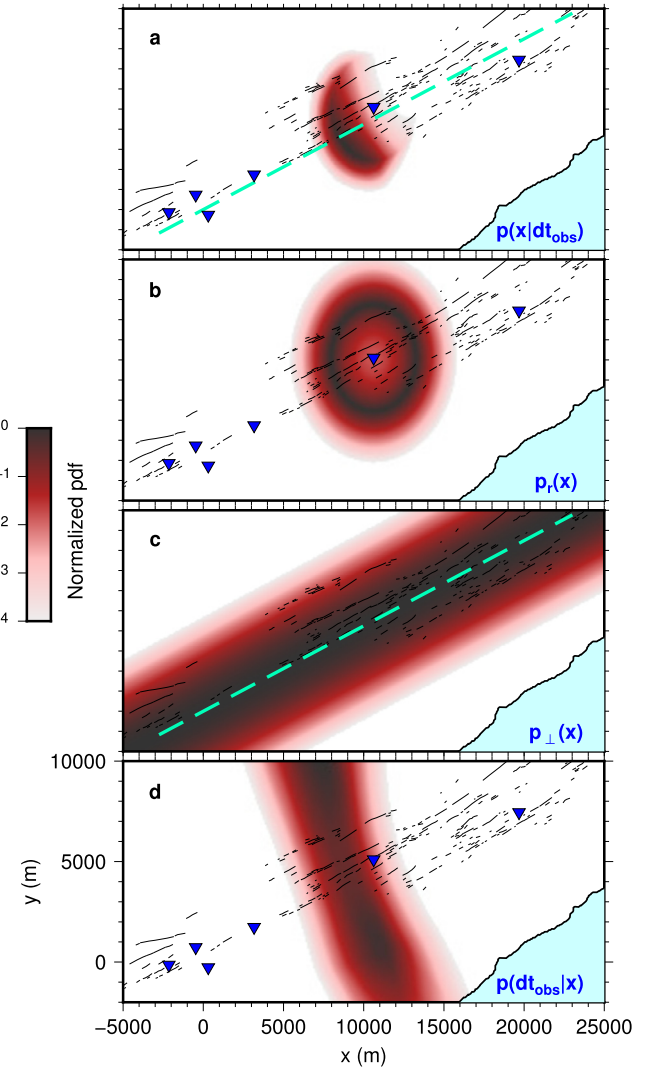


Fig. 4. Example of event localization from P-wave travel-time differences. The posterior probability density (a) $p(\mathbf{x}|\mathbf{dt}_{\text{obs}})$ on the event location \mathbf{x} given the observed travel-time differences \mathbf{dt}_{obs} is shown on top. We use the maximum of this function as the most probable event location. This posterior probability density is obtained from the combination of the data likelihood (d), $p(\mathbf{dt}_{\text{obs}}|\mathbf{x})$ with prior information on the event distance from JOKA (b), $p_r(\mathbf{x})$ and the event distance from the rift zone (c), $p_{\perp}(\mathbf{x})$. For more clarity, the probability density functions (pdf) are normalized with respect to their maximum amplitude.

advantage of this approach is that we do not need to identify individual events or pick arrival times, which is particularly useful to locate small earthquakes with low signal to noise ratio. Here we follow the processing procedure proposed by Taisne et al. (2011). We first deconvolve records from their instrumental response and band-pass filter them in the 5–15 Hz frequency range, as we are mainly interested in high frequency signals emitted by the propagating dike. We then compute the envelope of the signal and estimate its median in a moving time-window of 10 s. The signal originally sampled at 100 Hz is decimated to one point every 10 s. Finally, we apply a last median filtering with a moving window size of 5 minutes. This gives us the smoothed high frequency amplitude recorded at seismic stations. Here we consider the 3 stations that are located along the dike path (KUPD, KLUD and JOKA in Fig. 1). We compute ratio of seismic amplitude for the 3 possible pairs of stations. This amplitude ratio is defined as

$$\frac{U_i(t)}{U_j(t)} = \left(\frac{r_j(t)}{r_i(t)} \right)^n \exp[-B(r_i(t) - r_j(t))] \quad (16)$$

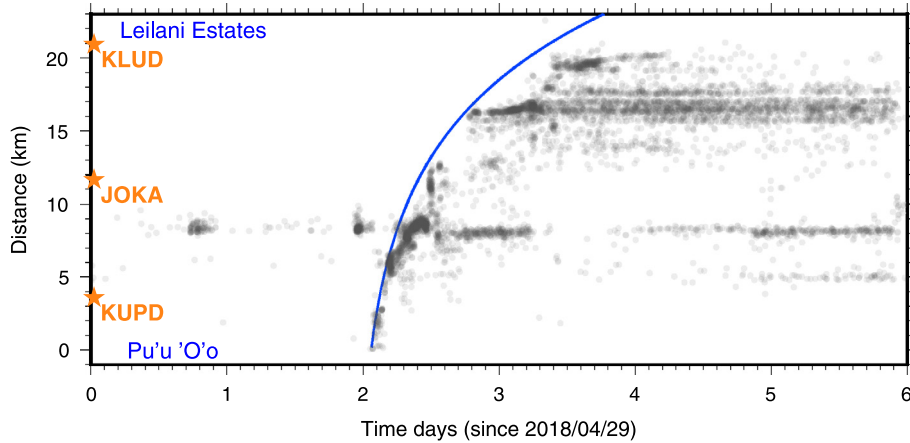


Fig. 5. Evolution of earthquake distance along the dike path as a function of time (gray circles). The three stars indicate the location of the 3 station JOKA, KUPD and KLUD. The blue line shows a fit of the form of Eq. (15) with $a = 8.2$ km and $\tau = 0.11$ day.

where $U_i(t)$ and $U_j(t)$ refer to the smoothed seismic amplitude measured at station i and j , $r_i(t)$ is the distance to station i and B is a factor defined as

$$B = \frac{\pi f}{Q V_S} \quad (17)$$

with V_S the shear wave velocity, f the frequency and Q is the quality factor for attenuation. The exponent n in Eq. (16) is equal to 1 for body waves. For simplicity, we consider an isotropic medium with constant V_S and Q . Using the fit of Eq. (15) to the event locations in Section 3.2, the distance of the dike tip to the stations is then estimated as a function of time. We then predict the amplitude ratios for the 3 possible pairs of stations using Eq. (16). As each station is associated with different local site effects, the predicted amplitude ratios must be corrected from the corresponding amplification of seismic waves. One way to estimate such amplification is to use the coda of large regional events (Aki and Ferrazzini, 2000). In this study, we invert for amplification factors minimizing differences between observed and predicted amplitude ratios given the previously inferred dike migration. Notice that these amplitude corrections are estimated for each station and are constant through time as we do not expect significant changes in site effects. Results presented in Fig. 6 indicate a good agreement between observed and predicted ratios of seismic amplitudes. Here we set $V_S = 4000/\sqrt{3}$ m.s⁻¹ and $Q = 170$ (the same quality factor as used by Taisne et al. (2011)). We also use $f = 10$ Hz, corresponding the middle of our frequency passband. We found that results are not much affected by change of these parameters. However, we observe that a source depth of 3 km as inferred for earthquakes in previous sections does not fit the observed amplitude ratios. The best agreement between our model and the observed data is obtained for a depth of 1 km (Fig. 6). We note here that we also do not take into account variation of topography (this corresponds to roughly a difference of 400 m between the two dike extremities).

5. Discussion

5.1. Limitations of the present results

We can notice all along the dike path, bursts of dike growth followed by pauses as well as gaps of seismicity at some locations. We first want to point that, because the dyke dynamics is uniquely inferred from seismicity, it has inevitably some limitations. For examples, volcano-tectonic earthquakes are only triggered, close to the dyke, at the location of pre-existing structures already near to failure Rubin et al. (1998). The absence of seismicity in some

areas may then possibly indicate that no pre-existing structures are present at these locations. It may also be possible that these structures exist and that they produce some small earthquakes but unfortunately we do not have any template event at that location which allows us to recover these small signals. Similarly burst of seismicity appearing during the dike growth may possibly be linked to our varying detection capability. Indeed, we see a lot of events located close to the station site JOKA, which may indicate the higher sensibility of our detection approach close to the recording instrument. These zones of earthquake clusters or gaps may also be linked to local changes of the dike or host rocks properties but and can also represent a real complex dike dynamics such that the model in Eq. (15) represents only an average description of the dike propagation. This model predicts an infinitely long dike propagation which is obviously not realistic as the dike stopped and reached the surface after a bit more than 20 km. A possible reason to explain the dike arrest is to propose that the dike overpressure, as governed by the pressure in the feeding magma chamber, becomes too small after a certain distance such that the fracture cannot propagate anymore. It may also be possible that, because the surface elevation above the dike is decaying as the dike propagates downrift, at some point the minimum compressive stress above the dike is low enough such that it becomes possible to propagate upward to the surface. Finally, we note there also exists models that predicts a finite dike length such as in Rivalta and Segall (2008) and could provide a different interpretation of our results.

5.2. Constraints on dike opening

The results above show that earthquake locations and seismic amplitudes are consistent with the logarithmic dike propagation described in Eq. (15). Here, we first investigate if geodetic data is also in agreement with this model. Station JOKA includes a GPS station and a tiltmeter in addition to the seismometer used in this study. Unfortunately, with a limited number of geodetic observations, estimating the evolution of dike opening is an undetermined problem with a wide range of possible solutions. We rather use geodetic time-series to get an independent constrain on the timing of the dike emplacement. Fig. 7 compares geodetic data recorded at JOKA with the distance of seismic events to this station. Assuming that seismicity is activated on pre-existing fractures close to the tip of dike, Fig. 7a shows that the dike tip reaches JOKA on May 1 around 9:40 UTC. At the same time, geodetic time-series show a slight change compared to the reference baseline observed before. As geodetic data is mostly sensitive to deformation in the

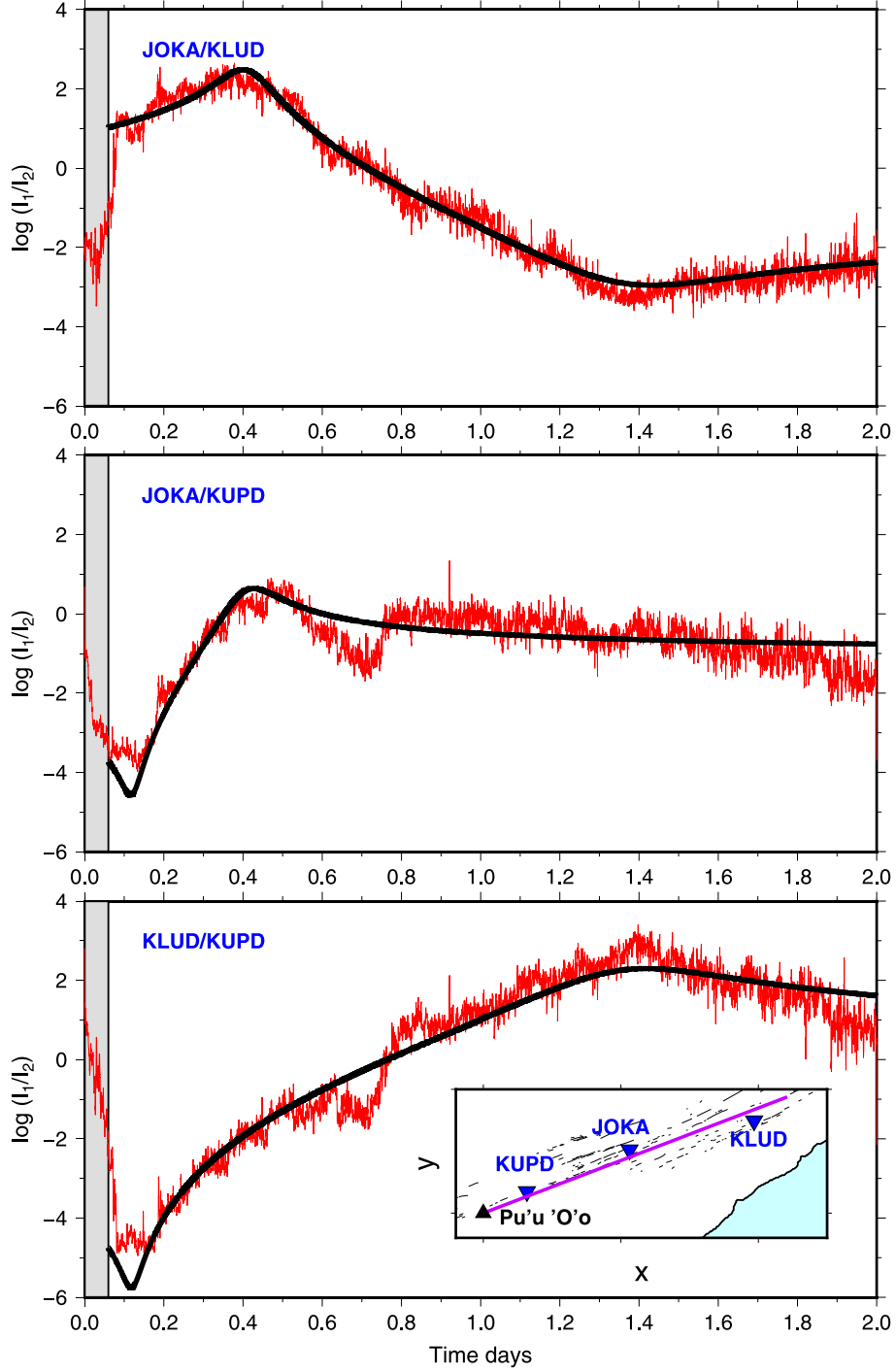


Fig. 6. Seismic amplitude ratio measured for 3 pairs of stations as a function of time (red curve). Black lines correspond to amplitude ratios predicted assuming sources located at the tip of a dike propagating according to Eq. (15). The gray rectangle at the beginning indicates the time period before the dike propagation. In the bottom figure, a map shows the location of the three used station and the assumed location of the dike.

vicinity of the instrument, we assume that these observations reflect dike opening close to the station. It suggests that the arrival of the tip brings little local deformation, but when the tip passes the station then opening really starts and it is basically complete in about 4 hours, at least locally.

5.3. Predicting magma chamber overpressure

We can also test if a model of a feeding magma chamber below the Pu'u 'O'o crater is consistent with the proposed dike propagation. To test this hypothesis, we compute the non-dimensional

pressure change in the supplying magma chamber following the model of Grossman-Ponemon et al. (2019). We here assumed some parameters, typical of basaltic volcanoes (similar to Grossman-Ponemon et al. (2019)), to perform this computation: magma chamber radius, $R = 1$ km, magma viscosity $\eta = 100$ Pa.s, deviatoric stress $S = 1$ MPa and shear modulus, $\mu = 30$ GPa. This model assumes that the dike is fed by a lateral reservoir and that the magma pressure within the dike is uniform. Using the parameters obtained from Eq. (15), it is then possible to estimate the non-dimensional pressure change in the reservoir associated with the dike intrusion in the MERZ. We can compare this predicted pres-

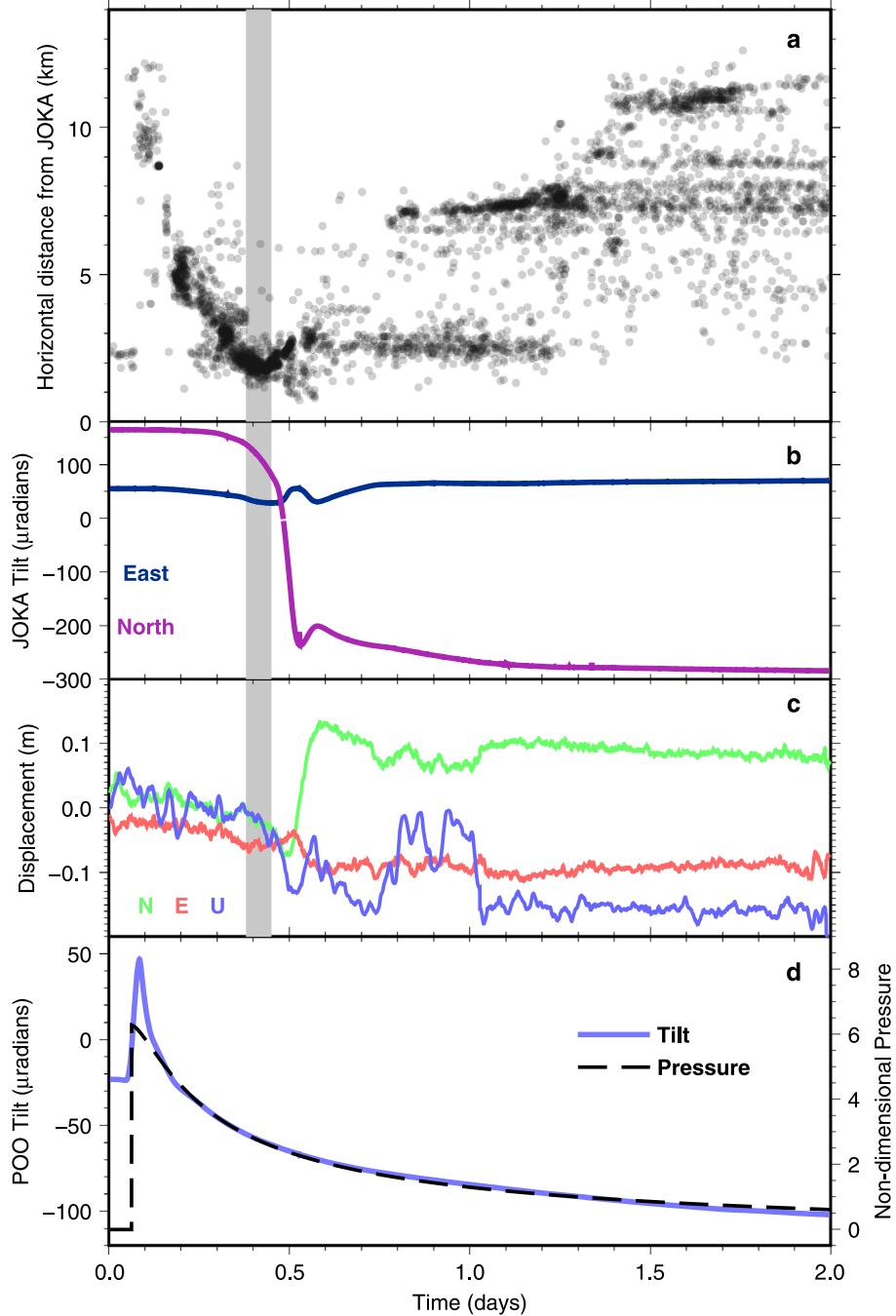


Fig. 7. Comparison between earthquake locations and geodetic observations. a) Epicentral distances between located seismic events and station JOKA (gray dots). The gray area, common of panel a, b and c, shows the time when the dike reaches the station as determined from the minimum distances of the earthquakes; b) Tiltmeter records at station JOKA on the East and North component; c) 30 s GPS displacement recorded at the same site (JOKA) (Miklius, 2007) in the 3 directions and processed using the method of Twardzik et al. (2019); d) radial tilt at station POO located less than 2 km away from Pu'u 'Ō'ō cone (blue curve). Decreasing curve indicates deflation in the direction of the cone. The black dashed line is the computed variation of pressure of the magma chamber feeding the dike. This value has been shifted and multiplied by a constant in order to fit the tilt data.

sure history with an observation reflecting the pressure change in the reservoir. With this purpose, we analyze tilt records at station POO which is located less than 2 km away from the Pu'u 'Ō'ō cone. The station POC located closer to the cone went off-scale during this episode and unfortunately cannot be considered here. We compute the radial tilt, and assume that this signal is linked to a spherical deflating magma source embedded in an elastic half space that we can model as a point source. If we suppose that elastic constants along with the size and location of the magma reservoir remain constants during deflationary episode, the tilt signal should be proportional to variations in the reservoir pressure

(Lisowski, 2007). Fig. 7d shows the shifted radial tilt and the inferred pressure variation multiplied by a constant. Overall, we observe a good agreement between tilt observations and predicted pressure variations in the magma reservoir. This good agreement allow us to infer some other properties derived from the model parameters, namely the total compressibility (the sum of the magma and chamber compressibility), $\beta = 1.8 \cdot 10^{-10}$ Pa, and the initial overpressure in the magma reservoir $\Delta P = 9.7$ MPa. The data misfit observed at the beginning of the intrusion is likely due to a contamination of the tilt signal by the dike starting its propagation near station POO. These results indicate that the deflationary be-

havior at the origin at the Pu'u 'Ō'ō crater floor collapse is mainly linked to the propagation of the dike in the MERZ. Although our simple model consider a single feeding magma chamber underneath the Pu'u 'Ō'ō vent, its ability to fit tilt observations suggests that this reservoir might have acted as an initial pressure source to the dike intrusion.

The deciphered scenario of dike intrusion that occurred during this episode show that inference of the dike dynamics can be mapped by seismological data. As the processing achieved here can be performed in near-real time, using these data in conjunction with a theoretical predictive model can help to estimate the future advance of the dike emplacement.

6. Conclusion

We track the dike intrusion that led to the 2018 Kīlauea eruption in the LERZ. Our results reveal that both earthquake locations and seismic amplitudes are consistent with a dike starting at Pu'u 'Ō'ō crater and propagating downrift in the northeast direction for more than 20 km. The observed dike migration is well modeled by logarithmic growth, whose parameters inform us about the pressure decrease in the magma reservoir. The resulting predicted pressure decay is in good agreement with tilt records near the Pu'u 'Ō'ō vent, showing that most of the observed deflation is associated with the dike intrusion. We emphasize that applying such a procedure in real time can help to estimate the dike movement.

CRediT authorship contribution statement

Olivier Lengliné: Conceptualization, Methodology, Validation, Visualization, Writing – original draft, Writing – review & editing.
Zacharie Duputel: Conceptualization, Methodology, Validation, Visualization, Writing – original draft, Writing – review & editing.
P.G. Okubo: Data curation, Resources, Validation, Writing – original draft, Writing – review & editing.

Declaration of competing interest

The authors declare that they have no known competing financial interests or personal relationships that could have appeared to influence the work reported in this paper.

Acknowledgements

We thank Brian Shiro from USGS HVO for discussion along Meredith Townsend and an anonymous reviewer for their suggestions. Sentinel-1A interferogram is provided by the European Space Agency's Sentinel-1satellite and was processed by University of Hawaii (http://pgf.soest.hawaii.edu/Kilauea_insar/). All figures are made with the GMT software (Wessel et al., 2013). This project has received funding from the European Research Council (ERC, under the European Union's Horizon 2020 research and innovation program under grant agreement No. 805256) and from Agence Nationale de la Recherche (project ANR-17-ERC3-0010). All seismic data are from HVO seismic network and can be accessed from IRIS (HVO, 1956). Tiltmeter and lava lake data shown here are from Johanson and Miklius (2019) and Patrick et al. (2019).

Appendix A. Supplementary material

Supplementary material related to this article can be found online at <https://doi.org/10.1016/j.epsl.2020.116653>.

References

- Aki, K., Ferrazzini, V., 2000. Seismic monitoring and modeling of an active volcano for prediction. *J. Geophys. Res.* 105, 23763.
- Baillard, C., Crawford, W.C., Ballu, V., Hibert, C., Mangeney, A., 2014. An automatic kurtosis-based P-and S-phase picker designed for local seismic networks. *Bull. Seismol. Soc. Am.* 104, 394–409.
- Battaglia, J., Aki, K., 2003. Location of seismic events and eruptive fissures on the Piton de la Fournaise volcano using seismic amplitudes. *J. Geophys. Res., Solid Earth* 108.
- Brandsdóttir, B., Einarsson, P., 1979. Seismic activity associated with the September 1977 deflation of the Krafla central volcano in northeastern Iceland. *J. Volcanol. Geotherm. Res.* 6, 197–212.
- Caudron, C., Taisne, B., Kugaenko, Y., Saltykov, V., 2015. Magma migration at the onset of the 2012–13 Tolbachik eruption revealed by seismic amplitude ratio analysis. *J. Volcanol. Geotherm. Res.* 307, 60–67.
- Caudron, C., White, R.S., Green, R.G., Woods, J., Ágústsdóttir, T., Donaldson, C., Greenfield, T., Rivalta, E., Brandsdóttir, B., 2018. Seismic amplitude ratio analysis of the 2014–2015 Bár arbunga-Holuhraun dike propagation and eruption. *J. Geophys. Res., Solid Earth* 123, 264–276.
- Chen, K., Smith, J.D., Avouac, J.P., Liu, Z., Song, Y.T., Gualandi, A., 2019. Triggering of the Mw 7.2 Hawaii earthquake of 4 may 2018 by a dike intrusion. *Geophys. Res. Lett.* 46, 2503–2510.
- Dieterich, J., Cayol, V., Okubo, P., 2000. The use of earthquake rate changes as a stress meter at Kīlauea volcano. *Nature* 408, 457–460.
- Duputel, Z., Lengliné, O., Ferrazzini, V., 2019. Constraining spatiotemporal characteristics of magma migration at Piton de la Fournaise volcano from pre-eruptive seismicity. *Geophys. Res. Lett.* 46, 119–127.
- Duputel, Z., Rivera, L., 2019. The 2007 caldera collapse of Piton de la Fournaise volcano: source process from very-long-period seismic signals. *Earth Planet. Sci. Lett.* 527, 115786.
- Grandin, R., Jacques, E., Nercessian, A., Ayele, A., Doubre, C., Socquet, A., Keir, D., Kassim, M., Lemarchand, A., King, G., 2011. Seismicity during lateral dike propagation: insights from new data in the recent Manda Hararo-Dabbahu rifting episode (Afar, Ethiopia). *Geochem. Geophys. Geosyst.* 12.
- Grandin, R., Socquet, A., Jacques, E., Mazzoni, N., de Chabalier, J.B., King, G., 2010. Sequence of rifting in Afar, Manda-Hararo rift, Ethiopia, 2005–2009: time-space evolution and interactions between dikes from interferometric synthetic aperture radar and static stress change modeling. *J. Geophys. Res., Solid Earth* 115.
- Grossman-Ponemon, B.E., Heimisson, E.R., Lew, A.J., Segall, P., 2019. Logarithmic growth of dikes from a depressurizing magma chamber. *Geophys. Res. Lett.* 47, e2019GL086230.
- Gudmundsson, A., 2002. Emplacement and arrest of sheets and dykes in central volcanoes. *J. Volcanol. Geotherm. Res.* 116, 279–298.
- Hansen, S., Thurber, C., Mandernach, M., Haslinger, F., Doran, C., 2004. Seismic velocity and attenuation structure of the east rift zone and south flank of Kīlauea volcano, Hawaii. *Bull. Seismol. Soc. Am.* 94, 1430–1440.
- HVO, USGS Hawaiian Volcano Observatory, 1956. Hawaiian Volcano Observatory Network. International Federation of Digital Seismograph Networks, Dataset/Seismic Network.
- Johanson, I., Miklius, A., 2019. Tiltmeter data from Kīlauea Volcano, Hawaii, spanning the 2018 eruption and earthquake sequence. U.S. Geological Survey data release. <https://doi.org/10.5066/P9310M9N>.
- Klein, F.W., 1981. A linear gradient crustal model for south Hawaii. *Bull. Seismol. Soc. Am.* 71, 1503–1510.
- Langet, N., Maggi, A., Michelini, A., Brenguier, F., 2014. Continuous kurtosis-based migration for seismic event detection and location, with application to Piton de la Fournaise volcano, la réunioncontinuous kurtosis-based migration for seismic event detection and location. *Bull. Seismol. Soc. Am.* 104, 229–246.
- Lengliné, O., Duputel, Z., Ferrazzini, V., 2016. Uncovering the hidden signature of a magmatic recharge at Piton de la Fournaise volcano using small earthquakes. *Geophys. Res. Lett.* 43, 4255–4262.
- Lisowski, M., 2007. Analytical volcano deformation source models. In: *Volcano Deformation*. Springer, pp. 279–304.
- Lundgren, P., Poland, M., Miklius, A., Orr, T., Yun, S.H., Fielding, E., Liu, Z., Tanaka, A., Szeliga, W., Hensley, S., et al., 2013. Evolution of dike opening during the March 2011 Kamoamoa fissure eruption, Kīlauea volcano, Hawaii. *J. Geophys. Res., Solid Earth* 118, 897–914.
- Maccafferri, F., Smittarello, D., Pinel, V., Cayol, V., 2019. On the propagation path of magma-filled dikes and hydrofractures: the competition between external stress, internal pressure, and crack length. *Geochem. Geophys. Geosyst.* 20, 2064–2081.
- Miklius, A., 2007. Hawaii GPS Network - JOKA-Jonika P.S. the GAGE Facility operated by UNAVCO, Inc., GPS/GNSS Observations Dataset. <https://doi.org/10.7283/T58P5XR4>.
- Montgomery-Brown, E.K., Sinnott, D., Poland, M., Segall, P., Orr, T., Zebker, H., Miklius, A., 2010. Geodetic evidence for en echelon dike emplacement and concurrent slow slip during the June 2007 intrusion and eruption at Kīlauea volcano, Hawaii. *J. Geophys. Res., Solid Earth* 115.
- Neal, C., Brantley, S., Antolik, L., Babb, J., Burgess, M., Calles, K., Cappos, M., Chang, J., Conway, S., Desmither, L., et al., 2019. The 2018 rift eruption and summit collapse of Kīlauea volcano. *Science* 363, 367–374.
- Owen, S., Segall, P., Lisowski, M., Miklius, A., Murray, M., Bevis, M., Foster, J., 2000. January 30, 1997 eruptive event on Kīlauea volcano, Hawaii, as monitored by continuous GPS. *Geophys. Res. Lett.* 27, 2757–2760.

- Patrick, M., Younger, E., Tollett, W., 2019. Lava Level and Crater Geometry Data During the 2018 Lava Lake Draining at Kilauea Volcano, Hawaii. U.S. Geological Survey, data release.
- Pinel, V., Carrara, A., Maccaferri, F., Rivalta, E., Corbi, F., 2017. A two-step model for dynamical dike propagation in two dimensions: application to the July 2001 Etna eruption. *J. Geophys. Res., Solid Earth* 122, 1107–1125.
- Rivalta, E., 2010. Evidence that coupling to magma chambers controls the volume history and velocity of laterally propagating intrusions. *J. Geophys. Res., Solid Earth* 115.
- Rivalta, E., Segall, P., 2008. Magma compressibility and the missing source for some dike intrusions. *Geophys. Res. Lett.* 35.
- Rivalta, E., Taisne, B., Bunger, A., Katz, R., 2015. A review of mechanical models of dike propagation: schools of thought, results and future directions. *Tectonophysics* 638, 1–42.
- Rubin, A.M., 1995. Propagation of magma-filled cracks. *Annu. Rev. Earth Planet. Sci.* 23, 287–336.
- Rubin, A.M., Gillard, D., Got, J.L., 1998. A reinterpretation of seismicity associated with the January 1983 dike intrusion at Kilauea Volcano, Hawaii. *J. Geophys. Res., Solid Earth* 103, 10003–10015.
- Segall, P., 2013. Volcano deformation and eruption forecasting. *Geol. Soc. (Lond.) Spec. Publ.* 380, 85–106.
- Segall, P., Anderson, K.R., Johanson, I., Miklius, A., 2019. Mechanics of inflationary deformation during caldera collapse: evidence from the 2018 Kilauea eruption. *Geophys. Res. Lett.*, 149.
- Shelly, D.R., Hill, D.P., 2011. Migrating swarms of brittle-failure earthquakes in the lower crust beneath Mammoth Mountain, California. *Geophys. Res. Lett.* 38.
- Shelly, D.R., Thelen, W.A., 2019. Anatomy of a caldera collapse: Kīlauea 2018 summit seismicity sequence in high resolution. *Geophys. Res. Lett.*
- Shiro, B., Burgess, M.K., Chang, J.C., Dotray, P., Okubo, P., Thelen, W.A., Waite, G.P., Antolik, L., Johanson, I.A., Anderson, K.R., Montgomery-Brown, E.K., 2018. Earthquake sequences of the 2018 Kīlauea Volcano eruption. In: AGU Fall Meeting Abstracts. V41B-01.
- Sigmundsson, F., Hooper, A., Hreinsdóttir, S., Vogfjörd, K.S., Ófeigsson, B.G., Heimisson, E.R., Dumont, S., Parks, M., Spaans, K., Gudmundsson, G.B., et al., 2015. Segmented lateral dyke growth in a rifting event at Bárðarbunga volcanic system, Iceland. *Nature* 517, 191–195.
- Smittarello, D., Cayol, V., Pinel, V., Peltier, A., Froger, J.L., Ferrazzini, V., 2019. Magma propagation at Piton de la Fournaise from joint inversion of InSAR and GNSS. *J. Geophys. Res., Solid Earth* 124, 1361–1387.
- Taisne, B., Brenguier, F., Shapiro, N., Ferrazzini, V., 2011. Imaging the dynamics of magma propagation using radiated seismic intensity. *Geophys. Res. Lett.* 38.
- Tarantola, A., 2005. *Inverse Problem Theory and Methods for Model Parameter Estimation*, vol. 89. SIAM.
- Tepp, G., Hotovec-Ellis, A., Shiro, B., Johanson, I., Thelen, W., Haney, M.M., 2020. Seismic and geodetic progression of the 2018 summit caldera collapse of Kīlauea volcano. *Earth Planet. Sci. Lett.* 540, 116250.
- Townsend, M.R., Pollard, D.D., Smith, R.P., 2017. Mechanical models for dikes: a third school of thought. *Tectonophysics* 703, 98–118.
- Trusdell, F.A., Wolfe, E.W., Morris, J., 2005. Digital Database of the Geologic Map of the Island of Hawaii. U.S. Geological Survey, Data Series 144.
- Twardzik, C., Vergnolle, M., Sladen, A., Avallone, A., 2019. Unravelling the contribution of early postseismic deformation using sub-daily gnss positioning. *Sci. Rep.* 9, 1–12.
- Walker, G.P., Sigurdsson, H., 2000. Basaltic volcanoes and volcanic systems. In: *Encyclopedia of Volcanoes*, pp. 283–289.
- Wessel, P., Smith, W.H., Scharroo, R., Luis, J., Wobbe, F., 2013. Generic mapping tools: improved version released. *Eos* 94, 409–410.
- Woods, J., Winder, T., White, R.S., Brandsdóttir, B., 2019. Evolution of a lateral dike intrusion revealed by relatively-relocated dike-induced earthquakes: the 2014–15 Bárðarbunga–Holuhraun rifting event, Iceland. *Earth Planet. Sci. Lett.* 506, 53–63.